

# Final Report

RS03-212F



**State of Wyoming  
Department of Transportation**



U.S. Department  
of Transportation  
**Federal Highway  
Administration**



## **Structural Health Monitoring of Highway Bridges Subjected to Overweight Trucks, Phase I – Instrumentation Development and Validation**



By:

Richard J. Schmidt

ORCID number 0000-0003-1672-2625

Department of Civil and Architectural Engineering

University of Wyoming

Laramie, Wyoming 82071

March 2016

## **FORWARD**

**Purpose of the Report:** This document is the final report of research sponsored by the Federal Highway Administration, the Wyoming Department of Transportation, and the Mountain Plains Consortium.

**Content Summary:** This report contains the results of Phase I of a research project intended to develop a structural health monitoring system for highway bridges using fiber Bragg gratings as the strain sensors. The objectives are to provide long-term sensing of bridges that are subjected to overweight and other permit vehicles such that the accuracy of bridge rating software can be evaluated.

**Interested Audience:** Bridge owners and operators, bridge maintenance personnel, individuals interested in structural health monitoring of bridges

**Previous Printings of the Publication:** none

**Publication Status:** Final

## **DISCLAIMER NOTICE**

This document is disseminated under the sponsorship of the U.S. Department of Transportation in the interest of information exchange. The U.S. Government assumes no liability for the use of the information contained in this document.

The U.S. Government does not endorse products or manufacturers. Trademarks or manufacturers' names appear in this report only because they are considered essential to the objective of the document.

The contents of this report reflect the views of the authors, who are responsible for the facts and the accuracy of the information presented. This document is disseminated under the sponsorship of the Department of Transportation, University Transportation Centers Program, in the interest of information exchange. The U.S. Government assumes no liability for the contents or use thereof.

## **QUALITY ASSURANCE STATEMENT**

The Federal Highway Administration (FHWA) provides high-quality information to serve Government, industry, and the public in a manner that promotes public understanding. Standards and policies are used to ensure and maximize the quality, objectivity, utility, and integrity of its information. FHWA periodically reviews quality issues and adjusts its programs and processes to ensure continuous quality improvement.

## **ACKNOWLEDGEMENTS**

This report is based largely on the research and Masters Theses by University of Wyoming graduate students Mr. Danial Maurais, Mr. Michael Jung, and Ms. McKenzie Danforth. The invaluable contributions of Mr. James Branscomb to development of the microprocessor controllers for this study are also acknowledged.

1. Report No. FHWA-CFL/TD-0x-00x	2. Government Accession No.	3. Recipient's Catalog No.	
4. Title and Subtitle <i>Structural Health Monitoring of Highway Bridges Subjected to Overweight Trucks, Phase I – Instrumentation Development and Validation</i>		5. Report Date January 2016	
		6. Performing Organization Code	
7. Author(s) Richard J. Schmidt; ORCID number 0000-0003-1672-2625		8. Performing Organization Report No.	
9. Performing Organization Name and Address Department of Civil and Architectural Engineering University of Wyoming, 1000 E. University Avenue Laramie, WY 82071		10. Work Unit No. (TRAIS)	
		11. Contract or Grant No. RS03-212	
12. Sponsoring Agency Name and Address Wyoming Department of Transportation 5300 Bishop Blvd Cheyenne, Wyoming 82002		13. Type of Report and Period Covered Final, June 2013 - Dec. 2015	
		14. Sponsoring Agency Code	
15. Supplementary Notes This project was co-funded by the Mountain Plains Consortium			
16. Abstract The long-term objectives of this project were to develop and validate an instrumentation package for structural health monitoring of bridges subjected to overweight trucks and to develop plans for field deployment of the instrumentation on a pilot scale. Ultimately, the objective is to accurately correlate long-term field performance data to the behavior of the bridges predicted by analysis and rating software. In Phase I of the project, instrumentation, packaging, installation techniques and data collection and storage for fiber Bragg grating (FBG) sensors were developed in the laboratory. The essential elements of the SHM system are in place and include (a) sensor installation and protection techniques for both concrete and steel host structures, (b) commercial and special-purpose instrumentation for interrogating the SHM network, and (c) a triggering system based in RFID technology to control the amount of data that is collected by the SHM network. Subsequent deployment of the system on a bridge in the WYDOT inventory will require additional development of data storage and transmission capabilities, which will be particular to the location and characteristics of the targeted bridge. Researchers engaged in Phase II of this study must coordinate with bridge engineers at WYDOT to identify a spectrum of SHM applications and objectives, for which individual data analysis techniques can be developed. Subsequent design and implementation of software to execute such data analysis will be needed to relieve bridge engineers from the burdensome and tedious tasks of sifting through raw SHM data streams themselves.			
17. Key Words <b>BRIDGE ENGINEERING, DURABILITY, FIBER OPTIC SENSORS, FIBER BRAGG GRATINGS, STRUCTURAL HEALTH MONITORING, OVER-WEIGHT TRUCKS, RATING AND ANALYSIS</b>		18. Distribution Statement No restriction.	
19. Security Classif. (of this report) Unclassified	20. Security Classif. (of this page) Unclassified	21. No. of Pages 71	22. Price

# METRIC CONVERSION CHART

<b>SI* (MODERN METRIC) CONVERSION FACTORS</b>				
<b>APPROXIMATE CONVERSIONS TO SI UNITS</b>				
<b>Symbol</b>	<b>When You Know</b>	<b>Multiply By</b>	<b>To Find</b>	<b>Symbol</b>
<b>LENGTH</b>				
in	inches	25.4	millimeters	mm
ft	feet	0.305	meters	m
yd	yards	0.914	meters	m
mi	miles	1.61	kilometers	km
<b>AREA</b>				
in <sup>2</sup>	square inches	645.2	square millimeters	mm <sup>2</sup>
ft <sup>2</sup>	square feet	0.093	square meters	m <sup>2</sup>
yd <sup>2</sup>	square yard	0.836	square meters	m <sup>2</sup>
ac	acres	0.405	hectares	ha
mi <sup>2</sup>	square miles	2.59	square kilometers	km <sup>2</sup>
<b>VOLUME</b>				
fl oz	fluid ounces	29.57	milliliters	mL
gal	gallons	3.785	liters	L
ft <sup>3</sup>	cubic feet	0.028	cubic meters	m <sup>3</sup>
yd <sup>3</sup>	cubic yards	0.765	cubic meters	m <sup>3</sup>
NOTE: volumes greater than 1000 L shall be shown in m <sup>3</sup>				
<b>MASS</b>				
oz	ounces	28.35	grams	g
lb	pounds	0.454	kilograms	kg
T	short tons (2000 lb)	0.907	megagrams (or "metric ton")	Mg (or "t")
<b>TEMPERATURE (exact degrees)</b>				
°F	Fahrenheit	$(F-32)/1.8$	Celsius	°C
<b>ILLUMINATION</b>				
fc	foot-candles	10.76	lux	lx
fl	foot-Lamberts	3.426	candela/m <sup>2</sup>	cd/m <sup>2</sup>
<b>FORCE and PRESSURE or STRESS</b>				
lbf	poundforce	4.45	newtons	N
lbf/in <sup>2</sup>	poundforce per square inch	6.89	kilopascals	kPa
<b>APPROXIMATE CONVERSIONS FROM SI UNITS</b>				
<b>Symbol</b>	<b>When You Know</b>	<b>Multiply By</b>	<b>To Find</b>	<b>Symbol</b>
<b>LENGTH</b>				
mm	millimeters	0.039	inches	in
m	meters	3.28	feet	ft
m	meters	1.09	yards	yd
km	kilometers	0.621	miles	mi
<b>AREA</b>				
mm <sup>2</sup>	square millimeters	0.0016	square inches	in <sup>2</sup>
m <sup>2</sup>	square meters	10.764	square feet	ft <sup>2</sup>
m <sup>2</sup>	square meters	1.195	square yards	yd <sup>2</sup>
ha	hectares	2.47	acres	ac
km <sup>2</sup>	square kilometers	0.386	square miles	mi <sup>2</sup>
<b>VOLUME</b>				
mL	milliliters	0.034	fluid ounces	fl oz
L	liters	0.264	gallons	gal
m <sup>3</sup>	cubic meters	35.314	cubic feet	ft <sup>3</sup>
m <sup>3</sup>	cubic meters	1.307	cubic yards	yd <sup>3</sup>
<b>MASS</b>				
g	grams	0.035	ounces	oz
kg	kilograms	2.202	pounds	lb
Mg (or "t")	megagrams (or "metric ton")	1.103	short tons (2000 lb)	T
<b>TEMPERATURE (exact degrees)</b>				
°C	Celsius	1.8C+32	Fahrenheit	°F
<b>ILLUMINATION</b>				
lx	lux	0.0929	foot-candles	fc
cd/m <sup>2</sup>	candela/m <sup>2</sup>	0.2919	foot-Lamberts	fl
<b>FORCE and PRESSURE or STRESS</b>				
N	newtons	0.225	poundforce	lbf
kPa	kilopascals	0.145	poundforce per square inch	lbf/in <sup>2</sup>

\*SI is the symbol for the International System of Units. Appropriate rounding should be made to comply with Section 4 of ASTM E380. (Revised March 2003)



# TABLE OF CONTENTS

Forward.....	ii
Disclaimer Notice .....	ii
Quality Assurance Statement.....	ii
Acknowledgements.....	ii
Metric Conversion Chart.....	ii
Table of Contents.....	iii
List of Figures.....	vi
Chapter 1 – Executive Summary .....	1
Purpose of the Study .....	1
General Approach .....	1
Findings and Conclusions .....	2
Task 1 .....	2
Task 2 .....	3
Task 3 .....	3
Task 4 .....	4
Task 5 .....	5
Recommendations.....	5
Chapter 2 – Problem Description.....	8
Problem Statement .....	8
Research Methods and Tasks.....	9
Research Benefits.....	10
Literature Review.....	11
Background on Fiber Bragg Grating Sensors.....	11
Transfer of Strain from Host Material to the FBG .....	13
FBG Sensor Placement.....	15
FBG Sensor Installation.....	16
FBG Protection Techniques.....	17
FBG Strain Verification Cases Based upon Laboratory and Field Testing.....	18
Chapter 3 – Optical Fiber Packaging.....	19
Bonding to a Concrete Host .....	19

Finite Element Study .....	19
Experimental Study .....	22
Bonding to a Steel Host.....	23
Chapter 4 – Instrumentation Package .....	26
Chapter 5 – Data Collection and Processing.....	27
Microcontroller and RFID Triggering System.....	28
System Overview.....	28
Instrumentation Design.....	30
System Validation Procedure and Results.....	31
Chapter 6 – Laboratory Validation .....	34
Laboratory Model.....	34
Multiplexed Sensor System Design .....	38
Temperature Compensation .....	39
Sensor Installation, Protection and Repair .....	39
Installation on Steel Elements .....	40
Protection on Steel Elements.....	41
Repair on Steel Elements.....	41
Sensing Concrete Elements.....	42
Installation on Concrete Elements.....	42
Protection on Concrete Elements .....	43
Repair on Concrete Elements .....	44
Experimental Procedures.....	44
Experimental Results and Analysis.....	45
Concrete Beam Results .....	46
Steel Beam Results.....	47
Chapter 7 – FBG Microbuckling in Compression .....	50
Chapter 8 – Findings and Conclusions .....	51
Task 1 .....	51
FBG Sensors Mounted on Concrete .....	51
FBG Sensors Mounted on Steel.....	54
Task 2 .....	54
Task 3 .....	55

Task 4 .....	56
Task 5 .....	57
Chapter 9 – Implementation recommendations .....	58
References.....	61
Appendix A – Practice Manual	
Appendix B-1 – M.S. Thesis by Daniel Maurais	
Appendix B-2 – M.S. Thesis by Michael Jung	
Appendix B-3 – M.S. Thesis by McKenzie Danforth	

## LIST OF FIGURES

Figure 2.1 – Illustration of FBG Signal Transmission (Heininger 2009)	11
Figure 3.1 – Notch embedded FBG configuration cross sections	19
Figure 3.2 – (a) V-notch FEM configuration, (b) Saw-notch FEM configuration	20
Figure 3.3 – Epoxy bond length comparison, saw-notch, 1.6 mm bond layer thickness	21
Figure 3.4 – Concrete test prisms notches: (a) V-notch (b) Saw-notch	22
Figure 3.5 – Strain transfer for V-notch, Eepoxy = 1800 MPa, 2.7 mm bond layer thickness	23
Figure 3.6 – Stress-Strain Comparison, Steel Specimen	25
Figure 6.1 – Schematic of Load Cart for Laboratory Test	35
Figure 6.2 – Laboratory Test Setup	36
Figure 6.3 – Sensor Locations on Beam Cross-Sections	36
Figure 6.4 – Sensor Locations Along Beam Length	37
Figure 6.5 – Sensor Placement for Concrete Beam	39
Figure 6.6 – Comparison of Analytical and Measured Curvatures for Concrete Beam	47
Figure 6.7 – Curvatures Measured by Sensors on Steel Beam	48
Figure 6.8 – Comparison of Analytical and Measured Curvatures on Steel Beam	49

# CHAPTER 1 – EXECUTIVE SUMMARY

## Purpose of the Study

State departments of transportation (DOTs) in the West have been under increasing pressure to permit and route overweight trucks transporting machinery and equipment for the energy sector through their state and interstate highway systems. DOT engineers are called upon daily to rate their bridges for overweight trucks to determine appropriate truck routing and to assess the impacts of the trucks on bridge safety and durability. Many of these overweight trucks have nonstandard configurations, which further complicates the rating and permitting process. Hence, it is critical that bridge engineers in the DOTs develop confidence that their bridge analysis and rating software accurately predicts the response of bridges to overweight trucks, especially for bridges on the most frequently traveled routes.

The long-term objectives of this project were to develop and validate an instrumentation package for structural health monitoring (SHM) of bridges subjected to overweight trucks and to develop plans for field deployment of the instrumentation on a pilot scale. Ultimately, the objective is to accurately correlate long-term field performance data to the behavior of the bridges predicted by analysis and rating software. The field instrumentation package incorporates use of optical fiber sensors, specifically fiber Bragg gratings (FBGs), to monitor strains at critical locations in bridges that are considered most vulnerable to overweight truck loads and are most difficult to effectively rate with currently used software.

## General Approach

In Phase I of the project, instrumentation, packaging, installation techniques and data collection and storage for fiber Bragg grating (FBG) sensors were developed in the laboratory. The laboratory investigation included the following primary tasks.

1. Development of optical-fiber packaging or other protection mechanisms suitable for installation in the target environments, including both steel and concrete girder bridges.
2. Development of a low-cost, compact, and energy-efficient instrumentation package for interrogating the sensor network. The approach involved a combination of design and fabrication of custom instrumentation linked to commercially available components with proven reliability.
3. Development of data collection, processing and transmission capabilities for an FBG sensor network on a bridge.
4. Validation of tasks 1, 2, and 3 in the laboratory using a mock-up of bridges having steel and concrete girders.
5. Determine if micro-buckling of FBG sensors strained in compression occurs and the means that can be employed to prevent it, thus allowing the sensors to accurately respond to compressive strain.

## Findings and Conclusions

### Task 1

#### *FBG Sensors Mounted on Concrete*

Both experimental and finite element methods were used to determine the elasto-mechanical behavior of FBG sensors attached to a concrete host. The conclusions drawn from the FEA and the experimental tests relate primarily to the strain measurement accuracy of the FBG sensors bonded to concrete in notches. It was found that the FEA slightly over-predicts the strain transfer to the FBG when compared to test results. This conclusion is supported by the fact that for 80% of the configurations that were compared, the FEA strain transfer results were 1% to 9% greater than those seen in the experimental tests. Despite the FEA over-prediction, it is still possible to conclude that there are some configurations that provide full strain transfer and some that do not.

After several laboratory and computer simulations of the FBG embedment procedure, it was concluded that the equipment and materials required to install an FBG in a notched concrete structural member are effective and obtainable for an engineering or construction crew. The embedment notches can be cut in the concrete with a masonry saw or formed as the concrete is placed. The Ultrabond 1300 epoxy was effective because of its short cure time and availability, however for overhead or vertical applications, a more paste-like adhesive with higher viscosity would be optimal.

The FEA results supported several conclusions about how the configuration parameters affect the strain transfer for the notch-embedment sensing method. One undeniable conclusion is that as epoxy bond length increases, so does the effective strain transfer length for a given configuration. This trend is true for all bond layer thicknesses and epoxy moduli. A second conclusion relates to the effect of epoxy elastic modulus on strain transfer. It was observed that strain transfer increases with an increase in the adhesive elastic modulus. This trend supports the conclusions of previous studies, which suggest that the closer the elastic modulus is to the concrete, the better the strain transfer.

The results of this study suggest an inverse relationship between bond layer thickness and strain transfer. It is seen that smaller bond layer thicknesses provide greater strain transfer. Additionally, the effect of bond layer thickness appears to have more of an impact on the V-notch configuration than the saw-notch configuration. This behavior is likely due to the fact that the V-notch is wider with a tapered shape while the saw-notch geometry is narrower and more uniform. The bigger V-notch provides a greater volume of epoxy for strain loss to occur in. The tapered V-notch shape provides more epoxy between the FBG and the concrete than the saw-notch as the bond layer thickens.

### ***FBG Sensors Mounted on Steel***

Fiber Bragg gratings (FBGs) and traditional foil gages (TGs) were installed on an S3x5.7 steel beam. There were six of each type of sensor, where one FBG and one TG were located in six different locations on the beam. The averaged results from each FBG and TG set at the various locations were compared for the six tests. The modulus of elasticity values were used for comparison because the averaged results were linear, so one slope value accurately represented the data set.

Given the assumptions of the tests and additional test properties, the results are within a reasonable range. Typically, when comparing strain gages on the market to foil gages through laboratory testing, strain results within 5% are a reasonable expectation. Set 6 displayed this comparison with a 2% difference. However, based upon the assumptions and additional test properties, results within 15% are realistic.

#### **Task 2**

Upon study of the market for commercially available instrumentation, particularly FBG network interrogators, it became evident that a commercial product was superior to anything that could be developed individually. Commercial products provide the low-cost, compact form-factor and energy-efficiently required for this project. Additional pursuit of custom instrumentation would have been wasteful of research time and funding. Consequently a two-channel SmartScan 02 Lite FBG interrogator developed by Smart Fibres, was purchased for the laboratory study. The only other resources required in the laboratory are a standard Windows-based desktop computer and an internet connection. This approach assured that the laboratory instrumentation conformed to the latest industry standards and had the reliability and durability to perform as required.

Selection of instrumentation for field application was merged with task 3 in order to successfully integrate commercially available hardware with a custom-designed microcontroller. Findings and conclusions for the instrumentation intended for field application follow.

#### **Task 3**

Future field deployment and operation of the SHM network emphasized proof of concept of the RFID triggering system for data collection and data storage capabilities. The research was focused on permitted vehicles. Additionally, the system was designed to correlate known vehicle data with the measured response of a bridge. The work focused on the RFID systematic description, the validation procedure, and the validation results for the proof of concept field tests.



The RFID system utilizes a transponder that wirelessly transmits data to and from the RFID tags. RFID transponders will be installed at a weigh station at a Wyoming port of entry and at the bridge of interest. At the port of entry, the permitted truck information, including the axle weights and configuration, will be assigned to an RFID tag with an identification code that would be placed on the windshield of the vehicle. Another transponder placed near the bridge will detect the presence of the RFID tag and trigger the system to store the bridge strain data when the tagged permitted vehicle passes over the bridge.

For the proof of concept testing, the triggering mechanism, data collection, and data storage were the specific parameters tested. The proof-of-concept tests were organized so that the initial positioning of each RFID component was established prior to testing the system at full speed, including positioning of the RFID transponder, RFID tag, and RFID vehicle. Each time the transponder detected the tag, the FBG strain data from three sensors were continuously recorded for the allotted 30-second time frame.

The proof-of-concept for the RFID triggering system was validated. It was determined that the success of the triggering is dependent upon the position of the tagged vehicle; the transponder, including the height and horizontal position; and the tag location in the vehicle. The proof-of-concept tests provided admissible results that were sufficient to move on to the next phase of instrumentation design and testing.

#### **Task 4**

The sensors installed on the concrete beam using methods developed in task 1 provided measurements similar to, but lower in magnitude than, what was predicted by the analytical model. It was necessary to account for averaging effects caused by the long gauge sensor configuration. Further discrepancies between the test results and the analytical model could be explained by a difference between the predicted and the as-built modulus of elasticity for the concrete.

The measurements taken on the steel beam were similar in magnitude to the values predicted by the analytical model. However, the measurements taken at different locations on the beam cross-section varied significantly, where they should have been similar. This variation could be explained by the presence of secondary load effects induced by an eccentricity in the load on the beam that was observed during the experiment. In a few locations on the steel beam, the sensors experienced a significant loss in pretension after installation. The wavelengths from these sensors did stabilize at a point that indicated that there was still adequate pretension to make the necessary measurements. However, the resulting measurements at these locations appeared inconsistent with measurements taken from other sensors during the tests. This may be due to an inadequate bond between the sensor and the beam. However, these sensors were located directly above the mid supports of the beam. So, the inconsistent measurements may have been the result of unpredicted localized effects from the supports.

## Task 5

Based on the findings in the literature and additional testing with steel specimens in this research, it can be reasonably concluded that effective strain transfer in compression can be achieved with proper bonding technique. Whether the ineffective transfer with the wood block specimens was a consequence of micro-buckling or some other phenomenon remains unknown, but also irrelevant. The important finding is that FBG sensors can indeed perform accurately when subjected to compressive strain.

## Recommendations

The research and development reported herein lays the groundwork for continued study involving field deployment of the FBG-based SHM system. The essential elements of the system are in place. These elements include the following:

- Sensor installation and protection techniques for both concrete and steel host structures
- Commercial and special-purpose instrumentation for interrogating the SHM network
- A novel triggering system based in RFID technology to control the amount of data that is collected from the SHM network.

Subsequent deployment of the system on a bridge in the WYDOT inventory will require additional development of data storage and transmission capabilities, which will be particular to the location and characteristics of the targeted bridge. In addition, the objectives of the SHM network (such as, for instance, observing the impacts of overweight and other permit vehicles, validating load-rating software, monitoring long-term health of the bridge, etc.) will dictate the nature of the sensor installation, the type and volume of data collected, and the required post-processing requirements. Hence, development of a general performance specification for real-time data analysis is not feasible. Rather researchers engaged in Phase II of this study must coordinate with bridge engineers at WYDOT to identify a spectrum of SHM applications and objectives, for which individual data analysis techniques can be developed. Subsequent design and implementation of software to execute such data analysis will be needed to relieve bridge engineers from the burdensome and tedious tasks of sifting through raw SHM data streams themselves.

In addition to the general recommendation above to move toward field deployment of the SHM system, the following specific recommendations are offered.

1. Special attention should be taken when purchasing FBGs. Knowledge about existing technologies and manufacturers will help to assure accurate, consistent, and reliable strain sensor results. Particular points of interest include the wavelength range that can be sensed by the interrogator and the required spacing between central wavelengths of

- FBGs on an individual channel. The interrogator range and the spacing determine the number of sensors that can be installed on a single optical fiber.
2. In design of the sensor network for a particular bridge, sensors should be placed at a sufficient distance away from the neutral axis to ensure that they are measuring meaningful flexural strain values. For many structures, the concrete deck will act integrally with the primary structural elements. This composite behavior (intended or otherwise) will shift the neutral axis toward the deck. Analysis should be performed for each structure to determine where the expected neutral axis will occur, and the neutral axis location should be considered when deciding where to locate the sensors on the cross-section.
  3. A two-sensor configuration makes it difficult to distinguish any contribution from out-of-plane bending. If a sensor is located on a location of the cross-section where strains from one load effect act counter to strains from another load effect, these readings would underestimate the response of the structure to the loading. If these values were used to load rate a bridge, they would overestimate the capacity of the bridge. Placing the sensors close to the minor neutral axis of the beam would minimize the contributions from these secondary load effects. However, if there are significant secondary load effects, it would be important to consider them and the interaction of the stresses.
  4. While the top flange of a girder is typically braced by the deck, the bottom flange often carries lateral loads along the girder line through bending until they reach a lateral brace that will transfer the loads into the deck. The significance of these lateral loads should be investigated as part of the design process for the sensor network.
  5. The SHM system will be capable of recording massive amounts of data. It will be necessary to develop methods to automatically decipher which data is significant and should be transmitted and saved by the system. An algorithm to save data with readings that exceed a certain threshold or the maximum response each day may be appropriate. Taking a relaxed-state reading each day may be appropriate for documenting changes in the structure or to verify the functionality of the sensing system.
  6. Since trucks pass over a bridge in a matter of seconds, it is highly unlikely that significant effects of temperature change will occurring during the load event. Hence, when the data acquisition system is triggered by the RFID signal, initial relaxed-state scans of the bridge can be used to establish a baseline of strains immediately prior to and perhaps after passage of the permitted vehicle. Such an approach effectively embeds temperature compensation in the software that drives data collection rather than in special-purpose sensors, which require additional cost and bandwidth in the interrogator.
  7. The RFID triggering system requires additional development. Developments include the port of entry system installation, firmware advancement, larger transponder range capabilities, cellular data transmission capabilities, database establishment, and software formation. For instance, use the E-ZPASS system, common in many states, could simplify application of the system at the port of entry, since it is already familiar to DOT officials and the trucking industry alike.
  8. A database should be established that can manage a large amount of vehicle and bridge information and can be accessed by approved personnel, for example WYDOT bridge engineers. Software as well as algorithms for automatic post-processing must be developed. One company that has been researched, Chandler Monitoring Systems, Inc.,

has developed some of these processes, and it may be worthwhile to pursue their guidance or services.

9. Port of entry sites would do well to couple weigh-in-motion systems to an RFID triggering system to automate collection of vehicle characteristics. Utilizing a static WIM system that already exists at the port of entries, bridge engineers can correlate that load to the bridge responses induced by permitted live loads.
10. Another possible enhancement to the SHM system could be a continuous load-rating system for permitted vehicles. Over time, a standard baseline could be built for specific permitted vehicles and bridge families. Instead of relying on a conservative analysis completed by BRASS-Girder, the actual responses would be measured and monitored for a variety of applied vehicle configurations. Algorithms and procedures would need to be developed to determine real-time bridge load ratings from bridge measurement data. By continuously monitoring the bridge, bridge management officials could potentially determine practices to safely increase the load ratings.
11. The SHM system could assist in identifying illegal loads and notifying law enforcement. Individuals or companies with overweight or oversize vehicles might not file for a permit in an attempt to by-pass permit fees. Strain-level triggers implemented in the sensing network, coupled to RFID tags in trucks entering the State could be used to detect and identify illegal loads.

## CHAPTER 2 – PROBLEM DESCRIPTION

### Problem Statement

State departments of transportation (DOTs) in the West have been under increasing pressure to permit and route overweight trucks transporting machinery and equipment for the energy sector through their state and interstate highway systems. DOT engineers are called upon daily to rate their bridges for overweight trucks to determine appropriate truck routing and to assess the impacts of the trucks on bridge safety and durability. Many of these overweight trucks have nonstandard configurations, which further complicates the rating and permitting process. Hence, it is critical that bridge engineers in the DOTs develop confidence that their bridge analysis and rating software accurately predicts the response of bridges to overweight trucks, especially for bridges on the most frequently traveled routes.

The long-term objectives of this project were to develop and validate an instrumentation package for SHM of bridges subjected to overweight trucks and to develop plans for field deployment of the instrumentation on a pilot scale. Ultimately, the objective is to accurately correlate long-term field-performance data to the behavior of the bridges predicted by analysis and rating software. The field instrumentation package incorporates use of optical fiber sensors, specifically fiber Bragg gratings (FBGs), to monitor strains at critical locations in bridges that are considered most vulnerable to overweight truck loads and are most difficult to effectively rate with currently used software.

This report documents the methods and outcomes of Phase I of what is envisioned to be a long-term, multi-phase project. Phase I involved a laboratory investigation, the objectives of which are to develop the instrumentation package; remote data collection and processing capabilities; and field installation and operations methods suitable for long-term SHM of bridges in remote locations. Methods appropriate for both steel and concrete girder bridges were developed. The monitoring system is capable of observing bridge behavior under both static and dynamic (wheel impact) loadings.

Continuation of the research reported herein in Phase II of the project will extend the laboratory developments to field deployment and operations. It will further include correlation of field measurements with analysis results from bridge rating software. Key elements of Phase II will include configuration of the SHM system to properly record bridge response data for load events of interest, development of data transmission capabilities from the instrumented bridge to a central server (a process that will require site-specific details on bridge location, proximity to the central server, and availability of power and computer network access), and development of automated data post-processing methods to transform SHM data into formats that inform bridge engineers of the alignment of bridge performance with predicted results from their rating models.

## Research Methods and Tasks

In Phase I of the project, instrumentation, packaging, installation techniques and data collection and storage for fiber Bragg grating (FBG) sensors were developed in the laboratory. The laboratory investigation included the following primary tasks.

1. Development of optical-fiber packaging or other protection mechanisms suitable for installation in the target environments. Both steel and concrete girder bridges were considered, with emphasis placed on girder-line response. Considerations included the following sub-tasks.
  - a. Protecting the optical fiber from damage due to the harsh environment and possible vandalism.
  - b. Positioning and bonding optical fibers to the host girder material. The bonding process must assure effective strain transfer from the host material to the optical fiber in the vicinity of the FBG sensor.
  - c. Repairing or replacing damaged optical fibers and sensors that do not survive the conditions in step 1.a.
  - d. Compensating for temperature sensitivity of the FBG sensors, likely achieved through use of companion unbonded sensors.
2. Development of a low-cost, compact, and energy-efficient instrumentation package for interrogating the sensor network. The approach involved a combination of design and fabrication of custom instrumentation linked to commercially available components with proven reliability. This approach achieved a balance among cost, reliability, and ease of maintenance and replacement.
3. Development of data collection, processing and transmission capabilities. An FBG sensor network on a bridge will have the capacity to collect an overwhelming volume of data, so much so that data storage and transmission could easily become a constraining bottleneck to the performance of the network. To avoid this bottleneck, real-time data processing is needed to convert the data collected by the interrogator into behavior parameters that are of value to bridge engineers at the state DOTs. Among others such parameters may include strains, stresses, accelerations, vibration histories, damping ratios and impact factors. The volume of even these behavior parameters could become overwhelming unless some control is provided to synchronize collection of the parameters with critical events, such as the passage of an overweight truck that has just been routed over the bridge, and then trigger delivery of the parameters to the DOT offices. For this project a general performance specification for real-time data analysis developed in cooperation with bridge engineers at WYDOT was considered but regarded as infeasible. Design and implementation of software to satisfy site-specific performance requirements will complete this task in Phase II of the research.
4. Validation of tasks 1, 2, and 3 was performed in the laboratory using a mock-up of bridges having steel and concrete girders. Pseudo-static and dynamic loading protocols, intended to simulate slow-moving and high-speed truck traffic, were applied to the mock-up to excite the FBG sensor network. Observed response was then compared to detailed analysis results to confirm the function and efficacy of the SHM system.
5. Research outcomes during Year 1 of Phase 1, plus reports by other investigators, suggest that FBG sensors must be pre-tensioned prior to installation so that, if the host structure is subjected to in-service compressive strain, the sensors will simply relieve some amount of pre-tension, rather than experience a net compressive strain. Spurious compression-

strain response of FBG sensors has been attributed to possible micro-buckling of the optical fibers, thus rendering the sensor output unreliable as a measure of host-structure strain. This task involved an attempt to determine if micro-buckling does indeed occur and what means can be employed such that micro-buckling can be prevented, thus allowing the sensors to accurately respond to compressive strain.

## **Research Benefits**

The proposed project will make direct positive contributions to the following strategic goals.

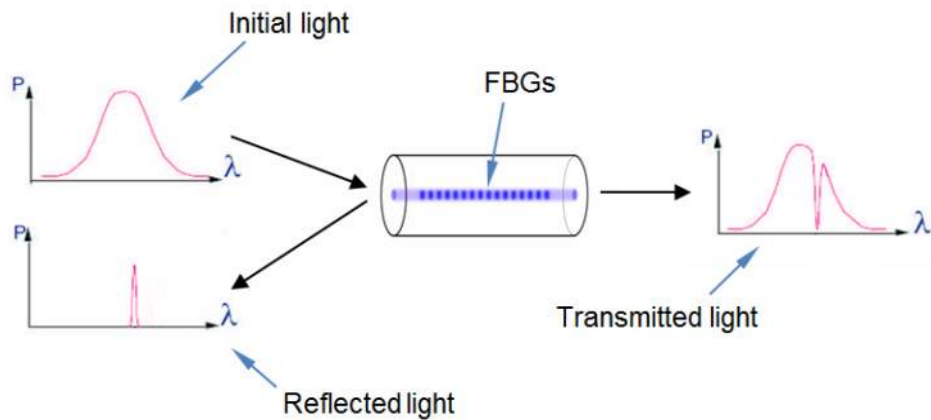
1. **State of Good Repair:** An effective SHM system for highway bridges will, over time, improve the ability of bridge engineers to predict the effect that overweight vehicles will have on the condition of their bridges. As engineers receive feedback on bridge performance to confirm or recalibrate their rating methods, they will have the capability to predict long-term durability of bridges. They will also be able to more effectively route overweight trucks and also specify appropriate reconfigurations of trucks that would otherwise not be permitted on certain routes.
2. **Safety:** Accurate real-time monitoring of bridge response will improve the operational safety of bridges during overload events by controlling the magnitude of the overload. Long-term safety will also be enhanced by use of the monitoring system to identify and quantify unanticipated overload events. Further, increased precision in defining the weight distribution in overweight trucks plus refinements in monitoring bridge response will reduce the inherent randomness in the demand (applied loads) as well as the variability in structural capacity to permit more refined predictions of bridge performance.
3. **Economic Competitiveness:** The proposed SHM system using relatively low-cost equipment with low power demand will provide the initial economic advantage to the project. The second advantage is in improved predictions of bridge durability and life-cycle. Effective scheduling of inspections and maintenance will be facilitated by an accurate and easy-to-use sensing network on the bridge. With suitable experience and calibration of the sensing network, engineers will be able to observe changes in bridge response that might suggest deterioration or damage, thus prompting more timely inspection and maintenance work. An SHM system that can be quickly deployed would be beneficial in instances in which a bridge may otherwise need to be restricted or closed due to advanced deterioration or impact damage. Monitoring a structure as the repairs are being designed could also help to ease the burden on the traveling public.



## Literature Review

### Background on Fiber Bragg Grating Sensors

Fiber Bragg Grating (FBG) strain sensors are beginning to achieve broad acceptance by the civil engineering field because they offer many advantages over other sensors available on the market (Zhou and Ou 2004). FBG sensors have been widely studied and used in structural testing and health monitoring applications, but are still less common than traditional foil strain gages because of the high cost of FBG sensors and interrogators. An FBG is an optical sensing device that consists of a grating etched into the core of an optical fiber at a precise spacing. When light is passed through the grating, a portion of the light is reflected back toward the source at a narrow band of wavelength centered about the Bragg peak wavelength. This process is illustrated in Figure 1.1. In the figure on the upper left, a broad spectrum of light enters the optical fiber from a laser or other light source. When the light spectrum encounters the FBG, a small portion of the spectrum, corresponding to the gage of the gratings is reflected back to an interrogator. The rest of the spectrum passes through the grating as transmitted light.



**Figure 2.1 – Illustration of FBG Signal Transmission (Heininger 2009)**

A change in the pitch of the grating, which can be induced by straining the fiber, results in a shift in the peak wavelength that is reflected back. This shift in reflected wavelength is proportional to the strain. Using this property, the strain in the fiber can be determined by measuring the shift in the reflected wavelength. The relationship between strain and wavelength shift is given by Equation 1.

$$\varepsilon = \frac{\lambda - \lambda_0}{G\lambda_0} \quad (\text{Eq. 1})$$

where:

- $\varepsilon$  = strain
- $\lambda$  = reflected wavelength
- $\lambda_0$  = unstrained reflected wavelength
- $G$  = gage factor (typically 0.78)

An interrogator is used to both send and receive the light signals for the gratings. The interrogator may have multiple channels, and multiple FBG sensors can be installed on a single fiber and interrogated by a single channel. Installing multiple sensors on one channel is called multiplexing. Multiplexing permits a large number of sensors to be installed on a structure and read by a single interrogator. Fibers can run the entire length of the structure and measure strains at multiple locations. Distributing a number of sensors along the length of just a few fibers simplifies the installation process and reduces the costs of equipment necessary to read the sensors. It is important to efficiently utilize the multi-channel and multiplexing capabilities of an interrogator in order to minimize the cost of an SHM system. Interrogators are by far the costliest components of a FBG monitoring system, accounting for as much as 70% of the component costs.

Because FBGs operate using light signals, the sensors are immune to electromagnetic interference, the behavior of the gage is extremely stable and does not need to be recalibrated (Guemes and Sierra-Perez 2013), and the signal can travel extremely long distances with almost no losses. Additionally, the silica material for the sensors is resistant to corrosion. So, the sensors can be applied almost anywhere so long as the optical fibers are protected from mechanical breakage.

Due to their many benefits and long lifespan, FBG sensors are beginning to be widely implemented in critical civil structures. Their benefits, however, may extend beyond just high profile projects and critical structures. As the technology becomes more widespread the cost of FBG systems may reach a point where it becomes economically viable for widespread implementation of FBG-based bridge rating and monitoring systems on highway networks.

In summary FBG sensors were selected for this application since they possess several advantages over alternative sensor technology. Some of these advantages include the following (Kreuzer, 2007).

- FBG sensors are effective in measuring strain to a high level of resolution. Changes in strain as small as  $1 \mu\epsilon$  can be observed with suitable interrogation instruments and signal processing techniques. The sensors can further measure very high strains, in excess of  $10,000 \mu\epsilon$ , thus increasing the likelihood that they will continue to function in the event of severe damage, such as due to vehicle collision with a bridge.
- FBG sensors are capable of high scan rates using relatively low-cost interrogation instruments. Frequency response rates of 5 kHz are easily achieved, allowing accurate determination of wheel impact factors.
- FBG sensors are immune to electromagnetic interference, which might otherwise limit the environments in which they can be used.
- FBG sensors can be interrogated over long distances (in excess of 5 km) without loss of signal strength and resolution.
- Multiple (25-50) FBG sensors can be located on a single optical fiber and interrogated with a single electronic device.

- FBG sensors, their interrogation instrumentation and data communications equipment consume relative low power, enabling an installation to function off-grid, using for instance a power supply consisting of only small solar cells and an automobile battery.

### **Transfer of Strain from Host Material to the FBG**

A study by Pak (1992) had the objective to determine strain transfer behavior of a fiber optic sensor (FOS) strand imbedded in an isotropic homogeneous host matrix with an applied longitudinal shear stress. A numerical analysis was conducted in which various material property relationships of the fiber and host matrix were compared. Pak considered two types of embedded fibers: one with a single layer coating and a second bare embedded fiber with no coating. Different thicknesses and shear moduli of the coating and fiber were tested in order to observe strain transfer variations. The results led to several relevant conclusions contributing to the understanding of the elastic behavior between an embedded FOS and its host material.

The most relevant trends seen in the study were derived from a comparison of the shear strain transfer in the optical fiber with various shear moduli and thicknesses of the fiber coating. It was found that strain transfer increased in the optical fiber as the coating layer got thinner but only when the shear modulus of the coating was less than that of the host matrix. Conversely, when the shear modulus of the coating was greater than that of the host matrix, the shear transfer increased as the coating layer got thicker. This relationship allowed determination of the shear modulus of the coating, which gives the greatest shear transfer to the fiber. The maximum shear transfer from the host material to the fiber occurs when the shear modulus of the coating is the geometric mean of the shear moduli of the host matrix material and the fiber. This relationship is true for all coating layer thicknesses.

Further analysis of the results showed that the most accurate shear transfer would occur if the bare fiber were embedded directly into the host matrix without a protective coating. As stated previously, the shear transfer across the coating improves as the coating gets stiffer, however since in most applications the coating (typically epoxy or plastic cladding) is less stiff than the host material (typically steel or concrete), it is correct to assume that the optimal fiber embedment configuration would have no coating. Furthermore, for a fiber with no coating, it was found that the best shear transfer occurs when the optical fiber stiffness is equal to or less than that of the host matrix material. The study conducted by Pak discovered several fundamental relationships about embedded fiber optic sensors that are useful in their implementation and optimization in civil engineering applications.

Zhou *et al.* (2010) investigated axial strain distributions of FBG sensors and the influencing parameters, which include the bonded length of the FBG sensor, adhesive thickness, and elastic modulus of the adhesive. Zhou *et al.* considered a four-layer cylindrical model consisting of the inner core of bare optical fiber sequentially wrapped by a protective coating, an adhesive layer, and an outer host material.

A finite element analysis was conducted to examine the strain transfer from the outer host material to the FBG core under an axial tensile stress of 50 MPa applied to the host material. The results of the FEA were then verified by laboratory testing of the FBG strand bonded to an aluminum alloy dog-bone specimen. The mechanisms that induce FBG chirping phenomena were also identified and analyzed. Chirping is a phenomenon that occurs when the period of the gratings along the grating section of the fiber is not constant. Chirping results in inaccurate sensing due to the fact that the reflected wavelength was formed by inconsistent grating periods.

The laboratory tests conducted by Zhou not only verified the FEA results but also revealed some insightful information about the chirping phenomena. Three dog-bone specimens were tested with adhesive bond lengths of 5 mm, 10 mm and 15 mm. The effective sensor lengths found for each specimen corresponded well with those found in the FEA. It was found that increased chirping occurred as the bond length decreased. When the bond length was equal to the grating length (5 mm) the chirping was unacceptably high, but when the bonded length was three times the grating length (15 mm), chirping was nearly nonexistent. Therefore it was concluded that a bonded length that is at least 3 times the grating length will minimize chirping and provide optimal strain transfer sensing.

Zhou's study discovered several important characteristics dealing with strain transfer of embedded FBG sensor. FBGs can be designed for optimal strain transfer as long as the material properties, bond configurations and grating lengths are all properly set. Additionally it is best to have a stiff adhesive layer that is as thin as possible but still provides an adequate bond.

The ability to determine the amount of strain transfer from a host material to the fiber core of an FOS is the subject of interest in a study by Ansari *et al.* (1998). In their research, a theoretical model was developed that calculates the strain in a host material using the values measured by an FOS. The investigation considers the strain loss through the protective coating of an FOS as well as the behaviors of a bare embedded FOS. The theoretical model is verified through experimental tests of FOS strands attached to a tapered cantilever beam. Results of the study suggest that strain transfer is a function of the mechanical properties of the fiber core, the protective coating and the fiber gage length (length of optical fiber in contact with the host material). The result of this research makes it possible to determine FOS gage length requirements, but also eliminates the need for calibration tests and statistical analysis to determine strain transfer. It was also found that having a bare embedded fiber (no protective coating) gives an optimal strain transfer, but is an unrealistic configuration due to the requirement for fiber protection when used in structural health monitoring applications.

The goal of the analysis conducted by Torres *et al.* (2010) was to understand the effectiveness of a new FBG packaging system that was adhered to the surface of a host structure. The packaging configuration consists of an FBG fiber covered by a single protective layer of composite material made up of glass fiber reinforced polyester resin. A second more common configuration was also tested and used as a comparison to the new configuration. The second configuration had

two protective layers of the glass fiber composite material, one on each side of the fiber. The two configurations were adhered to a host structure using a thin layer of adhesive. A finite element model (FEM) of the packaging was used to determine the configuration that produces optimal strain transfer between the host structure and the FBG sensor. The parameters that were adjusted in order to optimize the design included material properties, adhesive layer thickness, temperature, and the number of protective layers. A strain was applied on the lower face of the adhesive layer, which simulated strain induced in the host structure caused by temperature change. The response of the system to the induced strain was analyzed assuming an orthotropic adhesive layer, and only considering thermal expansion in the longitudinal direction.

A comparison of the new single layer packaging design and the more commonly used double layer design resulted in strong partiality towards the single layer configuration. The presence of a second 400  $\mu\text{m}$  thick protective composite layer between the fiber and the host structure caused a substantial strain transfer error of 15%. In addition, the extra layer caused an inconsistency in strain transfer measurements, which was thought to be a result of material manufacturing defects and material property variances. The single layer design not only eradicates this error but is also a more simple design.

### **FBG Sensor Placement**

For the purpose of performing load tests on bridges, the Manual for Bridge Rating through Load Testing (A.G. Lichtenstein and Associates, Inc. 1998), published by the National Cooperative Highway Research Program (NCHRP), states that sensors should be placed on critical members and in locations to gather data that can be used to verify the analytical model. In the following, a three digit notation of the form X.XX is used to describe a point of interest (POI) on a bridge. The number on the left of the decimal place indicates which span the POI is located in, and the two digit number to the right of the decimal place indicates how many tenths of the span the POI is from the left end of the span. For example, 1.00 indicates a position just inside of the first support of a bridge. Location 1.05 describes the middle (5/10) of span 1, and 1.10 describes the location just to the left of the second support. Location 2.00 would then describe the location just to the right of the second support.

In Barker, et al. (1999), six different standardized testing plans are detailed for measuring the different factors that can affect a load rating on a steel girder bridge. These testing plans provide guidance for placing the necessary sensors for performing the required tests. The six plans vary in complexity and effort required based on the amount of information the tester would like gain from the test. The simplest plan consists of a single strain gage placed on the bottom flange of the critical girder at the location of maximum moment determined from analysis. This simple plan can be used to post a bridge. The most complex plan consists of multiple sensors on each of the girder webs at the maximum moment regions and near each support. This more complex configuration can be used to determine load rating adjustments for: impact, lateral load distribution factors, bearing restraints, and composite behavior.

Chajes, Shenton III, & O'Shea (2000) performed diagnostic load tests on a bridge by placing sensors on the top and bottom flanges of girders at the middle of each of the three spans in a continuous multi-girder bridge. They did not discuss any analysis indicating that the mid-span locations were points of maximum load effect, and typical practice would indicate that the sensors in the exterior spans are not measuring the maximum load effects. The AASHTO Bridge Design Manual (AASHTO 2012) reports statistical moment data from the 1.04, 2.05, and 3.06 span locations from a number of bridges in the commentary discussing the calibration of the HL-93 live load and load factors. These span locations reflect a commonly accepted rule of thumb for estimating the anticipated maximum moment locations in a three-span bridge.

In Cardini and DeWolf (2008) sensors were placed on the web of the steel girders. They were located 2 inches below the top flange and 2 inches above the bottom flange. This placement allowed for the calculation of the neutral axis location. However, by being further from the extreme fibers, the strain gages were limited to measuring smaller strains. As it was a simple-span bridge being tested, sensors were installed only at mid-span for each of the girders on the bridge.

Doornink, et al. (2006) conducted a study to monitor a bridge for local failure in a girder web by placing sensors across the region of the expected failure and in other "non-target" areas. By tracking the paired response of these sensors to loading events over time, they were able to prevent false alarms that could have been triggered by systems monitoring sensors in the critical locations alone.

In addition to placing sensors to measure critical member behavior, Seo, Phares, Lu, Wipf, & Dahlberg (2012) placed sensors on the underside of the bridge deck in order to determine the approximate wheel locations and axle spacing of a vehicle during a load event.

### **FBG Sensor Installation**

Several considerations are important when determining an appropriate sensing system for bridge monitoring and testing. A good summary of issues to consider is presented in Farhey (2005). Many of the complications described in this summary are overcome by FBG sensors. However, the developed system must still consider appropriate sensor placement, ease of installation, gauge lengths, and procedures for protecting and replacing sensors. In addition, FBG sensors present some additional challenges that are not discussed in this paper, such as appropriately tensioning fibers, and adequately spacing the wavelengths of multiplexed sensors. These topics are addressed below.

The FBG sensors used in the study by Todd, et al. (1999) were installed on steel girders using a cyanoacrylate adhesive and protected with a silicone RTV sealant. This method of protection is simple to apply and provides protection from weather. However, it may not be adequate to withstand vandals and wildlife.

In Doornink, et al. (2006) FBG sensors were embedded in carbon fiber reinforced polymer packaging, which is commercially available, and installed on steel bridge members using cyanoacrylate adhesive. The strain measurements showed excellent agreement with the traditional strain transducers that were installed to verify the accuracy of the FBGs.

A different type of fiber optic sensor, called a Brillouin Optical Time-Domain Reflectometry sensor, was used in Matta, et al. (2005). The installation required for this type of sensor is similar to that required for FBG sensors. For this study, the researchers ordered the fibers to be factory-embedded into an FRP tape. The sensors and tape were then adhered to the steel bridge girders using a two-part epoxy encapsulation resin. Prior to adhering the sensors, the steel was prepped by manually roughening the surface with steel brushes and applying a lacquer thinner for degreasing.

### **FBG Protection Techniques**

A presentation by Micron Optics, one of the leading FOS manufactures in the United States, describes general misconceptions about the reliability of FOS (Micron Optics, 2014f).

1. A sense that FOS are still a “research” technology
2. Prior direct or anecdotal poor experiences with university or startup technology and/or deployments.
3. Prior poor experiences stemming from inadequate understanding or training with regard to FOS strengths, weaknesses, and deployment techniques

Various topics have been explored by Micron Optics including fiber breakage susceptibility, poor or inconsistent strain transfer from carrier to FBG, spectral distortions leading to measurement distortions, fiber or carrier creep, fiber debonding, repeatable thermal response, humidity exposure and cycling, and fatigue cycling. Micron Optics laboratory and field qualification tests have proven that the right materials, processes, and controls can provide accurate and reliable strain results (Micron Optics, 2014f).

The protective coating on a FBG must be removed in order to etch the grating into the core of the fiber, which designates a base wavelength for that specific fiber. Afterward, the FBGs must have their inner cores protected by recoating the fiber, enhancing the fiber’s strength and flexibility. The two most common types of recoating material currently available are polyimide and acrylate. Kuang, et al. (2006) at the National University of Singapore studied the performance of FBGs embedded in carbon fiber composites; some were recoated with acrylate and some were bare FBGs after the recoated acrylate was removed. It was discovered that the bare FBGs performed more accurately compared to the recoated acrylate fibers, which saw a significant amount of stress relaxation. A study completed by the University of Manitoba (Rivera, et al. 2005) discusses the main differences between polyimide and acrylate recoating. Tension tests were conducted for strain transfer performance; the FBGs were purchased from two different manufacturers, and the results were dependent on the manufacturer, not the type of recoat material. This finding led the researchers to believe that FBG recoating standards should be



implemented. An e-mail from a representative at Micron Optics (Baez, 2014), one of the leading FBG manufacturers in the United States, described acrylate recoat as a “spongy” cladding, commenting that polyimide coating accomplishes strain transfer more successfully and has a wider temperature range.

### **FBG Strain Verification Cases Based upon Laboratory and Field Testing**

Fiber optic sensors were first applied in the 1960s for commercial telecommunication purposes. They have been utilized in military and aerospace equipment fields, and have, within the last two decades, begun to gain acceptance into many fields including health monitoring for medicine, heritage culture, and various engineering fields. In the civil engineering industry, they are ultimately used to potentially increase the life of expensive and important structures as well as avoid crucial failures (Annanddas, 2011).

Ansari (2007) discussed the complications in using bare FBG sensors, or sensors without a type of carrier or protection method in field conditions. In Hong Kong China, forty sensors were installed on the Tsing Ma Bridge to measure temperature and strain. By using epoxy and a nitinol metal as a protection method, favorable strain results were seen from testing, agreeing with traditional foil gage measurements in similar locations (Chan, et al. 2005). Tests completed by a team at the University of Iowa Bridge Engineering Center displayed good agreement between FOS and traditional foil gage strain readings, which assured accuracy for field instrumentation on the US 30 Bridge near Ames, Iowa (Doornink, 2006). This study showed that FBGs perform accurately using a variety of different protection techniques.

Bridge Diagnostics Inc. (BDI) of Boulder, Colorado was hired to install their strain sensors adjacent to the FOS installed on the US 30 Bridge to compare readings based upon ambient traffic loads. The results from BDI’s sensors and the FOS were excellent, and the tests were deemed successful (Doornink, 2006). During construction of the Hulanhe Bridge, which crosses the Hulan River in northeast China, 15 FBGs and 15 traditional foil gages were installed. The FBGs performed as expected while only one traditional foil gage survived the installation procedure, proving the durability and reliability of FBGs over foil gages in this application (Zhou, et al.).

ISIS Canada and the University of Manitoba teamed up to install FOS onto various bridges in Canada (Tennyson, 2001). The Beddington Trail Bridge in Alberta, Canada was an example of FBGs as a reliable strain sensor with 18 out of 20 sensors still working accurately three years after installation. The Taylor Bridge in Manitoba, Canada was used to install 63 FBGs with traditional foil gages used to compare the data. Only 40% of the foil gages survived while the majority of the FBGs were still reading accurately.

## CHAPTER 3 – OPTICAL FIBER PACKAGING

Task 1 for this research project involved development of optical-fiber packaging or other protection mechanisms suitable for installation in the target environments. Both steel and concrete girder bridges were considered, with emphasis placed on girder-line response.

### Bonding to a Concrete Host

The elasto-mechanical problem involving use of FBG sensors in concrete host structures was studied by Maurais (2012). That study involved both experimental testing and FEM analyses to determine the strain transfer behavior of FBG sensors embedded in notches in the concrete host. Other researchers have examined strain transfer behavior of FBG sensors embedded in concrete as it is cast, but this research focused on installation of the sensors in existing structures, rather during the construction sequence.

### Finite Element Study

A three-dimensional finite element analysis (FEA) of a notched concrete host structure and a notch-embedded FBG strand (Figure 3.1) was conducted to study strain transfer behavior from the concrete to the FBG. The 90-degree V-notch configuration in Figure 3.1 shows an optical fiber with FBG sensors embedded in an epoxy-filled V-shaped notch. The V-notch configuration was studied, as the V-notch may be formed when the concrete host structure is cast or may be cut in after the concrete has cured, providing the opportunity for optical fiber installation following construction. The saw-notch configuration in Figure 3.1 involves a bull-nosed slot cut into the concrete after construction using a conventional abrasive saw blade. Again the optical fiber with its FBG sensors is bonded within the epoxy-filled notch. Bond layer thickness, adhesive bond length, adhesive elastic modulus, and notch geometry were all variables of interest in the study.

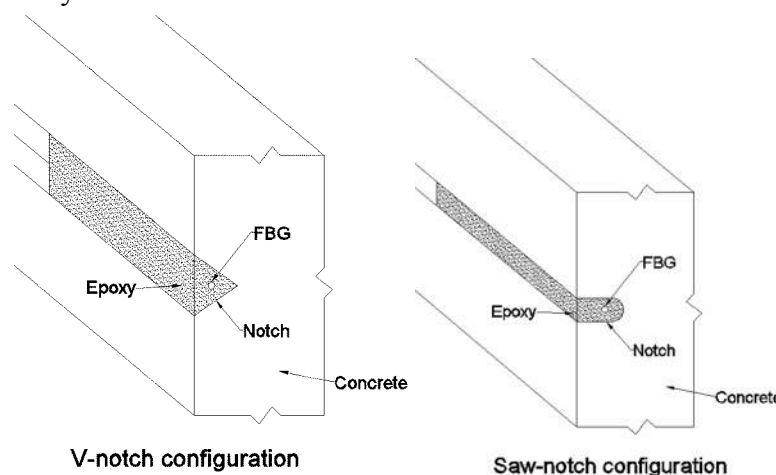
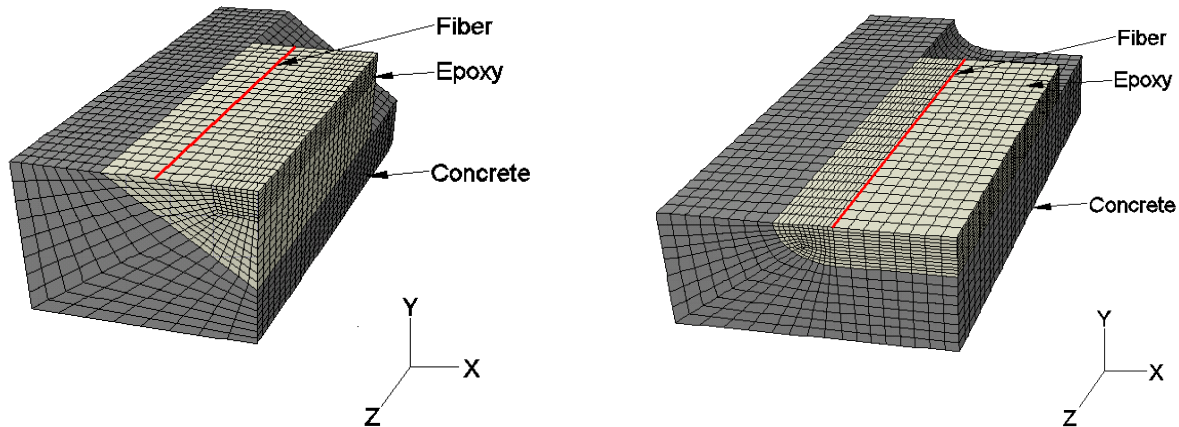


Figure 3.1 – Notch embedded FBG configuration cross sections

Each notch configuration was modeled with a different FEA model. Figure 3.2 illustrates the two models, which exploit the quarter-symmetry in of the notch configurations. The red line in the figure represents the optical fiber, which lies in the plane of symmetry. The light-gray elements represent the epoxy and the dark gray elements represent concrete.



**Figure 3.2 – (a) V-notch FEM configuration, (b) Saw-notch FEM configuration**

The epoxy bond length and bond layer thickness are two important parameters that affect strain transfer. The epoxy bond length is the length of epoxy in the concrete notch measured parallel to the optical fiber and bonds it to the concrete. Intuition suggests that the longer the epoxy bond length the better the strain transfer, however it is theorized that only a portion of the optical fiber needs to be bonded in the notch in order to achieve full strain transfer. Epoxy bond lengths of 10 mm, 20 mm, 30 mm, 40 mm, 50 mm and 60 mm were analyzed in the FEA in order to determine which lengths provide full strain transfer to the FBG. The bond layer thickness is the distance from the epoxy embedded fiber to the tip of the concrete notch. It is hypothesized that as bond layer thickness increases, i.e. the fiber moves further away from the notch tip, the strain transfer from the concrete to the fiber will decrease. To test this hypothesis, the strain transfer was analyzed with thicknesses of 0.875 mm, 1.75 mm and 3.5 mm for the V-notch configuration and 1.6 mm and 3.2 mm for the saw-notch configuration. All the bond layer thicknesses were tested for each epoxy bond length giving 18 different configurations for the V-notch and 12 configurations for the saw-notch.

The elastic modulus of the epoxy also has an effect on strain transfer. Studies discussed in the literature suggest that the closer the elastic modulus of the epoxy is to that of the host material (concrete), the better the strain transfer will be. Four different epoxy moduli were used in each of the aforementioned configurations to determine the relationship between epoxy modulus and strain transfer. After researching various epoxies that would be suitable for field applications, the following four elastic moduli were selected: 700 MPa, 1800 MPa, 3000 MPa and 6000 MPa. Each elastic modulus was tested for all the FEM configurations giving a total of 72 configurations for the V-notch and 48 configurations for the saw-notch. The elastic moduli for

the concrete and FBG were modeled as 25,000 MPa and 72,000 MPa respectively. Strain was induced in the concrete part of the FEM by applying an axial displacement to the free end of the concrete. Boundary conditions were applied to enforce symmetry. A perfect bond was assumed to exist between the concrete and the epoxy and between the epoxy and the fiber.

Strain transfer from the concrete over the epoxy bond layer to the fiber is the primary behavior parameter of interest. The strain transfer ratio  $r$  is represented as the ratio of the strain in the fiber to the strain in the concrete at adjacent locations in the model. In addition the strain transfer values at all nodes along the length of the fiber were determined to identify the *effective strain transfer length*  $l_e$  for a given model configuration. The effective strain transfer length is the length along the fiber that is experiencing fully developed strain transfer i.e.  $r = 1.0$ . In order to determine  $l_e$  of each configuration, the strain transfer along the length of the fiber was calculated and plotted.

As a sample of the FEA results, Figure 3.3 illustrates the relationship between strain transfer ratio and the distance from the center of the FBG sensor in the saw-notch FEA model with a 1.6 mm bond layer thickness and the epoxy bond lengths listed above. Each of the haystack-shaped curves in the figure is for a different epoxy bond length. As shown in the figure, an increase in epoxy bond length results in an increase in strain transfer ratio up to a value near 1.0. The haystack curves also flatten out with increasing epoxy bond length to illustrate the length over which full strain transfer occurs. The effective bond length is then defined as the length of the flat portion of the haystack curve. For a given model configuration to be fully effective in terms of strain transfer, the flat portion of the strain curve must be at least 10 mm long, which is the length of the grated sensor region in the FBG. Additional illustrations of the FEA results are found in the report by Maurais (2012).

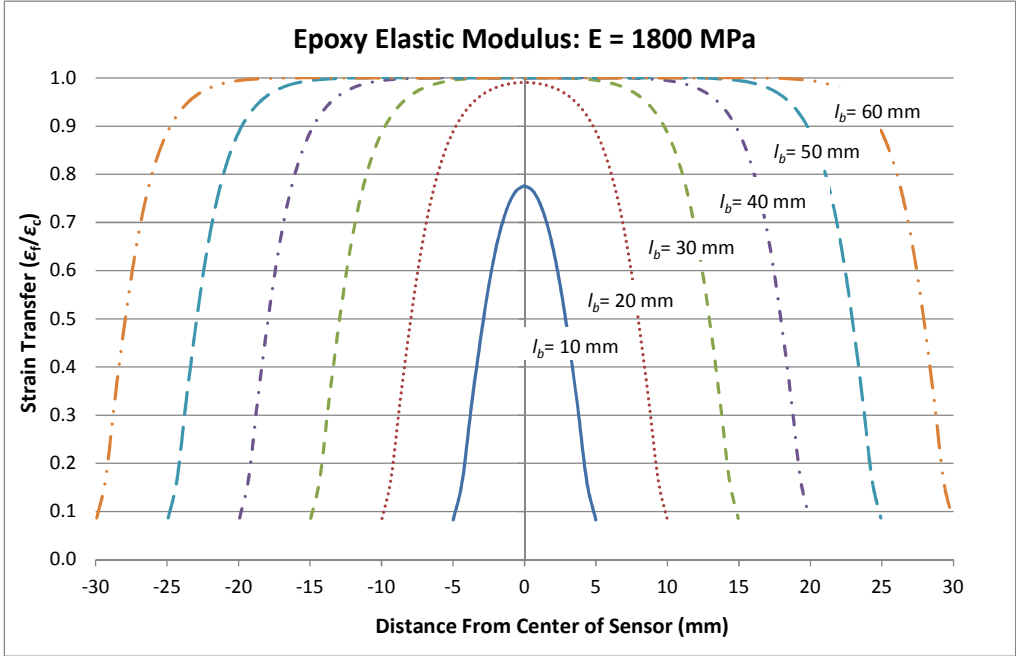


Figure 3.3 – Epoxy bond length comparison, saw-notch, 1.6 mm bond layer thickness

It is interesting to note that the amount by which the strain transfer decreases as bond layer thickens is greater for the V-notch than the saw-notch. This behavior is likely due to the fact that the V-notch is wider with a tapered shape while the saw-notch geometry is narrower and more uniform. The bigger V-notch provides a greater volume of epoxy for strain loss to occur in. The tapered V-notch shape causes the strain transfer to reduce more than the saw-notch as the bond layer thickens.

### **Experimental Study**

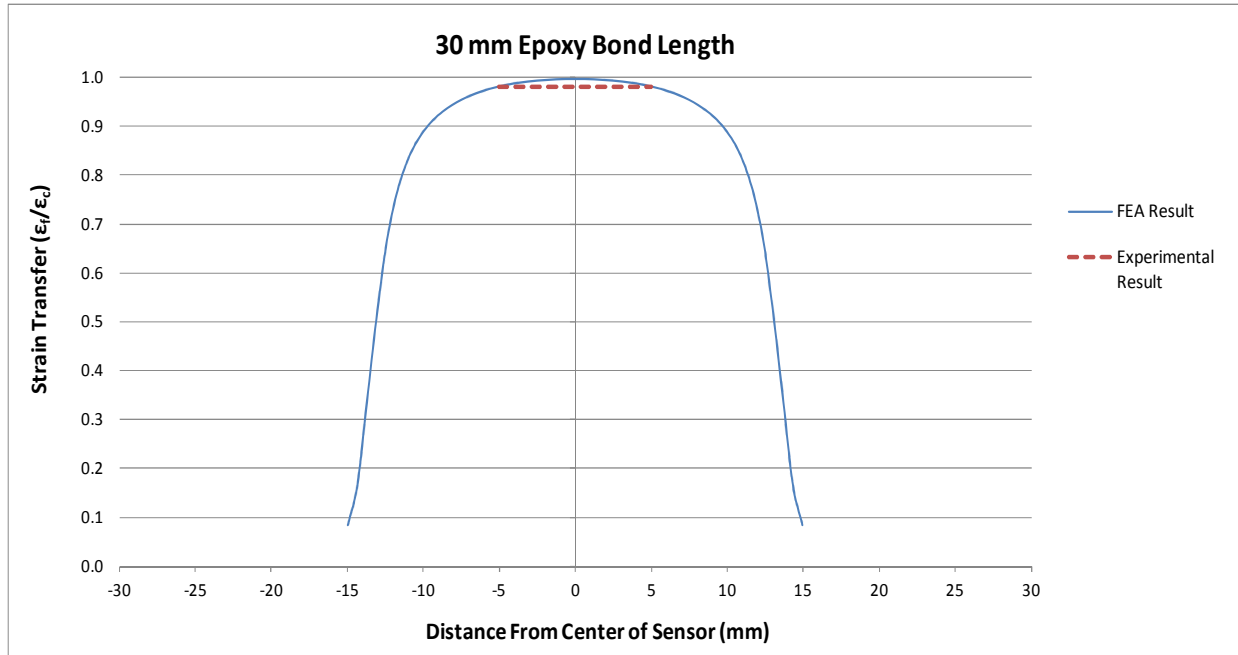
An experimental study was conducted on notched concrete prisms with adhered FBGs and conventional strain gages. The objectives of the tests were to confirm the results from the FEA as well as to develop an FBG application technique suitable for field implementation. Two types of concrete prisms were cast, both having the same dimensions but with different notch geometries. One prism type had V-notches and the other had saw-cut notches, with notch geometries matching those of the FEM. The prism dimensions were 8 in x 4 in x 4 in with one longitudinal notch on each of the four sides as seen in Figure 3.4. The prisms were notched on all four sides so that multiple fibers could be imbedded and tested simultaneously on the same prism.



**Figure 3.4 – Concrete test prisms notches: (a) V-notch (b) Saw-notch**

The FBG strain sensors were embedded into the notches of the concrete prisms in order to observe the strain transfer behavior from the loaded concrete prism to the FBGs. The prisms were axially compressed using an Instron 1332 servohydraulic loading machine. The FBGs were embedded into the prism notches using a common structural epoxy with an elastic modulus of 1800 MPa (Ultrabond 1300 manufactured by Adhesives Technology). Data from surface-adhered conventional strain gages was used to compare with the epoxy-embedded FBG strain data to establish strain transfer rates. The strain measured by the conventional strain gages was taken as the strain of the concrete in the comparison. Additional details of the test set-up and loading protocols are found in Maurais (2012).

Figure 3.5 is representative of the results of the experimental study compared to the FEA results. In the figure, the haystack curve from the FEA V-notch model with 30 mm epoxy bond length, 2.7 mm epoxy bond layer thickness, and epoxy modulus of 1800 MPa is compared to the strain transfer ratio from the companion experimental test. In the figure, the short dashed line represents the experimental strain transfer ratio. The dashed line is a 10 mm line segment, because the strain transfer of each experimental test was taken as a single averaged strain value. The 10 mm segment represents the strain transfer to the 10 mm FBG sensor region that was centered in the epoxy.



**Figure 3.5 – Strain transfer for V-notch,  $E_{\text{epoxy}} = 1800 \text{ MPa}$ , 2.7 mm bond layer thickness**

As shown in Figure 3.5 and in general, the FEA models predict slightly higher strain transfer ratios than the experimental test. A few influencing factors include the assumption of perfect bond in the FEA models, the influence of aggregate size in the concrete creating a nonhomogeneous strain state at the FBG sensor, the use of form oil on the concrete surface which might soften the bond between the epoxy and the concrete. Nevertheless, the experimental results match well with those from the FEA models, confirming that FEA modeling can be used reliably to predict the strain transfer behavior of notch-embedded FBG sensors in concrete.

## Bonding to a Steel Host

Verification of the strain transfer behavior of FBG sensors when adhered to a steel host was performed experimentally on a small four-point bending specimen (S3x5.7 cross section). The basis of comparison of FBG performance was that of traditional foil strain gages (TGs).

Micron Optics os3120 FBG sensors were selected for application with the steel host material. These sensors were chosen because they are protected by a steel carrier, installed easily with an epoxy, and used frequently in the field. This approach is beneficial as opposed to a spot welding model, because field welding on WYDOT bridges is prohibited. Micron Optics provides the following performance properties for the os3120 gages (Micron Optics, 2010a):

- Strain sensitivity  $\sim 1.4 \text{ pm}/\mu\epsilon$
- Gage length = 22 mm
- Operating temperature range =  $-104^\circ$  to  $248^\circ \text{ C}$
- Strain limits  $\pm 2,500 \mu\epsilon$
- Fatigue life =  $100(10^6)$  cycles,  $\pm 2,000 \mu\epsilon$

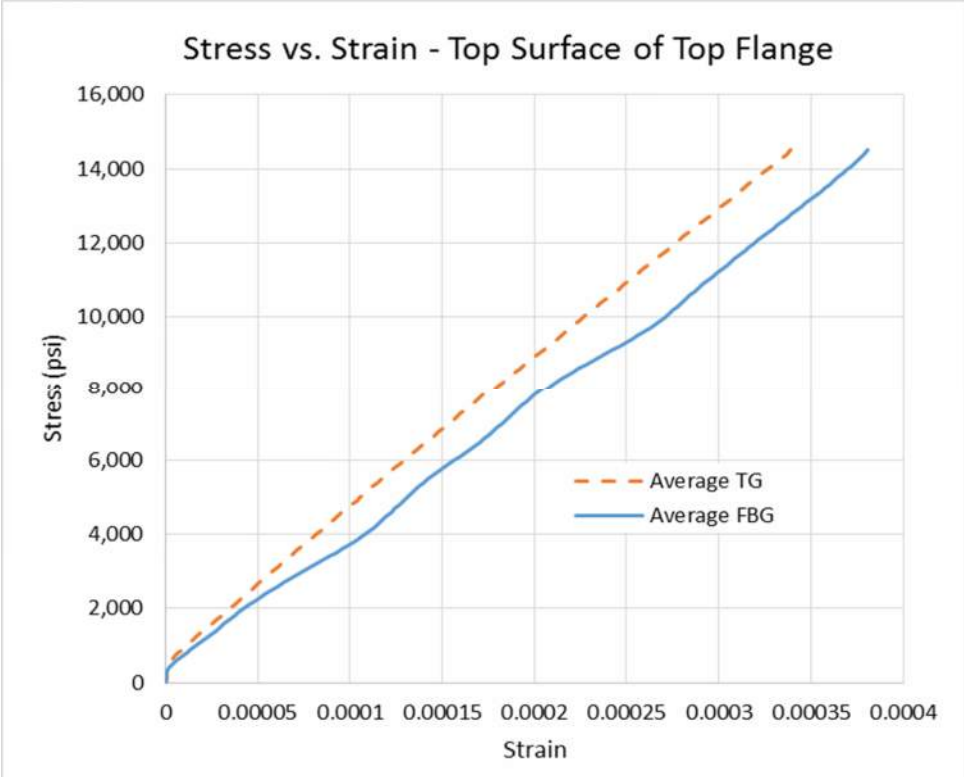
Both FBG and TG sensors were adhered to the steel specimen using Micron Optics recommended procedures. Sensors were placed at the following locations on the S3x5.7 beam specimen:

- Set 1: On the top surface of the top (compression) flange at midspan over the web
- Set 2: On the bottom surface of the top flange at midspan near the tips of the flanges
- Sets 3 & 4: At middepth of the cross section between load points and support points, oriented at 45-degrees from horizontal to measure shear strain
- Set 5: On the top surface of the bottom (tension) flange at midspan near the tips of the flanges
- Set 6: On the bottom surface of the bottom flange at midspan over the web

Additional details of the test specimen, set-up, and loading protocol are found in the thesis report by Danforth (2015).

Test results are mixed, in that, at a given load on the beam, in some cases the FBG sensors recorded higher strains than the TG sensors and other cases the FBG sensors recorded lower strains. As a representative illustration of the test results, Figure 3.6 contains the stress-strain curves for the FBG and TG sensors in set 1 – on the top surface of the top flange (loaded in compression). At a given applied stress, the FBG sensors record higher strains than the TG sensors. Nevertheless, the two curves track fairly uniformly and nearly linearly. Accuracy in placement of the sensors on the relatively small test specimen is the likely reason for the differences in behavior. However, in all cases, the results from the FBG sensors are reasonable and provide confidence that they will perform adequately in a field application.





**Figure 3.6 – Stress-Strain Comparison, Steel Specimen**

## **CHAPTER 4 – INSTRUMENTATION PACKAGE**

Task 2 involved development of a low-cost, compact, and energy-efficient instrumentation package for interrogating the sensor network. The approach involved a combination of design and fabrication of custom instrumentation linked to commercially available components with proven reliability. This approach achieved a balance among cost, reliability, and ease of maintenance and replacement.

A commercially available interrogation system was selected for proof of concept laboratory testing. A two-channel SmartScan 02 Lite FBG interrogator developed by Smart Fibres was purchased to interrogate the sensor network in the laboratory. The only other resources required in the laboratory are a standard Windows-based desktop computer and an internet connection.

For field application, we selected the four-channel FS2200XT BraggMETER from FiberSensing. The FS2200 extended temperature interrogator features high bandwidth, programming capabilities, Ethernet interface, and ability to handle harsh Wyoming weather. A custom microcontroller system to operate the BraggMETER interrogator was developed and implemented specifically for unattended, remote deployment at a bridge site. Details of this system are presented in the following chapter.

## CHAPTER 5 – DATA COLLECTION AND PROCESSING

Task 3 involved development of data collection, processing and transmission capabilities. An FBG sensor network on a bridge will have the capacity to collect an overwhelming volume of data, so much so that data storage and transmission could easily become a constraining bottleneck to the performance of the network. Compounding this problem, the need to sift through the huge amounts of data to locate and use behavior parameters of interest would be an overwhelming and tedious task for bridge engineers.

The first step in dealing with this challenge is to develop an interrogation control system that activates the SHM network interrogator only when needed and successfully stores the network data. Unattended operation of the system is essential to eliminate the need for DOT personnel to be at the bridge site with permit vehicles or other extreme events occur. A microcontroller system was developed as part of this research that satisfied the preceding first-step requirement.

Since Phase I of the research did not include deployment of the SHM network on a prototype bridge, it was not feasible to pursue further development of a real-time data processing and transmission capability. Such development will be specific to the particular bridge location, access to data networks, electrical power, and the performance parameters that are critical for the bridge. Hence continuation of this task must become a component of Phase II of the envisioned future research. That is to say, it was not possible to develop a general performance specification for real-time data analysis of an arbitrary bridge. Instead site-specific specifications must be developed in cooperation with bridge engineers at WYDOT. Subsequent design and implementation of software to satisfy the performance requirements will complete this task.

For Phase I of this research, an Ethernet-to-SPI (Serial Peripheral Interface) data link was established to the microcontroller from the interrogator through two Olimex mod-enc624J600 boards, which are comprised of Microchip's ENC624J600 10/100 Base-T Ethernet controller. The established SPI connection allows access and discrimination of streaming raw data through the use of an Atmel ATXMEGA64A3 microcontroller. The microcontroller was programmed with firmware triggers based on predetermined parameters in order to alleviate data bottlenecks and over-storage that inevitably occur as a result of transmission speed differences between the interrogator and the ethernet transmission device, as well as storage limitations associated with the unsegregated collection of data. Local post-filtered data storage was accomplished by an SD-card board also supplied by Olimex.

When the system is deployed for field application, it will have the capacity to implement remote data storage by software on a dedicated computer or server as data is received through the ethernet module. Two examples of Ethernet modules considered include radios or cellular gateways. Two cellular internet gateway modules have been considered: the OnCell G3150 by MOXA and the Airlink Raven XT by Sierra Wireless, which was recommended by Mr. Keith

Tupper with WYDOT. Both systems are suitable for industrial Supervisory Control and Data Acquisition (SCADA) applications. The selection of the gateway will be determined when the system is deployed in the follow up project. The connection from the microcontroller to the cellular module will be accomplished through an SPI connection using another Ethernet controller, which converts the SPI signals back to Ethernet for transmission.

Also of major importance is selection of a suitable power source from which the previously mentioned instrumentation will draw. Two primary methods have been considered. One option, assuming the equipment will be located close to a power grid source, is to connect directly to the grid. The second method under consideration would be the implementation of a solar panel with a bank of batteries.

Finally, a novel triggering mechanism has been developed to initiate data collection from the sensor interrogator and network. We have selected a radio frequency identification (RFID) tag reading system that employs passive RFID tags in the overweight vehicle to activate the data acquisition system. This approach will facilitate live, unscheduled collection of data for all permitted vehicles. The RFID tag can be placed in the cab of the permitted vehicle at the port of entry. Then the SHM system will automatically detect and record passing of the vehicle over the bridge. Bridge response data will be collected and transmitted as required to facilitate analysis of bridge response to the passing vehicle. The RFID system, supplied by Convergence Systems Limited, has been integrated with the microcontroller to activate data recording from the interrogator. For the system to function as intended, the interrogator must remain continuously active.

## **Microcontroller and RFID Triggering System**

One challenge with managing a continuous, long-term bridge monitoring system is collecting, storing, and prioritizing the copious amounts of bridge response data. The RFID triggering system was developed as a method to prioritize the collection and storage of data by triggering the system with a predetermined and recognizable vehicle. The triggering is important because storing continuous strain data can result in an unmanageable amount of information to be stored or to be passed through a cellular modem. The outcome of the system would provide the means to collect and store only the meaningful FBG strain data.

### **System Overview**

The RFID system operates by transferring information using radio-frequency electromagnetic fields, utilizing a transponder that wirelessly transmits data to and from the tags. In this specific application, RFID reader and antenna combinations, or transponders, will be installed at a weigh station at a Wyoming port of entry and at the bridge of interest. At the port of entry, the permitted truck information, including the axle weights and configuration, will be assigned to an RFID tag with an identification code. The tag would then be placed on the windshield of the

vehicle. At the bridge, a different transponder will detect the presence of the RFID tag and will trigger the data acquisition system to store the bridge strain data while the permitted vehicle passes over the bridge. The following subsections describe the process in detail.

The first transponder should be placed at a Wyoming port of entry. Along with detecting the presence of a tag, the transponder has the capabilities of writing specific information to a tag, enabling a transponder to read the data from the tag at a different point in time. All permitted vehicles are required to stop at the ports of entry when crossing over the state line to assure that they remain in compliance with their specified axle loads and gross vehicle weight requirements. When a permitted vehicle is weighed, it will be assigned a tag encoded with a vehicle identification number. At the weigh station, the axle weights, gross vehicle weight, and axle configuration will be determined. This information can then be entered into a database and associated with its assigned vehicle identification number. The vehicle will then travel across the highway with the tag in the vehicle.

When a tagged vehicle approaches an instrumented bridge and the tag is within range of the transponder, the transponder will send a signal to the data acquisition unit on the bridge to activate the data storage. The transponder will read the vehicle identification number written on the tag and send its information and the bridge's response to a database.

The FBG interrogator will be powered on and will interrogate its FBG sensors continuously. Once an RFID tag has been identified, the transponder will send a signal to the data acquisition unit to begin data storage and transmission to the server. The data system will collect and record data for an allotted time period. This system will provide controlled data collection because it is triggered by the presence of a tag in a permitted vehicle. It will also limit the amount of data to analyze because only data from permitted vehicles crossing the bridge will be collected. As the system develops, additional triggering features may be considered, for example when a certain strain threshold is reached.

The data collected from the interrogator will be stored on an external hard drive. The extent of required storage space will depend on the duration over which data for a vehicle is recorded, the number of sensors on the bridge, the sensor scan rate, and the frequency of triggered traffic events. As the RFID development continues, the storage must be sufficient to store strain measurement data until cellular data transmission is established.

Data transmission will be implemented by means of a cellular module. The FBG strain measurements will be temporarily stored on an external hard drive, and then after the triggered event occurs, the database would receive the bridge response data. To provide a secure connection, Verizon Wireless recommended the Feeney Wireless Skyus and the Option Cloudgate as suitable options.

The data will be transmitted through the cellular network to the database. The RFID identification number assigned to the permitted vehicle at the weigh station with the axle loads and configuration will correlate with the same identification number recorded at the bridge site with the bridge response data. This would form a single case that contains the vehicle identification number, vehicle axle weights, vehicle gross weight, vehicle axle configuration, the time the vehicle passed over the bridge of interest, and the bridge strain measurement data. The vehicle load effects can then be associated with the measured structural response data obtained from the FBGs.

The database will work in conjunction with software to provide limited access to the combined vehicle and bridge information. Individuals, such as WYDOT bridge engineers, will be able to log into the database to view the most recent bridge activity. This software will allow the bridge owner to perform the necessary analysis procedures, whether they be load rating procedures, permitted vehicle hysteresis, or long term monitoring to determine changes in bridge behavior.

### **Instrumentation Design**

The instrumentation was developed in collaboration with an electrical engineer, Mr. James Branscomb. Field instrumentation necessary for the discrimination of bridge strain data based on identified permitted vehicles primarily relies upon a robust FBG sensor interrogator, Ethernet controller, data processing microcontroller, data storage module, cellular transmission module, reliable power source, RFID transponder, and RFID tags.

As discussed earlier two Olimex mod-enc624J600 boards create the Ethernet to SPI data link from the interrogator and cellular network to the microcontroller. The boards' main components are Microchip's enc624J600 10/100 Base-T Ethernet controllers.

By using the Ethernet controller to form the SPI connection, the Atmel ATxmega64a3 microcontroller is able to receive continuous strain data from the FBG interrogator. The microcontroller allows the user to define which parameters will trigger the data storage of field measurements. As of now, the detection of an RFID tag is the trigger for storing the field test data.

As previously mentioned, two cellular modules, as advised by Verizon Wireless, were explored. A second Ethernet controller will be used to link the microcontroller and the cellular module. The purpose of the controller is to convert SPI signals back to Ethernet so that the field strain data can be directed through the cellular network.

The current system development consists of a printed circuit board (PCB) containing two Ethernet controllers, microcontroller, programming port, voltage supply and regulator, LED indicators, and general purpose input/output (GPIO) pins to be used for future programming. Detailed descriptions of the PCB along with images are found in Danforth (2015).

Solar panels would be effective power sources for the RFID system for a few reasons. Bridges in Wyoming are often located in remote areas, so access to power supply is limited. The Wyoming weather conditions often provide enough sunlight to power various electronic devices, for example the variable speed limit signs use this technology. Also, solar panels are economically feasible and are practical to install.

The RFID system that triggers the microcontroller consists of three main physical components: an RFID reader, antenna, and tags. The CS203ETHER Integrated RFID reader both reads and writes information to the tags and transmits data. It is designed to withstand extreme weather conditions, including water and dust, with a high read rate. The RFID antenna communicates with the tags using radio frequency signals. The antenna has a range of approximately 9 meters, however it can be coupled with an additional IP67 antenna for extended radio frequency range. The reader and antenna have thus far been referred to as the transponder, as they are physically enclosed in one unit that can be powered through an Ethernet connection.

The CS6710 Windshield RFID tags are each assigned a unique identification number, and they can store data transmitted from one transponder that can be read by another transponder at a different location. The tags are designed to be coupled with the CS203 integrated reader and placed on the inside of cars, buses, and trucks. The tags are passive, meaning that they do not require batteries in order to communicate with the reader and antenna and are more economical than active tags that need batteries.

### **System Validation Procedure and Results**

Field tests for the triggering mechanism validated the performance of the RFID system components. The validation procedure was considered successful when the RFID transponder recognized the presence of the RFID tag in an approaching vehicle, recorded the tag identification number, and triggered the storage of FBG strain data for a predetermined amount of time. This procedure was designed to test the system for a possible deployment project, so the focus was to demonstrate the capabilities of the triggering mechanism to provide a basis for future work.

Two operational modes were developed for the system: software and hardware. The software mode required use of a laptop computer that commands the microcontroller to store strain sensor data. This mode was utilized for field tests. Having a laptop in the field is not ideal, because it cannot handle extreme weather conditions, requires additional space in a weatherproof enclosure, and calls for an increase in power supply. The hardware mode was developed to prevent this scenario, and if the hardware mode is used, the laptop is not needed in the field. The hardware mode was under development at the time of testing; therefore, the software mode was used for field tests. However, the hardware mode has since been systematically validated, and it will be functional for field tests in the future.

The RFID triggering tests were performed on Highway 17 (Roger Canyon Road) north of Laramie. The equipment was powered by means of a vehicle using a power convertor. Highway 17 has two lanes that are each 11-feet wide, unlike interstate lanes that are typically 12-feet wide. The distance from the edge of the lane to the transponder was 6-feet, and the distance from the ground to the bottom of the transponder was also 6-feet. The transponder was on the south side of the highway facing west. The RFID tag that was placed in the car was 5-feet above the ground.

The tests were organized so that the initial positioning of each RFID component was established prior to testing the system at full speed, including the position and direction of the RFID transponder, RFID vehicle, and RFID tag. For all tests, the vehicle was driven in the east direction toward the transponder. Each time the transponder detected the tag, the FBG strain data from three sensors were recorded for the allotted 30-second time frame.

The horizontal direction to which the transponder would detect the tag most effectively was determined by three different arrangements. The tag was placed in the upper left-hand corner of the windshield, and the vehicle travelled at 65 MPH.

First, the transponder was faced parallel to the oncoming vehicle, or straight toward the tag. This method was successful when the vehicle travelled in the closest lane, however the transponder did not detect the tag when the vehicle was in the farther lane. Second, the transponder was directed perpendicular to the road. This angle was effective for the vehicle in the farthest lane, however it did not trigger when the vehicle was in the closest lane. Third, the transponder faced the northwest direction at a 45-degree angle. When the vehicle was located in the closest and farthest lanes, the transponder identified the tag and triggered the data to be saved onto a file.

The position of the transponder from the ground also varied throughout testing. It was determined that the system was triggered occasionally at a height of 5-feet, consistently at 6-feet, and rarely at 7-feet. Clearly, this distance will alter depending on the height of the tag target for permitted vehicles in future testing. Additionally, the transponder was initially located at a distance of 8-feet from the edge of the lane, however the distance was decreased to 6-feet for reliable triggering. The vertical angle that the transponder was directed was not tested because it is a feature that should be considered based upon the setup of the system in the future.

To determine the range from the transponder to the tag, the tag was placed in the upper left-hand corner of the vehicle windshield. The transponder was directed at a 45-degree angle northwest. The vehicle was located in the lane closest to the transponder and travelled at a speed of 10-MPH. The transponder detected the presence of the tag when the vehicle was approximately 10-feet from the reader, measuring parallel on the road. The vehicle then travelled in the farthest lane, again headed east. With the tag farther away, the transponder detected the tag when the vehicle was in line with the reader, or at zero feet parallel on the road.



The tags were designed to be placed on the inside of a vehicle's windshield. For the field tests, the tag was initially placed on the upper left-hand corner of the windshield. The vehicle was driven at 65-MPH in the closest lane, and the transponder detected the tag six out of six times consecutively. The vehicle was then driven in the farthest lane with the same tag positioning, and the tag was identified in two out of four runs. As a result, an additional tag was added to the upper right-hand corner of the vehicle. The transponder then detected the tag two out of two times while the vehicle was in the farthest lane. This test suggests that the maximum perpendicular distance for consistent triggering is approximately 18-feet, and inconsistent triggering occurs at a distance of 28-feet for a system using one antenna.

Up to this point, the positions of the transponder, vehicle, and tag were established, and the outcome of the three tested parameters had to be confirmed. The transponder was angled at 45-degrees facing the northwest direction; the vehicle was located in the farthest lane to test the worst-case scenario for vehicle placement; and the tag was placed in the upper right-hand corner of the windshield. The vehicle was driven at 65-MPH, and the transponder recognized the tag, triggering the data saving system six out of six times. These tests were sufficient to determine that the RFID triggering system functioned as intended.

After the vehicle event was triggered, the FBG strain measurement data automatically saved to a file onto the computer hard drive. The file included the wavelength readings, tag identification number, date, and time, respectively. The wavelength readings were recorded from three of the four available interrogator channels, where one FBG was located on each channel. The sensors were not the focus of the field tests nor were they adhered to a host material affected by traffic events, so the readings fluctuated only slightly due to noise and marginal temperature variations.

## CHAPTER 6 – LABORATORY VALIDATION

Task 4 was initially intended to validate tasks 1, 2 and 3 in the laboratory. However, it became feasible and more efficient to validate only task 1 in the laboratory and to prove the function of the systems developed in tasks 2 and 3 independently, as described in the foregoing chapters. To validate task 1, a laboratory model of a bridge was designed and constructed. The model bridge consisted of two girders that were vertically supported at four points resulting in a three-span continuous configuration. Utilizing a three-span design allowed for the measurement of bridge behavior undergoing positive and negative bending. In order to develop techniques for sensing both steel and concrete structures, one girder was constructed of a wide flange steel beam, and the other utilized a post-tensioned concrete beam.

The design of the experiment was loosely modeled after a three-span bridge on Interstate 80 between mile-posts 310 and 311 west of Laramie, Wyoming. Analysis of this bridge provided some approximation of the magnitude of measurements that will be required of the resulting system. The field study will provide an opportunity to field test the methodology developed in this study.

### Laboratory Model

The I-80 bridge that was modeled in the lab consisted of a three-span, continuous, non-composite steel girder design, utilizing W33x130 rolled-section girders spanning 40.5 feet, 50.5 feet, and 40.5 feet for a total length of 131.5 feet. A girder-line model of this bridge was developed using SAP2000 (Computers & Structures, Inc 2011) finite element structural analysis software and the model was analyzed for an HL-93 design truck, where it was assumed that one-half of each axle load would distribute to the beam-line, and no lane load was applied. Service-level loads were used to demonstrate that the SHM system will be capable of measuring the structural response of a bridge under elastic conditions. Based on this loading, the maximum curvature in the bridge was found to be  $0.000287 \text{ ft}^{-1}$ , corresponding to a maximum strain in the extreme fiber of the cross-section of  $792 \text{ } \mu\epsilon$ .

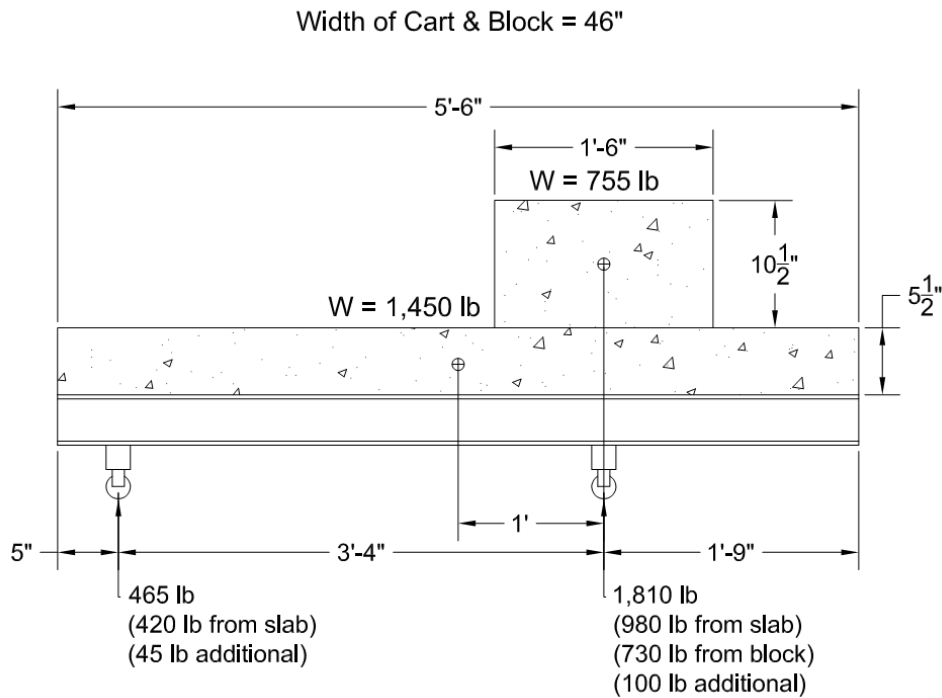
The laboratory experiment was designed to achieve the same maximum strains as those determined from analysis of the I-80 highway bridge. Due to constraints on support locations for the laboratory bridge, the span ratio for the laboratory setup was modified slightly, and the laboratory beams spanned 9 feet, 12 feet, and 9 feet for a total length of 30 feet.

A small cross-section rolled wide flange beam (W4x13) was used to form one girder for the laboratory bridge. A post-tensioned concrete beam was sized to produce approximately the same flexural rigidity as the steel beam while providing adequate strength to carry the required loads. The resulting section was a rectangular beam 6 inches deep by 4.5 inches wide. Use of a pre-

stressed beam allowed the beam to undergo the desired curvatures for the experiment while still supplying adequate strength to carry the necessary loads.

Based on the flexural rigidity of the steel section, the load necessary to induce a strain in the extreme fiber of the section equal to that predicted by the analysis of the highway bridge mentioned above was calculated by scaling the loads according to the section depths and resulting curvatures. The scaling process resulted in load applied to the laboratory bridge roughly equal to 6% of the load on the I-80 bridge from the HL-93 design truck.

The load cart consisted of a concrete block, a concrete slab, two mounting beams, four load cells, and four non-swiveling V-notched casters. The concrete block was placed directly above the rear wheels. A schematic of the load cart design is shown in Figure 6.1. Figure 6.2 shows the constructed laboratory experiment with the load cart, steel and concrete beams, and the support locations.

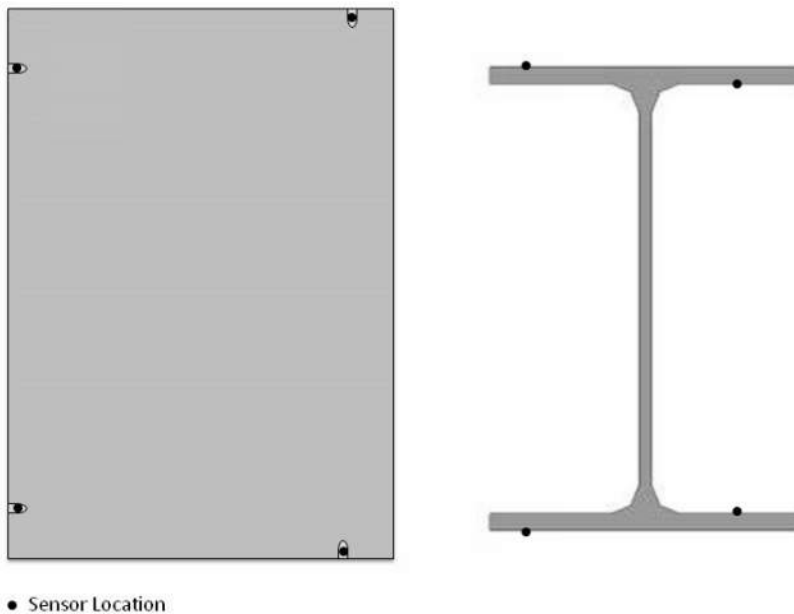


**Figure 6.1 – Schematic of Load Cart for Laboratory Test**

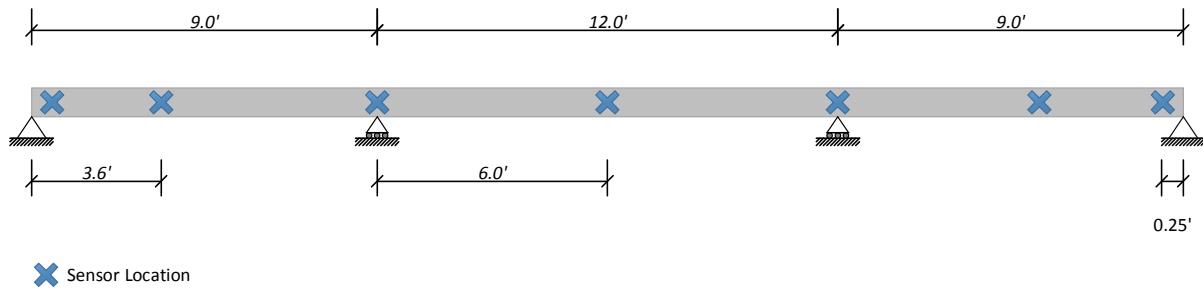


**Figure 6.2 – Laboratory Test Setup**

Fifty-six FBG sensors were installed on the beams for the laboratory experiment. For each beam, four sensors were installed about each beam cross-section at seven locations along the span of the beam. Figure 6.3 shows the sensor placement on the cross-section of each beam, and Figure 6.4 shows the locations of the sensors along the length of the beams.



**Figure 6.3 – Sensor Locations on Beam Cross-Sections**



**Figure 6.4 – Sensor Locations Along Beam Length**

On the cross-section of the beam, sensors were placed at the extreme fibers of the section for strong-axis bending to measure the curvature of the beam and the neutral axis depth. Measuring strain at the extreme fibers allows the strain sensors to read larger measurements for the same value of curvature.

Typically, three-span bridges achieve the maximum load effects due to bending over the supports, at mid-span of the middle span, and at approximately 40% of the span in from the end supports on the exterior spans. This rule of thumb is reflected in the AASHTO LRFD Design Specifications (2012) in the section discussing the calibration of the HL-93 live load and load factors and was echoed in discussions with WYDOT officials regarding points of interest for curvature measurement. Therefore, these locations were selected to take measurements on the bridge. The sensors placed at the end supports allowed for the measurement of rotational fixity in the supports, and the sensors located between the supports aided in determining the stiffness parameters of the beam.

The span configuration was modeled in SAP2000, with a moving unit load used to determine the analytical curvature envelope for the laboratory structure. The maximum positive load effects in the first and third spans would have occurred near the sensors placed at the 1.04 and 3.06 span locations. According to the simulation, the curvature at the maximum locations in the exterior spans was 3.52% higher than the curvature at the sensor locations. For the middle span, the analytical model calculated that the maximum positive curvature would occur at the mid-span where the sensors were located.

The analytical models indicated that the maximum negative load effects would occur over the supports for the structure, as would be expected. Sensors were placed as near to the ends of the beams as possible to measure any curvature due to rotational fixity in the end supports. For the steel beam, sensors were placed within 2 inches of the end. However, sensors on the concrete beam needed to be moved in approximately 8 inches from the ends due to requirements for strain averaging and adhesive development length. Because the sensors in the tests were inset along the span due to interference from connections, they could only measure the moment near the ends of the beam, but not at the ends. However, as the analytical moment distribution was linear for the loading, the curvature at the end of the beam was found by linearly extrapolating from the values at the sensor locations.

## Multiplexed Sensor System Design

For a multiplexed FBG system, a sensor plan should be carefully developed prior to installing any sensors, to ensure that the operating wavelength spectrum of each channel of the interrogator is efficiently utilized. The operating spectrum of an interrogator is often the largest constraint on the number of sensors that can be effectively multiplexed, and interrogators with wider spectra or more channels will incur significant costs.

Therefore, consideration must be given to the wavelength range that multiplexed sensors will experience under operating conditions. If the reflected peaks from two FBGs on the same channel overlap during operation, interrogators cannot differentiate the light returning from the two sensors, and the reflected light will register as a single peak returning from a single FBG. This overlapped peak confuses the data collection, and renders those sensors ineffective. This problem occurs if the unstrained FBG peaks are not spaced far enough apart on the wavelength spectrum to allow for the wavelength shift caused by the strain conditions.

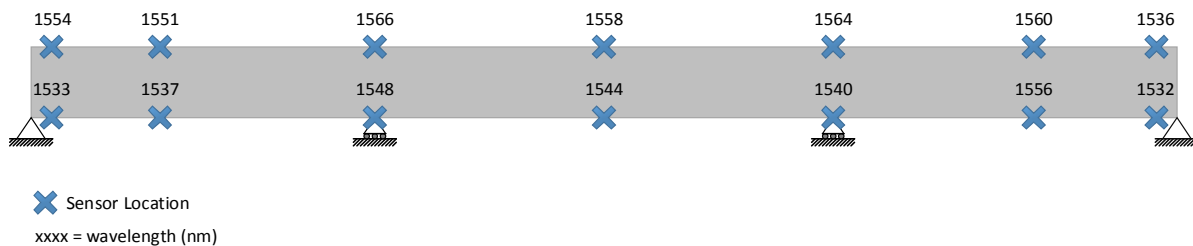
The wavelength spacing can be adjusted by applying different magnitudes of pretension to the fibers while they are being adhered to the structure. Enough pretension can be applied to a fiber to cause a wavelength shift of about 4-nm without causing concern for over-tensioning the fiber during the FBG installation.

To prevent overlapping peaks, preliminary analysis of the expected structural behavior should be performed to determine the appropriate location and pretensioning necessary to place multiplexed FBGs with adjacent wavelengths. The maximum shift on the light spectrum will be dictated primarily by the maximum strain that the fiber will undergo while in operation. For a maximum strain of 0.003, the corresponding shift in wavelength is approximately 4nm.

The maximum expected wavelength shift due to strain provides an estimate on the necessary spacing between wavelength peaks, but one must be judicious in spacing FBG wavelengths to also maximize the number of sensors that can be multiplexed onto a single channel. In areas of the structure where large strains are unlikely to occur, the wavelength spacing may be reduced. However, if two fibers possess adjacent wavelength peaks on the spectrum and are likely to experience concurrent opposing strains (one fiber undergoing positive strain, while the other experiences negative strain), bringing the wavelength peaks toward each other, then the wavelength spacing between them should be increased appropriately. Care can be taken to place FBGs with adjacent wavelengths in areas of the structure that will undergo concurrent strains in the same direction allowing for a reduction in the wavelength spacing.

A sensor plan that maps the locations of the FBGs on the structure with their corresponding wavelengths helps to design an effective layout for the FBG sensors that can efficiently utilize

the operational spectrum of the interrogator. System designers must determine appropriate wavelength spacing for the strains expected in the structural locations being measured. A sample sensor plan, which was used in the laboratory experiment design, is provided in Figure 6.5. In the figure, sensor locations are indicated with the letter X and the four-digit numeral indicates the wavelength of the sensor in nanometers.



**Figure 6.5 – Sensor Placement for Concrete Beam**

## Temperature Compensation

FBG sensors are sensitive to changes in temperature and are not self-compensating for temperature variations. Therefore, it is necessary to separate the wavelength shift due to temperature variation from the wavelength shift due to mechanical strain in the host material. While the relationship between temperature and wavelength shift is well established, measuring temperature introduces complexity to the system. It is easier to measure the temperature effect on wavelength directly by using an FBG that is isolated from mechanical strain, and directly subtracting this apparent strain from the other bonded sensors on the structure to determine the resulting mechanical strain. The computations for this procedure are outlined in detail in Jung (2015).

To measure the thermal effect on FBG readings, it was necessary to develop a method for isolating an FBG sensor from mechanical strain while providing adequate protection to ensure durable operation. To achieve this, an FBG sensor was inserted into a protective heat shrinking tube, which is typically used for protecting splices in optical fibers. Using a heat source, one of the tips was heated until it shrank and secured a bond with the fiber. Then the fiber was compressed to induce a buckled shape inside the protective sleeve. Finally the other tip was heated to lock the fiber into place while being careful to maintain the buckled shape. The resulting protective sleeve was pinched at the ends, and a gap remained in the middle to allow the sleeve to expand and contract as temperature fluctuates without inducing mechanical strain in the fiber.

## Sensor Installation, Protection and Repair

In adhering the fiber Bragg gratings to bridges, care must be taken to ensure good strain transfer and reliable readings. The fibers need to be aligned along the desired axis of strain measurement,

and it must be ensured that the fibers are securely attached to the host material without any slack or buckling in the fiber across the sensing region. Slack and buckling in the fiber is prevented by applying a slight pretension to the fiber while adhering it to the host element. While a nominal amount of pretension is necessary to ensure a sensor is installed straight and with a good bond, the specific amount of pretension necessary will be dictated by the wavelength required by the sensor plan. Care must be taken not to over-tension the FBGs, as they can be brittle and have a tendency to break across the sensing region, which is slightly weakened during the manufacturing process (Li, Ren and Li 2012). Therefore, when ordering FBGs it is important to order sensors with base wavelengths that vary all across the effective spectrum of the interrogator.

Separate methods were developed for installing, protecting, and replacing FBG sensors for steel and concrete structures. The specific methodology is detailed in the following subsections.

### **Installation on Steel Elements**

As steel is a homogeneous material, the strain sensor can be adhered directly to the region where measurement is desired. It was determined that adhering an FBG directly to the surface of steel elements using cyanoacrylate adhesive achieves satisfactory strain transfer. This was shown in previous work (Maurais 2012), where an FBG was adhered to a steel dog-bone specimen that was also instrumented with a traditional foil resistive strain gage and subjected to cyclic axial loading. The average discrepancy in strain measurements between the FBG and the strain gage at the peak load was 0.13%, demonstrating that this method of adhering FBGs produces strain readings comparable to commonly accepted practices for traditional strain gages.

The specific type of adhesive used for the installation procedure on this project was a thickened fast curing cyanoacrylate adhesive called Lightning Bond™, which comes with an activator spray that accelerates the curing process. Loctite™ produces a similar product. Applying the FBGs to the steel material with the proper pretension requires methodical precision. The method devised for achieving an adequate bond with the appropriate pretension is as follows:

1. Remove any mill scale or paint using a grinder or wire brush. Then clean the material surface, removing all oil, and slightly roughen it with sand paper.
2. Carefully mark the location to be measured on the element and draw a straight line along the axis of measurement. Then position the fiber along the axis of measurement so that the FBG region of the fiber is positioned at the location of interest. Tape one end of the fiber to the structure to aid in aligning the fiber for the next step.
3. Apply the cyanoacrylate adhesive approximately 2 inches away from the sensing region along the axis of measurement. Set the fiber into the adhesive so that the FBG is aligned and positioned correctly and spray the activator over the adhesive region to accelerate the curing process. Hold the fiber in place until the adhesive cures (about 30 seconds).
4. Once the adhesive has cured apply the cyanoacrylate adhesive to the region to be measured ensuring a minimum adhesive length of 1.5 inches. Then, gently adjust the tension on the fiber until the target wavelength is achieved. Next, press the fiber against the steel so that it is aligned with the axis of measurement and in good contact with the



adhesive. Hold the fiber steady, ensuring that it is tensioned to the appropriate wavelength, and apply the activator to the adhesive. Hold the fiber in place until the adhesive cures (about 30 seconds). (As an alternative to manually holding the fibers in place while the glue cures, a pair of flat clamps or strong magnets may be used to hold the fiber in tension against the steel member. For this approach, the fiber should be protected from the clamps or magnets using a thin piece of rubber or similar cushioning material. Prior to applying the activator spray, verify that the pre-tension is stable by monitoring the wavelength for any change.)

5. Slowly release hold of the fiber while monitoring the wavelength for any significant drop in wavelength. If the wavelength of the applied FBG fails to stabilize at a higher wavelength than the base wavelength, then adequate bond has not been achieved. If a satisfactory bond is not achieved, refer to the subsequent replacement procedure.

Variations on these methods were tried during the installation of sensors on the laboratory structure as the procedure was refined. The devised attachment method was generally effective. Out of the 28 sensors installed on the steel beam, three experienced a loss of pretension greater than 25% between the time of installation and the time that test were performed. For the remaining sensors, the average pre-tension loss was 10%.

### **Protection on Steel Elements**

For steel material it was decided that covering the fiber with a rugged, durable tape would be the simplest method for providing protection. The tape provides adequate protection and also holds the fibers in place. Fiber with the additional plastic protective coating should be spliced between FBG sensors to provide further durability under the tape. Various tapes were investigated for their bond quality, weatherproof capability, and ability to provide protection. A modified butyl rubber tape produced by Permatite™ was selected as the best option. It is rated for exterior exposure with a temperature range from -40°F to 250°F and a watertight seal. The tape is approximately 1/8" thick with a soft rubber-clay consistency, and it is available in various widths. The tape bonds well to steel, although no long term environmental exposure tests were performed. The steel should be clean and free of mill scale and oil prior to applying the tape.

### **Repair on Steel Elements**

If a fiber breaks on a multiplexed channel, then the signal from all FBGs beyond the break will be lost. The location of the last FBG reflecting a signal back to the interrogator can be used to locate the break in the optical fiber, as the break will be located somewhere between this last reporting FBG and the next sensor on the fiber. To replace the damaged fiber, at least one foot of the protective tape must be removed from each side of the break to allow enough slack in the fiber to perform a splice. In regions where the lead fiber is protected by the additional sleeve, the tape can be carefully removed with a putty knife. In regions where the fiber lacks this protective sleeve it will be difficult to remove the tape without breaking the fiber.

If the break occurs near a sensor, where a fiber cannot be repaired by simply splicing in an additional length of fiber at the break, the damaged fiber will need to be removed and replaced.

Once the tape has been removed, a putty knife or a razorblade can be used to scrape off the old fiber and adhesive. Sandpaper should be used to re-clean and roughen the surface. Then the new FBG can be spliced and installed according to the preceding installation instructions.

## **Sensing Concrete Elements**

### **Installation on Concrete Elements**

The method developed and tested by Maurais (2012) and discussed above was employed to embed FBG sensors in the concrete beam. Based on those tests, a bond length of 2.4 inches (60 mm) was deemed sufficient to achieve adequate strain transfer for fibers embedded at reasonable depths in saw notches 0.125 in wide and 0.125 in deep. While embedding the fibers in a notch provides a good mechanism for strain transfer, it does present some accessibility challenges for installing fibers with adequate pretension. Furthermore, the majority of high-strength epoxies require at least 24 hours to fully cure. This makes it impractical for the fiber to be held in place manually until the epoxy reaches full strength. Therefore, a procedure was devised to apply an FBG fiber into a notch with adequate pretension and hold it in place long enough for the epoxy to cure. The devised method involves installing a heat shrink protective sleeve on the fiber, which bonds to the fiber and provides a means to grasp and tension the fiber. These protective sleeves can be affixed to concrete using cyanoacrylate. While this bond is not adequate for permanent installation in service conditions, it is sufficient to hold the fiber in place temporarily while the epoxy cures.

The protocol developed for installing FBGs onto concrete members is as follows:

1. Prior to splicing the FBG into the channel line, slide a heat shrink protective sleeve onto each side of the FBG approximately 5 inches away from the center of the sensor. Being careful to keep the sleeve in place on the fiber, set each sleeve into the heating unit on the splicer to bond it into place. Once the sleeves are in place, the FBG fiber can be spliced onto other fibers or leads following typical procedures.
2. Carefully mark the location to be measured on the host structure and draw a straight line along the axis of measurement. Then, using a 1/8 in thick masonry blade, cut a straight shallow notch into the beam along the axis of measurement approximately 1/8 inch deep and 12 inches long.
3. Align the fiber with the notch and mark off the locations for the FBG sensor, the unepoxied region (approximately 3-5 inches), the epoxied regions on each side (2.5 inches), and the protective sleeves. Then using these marks as a guide, apply a thin layer of cyanoacrylate adhesive to one of the protective sleeves and position it in the notch. Ensure that it is in the appropriate position, and firmly press it down until the adhesive cures.
4. Using a small flat head screwdriver or similar tool, distribute the epoxy into the bottom of the notch, filling it approximately halfway up in the epoxied regions. Note: for sensors being installed overhead or on vertical faces, it may be necessary to wait approximately 10 minutes after mixing the two parts of the epoxy for it to establish adequate viscosity to prevent it from running.

5. Apply a thin layer of cyanoacrylate adhesive to the remaining unattached protective sleeve and to the corresponding region of the notch. Then, gently apply the appropriate pretension to the fiber and press the sleeve into the notch. Firmly hold the sleeve in place to maintain the pretension in the fiber. Then spray the activator on the cyanoacrylate adhesive and continue to hold the sleeve until the bond is secure.
6. Using the flathead screwdriver, fill the epoxy region to the top of the notch with epoxy, being careful not to damage the fiber. Then monitor the wavelength for any significant drop in wavelength. If the wavelength fails to stabilize above the base wavelength, it indicates an inadequate bond between the sensor and host material. If a satisfactory bond is not achieved, refer to the subsequent replacement procedure.

This procedure was used for installing the sensors on the concrete beam in the laboratory structure. Of the 28 FBG sensors installed using this approach, 3 sensors experienced a loss of pretension greater than 25%, and the average pretension loss in the remaining sensors was 13%.

### **Protection on Concrete Elements**

Affixing protective materials to concrete is more difficult than affixing to steel due to the rough surface, to which the tape does not adhere well. Two methods were developed to protect fibers attached to concrete elements. The first method requires a more intricate installation process, but results in a more permanent system. However, if for some reason an element in the SHM system breaks, all of the sensors on the channel must be replaced. To begin, a notch is cut the full length of the bridge, and each sensor must be installed so that the fiber lies within the notch for the full length of the bridge. To ensure that the optical fibers fit into the notch, the fibers between sensors must be measured out to be the same length as the notch between sensors, so that the fibers can be installed onto the structure with very little slack. Once all of the sensors have been installed, the entire length of fiber for each channel is laid into the notch and covered with epoxy, except for the unepoxied regions where FBG's have been installed. Over the unepoxied regions, a thin 1 inch wide cover plate, made of either plastic or metal, can be attached to the concrete using epoxy to seal off the notch. This method results in a very durable, permanent system. However, the installation process is complicated by the necessity of having a taught fiber between sensors, and it can be cumbersome to saw a notch the full length of the bridge. Finally, if a problem is discovered in any of the sensors after the protection system is in-place, then the entire line of sensors must be cut out, and new sensors must be installed.

The second method does not provide as robust protection, however it is easier to implement, and it allows for repairs to be performed without replacing all of the sensors on a channel. For this method, shallow, 1 foot long notches are cut at sensor locations, and the FBGs are installed according to the installation procedure. Between sensors the more durable fiber with a 900 micron protective sleeve is spliced leaving enough slack between sensors to maintain workability. A strip of clear spray paint is applied along the length of the element and allowed to dry in order to produce a smooth surface. Then the fiber is attached to the element using the butyl rubber tape discussed in the steel protection method section. The tape must be pressed firmly onto the concrete to ensure an adequate bond. If there is excess fiber, it can be wound into a loop and covered with butyl rubber tape. Care must be taken not to wind the fibers into

too tight of a loop, which would result in a loss of signal. A diameter of about 2 to 3 inches is acceptable. The butyl rubber tape can be installed over the notched regions where sensors are installed, or a thin cover plate may be epoxied into place to provide extra protection for the bare fiber in the notch.

### **Repair on Concrete Elements**

If protection method 1 was used, and it is discovered that a sensor is not performing, then all of the fiber will need to be removed from the notch, and new sensors will need to be installed. The epoxy may be removed using a file and similar hand tools, or it may be easier to recut the notch using a masonry blade. Once all of the sensors are removed, new sensors must be installed and protected according to the previous instructions.

If protection method 2 was used, the butyl rubber tape can be gently removed from the structure using a putty knife. Care must be taken not to damage the underlying protective coated fiber. If the break occurred along the fiber between sensors, then the disjointed fiber ends can be stripped, cleaved, and spliced according to common practice. The fiber can then be re-adhered to the structure using a fresh strip of the butyl rubber tape.

If the break occurred at, or close to, the sensor, then the sensor will need to be replaced. If a cover plate was used, it should be removed by scraping the underlying epoxy away with a putty knife. Otherwise the butyl rubber tape can be removed by gently pulling it back using a putty knife. Enough of the lead fiber should be liberated to splice a new FBG onto the channel. To remove the old sensor, the epoxy can be removed with a file, and the glued fiber protectors can be pried out using a flathead screwdriver. Once the old fiber is removed and the notch is cleaned, a new sensor can be installed according to the preceding instructions.

### **Experimental Procedures**

Experiments were performed on each beam to compare the measured behavior of the structure with the predicted behavior from analysis. For each beam, three types of tests were performed: a static test, a pseudo-static (crawl-speed) test, and a full-speed test. These are typical of the types of tests traditionally performed in load rating tests for bridges. The static test provides the most reliable results, as there is less uncertainty about the position of the load, and any dynamic amplification is eliminated. The goal of the crawl speed test is to approximate the results of the static test with a less time-consuming method. Crawl speed tests were performed in the lab to verify their accuracy. Dynamic test results are typically compared to static or pseudo-static tests in order to calculate a dynamic impact factor. This report focuses on the statics tests; details of the crawl-speed and dynamics tests are found in Jung (2015).

During each test, three parameters were measured: the location of the wheels, the magnitude of the loads applied by the wheels, and the strains measured by the FBG sensors. In order to

correlate these data, a stopwatch was used along with the timer mechanism built into the data acquisition software. Each wheel of the load cart contained a 2-kip Interface© 1210AF load cell connected to a computer using a data acquisition unit connected through a USB port. A program written in Labview© was used to record the data from the load cells along with the time of the measurement.

In order to achieve a consistent load distribution during the tests, the cart configuration was modified to bear on three wheels rather than four. This was achieved by raising the height of one wheel on the cart until it was not in contact with the beam. The result was a load cart that was supported by three wheels, one on the measured beam, and two on the non-measured beam. This configuration provided a stable system that could produce a single point load traveling down the beam of interest with more consistent load distribution than the original four-wheel configuration.

The sensors used in the laboratory experiment were 5 mm FBGs in SMF-28 acrylate fiber with base wavelengths ranging from 1530 nm to 1566 nm. The FBG data were recorded using a two-channel SmartScan© interrogator. Each channel was connected to 14 multiplexed FBG sensors installed along the length of the beam. One channel was connected to the sensors oriented on the extreme fibers of the cross-section of the test beam. The other channel was connected to the sensors oriented on the inside of the test-beam cross section. The sample rate of the FBG data was set to 4 Hz, and the data were averaged to produce one data point per second. The averaging of the data was done to limit the quantity of data recorded during the test and to reduce the noise of the data collected.

For the static load test, the load cart was moved incrementally along the beam at 1 ft intervals for the entire length of the beam. At each interval the load cart was held in position for approximately 10 seconds while measurements were recorded. The interval that the load was held stationary for data collection is referred to as a load condition. Six static tests were performed on each beam to test the repeatability of the results. In-depth analysis was performed for the load condition that induced the largest curvatures measured in each span: a point load at 4 ft, a point load at 15 ft, and a point load at 26 ft.

## **Experimental Results and Analysis**

In-depth analysis was performed with the load positioned at three locations on each beam: at 40% of the first span (1.04), the middle of the second span (2.05), and 60% of the third span (3.06). The load effects and the structural response were calculated from the raw data at each point, and the structural properties of interest were calculated for comparison with values found through analysis. Multiple data points were collected while the load was held stationary at a single position. The data collected over the time that the load was held in position was averaged to produce a single average strain value for each load location, which was used in the analysis.

The raw wavelength measurements from the FBG sensors were converted to strain using Equation 1.

Equation 2 was then used to calculate the curvature at each position on the bridge using these strain values. By considering the strain at two different cross-section depths, Equation 2 eliminates the need for knowing the neutral axis depth to calculate curvature, assuming that the strain distribution is linear through the depth of the bending member.

$$\phi = \frac{\varepsilon_T - \varepsilon_B}{d} \quad (\text{Eq. 2})$$

where:  $\phi$  = curvature  
 $\varepsilon_T$  = strain in top sensor  
 $\varepsilon_B$  = strain in bottom sensor  
 $d$  = depth between top and bottom sensors

In order to calculate the analytical load effects for comparison with the laboratory measurements, a beam was modeled in SAP2000 with the flexural rigidity  $EI$  set to unity; nodes were placed at sensor locations, support locations, and load locations; a unit load was positioned at the appropriate location to replicate the load condition of the laboratory test; and the model was analyzed for the resulting moment. The supports were modeled to provide vertical and lateral restraint only. The values resulting from the simulation provided the moment function for a load at the location modeled. This moment function could then be scaled by the analytical flexural rigidity of the beam and the measured load magnitude to determine the analytical load effects, such as strains and curvatures, for a given load configuration.

## Concrete Beam Results

The results from all six static tests were averaged to produce a curvature distribution for each of the three load cases that were analyzed in depth: a point load at the 1.04, 2.05, and 3.06 locations. In all three load cases, the analytical model predicted curvatures higher in magnitude than those measured during the tests, except at the beam ends, where the end-conditions assumed in the analytical model forced the curvature to a value of zero. The elastic modulus ( $E$ ) that was used for the analytical concrete model was based on Equation 5.4.2.4-1 in the AASHTO LRFD Design Manual (2012). This equation does not account for the stiffness of the aggregate used. A direct test of the elastic modulus for the batch of concrete used to construct the beams would have given better results. However due to a malfunction of the testing machine, reliable data was not available.

In order to determine a modulus of elasticity that better approximated the experimental data than the value calculated using the AASHTO equation, the analytical statical moment distribution was scaled by increasing the modulus of elasticity value to approximate the experimental curvature

distribution. The resulting modulus of elasticity was increased by 32.3% from 4,031 ksi to 5,333 ksi. An additional analytical model was developed using this adjusted modulus of elasticity.

The curvature distributions calculated from the analytical model, the experimental data, and the adjusted modulus of elasticity analytical model for the load position at 1.04 location are shown for comparison in Figure 6.6. The figure shows that the analytical model curvature tracks closely with the experimental curves for the various sensors along the length of the beam. However the analytical curve indicates greater curvature at all positions along the length of the beam.

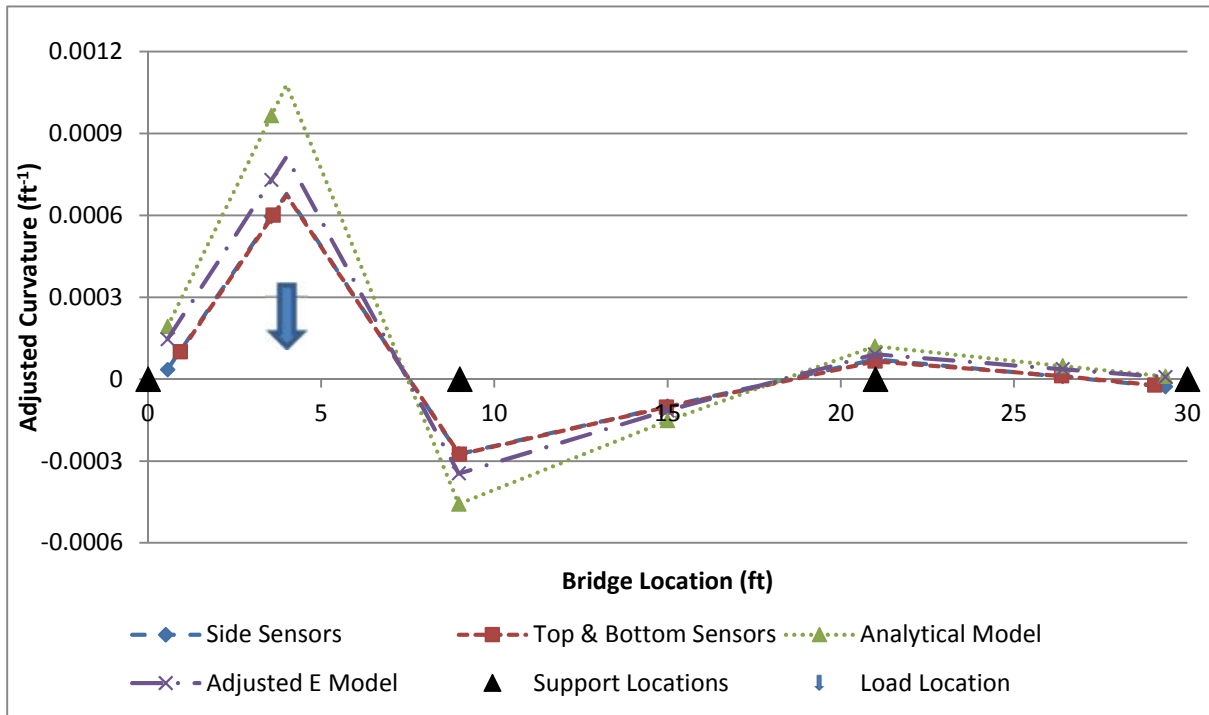


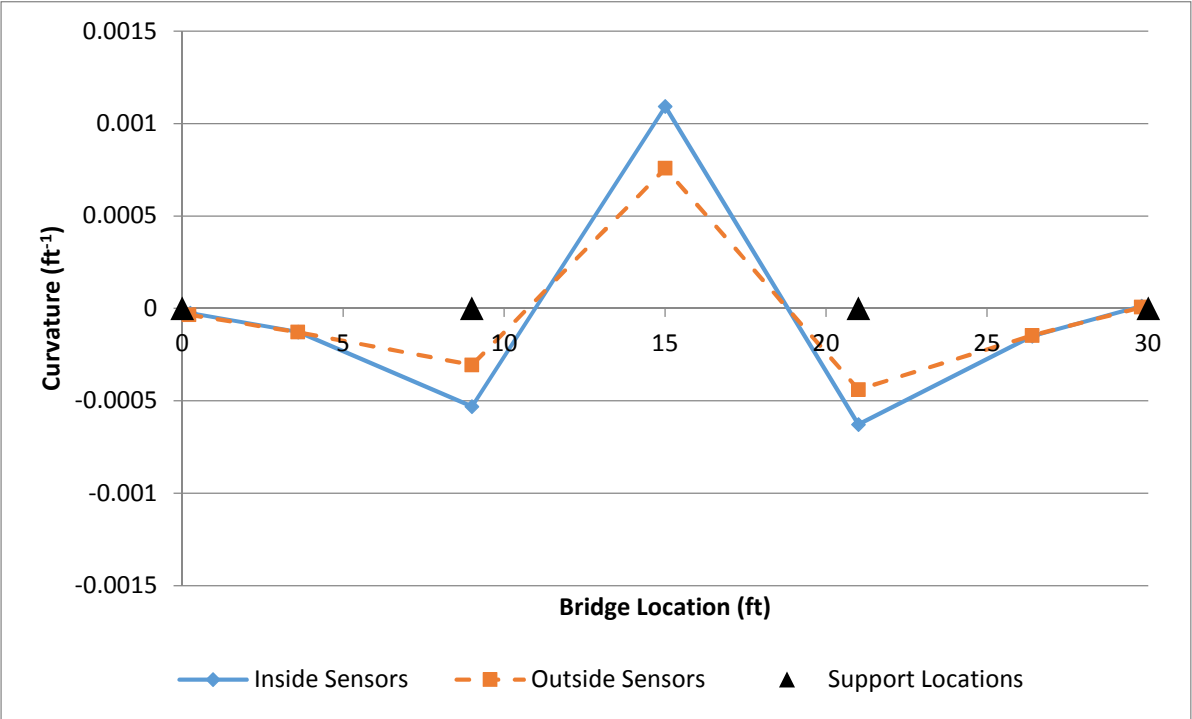
Figure 6.6 – Comparison of Analytical and Measured Curvatures for Concrete Beam

## Steel Beam Results

On the steel beam, there were significant discrepancies between the curvatures from the sensors placed at the extreme fibers and the curvatures measured by the sensors placed on the inside of the flanges. Figure 6.7 shows the average curvatures measured for the load positioned at the 2.05 location. The curvature for the inside sensors should have corresponded precisely with that for the outside sensors, as was the result for the concrete beam. However, in this case the inside sensors predicted higher curvature. For the three load configurations analyzed during the six static load tests, the average discrepancy between values measured by the two configurations was 30.5% of the mean value for the maximum positive curvature values and 29.3% of the mean value for the maximum negative curvature values.

Various factors may have contributed to the discrepancies in the measured values between the sensor configurations on the steel beam. The top sensors at the mid-support locations (9 ft and 21 ft) for both the inside and outside configurations experienced significant loss in pretension during the installation process. So they may not represent accurate results. Additionally, the strains in these locations may be affected by local bearing effects induced by the supports.

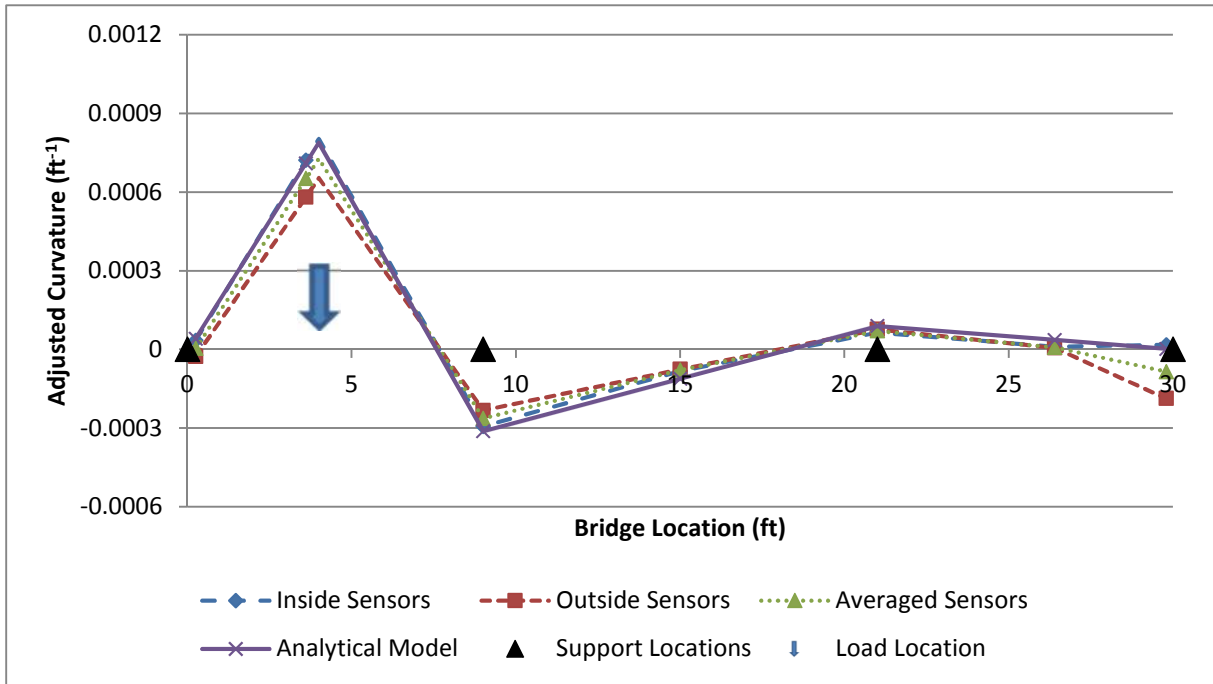
The curvature calculated from the top and bottom sensors on the same side of the beam were not equal in magnitude. However, there appears to be some correspondence in the strains measured by the inside top and outside bottom sensors, located near the top right and bottom left corners of the cross-section. Similarly, there is an apparent correspondence between the outside top and inside bottom sensors, located near the top left and bottom right corners of the cross-section. This symmetry could indicate the presence of out of plane bending, which would result in a rotation of the neutral axis. During the experiment, it was observed that the cart's wheel was bearing close to the edge of the flange rather than directly over the web. The beams constructed in the lab were not perfectly straight and the rigidity of the load cart may have pulled the steel beam toward the stiffer concrete beam, resulting in minor-axis bending. This notion is consistent with observations from the neutral axis locations on the concrete beam. Furthermore, the eccentric load condition observed would result in a combined torsion and bending of the beam, which can result in secondary minor axis bending (Bremault, Driver and Grondin 2008). The minor axis bending would result in a tensile strain in both the top and bottom sensors on one side of the cross-section, and a compressive strain in the top and bottom sensors on the other side of the cross-section.



**Figure 6.7 – Curvatures Measured by Sensors on Steel Beam**



Figure 6.8 compares the curvatures obtained from the sensors to the analytical values predicted by analysis of the steel beam subjected to strong axis bending for the load placed at the 1.04 position. In this case, the analytical model closely aligns with the curvatures predicted by the sensors in the experiment.



**Figure 6.8 – Comparison of Analytical and Measured Curvatures on Steel Beam**

As was previously discussed, the discrepancy between the measurements taken by the inside sensors and the outside sensors may be the result of secondary load effects like minor-axis bending. Averaging the measurements taken from all four sensors would have the effect of neutralizing these secondary load contributions on the data, as tensile strains on one side of the beam would be counteracted by compressive strains in the opposite side of the beam when the data is combined. The previous plot shows some of this behavior, where the averaged curvatures tend to approach the analytically predicted values. Additional discussion of the secondary load effects and the performance of the steel beam is found in Jung (2015).

## CHAPTER 7 – FBG MICROBUCKLING IN COMPRESSION

Generally FBG sensors are installed after some pretension is applied to the sensor. This process is intended to maintain a net tension in the sensor when compressive strain is applied. When an FBG is unstrained, it has a base wavelength that is determined when the FBG is created. For strain sensing applications, FBGs are typically pre-tensioned to a wavelength of 2 nm to 5 nm above the base wavelength, depending on the expected strains that the FBG will experience. Pre-tensioning ensures that the FBG will remain in tension when strained throughout its service life. For the applications in this research it was important to examine how the FBG performs in the compression zone without pre-tensioning. It was hypothesized that since the fiber is embedded in epoxy, it is restrained from buckling in compression and will therefore maintain functionality in its compression range.

To test the FBG compression range functionality, an un-tensioned FBG was surface adhered to a wood block with a 70 mm bond length. A strain gage was also surface adhered to the block adjacent to the FBG sensor. Cyanoacrylate adhesive was used to bond both sensors to the block. The strain gage data was used for comparison to the FBG strain data during the compression test. Wood was selected as the host structure material because it is easily strained in compression. Two ramp loading tests were run and the strain differences between the two sensors were compared.

The wood block was loaded up to a maximum strain magnitude of about 0.003, which is the design strain limit for concrete. The FBG maximum compression wavelength shift experienced by the FBG was 3 nm below its base wavelength. The block was loaded twice and the results of each repetition averaged to demonstrate that the FBG only measured about 83% of the strain measured by the strain gage.

One possible reason for the strain sensing inaccuracy of the FBG is local buckling of the fiber when compressed. FBG fibers buckle very easily due to their thin silica-glass structure (Mohammad, et al., 2004). Accurate compression range sensing by embedding an FBG in epoxy has been achieved in previous studies but requires an epoxy with specific properties and a specific embedment configuration (Le Blanc, *et al.*, 1994). It was found in previous studies that adequate thickness and stiffness of the epoxy that embeds the FBG to the host are essential in order to prevent local buckling of the FBG. Other techniques that utilize magnetic actuators or fiber-guiding systems have proven to be effective in preventing local buckling of FBGs, but are not feasible for strain sensing applications of structural members (Mohammad, et al., 2004).

## CHAPTER 8 – FINDINGS AND CONCLUSIONS

A rise in the energy sector has resulted in a greater number of trucks travelling with overweight loads or non-standard vehicle configurations. State bridge managers are responsible for assuring safe and efficient routes for these permitted vehicle loads over bridges. As a result, bridge engineers are developing methods to quantify the actual capacities of in-service bridges, which are generally higher than the analytical analysis indicates. A field-tested bridge analysis can lead to improved load ratings or the removal of bridge postings, allowing permitted vehicles to travel through the state safely without costly detours.

The University of Wyoming team executed the following research tasks:

- 1) Develop optical-fiber packaging, installation, and protection mechanisms for implementation in harsh environments.
- 2) Develop a low-cost, compact, and energy-efficient instrumentation package for SHM of bridges using FBG sensors
- 3) Develop data collection, processing and transmission capabilities for the SHM network.
- 4) Validate the developments in tasks 1, 2 and 3 in a laboratory environment.
- 5) Study the behavior of FBG sensors subjected to compressive strains in excess of initial tensile straining.

Each of the research tasks achieved meaningful outcomes as described in the following.

### Task 1

Fiber Bragg Gratings have been used in various fields for decades; more recently, they have been introduced into the structural engineering field. FBGs are more commonly replacing TGs for field testing bridges. Regardless, some engineers are skeptical of replacing the TGs. To reestablish confidence in the performance of FBGs and to understand and describe the installation process for future possible deployment, the University of Wyoming used TGs to verify FBGs.

#### FBG Sensors Mounted on Concrete

Both experimental and finite element methods were used to determine the elasto-mechanical behavior of FBG sensors attached to a concrete host. The conclusions drawn from the FEA and the experimental tests relate primarily to the strain measurement accuracy of the FBG sensors bonded to concrete in notches. It was found that the FEA slightly over-predicts the strain transfer to the FBG when compared to test results. This conclusion is supported by the fact that for 80% of the configurations that were compared, the FEA strain transfer results were 1% to 9% greater than those seen in the experimental tests. Despite the FEA over-prediction, it is still

possible to conclude that there are some configurations that provide full strain transfer and some that do not. Before more detailed specifications can be made about which configurations are most effective, it is important to consider the feasibility of field implementation. Several issues such as the equipment, time, and level of installation complexity required for field applications must be evaluated.

After several laboratory and computer simulations of the FBG embedment procedure, it was concluded that the equipment and materials required to install an FBG in a notched concrete structural member are effective and obtainable for an engineering or construction crew. The embedment notches can be cut in the concrete with a masonry saw or formed as the concrete is placed. The Ultrabond 1300 epoxy was effective because of its short cure time and availability, however for overhead or vertical applications, a more paste-like adhesive with higher viscosity would be optimal.

The process of embedding an FBG in a concrete notch is fairly straight forward and feasible for field applications. After a notch is formed or cut into a concrete structural member, a thin layer of adhesive is placed in the bottom of the notch. An FBG is then placed onto the first layer of adhesive followed by a second layer of adhesive that covers the FBG and fills the notch. The specified adhesive cure time should be allowed before strain monitoring begins. The FBG embedment process takes less than 20 minutes per sensor, excluding the adhesive cure time.

An evaluation of the strain transfer test results reveals minor differences between the FEA and the experimental tests. The slightly lower strain transfer seen in the experimental results is attributed to several influential factors. One is the assumption of perfect bonds between the adhesive and the concrete as well as between the adhesive and the fiber in the FEA. This assumption is unrealistic in real conditions and resulted in greater strain loss in the experimental tests. Additionally, the form oil on the surface of the concrete prisms was not fully removed before applying the epoxy possibly resulting in a softening of the concrete-epoxy bond interface. The size of the aggregate in the concrete may have also affected the strain sensing of the FBG. The maximum aggregate diameter was 20 mm which is twice the length of the FBG sensor region. If the FBG sensor region was adhered directly over a single piece of aggregate, the strain measured by the FBG would have been more representative of that piece of aggregate rather than the prism as a whole. The conventional strain gage had a sufficiently long sensor region, however electrical noise and sensitivity level are two parameters that may have affected the accuracy of the strain gage when compared to the FBG strain measurements.

Non-uniformities in the epoxy and the notch shapes may have also caused variations in the strain transfer in the experimental tests. The concrete notches were not formed in the concrete exactly as they were modeled in the FEA. There were imperfections such as air bubbles and non-exact geometries in the concrete notches that could have contributed to the difference in strain transfer between the FEA and the experimental tests. The epoxy may have also had air bubbles or long-term shrinkage behavior that influenced the strain measurements of the embedded FBG. Despite

the various factors that affected the strain sensing accuracy in the experimental tests, good correlation between the physical tests and the FEA data was seen. The differences in strain transfer (1% to 9%) between the FEA and experimental tests for the five configurations that were compared were reasonably low. The FEA was therefore considered an effective tool for analyzing the FBG notch embedment strain sensing method.

The FEA results supported several conclusions about how the configuration parameters affect the strain transfer for the notch-embedment sensing method. One conclusion is that as epoxy bond length increases, so does the effective strain transfer length for a given configuration. This trend is true for all bond layer thicknesses and epoxy moduli. A second conclusion relates to the effect of epoxy elastic modulus on strain transfer. It was observed that strain transfer increases with an increase in the adhesive elastic modulus. This trend supports the conclusions of previous studies, which suggest that the closer the elastic modulus is to the concrete, the better the strain transfer.

The results of this study revealed an inverse relationship between bond layer thickness and strain transfer. It is seen that smaller bond layer thicknesses provide greater strain transfer. Additionally, the effect of bond layer thickness appears to have more of an impact on the V-notch configuration than the saw-notch configuration. This behavior is likely due to the fact that the V-notch is wider with a tapered shape while the saw-notch geometry is narrower and more uniform. The bigger V-notch provides a greater volume of epoxy for strain loss to occur in. The tapered V-notch shape provides more epoxy between the FBG and the concrete than the saw-notch as the bond layer thickens.

The results also suggest that the saw-notch provides better strain transfer than the V-notch. It is expected that the configuration with the smaller bond layer thickness will provide enhanced strain transfer. It is seen however, that the saw-notch configuration with a 3.2 mm bond layer thickness provides better strain transfer than the V-notch configuration with a smaller 1.75 mm bond layer thickness. In other words, even though the FBG is further away from the host structure in the saw-notch than in the V-notch, the saw-notch still provides higher strain transfer. This implies that the saw-notch will provide better strain transfer than the V-notch in any situation where the epoxy modulus, epoxy bond length, and bond layer thickness are the same in both notch types.

The experimental test results also offer some insight towards what configurations will provide effective strain transfer in field applications. Results show a nearly fully developed experimental strain transfer value of 0.98 for the V-notch configuration with a 2.7 mm bond layer thickness and a 30 mm epoxy length. This implies that any V-notch configuration that has an epoxy length of 30 mm or greater with a bond layer thickness of 2.7 mm or less, will have a strain transfer rate of 0.98 or greater. This conclusion also applies to the saw-notch configuration since it was found that the saw-notch provides better strain transfer than the V-notch. A final conclusion is that decreasing the epoxy length and increasing the bond layer thickness will decrease strain transfer as seen with the 4.2 mm bond layer thickness configuration.

## **FBG Sensors Mounted on Steel**

The FBGs and TGs were installed on an S3x5.7 steel beam. There were six of each type of sensor, where one FBG and one TG were located in six different locations on the beam. The averaged results from each FBG and TG set at the various locations were compared for the six tests. The modulus of elasticity values were used for comparison because the averaged results were linear, so one slope value accurately represented the data set.

Set 1 had an FBG and TG located at the extreme compression fiber. At this location, the TG results were 11.3% higher than the FBG results. Set 2 was located on the underside of the top flanges with FBG results 14.8% higher than the TG results. Sets 3 and 4 were installed on the web of the beam on the same side at a 45-degree angle to record shear strain results. Set 3 FBG results were 8.8% higher than TG results while set 4 showed FBG results 14.2% higher. Set 5 was located on the top of the bottom flanges and the FBG results were 20.3% higher than TG results. Lastly, set 6 was mounted on the bottom of the bottom flange; the FBG resulted in an average of 2% higher than the TG results.

The FBG results based upon the six tests were within a reasonable range of the TG results. Set 5 is an exception that displayed unusual results, possibly due to an epoxy bond failure. Many assumptions were made for the verification tests that could explain the strain measurement discrepancies. Assumptions include a perfectly flat, sanded, and clean surface; flawless sensor application, resulting in a perfect bond; reliable foil gage measurements; exact angle alignment of sensors at 45-degrees and sensors parallel to each other; the beam stays within its elastic range; and that a difference in strain due to the distance between sensor sets is negligible. Although the assumptions represent ideal testing conditions, this is rarely the case.

Given the assumptions of the tests and additional test properties, the results are within a reasonable range. Typically, when comparing strain gages on the market to foil gages through laboratory testing, strain results within 5% are a reasonable expectation. Set 6 displayed this comparison with a 2% difference. However, based upon the assumptions and additional test properties, results within 15% are realistic.

## **Task 2**

Upon study of the market for commercially available instrumentation, particularly FBG network interrogators, it became evident that a commercial product was superior to anything that could be developed individually. Commercial products provide the low-cost, compact form-factor and energy-efficiently required for this project. Additional pursuit of custom instrumentation would have been wasteful of research time and funding. Consequently a two-channel SmartScan 02 Lite FBG interrogator developed by Smart Fibres, was purchased for the laboratory study. The only other resources required in the laboratory are a standard Windows-based desktop computer

and an internet connection. This approach assured that the laboratory instrumentation conformed to the latest industry standards and had the reliability and durability to perform as required.

Selection of instrumentation for field application was merged with task 3 in order to successfully integrate commercially available hardware with a custom-designed microcontroller. Findings and conclusions for the instrumentation intended for field application follow.

### **Task 3**

Future field deployment and operation of the SHM network emphasized proof of concept of the RFID triggering system for data collection and data storage capabilities. The research was focused on permitted vehicles. Additionally, the system was designed to correlate known vehicle data with the measured response of a bridge. The work focused on the RFID systematic description, the validation procedure, and the validation results for the proof of concept field tests.

The RFID system utilizes a transponder that wirelessly transmits data to and receives data from the RFID tags. RFID transponders will be installed at a weigh station at a Wyoming port of entry and at the bridge of interest. At the port of entry, the permitted truck information, including the axle weights and configuration, will be assigned to an RFID tag with an identification code that would be placed on the windshield of the vehicle. Another transponder placed near the bridge will detect the presence of the RFID tag and trigger the system to store the bridge strain data when the tagged permitted vehicle passes over the bridge.

Mr. James Branscomb was the primary developer of the instrumentation for the RFID triggering system and the microcontroller that drives the FBG interrogator. For the proof of concept testing, the triggering mechanism, data collection, and data storage were the specific parameters tested. The proof-of-concept tests were organized so that the initial positioning of each RFID component was established prior to testing the system at full speed, including positioning of the RFID transponder, RFID tag, and RFID vehicle. Each time the transponder detected the tag, the FBG strain data from three sensors were continuously recorded for the allotted 30-second time frame.

The proof-of-concept for the RFID triggering system was successful. It was determined that the success of the triggering is dependent upon the position of the tagged vehicle; the transponder, including the height and horizontal position; and the tag location in the vehicle. The proof-of-concept tests provided admissible results that were sufficient to move on to the next phase of instrumentation design and testing.

## Task 4

The sensors installed on the concrete beam using methods developed in task 1 provided measurements similar to, but lower in magnitude than, what was predicted by the analytical model. It was necessary to account for averaging effects caused by the long gauge sensor configuration. Further discrepancies between the test results and the analytical model could be explained by a difference between the predicted and the as-built modulus of elasticity for the concrete.

The measurements taken on the steel beam were similar in magnitude to the values predicted by the analytical model. However, the measurements taken at different locations on the beam cross-section varied significantly, where they should have been similar. This variation could be explained by the presence of secondary load effects induced by an eccentricity in the load on the beam that was observed during the experiment. In a few locations on the steel beam, the sensors experienced a significant loss in pretension after installation. The wavelengths from these sensors did stabilize at a point that indicated that there was still adequate pretension to make the necessary measurements. However, the resulting measurements at these locations appeared inconsistent with measurements taken from other sensors during the tests. This may be due to an inadequate bond between the sensor and the beam. However, these sensors were located directly above the mid supports of the beam. So, the inconsistent measurements may have been the result of unpredicted localized effects from the supports.

Analysis of the curvature did not yield values similar to the analytical model. Comparing the measured experimental values with different hypothesized properties and loading scenarios on the analytical model allowed for reasonable postulations of the behavior that may have induced the recorded test data. The sensor data appeared to be significantly influenced by local effects at the support locations. Therefore, placing sensors directly over the support locations should be avoided. It may be necessary to offset the sensors a distance away from the support locations to minimize the influence of local bearing effects.

The curvatures measured by the sensors located at the extreme fibers of the concrete beam cross-section were similar to the curvatures measured by the sensors inset from the edges of the beam cross-section. This similarity in results supports the conclusion that the FBG sensors do not need to be located at the extreme fibers of the cross-section in order to measure accurate values. The neutral axis height values indicated that locating sensors near the sides of the cross-sections may incur unanticipated load effects due to minor-axis bending.

The sensors at the four locations on the steel beam cross-section each reported different magnitudes of curvature. It was postulated that this variation in results was caused by unanticipated secondary load effects such as minor-axis bending and torsional warping, based on observations of the load condition during the experiment. The presence of these incongruent



curvature values makes it difficult to confirm that sensors located on the inside of the cross-section can accurately measure major-axis bending effects.

The presence of FBG sensors at multiple locations on the beam cross-section enabled the sensing system to detect discrepancies that were likely due to secondary load effects. To improve on the sensor arrangement used during these tests, sensors could be placed at the top and bottom of the beam cross-section along the minor neutral axis in addition to near the side of the beam. The sensors on the minor neutral axis would provide a more direct measure of the major-axis bending, and could be compared to the measurements taken near the sides of the cross-section to quantify secondary load effects.

The calculated load effects from the laboratory tests on the concrete beam are compared with the values predicted by an analytical model based on common structural analysis and bridge design practices. The measured curvatures from the laboratory tests were consistently lower than those predicted by the analytical model. It was postulated that the modulus of elasticity of the laboratory beam was higher than what was assumed in the analytical model. Lack of additional experimental data makes it impossible to confirm several of the foregoing explanations.

## **Task 5**

Based on the findings in the literature and additional testing with steel specimens in this research, it can be reasonably concluded that effective strain transfer in compression can be achieved with proper bonding technique. Whether the ineffective transfer with the wood block specimens was a consequence of micro-buckling or some other phenomenon remains unknown, but also irrelevant. The important finding is that FBG sensors can indeed perform accurately when subjected to compressive strain.

## CHAPTER 9 – IMPLEMENTATION RECOMMENDATIONS

The research and development reported herein lays the groundwork for continued study involving field deployment of the FBG-based SHM system. The essential elements of the system are in place. These elements include the following:

- Sensor installation and protection techniques for both concrete and steel host structures
- Commercial and special-purpose instrumentation for interrogating the SHM network
- A novel triggering system based in RFID technology to control the amount of data that is collected from the SHM network.

Subsequent deployment of the system on a bridge in the WYDOT inventory will require additional development of data storage and transmission capabilities, which will be particular to the location and characteristics of the targeted bridge. In addition, the objectives of the SHM network (such as, for instance, observing the impacts of overweight and other permit vehicles, validating load-rating software, monitoring long-term health of the bridge, etc.) will dictate the nature of the sensor installation, the type and volume of data collected, and the required post-processing requirements. Hence, development of a general performance specification for real-time data analysis is not feasible. Rather researchers engaged in Phase II of this study must coordinate with bridge engineers at WYDOT to identify a spectrum of SHM applications and objectives, for which individual data analysis techniques can be developed. Subsequent design and implementation of software to execute such data analysis will be needed to relieve bridge engineers from the burdensome and tedious tasks of sifting through raw SHM data streams themselves.

In addition to the general recommendation above to move toward field deployment of the SHM system, the following specific recommendations are offered.

1. Special attention should be taken when purchasing FBGs. Knowledge about existing technologies and manufacturers will help to assure accurate, consistent, and reliable strain sensor results. Particular points of interest include the wavelength range that can be sensed by the interrogator and the required spacing between central wavelengths of FBGs on an individual channel. The interrogator range and the spacing determine the number of sensors that can be installed on a single optical fiber.
2. In design of the sensor network for a particular bridge, sensors should be placed at a sufficient distance away from the neutral axis to ensure that they are measuring meaningful flexural strain values. For many structures, the concrete deck will act integrally with the primary structural elements. This composite behavior (intended or otherwise) will shift the neutral axis toward the deck. Analysis should be performed for each structure to determine where the expected neutral axis will occur, and the neutral axis location should be considered when deciding where to locate the sensors on the cross-section.

3. A two-sensor configuration makes it difficult to distinguish any contribution from out-of-plane bending. If a sensor is located on a location of the cross-section where strains from one load effect act counter to strains from another load effect, these readings would underestimate the response of the structure to the loading. If these values were used to load rate a bridge, they would overestimate the capacity of the bridge. Placing the sensors close to the minor neutral axis of the beam would minimize the contributions from these secondary load effects. However, if there are significant secondary load effects, it would be important to consider them and the interaction of the stresses.
4. While the top flange of a girder is typically braced by the deck, the bottom flange often carries lateral loads along the girder line through bending until they reach a lateral brace that will transfer the loads into the deck (AASHTO 2012). The significance of these lateral loads should be investigated as part of the design process for the sensor network.
5. The SHM system will be capable of recording massive amounts of data. It will be necessary to develop methods to automatically decipher which data is significant and should be transmitted and saved by the system. An algorithm to save data with readings that exceed a certain threshold or the maximum response each day may be appropriate. Taking a relaxed-state reading each day may be appropriate for documenting changes in the structure or to verify the functionality of the sensing system.
6. Since trucks pass over a bridge in a matter of seconds, it is highly unlikely that significant effects of temperature change will occurring during the load event. Hence, when the data acquisition system is triggered by the RFID signal, initial relaxed-state scans of the bridge can be used to establish a baseline of strains immediately prior to and perhaps after passage of the permitted vehicle. Such an approach effectively embeds temperature compensation in the software that drives data collection rather than in special-purpose sensors, which require additional cost and bandwidth in the interrogator.
7. The RFID triggering system requires additional development. Developments include the port of entry system installation, firmware advancement, larger transponder range capabilities, cellular data transmission capabilities, database establishment, and software formation. For instance, use the E-ZPASS system, common in many states, could simplify application of the system at the port of entry, since it is already familiar to DOT officials and the trucking industry alike.
8. A database should be established that can manage a large amount of vehicle and bridge information and can be accessed by approved personnel, for example WYDOT bridge engineers. Software as well as algorithms for automatic post-processing must be developed. One company that has been researched, Chandler Monitoring Systems, Inc., has developed some of these processes, and it may be worthwhile to pursue their guidance or services.
9. Port of entry sites would do well to couple weigh-in-motion systems to an RFID triggering system to automate collection of vehicle characteristics. Utilizing a static WIM system that already exists at the port of entries, bridge engineers can correlate that load to the bridge responses induced by permitted live loads.
10. Another possible enhancement to the SHM system could be a continuous load-rating system for permitted vehicles. Over time, a standard baseline could be built for specific permitted vehicles and bridge families. Instead of relying on a conservative analysis completed by BRASS-Girder, the actual responses would be measured and monitored for a variety of applied vehicle configurations. Algorithms and procedures would need to be

developed to determine real-time bridge load ratings from bridge measurement data. By continuously monitoring the bridge, bridge management officials could potentially determine practices to safely increase the load ratings.

11. The SHM system could assist in identifying illegal loads and notifying law enforcement. Individuals or companies with overweight or oversize vehicles might not file for a permit in an attempt to by-pass permit fees. Strain-level triggers implemented in the sensing network, coupled to RFID tags in trucks entering the State, could be used to detect and identify illegal loads.

## REFERENCES

- A.G. Lichtenstein and Associates, Inc. 1998. "Manual for Bridge Rating Through Load Testing." *National Cooperative Highway Research Program Research Results Digest* (Transportation Research Board) (No. 234).
- AASHTO. 2012. *AASHTO LRFD Bridge Design Specifications*. Washington, D.C.: AASHTO.
- Annamdas, Venu Gopal Madhav (2011). "Review on Developments in Fiber Optical Sensors and Applications." *IJME International Journal of Materials Engineering*: 1-16. Scientific & Academic Publishing.
- Ansari, F., & Libo, Y. (1998). Mechanics of Bond and Interface Shear Transfer in Optical Fiber Sensors. *Journal of Engineering Mechanics*, 385-394.
- Ansari, F. (2007) Practical Implementation of Optical Fiber Sensors in Civil Structural Health Monitoring, *Journal of Intelligent Material Systems and Structures*, v.18: 879-889, August.
- Baez, Michael (13 May 2014). "Phase II." Message to McKenzie Danforth. Personal communication.
- Barker, Michael, Cory Imhoff, Travis McDaniel, and Troy Frederick. 1999. *Field Testing and Load Rating Procedures for Steel Girder Bridges*. Jefferson City, MO: Missouri Department of Transportation.
- Branscomb, James (Mar. 2013-Oct. 2015). Electrical Design Engineer. Wyoming Department of Transportation. Personal communication.
- Bremault, Dennis, Robert G Driver, and Gilbert Y Grondin. 2008. *Limit States Design Approach for Rolled Wide Flange Beams Subject to Combined Torsion and Flexure*. University of Alberta.
- Cardini, A, and J DeWolf. 2008. "Long-term Structural Health Monitoring of a Multi-girder Steel Composite Bridge Using Strain Data." *Structural Health Monitoring* 47-58.
- Chajes, Michael, Harry Shenton III, and Dennis O'Shea. 2000. "Bridge-Condition Assessment and Load Rating Using Nondestructive Evaluation Methods." *Transportation Research Record*.
- Chan, T.h.t., L. Yu, H.y. Tam, Y.q. Ni, S.y. Liu, W.h. Chung, and L.k. Cheng (2005). "Fiber Bragg Grating Sensors for Structural Health Monitoring of Tsing Ma Bridge: Background and Experimental Observation." *Engineering Structures* 8.5: 648-59.
- Computers & Structures, Inc. 2011. "SAP 2000 Version 15."
- Danforth, McKenzie. 2015. *Laramie River Bridge Load-Testing Plan with Sensor Verification and RFID Feasibility of Permitted Vehicles*. Thesis, Laramie, WY: University of Wyoming.
- Doornick, J. D., Phares, B. M., Wipf, T. J., & Wood, D. L. (2006) Damage detection in bridges through fiber optic structural health monitoring, *Photonic Sensing Technologies, Proc. Of SPIE*, v. 6371, 637102-1 – 637102-12
- Farhey, Daniel N. 2005. "Bridge Instrumentation and Monitoring for Structural Diagnostics." *Structural Health Monitoring* 301-318.

- Guemes, Alfredo, and Julian Sierra-Perez. 2013. "Fiber Optic Sensors." In *New Trends in Structural Health Monitoring*, by W. Ostachowicz, 265-316. Udine: International Centre for Mechanical Sciences.
- Heininger, Hilmar. 2009. "Research proposal, Faseroptische Sensoren zur Bauwerksüberwachung." Mannheim Germany.
- Jung, Michael, 2015. *Development of a Fiber Optic Based Load Testing System for Highway Bridges*. Thesis, Laramie, WY: University of Wyoming. December
- Kreuzer, M. (2007) Strain Measurement with Fiber Bragg Grating Sensors, HBM, Darmstadt Germany, July 16, <http://www.hbm.com>.
- Kuang, K. S. C., M. Maalej, and S. T. Quek (2006). "Hybrid Optical Fiber Sensor System Based on Fiber Bragg Gratings and Plastic Optical Fibers for Health Monitoring of Engineering Structures." *Smart Structures and Materials 2006: Sensors and Smart Structures Technologies for Civil, Mechanical, and Aerospace Systems* 6174.
- Le Blanc, M., Huang, S. Y., Ohn, M. M., & Measures, R. M. (1994). Tunable chirping of a fiber bragg grating using a tapered cantilever bed. *Electronics Letters*.
- Li, Dongsheng, Liang Ren, and Hongnan Li. 2012. "Mechanical Property and Strain Transferring Mechanism in Optical Fiber Sensors." In *Fiber Optic Sensors*, by Dr. Moh. Yasin, 439-458. Shanghai: InTech.
- Matta, F, F Bastianini, N Galati, P Casadei, and A Nanni. 2005. *In-Situ Load Testing of Bridge A6358*. MoDOT.
- Maurais, Daniel. 2012. *Strain Transfer of Notch Embedded Fiber Bragg Gratings*. Thesis, Laramie, WY: University of Wyoming.
- Micron Optics (2010a). "Optical Strain Gage os3100." Web. 19 Mar. 2014.
- Micron Optics (13 May 2014f). "Requirements and Considerations for Successful FBG Sensing Solutions." PowerPoint.
- Mohammad, N., Syszkowski, W., Zhang, W., Haddad, E., Zou, J., Jamroz, W., et al. (2004). Analysis and Development of a Tunable Fiber Bragg Grating Based on Axial Tension/Compression. *Journal of Lightwave Technology*.
- Pak, E. (1992). Longitudinal shear transfer in fiber optic sensors. *Smart Mater. Struct.*, 1, 57-62.
- Rivera, E., D. J. Thomson, and A. A. Mufti (2005). "Comparison of Recoated Fiber Bragg Grating Sensors under Tension on a Steel Coupon." *Nondestructive Evaluation and Health Monitoring of Aerospace Materials, Composites, and Civil Infrastructure IV* 5767.1: 163-74.
- Seo, Junwon, Brent M. Phares, Ping Lu, Terry J. Wipf, and Justin Dahlberg (2012). "Use of a Structural Health Monitoring System for the Assessment of Bridge Load Rating." *Forensic Engineering 2012*: 18-27.
- Tennyson, R. C., A. A. Mufti, S. Rizkalla, G. Tadros, and B. Benmokrane (2001). "Structural Health Monitoring of Innovative Bridges in Canada with Fiber Optic Sensors." *Smart Materials and Structures* 10: 560-73.
- Todd, M, C Chang, G Johnson, S Vohra, J Pate, and R Idriss. 1999. "Bridge Monitoring Using a 64-Channel Fiber Bragg Grating System." *17th International Modal Analysis Conference*. Kissimmee, FL: Society for Experimental Mechanics. 1719-1725.

- Torres, B., Paya-Zaforteza, I., Caldron, P., & Adam, J. (2010). Analysis of the strain transfer in a new FBG sensor for Structural Health Monitoring. *Engineering Structures*, 539-548.
- Zhou, Zhi, and Jinping Ou. 2004. "Development of FBG Sensors for Structural Health Monitoring in Civil Infrastructures." *Sensing Issues in Civil Structural Health Monitoring*. Oahu: North American Euro-Pacific Workshop.
- Zhou, J., Zhou, Z., & Zhang, D. (2010). Study on Strain Transfer Characteristics of Fiber Bragg Grating Sensors. *Intelligent Material Systems and Structures*, 1117-1122.
- Zhou, Zhi et al (20 July 2015). "The Application of FBG Sensing in Monitoring Hulanhe Bridge in Heilong Jiang Province." *Micron Optics*.

**APPENDIX A**  
**PRACTICE MANUAL**



# Practice Manual

## Structural Health Monitoring of Bridges with Fiber Bragg Gratings

RS03-212F



**State of Wyoming  
Department of Transportation**



**U.S. Department  
of Transportation  
Federal Highway  
Administration**



### Structural Health Monitoring of Highway Bridges Subjected to Overweight Trucks, Phase I – Instrumentation Development and Validation



By:

Richard J. Schmidt

Department of Civil and Architectural Engineering

University of Wyoming

Laramie, Wyoming 82071

February 2016

## **Acknowledgements**

This document is based largely on and excerpted from the Masters Theses by University of Wyoming graduate students Mr. Danial Maurais, Mr. Michael Jung, and Ms. McKenzie Danforth. Documentation of the schematic design and fabrication of instrumentation developed during the project has been prepared by Mr. James Branscomb, MSEE

**COPYRIGHT 2016** – State of Wyoming,  
Wyoming Department of Transportation,  
University of Wyoming

# Table of Contents

Overview.....	1
Part 1 – Fiber Splicing and Sensor Interrogation.....	2
Overview.....	2
Preparation.....	2
Coating Removal.....	3
Cleaving.....	4
Splicing.....	5
Reinforcing.....	6
Troubleshooting.....	7
Part 2 –SMARTSCAN Interrogation OPERATION.....	8
SmartScan Setup Instructions.....	9
SmartSoft Instructions.....	9
Part 3 – Installing, Protecting and Repairing Optical Fiber Sensors.....	12
Multiplexed Sensor System Design.....	12
Sensor Installation.....	13
Sensing Steel Elements.....	14
Sensing Concrete Elements.....	18
Part 4 – Temperature Compensation for FBG Sensors.....	23
Part 5 – Schematic Design and Fabrication of Instrumentation.....	26
Introduction.....	26
System Overview.....	27
Assembly Guidelines and Quick-Start Guides.....	33
Part 6 – Data Analysis Methods.....	42
Objective.....	42
Methodology for Determining the Instrumentation Plan.....	42
Instrumentation Plan.....	43
Factors Affecting Sensor Placement.....	43
Sensor Placement on Beams.....	44
Critical Longitudinal Locations.....	45
Vehicle Loading Plan.....	45
Experimental Test Vehicle.....	47

Data Analysis ..... 47

Use of Experimental Lateral Distribution Factor ..... 51

## OVERVIEW

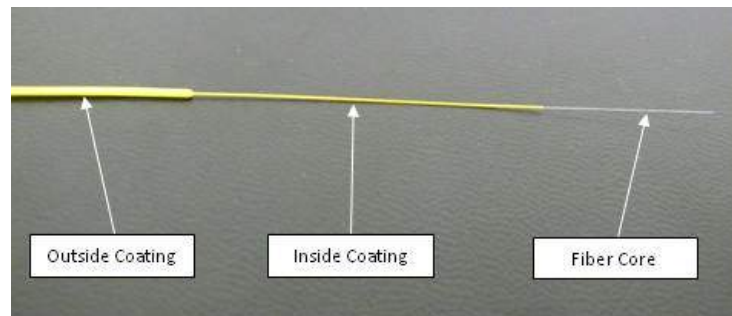
This report contains the essential elements of the WYDOT-MPC sponsored project: *Structural Health Monitoring of Highway Bridges Subjected to Overweight Trucks, Phase I – Instrumentation Development and Validation* required by bridge engineers and maintenance personnel to understand and implement a fiber Bragg grating (FBG) sensor network for structural health monitoring of bridges. The report contains the following parts.

1. Instructions for splicing optical fibers
2. Instructions for operating the Smart Scan FBG interrogator
3. Procedure for installing, protecting, and repairing optical fiber sensors on both concrete and steel host structures
4. Methods for temperature compensation of FBG sensor readings
5. Schematic design and fabrication of instrumentation to interrogate the sensor network and collect the sensor response
6. Methods for data analysis to efficiently deliver system response parameters that are of direct use to bridge engineers

# PART 1 – FIBER SPLICING AND SENSOR INTERROGATION

## Overview

Typical single-mode optical fibers are comprised of three distinct layers. There is the glass core ( $\varphi \approx 125 \mu\text{m}$ ), an inside coating ( $\varphi \approx 250 \mu\text{m}$ ), and an outside coating ( $\varphi \approx 850 \mu\text{m}$ ). These can be seen in Figure 1.1.



**Figure 1.1: Components of an optical fiber**

When splicing a fiber, the fiber core of two fibers is joined through an arc fusion process. In order to achieve this, the coatings must be removed, and the fiber core must be cleaved to provide a clean flat surface for the connection. The two fibers to be joined must then be aligned with extreme precision, and the fusing process can proceed. Once the fibers are joined, a protective sleeve must be affixed to reinforce this delicate connection.

## Preparation

To begin, all of the necessary tools should be removed from the case: protective sleeves, strippers, cleaver and splicer. Next, plug in the splicer, and turn the white switch on the side of the machine to "A/C ON". Open the outside cover of the splicing machine, and lift the screen into position. Then, slide a protective sleeve onto one of the fibers that is to be joined, careful to place it within the inside tube as shown if Figure 1.2.



**Figure 1.2: Protective Sleeve**

## Coating Removal

As mentioned above, optical fibers are typically coated with two protective layers that must be removed before a splice can be performed. Some fibers, however, only have the thinner "inside" coating.

For fibers that have the additional outside coating, this layer should be stripped off independently from the inside coating. It is important to strip off enough of the outside coating so that it will not interfere with the cleaving and splicing instruments. Approximately five inches should suffice. To do this, use regular 26 - 28 gauge wire strippers to notch around the coating as demonstrated in Figure 1.3; then use pliers to gently grip and pull the coating straight off of the fiber. It is important to pull the coating straight along the fiber; fibers are very weak in shear, and if the uncoated fiber is bent it is liable to break.



**Figure 1.3: Stripping outer coating of optical fiber.**

Once the end of the fiber has been reduced to just the inside coating and core, a length of the inside coating must be removed. This bare portion must be of adequate length to perform proper cleaving and alignment in the splicing instrument. Typically a length of about 1.5 inches is sufficient. Depending on the type of inside coating used, it may be necessary to strip the coating, or to burn the coating off. Most fibers have a plastic type coating that should strip off easily using the proper optical fiber strippers. Some fibers however, have a slightly thinner coating that is hard and brittle. If this type of coating is stripped off it will either slip through the strippers without removing the coating, or it will break off along with the glass core. For these fibers it is necessary to use the burning method described below.

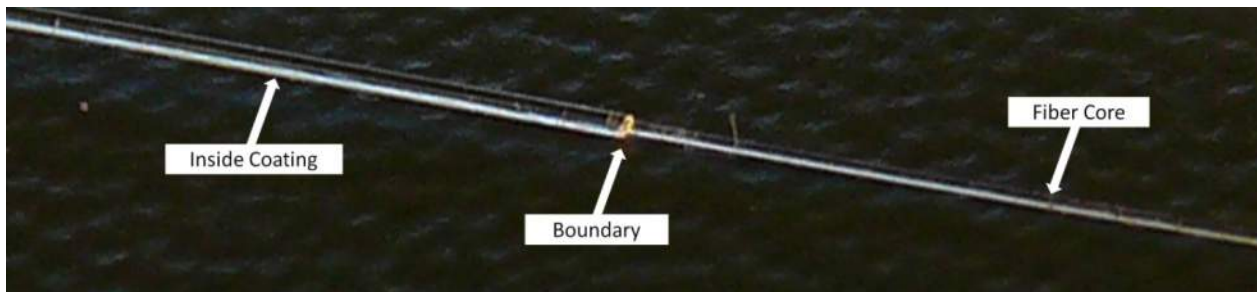
If the inside coating is of the plastic type then, it should be stripped. In order to strip the inside coating, insert the coated fiber into the small opening in the optical fiber strippers, squeeze the strippers, and slide them straight along the fiber toward the end. There will be some resistance, but it should not be difficult. Once again, it is important to pull the strippers straight along the fiber, as any bending can result in a broken fiber. See Figure 1.4 for photos of the optical fiber strippers. If the strippers move too easily, then the inside coating may already be stripped, or the coating may be of the more brittle type which must be burned off.



**Figure 1.4: Optical Fiber Strippers (left). Stripping of inner coating (right).**

If the fiber is of the type that must be burned off, use a lighter and briefly hold the fiber over the flame just long enough for the coating to turn black. Move the flame along the fiber burning off the length of coating that needs to be removed. Be careful not to hold the flame in one spot for too long as this can damage the fiber core. Next, take a soft tissue or chem-wipe, and coat it in *100% pure* isopropyl alcohol. Fold the tissue or wipe around the burned fiber, and gently pull the fiber straight through the wipe, repeating until the black remnants of the coating have been removed. If there are persistent spots of coating that will not wipe off, it may be necessary to quickly expose them to the flame again. Though, as long as the portion of fiber that is close to the cleave is clean, it is not necessary to make the whole length of bare fiber spotless.

The inside coating may be colored, or it may be clear. If it is clear, it is difficult to differentiate between the inside coating and the glass core, and you must look for the change in diameter to find the boundary between the coated fiber and the bare core as illustrated in Figure 1.5.



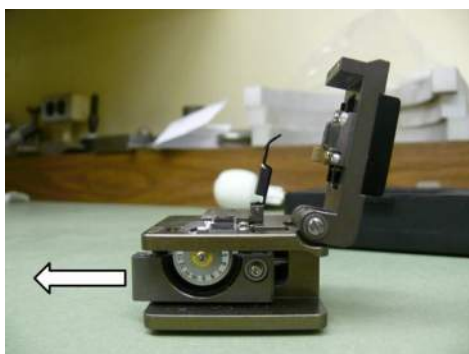
**Figure 1.5: Optical Fiber with clear inside coating partially stripped.**

### **Cleaving**

Once a fiber has been properly stripped it must be cleaved to provide a flat uniform surface for bonding. Before proceeding, open both latches on the cleaver, and use the sliding carriage to position the cutting wheel out toward the user as depicted in Figure 1.6. Note; the cleaving wheel is extremely sharp and should not be touched.

There are two notches that run the length of the fiber cleaver. For single mode fibers the smaller notch should be used. The fiber must be laid straight and flat in the notch, and it must be aligned so that the boundary between the inside coating and the bare fiber core lies at the 16 mm mark as shown in Figure 1.7. The bare fiber should span across the gap, and rest on the two pads on either side of the cutting wheel. The bare fiber should also overhang the edge of the far pad.





**Figure 1.6: Readied Fiber Cleaver**



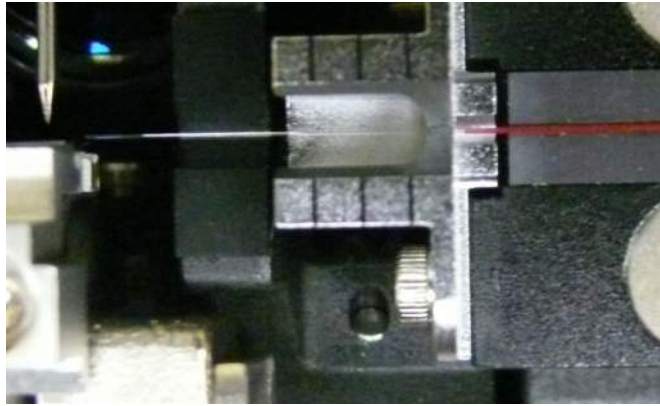
**Figure 1.7: Fiber aligned on Cleaver.**

Once the fiber is aligned, the first latch should be lowered to hold the fiber in place. Then check that the fiber is still aligned, and carefully lower the second latch. Push the cleaving wheel forward to cleave the fiber. Next, raise the latch over the cleaving wheel, and dispose of the loose piece of fiber. Then raise the other latch, move the fiber directly from the cleaver and align it in the splicing machine being careful not to touch the bare fiber end.

### **Splicing**

To align the fiber in the splicing machine, lift the inside cover and both latches (there are two latches per side). Then lay the fiber straight and flat on the surface ensuring that the fiber rests at the bottom of the V-notch, and align the boundary between the coating and bare fiber according to the reference printed on the inside cover. For fibers that have been stripped to 16 mm as described in these instructions, the end of the coating should match up with the face of the notched metal plate as in Figure 1.8. Close the first latch, and check that the fiber is still aligned, and that the fiber is seated in the bottom of the V-notch, then close the second latch. Repeat these steps to prepare and align the second fiber.

Once both fibers are aligned, close the inside cover, and press the "SET" button. The splicing machine will bring the two fibers together, and burn off minor dust particles. Then the machine will pause and ask if the fibers are ok. Inspect the fibers on the screen to ensure that there are no clumps of dust, and that there is a well cleaved surface for splicing. Fibers that are good for splicing will look like those shown in Figure 1.9. If the fibers look good, press set again, and the splicer will attempt to align the fibers and splice them automatically. If the fibers do not look good, or if the machine fails to automatically splice the fibers, refer to the troubleshooting section.



**Figure 1.8: Fiber aligned on Splicing**

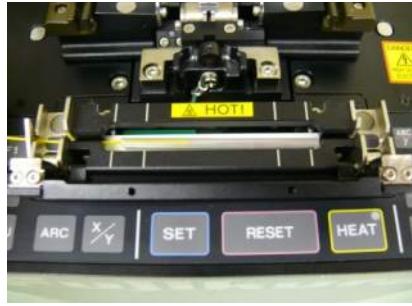


**Figure 1.9: Well Prepared Fibers**

Once the fibers have been spliced, the machine will attempt to analyze the quality of the connection. This is not necessarily important, and can be canceled by pressing the reset button. Open the inner cover, and while gently holding the fiber in place lift the two latches on either side of the machine to release the newly joined fiber. Be careful while handling this newly joined fiber as the connection is quite delicate. Carefully slide the reinforcing tube over the newly spliced connection.

### **Reinforcing**

To reinforce the splice, open the cover and latches on the heating unit, shown in Figure 1.10, carefully slide the reinforcing tube over the newly spliced connection, pull back the metal catch on the left side of the heating unit, and set the covered splice into the heating area with the fibers set into the notches on the ends. Then, close the cover, and latches, and press the "HEAT" button. The machine will then heat up the shrinkwrapping reinforcing tube automatically. When it is finished, the machine will beep. Open the cover and latches, and remove the fiber from the machine. The splice is now complete.



**Figure 1.10: Reinforcing Tube Heater**

## Troubleshooting

### *Cleaving:*

A bad cleave will be apparent when viewing the fibers on the splicing screen. The ends of the fiber will be rounded or jagged rather than square. Fibers sometimes break in the cleaving device but not at the cleaving wheel. This result will not provide a good surface for splicing. If this happens:

- Make sure that enough of the inside coating has been removed so that it is not interfering with any parts of the cleaver.
- Ensure that there is a short length of fiber that overhangs the pad on the far side of the cleaving wheel
- Be very careful when lowering the latch above the cleaving wheel.

### *Splicing:*

- Dirty fibers will have black clumps or spots showing on the fiber when viewed through the splicing screen. The machine will attempt to burn off this dust when it brings the fibers together, but this is not always enough. If the fibers are too dirty to splice, remove the fiber, and gently pull it through a soft tissue or chem-wipe soaked in *100% pure* isopropyl alcohol.
- Dust can fall onto the mirrors and optics of the splicing machine. If there are a lot of spots on the splicing screen, take the air bulb, and direct air at the mirrors and lenses in the machine. Never blow with your mouth or use aerosols to do this.
- If there is an error of the “ZL Overrun”, “ZR Overrun”, or “Set Error” type, it means one or more fibers are not aligned properly in the machine. Try resetting both fibers.
- If the fibers are well cleaved, clean, and correctly aligned, but the splicer still can not make a splice, it may be necessary to manually operate the splicer. Instructions for doing this are listed in the Instruction Manual starting on page 33. If possible it is best to use the method with Automatically Initial GAP Setting, though this does not always work. When performing a manual splice, it helps to have the fiber connected to an interrogator, and adjust the fiber in the machine to maximize the intensity of the reported signal.

## PART 2 –SMARTSCAN INTERROGATION OPERATION

The SmartScan Interrogator shown in Figure 2.1 is a device used to measure the wavelength of a fiber Bragg grating (FBG). It must be connected to the internet or a computer network via the Ethernet port located at the bottom of the interrogator. The SmartScan communicates with a computer with the SmartSoft software through this network connection. The input located directly above the Ethernet port is the power input and must be plugged in before turning on the device. The switch located to the left of the power input is the on/off switch. The four inputs labeled CH1, CH2, CH3 and CH4 identify the four FBG input channels. In Figure 2.1 there is only one FBG fiber (yellow wire) plugged into the SmartScan CH1 input. In general, the device has the capability of having four FBG fibers plugged in each of the four inputs simultaneously. The device shown contains just two channels.



**Figure 2.1 – SmartScan Interrogator**

The Software that drives the SmartScan interrogator is called SmartSoft. SmartSoft (desktop icon shown in Figure 2.2) is used to adjust settings and view the data inputs of the FBGs. The following two sections provide more detailed instruction on the setup and use of the SmartScan interrogator and the SmartSoft software.

Note: The SmartSoft User Manual provides detailed instruction on all instrument operations and can be found at [www.smartfibres.com/docs/Example\\_SmartSoft\\_Manual.pdf](http://www.smartfibres.com/docs/Example_SmartSoft_Manual.pdf).



**Figure 2.2 – SmartSoft Desktop Icon**

### **SmartScan Setup Instructions**

- 1) First ensure that the SmartScan on/off switch is in the off position.
- 2) Plug the Ethernet cable and power cord into respective ports as described previously. The Ethernet cable must be connected to a computer or a local computer network.
- 3) Remove the white cap from the channel port and put in a safe place.
- 4) Remove the clear plastic cap from the plug end of the FBG cable and put in a safe place. Ensure that the exposed plug end and channel port are clean. Use compressed air to clean if needed.
- 5) Line up the notch on the FBG plug end with the groove on the channel port and push in the FBG plug. Screw the FBG plug end tight.
- 6) Switch on the SmartScan interrogator.

### **SmartSoft Instructions**

- 1) Make sure the SmartScan interrogator is turned on before opening the SmartSoft software.
- 2) Open the SmartSoft software. You will be prompted with an IP address window, which should already have the correct IP address entered. Click OK. In case of trouble with the IP address, see the SmartSoft User manual pg. 32 for further instructions.
- 3) The SmartSoft window has five main tabs at the top as seen in Figure 2.3. The Post Process Suite is not currently installed and should not be needed. The following steps will go through the remaining 4 tabs.
  - a. **Instrument Setup tab:** This tab has five sub-tabs that are used to adjust the settings of the FBG setup.
    - i. The **Acquisition rate** tab shows a plot of the Wavelength vs. Relative intensity (response spectra) of the FBG. It may take a few seconds for the response spectra and number labels to appear. If there is no response peak on the response spectra as seen in Figure 2.3 then there is something wrong with the setup. Possible problems could be a bad fiber splice or a bad connection. The number at the top of the response peak should match the labeled wavelength of the FBG when there is no strain on the FBG. Here it is also possible to set the frequency of the wavelength readings that

will be saved to the output data file for a given acquisition time. For example if you want two wavelength readings per second then set the sample size to 125. The acquisition rate is always set at 250 Hz.  
 [ 250Hz / 125 samples = 2 readings per second ]

- ii. The **Gain Slots** tab is used for Enhanced Acquisition to assign individual wavelength windows to multiple FBGs. See SmartSoft User manual pg. 15 for more details.
- iii. The **Peak detection** tab is used to set a peak detection threshold on the reflected FBG wavelengths. This function filters out background reflection that is less than the FBG peaks. See SmartSoft User manual pg. 17 for more details.
- iv. The **Network** tab is used to change the IP address, subnet mask and gateway configurations. Such changes should only be necessary if network connections are altered. See SmartSoft User manual pg. 18 for more details.
- v. The **Load and Save** tab is used to save the instrumentation settings to a file that can be recalled during different sessions. See SmartSoft User manual pg. 19 for more details.

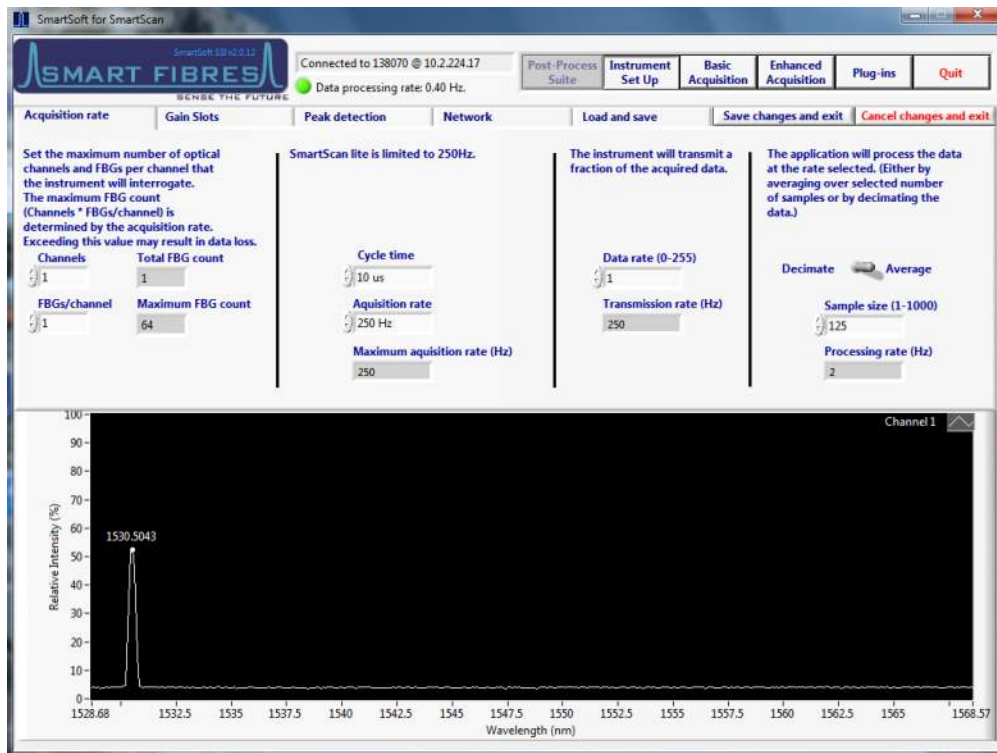


Figure 2.3 – SmartScan Main Window

- b. **Basic Acquisition tab:** This tab has three sub-tabs used to collect data from the FBGs over set time periods.
  - i. The ***Spectrum*** tab is used to view the spectrums of the FBGs of a specific channel. The channel being viewed can be changed. See SmartSoft User manual pg. 10 for more details.
  - ii. The ***Sensors*** tab has a table to the left which shows the wavelengths of the FBGs which updates every few seconds. To the right there is a log file box which is where the save location of the output data file is specified. Below that are the log controls. In the log time box enter the number of seconds that you would like to record wavelength data for. When you are ready to start recording, press the log button and a log progress bar will appear. See SmartSoft User manual pg. 11 for more details.
  - iii. The ***Charts*** tab is used to plot FBG variables such as temperature, strain, wavelength or pressure. See SmartSoft User manual pg. 12 for details.
- c. **Enhanced Acquisition tab:** The ***Spectrum*** tab has similar functions to those of the spectrum tab in the basic acquisition tab as described previously. See SmartSoft User manual pg. 21 for details.
  - i. The ***Select sensors*** tab allows the user to record data from a specific FBG sensor in a situation where there are multiple connected FBGs. The units of the wavelength can be set, and the sensor type can be selected. See SmartSoft User manual pg. 23 for details.
  - ii. The ***Charts*** tab has similar functions to those of the charts tab in the basic acquisition tab as described previously. Only the FBGs added in the select sensors tab will be selectable in the charts tab. See SmartSoft User manual pg. 27 for details.
  - iii. The ***Graphic*** tab can be used to import an image that can then be labeled with charts or graphs taken from the acquired FBG data. See SmartSoft User manual pg. 28 for details.
  - iv. The ***Event capture*** tab is used to record a plot of FBG wavelength data over a specified time period. The plot can be saved to file. See SmartSoft User manual pg. 29 for details.
  - v. The ***Plugins*** tab is used to run Lab View source code for more customized data acquisition. The software comes with a built in plugin setup for Fast Fourier Transform analysis. See SmartSoft User manual pg. 29 for details.
- d. **Plugins tab:** The ***Plugins*** tab serves the same function as the plugins tab described previously in the enhanced acquisition section.



## PART 3 – INSTALLING, PROTECTING AND REPAIRING OPTICAL FIBER SENSORS

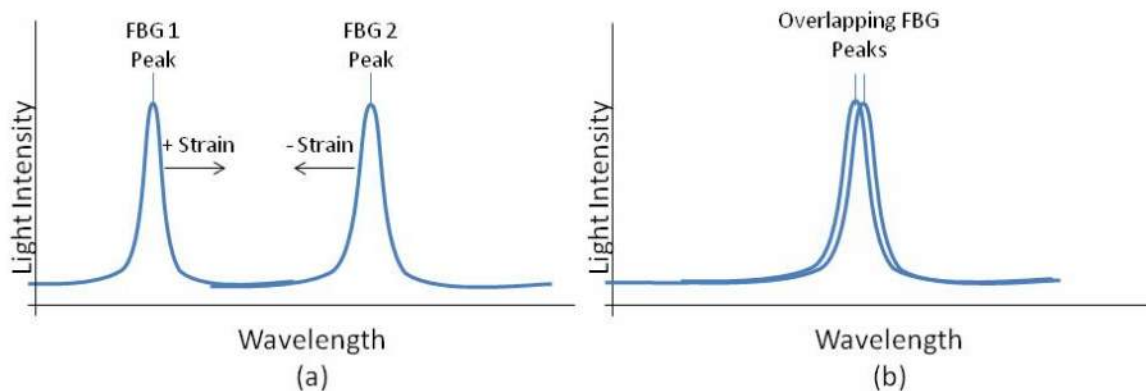
Methods were developed for installing, protecting, and replacing FBG sensors on bridges. Of primary concern was the feasibility and ease of using the installation methods in the field, the durability and ruggedness of the sensing system, and the practicality of repairing damaged fibers or sensors once installed.

### Multiplexed Sensor System Design

Multiplexing, or the ability to attach multiple sensors on a single channel, is one of the main advantages of using an FBG-based SHM system. It allows a single interrogator, which is generally the most expensive component of an FBG based system, to read a large number of sensors. Ideally, a single interrogator would be used to read all of the sensors on a bridge.

For a multiplexed FBG system, a sensor plan should be carefully developed prior to installing any sensors, to ensure that the operating wavelength spectrum of each channel of the interrogator is efficiently utilized. The operating spectrum of an interrogator is often the largest constraint on the number of sensors that can be effectively multiplexed, and interrogators with wider spectra or more channels will incur significant costs.

Therefore, consideration must be given to the wavelength range that multiplexed sensors will experience under operating conditions. If the reflected peaks from two FBG's on the same channel overlap during operation, interrogators cannot differentiate the light returning from the two sensors, and the reflected light will register as a single peak returning from a single FBG. This overlapped peak confuses the data collection, and renders those sensors ineffective. This problem occurs if the unstrained FBG peaks are not spaced far enough apart on the wavelength spectrum to allow for the wavelength shift caused by the strain conditions. An illustration of this issue is provided in Figure 3.1.



**Figure 3.1 - Interrogation Overlap Due to Inadequate Sensor Spacing**

(a) Unstrained sensor reflected peaks, (b) Strained sensor reflected peaks



The wavelength spacing can be adjusted by applying different magnitudes of pretension to the fibers while they are being adhered to the structure. Enough pretension can be applied to a fiber to cause a wavelength shift of about 4nm without causing concern for over-tensioning the fiber during the FBG service.

To prevent overlapping peaks, preliminary analysis of the expected structural behavior should be performed to determine the appropriate location and pretensioning necessary to place multiplexed FBGs with adjacent wavelengths. The maximum shift on the light spectrum will be dictated primarily by the maximum strain that the fiber will undergo while in operation. For a maximum strain of 0.003, the corresponding shift in wavelength is approximately 4nm.

The maximum expected wavelength shift due to strain provides an estimate on the necessary spacing between wavelength peaks, but one must be judicious in spacing FBG wavelengths to also maximize the number of sensors that can be multiplexed onto a single channel. In areas of the structure where large strains are unlikely to occur, the wavelength spacing may be reduced. However, if two fibers possess adjacent wavelength peaks on the spectrum and are likely to experience concurrent opposing strains (one fiber undergoing positive strain, while the other experiences negative strain), bringing the wavelength peaks toward each other, then the wavelength spacing between them should be increased appropriately. Often, care can be taken to place FBGs with adjacent wavelengths in areas of the structure that will undergo concurrent strains in the same direction allowing for a reduction in the wavelength spacing.

A sensor plan, which maps the locations of the FBGs on the structure with their corresponding wavelengths, helps to design an effective layout for the FBG sensors that can efficiently utilize the operational spectrum of the interrogator. System designers must determine appropriate wavelength spacing for the strains expected in the structural locations being measured.

### **Sensor Installation**

In adhering the fiber Bragg gratings to bridges, care must be taken to ensure good strain transfer and reliable readings. The fibers need to be aligned along the desired axis of strain measurement, and it must be ensured that the fibers are securely attached to the host material without any slack or buckling in the fiber across the sensing region. Slack and buckling in the fiber is prevented by applying a slight pretension to the fiber while adhering it to the host element.

While a nominal amount of pretension is necessary to ensure a sensor is installed straight and with a good bond, the specific amount of pretension necessary will be dictated by the wavelength required by the sensor plan. Often the sensors provided by an FBG manufacturer may not have base wavelengths corresponding to the necessary peak wavelengths required by the sensing plan. The peak wavelength can be increased by as much as 4 nm by applying pretension to the sensor during installation on the structure. Care must be taken not to over-tension the FBGs, as they can be brittle and have a tendency to break across the sensing region, which is slightly weakened during the manufacturing process. Therefore, when ordering FBGs it is important to order sensors with base wavelengths that vary all across the effective spectrum of the interrogator.

It was desired to develop a simple and effective method for adhering FBG sensors to steel and concrete elements. Of primary concern was achieving an effective bond capable of delivering adequate strain transfer to the FBG and devising an efficient method for installation that would be simple to perform in field conditions.

After an FBG is installed, the sensor and lead fiber must be protected from weather, vandals, and wildlife. For the portions of the optical fiber between sensors or leading to the interrogator, a much more durable fiber that is secured in a 900 micron plastic sleeve should be spliced in. This additional sleeve provides much more flexibility and durability than the standard acrylate coating. However, it would still be vulnerable to wildlife and vandals; so additional protection methods may be necessary.

Separate methods were developed for installing, protecting, and replacing FBG sensors for steel and concrete structures. The specific methodology is detailed in the following subsections.

### ***Sensing Steel Elements***

#### ***Installation of Bare Fibers on Steel Elements***

As steel is a homogeneous material, the strain sensor can be adhered directly to the region where measurement is desired. Adhering an FBG directly to the surface of steel elements using cyanoacrylate adhesive achieves satisfactory strain transfer. A specific type of adhesive that has proved useful for the installation procedure is a thickened fast-curing cyanoacrylate adhesive called Lightning Bond™, which comes with an activator spray that accelerates the curing process. Loctite™ produces a similar product. Applying the FBGs to the steel material with the proper pretension requires methodical precision. The method devised for achieving an adequate bond with the appropriate pretension is as follows:

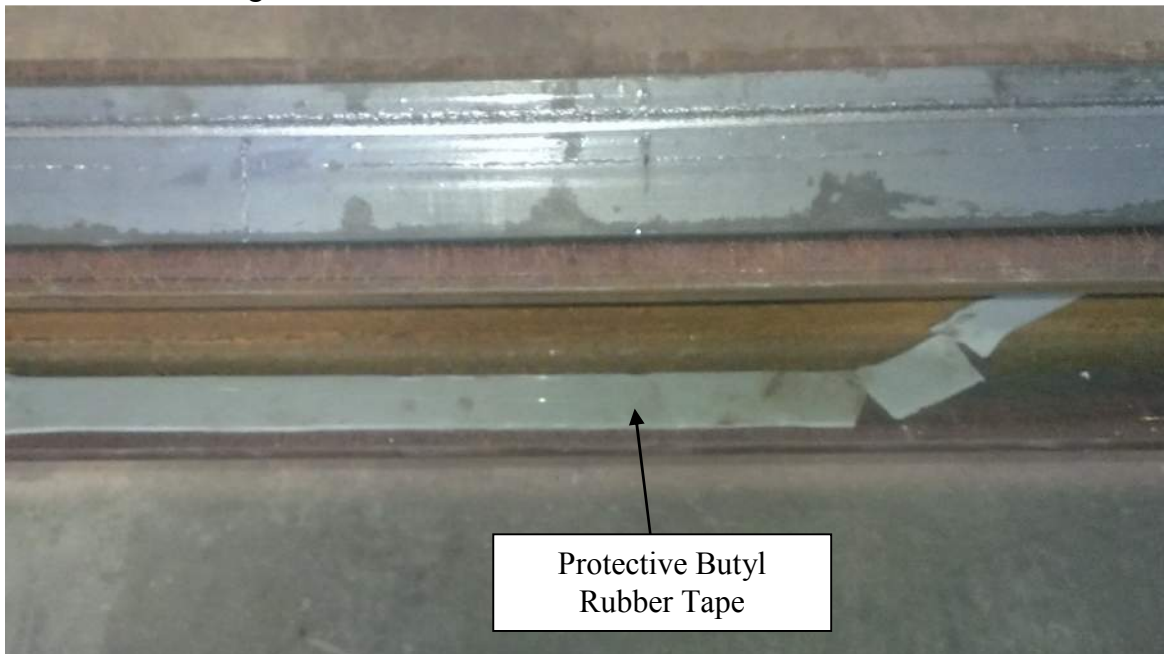
1. Remove any mill scale or paint using a grinder or wire brush. Then clean the material surface, removing all oil, and slightly roughen it with sand paper.
2. Carefully mark the location to be measured on the element and draw a straight line along the axis of measurement. Then position the fiber along the axis of measurement so that the FBG region of the fiber is positioned at the location of interest. Then tape one end of the fiber to the structure to aid in aligning the fiber for the next step.
3. Apply the cyanoacrylate adhesive approximately 2 inches away from the sensing region along the axis of measurement. Set the fiber into the adhesive so that the FBG is aligned and positioned correctly and spray the activator over the adhesive region to accelerate the curing process. Hold the fiber in place until the adhesive cures (about 30 seconds).
4. Once the adhesive has cured apply the cyanoacrylate adhesive to the region to be measured ensuring a minimum adhesive length of 1.5 inches. Then, gently adjust the tension on the fiber until the target wavelength is achieved. Next, press the fiber against the steel so that it is aligned with the axis of measurement and in good contact with the adhesive. Hold the fiber steady, ensuring that it is tensioned to the appropriate wavelength, and apply the activator to the adhesive. Hold the fiber in place until the adhesive cures (about 30 seconds). As an alternative to manually holding the

fibers in place while the glue cures, a pair of flat clamps or strong magnets may be used to hold the fiber in tension against the steel member. For this approach, the fiber should be protected from the clamps or magnets using a thin piece of rubber or similar cushioning material. Prior to applying the activator spray, verify that the pre-tension is stable by monitoring the wavelength for any change

5. Slowly release hold of the fiber while monitoring the wavelength for any significant drop in wavelength. If the wavelength of the applied FBG fails to stabilize at a higher wavelength than the base wavelength, then adequate bond has not been achieved. If a satisfactory bond is not achieved, refer to the subsequent replacement procedure.

### ***Protection on Steel Elements***

For steel material, application of a rugged, durable tape over the fiber is the simplest method for providing protection. The tape provides adequate protection and also holds the fibers in place. Fiber with the additional plastic protective coating should be spliced between FBG sensors to provide further durability under the tape. A modified butyl rubber tape produced by Permatite™ is recommended. The tape is rated for exterior exposure with a temperature range from -40°F to 250°F and provides a watertight seal. The tape is approximately 1/8" thick with a soft rubber or clay-like consistency, and it is available in various widths. The tape bonds well to steel, although no long term environmental exposure tests were performed. The steel should be clean and free of mill scale and oil prior to applying the tape. An example of this protection method is shown in Figure 3.2.



**Figure 3.2 - Protected FBG Fiber on Steel Beam**

### ***Replacement on Steel Elements***

If a fiber breaks on a multiplexed channel, then the signal from all FBGs beyond the break will be lost. The location of the last FBG reflecting a signal back to the interrogator can be used to locate the break in the optical fiber, as the break will be located somewhere between this

last reporting FBG and the next sensor on the fiber. To replace the damaged fiber, at least one foot of the protective tape must be removed from each side of the break to allow enough slack in the fiber to perform a splice. In regions where the lead fiber is protected by the additional sleeve, the tape can be carefully removed with a putty knife. In regions where the fiber lacks this protective sleeve it will be difficult to remove the tape without breaking the fiber.

If the break occurs near a sensor, where a fiber cannot be repaired by simply splicing in an additional length of fiber at the break, the damaged fiber will need to be removed and replaced. Once the tape has been removed, a putty knife or a razorblade can be used to scrape off the old fiber and adhesive. Sandpaper should be used to re-clean and roughen the surface. Then the new FBG can be spliced and installed according to the preceding installation instructions.

### ***Installation of Carrier-Mounted Sensors on Steel Elements***

The process for installing FBG sensors on a steel host varies when the sensors are mounted on a carrier, such as the case with Micron Optics' os3120 FBG sensors. The installation process is summarized below. An effective Youtube video is available at: <https://www.youtube.com/watch?v=PejlfJxzNmE>

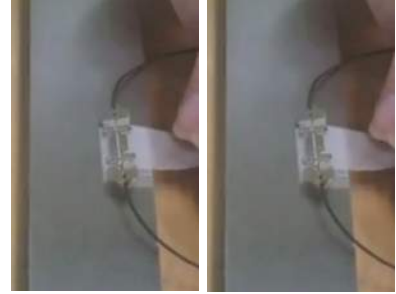
1. Mix Epoxy: Fill dropper with Curing Agent 10 exactly to the number 10 and dispense the contents into the center of the jar of Resin AE. Immediately cap the bottle of Curing Agent 10 to avoid moisture absorption. Mix thoroughly for five minutes, using one of the plastic stirring rods. Discard the dropper after use.



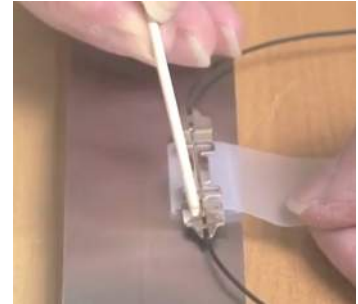
2. Prepare Surface: Sand the surface lightly to remove debris down to sound metal. Spray degreaser directly onto the surface and wipe down. Apply conditioner directly onto the surface. Use a new cloth to wipe the surface. Apply neutralizer directly onto the surface and wipe with a new cloth.



3. Position Sensor: Place the sensor along the axis of strain measurement. Tape the sensor to the surface, then pull back the tape on one side.



4. Apply Epoxy: Apply enough epoxy to cover each end of the sensor mount using a wooden dowel. Tape the sensor back on the surface.



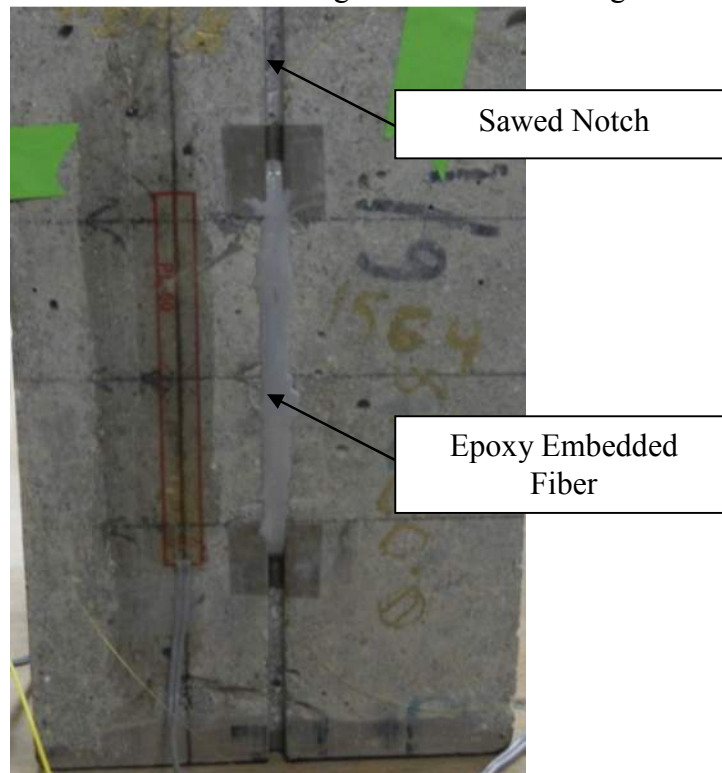
5. Cure Epoxy: Plate a metal plate over the os3120 and secure by taping. Clamp the plate to the surface. Allow epoxy to cure at room temperature for approximately six hours.



## ***Sensing Concrete Elements***

### ***Installation on Concrete Elements***

Because of the porous nature of concrete, it is difficult to achieve a high-quality, long-lasting bond using cyanoacrylate adhesive. In other studies, FBG fibers have been embedded in concrete using mechanical anchors or affixed to rebar. However, the intent here is on methods for installing an SHM system post-construction. Therefore, a method was necessary for applying FBG sensors to in-service concrete structures. The recommended approach is to adhere FBG sensors to concrete by placing the fiber in a shallow channel on the concrete surface, which can be cut using a masonry saw, and embedding the fiber in a stiff high-strength epoxy. The epoxy used in this study was Ultrabond 1300™. The resulting bond is shown in Figure 3.3.



**Figure 3.3 – Bond Resulting From Notch Embedded Epoxy Procedure For Concrete Fiber Installation**

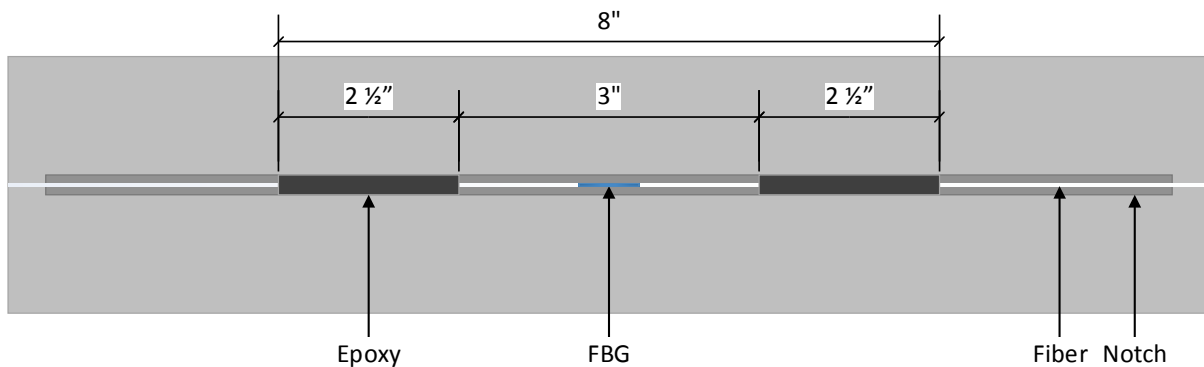
Based on physical, a bond length of 2.4 inches (60 mm) is regarded as sufficient to achieve adequate strain transfer for fibers embedded at reasonable depths in saw notches 0.125 in wide and 0.125 in deep.

While embedding the fibers in a notch provides a good mechanism for strain transfer, it does present some accessibility challenges for installing fibers with adequate pretension. Furthermore, the majority of high-strength epoxies require at least 24 hours to fully cure. This makes it impractical for the fiber to be held in place manually until the epoxy reaches full strength. Therefore, a procedure was devised to apply an FBG fiber into a notch with adequate pretension and hold it in place long enough for the epoxy to cure. The devised method involves installing a heat-shrink protective sleeve on the fiber, which bonds to the fiber and provides a

means to grasp and tension the fiber. These protective sleeves can be affixed to concrete using cyanoacrylate. While this bond is not adequate for permanent installation in service conditions, it is sufficient to hold the fiber in place temporarily while the epoxy cures. This procedure is presented in detail in the following installation instructions for concrete.

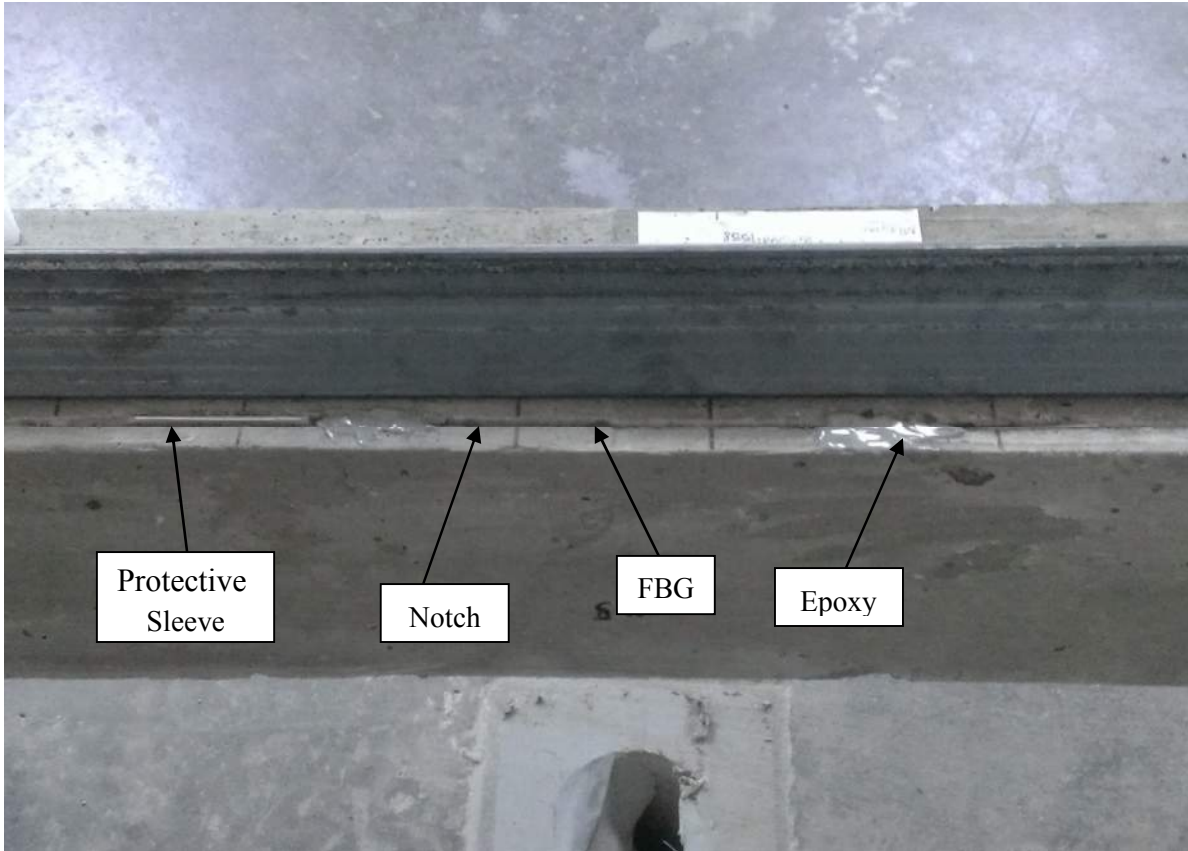
Unlike steel, concrete is a heterogeneous material and the strain field is not constant across the material. For normal strength concrete, the stiffer aggregate will strain less than the cementitious material. As the strain increases, cracks will form, creating regions where most of the deformation is distributed into crack widening and almost no strain is experienced by the regions between cracks. Thus, it is necessary to average the strain across a long gage length for concrete rather than sensing strain locally. A gage length of 8 inches (20 cm) for concrete and asphalt materials is recommended.

The configuration devised to achieve a long-gage strain sensor with adequate bond length consists of a shallow notch in the host concrete structure with two regions of epoxy approximately 2.5 inches long separated by an unepoxied region of at least 3 inches. The FBG is positioned in the center of the unepoxied region. A diagram of the long-gage FBG strain sensor is shown in Figure 3.4. This configuration shows the minimum gap between the epoxied regions. The strain over the epoxy region may not be uniform as the bond is developed. However, in the analysis the strain obtained will be treated as a reading at a localized point, likely located at a point of maximum strain. A photo of an FBG installed according to this configuration is shown in Figure 3.5. As the FBG is not directly affixed to the material, it is critical to maintain enough pretension in the fiber to prevent it from reaching a relaxed state during service. Therefore, the maximum expected compressive strain should be considered when determining the proper pretension to apply to the sensors for the system.



**Figure 3.4 – Minimum Configuration for Long-Gage Strain Sensing of Concrete Using an FBG**





**Figure 3.5 – Photo of Long-Gage FBG Installed on Concrete Beam**

The protocol developed for installing FBGs onto concrete members is as follows:

1. Prior to splicing the FBG into the channel line, slide a heat shrink protective sleeve onto each side of the FBG approximately 5 inches away from the center of the sensor. Being careful to keep the sleeve in place on the fiber, set each sleeve into the heating unit on the splicer to bond it into place. Once the sleeves are in place, the FBG fiber can be spliced onto other fibers or leads following typical procedures.
2. Carefully mark the location to be measured on the host structure and draw a straight line along the axis of measurement. Then, using a 1/8 in thick masonry blade, cut a straight shallow notch into the beam along the axis of measurement approximately 1/8 inch deep and 12 inches long.
3. Align the fiber with the notch and mark off the locations for the FBG sensor, the unepoxied region (approximately 3-5 inches), the epoxied regions on each side (2.5 inches), and the protective sleeves. Then using these marks as a guide, apply a thin layer of cyanoacrylate adhesive to one of the protective sleeves and position it in the notch. Ensure that it is in the appropriate position, and firmly press it down until the adhesive cures.
4. Using a small flat head screwdriver or similar tool, distribute the epoxy into the bottom of the notch, filling it approximately halfway up in the epoxied regions.



*Note:* For sensors being installed overhead or on vertical faces, it may be necessary to wait approximately 10 minutes after mixing the two parts of the epoxy for it to establish adequate viscosity to prevent it from running.

5. Apply a thin layer of cyanoacrylate adhesive to the remaining unattached protective sleeve and to the corresponding region of the notch. Then, gently apply the appropriate pretension to the fiber and press the sleeve into the notch. Firmly hold the sleeve in place to maintain the pretension in the fiber. Then spray the activator on the cyanoacrylate adhesive and continue to hold the sleeve until the bond is secure.
6. Using the flathead screwdriver, fill the epoxy region to the top of the notch with epoxy, being careful not to damage the fiber. Then monitor the wavelength for any significant drop in wavelength. If the wavelength fails to stabilize above the base wavelength, it indicates an inadequate bond between the sensor and host material. If a satisfactory bond is not achieved, refer to the subsequent replacement procedure.

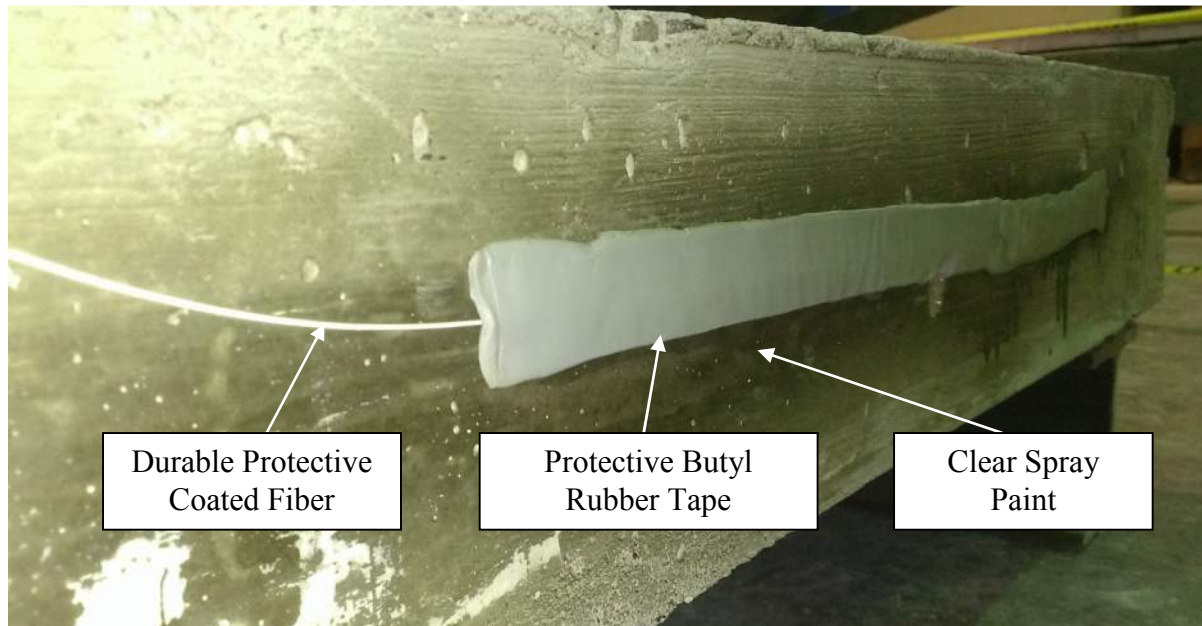
### ***Protection on Concrete Elements***

Affixing protective materials to concrete is more difficult than affixing to steel due to the rough surface, to which the tape does not adhere well. Two methods were developed to protect fibers attached to concrete elements.

The first method requires a more intricate installation process, but results in a more permanent system. However, if for some reason an element in the SHM system breaks, all of the sensors on the channel must be replaced. To begin, a notch is cut the full length of the bridge, and each sensor must be installed so that the fiber lies within the notch for the full length of the bridge. To ensure that the optical fibers fit into the notch, the fibers between sensors must be measured out to be the same length as the notch between sensors, so that the fibers can be installed onto the structure with very little slack. Once all of the sensors have been installed, the entire length of fiber for each channel is laid into the notch and covered with epoxy, except for the unepoxied regions where FBG's have been installed. Over the unepoxied regions, a thin 1-inch wide cover plate, made of either plastic or metal, can be attached to the concrete using epoxy to seal off the notch. This method results in a very durable, permanent system. However, the installation process is complicated by the necessity of having a taught fiber between sensors, and it can be cumbersome to saw a notch the full length of the bridge. Finally, if a problem is discovered in any of the sensors after the protection system is in-place, then the entire line of sensors must be cut out, and new sensors must be installed.

The second method does not provide as robust protection, however it is easier to implement, and it allows for repairs to be performed without replacing all of the sensors on a channel. For this method, shallow, 1-foot long notches are cut at sensor locations, and the FBGs are installed according to the installation procedure. Between sensors the more durable fiber with a 900-micron protective sleeve is spliced leaving enough slack between sensors to maintain workability. A strip of clear spray paint is applied along the length of the element and allowed to dry in order to produce a smooth surface. Then the fiber is attached to the element using the butyl rubber tape discussed in the steel protection method section. The tape must be pressed firmly onto the concrete to ensure an adequate bond. If there is excess fiber, it can be wound

into a loop and covered with butyl rubber tape. Care must be taken not to wind the fibers into too tight of a loop, which would result in a loss of signal. A diameter of about 2 to 3 inches is acceptable. The butyl rubber tape can be installed over the notched regions where sensors are installed, or a thin cover plate may be epoxied into place to provide extra protection for the bare fiber in the notch. A figure of the second protection method is shown in Figure 3.6.



**Figure 3.6 – Protection Method 2 for Fibers Installed on Concrete**

### ***Replacement on Concrete Elements***

If protection method 1 was used, and it is discovered that a sensor is not performing, then all of the fiber will need to be removed from the notch, and new sensors will need to be installed. The epoxy may be removed using a file and similar hand tools, or it may be easier to recut the notch using a masonry blade. Once all of the sensors are removed, new sensors must be installed and protected according to the previous instructions.

If protection method 2 was used, the butyl rubber tape can be gently removed from the structure using a putty knife. Care must be taken not to damage the underlying protective coated fiber. If the break occurred along the fiber between sensors, then the disjointed fiber ends can be stripped, cleaved, and spliced according to common practice. The fiber can then be re-adhered to the structure using a fresh strip of the butyl rubber tape.

If the break occurred at, or close to, the sensor, then the sensor will need to be replaced. If a cover plate was used, it should be removed by scraping the underlying epoxy away with a putty knife. Otherwise the butyl rubber tape can be removed by gently pulling it back using a putty knife. Enough of the lead fiber should be liberated to splice a new FBG onto the channel. To remove the old sensor, the epoxy can be removed with a file, and the glued fiber protectors can be pried out using a flathead screwdriver. Once the old fiber is removed and the notch is cleaned, a new sensor can be installed according to the preceding instructions.

## PART 4 – TEMPERATURE COMPENSATION FOR FBG SENSORS

FBG sensors are sensitive to changes in temperature and are not self-compensating for temperature variations. Therefore, it is necessary to separate the wavelength shift due to temperature variation from the wavelength shift due to mechanical strain in the host material. While the relationship between temperature and wavelength shift is well established (Eq. 4.1), measuring temperature introduces complexity to the system. It is easier to measure the temperature effect on wavelength directly by using an FBG that is isolated from mechanical strain, and directly subtracting this apparent strain from the other bonded sensors on the structure to determine the resulting mechanical strain. The computations for this procedure are illustrated in the following.

The relationship between temperature change  $\Delta T$  and wavelength shift is given by:

$$\Delta\lambda_T = \lambda_0(\alpha_A + \alpha_\eta)\Delta T \quad (4.1)$$

where:  $\Delta\lambda_T$  = wavelength shift due to temperature change  
 $\lambda_0$  = base wavelength of FBG  
 $\alpha_A$  = thermal expansion coefficient of fiber ( $\approx 0.55 \times 10^{-6}/^\circ\text{C}$ )  
 $\alpha_\eta$  = thermo-optic coefficient ( $\approx 8.60 \times 10^{-6}/^\circ\text{C}$ )  
 $\Delta T$  = change in temperature

For a given change in temperature, the strain sensing FBG would read a total wavelength shift of:

$$\Delta\lambda = \Delta\lambda_M + \Delta\lambda_T \quad (4.2)$$

where:  $\Delta\lambda$  = total wavelength shift  
 $\Delta\lambda_M$  = wavelength shift due to mechanical strain  
 $\Delta\lambda_T$  = wavelength shift due to temperature change

The relationship between strain and wavelength shift in an FBG is given by Equation 4.3.

$$\varepsilon = \frac{\lambda - \lambda_0}{G\lambda_0} \quad (4.3)$$

where:  $\varepsilon$  = strain  
 $\lambda$  = reflected wavelength  
 $\lambda_0$  = unstrained reflected wavelength  
 $G$  = gage factor (typically 0.78)

Rearranging Equation 4.3 gives:

$$\Delta\lambda_M = \lambda_0 G \varepsilon \quad (4.4)$$

where:  $G$  = FBG gauge factor  
 $\varepsilon$  = strain

Substituting for  $\Delta\lambda_M$  and  $\Delta\lambda_T$  gives:

$$\Delta\lambda = \lambda_0 G \varepsilon + \lambda_0 (\alpha_A + \alpha_\eta) \Delta T \quad (4.5)$$

The value for  $\Delta T$  can be obtained by the temperature compensating FBG by rearranging equation 4.1:

$$\Delta T = \frac{\Delta\lambda_{TC}}{\lambda_{0TC} (\alpha_A + \alpha_\eta)} \quad (4.6)$$

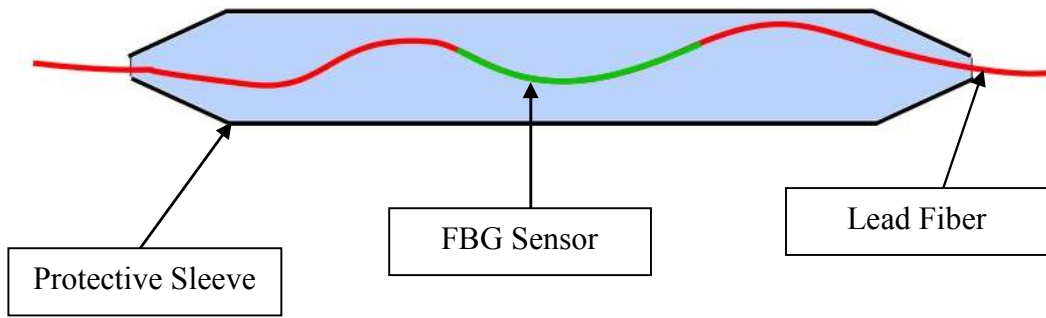
where the subscript  $TC$  denotes the values are obtained from the temperature compensating FBG sensor. Substituting equation 4.6 into equation 4.5 and simplifying results in the formula:

$$\Delta\lambda = \lambda_0 G \varepsilon + \frac{\lambda_0}{\lambda_{0TC}} \Delta\lambda_{TC} \quad (4.7)$$

Then solving equation 4.7 for strain  $\varepsilon$  gives the equation for field measured strain using a temperature compensating FBG sensor:

$$\varepsilon = \frac{\Delta\lambda - \frac{\lambda_0}{\lambda_{0TC}} \Delta\lambda_{TC}}{\lambda_0 G} \quad (4.8)$$

To measure the thermal effect on FBG readings, it was necessary to develop a method for isolating an FBG sensor from mechanical strain while providing adequate protection to ensure durable operation. To achieve this, an FBG sensor is inserted into a protective heat shrinking tube, which is typically used for protecting splices in optical fibers. Using a heat source, one of the tips is heated until it shrinks and achieves a bond with the fiber. Then the fiber is compressed to induce a buckled shape inside the protective sleeve. Then the other tip is heated to lock the fiber into place while being careful to maintain the buckled shape. The resulting protective sleeve is pinched at the ends, and a gap remains in the middle to allow the sleeve to expand and contract as temperature fluctuates without inducing mechanical strain in the fiber. The devised encasement for a temperature compensating FBG is illustrated in Figure 4.1.

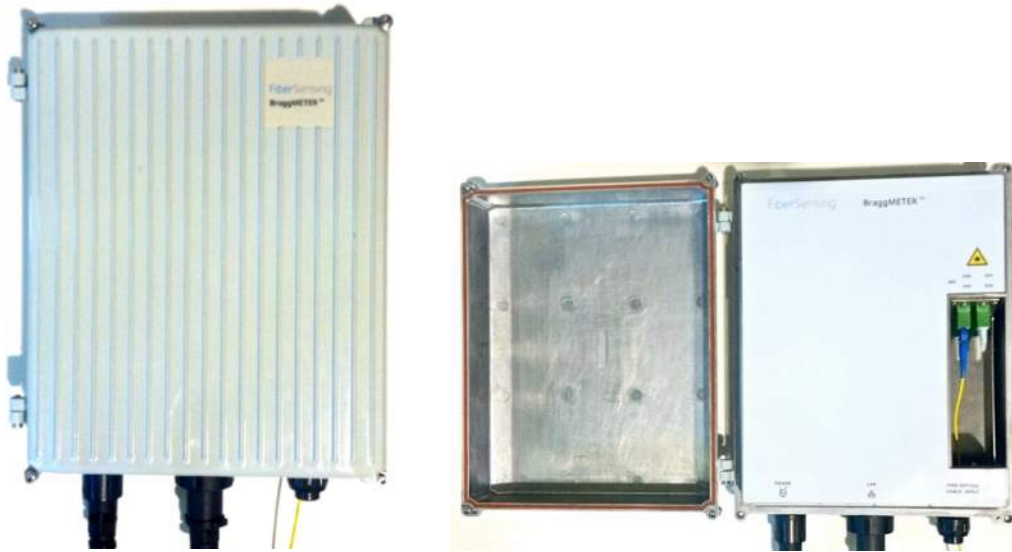


**Figure 4.1 – Temperature Compensation FBG**

## PART 5 – SCHEMATIC DESIGN AND FABRICATION OF INSTRUMENTATION

### Introduction

Field instrumentation necessary for the discrimination of bridge strain data based on critical events, such as the passing of an overloaded truck, primarily relies on a robust fiber Bragg grating (FBG) sensor interrogator, data processing microcontroller, and data storage capability. The FS2200 extended temperature BraggMETER by HBM FiberSensing was chosen as the FBG sensor interrogator for field deployment due to its programming capabilities, ethernet interface, and ability to handle harsh environments (Figure 5.1). The FBG interrogator strictly interrogates and interprets optical strain sensor response and transmits that data over a standard ethernet interface. Therefore, in a remote installation where power and data transmission requirements are to be minimized based on predetermined criteria, the designer is forced to build a low-power controller that will autonomously communicate with the interrogator on a localized basis.



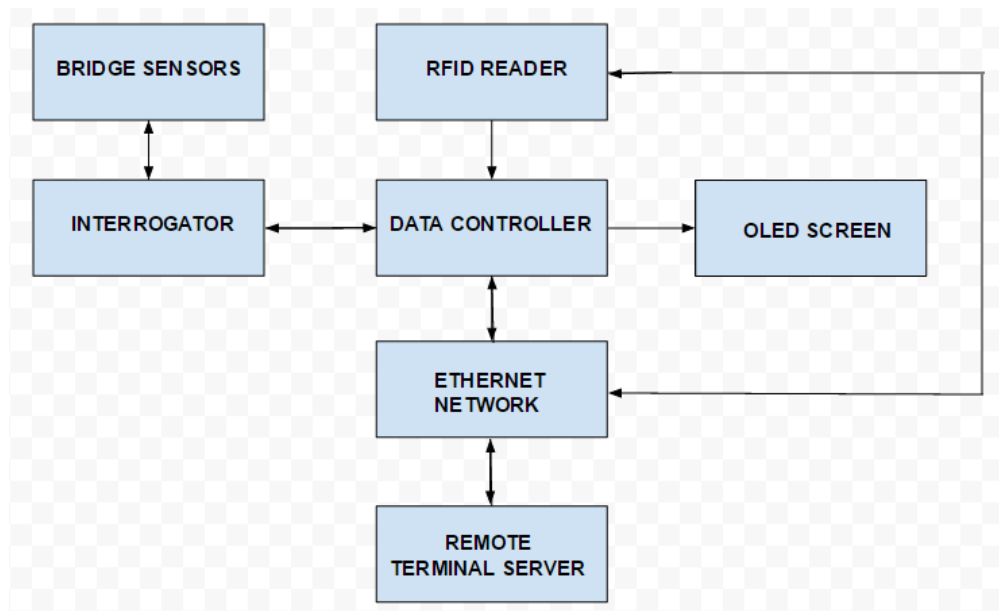
**Figure 5.1: The FS2200 extended temperature BraggMETER by HBM FiberSensing.**

The designed data controller can be programmed to only allow data that meets particular requirements (such as minimum or maximum strain) and/or be programmed to only allow data following a trigger from an external device (such as an RFID reader). The purpose of the data controller is to act as an intermediary between the interrogator and the network, through which decisions can be made based on predetermined parameters or an external trigger mechanism. For this system, an RFID reader was selected to provide a trigger response to the data controller in order to signal the beginning and end of a data transmission from the interrogator. The CS203 from Convergence Systems Limited was selected as the RFID reader in conjunction with

CS6710 RFID tags for this application. Before a description of the controller design is given, it is important for the reader to understand that the BraggMETER FS2200 has not been altered in any way. The interrogator still functions as it was originally intended (without the data controller), therefore, the user should refer to the operating manual for specific details concerning the operation of the FS2200, if it is to be used in this fashion.

### System Overview

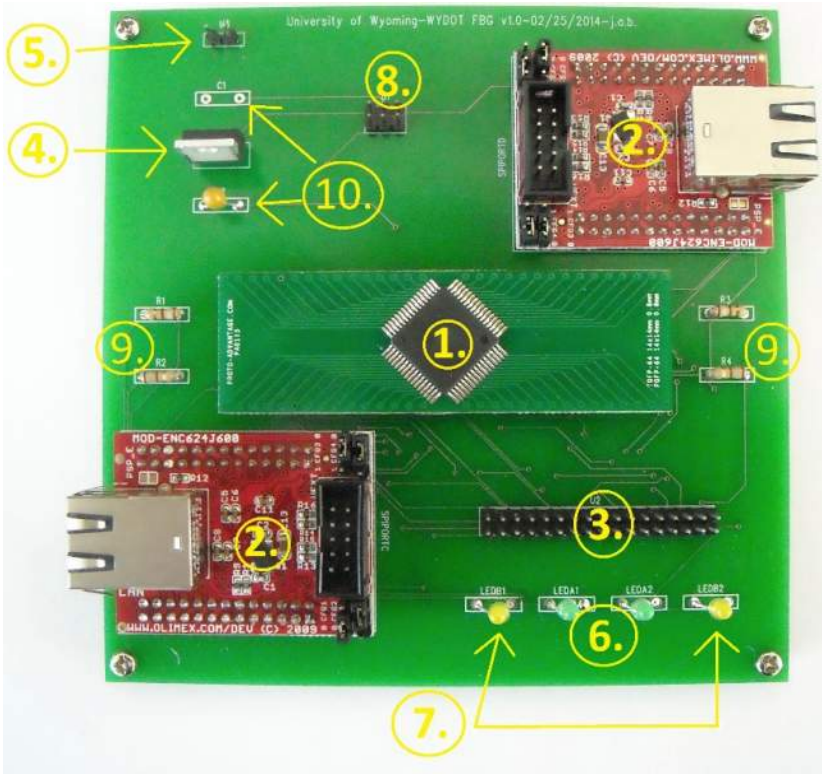
Figure 5.2 illustrates the basic interactions among components in the system. The optical bridge sensors connect to the four channels of the FS2200 interrogator through APC optical connectors (See Figure 5.1). Two CAT5e cables with RJ45 connectors extending from the data controller are used to connect the controller to the interrogator and the ethernet network. On the printed circuit board, two ethernet controllers are labeled “PORT C” and “PORT D” (see Figure 5.3). The ethernet controller labeled “PORT C” should be connected to the interrogator and the ethernet controller labeled “PORT D” should be connected to the network. The RFID reader is connected to the data controller through the provided GPIO cable from Convergence Systems Limited. The term “Ethernet Network” should be interpreted as a Cell Modem, Switch, Router, Radio, or by any intermediary ethernet equipment between the data controller and the network connected terminal server. The data controller and RFID reader can also be connected directly to the terminal server’s network interface card if there are enough ports available, otherwise a switch must be used. Nevertheless, it is important to mention that any device that is used to connect to the terminal server should support Auto-MDIX for the data controller to function properly.



**Figure 5.2: Block diagram illustrating system component interactions.**

The data controller consists primarily of two enc624J00 ethernet controllers, an Atxmega64a3 microcontroller, a 6-pin PDI programming port for the microcontroller, a 34-pin

GPIO microcontroller breakout port, and a power supply (see circuit schematics of Figures 5.3, 5.4, 5.5, 5.6 and 5.7). Data from the interrogator passes from the ethernet controller labeled PORT C, through the microcontroller, and to the terminal server or network through the ethernet controller labeled PORT D. Most of the GPIO pins are unused; exceptions are the OLED screen and the RFID input. The OLED screen is connected to pins D3, VCC, and GND, whereas, the RFID is connected to pin A0. The ethernet controllers “talk” to the microcontroller over a serial peripheral interface (SPI), the OLED screen through a universal asynchronous receive transmit (UART), and the RFID through a simple on-off (0-3.3v) signal. There are two pairs of green and yellow colored LEDs on the circuit board that relate to both of the ethernet controllers. On the finished product, these LEDs have been brought out to the side of the enclosure that houses each controller. There is one green and one yellow LED for each controller. The green LED will illuminate when the ethernet controller has established a PHY connection and the yellow LED will illuminate when the ethernet controller either receives or transmits data from the server or client. The OLED Screen can be programmed further, but is currently used to give system information upon startup regarding initialization status with the network and interrogator.

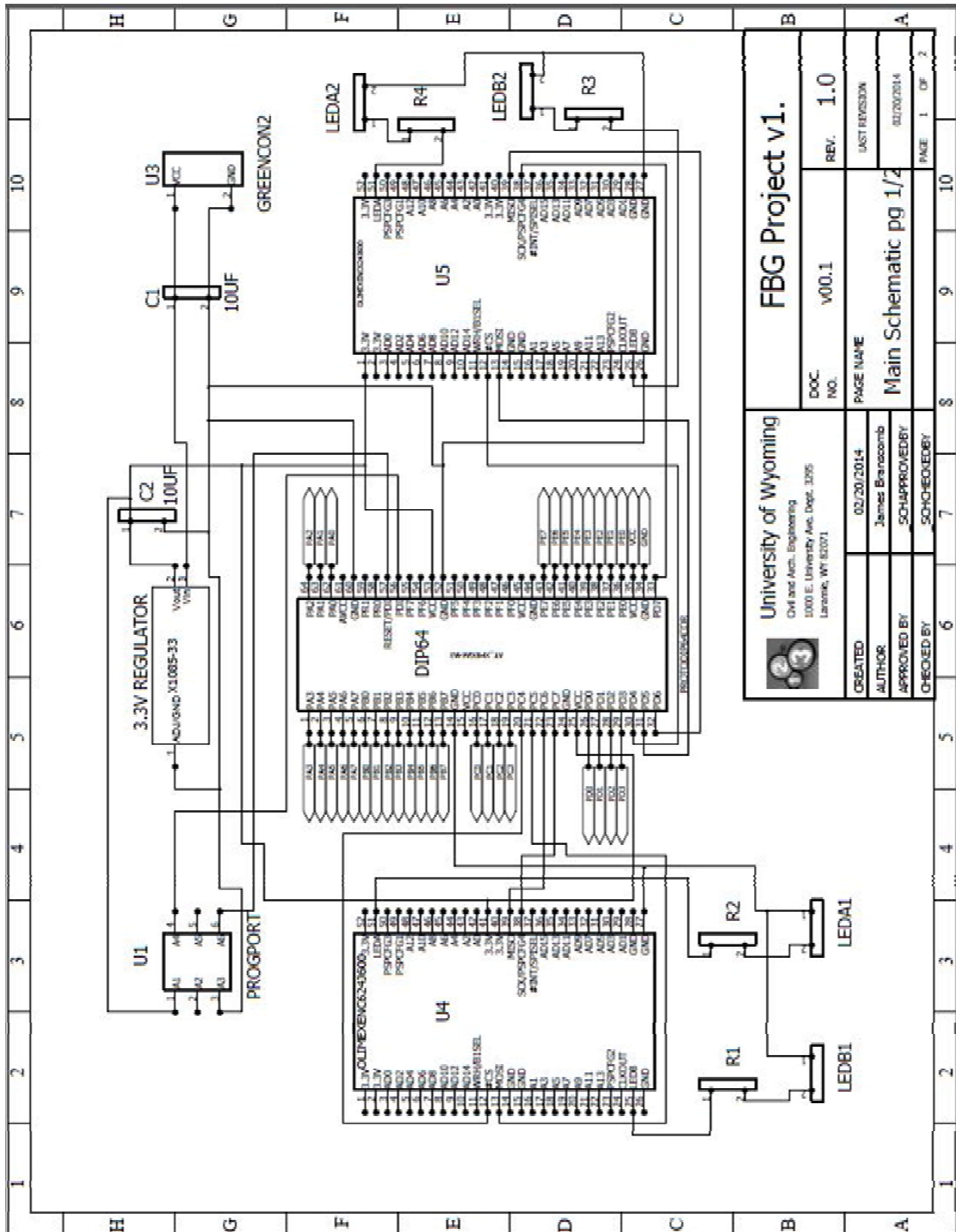


**Figure 5.3: Diagram of the finished printed circuit board (PCB)**



The following components are identified in Figure 5.3:

- 1) Atmel Atxmega64a3 microcontroller
- 2) Olimex mod-enc624J600 Ethernet controllers
  - PORT C to Interrogator (on bottom as pictured)
  - PORT D to Network (on top as pictured)
- 3) General purpose input/output (GPIO) pins/UART/SPI/VCC/GND for OLED screen, RFID Reader, and future device implementation
  - OLED Screen data pin on D3 (see Figure 5.6)
  - OLED Screen power pin on VCC (see Figure 5.6)
  - OLED Screen ground pin on GND (see Figure 5.6)
  - RFID GPIO pin on A0 (see Figure 5.6)
- 4) LM1085it-3.3v fixed voltage regulator (27V maximum input-to-output differential)
- 5) Voltage Supply
- 6) LED Ethernet link status indicators for the two Ethernet controllers (programmable)
- 7) LED Ethernet activity indicators for the two Ethernet controllers (programmable)
- 8) PDI programming port for the Atxmega64a3 microcontroller
- 9) 180 $\Omega$  current-limiting resistors for LED Ethernet indicators
- 10) 10uF Bypass capacitors




 <b>University of Wyoming</b> Civil and Arch. Engineering 1000 E. University Ave. Dept. 3205 Laramie, WY 82071		<b>FBG Project v1.1.</b>	
CREATED 02/20/2014	AUTHOR James Brancomb	DOC NO. v00.1	REV. 1.0
APPROVED BY SCHAPROVEDBY	CHECKED BY SCHAPROVEDBY	PAGE NAME Main Schematic pg 1/2	
			LAST REVISION 02/20/2014
			PAGE 1 OF 2

Figure 5.4: PCB circuit schematic PG 1

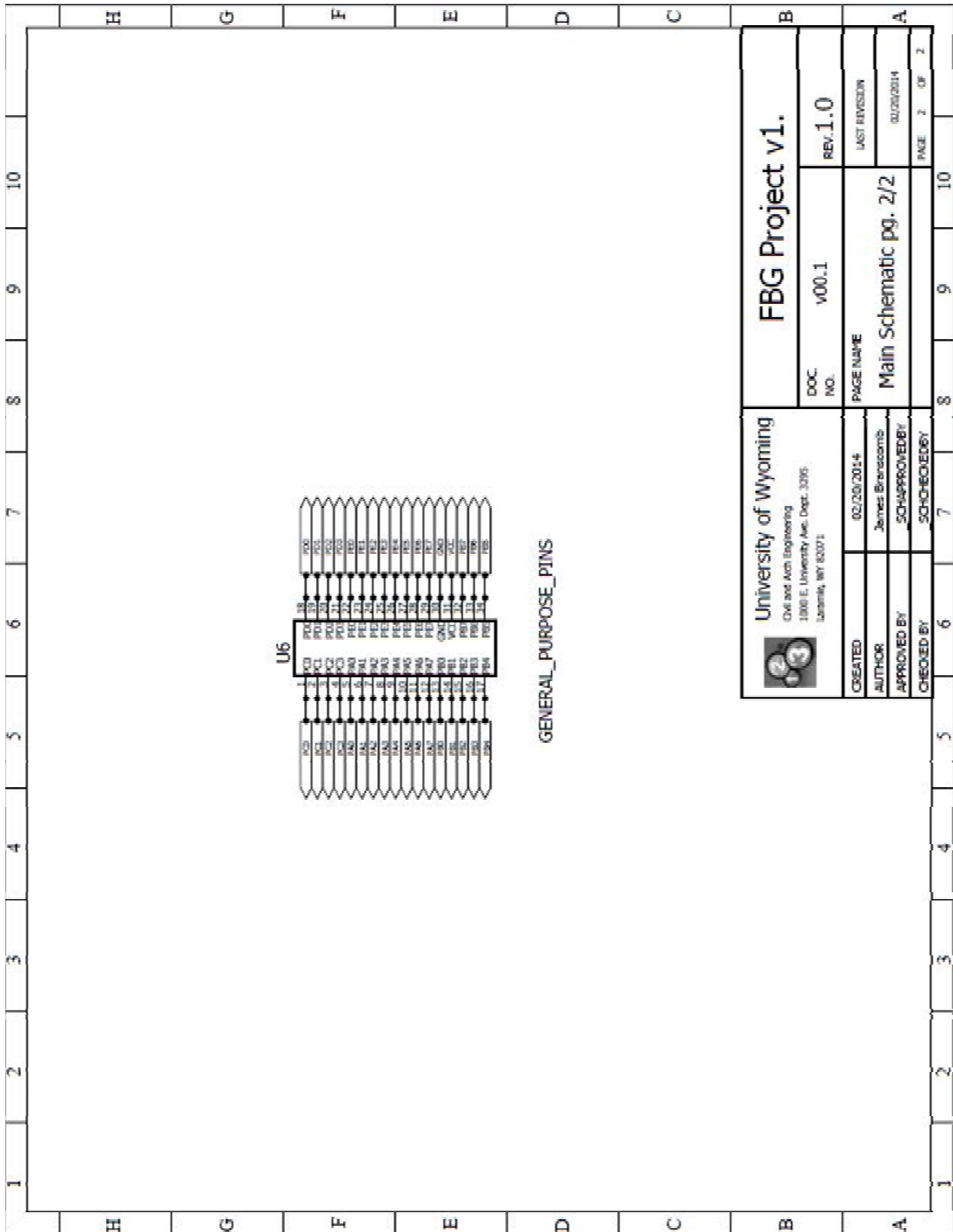
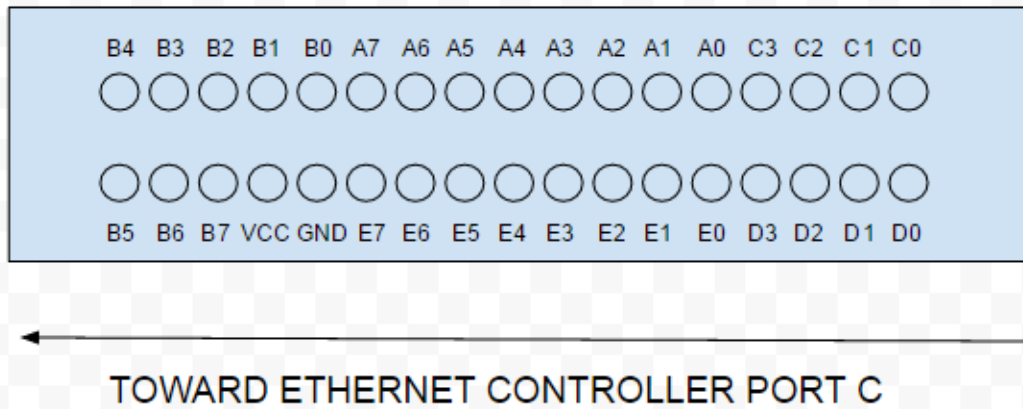


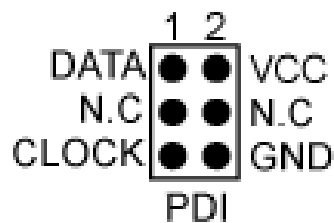
Figure 5.5: PCB circuit schematic PG 2

Figure 5.6 gives the orientation and pinout of the PCBs microcontroller breakout pins. Each pin corresponds to a particular port on the Atxmega64a3. Pins that are not already dedicated to the OLED (VCC, GND, and D3) and the RFID (A0) can be used for future external additions. If these pins are used in the future, it will be necessary to program the Atxmega64a3 microcontroller accordingly.



**Figure 5.6: Pinout of the PCB GPIO pins relating to microcontroller ports**

The PCB has the built-in PDI programming port shown in Figure 5.7. For this development version, an AVRISPMkII in-system programmer by Atmel was used in conjunction with Atmel Studio 6.1 for all firmware programming of the Atxmega64a3. However, there are a number of programmers/debuggers available from Atmel that will also allow for programming the Atxmega64a3.



**Figure 5.7: AVRISPMkII and pinout of the PCB PDI programming port**

## Assembly Guidelines and Quick-Start Guides

Assembling the system is a matter of matching male-to-female plugs. The FS2200 Interrogator has three types of inputs: its power supply (connected through the provided cable), network input (connected to data controller as shown in Figure 5.8), and optical inputs for FBG sensors. Plugging in the devices, one must be careful that the two CAT5e cables extending from the data controller are connected to the appropriate devices. Refer to Figure 5.8 for the proper orientation and connections of the data controller to the interrogator and the network. If it is necessary to remove the lid to the data controller enclosure, be careful to lift carefully as it is possible to pull loose the wires connecting the OLED screen to the PCB. A step-by-step assembly guide follows below. Both green lights should light up on each side of the data controller indicating the establishment of a PHY connection with the network and interrogator.

### Step-by-Step Assembly:

1. Plug the ethernet cable from the data controller into the interrogator LAN input (see Figure 5.8).
2. Plug the ethernet cable from the data controller into the network switch (see Figure 5.8).
3. Plug the GPIO cable from the CS203 RFID reader into the blue female connector on the data controller (see Figure 5.8).
4. Plug the ethernet cable from the CS203 into the network switch.
5. Use an ethernet cable and plug the network switch into the computer.
6. Plug all optical sensors into the FS2200 FBG interrogator.
7. Plug all power cables (network switch, FS2200, CS203, data controller) into a 120V wall outlet and turn on the power switch to the data controller (see Figure 5.8). The OLED Screen on the data controller should indicate that the system initialized and running (Figure 5.9).

Note: The RFID reader and interrogator will power on automatically when plugged in. The interrogator will take some time to ready itself (refer to FS2200 user manual).



**Figure 5.8: Diagram of appropriate connections to the data controller**



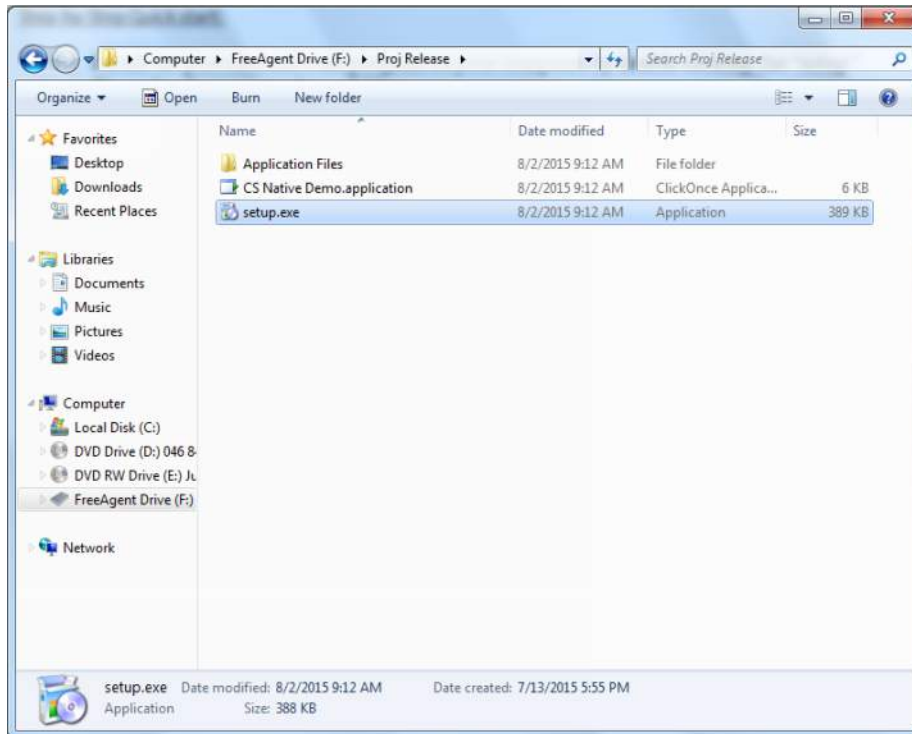
**Figure 5.9: Data controller OLED Screen indicating a successful startup**

### ***Software Overview***

The software required to run the system was built from a Convergence Systems Limited software development kit (SDK) and written in C# language in Visual Studio 2010. In particular, the visual studio solution “CSL Demo Apps for VS2008” was used as the base for the program. Several additional forms and functions were added to this solution to incorporate the data controller and interrogator. Any functionality in this software that is specific to the RFID reader can be found on the company website. The following quick start guide and subsequent figures describe the basic software operation, including the acquisition of interrogator strain sensor data.

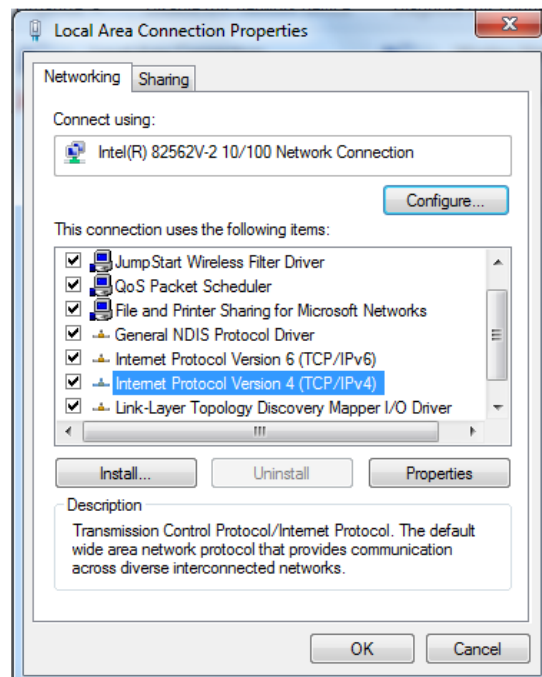
Step-by-Step Software Quick start:

1. Complete assembly as outlined in *Step-by-Step Assembly* above.
2. Install the provided software program on your computer by double clicking the “setup.exe” file under the project release folder (Figure 5.10).

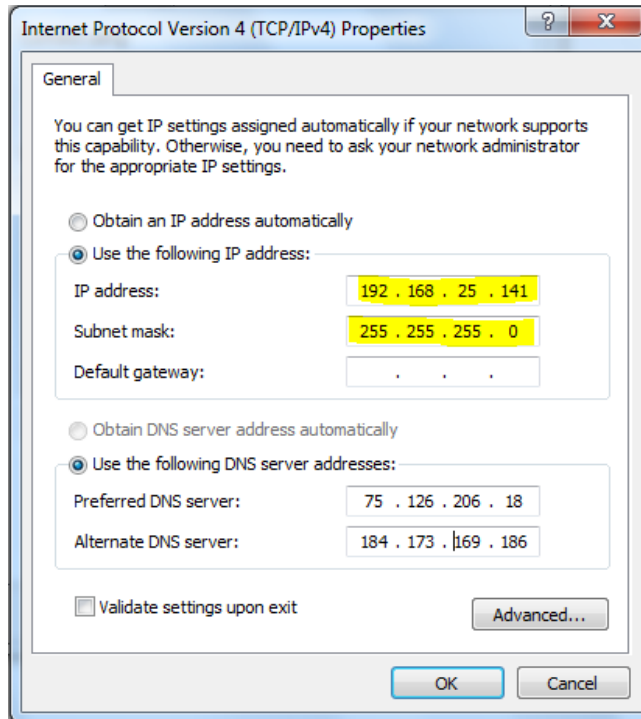


**Figure 5.10: Setup file for installing the system software**

3. Change the network adapter settings in the computer’s “Local Area Connection Properties” (Figure 5.11). Select the properties button and enter the information shown in Figure 5.12 for the IP address and Subnet mask. Click “OK” to save the changes.

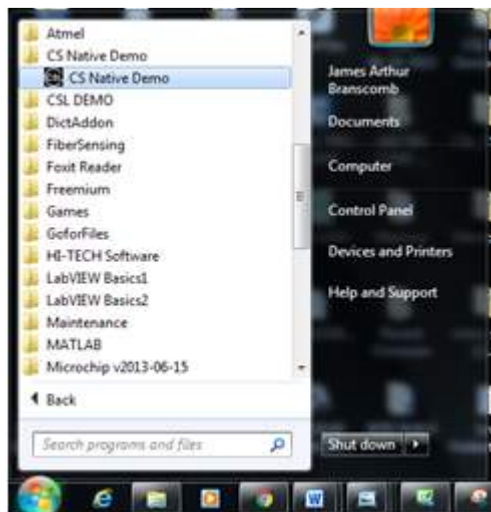


**Figure 5.11: Local Area Connection Properties with “Internet Protocol Version 4 (TCP/IPv4) selected. The user will click on the properties button to change IP settings**



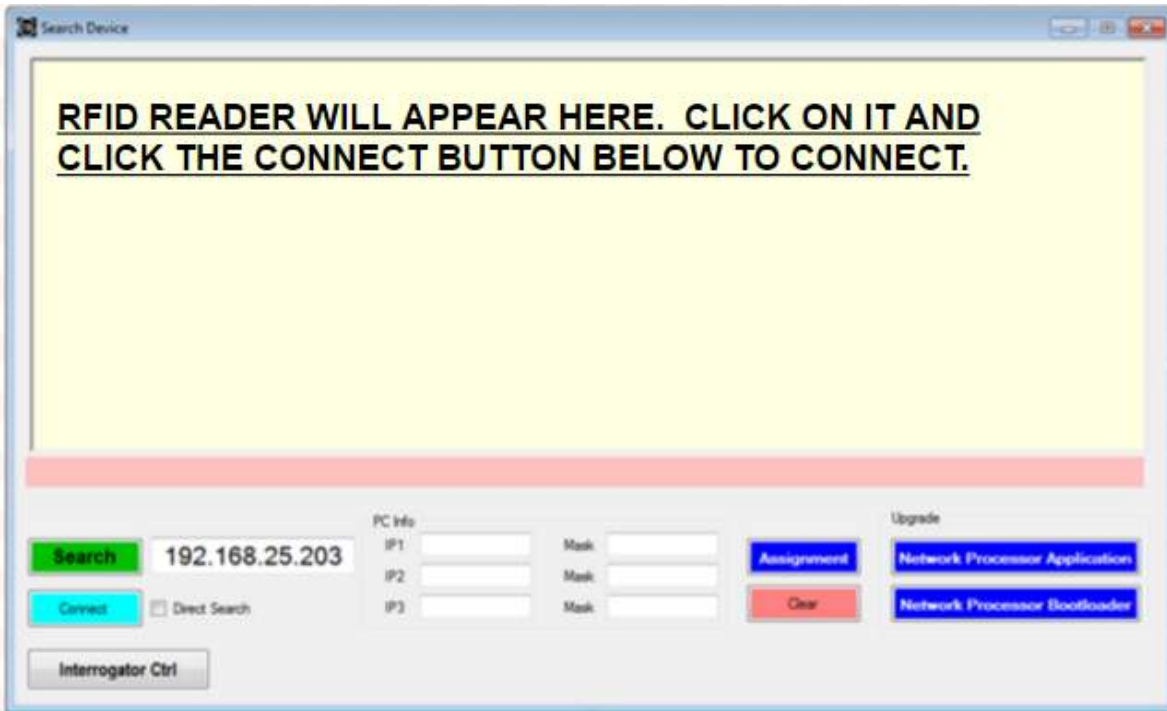
**Figure 5.12: IP address and Subnet mask to be entered as shown**

4. Open the installed program “CS Native Demo” through the windows start menu as shown in Figure 5.13. The opening page should look the same as that of Figure 5.14.



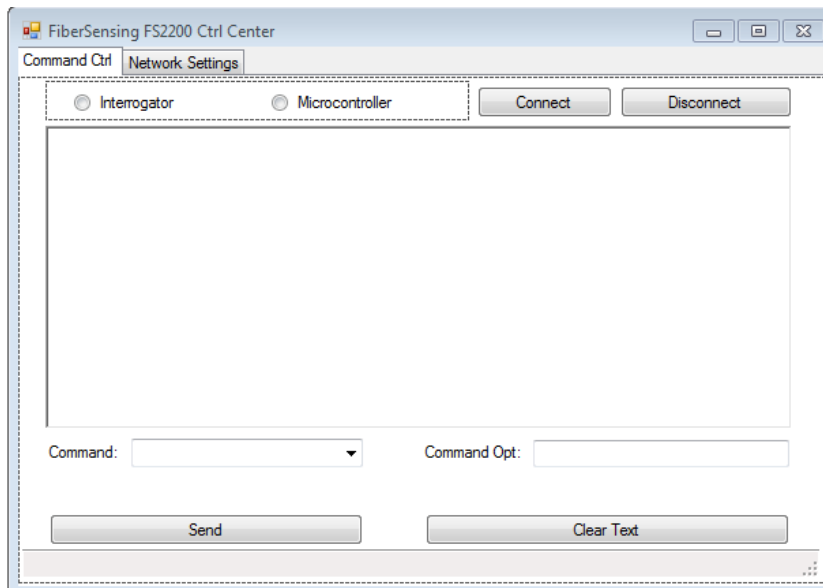
**Figure 5.13: CS Native Demo program in windows start menu after install**



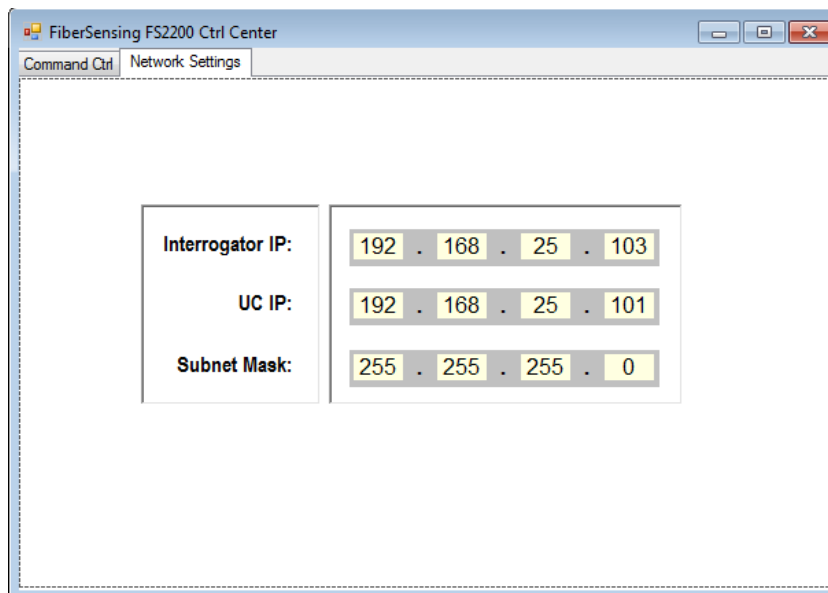


**Figure 5.14: Opening page of CS Native Demo software**

5. Click on the button labeled “Interrogator Ctrl” at the bottom left of the window as shown in Figure 5.14. This program is specific to the interrogator.
  - Clicking on the “Connect” button will establish a connection to the interrogator and subsequently display an “ACK” response in the informational box signaling a successful response from the interrogator.
  - After connecting to the interrogator, select the “Interrogator” radio button. This button will fill the drop down box labeled “Command:” with all available commands for the interrogator. After selecting the command, the command is sent through the “Send” button. Refer to the FS2200 user manual for all available commands and command options.
  - The “Microcontroller” radio button will populate the “Command:” drop down box with a few experimental and relatively untested data controller commands. For future expansion, various commands could be programmed into the data controller and sent through this manner. This allows for a quick way to change data controller settings without having to program the microcontroller through the use of a programmer/debugger in Atmel Studio.
  - When finished with the program, click the “Disconnect” button to disconnect the interrogator and data controller from the software.
  - The “Network Settings” tab in the upper left hand corner of the window is displayed in Figures 5.15 and 5.16. This is for informational purposes only and should not be changed. “Interrogator IP” lists the IP address that the interrogator is using. “UC IP” lists the IP address that the data controller is set to and “Subnet Mask” is the system subnet mask.



**Figure 5.15: Window display for controlling the FS2200 interrogator**



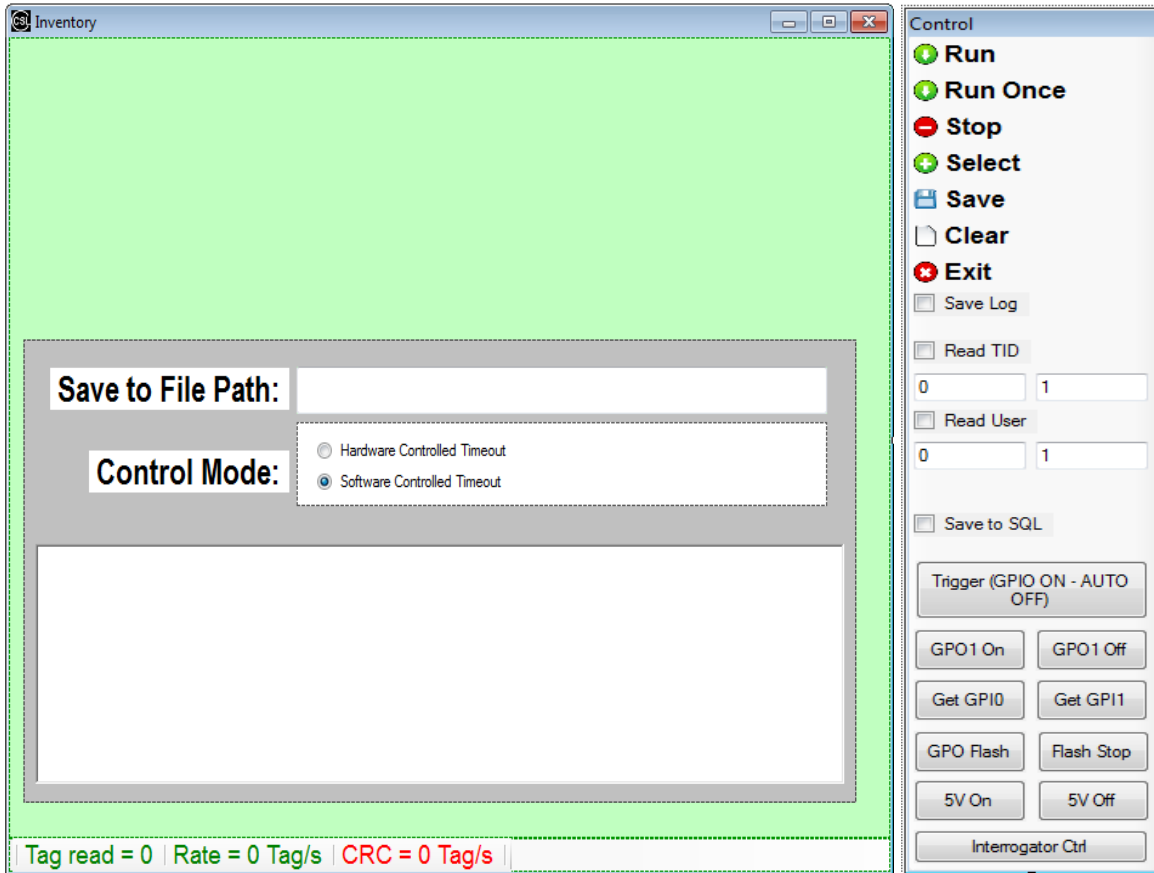
**Figure 5.16: Network Settings tab displaying system IP and mask information**

6. Close the program from the previous step (step 5.). The IP address for the RFID Reader should be the same as shown in Figure 5.14. Click the “Search” button. The program should find the RFID reader and display it in the top part of the window (Figure 5.14).
7. Once the software has found the RFID reader, select the found reader and click the connect button (Figure 5.14).

8. The window shown in Figure 5.17 should open and is primarily related to the RFID reader. If the user is to use these functions, refer to <http://www.convergence.com.hk/download/2/cs203/>. The main focus here is the button “GPIO Trigger”.
9. With the window shown in Figure 5.17 still open, select the button labeled “GPIO Trigger”. A window similar to that shown in Figure 5.18 will open.



Figure 5.17: Software page which displays upon connecting to RFID Reader.



**Figure 5.18: Window display for primary interrogator data acquisition**

- To set the system in data acquisition mode:
  - a) Copy and paste a file path that you want the data file to save to. Example:  
C:\users\yourname\desktop\  
**Note: be sure to place a backslash at the end of the file path**
  - b) Select either “Hardware Controlled Timeout” or “Software Controlled Timeout” definitions follow:  
**Hardware Controlled Timeout:** This mode would be selected in a remote deployment. Selecting the “Hardware Controlled Timeout” radio button essentially places the data controller in a ready and waiting state. Meaning, the data controller is waiting for a physical signal from the RFID reader in order to begin releasing data to the network. Once the data controller receives the trigger from the RFID reader (meaning a vehicle with a RFID tag has been read by the reader), the data controller will automatically establish the necessary connections to the network and interrogator and begin releasing sensor data to the network for a predetermined amount of time (programmed into the Atxmega64a3 – currently set to approx. 30 seconds).

**Software Controlled Timeout:** This mode would be selected in a local deployment. Selecting the “Software Controlled Timeout” radio button allows the entire data acquisition process to be controlled through the software from start to finish. Only the software is able to “see” that a tag has been read by the RFID reader and data is only passed through the data controller instead of acting as a client to the interrogator. After selecting the radio button for this option you will be prompted to enter a timeframe (in seconds) for which you would like the system to collect data.

- c) After selecting the appropriate radio button in step b), click the “Run” button. The system is now in a ready and waiting state. Once a tag is read by the RFID reader the yellow lights on the data controller should flash indicating the transference of strain data through the controller. Additionally, the table in the window of Figure 5.17 will display that particular tags data. The RFID reader can read multiple tags at once, however, the system will trigger only on the first tag read by the reader. The yellow lights will flash until the 30 seconds (hardware controlled) or user entered (software controlled) time has expired.
  - d) After the system has finished transferring data (yellow lights on data controller have ceased flashing), the software program will automatically save the collected data at the location specified earlier with the date and time it was received.
- Refer to step 5 above regarding the button labeled “Interrogator Ctrl”.
  - Button “Trigger (GPIO ON-AUTO OFF)” was experimental and should not have any function.
  - Buttons “GP01 On”, “GP01 Off”, “Get GPIO”, “Get GPI1”, “GP0 Flash”, “Flash Stop”, “5V On”, and “5V Off” are specific to the GPIO output of the RFID reader and should **not** be clicked as part of a standard interrogator data acquisition. If the user is interested in these functions refer to the link shown in step 9.
  - Check boxes “Save Log”, “Read TID”, “Read User”, and “Save to SQL” are specific only to the RFID reader and are not needed as part of a standard interrogator data acquisition. Again, refer to the link in step 9 for further details.

## **PART 6 – DATA ANALYSIS METHODS**

### **Objective**

The primary interest in load rating of bridges expressed by WYDOT engineers was to obtain the lateral distribution factors (DFs) to validate or potentially improve the existing load ratings. The following discussion presents the process behind obtaining the DFs through the means of experimental field testing. A methodology used for instrumentation design for the Laramie River bridge on I-80 in Laramie, the instrumentation plan, the design vehicle loading plan, and the data collection and analysis procedures is included.

### **Methodology for Determining the Instrumentation Plan**

There are various methods used for field testing bridges to determine more accurate analyses of structures. A common method is to fully instrument a bridge with strain sensors, conduct field load rating tests, gather and analyze strain data to develop a field-tested model, and then compare this model to the analytical design model. By comparing the two models, a tuned analysis of the bridge can result in a quantitative representation of the structure's true behavior. While this method results in a fairly accurate representation of a bridge's response, the data acquisition system and analysis are costly and time consuming due to the price and number of sensors, installation time, and data reduction and analysis procedures. A tuned model and analysis of a bridge is not always necessary, depending on the goals of the field tests.

A simplified and economical field instrumentation plan may be implemented to measure accurate DFs. Then, these DFs can be used in an analytical rating, such as with BRASS- Girder, to determine more accurate load ratings. Past research has resulted in development of a total of six instrumentation plans to be used on slab-on-steel girder bridges. The premise is based on the idea that the majority of bridges have a higher capacity than design indicates. The following eight factors are known to contribute to additional bridge performance capacity, and these factors are not normally accounted for in initial design using specification procedures.

1. Impact factor
2. Experimental dead load
3. Actual dimensions
4. Unintended composite action
5. Lateral distribution factor
6. Bearing restraint
7. Longitudinal distribution
8. Unaccounted system stiffness

The bridge instrumentation plan can be developed based upon which of the eight factors are parameters of interest. The bridge engineer must decide which factors should be accounted for based upon an initial analysis, determining the complexity of the instrumentation plan for the field tests.

## Instrumentation Plan

The experimental response of the noncomposite Laramie River Bridge would include contributions from all eight factors that could affect the additional bridge capacity over design procedures as previously discussed. Because the purpose of instrumenting the bridge is to obtain DFs, several of these parameters are regarded as irrelevant for this field testing. These considerations are discussed in the following, as they formed the basis for developing the strain sensor instrumentation plan.

### *Factors Affecting Sensor Placement*

After careful consideration and input from WYDOT bridge engineers, it was decided that the DFs were the most vital parameters for establishing an experimental load rating capacity. The experimental DFs are input values for BRASS load rating analysis and affect the load rating of a structure. It provides bridge engineers a more accurate representation of the bridge's behavior and allows potentially higher load ratings without the cost to develop a fully tuned bridge model.

Since the objective of the field test is to determine the DFs, an instrumentation plan that determines the DFs has been developed; all other factors that affect the bridge response were considered irrelevant. Table 1 is a summary of the eight contributing factors and describes why each factor is or is not considered relevant for the purpose of this work.

*Table 1 – Factors Taken into Consideration for Field Testing*

<b>Contributing Factors</b>	<b>Considered</b>	<b>Reasoning</b>
1. Impact Factor	No	Expensive to determine as it involves in-depth static and dynamic testing and analysis.
2. Experimental Dead Load	No	Assumed to be equal to design dead loads.
3. Actual Dimensions	No	Assumed that actual dimensions are equal to design dimensions because measuring the true dimensions of each member would take additional time to complete during bridge inspections.
4. Unintended Composite Action	No	Cannot be relied upon for determining the ultimate capacity of a bridge.
5. Lateral Distribution	Yes	Can be quantified as an input factor for BRASS analysis, affecting the load rating of a structure. Can provide bridge engineers a general idea of the bridge's behavior in order to calculate a potentially higher load rating without the cost for a tuned bridge model.
6. Bearing Restraint	No	Cannot be relied upon for determining the ultimate capacity of a bridge.
7. Longitudinal Distribution	No	Is not quantified or accounted for as an input parameter to improve a calculated load rating through BRASS.
8. Unaccounted System Stiffness	No	Is not quantified or accounted for as an input parameter to improve a calculated load rating through BRASS.

### ***Sensor Placement on Beams***

In order to calculate an approximate DF for each girder, a single strain gage is required on the bottom flange of each girder. This would allow Equation 6.1 to be used:

$$DF = \frac{\varepsilon_{GirderMax}}{\sum \varepsilon_{AllGirders}} \quad (6.1)$$

where the DF for the girder of interest is equal to the maximum strain measured in that girder divided by the sum of all the girder strains at the critical locations. This approach is straightforward, however this simplified sensor configuration will result in approximated DFs, and it does not provide redundancy of experimental sensors or the means to calculate cross-sectional stress, moments, or the location of the neutral axis.

Although this was designed as a noncomposite bridge, the bridge will act with at least partially composite action. Because of this behavior, the location of the neutral axis must be determined in order to obtain a more accurate DF. By calculating the actual neutral axis location and total bending moment, the engineer is also able to check global equilibrium to validate the system's performance.

Instead of having a single FBG installed at the extreme fibers of the bottom flange, there will be a total of four FBGs. This will include two FBGs located on the web, each positioned at mid-depth of the girder but on different sides of the web. Additionally, two FBGs will be located on the underside of the bottom flange, each placed an equal distance away from the longitudinal center of the flange and the outside edge of the flange. This configuration is displayed in Figure 6.1.



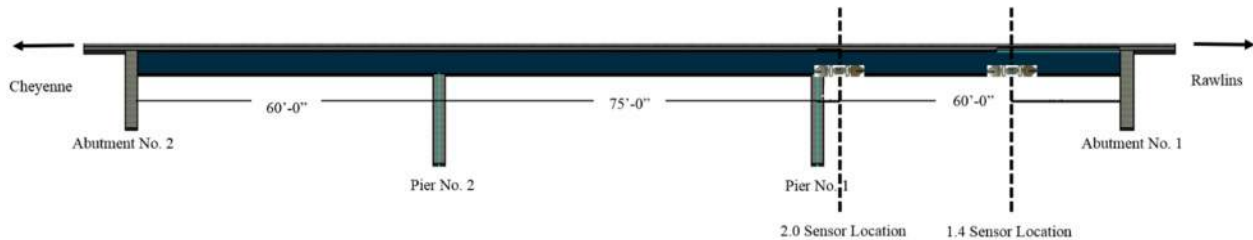
**Figure 6.1 – Cross-Sectional View with FBG Sensors on the Web and Bottom Flange**

The strain measurements can be averaged at the two locations to remove the effects of weak axis bending and torsion. The two different locations for strain measurements allow the strain profile for the section to be calculated, and then the location of the neutral axis can be determined. This process is described later.

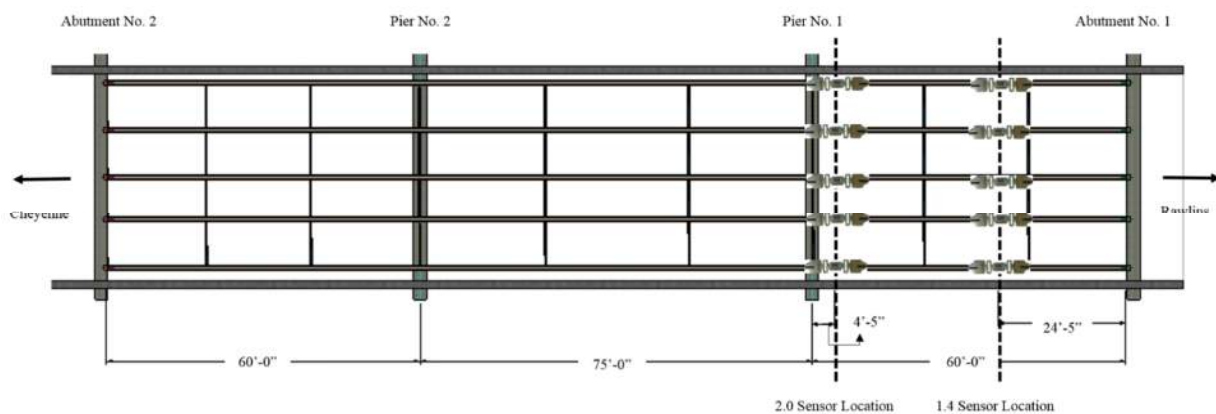


### ***Critical Longitudinal Locations***

Based on results from the BRASS LFR load rating analysis, the critical cross section for sensor placement is at the 1.4 location, which is at 40% of the first span, and at the 2.0 location, which is the start of the second span. The 1.4 critical location is controlled by the following commercial vehicle configurations for the strength limit state: HS20, HS25, and Type 3. The 2.0 critical location is also controlled by the strength limit state for Type 3S2 and Type 3-3 vehicles. The critical locations are shown in an elevation view in Figure 6.2 and a plan view in Figure 6.3.



**Figure 6.2 – Elevation View with Critical Locations for Sensor Placements**



**Figure 6.3 – Plan View with Critical Locations for Sensor Placements**

One should note that the sensors are not directly placed at the 1.4 or 2.0 locations. By installing the sensors a distance of the height of the girder away from locations of concentrated load or reaction, localized effects can be avoided. The 1.4 location of 24-feet from abutment 1 was adjusted an additional 5-inches due to a cross frame. The 2.0 sensor location also shifted 4-foot, 5-inches toward abutment 1 to avoid concentrated load effects due to pier 1.

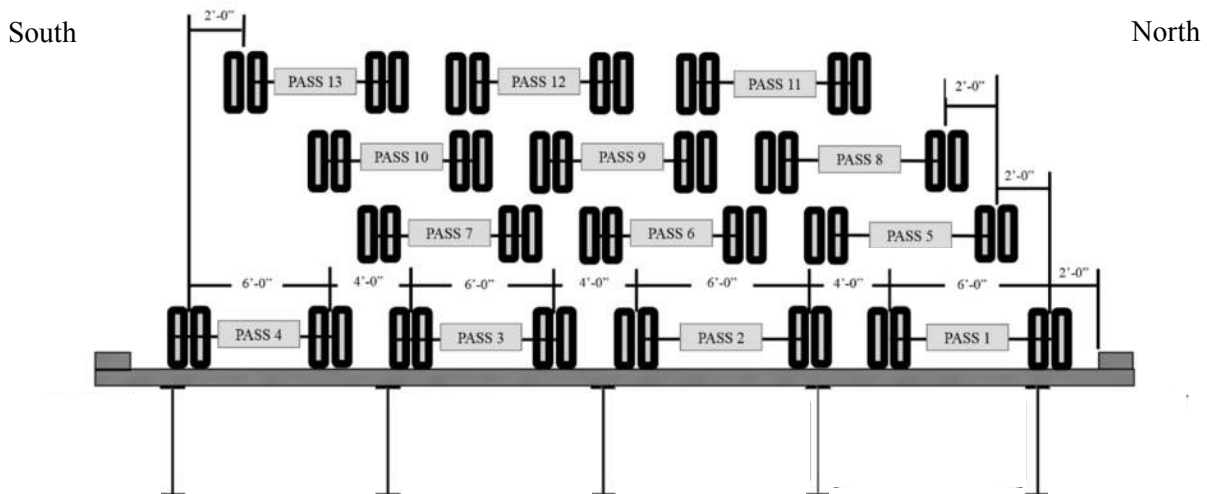
### **Vehicle Loading Plan**

The purpose of developing a vehicle-loading plan is to determine the maximum resistance of each girder against a known load. It is important that each girder be tested for its maximum live-load effect under static testing of individual vehicle loads. Static testing can be accomplished by driving a vehicle at crawl speed. Most field tests are not completed with multiple test load vehicles. Thus to induce the effect of multiple vehicles, the method of superposition is applied.

As long as the bridge stays within its elastic range, the effect from an individual vehicle can be added or superimposed on the effect of another vehicle when loaded in an adjacent lateral position. Field testing should take place first where an individual vehicle passes over the bridge in a predetermined lateral position. Based upon the field testing results, an engineer can determine which combinations of truck position caused the greatest stress in the girder of interest. The strain effects from the selected truck positions that cause the beam maximum stress can be superimposed, resulting in the maximum total strain induced from the vehicle passes on the girder of interest.

The design vehicle placement plan is displayed in Figure 6.4, where the principle of superposition should be used to maximize the load effects on each girder for a total of 13 passes. The outside wheel was placed 2-feet from the right, or north, curb because the overhang on the north side is wider and should produce a greater DF. With a design lane load of 10-feet, four design vehicle loads are included. However, it is not expected that four lanes loaded would control.

From the north side, the design vehicle should be placed 2-feet toward from the north curb for passes 1, 2, 3, and 4. Then the vehicle's path should be 2-feet toward the south for passes 5, 6, and 7 and then another 2-feet for passes 8, 9, and 10. Passes 11, 12, and 13 should be positioned 2-feet north from the south most wheel load of pass 4. By completing each pass with an individual test vehicle, load combinations of design vehicles can dictate the maximized live-load effects of each girder. It is important that various traffic positions are tested to determine the worst-case scenario.



**Figure 6.4 – Vehicle Load Test Plan**

The tests are designed so that passes 1 through 13 are completed in sequential order with the layout of the passes marked on the bridge. As stated earlier, deflections should be measured throughout the duration of the testing. After the strain data is collected, the values should be used to find stresses. By plotting stress versus time for the girder of interest, one is able to distinguish which load cases created the maximum moment on the girder. The critical vehicle

passes must be selected, which forms a maximized load case combination. The combination should be checked to assure that the selected load cases all fit on the clear roadway width with 4-feet in between axles as some passes are overlapped in the vehicle load test plan. Superposition of the applicable load cases will determine the maximum response for each girder.

Table 2 gives examples of which vehicle load cases may maximize the live load effects of each girder and should be analyzed.

**Table 2 – Potential Controlling Vehicle Load Combinations**

<b>Girder</b>	<b>Load Combination</b>
South	Pass 3 + Pass 4
South Interior	Pass 3 + Pass 4 Pass 4 + Pass 12 Pass 12 + Pass 13
Middle	Pass 2 + Pass 3 Pass 6 + Pass 7 Pass 8 + Pass 9 Pass 9 + Pass 10 Pass 11 + Pass 12
North Interior	Pass 1 + Pass 2 Pass 5 + Pass 6
North	Pass 1 + Pass 2

***Experimental Test Vehicle***

The purpose of using an experimental load truck is to accurately measure the bridge’s strain responses to known loads using typical highway truck configurations. Typically during field testing, any type of available truck with the appropriate dimensions that can be loaded to the required axle weights may be used. When developing a field tested load rating factor using LFR Specifications, the load testing vehicle used must be analytically equated to an AASHTO approved vehicle. Often this approved vehicle is an HS20 design truck.

The determination of the DFs is based on the gage distance of the test vehicle, not the longitudinal configuration of the axles. Any load-testing vehicle that has wheel lines that are 6-feet apart can be utilized where the next adjacent vehicle is separated by 4-feet. This configuration creates a lane width of 10-feet used for applying the live load. An experienced bridge engineer should determine the actual weight placed in the testing vehicle, however it should not exceed the operating rating tonnage limit.

**Data Analysis**

Ultimately, the goal of the Laramie River Bridge field testing is to determine the actual DFs. Although Equation 6.1 determines an approximate DF, it cannot determine girder

moments. A more accurate procedure for determining the DF is to place additional sensors as shown in Figure 6.1 and determine individual girder moments and calculate the DF using Equation 6.2:

$$DF = \frac{M_{GirderMax}}{\left(\frac{\Sigma M_{AllGirders}}{2}\right)} \quad (6.2)$$

where  $M_{GirderMax}$  is the maximum moment in the girder of interest, and  $\Sigma M_{AllGirders}$  is the sum of the concurrent moments in the individual girders across the bridge section.

To account for one-lane loaded in order to compare to LFD DFs, the sum is divided by 2 because two vehicle wheels lines are applied. If for example, the superimposed load consisted of two vehicles to maximize the girder, the sum should be divided by 4, etc. Additionally, the multiple presence factors should be included. If one- or two-lanes loaded controls, then Equation 6.1 is multiplied by 1.0. If three- or more-lanes loaded controls, which is unlikely, Equation 6.1 is multiplied by 0.9.

Two methods are described for finding the maximum moment for the bridge girders. The first method assumes full composite action using the transformed section and could be used for a preliminary analysis. The second method is the more accurate and is recommended, as it takes into account the partial composite action from field testing.

The first method uses the calculation for the bending moment shown in Equation 6.3:

$$M_{Girder} = S_{TR} E \epsilon \quad (6.3)$$

where  $E$  is equal to the modulus of elasticity of steel;  $\epsilon$  is the maximum superimposed strain value obtained from field testing.  $S_{TR}$  is the transformed section modulus shown by Equation 6.4:

$$S_{TR} = \frac{I_{TR}}{c} \quad (6.4)$$

where  $I_{TR}$  is the transformed analytical moment of inertia of the cross section, and  $c$  is the distance to the neutral axis from the bottom of the bottom flange.

The strain sensor configuration described above allows the location of the neutral axis location to be determined as explained in Equation 6.5 and displayed in Figure 6.5.

$$c = \frac{\epsilon_b}{(\epsilon_b - \epsilon_m)} d \quad (6.5)$$

where  $\epsilon_b$  is the strain measured at the bottom of the bottom flange,  $\epsilon_m$  is the strain measured at middepth of the girder, and  $d$  is the distance between the two sets of sensors.

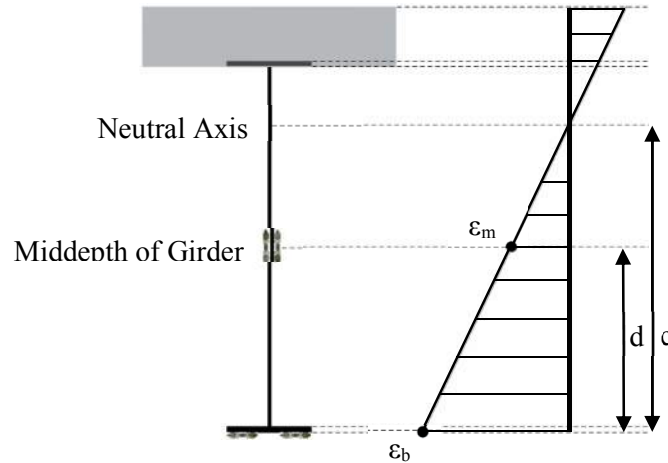


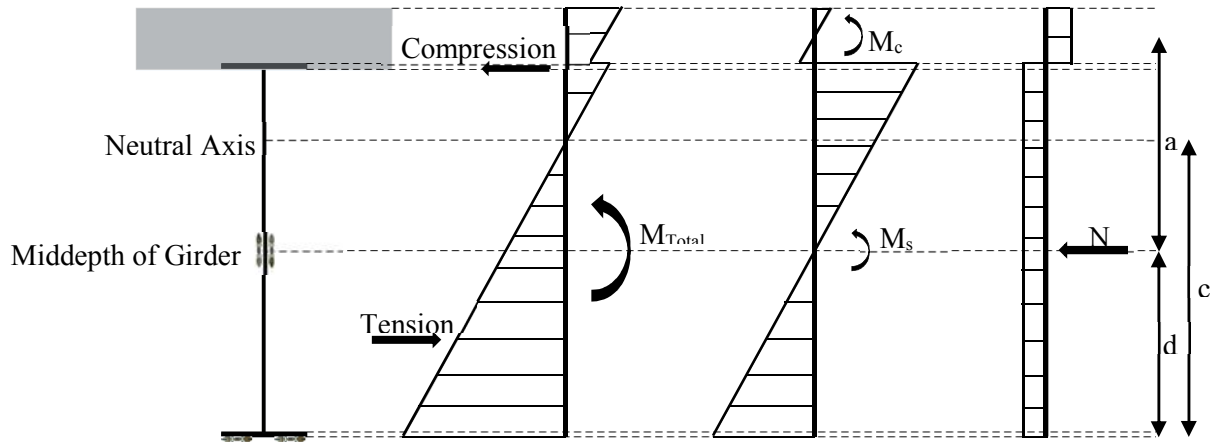
Figure 6.5 – Strain Profile for Girder with Partially Composite Behavior

The second method calculates the total moment shown in Equation 6.6. This calculation is useful because it takes into account the bending moment contributions from the steel girder and the concrete deck. This method accounts for the experimental moment of inertia, including the moment contribution of the concrete slab; yields more accurate DFs; and provides the means to complete a global equilibrium check.

$$M_{\text{GirderTotal}} = M_s + M_c + Na \quad (6.6)$$

where the total moment is equal to the sum of  $M_s$ , the steel girder bending about its own neutral axis,  $M_c$ , the concrete area bending about its own neutral axis, and  $Na$ , a function developed to quantify the unintended composite action between the steel and concrete.

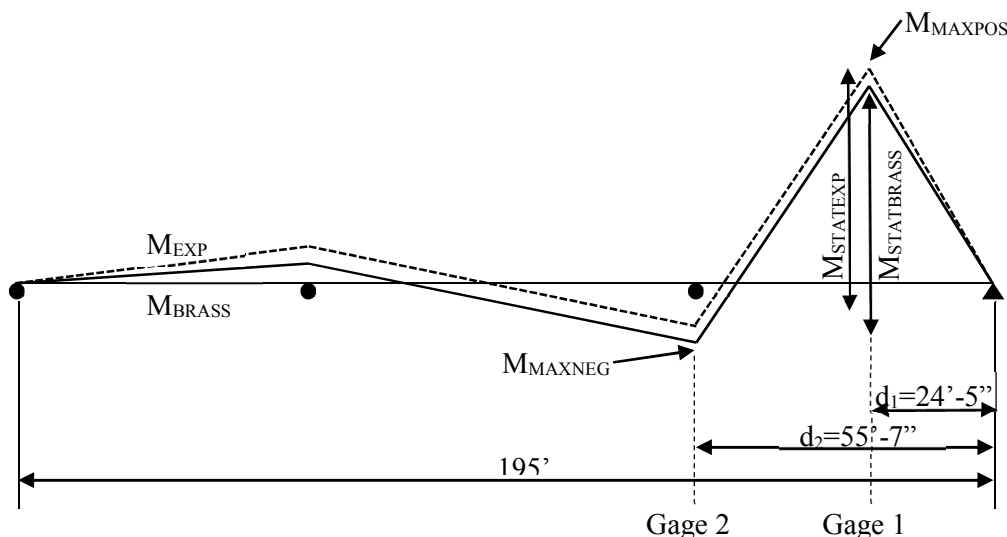
This process is demonstrated in Figure 6.6 where the total stress distribution is shown, and a breakdown of the individual total moment components is displayed. Typically a noncomposite beam would have the neutral axis close to middepth of the girder. Although the Laramie River Bridge was built to perform noncompositely, unintended composite action will occur. This behavior causes the neutral axis location to be higher than middepth of the girder where a larger area of the girder is in tension with the concrete area acting in compression.



**Figure 6.6 – Total Moment for Girder with Partially Composite Behavior**

Engineers are able to verify the accuracy of the system by checking that static equilibrium exists, where the sum of the moments in the girders is equal to the applied moment. Comparisons can be made between the experimental statical moments and the analytical statical moments to gain a better overall understanding of a bridge’s true behavior. Often the bridge performs better than the design model.

Figure 6.7 is an example of the statical moment with the load located for maximum positive moment, the 1.4 location, plotted along the length of the Laramie River Bridge. The solid line represents moment results one might see from the BRASS-Girder file, while the dashed line represents possible experimental results from field testing. The figure also shows a strain gage located near the 1.4 location and another strain gage near the 2.0 location.



**Figure 6.7 – Analytical and Experimental Moments**

The experimental statical moment can be determined by Equation 6.7:

$$M_{\text{STATEXP}} = \frac{d_1}{d_2} \times \mathbf{M}^{\text{NEG-GAGE}} + \mathbf{M}^{\text{POS-GAGE}} \quad (6.7)$$

where  $d_1$  is equal to the distance to the strain gage located near the 1.4 location, and  $d_2$  is equal to the distance to the strain gage located near the 2.0 location.  $M^{\text{NEG-GAGE}}$  is the maximum negative moment measured by strain gage 2, and  $M^{\text{POS-GAGE}}$  is the maximum positive moment measured by strain gage 1.

The analytical moment can be determined by Equation 6.8:

$$M_{\text{STATEXP}} = \frac{d_1}{d_2} \times \mathbf{M}^{\text{NEG-BRASS}} + \mathbf{M}^{\text{POS-BRASS}} \quad (6.8)$$

where  $d_1$  is again equal to the distance to the strain gage located near the 1.4 location, and  $d_2$  is equal to the distance to the strain gage located near the 2.0 location.  $M^{\text{NEG-BRASS}}$  is the maximum negative moment from the BRASS-Girder analysis near the 2.0 location, and  $M^{\text{POS-BRASS}}$  is the maximum positive moment from the BRASS-Girder analysis near the 1.4 location.

### Use of Experimental Lateral Distribution Factor

The purpose of field testing the Laramie River Bridge is to obtain the accurate DFs as input parameters for BRASS-Girder. These input values are controlled by the user under the “Wheel Fractions” control panel, which uses the LFR Standard Specifications for load ratings. There are two options presented in the control panel: one-lane loaded and multiple-lanes loaded. If the input values are left empty, the load rating analysis will be determined automatically using the AASHTO Specification values. However, by specifying the field-tested DFs calculated from Equation 6.2, a more accurate load rating can be determined.

Again, it is important to have the DFs in the correct form because BRASS-Girder uses the values as a wheel fraction. When using Equation 6.2, one must take note of how many load vehicles create the maximum moment in the girder of interest because it affects the DFs. If the engineer is interested in comparing the experimental DFs with the analytical LRFR factors, the values should be in terms of lanes per girder, and determined by multiplying Equation 6.2 by 0.5 to account for two wheel lines per lane.

The user should calculate the experimental DFs for one-lane loaded and multiple-lanes loaded to input into BRASS-Girder. A table could be formed comparing the difference between the LFR Specifications versus the experimental DFs, where a percent difference is presented. An example of how this comparison may be arranged is displayed in Table 3 with the highlighted values examples of the BRASS-Girder input values.

**Table 3 – Example Comparison of Analytical and Experimental Distribution Factors**

Analysis	Bending Moment	One Lane Loaded		Two Lanes Loaded		Three Lanes Loaded	
		Interior Girder	Exterior Girder	Interior Girder	Exterior Girder	Interior Girder	Exterior Girder
Analytical	Positive and Negative	0.64	0.72	0.82	0.72	0.74	0.65
Experimental (Example)	Positive	<b>0.62</b>	0.58	0.61	<b>0.65</b>	0.59	0.53
	Negative	0.56	0.61	0.63	0.59	0.61	0.50
Percent Difference		14		21			

The experimental DFs for one-lane loaded for BRASS-Girder will be the maximum value from the 1.4 and 2.0 critical locations, including the interior and exterior girders for one-lane loaded. The maximum experimental value will be divided by the maximum LFD analytical value to obtain the percent difference; for this example the difference would be 0.62 divided by 0.72 to obtain a 14% improvement. The experimental DFs for multiple-lanes loaded will be the maximum value from the 1.4 and 2.0 locations, including the interior and exterior girders for two- or more-lanes loaded. Again, the maximum experiment value will be compared to the maximum LFD factor to obtain the percent difference of the DFs; for this example the difference would be 0.65 divided by 0.82 resulting in a 21% increase.



**APPENDIX B-1**

**M.S. THESIS  
BY DANIEL MAURIS**

To the University of Wyoming:

The members of the Committee approve the thesis of Daniel Thomas Maurais Presented on November 27th, 2012.

Dr. Richard Schmidt, Chairperson

Dr. Ray Fertig, External Department Member

Dr. Jennifer Tanner

APPROVED:

Dr. Richard Schmidt, Department Head, Civil and Architectural Engineering Department.

Dr. Robert Ettema, Dean, College of Engineering and Applied Sciences

## ABSTRACT

The vehicle loads seen on Wyoming roadways are continuously increasing due to the demanding transportation needs of Wyoming's expanding energy industry. The resulting overload conditions experienced by Wyoming's aging bridges have called for the implementation of a structural health monitoring (SHM) system. A SHM system utilizing fiber optic strain sensors called Fiber Bragg Gratings (FBGs) have proven in recent years to be an innovative and effective solution for monitoring bridge conditions. Such a system will allow WYDOT engineers to monitor the damages and fatigue effects of overloaded Wyoming bridges over years of service. This research examined a new method of attaching FBG strain sensors to concrete structural members via adhesive embedment in concrete notches. The proposed method is ideal because it provides ample fiber protection from weathering and vandalism. Additionally, the FBG becomes a rooted component of the structure that is unlikely to detach or be scraped off throughout years of service.

Both a finite element analysis (FEA) and an experimental investigation were conducted to analyze the effectiveness and feasibility of the proposed concrete strain monitoring method. The strain loss over the adhesive layer between the concrete and the FBG sensor was the primary variable of interest in the study. The strain loss directly affects the accuracy of the sensors in measuring the strain of the concrete. Several attachment configurations with different parameters were tested.

The results of this study support the conclusion that there are certain notch embedment configurations that will provide accurate strain measurement of a concrete structural member. It was found that the FEA predicts slightly higher strain transfer than what occurs in real conditions. A feasible procedure for implementing the proposed sensing method in field conditions was developed during the experimental tests.

**STRAIN TRANSFER BEHAVIOR OF NOTCH EMBEDDED FIBER BRAGG  
GRATINGS**

By

Daniel Thomas Maurais

A thesis submitted to the Civil and Architectural Engineering Department

and The University of Wyoming

in partial fulfillment of the requirements

for the degree of

MASTERS OF SCIENCE

in

CIVIL ENGINEERING

Laramie, Wyoming

November 2012

## DEDICATION PAGE

To my family

## ACKNOWLEDGMENTS

I would like to thank the Wyoming Department of Transportation, the Mountain-Plains Consortium and the Department of Civil and Architectural Engineering at UW for their funding and support of my graduate work. This thesis was made possible through their commitment to the research and development of structural engineering methods for Wyoming infrastructure.

Thank you to my committee members who advised and helped me throughout my graduate experience: Dr. Richard Schmidt, Dr. Jennifer Tanner and Dr. Ray Fertig. A second special thanks to Dr. Schmidt for serving as my advisor and providing me with the opportunity to earn a graduate education at the University of Wyoming.

I would like to thank Dr. Rob Erikson, Bridget Schabron and the gentlemen in the UW machine shop for their assistance with the testing instrumentation and machinery. Finally I would like to thank my fellow research partners without whom this research would have never been possible: Mike Jung and Hilmar Heiningner.

# TABLE OF CONTENTS

CHAPTER 1: INTRODUCTION.....	1
1.1 Background .....	1
1.2 Research Significance.....	2
1.3 Research Objective .....	2
CHAPTER 2: LITERATURE REVIEW .....	4
2.1 Overview .....	4
2.2 Fiber Bragg Grating Background .....	5
2.3 Civil Engineering Applications of Fiber Bragg Gratings.....	8
2.4 FBG Strain Transfer .....	12
CHAPTER 3: FINITE ELEMENT STUDY .....	22
3.1 Test Objective .....	22
3.2 Finite Element Model Configurations .....	22
3.3 FEA Convergence Study .....	26
3.4 FEM Strain Transfer Analysis.....	27
3.5 FEA Results .....	28
CHAPTER 4: EXPERIMENTAL INVESTIGATION .....	32
4.1 Test Specimens .....	32
4.2 FBG Test Configuration .....	33
4.3 Loading and Strain Measurement.....	37

4.4 Notched Prism Test Results .....	38
4.5 Gage Factor Calibration .....	46
4.6 FBG Compression Range Functionality Test .....	49
CHAPTER 5: CONCLUSIONS .....	52
5.1 Field Implementation Considerations.....	52
5.2 Strain Transfer Analysis Conclusions.....	53
5.3 Gage Factor Calibration Test Conclusions.....	56
5.4 FBG Compression Range Test Conclusions .....	56
CHAPTER 6: FUTURE WORK .....	58
6.1 Development of FBG Steel Application Method.....	58
6.2 Sensing Scheme Development and Laboratory Simulation .....	59
6.3 Development of Data Processing, Transmission, and Analysis.....	59
6.4 Field Implementation.....	60
CHAPTER 7: REFERENCES .....	61
APENDIX A: FEA TEST DATA .....	63
APENDIX B: PICTURES OF TESTS.....	83



## LIST OF FIGURES

Figure 2-1: FBG light reflection process.....	6
Figure 2-2: Cylindrical FBG model test configuration .....	14
Figure 2-3: Normalized strain distribution for various FOS gage lengths.....	17
Figure 2-4: Reinforced concrete prism test specimens .....	18
Figure 2-5: (a) Single protective layer configuration (b) Double protective layer configuration .....	20
Figure 3-1: Notch embedded FBG configuration cross sections.....	22
Figure 3-2: (a) V-notch FEM configuration (b) Saw-notch FEM configuration .....	23
Figure 3-3: Notched concrete prism symmetry axes.....	23
Figure 3-4: FEM part indication .....	24
Figure 3-5: Notch geometry details .....	24
Figure 3-6: FEM boundary conditions: (a) V-notch FEM configuration (b) Saw-notch FEM configuration	27
Figure 3-7: Epoxy bond length comparison for saw-notch with 1.6 mm bond layer thickness .....	29
Figure 3-8: Epoxy elastic modulus comparison for v-notch with 1.75 mm bond layer thickness .....	30
Figure 3-9: Bond layer thickness comparison .....	31
Figure 3-10: Bond layer thickness comparison .....	31
Figure 4-1: Concrete prism forms .....	32
Figure 4-2: Concrete test prisms notches: (a) V-notch (b) Saw-notch.....	33
Figure 4-3: Laboratory test schematic .....	34
Figure 4-4: Epoxy stiffness test .....	35
Figure 4-5: FBG notch embedment setup.....	36
Figure 4-6: Epoxy bond length .....	36
Figure 4-7: Typical test load pattern as a function of failure load.....	37
Figure 4-8: V-notch configuration results with $E_{\text{epoxy}} = 1800 \text{ MPa}$ .....	40

Figure 4-9: Result comparison for v-notch with $E_{\text{epoxy}} = 1800$ MPa, 2.7 mm bond layer thickness.....	41
Figure 4-10: Result comparison for v-notch with $E_{\text{epoxy}} = 1800$ MPa, 3.2 mm bond layer thickness.....	41
Figure 4-11: Result comparison for v-notch with $E_{\text{epoxy}} = 1800$ MPa, 4.2 mm bond layer thickness .....	42
Figure 4-12: Saw-notch configuration results with $E_{\text{epoxy}} = 1800$ MPa .....	44
Figure 4-13: Result comparison for saw-notch with $E_{\text{epoxy}} = 1800$ MPa, 3.6 mm bond layer thickness .....	44
Figure 4-14: Result comparison for saw-notch with $E_{\text{epoxy}} = 1800$ MPa, 3.4 mm bond layer thickness .....	45
Figure 4-15: Notched prism load test for saw-notch with 3.4 mm bond layer thickness .....	46
Figure 4-16: Steel dogbone gage factor calibration test.....	47
Figure 4-17: FBG gage factor calibration test result .....	48
Figure 4-18: FBG compression range test setup.....	50
Figure 4-19: FBG compression range strain plot repetition 1.....	51
Figure 4-20: FBG compression range strain plot repetition 2.....	51
Figure 5-1: Local buckling effect of epoxy embedded FBG.....	57
Figure A1-1a: Epoxy length comparison for 0.875 mm bond layer thickness v-notch configuration .....	63
Figure A1-1b: Epoxy length comparison for 0.875 mm bond layer thickness v-notch configuration .....	63
Figure A1-1c: Epoxy length comparison for 0.875 mm bond layer thickness v-notch configuration.....	64
Figure A1-1d: Epoxy length comparison for 0.875 mm bond layer thickness v-notch configuration .....	64
Figure A1-2a: Epoxy length comparison for 1.75 mm bond layer thickness v-notch configuration .....	65
Figure A1-2b: Epoxy length comparison for 1.75 mm bond layer thickness v-notch configuration .....	65
Figure A1-2c: Epoxy length comparison for 1.75 mm bond layer thickness v-notch configuration.....	66
Figure A1-2d: Epoxy length comparison for 1.75 mm bond layer thickness v-notch configuration .....	66
Figure A1-3a: Epoxy length comparison for 3.5 mm bond layer thickness v-notch configuration .....	67
Figure A1-3b: Epoxy length comparison for 3.5 mm bond layer thickness v-notch configuration .....	67
Figure A1-3c: Epoxy length comparison for 3.5 mm bond layer thickness v-notch configuration.....	68

Figure A1-3d: Epoxy length comparison for 3.5 mm bond layer thickness v-notch configuration .....	68
Figure A1-4a: Epoxy length comparison for 1.6 mm bond layer thickness saw-notch configuration .....	69
Figure A1-4b: Epoxy length comparison for 1.6 mm bond layer thickness saw-notch configuration .....	69
Figure A1-4c: Epoxy length comparison for 1.6 mm bond layer thickness saw-notch configuration .....	70
Figure A1-4d: Epoxy length comparison for 1.6 mm bond layer thickness saw-notch configuration .....	70
Figure A1-5a: Epoxy length comparison for 3.2 mm bond layer thickness saw-notch configuration .....	71
Figure A1-5b: Epoxy length comparison for 3.2 mm bond layer thickness saw-notch configuration .....	71
Figure A1-5c: Epoxy length comparison for 3.2 mm bond layer thickness saw-notch configuration .....	72
Figure A1-5d: Epoxy length comparison for 3.2 mm bond layer thickness saw-notch configuration .....	72
Figure A2-1a: Epoxy modulus comparison for 0.875 mm bond layer thickness v-notch configuration .....	73
Figure A2-1b: Epoxy modulus comparison for 0.875 mm bond layer thickness v-notch configuration .....	73
Figure A2-1c: Epoxy modulus comparison for 0.875 mm bond layer thickness v-notch configuration .....	73
Figure A2-1d: Epoxy modulus comparison for 0.875 mm bond layer thickness v-notch configuration .....	74
Figure A2-1e: Epoxy modulus comparison for 0.875 mm bond layer thickness v-notch configuration .....	74
Figure A2-1f: Epoxy modulus comparison for 0.875 mm bond layer thickness v-notch configuration .....	74
Figure A2-2a: Epoxy modulus comparison for 1.75 mm bond layer thickness v-notch configuration .....	75
Figure A2-2b: Epoxy modulus comparison for 1.75 mm bond layer thickness v-notch configuration .....	75
Figure A2-2c: Epoxy modulus comparison for 1.75 mm bond layer thickness v-notch configuration .....	75
Figure A2-2d: Epoxy modulus comparison for 1.75 mm bond layer thickness v-notch configuration .....	76
Figure A2-2e: Epoxy modulus comparison for 1.75 mm bond layer thickness v-notch configuration .....	76
Figure A2-2f: Epoxy modulus comparison for 1.75 mm bond layer thickness v-notch configuration .....	76
Figure A2-3a: Epoxy modulus comparison for 3.5 mm bond layer thickness v-notch configuration .....	77
Figure A2-3b: Epoxy modulus comparison for 3.5 mm bond layer thickness v-notch configuration .....	77
Figure A2-3c: Epoxy modulus comparison for 3.5 mm bond layer thickness v-notch configuration .....	77

Figure A2-3d: Epoxy modulus comparison for 3.5 mm bond layer thickness v-notch configuration .....	78
Figure A2-3e: Epoxy modulus comparison for 3.5 mm bond layer thickness v-notch configuration.....	78
Figure A2-3f: Epoxy modulus comparison for 3.5 mm bond layer thickness v-notch configuration .....	78
Figure A2-4a: Epoxy modulus comparison for 1.6 mm bond layer thickness saw-notch configuration ....	79
Figure A2-4b: Epoxy modulus comparison for 1.6 mm bond layer thickness saw-notch configuration ....	79
Figure A2-4c: Epoxy modulus comparison for 1.6 mm bond layer thickness saw-notch configuration ....	79
Figure A2-4d: Epoxy modulus comparison for 1.6 mm bond layer thickness saw-notch configuration ....	80
Figure A2-4e: Epoxy modulus comparison for 1.6 mm bond layer thickness saw-notch configuration ....	80
Figure A2-4f: Epoxy modulus comparison for 1.6 mm bond layer thickness saw-notch configuration.....	80
Figure A2-5a: Epoxy modulus comparison for 3.2 mm bond layer thickness saw-notch configuration ....	81
Figure A2-5b: Epoxy modulus comparison for 3.2 mm bond layer thickness saw-notch configuration ....	81
Figure A2-5c: Epoxy modulus comparison for 3.2 mm bond layer thickness saw-notch configuration ....	81
Figure A2-5d: Epoxy modulus comparison for 3.2 mm bond layer thickness saw-notch configuration ....	82
Figure A2-5e: Epoxy modulus comparison for 3.2 mm bond layer thickness saw-notch configuration ....	82
Figure A2-5f: Epoxy modulus comparison for 3.2 mm bond layer thickness saw-notch configuration.....	82
Figure B1: Example of FEA longitudinal strain distribution with deflected shape.....	83
Figure B2: Axially loaded concrete prism test setup.....	83
Figure B3: FBG epoxy embedment technique with tensioning devise .....	84
Figure B4: FBG compression range test setup .....	84
Figure B5: FBG gage factor calibration test .....	85
Figure B6: Epoxy stiffness test .....	85

## LIST OF TABLES

Table 3-1: FEM material data.....	26
Table 3-2: Convergence study data .....	26
Table 4-1: Concrete prism properties .....	33
Table 4-2: Epoxy stiffness test data .....	35
Table 4-3: V-notch prism test results with FEA comparison.....	39
Table 4-4: Saw-notch prism test results with FEA comparison .....	43
Table 4-5: FBG gage factor calibration results .....	48
Table 4-6: FBG compression range test results .....	50
Table 5-1: V-notch prism results comparison.....	55
Table 5-2: Saw-notch prism results comparison.....	55

## LIST OF NOTATION

FBG = Fiber Bragg Grating

FEA = Finite Element Analysis

FOS = Fiber Optic Sensor

SHM = Structural Health Monitoring

$d_c$  = thickness of FBG epoxy coating

$E_{\text{epoxy}}$  = elastic modulus of epoxy

$E_m$  = elastic modulus of FBG host material

$k$  = FBG gage factor

$L$  = FBG gage length

$l_e$  = effective strain transfer length

$l_b$  = epoxy bond layer length

$p$  = photoelastic coefficient

$t_b$  = epoxy bond layer thickness

$w$  = property constant

$\alpha$  = constant of proportionality

$\Delta\lambda$  = FBG wavelength shift

$\varepsilon_c$  = strain in concrete

$\varepsilon_f$  = strain in FBG

$\varepsilon_g$  = normal strain in FBG

$\varepsilon_{sg}$  = strain in strain gage

$\eta_{eff}$  = modal refractive index

$\Lambda$  = FBG grating period

$\lambda$  = light wavelength

$\lambda_b$  = base light wavelength

$\lambda_o$  = FBG base wavelength

$\lambda_s$  = strongest interaction light wavelength

$\mu^c$  = shear modulus of FBG coating

$\mu^F$  = shear modulus of FBG

$\mu^m$  = shear modulus of FBG host material

$\sigma_m$  = longitudinal stress in FBG host material

# CHAPTER 1: INTRODUCTION

## 1.1 Background

Structural Health Monitoring (SHM) is the process of implementing a damage detection strategy for civil infrastructure (Sohn, *et al.*, 2001). The condition of a structure is defined as its response to external and internal forces resulting in deflections, damage and fatigue. SHM has become increasingly relevant in the civil engineering industry due to the increasing loads on aging infrastructure as well as the growth in innovative, complex structural designs (Clarke, *et al.*, 2009). Various methods of SHM have been developed, however one that utilizes Fiber Bragg Grating (FBG) strain sensors has proven to be superior. The research for this thesis focused primarily on the attachment method of FBG sensors to be utilized as strain gages in a concrete SHM system.

A FBG is an optical fiber with an inner core made of silica glass. The inner core is encased by three layers composed of glass cladding, polymer coating and a protective outer jacket (typically metal or plastic) (Kersey, *et al.*, 1955). The purpose of the encasing layers is to protect the inner core from damage, breakage, and corrosion. Within the silica glass core are sections of gratings that are spaced longitudinally along the fiber and typically range from 5 mm to 30 mm in length. These grating sections are the locations where the strain sensing occurs. As light is launched through a FBG it passes through the grating sensor section. A portion of the passing light with a specific wavelength is reflected by the spaced gratings while the remainder passes through. When the grating sensor region is strained, the spacing of the gratings changes, causing a shift in the wavelength of the reflected light. By observing the shift in the reflected wavelength, it is possible to calculate the strain that the sensor region is experiencing. This method of strain sensing has proven to be ideal for SHM due to key characteristics of FBGs that include durability, embeddability, immunity to electromagnetism, and multiplexing capability (Glisic & Daniele, 2007).

## 1.2 Research Significance

The research reported herein is in support of the development of a SHM system for bridges managed by the Wyoming Department of Transportation (WYDOT). The necessity of a SHM system for Wyoming bridges stems from the increasing loads seen on Wyoming motorways. The expanding energy industry throughout Wyoming has produced the need for transportation of extremely heavy objects that induce overweight loadings on aging highway bridges. These overweight loads are often carried on trucks with nonstandard axle configurations which further challenge the analysis capabilities of the software used by WYDOT bridge engineers. Additionally, the frequent road closures in Wyoming due to severe weather conditions cause tandem overloading on bridges. It is therefore necessary to monitor the damage and degradation inflicted on overloaded bridges as they age.

The project proposed to WYDOT puts forward a two phase plan for the development and implementation of a SHM system that utilizes FBGs. Phase I of the proposal focuses primarily on the development of a SHM system through academic research and testing. The objective of Phase II is to implement the system developed in Phase I on critical Wyoming bridges. The ultimate goal of the project is to collect bridge structural health data from a SHM system that can be correlated with existing bridge rating software and inspection methods. It is also desirable to confirm the results provided by current bridge rating software for overweight trucks and those with nonstandard axle configurations.

## 1.3 Research Objective

An important objective of this project is to determine effective methods of attaching the FBGs to structural members. Two primary concerns with the attachment of the FBGs to concrete members are their accuracy in measuring the strain in the host structure as well as the feasibility of the attachment method for field applications. The strain transfer from the host structure to the FBG sensor over the adhesive layer is the primary variable that affects the accuracy of the FBG as a strain sensor.



Little research has been conducted on the strain transfer behavior of FBGs epoxy-bonded to concrete members in shallow surface notches. The aim of this thesis is to determine the bond layer thickness, adhesive bond length, adhesive elastic modulus, and notch geometry that optimize the strain transfer between a strained concrete member and a notch-embedded FBG sensor. The strain transfer is studied through finite element analysis (FEA) as well as experimental tests. The notch embedment attachment configuration is ideal because it not only protects the FBG from weathering and vandalism, but also makes the FBG a rooted component of the structural member that will not detach or be scrapped off in service conditions.

This thesis is organized into several chapters that encompass the abovementioned study. It begins with a review of previous research on FBGs relating primarily to their use as SHM devices. The FEA and test methodologies are then described along with a report of the results. The thesis then closes with conclusions drawn from the test results and a discussion of the future work that will continue the project.

## CHAPTER 2: LITERATURE REVIEW

This chapter reviews several studies related to the research and concepts of this thesis. The literature review is organized in three parts including a section on the background of FBGs, followed by a section discussing the applications of FBGs in civil engineering, and finally a section that examines the strain transfer characteristics of FBGs in civil engineering applications. The overview section provides a summary of the three sections focusing on key concepts and conclusions.

### 2.1 Overview

The capabilities and applications of Fiber Bragg Gratings (FBGs) since their invention in 1978 have been subjects of great interest in engineering research. Characteristics such as multiplexity, compact size and ability to monitor strain and temperature concurrently make FBGs a unique tool with a wide range of applicability (Chan, et al., 2005). Using FBGs, researchers have made technological advances in such fields as telecommunications, aerospace and civil engineering that were never possible before. Applications include vibration measurement, pressure sensing, temperature sensing and strain sensing (Measures, 2001). The primary objective of past research for strain sensing applications was to determine what variables affect the accuracy of the FBGs in measuring the mechanical strain of the host structure. The amount of strain that is transferred from the host structure over the protective and adhesive layers to the FBG sensing core is of primary interest. Optimizing FBG accuracy by maximizing strain transfer, or at least determining a compensation parameter, is of great importance in the usefulness of FBGs as structural health monitoring devices. Section 2.2 of this chapter discusses the development of FBGs and how they function as strain sensors. It is found that FBGs are superior to traditional strain sensing devices for many civil engineering applications.

FBGs show high functionality as structural health monitoring systems in civil structures like buildings, bridges, roads and offshore platforms. Structures frequently experience dilapidation due to

damaging events such as seismic activity, corrosion, impacts, wind, and fire (Ansari, 2009). A structure instrumented with FBG strain sensors, also known as a “smart structure”, has the ability to self-monitor its structural condition and indicate when damage or degradations are present (Lopez-Higuera, *et al.*, 2005). The sensor network can act as a nervous system for a structure, reporting structural health by measuring strain. Section 2.3 reviews examples of how FBGs are used in civil engineering industry primarily as structural health monitoring tools. Application techniques such as surface adhesion, concrete embedment and tension-cable attachment are examined, each having their own benefits and limitations.

Various studies have been conducted that investigate the optimal attachment configuration of fiber optic sensor (FOS) strands to structural materials. Several attachment techniques such as full embedment of the FOS in the host material, surface bonding of the FOS, and notch embedment have been tested. Variables of interest with each attachment method include fiber protective coating arrangements, material properties, adhesive bond thickness and adhesive bond length. How these variables affect the strain transfer from the host structure to the FOS is the main subject of Section 2.4. Several studies on FOS strain transfer relating specifically to the research of this thesis are discussed. The results identify key parameters that affect strain transfer such as the stiffness of the host material and the attachment configuration of the FBG to the host material.

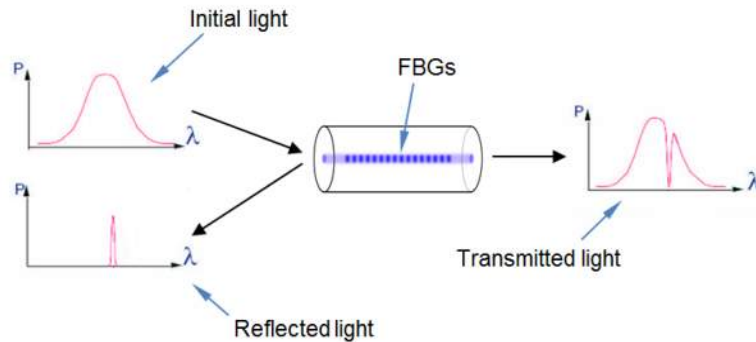
## **2.2 Fiber Bragg Grating Background**

### **2.2.1 Fiber Bragg Grating Technology Fundamentals and Overview, Hill and Meltz (1997)**

Hill and Meltz (1997) discuss the development and functions of FBG technology. FBGs were first conceived at the Canadian Communications Research Center in Ottawa, Ont., Canada in 1978 by Hill *et al.* The formation of the gratings within an optical fiber was achieved by passing high intensity Argon laser light through a germania-doped silica fiber at increasing intensities. The light reflectivity in the

fiber increased with exposure intensity until nearly all the light was reflected. At this point it was observed that the refractive index of the fiber had changed, and that a region of spaced reflective gratings had formed over a 1 mm portion of the fiber. The formation of the grating section proved the existence of photosensitivity in the silica fiber and marked the invention of Fiber Bragg Gratings. Further research was conducted to develop the new technology, and several applications were discovered, including fiber optic communication and strain sensors.

The spacing of the gratings within the grating portion of the FBG strand is the primary variable that allows for strain sensing. When light passes through the grating portion of a FBG strand, a small portion is reflected by each grating. While the majority of the light passes through the gratings, the fractional amount of reflected light provides vital information for FBG strain measurement. The reflected light is shown on a response spectrum as a wavelength peak as seen in Figure 2-1 where P is the light intensity and  $\lambda$  is the light wavelength.



**Figure 2-1: FBG light reflection process (Heininger)**

The wavelength of the reflected light is dependent on the grating spacing, which changes in response to strain, temperature, pressure, and polarization variations. It is possible to determine the corresponding engineering strain in the fiber by measuring the wavelength of the reflected light. Equation 2-1 describes the relationship between the strongest light interaction wavelength ( $\lambda_s$ ) and the grating spacing of an FBG:

$$\lambda_s = 2\eta_{eff}\Lambda \quad \text{Equation 2-1}$$

where  $\Lambda$  is the grating period (spacing) and  $\eta_{eff}$  is the modal refractive index that describes how light propagates through the gratings. By attaching or embedding FBG fibers to a structure, it is possible to monitor the strain induced under in-service conditions.

### 2.2.2 Strain Measurement with Fiber Bragg Grating Sensors, Kreuzer (2006)

The increase in use of FBGs over the past 30 years is due to their superiority over conventional electrical-resistance strain gages. Kreuzer explicates the advantages and disadvantages of FBGs and compares them to those of a conventional metal-foil strain gage. It is found that FBGs are superior in some applications, such as sensing in extreme conditions, but also possess some adverse characteristics such as the need for temperature compensation.

The advantages of FBG sensors stem from a few of their basic characteristics, which include small size, durability and ease of installation. Because of their small size and light weight, FBGs can be attached or embedded with very little disruption of the host material. The silica glass core and cladding that make up a FBG strand not only provide long-term stability but also resist corrosion and electromagnetic interference. FBGs have low thermal conductivity and require no electrical power, which allows them to function in combustible environments as well as in areas with extreme temperatures and high electro-magnetic interference. They possess the ability to measure very high strains, making them applicable for highly stressed structures. A single FBG strand can span great distances (up to 50 km) and have grating sensor sections spaced along the strand length, eliminating the need for a return cable. FBGs are applicable to common materials such as steel and concrete but are especially useful for more contemporary structural materials, such as fiber reinforced composites.

Although there are many unique advantages of FBGs, there are some drawbacks worth noting. The disadvantages of FBGs are primarily attributed to material composition, size, and precision. Because of FBG temperature sensitivity, separation of temperature and mechanical strain effects is an

issue. FBGs are not capable of self-compensating for temperature variations and therefore require a separate temperature compensating device in conditions with temperature gradients.

The high stiffness of optical fibers can also cause strain measurement inaccuracies. In most cases the optical fiber is stiffer than its host material, which causes a reactive friction force in the bond interface imposed by the fiber onto the strained host material. Also, the distance between the FBG sensor and the bonded surface can vary causing strain transfer inconsistencies and calibration complications. A final disadvantage is related to the FBG gage factor. The gage factor of an FBG is needed to convert the reflected light wavelengths into strain, and can vary from fiber type to fiber type.

## 2.3 Civil Engineering Applications of Fiber Bragg Gratings

### 2.3.1 Fiber Optic Civil Structural Monitoring System, Lopez-Higuera, *et al.* (2005)

Traditional methods of monitoring structural health are largely based on visual inspection of structural damage. These methods recognize structural deficiencies after the damage has occurred and often lead to costly repairs. A better alternative to this approach is one that internally monitors structural deficiencies throughout a structure's lifetime. Internal monitoring is achieved by securing strain monitoring transducers to or within a structure for extended periods of time. Surface secured strain monitoring with conventional strain gages is implausible due to their lack of durability and inability to monitor long term behavior. Fiber optic sensors like FBGs possess the necessary characteristics to effectively monitor structural health throughout a structure's lifetime. The enabling characteristics of FBGs include durability, absence of flowing electricity, multiplexing capabilities, and ability to monitor strain and temperature simultaneously. Higuera *et al.* (2005) discuss how FBG dog-bone shaped transducers can be used to monitor structural health of beams and bridges.

The first technique proposed by Higuera *et al.* for FBG structural health monitoring was to embed an FBG transducer within a concrete structure. In this application, the transducer had to be

specially designed to accommodate full encasement in concrete. This was achieved by using a concrete-compatible plastic called polymethylmethacrylate as the transducer body material. In order to compensate for thermal effects, the transducer required two separate FBGs. One responded to both strain and temperature change while the second acted as a compensator by only measuring temperature. The FBG strands were bonded within the transducer using cyanocrylate-based strain-gage glue, which was found to have optimal strain transfer characteristics. The resulting embeddable transducers were tested in laboratory demonstrations, field tests and in two reinforced concrete bridges located in Spain. The results of the tests indicated that the transducers were highly effective in monitoring both strain and temperature in structures as complex as a twelve span bridge. The tests also demonstrated that the transducers are capable of surviving the construction process, as they were attached to the steel reinforcement elements before concrete casting.

The second application method was to monitor mechanical strain and temperature by surface adhesion of FBG transducers to a structure. The objective here was to develop a structural health monitoring system using FBGs that is very similar to traditional methods with conventional strain gages. The similarity is meant to induce a smooth transition for users between modern strain-gage application techniques to the newer FBG systems. As with the embedded transducers, a level of protection and compatibility with the host material is required for surface bonded transducers. The sensing regions of the surface-mounted FBGs were protected by encasing them in plastic tubes as well as the application of two layers of Kapton<sup>®</sup>, a material used with standard strain gages. The surface transducers were tested along with the embedded sensors in the laboratory and in the field tests mentioned previously.

The embedded and the surface mounted FBG sensors not only proved to be superior to traditional methods as strain monitoring systems, but also monitored more complex structural responses such as the effects of dynamic loadings over time. Quasistatic and dynamic loading tests were conducted using trucks on bridges fitted with the FBG transducers. The transducers were placed

on the tops and bottoms of the bridge cross-sections in order to monitor the tensile and compressive strains of each load case. In the quasistatic tests, the transducers accurately reported positive and negative strains corresponding to regions of positive and negative flexure. The dynamic tests were performed by driving trucks over the bridge at various speeds and intervals. The FBGs reported the anticipated strain responses due to the dynamic loadings with spikes at instances where the truck axels passed over the monitored bridge locations. The durability of the FBGs was proved through their survival of the construction process and continuing functionality throughout years of embedment. Additionally, the accuracy of the fully embedded and surface bonded strain and temperature FBG monitoring systems was verified in a comparison of laboratory and field tests.

### 2.3.2 Structural Health Monitoring with Fiber Optic Sensors, Ansari (2009)

Ansari explores the different ways in which optic fiber sensing has been researched, tested and put into service in civil engineering industry. The paper consists of summaries of several different studies related to FBG implementation methods conducted by other researchers. Implementation methods include monitoring of fiber reinforced polymer (FRP) composites, weigh-in-motion (WIM) sensing, surface-adhered deformation sensing, embedded sensing, and tension-cable monitoring. Ansari concludes that the most important advantage of fiber optic sensing is their ability to conform to different structural elements and geometries while monitoring various types of structural deficiencies.

Fiber optic sensing of FRP composites is focused on monitoring the interface bond between FRP strips and the host concrete structural member. FRPs are often adhered to structural elements to increase strength in tension zones. Debonding of the FRP reinforcement from the host surface during fatigue loading is an area of concern with FRP applicability. Tests conducted by Dong *et al.* found that fiber optic sensors (FOS) bonded to the surface of FRP are effective at sensing the onset of bond failures under fatigue loadings (Dong, 2007).



Yuan *et al.* examined the dynamic effects of weigh-in-motion (WIM) sensors using FOS. WIM sensors are devices that measure the weight of a vehicle as the vehicle passes over the sensor. Such devices include capacitive mats, hydraulic load cells, and bending-plate load cells. Yuan developed a cheaper and simpler system that uses FOS to measure dynamic loadings like those of a passing vehicle. A dynamic ramp function loading test was conducted using the fiber optic sensing WIM system. The results indicated that the sensors could not only determine the loads but also accurately measure both the dynamic and static weights of a moving vehicle (Yuan, 2005).

Surface adhesion of fiber optic sensors is appropriate in conditions where the structure is not exposed to extreme environmental conditions. Even in mild conditions however, it is still necessary to provide protection to the FOS to shield against influences like extreme temperature gradients, large deformations and moisture penetration. Fiber protection is typically provided by one or more encasing layers of materials such as plastic, composite and adhesive. Bassam *et al.* provides an example of an effective method of protecting surface adhered FOS in an experiment with reinforced concrete columns under seismic loadings. In the experiment, FBG strands were used to monitor the effects of shake-table induced dynamic loads on large concrete columns. The FOS strands were encased in protective polyimide sheets and were prestressed to allow for compressive and tensile strain readings. The test results proved the adequacy of FBG sensors for monitoring crack behavior and other structural health monitoring factors in concrete applications. However, it was deduced that a better method for monitoring members with large cracks is to use a surface attached steel arch encasement for the sensors rather than a fully adhered strip. This arrangement accounts for the large dynamic deformation range induced by large cracks (Bassam & Ansari, 2008).

The ability to fully embed fiber optic sensors in a structural material is vital to their usefulness. In order to have functional full embedment, the sensors must have proper protection, which can be achieved in several ways. Ansari discusses a common embedment method that utilizes a metallic tube

with two circular metal end flanges. The FBG is housed by a tube that is attached to a flange at each end allowing for strain sensing over the gage length. The device provides sufficient durability and strain transfer capability when embedded in a structure.

The final application method of FOS discussed by Ansari is tension-cable monitoring. This method pertains primarily to structural tension cables and post-tensioning strands. The approach is similar to the previously discussed embedment technique in that a steel tube is used with circular metal end flanges. In this case however, the tensioned cable runs through the center of enlarged end flanges and the metal sensor tubes are offset from the center. This allows for multiple sensor tubes to be placed around the tension cable in order to monitor multiple variables, such as displacements, tension force, temperature and referencing of cable post tensioning strain.

## **2.4 FBG Strain Transfer**

### **2.4.1 Longitudinal Shear Transfer in Fiber Optic Sensors, Pak (1992)**

The primary objective of Pak's study was to determine strain transfer behavior of an FOS strand imbedded in an isotropic homogeneous host matrix with an applied longitudinal shear stress. A numerical analysis was conducted in which various material property relationships of the fiber and host matrix were compared. Pak considered two types of embedded fibers: one with a single layer coating and a second bare embedded fiber with no coating. Different thicknesses and shear moduli of the coating and fiber were tested in order to observe strain transfer variations. The results led to several relevant conclusions contributing to the understanding of the elastic behavior between an embedded FOS and its host material.

The most relevant trends seen in the study were derived from a comparison of the shear strain transfer in the optical fiber with various shear moduli and thicknesses of the fiber coating. It was found that strain transfer increased in the optical fiber as the coating layer got thinner but only when the shear

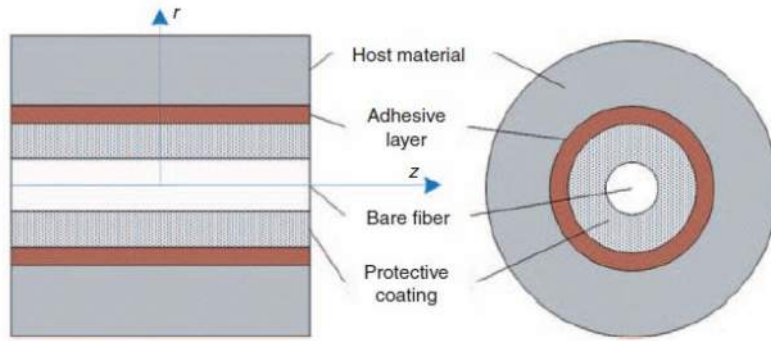
modulus of the coating was less than that of the host matrix. Conversely, when the shear modulus of the coating was greater than that of the host matrix, the shear transfer increased as the coating layer got thicker. This relationship allowed determination of the shear modulus of the coating, which gives the greatest shear transfer to the fiber. The result is seen in Equation 2-2 and states that the maximum shear transfer from the host material to the fiber occurs when the shear modulus of the coating ( $\mu^C$ ) is the geometric mean of the shear moduli of the host matrix material ( $\mu^M$ ) and the fiber ( $\mu^F$ ). The relationship in Equation 2-2 is true for all coating layer thicknesses.

$$\mu^C = \sqrt{\mu^M \mu^F} \quad \text{Equation 2-2}$$

Further analysis of the results showed that the most accurate shear transfer would occur if the bare fiber were embedded directly into the host matrix without a protective coating. As stated previously, the shear transfer across the coating improves as the coating gets stiffer, however since in most applications the coating (typically epoxy or plastic cladding) is less stiff than the host material (typically steel or concrete), it is correct to assume that the optimal fiber embedment configuration would have no coating. Furthermore, for a fiber with no coating, it was found that the best shear transfer occurs when the optical fiber stiffness is equal to or less than that of the host matrix material. The study conducted by Pak discovers several fundamental relationships about embedded fiber optic sensors that are useful in their implementation and optimization in civil engineering applications.

#### 2.4.2 Study on Strain Transfer Characteristics of Fiber Bragg Grating Sensors, Zhou (2010)

Zhou *et al.* investigated axial strain distributions of FBG sensors and the influencing parameters, which include the bonded length of the FBG sensor, adhesive thickness, and elastic modulus of the adhesive. Figure 2-2 taken from Zhou *et al.* shows the four-layer test configuration comprised of an outer host material, an adhesive layer, a protective coating and an inner FBG core.



**Figure 2-2: Cylindrical FBG model test configuration**

A finite element analysis was conducted to examine the strain transfer from the outer host material to the FBG core under an axial tensile stress of 50 MPa applied to the host material. The results of the FEA were then verified by laboratory testing of the FBG strand bonded to an aluminum alloy dog-bone specimen. The mechanisms that induce FBG chirping phenomena were also identified and analyzed. Chirping is a phenomenon that occurs when the period of the gratings along the grating section of the fiber is not constant. Chirping results in inaccurate sensing due to the fact that the reflected wavelength was formed by inconsistent grating periods.

The finite element model (FEM) had a fiber grating length of 5 mm, adhesive bond lengths ranging from 4 mm to 20 mm, adhesive thicknesses ranging from 0.1 mm to 2.0 mm and adhesive elastic moduli ranging from 1 GPa to 10 GPa. Each cylindrical layer of the model had material properties corresponding to their representative materials (steel host material, silica glass fiber etc.) and were assumed to be isotropic and linear elastic. The FEA results provided the effective sensing lengths of the fiber for each of the adhesive bond lengths. The effective sensing length is the region of the FBG fiber that has a strain transfer rate of 99% or greater and is considered to be the optimal location for the fiber gratings. A linear relationship was found between the bond length and the effective sensing length. It was seen that as the thickness of the adhesive layer decreased, the strain transfer rate and the effective sensing length increased. Another relevant trend was that the effective sensing length increased as the elastic modulus of the adhesive increased.

The laboratory tests conducted by Zhou not only verified the FEA results but also revealed some insightful information about the chirping phenomena. Three dog-bone specimens were tested with adhesive bond lengths of 5 mm, 10 mm and 15 mm. The effective sensor lengths found for each specimen corresponded well with those found in the FEA. By analyzing the reflection spectra of the FBG for each specimen, it was possible to draw conclusions about when exactly the chirping phenomenon occurs. It was found that increased chirping occurred as the bond length decreased. When the bond length was equal to the grating length (5 mm) the chirping was unacceptably high, but when the bonded length was three times the grating length (15 mm), chirping was nearly nonexistent. Therefore it was concluded that a bonded length that is at least 3 times the grating length will minimize chirping and provide optimal strain transfer sensing.

Zhou's study discovered several important characteristics dealing with strain transfer of embedded FBG sensor. FBGs can be designed for optimal strain transfer as long as the material properties, bond configurations and grating lengths are all properly set. Additionally it is best to have a stiff adhesive layer that is as thin as possible but still provides an adequate bond.

#### 2.4.3 Mechanics of Bond and Interface Shear Transfer in Optical Fiber Sensors, Ansari and Libo (1998)

The ability to determine the amount of strain transfer from a host material to the fiber core of an FOS is the subject of interest in a study by Ansari *et al.* In their research, a theoretical model was developed that calculates the strain in a host material using the values measured by an FOS. The investigation considers the strain loss through the protective coating of an FOS as well as the behaviors of a bare embedded FOS. The theoretical model is verified through experimental tests of FOS strands attached to a tapered cantilever beam. Results of the study suggest that strain transfer is a function of the mechanical properties of the fiber core, the protective coating and the fiber gage length (length of optical fiber in contact with the host material).

The configuration used to develop the theoretical model included a fiber core, a protective coating layer and a host material layer. The model was developed under the following simplifying assumptions:

1. The host materials are subjected to a structural strain acting parallel to the fiber.
2. All the materials involved in the model behave linear elastically.
3. A perfect bond exists between all adhered surfaces in the model.
4. The mechanical properties of the glass core and the encasing cladding are taken to be the same, resulting in a single fiber core unit.

A mathematical derivation yielded the following equation that gives the normal strain in the fiber core along the gage length ( $\varepsilon_g(x)$ ):

$$\varepsilon_g(x) = \frac{\sigma_m}{E_m} \left[ 1 - \frac{\sinh(wx)}{\sinh(wL)} \right] \quad \text{Equation 2-3a}$$

where  $\sigma_m$ ,  $E_m$ , and  $L$  are the longitudinal stress in the host material, elastic modulus of the host material, and the gage length respectively. The variable  $w$  (property constant) is a coefficient that accounts for how the mechanical properties of the protective coating influence the strain transfer of the fiber. Figure 2-3 taken from Ansari *et al.* (1993) is a distribution plot of the above equation plotted as a function of gage length.

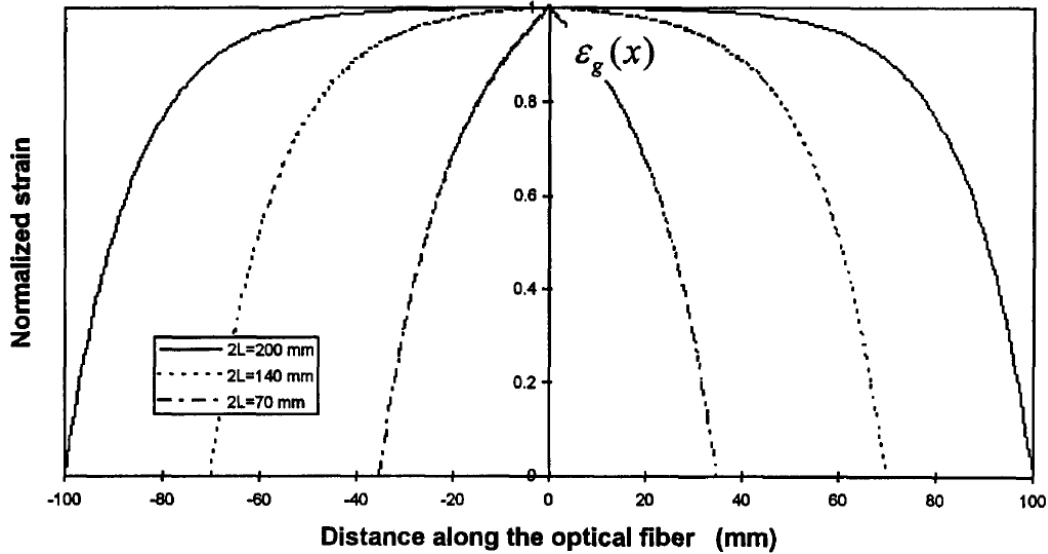


Figure 2-3: Normalized strain distribution for various FOS gage lengths

The plot shows that longer gage lengths provide a better transfer of strain from the host material to the fiber core.

A cantilevered beam flexure test with an epoxied FOS and conventional strain gage was conducted to confirm the aforementioned theory. A beam with a tapered geometry was used so that there was a uniform strain along the length of the beam when a bending end load was applied. The beam was tested with several different FOS gage lengths, and the resulting strains of the FOS and the strain gage were compared. By assuming a correspondence between the strain measured by the strain gage and the actual strain in the beam, it was possible to determine an equation that predicts the strain transfer to the fiber as a function of the gage length and the material properties of the coating:

$$\alpha(k, L) = \left[ 1 - \frac{\cosh(wL)}{wL \sinh(wL)} \right] \quad \text{Equation 2-3b}$$

where  $w$  and  $L$  are as defined previously, and  $\alpha$  is the constant of proportionality between the actual structural strain and the FOS strain measurement. The values for  $\alpha$  determined from the experimental tests compared well with those found using the above equation.

The determination of Equation 2-3b is significant for the applicability of FOS. The relationship not only makes it possible to determine FOS gage length requirements, but also eliminates the need for

calibration tests and statistical analysis to determine strain transfer. It was also found that having a bare embedded fiber (no protective coating) gives an optimal  $\alpha = 1$ , but is an unrealistic configuration due to the requirement for fiber protection when used in structural health monitoring applications.

#### 2.4.4 Investigation on Strengthening and Strain Sensing Techniques for Concrete Structures Using FRP Composites and FBG Sensors, Lau *et al.* (2001)

The study conducted by Lau *et al.* discovered the unique ability of FBG sensors to measure strain in concrete prisms reinforced with fiber reinforced plastics (FRP). The objective of the experiment was to determine the reinforcing capabilities of FRPs on concrete beams subjected to flexural loads. Twenty-inch long concrete prisms were retrofitted with FRP plates that were adhered to their tensile faces in four different configurations as seen in Figure 2-4.

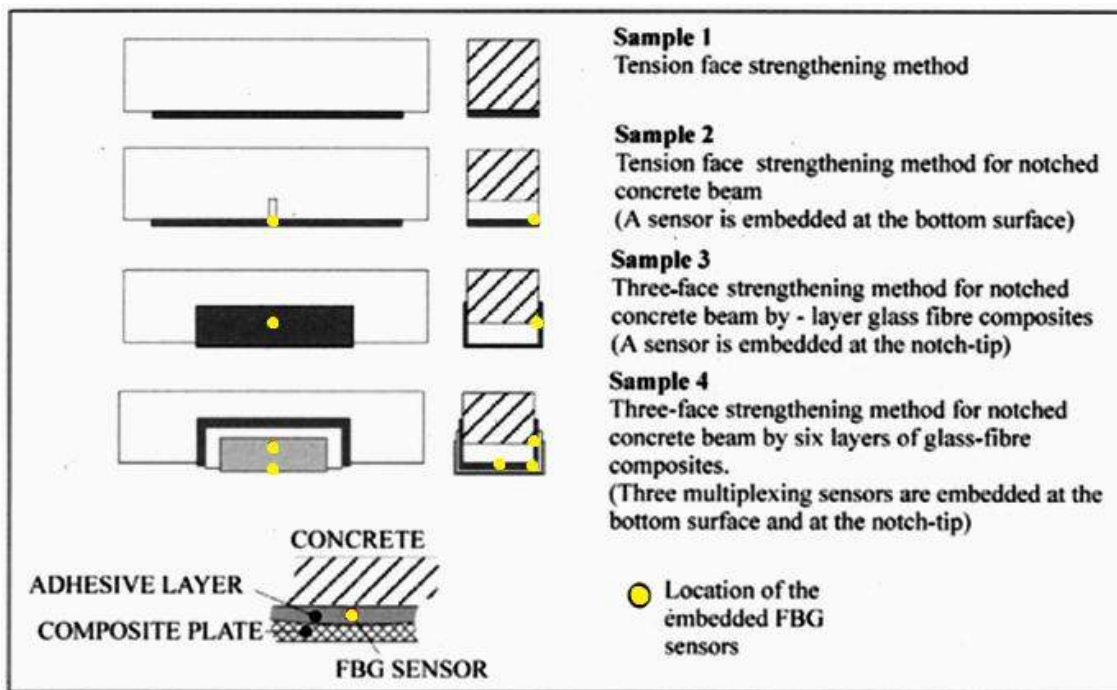


Figure 2-4: Reinforced concrete prism test specimens (Lau, Zhou, & Wu, 2001)

FBG sensors were surface adhered to the concrete prisms at midspan on both the bottom and vertical faces. The FBGs measured the longitudinal strains at the concrete-FRP interface during flexural loading. The FBG strains were compared to those measured by conventional strain gages that were adhered to



the surface of the FRP plates at the same locations of the FBGs. A notch running in the transverse direction was cut into the bottom of the prisms to induce stress concentrations and insure that the FRP reinforcement and the concrete failed at the midspan location. The notch was filled with epoxy so that FBGs could be adhered across the notch at the notch-tip and notch-mouth.

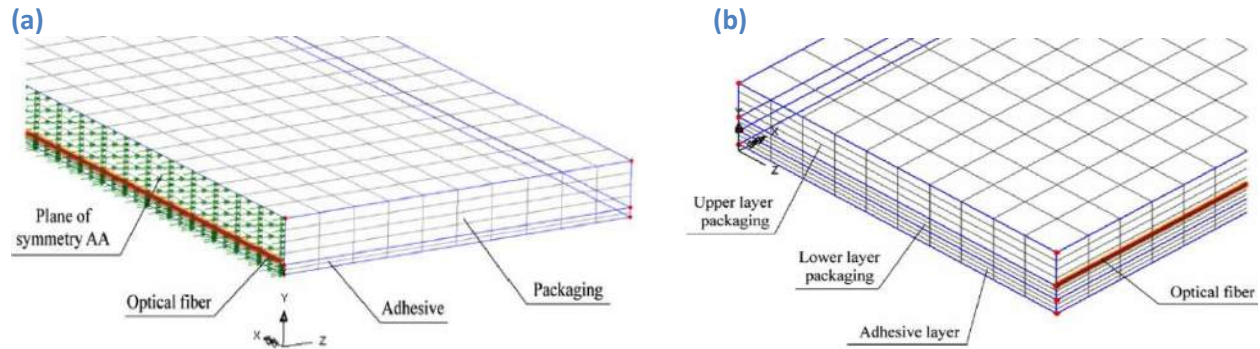
Several pertinent behaviors of FRP reinforced concrete beams were revealed by the test results. The positioning of the FBGs across the concrete notch was critical in determining the effects of the reinforcing FRP plates. By comparing the strains at the concrete-FRP interface with the strains at the corresponding FRP surface location, it was possible to evaluate the strain behavior of the two materials as they were loaded to failure. It was found that just before concrete failure, the strain in the concrete was four times greater than the strain at the surface of the FRP reinforcement. This relationship implies that the FRP reinforcement provides considerable additional strength for the concrete beam.

Unique strain sensing capabilities of FBGs were discovered in the tests. It was seen that the FBGs were effective strain measuring devices throughout all the load ranges, while the surface mounted strain gages were only accurate in the low-loading conditions. The FBG sensors were able to detect debonding of the FRP plates as well as concrete failure, which was not possible with the surface mounted strain gages. Accurate strain measurement by the FBGs was achieved by adhering them to the concrete over a 150 mm length. This length provided full strain transfer from the concrete to the FBG according to the theory developed by Ansari *et al.* discussed in the previous section.

#### 2.4.5 Analysis of the Strain Transfer in a New FBG Sensor for Structural Health Monitoring, Torres *et al.* (2010)

The goal of the analysis conducted by Torres *et al.* was to understand the effectiveness of a new FBG packaging system that was adhered to the surface of a host structure. The packaging configuration consists of an FBG fiber covered by a single protective layer of composite material made up of glass fiber reinforced polyester resin. A second more common configuration was also tested and used as a

comparison to the new configuration. The second configuration had two protective layers of the glass fiber composite material, one on each side of the fiber. The two configurations were adhered to a host structure using a thin layer of adhesive. Figure 2-5 taken from Torres *et al.* illustrates the FEMs of the two configurations in which the packaging layers represent the aforementioned protective composite layers.



**Figure 2-5: (a) Single protective layer configuration (b) Double protective layer configuration**

A FEM of the packaging was used to determine the configuration that produces optimal strain transfer between the host structure and the FBG sensor. The parameters that were adjusted in order to optimize the design included material properties, adhesive layer thickness, temperature, and the number of protective layers. A strain was applied on the lower face of the adhesive layer, which simulated strain induced in the host structure caused by temperature change. The response of the system to the induced strain was analyzed assuming an orthotropic adhesive layer, and only considering thermal expansion in the longitudinal direction.

The response of the system to different packaging material properties and varying adhesive thicknesses resulted in relevant guidelines towards the best strain transfer design. It was found that the optimal material properties of the composite layer in the single layer configuration were those with a high elastic modulus and a low Poisson's ratio. Adhesive layer thicknesses ranging from 100  $\mu\text{m}$  to 1000  $\mu\text{m}$  were tested, and a positive correlation between thickness and strain error was found. However, the effect of adhesive layer thickness was not considered to be significant because of the low difference

(4%) in strain loss between a typical adhesive thickness (400  $\mu\text{m}$ ) and a large adhesive thickness (1000  $\mu\text{m}$ ). An adhesive thickness greater than 1000  $\mu\text{m}$  is not recommended by the authors due to resulting low adhesion.

A comparison of the new single layer packaging design and the more commonly used double layer design resulted in strong partiality towards the single layer configuration. The presence of a second 400  $\mu\text{m}$  thick protective composite layer between the fiber and the host structure caused a substantial strain transfer error of 15%. In addition, the extra layer caused an inconsistency in strain transfer measurements, which was thought to be a result of material manufacturing defects and material property variances. The single layer design not only eradicates this error but is also a more simple design.

The final parameter analyzed in the study was the effect of temperature change on the packaging design. FBG temperature change is a realistic in-service condition and has an effect on the spectrum of light that is reflected by the gratings, which is directly related to sensor accuracy. In order to determine the type of composite packaging that performs best under temperature-variant conditions, two packaging material types were tested in the configurations discussed previously. One composite type was comprised of a volume fraction of glass fibers, while the second type had a uniform glass fiber volume. The resulting reflected light spectra of the FBGs with the two composite types subjected to a thermal variation test showed that the uniform glass volume composite is ideal for FBG thermal gradient applications. The non-uniform composite test produced a spectrum of inconsistent and varying responses, while that produced by the uniform composite was consistent throughout the temperature variations.

## CHAPTER 3: FINITE ELEMENT STUDY

### 3.1 Test Objective

A 3D finite element analysis (FEA) of a notched concrete host structure and a notch-embedded FBG strand (see Figure 3-1) was conducted to study strain transfer behavior from the concrete to the FBG. The bond layer thickness, adhesive bond length, adhesive elastic modulus, and notch geometry were all variables of interest in the study. An experimental laboratory investigation with similar parameters was also conducted for comparison with the numerical analysis. The experimental investigation is discussed further in Chapter 4.

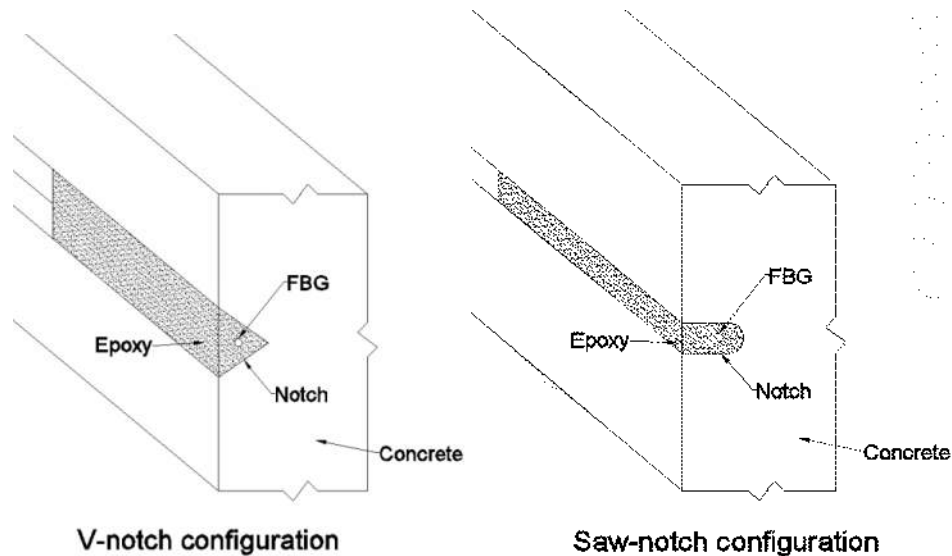


Figure 3-1: Notch embedded FBG configuration cross sections

### 3.2 Finite Element Model Configurations

Two different model configurations were tested in the numerical analysis, each having different notch geometries. Figure 3-2 illustrates both the v-notch and saw-notch finite element model (FEM) configurations. Both configurations represent quarter symmetry parts of a full concrete prism. The symmetry axes can be seen in Figure 3-3. Figure 3-4 indicates the portion of the concrete prism that is used in the FEMs. Both notch configurations were chosen because of the practicality of their field

implementation. The saw-notch configuration can be easily cut into concrete surfaces using a saw with a 3.2 mm (1/8 inch) masonry blade. The 90 degree v-notch configuration was selected because it is a common notch seen in concrete structural members and can either be cut with a masonry saw or formed directly when the concrete is placed. Detailed dimensions of the two notch geometries can be seen in Figure 3-5.

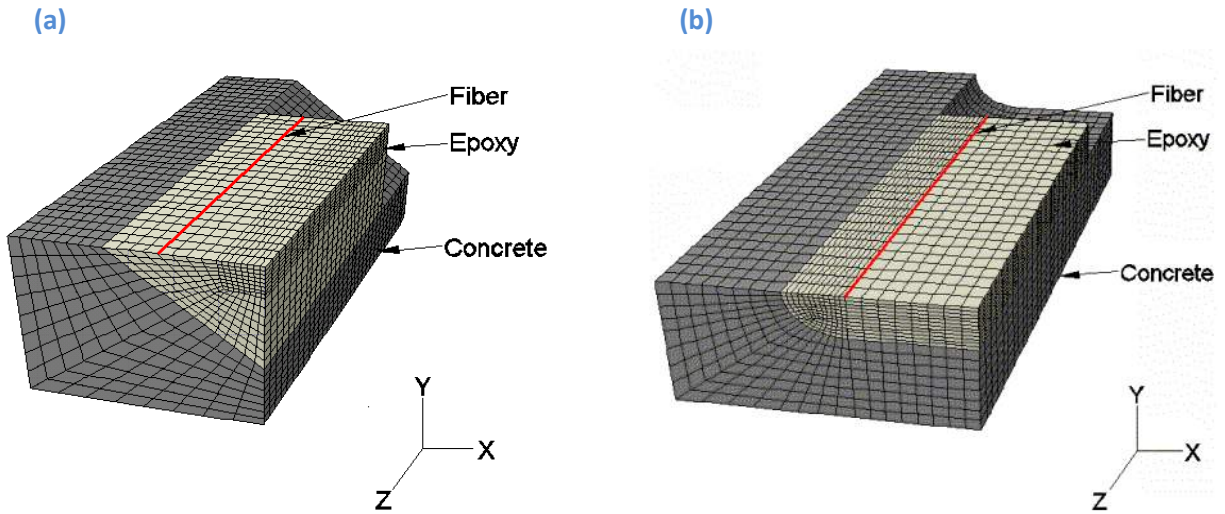


Figure 3-2: (a) V-notch FEM configuration (b) Saw-notch FEM configuration

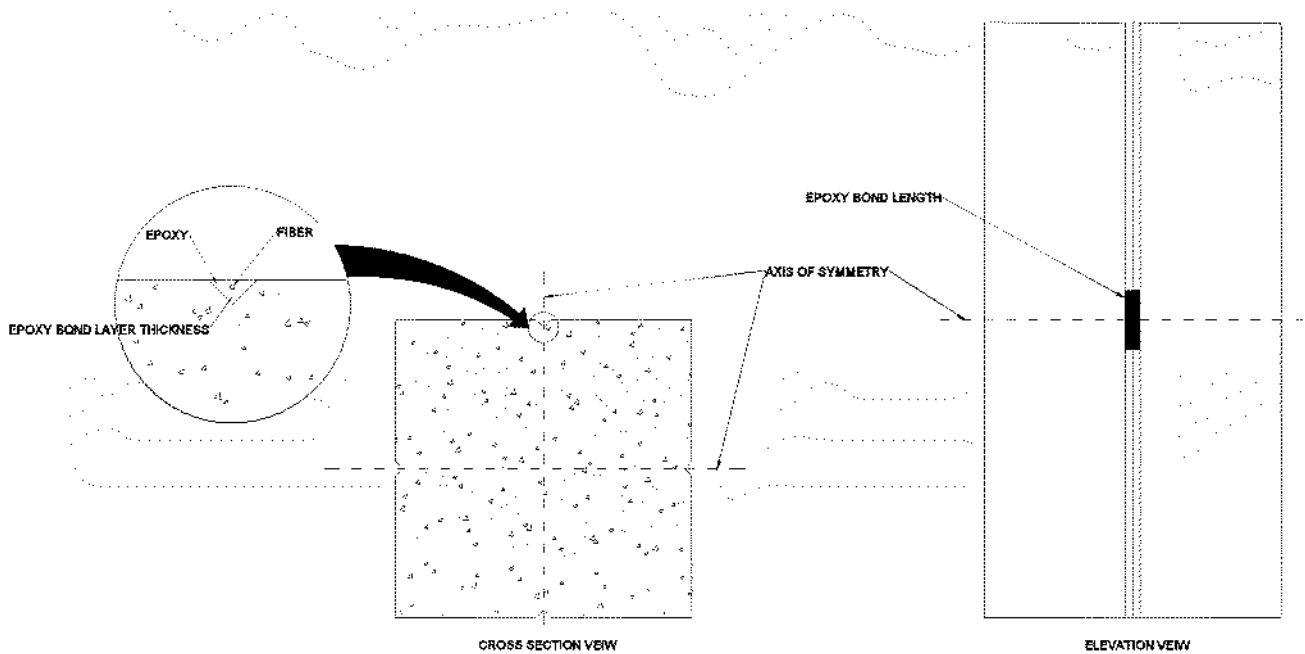
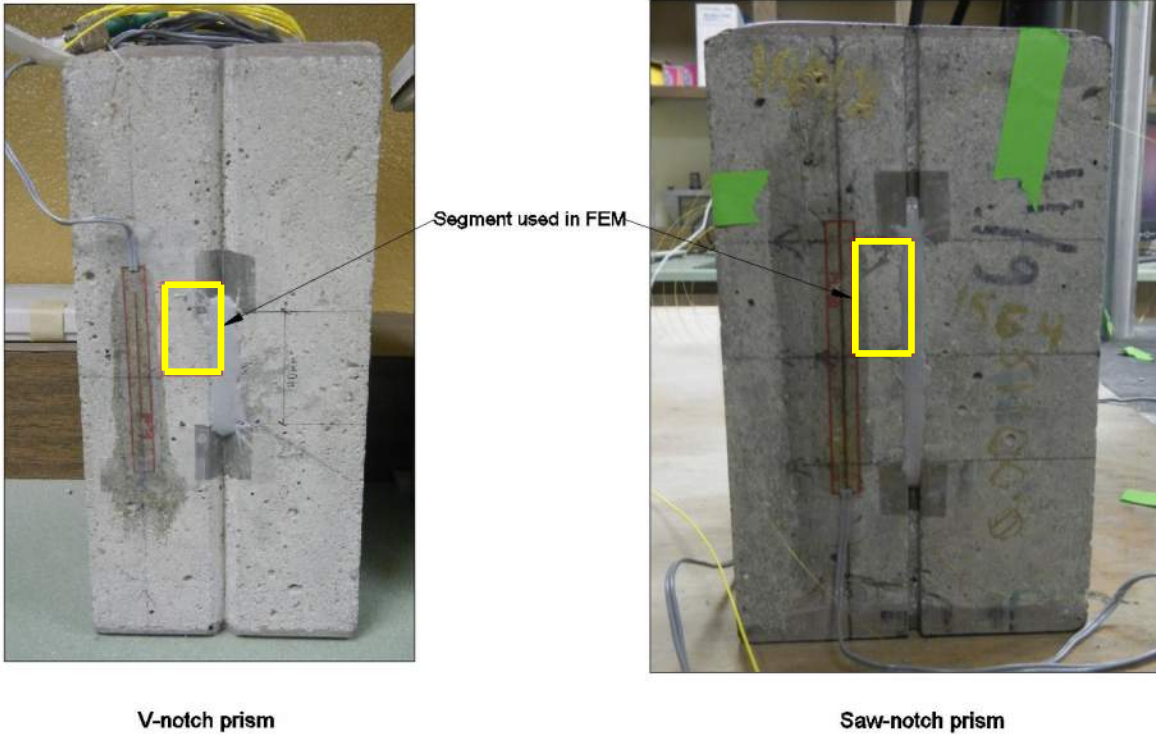


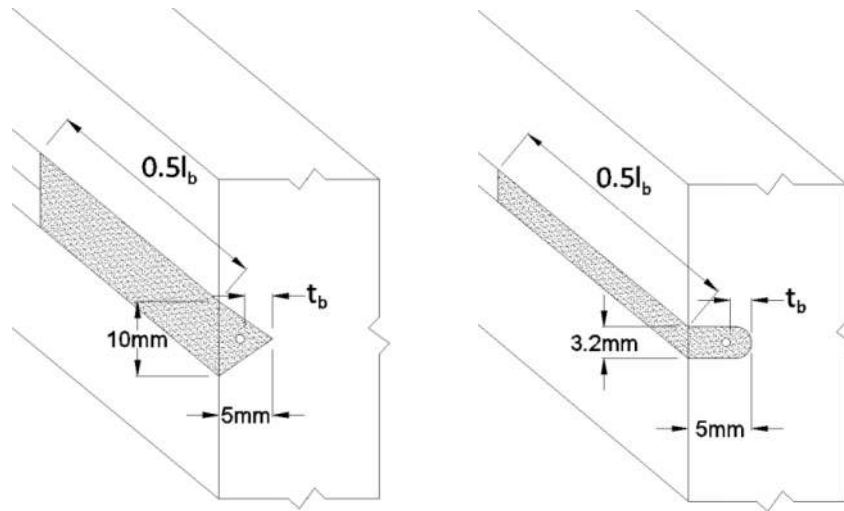
Figure 3-3: Notched concrete prism symmetry axes



V-notch prism

Saw-notch prism

Figure 3-4: FEM part indication



V-notch configuration

Saw-notch configuration

Figure 3-5: Notch geometry details

The epoxy bond length ( $l_b$  in Figure 3-5) and the bond layer thickness ( $t_b$  in Figure 3-5) are two important parameters that affect strain transfer. The epoxy bond length is the length of epoxy in the concrete notch that encases the grated section of the FBG and bonds it to the concrete as seen in Figure

3-5. Intuition suggests that the longer the epoxy bond length the better the strain transfer, however it is theorized that only a portion of the FBG needs to be bonded in the notch in order to achieve full strain transfer. Epoxy bond lengths of 10 mm, 20 mm, 30 mm, 40 mm, 50 mm and 60 mm were analyzed in the FEA in order to determine which lengths provide full strain transfer to the FBG.

The bond layer thickness ( $t_b$ ) is the distance from the epoxy embedded fiber to the tip of the concrete notch. It is hypothesized that as  $t_b$  increases, i.e. the fiber moves further away from the concrete, the strain transfer from the concrete to the fiber will decrease. To test this hypothesis, the strain transfer was analyzed with  $t_b = 0.875$  mm,  $t_b = 1.75$  mm and  $t_b = 3.5$  mm for the v-notch configuration and  $t_b = 1.6$  mm and  $t_b = 3.2$  mm for the saw-notch configuration. All the bond layer thicknesses were tested for each epoxy bond length giving 18 different configurations for the v-notch and 12 configurations for the saw-notch.

The elastic modulus of the epoxy also has an affect on strain transfer. Studies discussed in Chapter 2 suggest that the closer the elastic modulus of the epoxy is to that of the host material (concrete), the better the strain transfer will be. Four different epoxy moduli were used in each of the aforementioned configurations to determine the relationship between epoxy modulus and strain transfer. After researching various epoxies that would be suitable for field applications, the following four elastic moduli were selected: 700 MPa, 1800 MPa, 3000 MPa and 6000 MPa. Each elastic modulus was tested for all the FEM configurations giving a total of 72 configurations for the v-notch and 48 configurations for the saw-notch. The elastic moduli for the concrete and FBG were modeled as 30,000 MPa and 72,000 MPa respectively. Poisson's ratios remained constant for each material due to their minute effect on strain transfer (Zhou, *et al.*, 2006). See Table 3-1 for further information on material properties.

**Table 3-1: FEM material data**

<b>Material type</b>	<b>Elastic Modulus (MPa)</b>	<b>Poisson's ratio</b>
Concrete	25,000	0.15
Epoxy	700-6000	0.35
FBG strand	72,000	0.17

### 3.3 FEA Convergence Study

A convergence study was conducted on the saw-notch model to determine the necessary level of mesh refinement for the FEA. Convergence was determined by examining the change in strain at a particular node for several different levels of mesh refinement. The node that was selected was located at the base of the fiber at the fixed end of the model. This location represents the exact center location of the embedded FBG sensor. As the mesh became more refined from one level to the next, the change in the strain at the node of interest decreased. Four levels of mesh refinement were examined and it was found that the third level was acceptable. Convergence was achieved at the third level of mesh refinement because the amount of strain change between levels three and four was sufficiently low.

Table 3-2 provides convergence data.

**Table 3-2: Convergence study data**

<b>Mesh</b>	<b>Total # of nodes</b>	<b>Strain at fiber center (<math>\mu\epsilon</math>)</b>	<b>% change in strain</b>
1	437	3923.78	-
2	2676	3915.37	0.215%
3	18,518	3908.04	0.188%
4	137,322	3905.08	0.076%

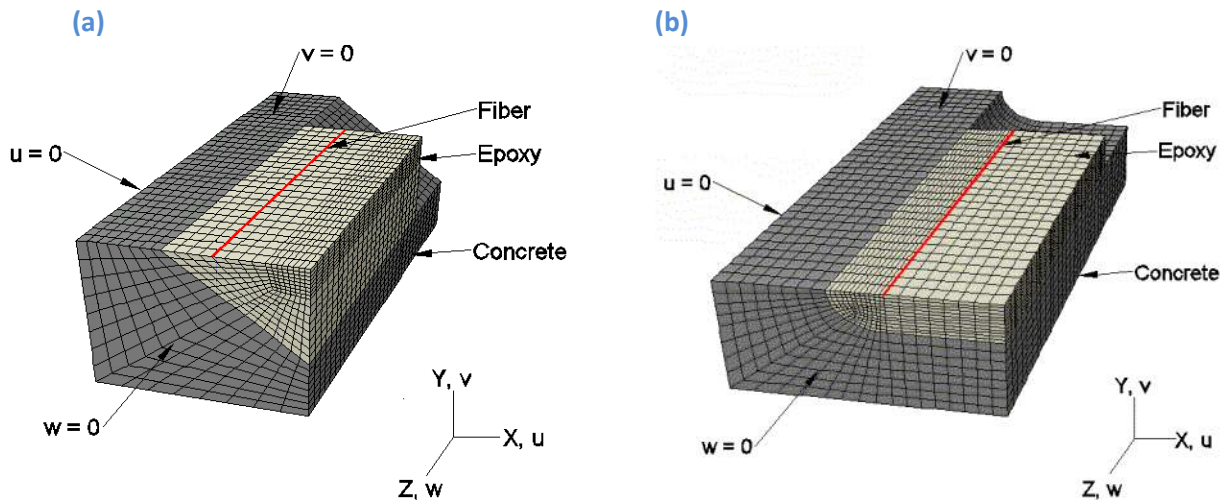
The FEM was created and analyzed using FEA software called Abaqus. The three parts (epoxy, concrete and fiber) of the FEM were modeled as 3D elastic isotropic solids. The elements of the concrete and epoxy parts were eight-node hexahedral bricks (C3D8R) with linear strain variation modes. C3D8R elements were selected because of their fast, accurate, and reliable analysis capabilities when compared to other element types such as six-node triangles or ten-node tetrahedrals. Reduced integration with one integration point per eight-node brick was used to evaluate the model. The fiber



part was modeled with 2-node linear 3D truss (T3D2) elements. These elements were selected for the fiber because they allow strain in the axial direction only which is representative of how FBGs measure strain.

### 3.4 FEM Strain Transfer Analysis

Strain was induced in the concrete part of the FEM by applying an axial displacement to the free end of the concrete. Several other boundary conditions seen in Figure 3-6 were applied to enforce symmetry conditions.



**Figure 3-6: FEM boundary conditions: (a) V-notch FEM configuration (b) Saw-notch FEM configuration**

The epoxy portion of the FEM was modeled as an extension of the concrete part but with different material properties. This modeling method allows for the assumption that a perfect bond exists between the concrete and the epoxy parts. The fiber part was attached to the epoxy part using a tie constraint, which also allows for the assumption of a perfect bond between the fiber and the epoxy.

As discussed earlier in this chapter, the strain transfer from the strained concrete over the epoxy bond layer to the fiber is the primary variable of interest. The strain transfer is represented as the ratio of the strain in the fiber to the strain in the concrete as shown in Equation 3-1.

$$\text{strain transfer} = \frac{\varepsilon_f}{\varepsilon_c} \quad \text{Equation 3-1}$$

In Equation 3-1 the fiber strain value is taken at a node along the length of the fiber. The concrete strain value is taken at the node of the concrete element located at the tip of the concrete notch. This concrete node is located at the same longitudinal distance from the fixed end of the model as the corresponding fiber node.

It was critical to determine the strain transfer values at all the nodes along the length of the fiber. This was necessary to determine what is known as the *effective strain transfer length* ( $l_e$ ) for a given model configuration. The  $l_e$  is the length along the fiber that is experiencing fully developed strain transfer i.e. *strain transfer* = 1.0 in Equation 3-1. In order to determine the  $l_e$  of each configuration, the strain transfer along the length of the fiber was calculated and plotted. The following section provides a discussion of the results along with graphical representations of strain transfer.

### 3.5 FEA Results

The strain transfer characteristics of the various model configurations in the FEA were analyzed by plotting three different graph types. An example of the first graph type, seen in Figure 3-7, compares the effects of epoxy bond length on strain transfer by plotting the strain transfer curves for six epoxy bond lengths. The variable  $l_b$  indicates the epoxy bond length for each curve, and  $l_e$  is represented by the flat portions of the curves. The primary trend seen in these plots is that the  $l_e$  increases as  $l_b$  increases. For a configuration to be fully developed in terms of strain transfer, the flat portion of the strain curve must be at least 10 mm long, which is the length of the grated sensor region in the FBG. Figures A1-1 through A1-5 in Appendix A illustrate the results for the first graph type for all the configurations that were tested. In all of the simulations, the  $l_b = 10$  mm curve never flattens out suggesting that 10 mm is an ineffective epoxy bond length for all configurations.

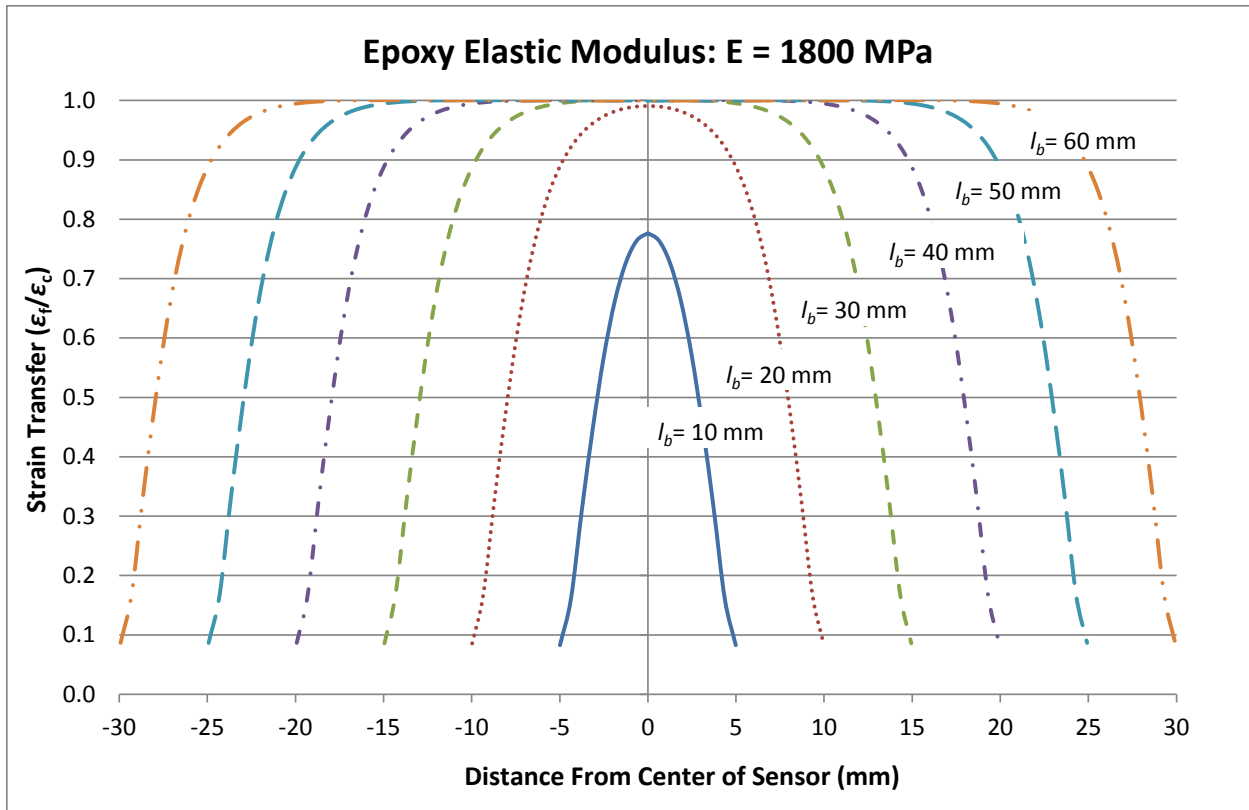


Figure 3-7: Epoxy bond length comparison for saw-notch with 1.6 mm bond layer thickness

An example of the second graph type, seen in Figure 3-8, provides an assessment of the effects of epoxy modulus on strain transfer. The strain curves for the four different epoxy moduli are plotted on the same graph. It is seen that the strain transfer improves modestly as the epoxy modulus increases. Figures A2-1 through A2-5 in Appendix A illustrate the results for all the configurations tested for the second graph type. These plots show that as epoxy bond length increases, the epoxy modulus strain curves become more tightly grouped for a given configuration. This trend implies that the greater the epoxy bond length, the less effect the epoxy modulus has on strain transfer.

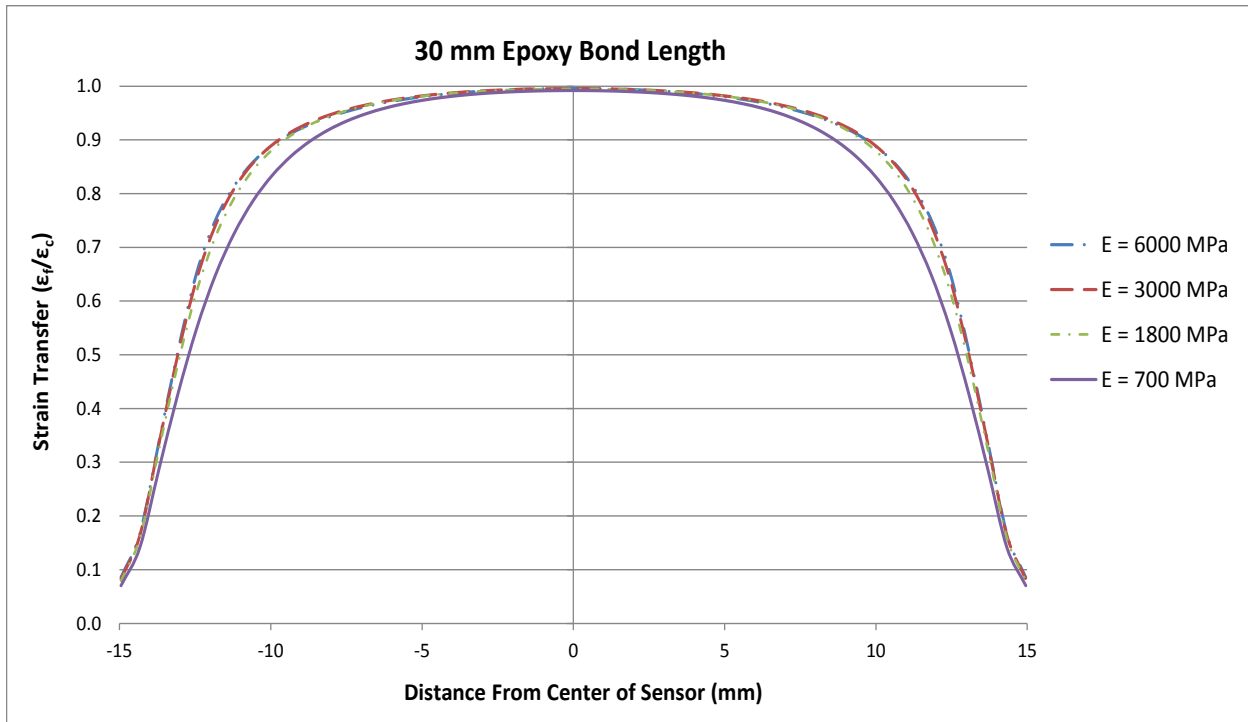


Figure 3-8: Epoxy elastic modulus comparison for v-notch with 1.75 mm bond layer thickness

The third graph type resulting from the FEA is seen in Figures 3-9 and 3-10 and indicates the effects of bond layer thickness on strain transfer. The bond layer thicknesses analyzed for the v-notch configurations are plotted in Figure 3-9 and the saw-notch bond layer thicknesses are seen in Figure 3-10. An epoxy bond length of 30 mm and an epoxy modulus of 1800 MPa were selected for both comparisons because they are configurations that can be compared to laboratory tests. Both graphs show that as the bond layer thickens, strain transfer decreases.

It is interesting to note that the amount by which the strain transfer decreases as bond layer thickens is greater for the v-notch than the saw-notch. This behavior is likely due to the fact that the v-notch is wider with a tapered shape while the saw-notch geometry is narrower and more uniform. The bigger v-notch provides a greater volume of epoxy for strain loss to occur in. The tapered v-notch shape causes the strain transfer to reduce more than the saw-notch as the bond layer thickens.

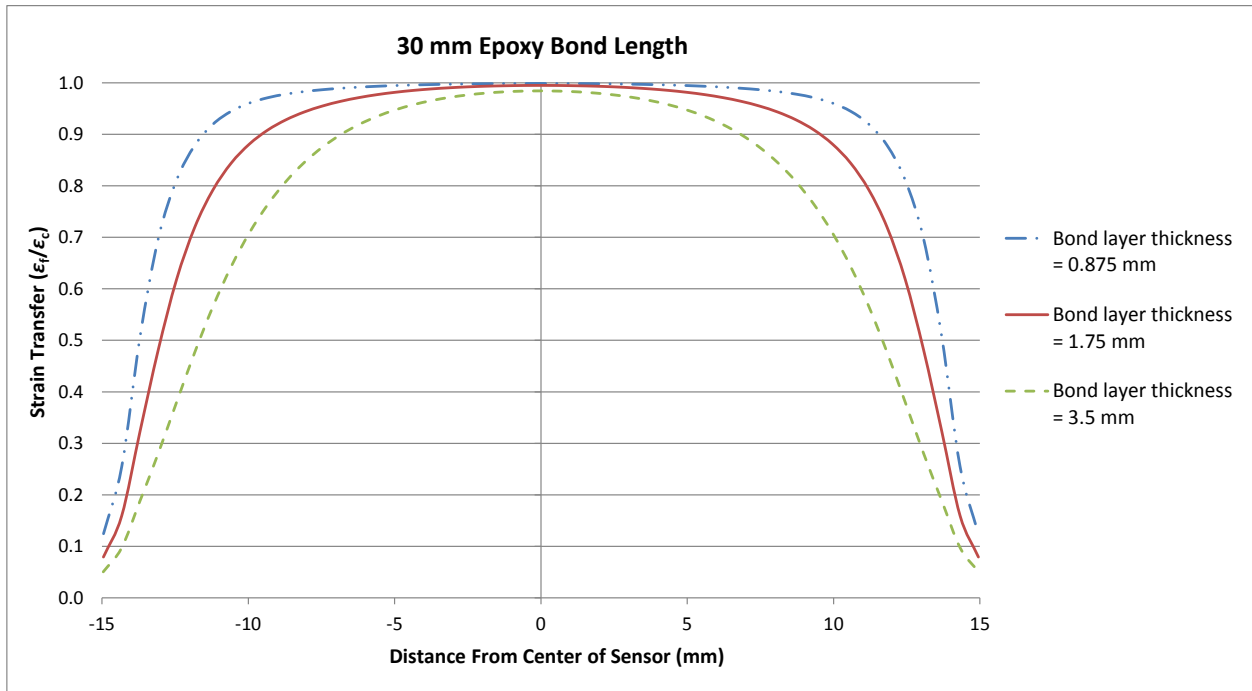


Figure 3-9: Bond layer thickness comparison for v-notch with  $E = 1800 \text{ MPa}$

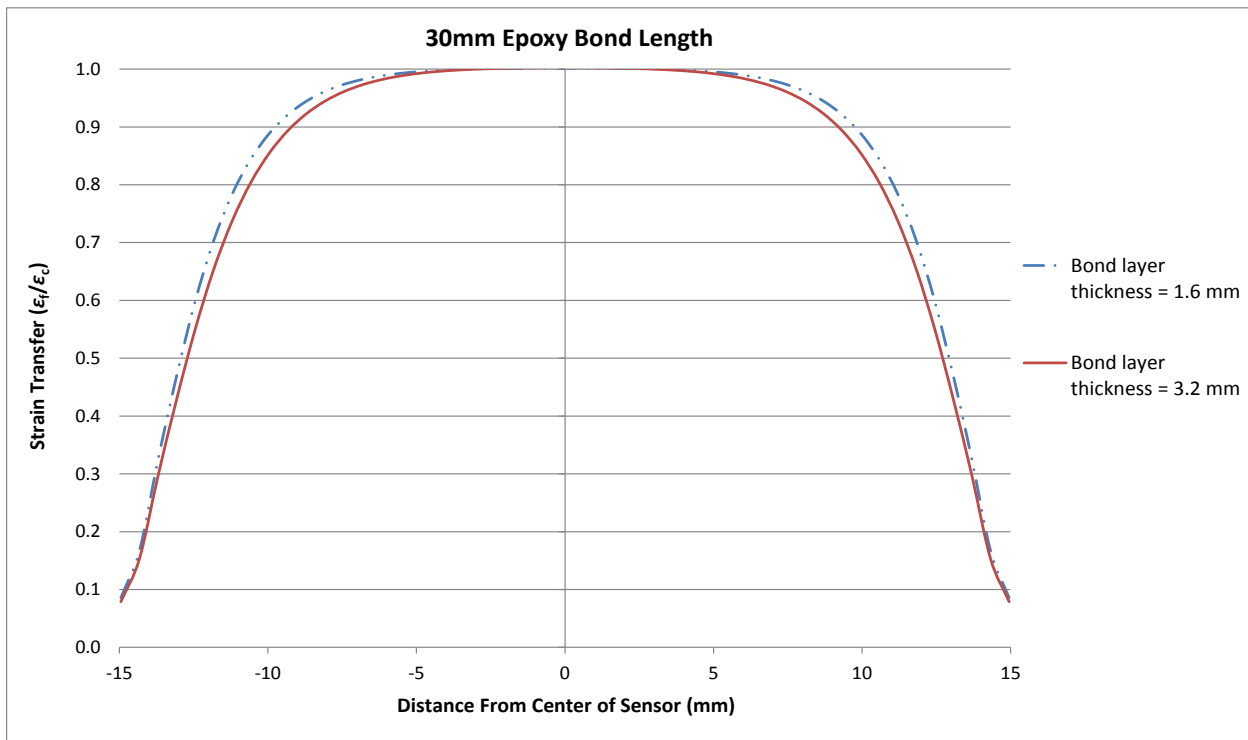


Figure 3-10: Bond layer thickness comparison for saw-notch with  $E = 1800 \text{ MPa}$

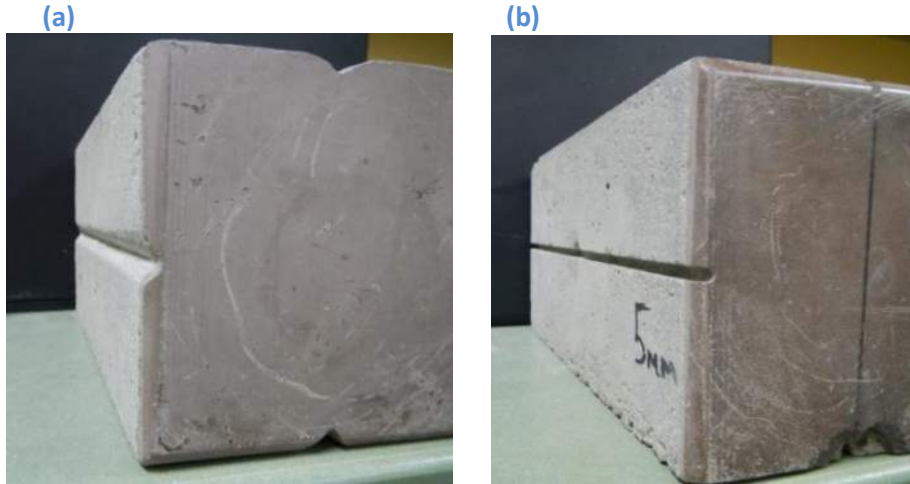
## CHAPTER 4: EXPERIMENTAL INVESTIGATION

### 4.1 Test Specimens

Experimental laboratory tests were conducted on notched concrete prisms with adhered FBGs and conventional strain gages. The objectives of the tests were to confirm the results from the FEA as well as to develop an FBG application technique suitable for field implementation. Two types of concrete prisms were cast, both having the same dimensions but with different notch geometries. One prism type had v-notches that were created using the aluminum forms seen in Figure 4-1. The saw-notched prism was formed using the unnotched aluminum form, and the notches were cut into the prisms with a 3.2 mm (1/8 in) thick masonry saw after curing. Form oil was used in the casting process, and the concrete surfaces were wiped clean with a dry cloth after curing. Both notch geometries were designed to match those of the FEM. The prism dimensions were 8 in x 4 in x 4 in with one longitudinal notch on each of the four sides as seen in Figure 4-2. The prisms were notched on all four sides so that multiple fibers could be imbedded and tested simultaneously on the same prism. The strength properties and batch mixture details of the prisms can be seen in Table 4-1.



**Figure 4-1: Concrete prism forms**



**Figure 4-2: Concrete test prisms notches: (a) V-notch (b) Saw-notch**

**Table 4-1: Concrete prism properties by weight**

Fine aggregate (passing No. 4 sieve)	36%
Coarse aggregate (retained before No. 4 sieve)	34%
Type I,II Portland Cement	20%
Water/cement ratio	0.50
Compressive strength	40 MPa

## 4.2 FBG Test Configuration

The FBG strain sensors were embedded into the notches of the concrete prisms in order to observe the strain transfer behavior from the loaded concrete prism to the FBGs. The prisms were axially compressed using an Instron 1332 servohydraulic loading machine. The load pattern was a cyclic ramp loading applied with steel bearing load plates. The FBGs were embedded into the prism notches using a common structural epoxy anchoring gel (Ultrabond 1300) manufactured by Adhesives Technology. Data from surface-adhered conventional strain gages was used to compare with the epoxy-embedded FBG strain data to establish strain transfer rates. The strain measured by the conventional strain gages was taken as the strain of the concrete in the comparison.

Various instruments were used to setup and run the experimental tests. The FBGs first had to be spliced to a fiber tail so that they could be connected to a commercial FBG interrogator device. Splices were made using an optical splicer along with fiber reinforcing tubes that protect the spliced

region. The SmartScan FBG interrogator, manufactured by Smart Fibres, is a device that relays FBG sensing information to a PC. It works by launching light through an FBG and then collecting the wavelength of the light reflected back by the gratings. The wavelength information is then relayed to a PC with SmartSoft software where it is displayed and recorded.

The surface mounted electrical resistance strain gages were attached to the smoothed concrete surface using cyanoacrylate adhesive. They were then wired into a National Instruments model cDAQ-9174 strain gage module. The strain gage data was viewed and recorded on a PC using LabView software. See Figure 4-3 for a schematic of the test configuration.

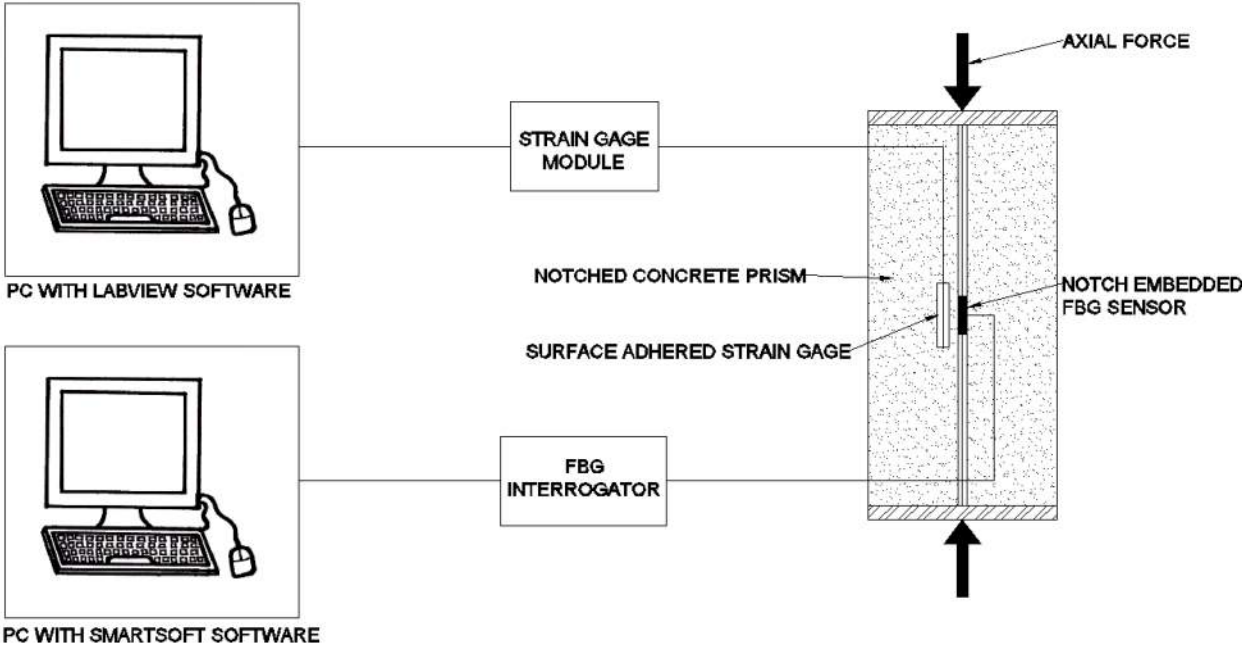


Figure 4-3: Laboratory test schematic

The epoxy used to imbed the fiber in the concrete prism notch was selected based on availability and field application feasibility. Ultrabond 1300 structural epoxy anchoring gel was chosen because it is readily available and has desirable material properties. Ultrabond 1300 has a high elastic modulus of 1800 MPa, a working time of 20 minutes, and a full cure time of 24 hours. The high elastic modulus is good for strain transfer while the 20-minute working time provides a sufficient window for fiber embedment. The 24-hour cure time is reasonably short and appropriate for field applications.



Ultrabond 1300 is typically used for anchoring and grouting dowels and tie bars for concrete pavement repairs, making it a common product that may already be found on DOT construction sites.

In order to confirm the elastic modulus of the epoxy, compressive and tensile stiffness tests were conducted on fully cured epoxy rods as seen in Figure 4-4. Both the compressive and tensile moduli were found to be the same and agreed well with the manufacturer specified value of 1800 MPa. See Table 4-2 for epoxy stiffness test data.



Figure 4-4: Epoxy stiffness test

Table 4-2: Epoxy stiffness test data

Compressive stiffness data		Tensile stiffness data	
Test	Compressive modulus (MPa)	Test	Tensile modulus (MPa)
1	2126	1	1872
2	1489	2	1774
Average	1807	Average	1823

Embedment of the FBGs in the prism notches was executed one at a time using the Instron machine and the fiber tensioning mechanism seen in Figure 4-5. The FBGs were pre-tensioned before embedment for two reasons: (1) to allow for easy placement into the epoxy gel and (2) to ensure that the FBG remains in tension when strained. If the fiber is untensioned when embedded into the epoxy, it could buckle when compressed resulting in inaccurate strain measurement. FBG compression range functionality was tested and is discussed later in this chapter.

The optical fiber was placed in the prism notch by raising the aligned prism up to the tensioned fiber as seen in Figure 4-5. A layer of epoxy was first placed in the bottom of the bare notch. The FBG fiber was then lowered into the epoxy followed by a second layer of epoxy that covered the fiber and filled the notch. The epoxy layering was done to avoid the formation of air pockets within the epoxy. The epoxy was allowed to cure for 24 hours before releasing the fiber from the tension clamps. The desired bond layer thickness was approximated using displacement control on the Instron machine. In order to confirm the bond layer thicknesses, the prisms were cut in half after testing and the bond layer thicknesses were measured. The desired epoxy bond length was achieved by placing metallic spacers in the notch to prevent the epoxy from bonding to the concrete at desired locations, as seen in Figure 4-6. Several embedment configurations were tested in order to confirm the FEA results, as further discussed in the results section.



**Figure 4-5: FBG notch embedment setup**



**Figure 4-6: Epoxy bond length**

### 4.3 Loading and Strain Measurement

A specific load pattern was selected to evaluate the strain transfer behavior from the concrete prism to the epoxy embedded FBG sensor. The load pattern seen in Figure 4-7 was selected because the series of ramp cycles not only show strain transfer trends under varying load magnitudes, but also reveal any viscoelastic lag behavior in the epoxy. Viscoelastic lag is the delay of the epoxy in recovering its original shape after it has been deformed. Since the epoxy is less stiff than the concrete, it was important to use a load pattern that identifies any viscoelastic lag behavior. At the end of the load pattern, the applied force was held at a constant magnitude for several minutes to allow for any gradual reformation of the epoxy to its undeformed state. A load rate of 200 lb/sec was found to be suitable for the tests. The maximum load magnitude in each test was roughly 25% of the failure strength of each prism. This load limit was selected to prevent any concrete failures from occurring and to ensure that all the induced stresses remained in the elastic range of the concrete.

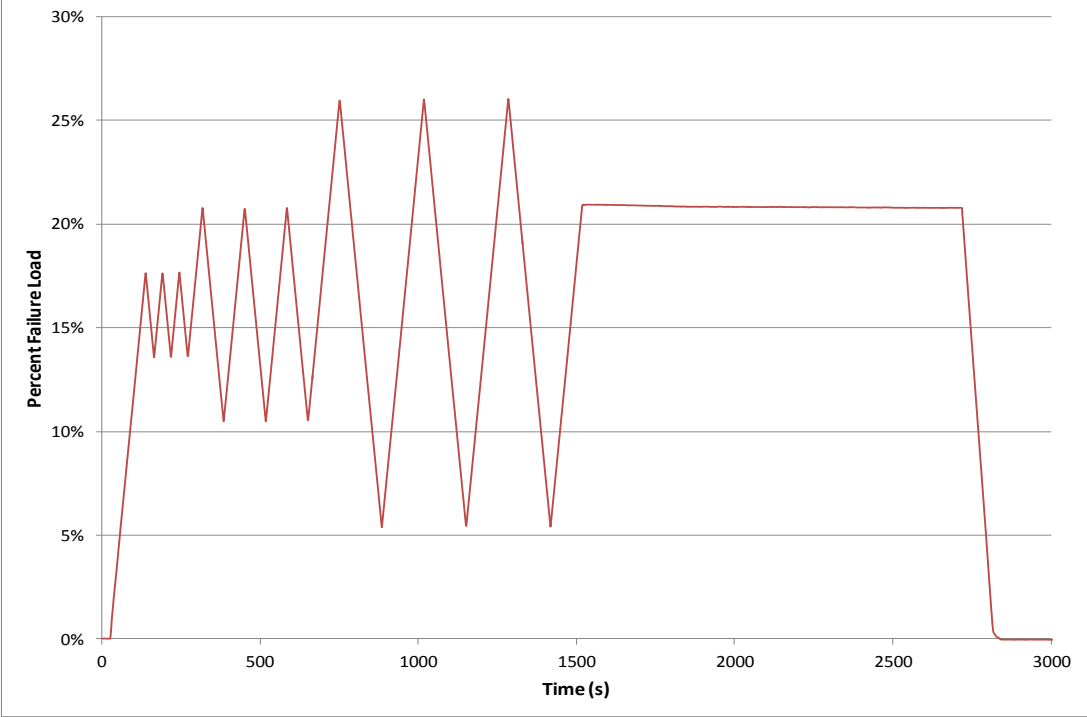


Figure 4-7: Typical test load pattern as a function of failure load

The strain transfer from the concrete to the FBG sensors was calculated by dividing the FBG strain at a given instant by the strain experienced by an adjacent electrical resistance strain gage at the same instant. The time stamps for the two sensors were correlated by simply starting the data acquisition recorders of both sensors at the same time. Strain ratios were calculated at half second intervals over the duration of the test. The strain ratios were then averaged to give a single strain transfer value for each test.

The data acquisition system for the FGBs reports the wavelength of the reflected light within the fiber in nanometers. In order to get a quantitative strain value for the FBG sensor, the wavelength of the reflected light must be converted into mechanical strain using Equation 4-1:

$$\varepsilon_f = \frac{\Delta\lambda}{(k)(\lambda_o)} \quad \text{Equation 4-1}$$

where  $\Delta\lambda$  is the wavelength shift,  $\lambda_o$  is the base wavelength (values range from 1540 nm to 1570 nm), and  $k$  is the FBG gage factor ( $k = 0.78$ ). The FBG strain values were calculated using Equation 4-1 after testing.

#### 4.4 Notched Prism Test Results

Several cyclic axial load tests were run on the FBG instrumented v-notch and saw-notch prisms. Eight repetitions of the load cycle seen in Figure 4-7 were run on the v-notch prism. The v-notch prism had two FBGs embedded in different notches with different configurations for the first six repetitions. One FBG had a bond layer thickness of 2.7 mm and an epoxy bond length of 30 mm while the second had a 3.5 mm bond layer thickness and a 60 mm epoxy bond length. A third embedded FBG with a different configuration was added to the v-notch prism for the last two repetitions. The third FBG configuration had a bond layer thickness of 4.2 mm and an epoxy bond length of 10 mm. The third configuration was tested with the intension that it would produce an undeveloped strain transfer result

as indicated by the FEA. Table 4-3 summarizes the results of the v-notch prism test and provides a comparison with the FEA results for the same configurations.

The scatter plot seen in Figure 4-8 compares the strain transfer results of the FEA and the experimental tests for the v-notch configuration. The FEA strain transfer values are represented as a flat line since the FEA result is one constant strain transfer value for a given configuration. It is seen that there is some scatter in the experimental values and that they vary slightly from the FEA values. Overall, the strain transfer values for the FEA and the experimental tests are well correlated with differences ranging from 1% to 9%.

**Table 4-3: V-notch prism test results with FEA comparison**

Test repetition	Bond layer thickness (mm)	Epoxy length (mm)	FEM strain transfer	Experimental strain transfer
1	2.7	30	0.99	0.972
	3.2	60	1.00	0.893
2	2.7	30	0.99	0.978
	3.2	60	1.00	0.886
3	2.7	30	0.99	0.979
	3.2	60	1.00	0.931
4	2.7	30	0.99	1.000
	3.2	60	1.00	0.904
5	2.7	30	0.99	0.998
	3.2	60	1.00	0.898
6	2.7	30	0.99	0.999
	3.2	60	1.00	0.924
7	2.7	30	0.99	0.982
	3.2	60	1.00	0.894
	4.2	10	0.32	0.337
8	2.7	30	0.99	0.971
	3.2	60	1.00	0.866
	4.2	10	0.32	0.332

**Summary table**

Bond layer thickness (mm)	Epoxy length (mm)	FEM strain transfer	Average experimental strain transfer
2.7	30	0.99	0.98
3.2	60	1.00	0.90
4.2	10	0.32	0.33

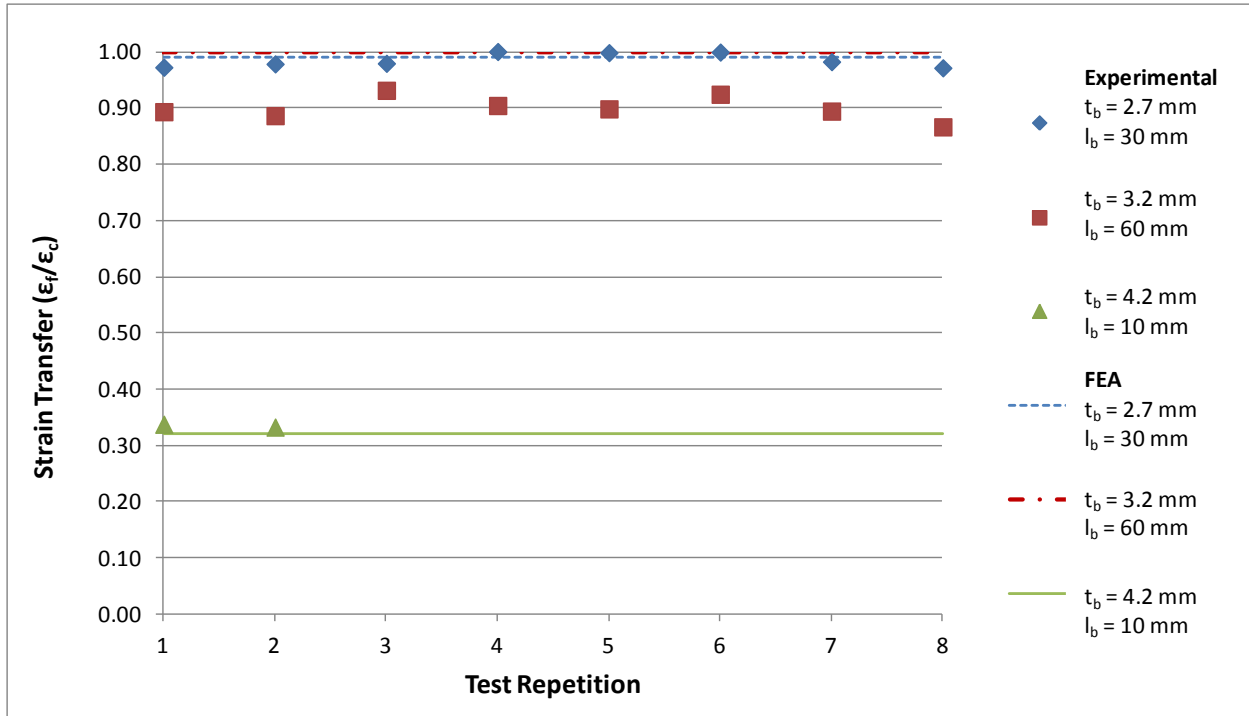


Figure 4-8: V-notch configuration results with  $E_{\text{epoxy}} = 1800$  MPa

Figures 4-9 through 4-11 graphically compare the FEA and experimental results by plotting strain transfer along the length of the epoxy. In these figures, the solid curve represents the FEA strain transfer while the dashed line represents the experimental strain transfer. The experimental result is represented by a flat 10 mm line-segment because the strain transfer of each experimental test was taken as a single averaged strain value. The 10 mm segment represents the strain transfer to the 10 mm FBG sensor region that was centered in the epoxy.

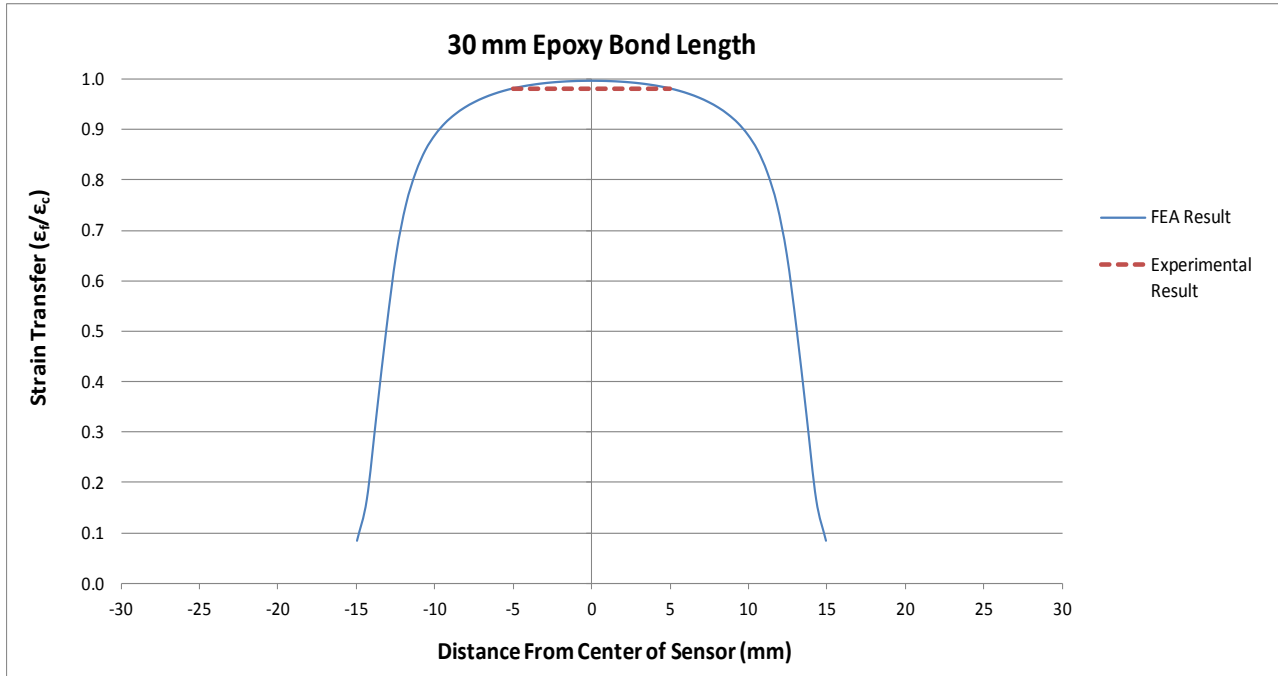


Figure 4-9: Result comparison for v-notch with  $E_{\text{epoxy}} = 1800 \text{ MPa}$ , 2.7 mm bond layer thickness

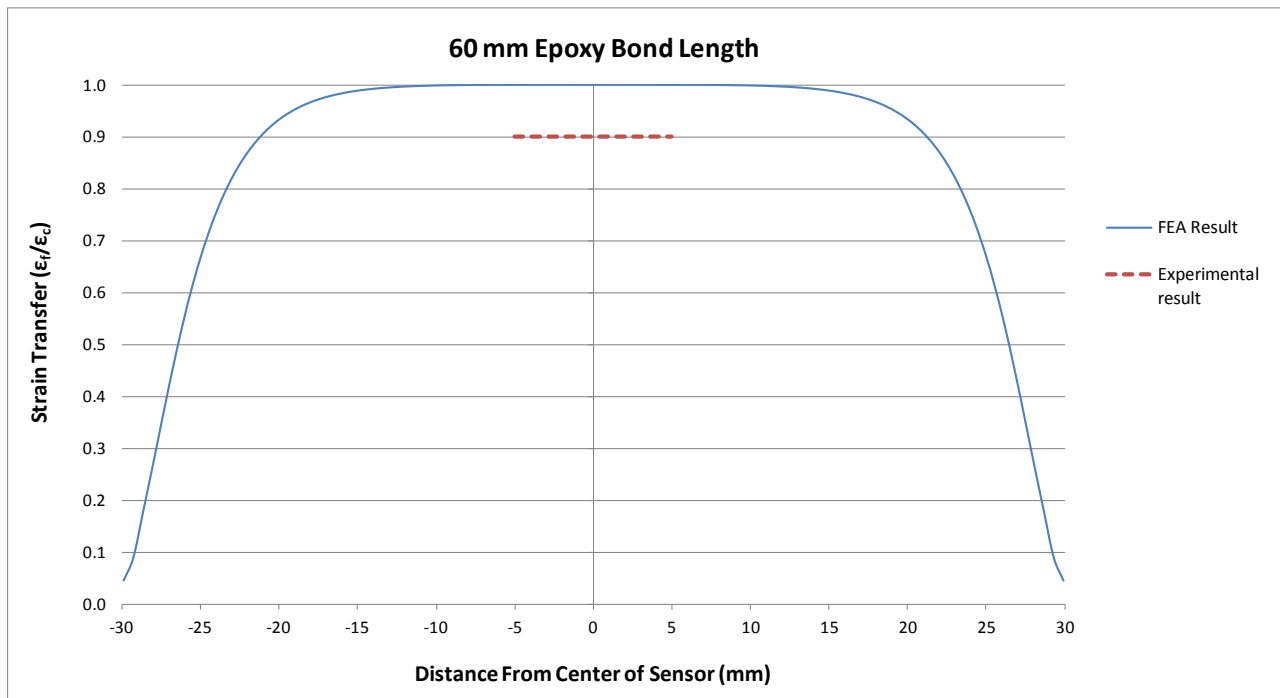
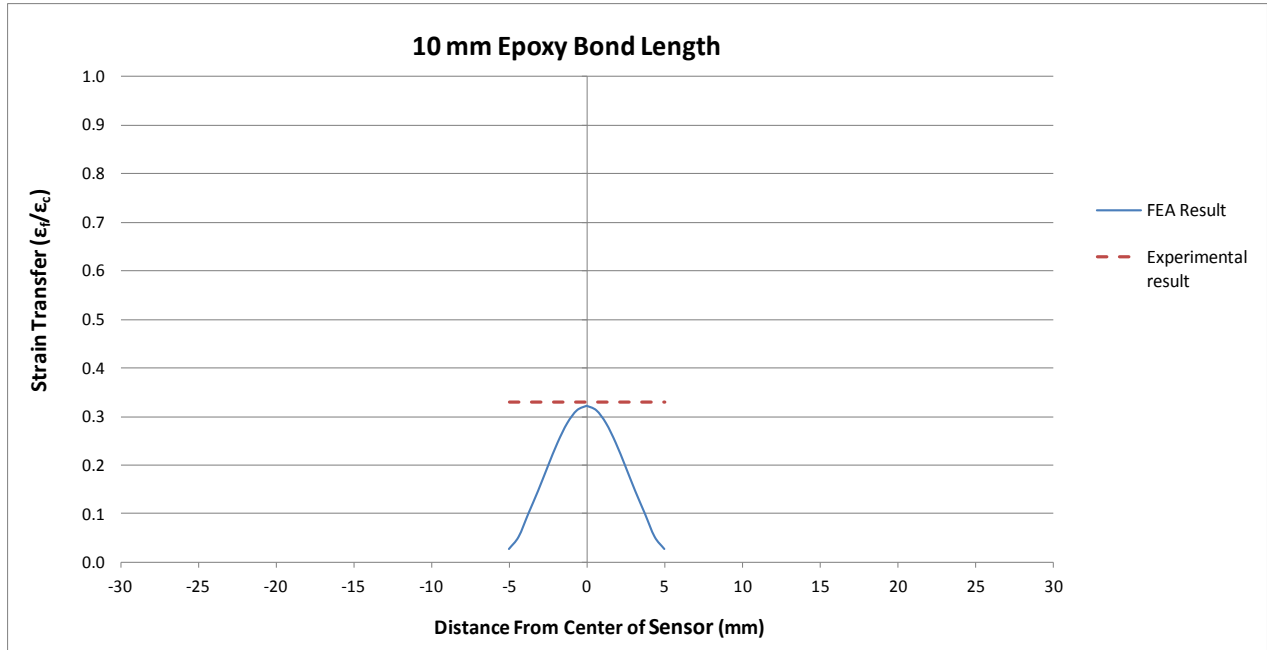


Figure 4-10: Result comparison for v-notch with  $E_{\text{epoxy}} = 1800 \text{ MPa}$ , 3.2 mm bond layer thickness



**Figure 4-11: Result comparison for v-notch with  $E_{\text{epoxy}} = 1800 \text{ MPa}$ , 4.2 mm bond layer thickness**

It is seen that the FEA strain transfer results are greater than the experimental results for the 30 mm and 60 mm epoxy bond length, and less for the 10 mm bond length. There are several possible reasons why the FEA generally predicts greater strain transfer than the experimental test. A few influencing factors include the assumption of perfect bonds in the FEA, the aggregate size in the concrete, the use of form oil on the concrete surface, imperfect concrete notches, and shrinkage of the epoxy over time. The effects of these factors are further evaluated in the Chapter 5.

The experimental and FEA strain transfer results for 10 mm epoxy bond length configuration are very low due to the thick bond layer and short bond length. The FEA strain transfer for the 10 mm epoxy bond length peaks at 0.32 but has an average strain transfer of 0.19, which is much lower than the experimental value of 0.33. The thick bond layer and short bond length cause low accuracy in strain measurement which is a possible explanation for why the FEA strain transfer is less than the experimental strain transfer despite the assumption of perfect bond in the FEA. The triangular shaped FEA curve in Figure 4-11 also suggests that high chirping (non-constant strain) occurred over the 10 mm FBG sensor region, which can also result in inaccurate strain sensing.



The saw-notch prism test consisted of six load repetitions with two different embedded FBG configurations. One embedment configuration had a 30 mm epoxy length with a 3.6 mm bond layer thickness while the second had a 60 mm epoxy length with a 3.4 mm bond layer thickness. The strain transfer data of the test along with a comparison to the FEA results are represented in Table 4-4. Figures 4-12 through 4-14 provide graphical comparisons of the results. Once again, these data reiterate the fact that the FEA generally over-predicts the strain transfer seen in the experimental tests.

**Table 4-4: Saw-notch prism test results with FEA comparison**

Test repetition	Bond layer thickness (mm)	Epoxy length (mm)	FEM strain transfer	Experimental strain transfer
1	3.6	30	0.99	1.08
	3.4	60	1.00	1.09
2	3.6	30	0.99	0.94
	3.4	60	1.00	0.96
3	3.6	30	0.99	0.91
	3.4	60	1.00	0.97
4	3.6	30	0.99	0.91
	3.4	60	1.00	0.94
5	3.6	30	0.99	0.89
	3.4	60	1.00	0.96
6	3.6	30	0.99	0.90
	3.4	60	1.00	0.92

**Summary table**

Bond layer thickness (mm)	Epoxy length (mm)	FEM strain transfer	Average experimental strain transfer
3.6	30	0.99	0.94
3.4	60	1.00	0.97

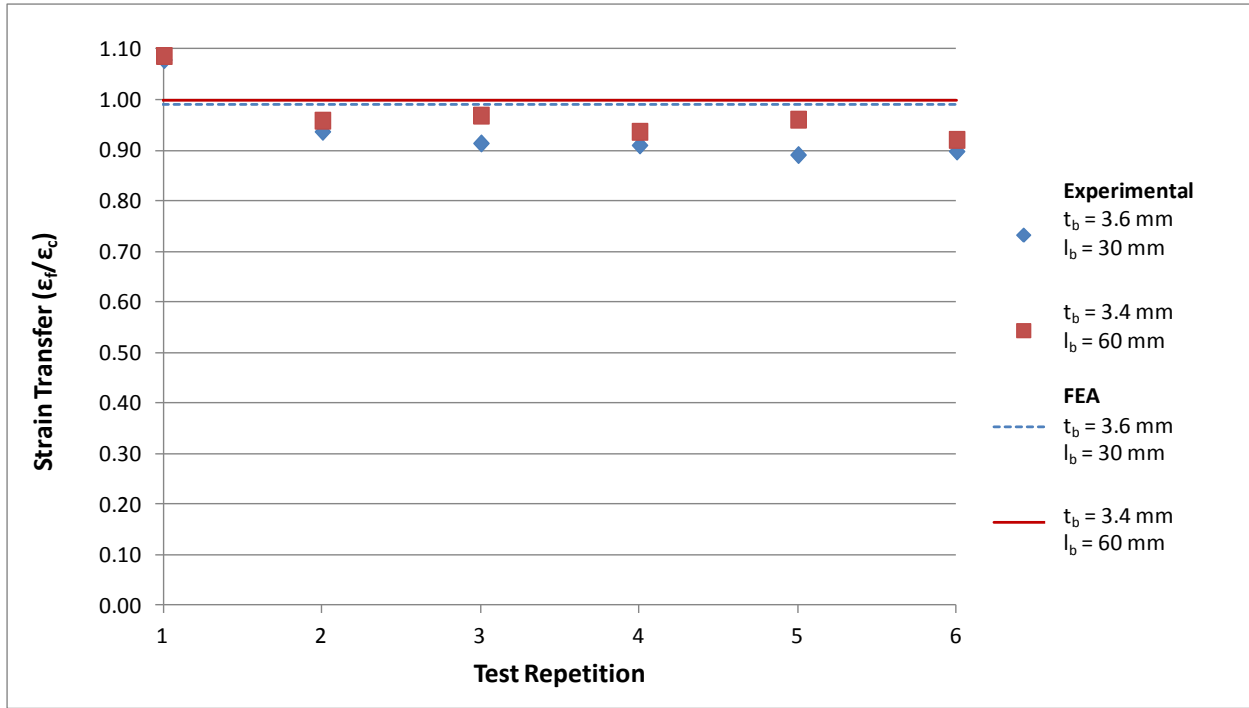


Figure 4-12: Saw-notch configuration results with  $E_{\text{epoxy}} = 1800 \text{ MPa}$

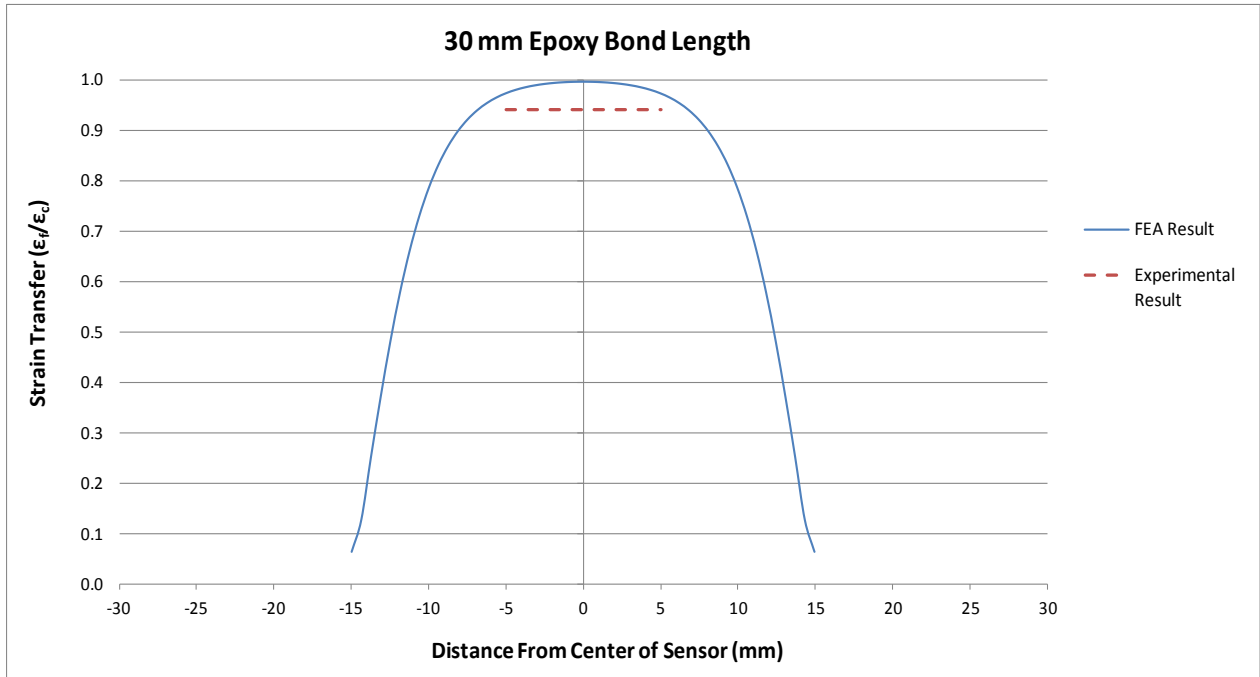
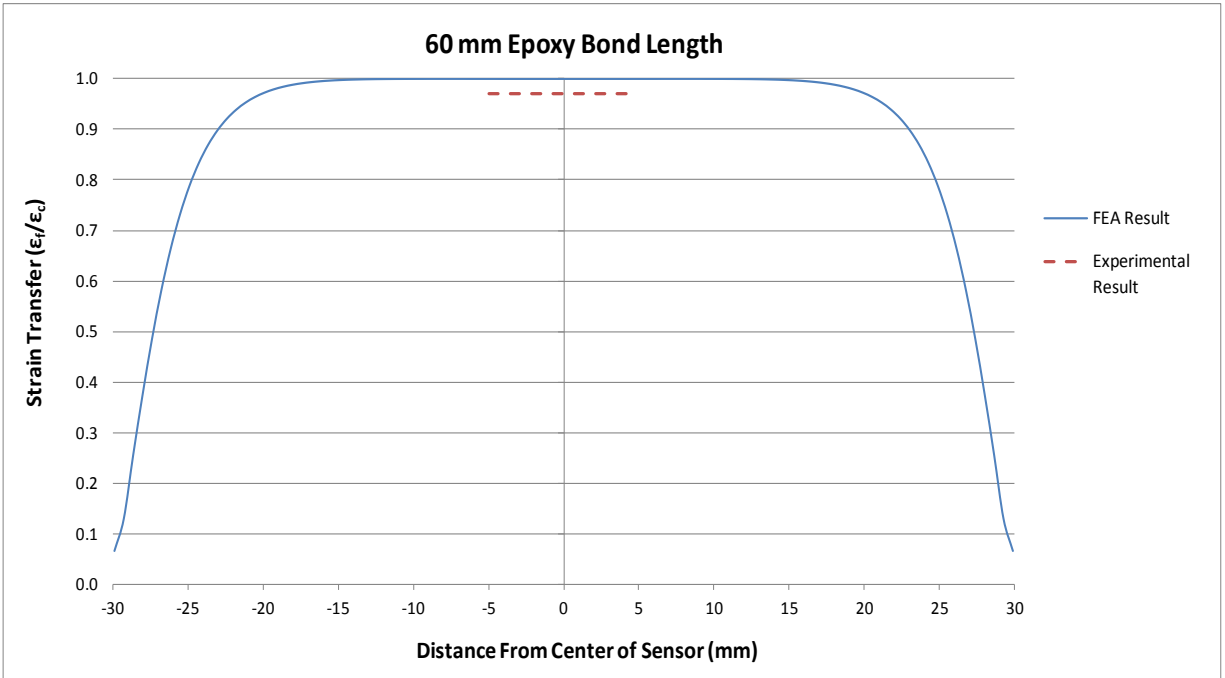


Figure 4-13: Result comparison for saw-notch with  $E_{\text{epoxy}} = 1800 \text{ MPa}$ , 3.6 mm bond layer thickness



**Figure 4-14: Result comparison for saw-notch with  $E_{\text{epoxy}} = 1800 \text{ MPa}$ , 3.4 mm bond layer thickness**

Figure 4-15 provides an example of a strain plot for the prism tests in which the difference in strain can be seen between the FBG and the strain gage. In Figure 4-15, the gaps between two the strain plots seen at the peaks and over the constant strain portion of the test demonstrate that the FBG is sensing a lesser strain than the strain gage. The FBG is expected to sense a smaller strain because of the strain loss over the epoxy bond layer. It is also seen that the strain plots do not converge when the strains is held constant, which suggests that there is no viscoelastic behavior occurring.

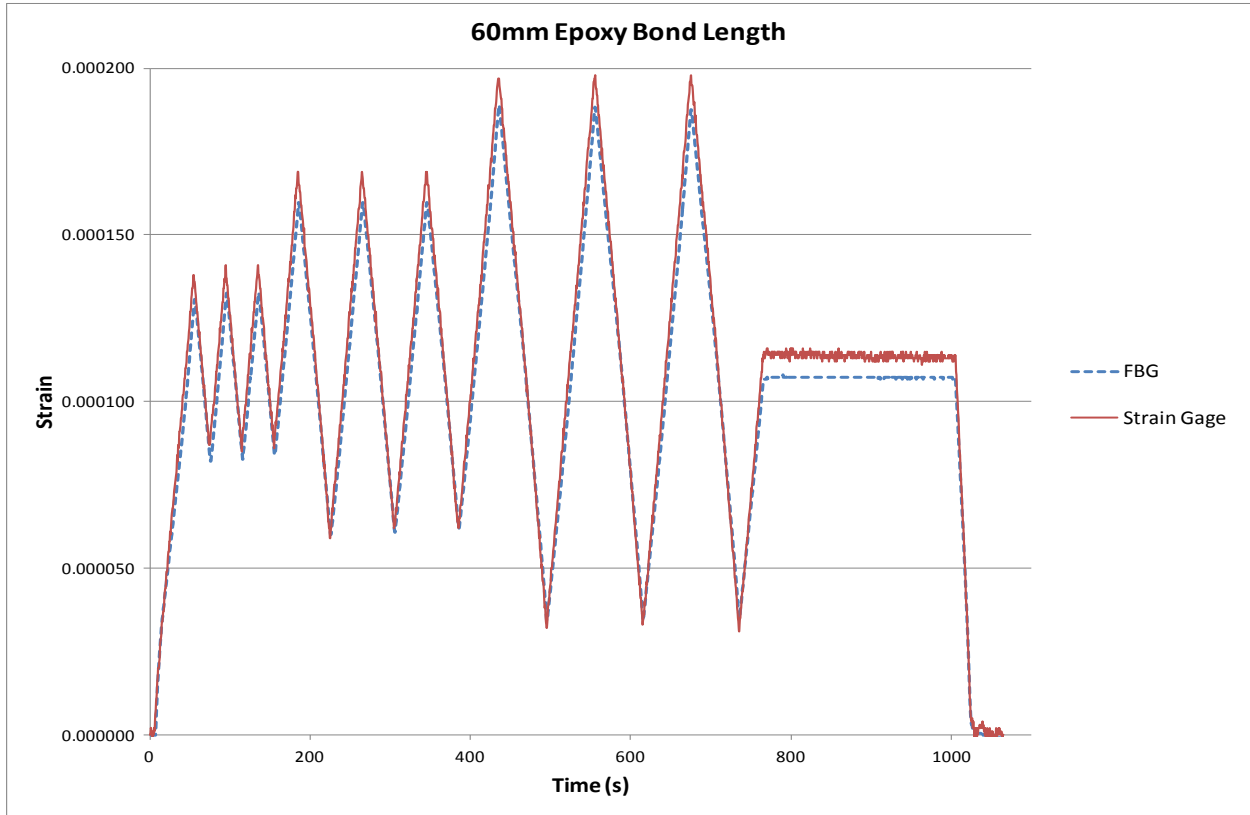


Figure 4-15: Notched prism load test for saw-notch with 3.4 mm bond layer thickness

## 4.5 Gage Factor Calibration

The gage factor (variable  $k$  in Equations 4-1 and 4-2) for the type of FBG used in this research is specified by the FBG manufacturer to be 0.78. This value is often times not exact and can vary slightly depending on FBG type.  $k$  is calculated using Equation 4-2 where  $p$  is the photoelastic coefficient of FBG silica glass core.

$$k = 1 - p \quad \text{Equation 4-2}$$

The value of  $p$  for the silica glass is typically taken as 0.22, however there are several different methods for determining the photoelastic coefficient of glass and the results are not always consistent.  $p$  values for silica glass (FBG core material) have been found to range from 0.206 to 0.22 (Mohammad N. , 2005). An experimental investigation was conducted to confirm the manufacturer-specified gage factor value of 0.78 for the FBGs used in this research. In the experiment, a FBG and a conventional strain gage were

surface adhered to a steel dogbone specimen using cyanoacrylate adhesive as seen in Figure 4-16. Since both strain sensors were directly bonded to the specimen, it was expected that the FBG strain results would be closest to those of the strain gage when using a FBG gage factor of 0.78. Steel was selected as the material for this test because of its high predictability and linear elastic characteristics. Five tensile load repetitions were run on the specimen using a cyclic load pattern.



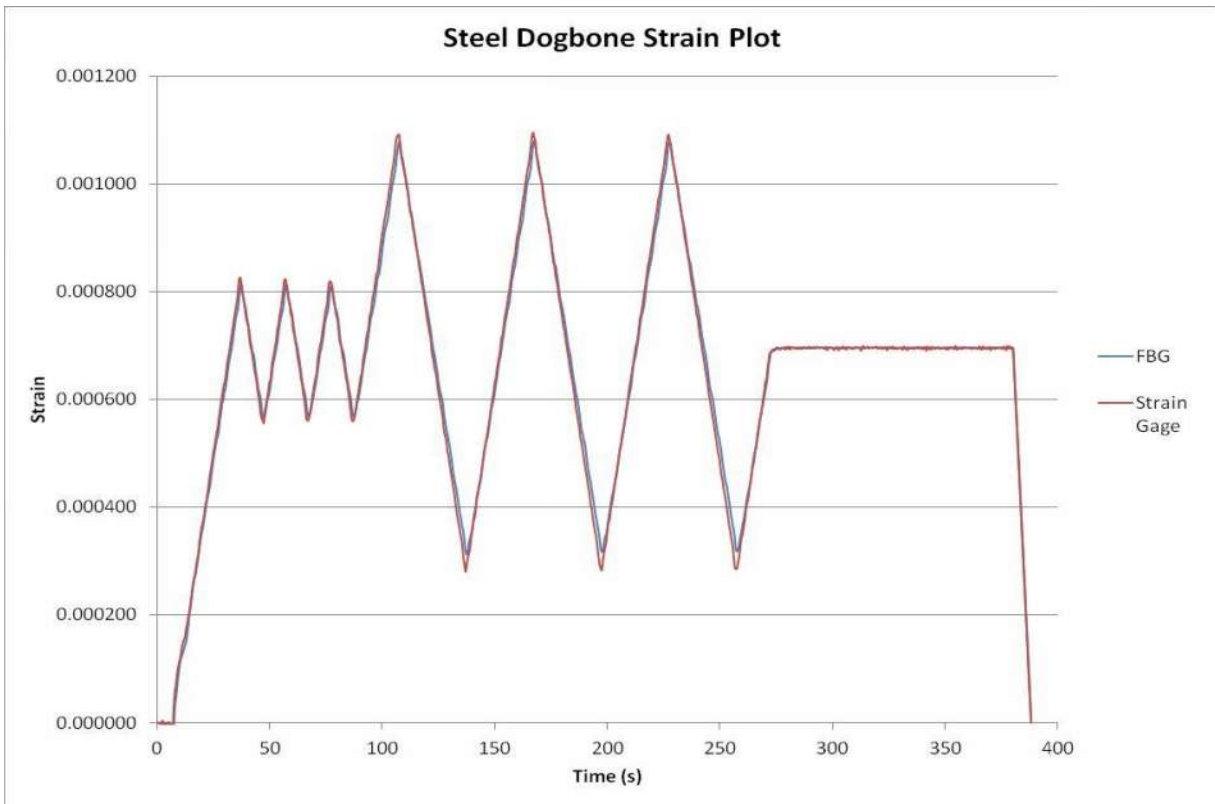
**Figure 4-16: Steel dogbone gage factor calibration test**

The gage factor of the FBG was set as the manufacturer specified value of 0.78 for the five load repetitions. The strains of the two sensors were compared by dividing the strain of the FBG by the strain of the strain gage as seen in Table 4-5. Table 4-5 shows the results of the five repetitions and it is seen that the average of the strain ratio (0.995) is very close to 1. This result supports the assumption that the true gage factor of the FBG is equal to the manufacturer specified value of 0.78.

**Table 4-5: FBG gage factor calibration results**

Test repetition	$\epsilon_f/\epsilon_{sg}$
1	0.989
2	0.985
3	0.981
4	1.007
5	1.014
<b>Average:</b>	<b>0.995</b>

Figure 4-17 shows an example strain plot of the steel dogbone test in which the tight correlation in strain is illustrated. The difference in strain between the FBG and the strain gage in Figure 4-15 when compared with Figure 4-17 is clearly greater. This observation verifies the fact that strain loss is occurring when the FBG is embedded in the epoxy and adhered in the prism notch. When the FBG is surface adhered to steel dog-bone specimen there is very little difference in strain between the two sensors as seen in Figure 4-17.

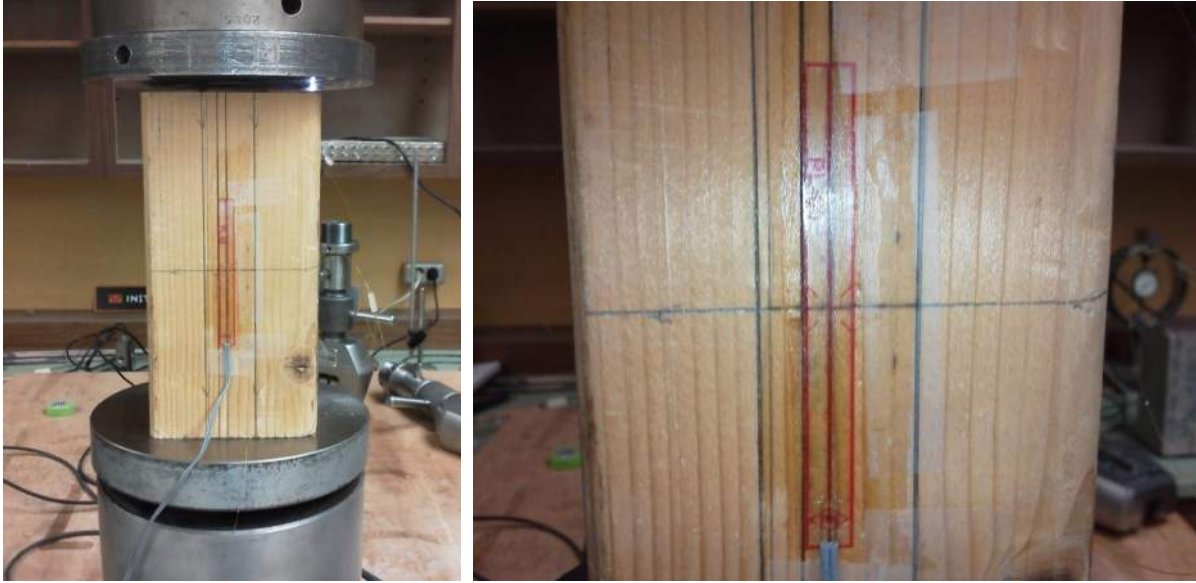


**Figure 4-17: FBG gage factor calibration test result**

## 4.6 FBG Compression Range Functionality Test

An experiment was conducted to examine the performance of the FBG sensors when strained into their compressive range. When a FBG is unstrained, it has a base wavelength that is determined when the FBG is created. For strain sensing applications, FBGs are typically pre-tensioned to a wavelength of 2 nm to 5 nm above the base wavelength, depending on the expected strains that the FBG will experience. Pre-tensioning ensures that the FBG will remain in tension when strained throughout its service life. For the applications in this thesis it was important to examine how the FBG performs in the compression zone i.e. without pre-tensioning. It was hypothesized that since the fiber is embedded in epoxy, it is restrained from buckling in compression and will therefore maintain functionality in its compression range.

To test the FBG compression range functionality, an un-tensioned FBG was surface adhered to a wood block with a 70 mm bond length. A strain gage was also surface adhered to the block adjacent to the FBG sensor as seen in Figure 4-18. Cyanoacrylate adhesive was used to bond both sensors to the block. The strain gage data was used for comparison to the FBG strain data during the compression test. Wood was selected as the host structure material because it is easily strained in compression. The experiment was attempted with a concrete prism, however the compression machine load cell capacity (55 kips) was not high enough to induce sufficient strain in the FBG for conclusive results. Two ramp loading tests were run and the strain differences between the two sensors were compared.



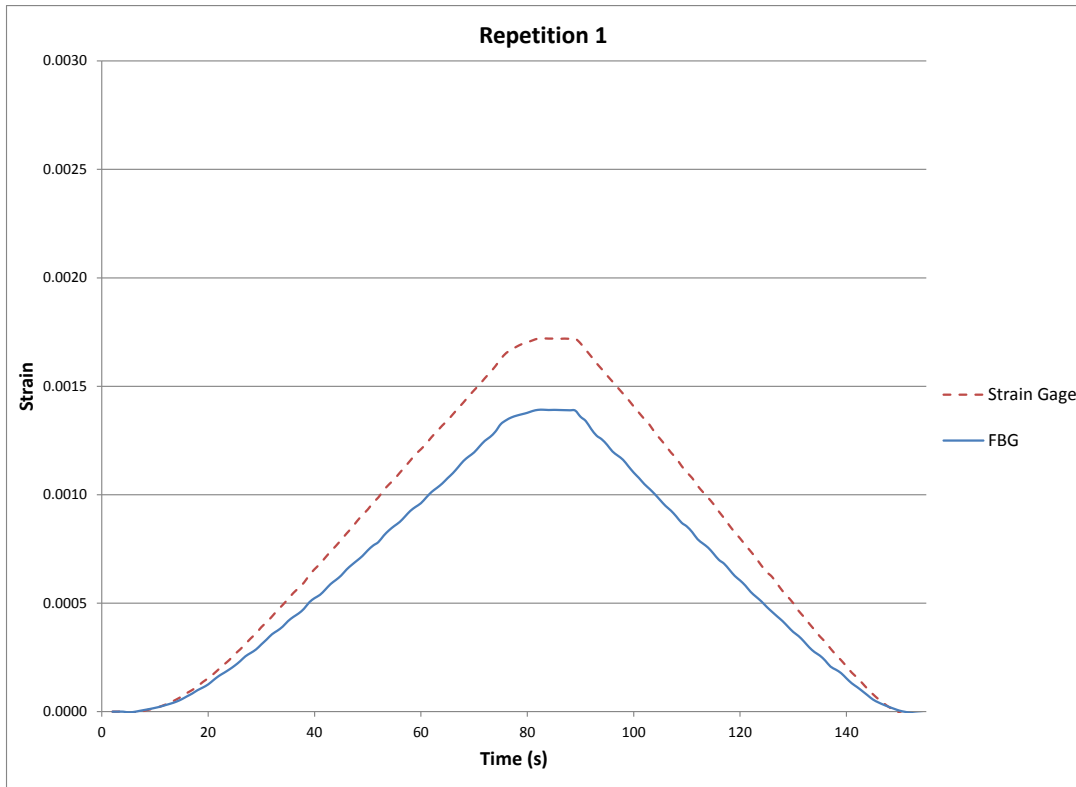
**Figure 4-18: FBG compression range test setup**

The wood block was loaded up to a maximum strain magnitude of about 0.003, which is the design strain limit for concrete. The FBG maximum compression wavelength shift experienced by the FBG was 3 nm below its base wavelength. The block was loaded twice and the results of each repetition are shown in Table 4-6. The strain ratio values in Table 4-6 are the average strain of the FBG over the duration of the test divided by that of the strain gage. It is seen that the FBG only measures about 83% of the strain measured by the strain gage. Two possible reasons for the difference in strains are local buckling of the FBG and geometric nonlinearities of the fiber. The adhesive that bonded the FBG to the wood surface may not have fully restrained the FBG from buckling which caused a reduction in strain measurement accuracy of the FBG. Additionally, the FBG may have been adhered to the block at a slight angle causing a nonlinear strain response. Further analysis of the strain difference is provided in Chapter 5. Figures 4-19 and 4-20 illustrate the strain plots of the compression test in which the difference in strains of the two sensors is seen.

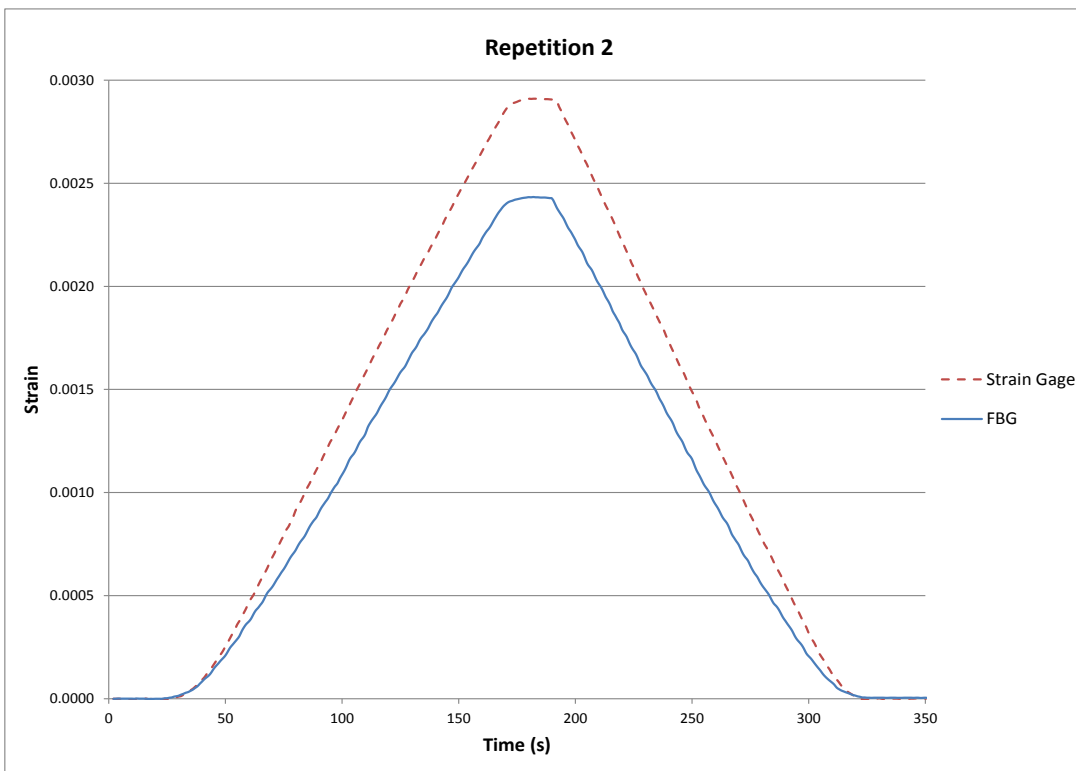
**Table 4-6: FBG compression range test results**

<b>Test repetition</b>	<b><math>\epsilon_f/\epsilon_{sg}</math></b>
1	0.834
2	0.822
<b>Average</b>	<b>0.828</b>





**Figure 4-19: FBG compression range strain plot repetition 1**



**Figure 4-20: FBG compression range strain plot repetition 2**

## CHAPTER 5: CONCLUSIONS

The conclusions drawn from the FEA and the experimental tests relate primarily to the strain measurement accuracy of the FBG sensors bonded to concrete in notches. It was found that the FEA generally over-predicts the strain transfer to the FBG when compared to tests in real life conditions. This conclusion is supported by the fact that for 80% of the configurations that were compared, the FEA strain transfer results were 1% to 9% greater than those seen in the experimental tests. Despite the FEA over-prediction, it is still possible to conclude that there are some configurations that provide full strain transfer and some that do not. Before more detailed specifications can be made about which configurations are most effective, it is important to discuss the feasibility of field implementation. Several issues such as the equipment, time, and level of installation complexity required for field applications must be evaluated.

### 5.1 Field Implementation Considerations

After several laboratory simulations of the FBG embedment procedure, it was concluded that the equipment and materials required to install an FBG in a notched concrete structural member are effective and obtainable for an engineering or construction crew. The embedment notches can be cut in the concrete with a masonry saw or formed as the concrete is placed. The Ultrabond 1300 epoxy was effective because of its short cure time and availability, however for overhead or vertical applications, a more paste-like adhesive with higher viscosity would be optimal.

The process of embedding an FBG in a concrete notch is fairly straight forward and feasible for field applications. After a notch is formed or cut into a concrete structural member, a thin layer of adhesive is placed in the bottom of the notch. An FBG is then placed onto the first layer of adhesive followed by a second layer of adhesive that covers the FBG and fills the notch. The full specified

adhesive cure time should be allowed before strain monitoring begins. The FBG embedment process takes less than 20 minutes, excluding the adhesive cure time.

## 5.2 Strain Transfer Analysis Conclusions

An evaluation of the strain transfer test results reveals important differences between the FEA and the experimental tests. The lower strain transfer seen in the experimental results is attributed to several influential factors. One is the assumption of perfect bonds between the adhesive and the concrete as well as between the adhesive and the fiber in the FEA. This assumption is unrealistic in real conditions and resulted in greater strain loss in the experimental tests. Additionally, the form oil on the surface of the concrete prisms was not fully removed before applying the epoxy resulting in a softening of the concrete-epoxy bond interface. The size of the aggregate in the concrete may have also affected the strain sensing of the FBG. The maximum aggregate diameter was 20 mm which is twice the length of the FBG sensor region. If the FBG sensor region was adhered directly over a single piece of aggregate, the strain measured by the FBG would have been more representative of that piece of aggregate rather than the prism as a whole. The conventional strain gage had a sufficiently long sensor region, however electrical noise and sensitivity level are two parameters that may have affected the accuracy of the strain gage when compared to the FBG strain measurements.

Non-uniformities in the epoxy and the notch shapes may have also caused variations in the strain transfer in the experimental tests. The concrete notches were not formed in the concrete exactly as they were modeled in the FEA. There were imperfections such as air bubbles and non-exact geometries in the concrete notches that could have contributed to the difference in strain transfer between the FEA and the experimental tests. The epoxy may have also had air bubbles or long-term shrinkage behavior that influenced the strain measurements of the embedded FBG. Despite the various factors that affected the strain sensing accuracy in the experimental tests, a good data correlation with

the FEA was seen. The differences in strain transfer (1% to 9%) between the FEA and experimental tests for the five configurations that were compared were reasonably low. The FEA was therefore considered an effective tool for analyzing the FBG notch embedment strain sensing method.

The FEA results supported several conclusions about how the configuration parameters affect the strain transfer for the notch-embedment sensing method. One undeniable conclusion is that as epoxy bond length increases, so does the effective strain transfer length for a given configuration. This behavior is seen in Appendix A, Figures A1-1 through A1-5, where the flat portions of the strain curves lengthen as the epoxy length increases. This trend is true for all bond layer thicknesses and epoxy moduli. A second conclusion is drawn from Figures A2-1 through A2-3 and relates to effect of epoxy elastic modulus on strain transfer. It was observed that strain transfer increases with an increase in the adhesive elastic modulus. This trend supports the conclusions of previous studies discussed in Section 2.4, which suggest that the closer the elastic modulus is to the concrete, the better the strain transfer.

Figures A3-1 and A3-2 imply an inverse relationship between bond layer thickness and strain transfer. It is seen that smaller bond layer thicknesses provide greater strain transfer. Additionally, the effect of bond layer thickness appears to have more of an impact on the v-notch configuration than the saw-notch configuration. This behavior is likely due to the fact that the v-notch is wider with a tapered shape while the saw-notch geometry is narrower and more uniform. The bigger v-notch provides a greater volume of epoxy for strain loss to occur in. The tapered v-notch shape provides more epoxy between the FBG and the concrete than the saw-notch as the bond layer thickens.

The FEA strain plots in Figures A3-1 and A3-2 also show that the saw-notch provides better strain transfer than the v-notch. It is expected that the configuration with the smaller bond layer thickness will provide more strain transfer. It is seen however, that the saw-notch configuration with a 3.2 mm bond layer thickness provides better strain transfer than the v-notch configuration with a smaller 1.75 mm bond layer thickness. In other words, even though the FBG is further away from the

host structure in the saw-notch than in the v-notch, the saw-notch still provides more strain transfer. This implies that the saw-notch will provide better strain transfer than the v-notch in any situation where the epoxy modulus, epoxy bond length, and bond layer thickness are the same in both notch types.

The results of the experimental tests also support the conclusion that the saw-notch provides better strain transfer than the v-notch. A comparison of the saw-notch configuration with a 60 mm epoxy length to the v-notch configuration with a 60 mm epoxy length (see Tables 5-1 and 5-2) shows that the saw-notch provides more strain transfer even with a greater bond layer thickness.

**Table 5-1: V-notch prism results comparison**

<b>Summary table</b>			
<b>Bond layer thickness (mm)</b>	<b>Epoxy length (mm)</b>	<b>FEM strain transfer</b>	<b>Average experimental strain transfer</b>
2.7	30	0.99	0.98
3.2	60	1.00	0.90
4.2	10	0.32	0.33

**Table 5-2: Saw-notch prism results comparison**

<b>Summary table</b>			
<b>Bond layer thickness (mm)</b>	<b>Epoxy length (mm)</b>	<b>FEM strain transfer</b>	<b>Average experimental strain transfer</b>
3.6	30	0.99	0.94
3.4	60	1.00	0.97

The experimental test results also offer some insight towards what configurations will provide effective strain transfer in field applications. Table 5-1 shows a nearly developed experimental strain transfer value of 0.98 for the v-notch configuration with a 2.7 mm bond layer thickness and a 30 mm epoxy length. This implies that any v-notch configuration that has an epoxy length of 30 mm or greater with a bond layer thickness of 2.7 mm or less, will have a strain transfer rate of 0.98 or greater. This conclusion also applies to the saw-notch configuration since it was found that the saw-notch provides better strain transfer than the v-notch. A final conclusion drawn from Table 5-1 is that decreasing the epoxy length and increasing the bond layer thickness will decrease strain transfer as seen with the 4.2 mm bond layer thickness configuration.

### 5.3 Gage Factor Calibration Test Conclusions

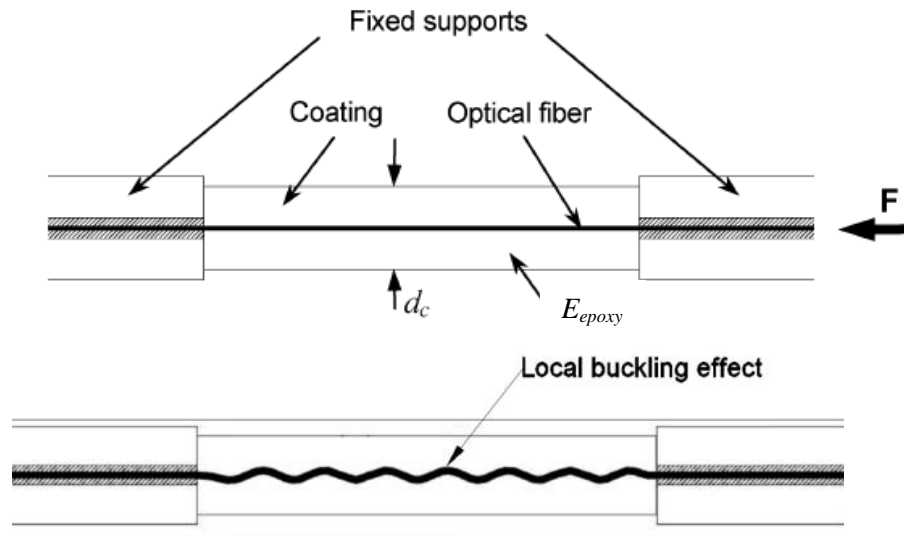
The primary goal of the steel dogbone tensile test was to determine the gage factor of a directly surface bonded FBG and compare it to the manufacturer specified value of 0.78. It was found that the FBG with a 0.78 gage factor measures almost exactly (0.5% difference) the same strain measured by a conventional strain gage. This strong agreement validates the use of a 0.78 FBG gage factor for all applications of the FBGs used in this research.

### 5.4 FBG Compression Range Test Conclusions

As discussed in Chapter 4, FBGs are typically pre-tensioned before application as strain sensors to ensure that they do not bend or buckle when compressed. For the applications in this research, the FBGs are encased in epoxy, which provides elastic lateral restraint to the FBG. It was important to determine if it is necessary to pre-tension the FBGs before use in epoxy embedment configurations. The results of the compression range test showed that the FBG only measured 83% of the strain measured by the adjacent strain gage. This result does not support the theory that FBGs are fully functional when in their compression range.

One likely reason for the strain sensing inaccuracy of the FBG is local buckling of the fiber when compressed. FBG fibers buckle very easily due to their thin silica-glass structure (Mohammad, et al., 2004). Figure 5-1 illustrates the local buckling effect of an FBG that is embedded in an epoxy coating and compressed axially. In Figure 5-1,  $d_c$  represents the thickness of the encasing epoxy coating and  $E_{epoxy}$  is the elastic modulus of the epoxy. Accurate compression range sensing by embedding an FBG in epoxy has been achieved in previous studies but requires an epoxy with specific properties and a specific embedment configuration (Le Blanc, et al., 1994). It was found in previous studies that parameters  $d_c$  and  $E_{epoxy}$  must be specific values in order to prevent local buckling of the FBG. Other techniques that utilize magnetic actuators or fiber-guiding systems have proven to be effective in

preventing local buckling of FBGs, but are not feasible for strain sensing applications of structural members (Mohammad, et al., 2004).



**Figure 5-1: Local buckling effect of epoxy embedded FBG (Mohammad, et al., 2004)**

A misalignment of the FBG fiber on the wood block in the compressive test could have also contributed to the inaccurate strain sensing of the FBG. The fiber may have been adhered to the block at a slight angle from the longitudinal axis of the block causing a reduction in the longitudinal strain measured by the FBG. The results of the compression test imply that surface adhesion of the FBG to a structural member using cyanoacrylate adhesive is not an accurate strain sensing technique if the FBG is in its compression range. It is recommended that if a FBG is to be used in its compression range that the proposed configuration be tested for accuracy before field application.

## CHAPTER 6: FUTURE WORK

The goal of the research following this thesis will be to complete Phases I and II of the project discussed in Chapter 1. The remaining objectives to be achieved in Phase I relate primarily to developing an FBG application method for steel bridges as well as a remote data collection system with long-range processing and transmission capabilities. Phase II of the project will be to implement the developed FBG structural health monitoring (SHM) system on WYDOT bridges. Data collected from the field implemented system will not only be used to monitor the health of the bridges but also to confirm existing bridge rating software results.

### 6.1 Development of FBG Steel Application Method

A method that effectively measures the strain of steel bridge members is crucial for the successful implementation of the proposed SHM system. The necessary attributes of the steel measurement system are strain measurement accuracy, durability, and application feasibility. As with the development of the concrete application method, strain transfer effects must be considered for the steel attachment configuration. The strain transfer investigation may require laboratory tests and or finite element analysis. It is recommended that both existing commercial FBG sensors designed for steel applications as well as designs developed by the research team on this project be considered and tested.

The steel application method should be designed to endure years of weathering and vandalism, while maintaining accurate strain sensing. The application method will likely be a surface adhered configuration that calls for sufficient protection of the FBG to achieve long-term stability. Additionally, it would be ideal for the installation process to have limited time and resource requirements. A technique proposed by the research team on this project is to imbed multiplexed FBGs into fiber reinforced polymer strips that could be adhered to steel surfaces.



## 6.2 Sensing Scheme Development and Laboratory Simulation

As part of the development of an implementable SHM system, it is necessary to generate a schematic for the locations on the bridge superstructure to which the FBGs will be attached. Likely locations for FBG attachment will be, but are not limited to, high stress zones or any critical locations with structural concerns. These application points may include girder midspans, supports, or connections. It will be necessary to verify the functionality of the FBGs at critical locations through laboratory testing before field implementation. A proposed laboratory test method is to simulate dynamic truck loads by rolling a load across an FBG instrumented beam and analyzing the measured FBG strain values.

## 6.3 Development of Data Processing, Transmission, and Analysis

An efficient data processing method will need to be developed for the SHM system. It will be necessary to have a system that wirelessly transmits the data collected at a bridge site to WYDOT officials for analysis. Wireless data transmission would prevent the necessity for frequent bridge site visits and allow for real-time monitoring from a WYDOT engineering office. Proposed wireless transmission systems include the use of a solar-powered wireless signal transmitter located at the bridge site that communicates data over a 4G wireless network.

The ability to identify and filter significant data collected by the FBGs will also be essential. Since data from the FBG system will be collected continuously over long periods of time, it will be necessary to identify when a bridge is overloaded and experiencing critical stress conditions. A proposed method for identifying critical stress conditions is to put a triggering mechanism in overweight trucks that will alert a bridge's SHM system when the truck passes over the bridge. The development of a program that also converts the wavelength data provided by an FBG into useful values such as strain, stress or deflections will be highly beneficial. An analysis method that considers fatigue of bridge

components over years of service will also be relevant. For example if a bridge experiences an overload at one point in time and then experiences a similar load years later, it will be of interest to see if the bridge behaves differently after years of service.

## **6.4 Field Implementation**

Phase II of the research focuses primarily on the field implementation of the SHM system developed in Phase I. The objective after the SHM system has been field implemented will be to correlate collected data with existing bridge rating software and in doing so optimize the SHM system. After the system has been refined it will be implemented on a larger scale to more bridges throughout Wyoming. The resulting SHM network will not only improve the safety and condition of Wyoming bridges but also advance existing bridge rating and inspection techniques.

## CHAPTER 7: REFERENCES

- Ansari, F. (2009). *Structural Health Monitoring with Fiber Optic Sensors*. Chicago: Higher Education Press and Springer-Verlag.
- Ansari, F., & Libo, Y. (1998). Mechanics of Bond and Interface Shear Transfer in Optical Fiber Sensors. *Journal of Engineering Mechanics* , 385-394.
- Bassam, S., & Ansari, F. (2008). Post-seismic Structural Health Monitoring of a Column Subjected to Near Source Ground Motions. *Journal of Intelligent Material Systems and Structures* , 1163-1172.
- Belanger, E., Bernier, M., Berube, J. P., Gagnon, S., Cote, D., & Vallee, R. (2008). Purely axial compression of fiber Bragg gratings embedded in a highly deformable polymer. *Optical Society of America* .
- Chan, T., Yu, L., Tam, H., Ni, Y., Liu, S., Chung, W., et al. (2005). Fiber Bragg grating sensors for structural health monitoring of Tsing Ma bridge: Background and experimental observation. *Engineering Structures* , 648-659.
- Clarke, T., Cawley, P., Wilcox, P., & Anthony, C. (2009). Evaluation of the Damage Detection Capability of a Sparse-Array Guided-Wave SHM System Applied to a Complex Structure Under Varying Thermal Conditions. *IEEE Transactions on Ultrasonics, Ferroelectrics, and Frequency Control* , 2666-2678.
- Dong, Y. (2007). *Fatigue performance of reinforced concrete beams with externally bonded CFRP reinforcement*. Florence: Taylor and Francis.
- Glisic, B., & Daniele, I. (2007). *Fiber Optic Methods for Structural Health Monitoring*. Chichester: John Wiley and Sons Ltd.
- Heininger, H. Pforzheim University, Pforzheim.
- Hill, K., & Meltz, G. (1997). Fiber Bragg Grating Technology Fundamentals and Overview. *Journal of Lightwave Technology* , 1263-1276.
- Kersey, A., Friebele, E., & Merzbacher, C. (1995). *Fiber optic sensors in concrete structures: a review*. Washington DC: IOP Publishig.
- Kesavan, K., Ravisankar, K., Parivallal, S., Sreeshylam, P., & Sridhar, S. (2009). Experimental studies on fiber optic sensors embedded in concrete. *Measurement* , 157-163.
- Krawinkler, H. (2009). *Load Histories for Cyclic Tests in Support of Performance Assessment of Structural Components*. Stanford, CA: Dept. of Civil and Environmental Engineering, Stanford University.
- Kreuzer, M. (2006). *Strain Measurement with Fiber Bragg Grating Sensors*. Darmstadt: HBM.
- Lau, K. T., Zhou, L. M., & Wu, J. S. (2001). Investigation on strengthening and sensing techniques for concrete structures using FRP composites and FBG sensors. *Materials and Structures* , 42-50.

- Le Blanc, M., Huang, S. Y., Ohn, M. M., & Measures, R. M. (1994). Tunable chirping of a fiber bragg grating using a tapered cantilever bed. *Electronics Letters* .
- Lopez-Higuera, J. M., Misas, C. J., Incera, A. Q., & Cuenca, J. E. (2005). *Fiber optic civil structure monitoring system*. Santander: Society of Photo-Optical Instrumentation Engineers.
- Measures, R. (2001). *Structural Monitoring with Fiber Optic Technology*. San Diego: Academic Press.
- Mohammad, N. (2005). *Analysis and Development of a Tunable Fiber Bragg Grating Filter Based on Axial Tension/Compression*. Saskatoon: University of Saskatchewan.
- Mohammad, N., Syszkowski, W., Zhang, W., Haddad, E., Zou, J., Jamroz, W., et al. (2004). Analysis and Development of a Tunable Fiber Bragg Grating Based on Axial Tension/Compression. *Journal of Lightwave Technology* .
- Pak, E. (1992). Longitudinal shear transfer in fiber optic sensors. *Smart Mater. Struct.* , 1, 57-62.
- Sohn, H., Farrar, C., Fugate, M., & Czarnecki, J. (2001). Structural Health Monitoring of Welded Connections. *The First International Conference on Steel & Composite Structures* .
- Torres, B., Paya-Zaforteza, I., Caldron, P., & Adam, J. (2010). Analysis of the strain transfer in a new FBG sensor for Structural Health Monitoring. *Engineering Structures* , 539-548.
- Yuan, S. (2005). Optic fiber-based dynamic pressure sensor for WIM system. *Sensors and Actuators A: Physical* , 1, 53-58.
- Zhou, G.-d., Li, H.-n., Ren, L., & Li, D.-s. (2006). Influencing parameters analysis of strain transfer in optic fiber Bragg grating sensors. *Advanced Sensor Technologies for Nondestructive Evaluation and Structural Health Monitoring II* .
- Zhou, J., Zhou, Z., & Zhang, D. (2010). Study on Strain Transfer Characteristics of Fiber Bragg GRating Sensors. *Intelligent Material Systems and Structures* , 1117-1122.

## APENDIX A: FEA TEST DATA

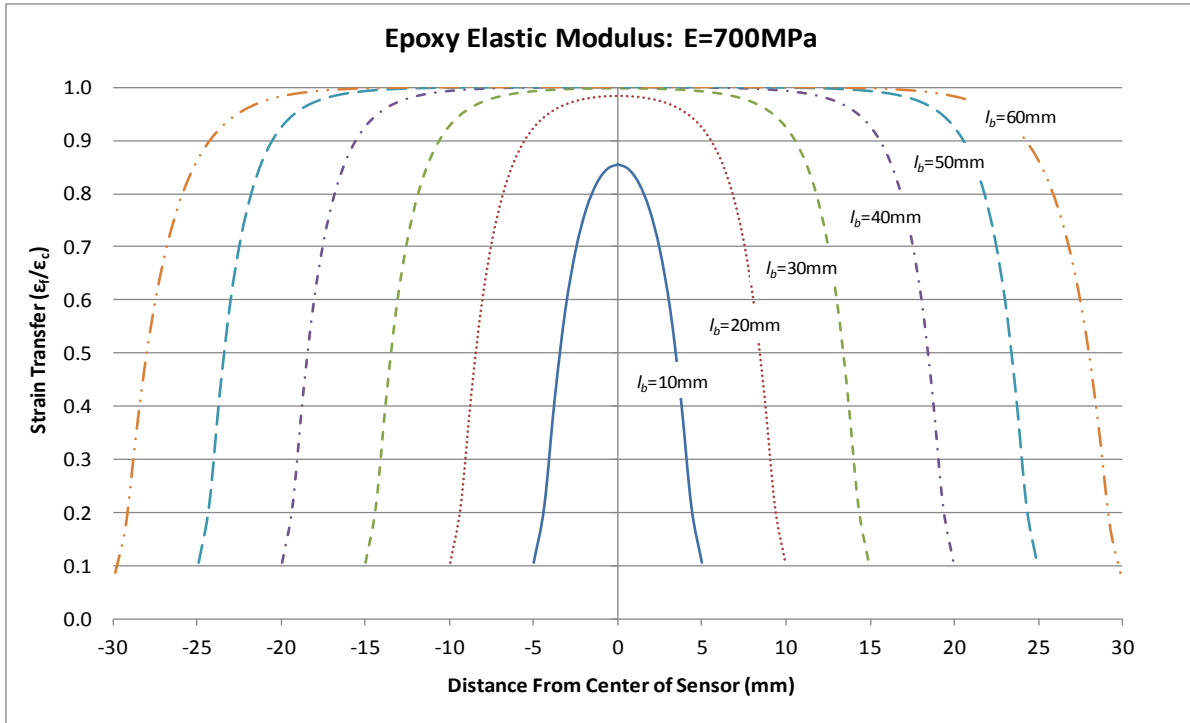


Figure A1-1a: Epoxy length comparison for 0.875 mm bond layer thickness v-notch configuration

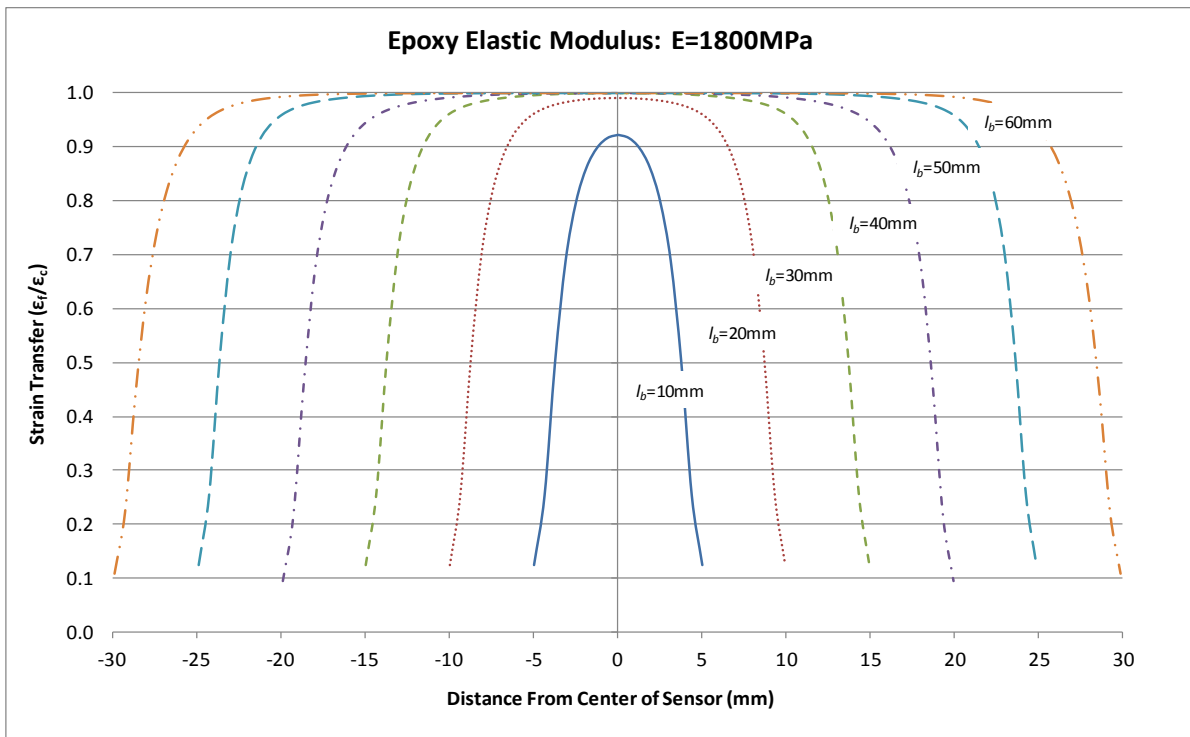


Figure A1-1b: Epoxy length comparison for 0.875 mm bond layer thickness v-notch configuration

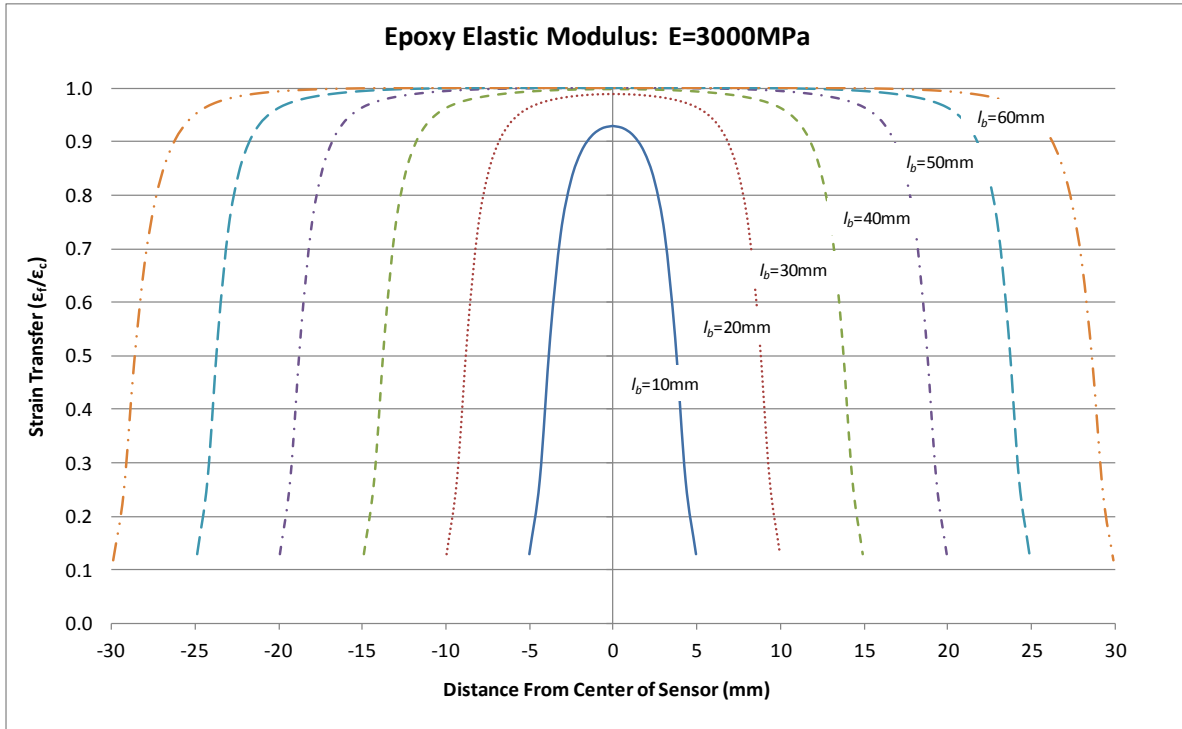


Figure A1-1c: Epoxy length comparison for 0.875 mm bond layer thickness v-notch configuration

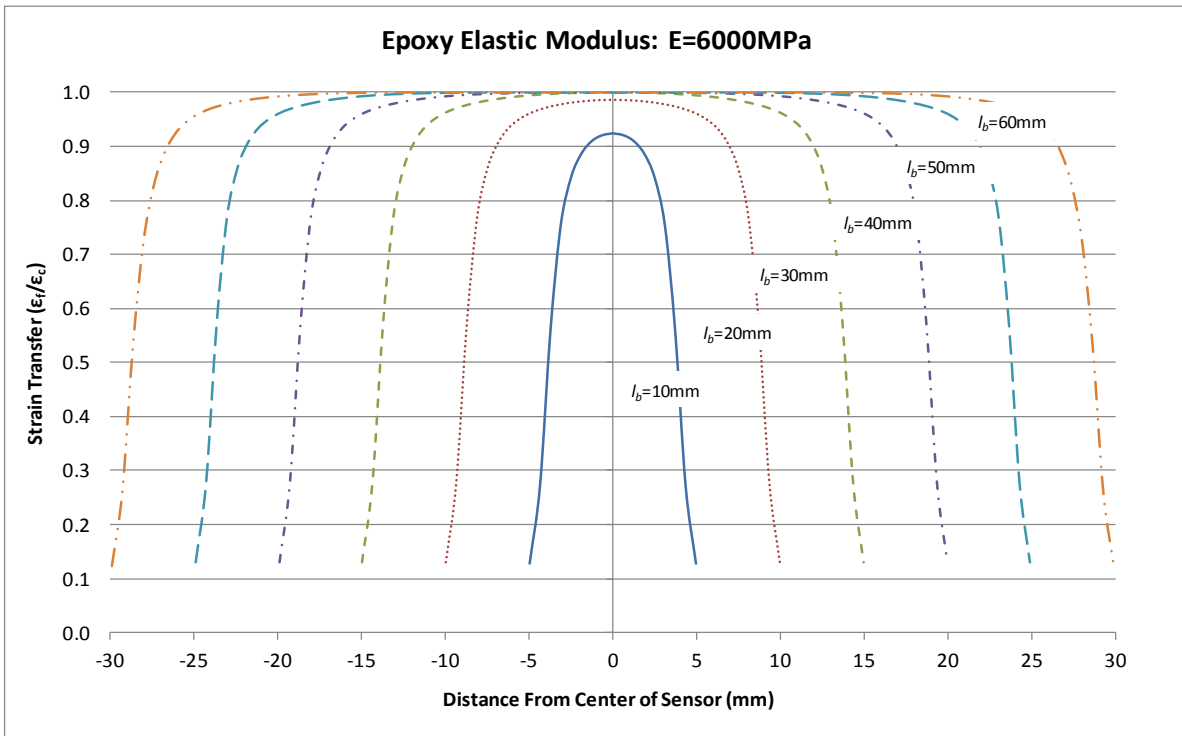


Figure A1-1d: Epoxy length comparison for 0.875 mm bond layer thickness v-notch configuration

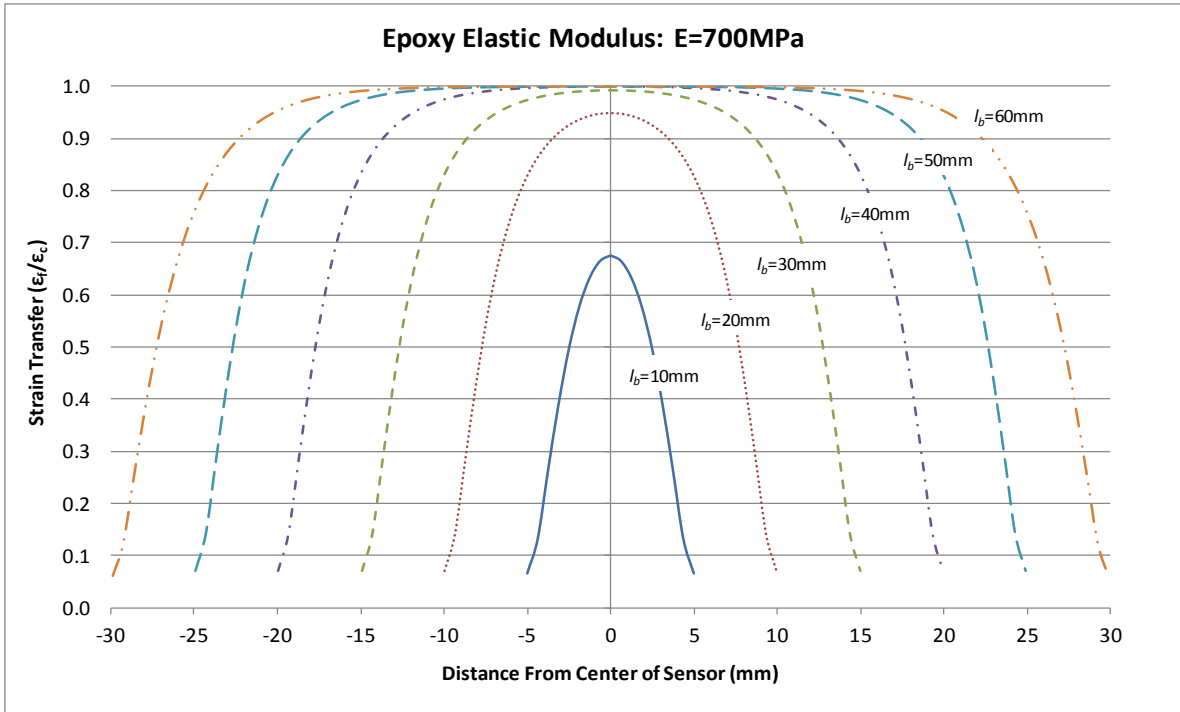


Figure A1-2a: Epoxy length comparison for 1.75 mm bond layer thickness v-notch configuration

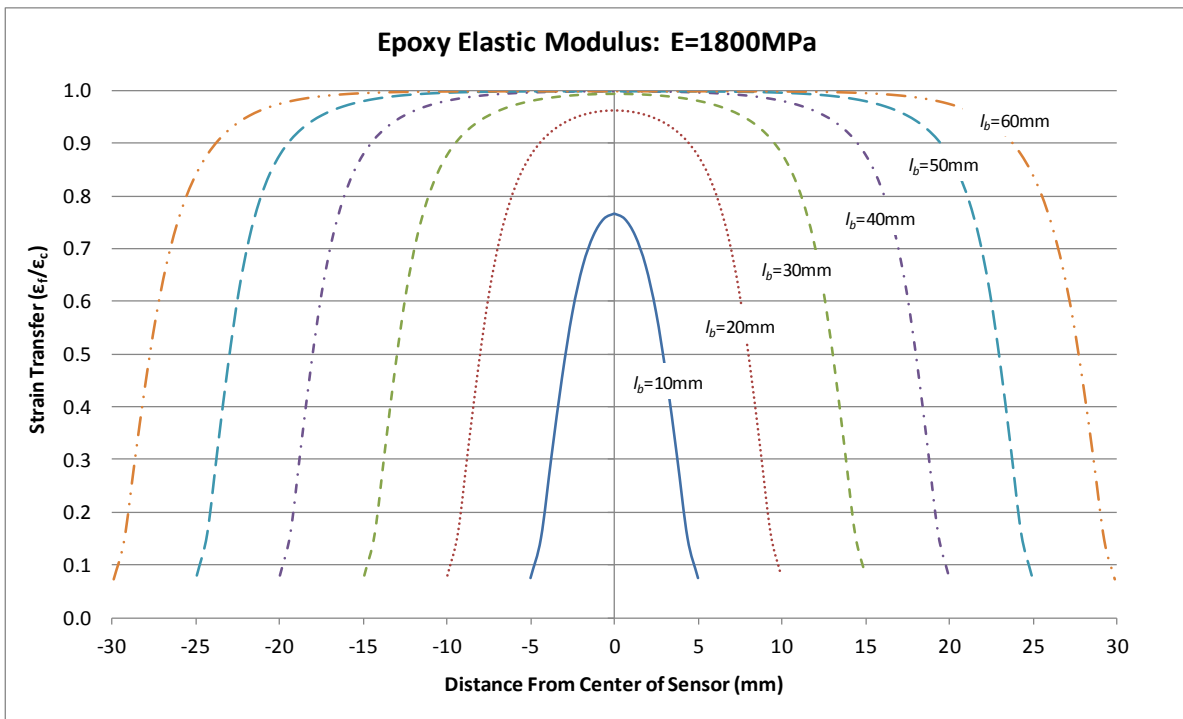


Figure A1-2b: Epoxy length comparison for 1.75 mm bond layer thickness v-notch configuration

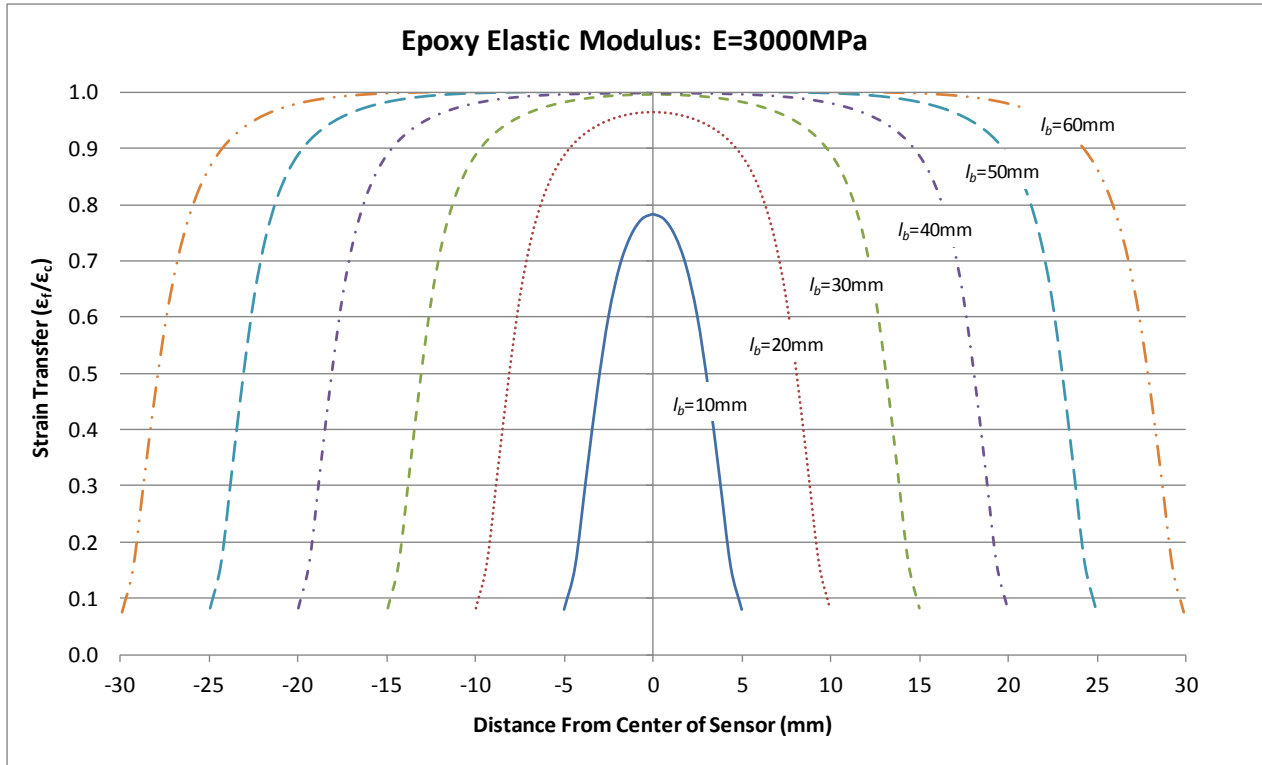


Figure A1-2c: Epoxy length comparison for 1.75 mm bond layer thickness v-notch configuration

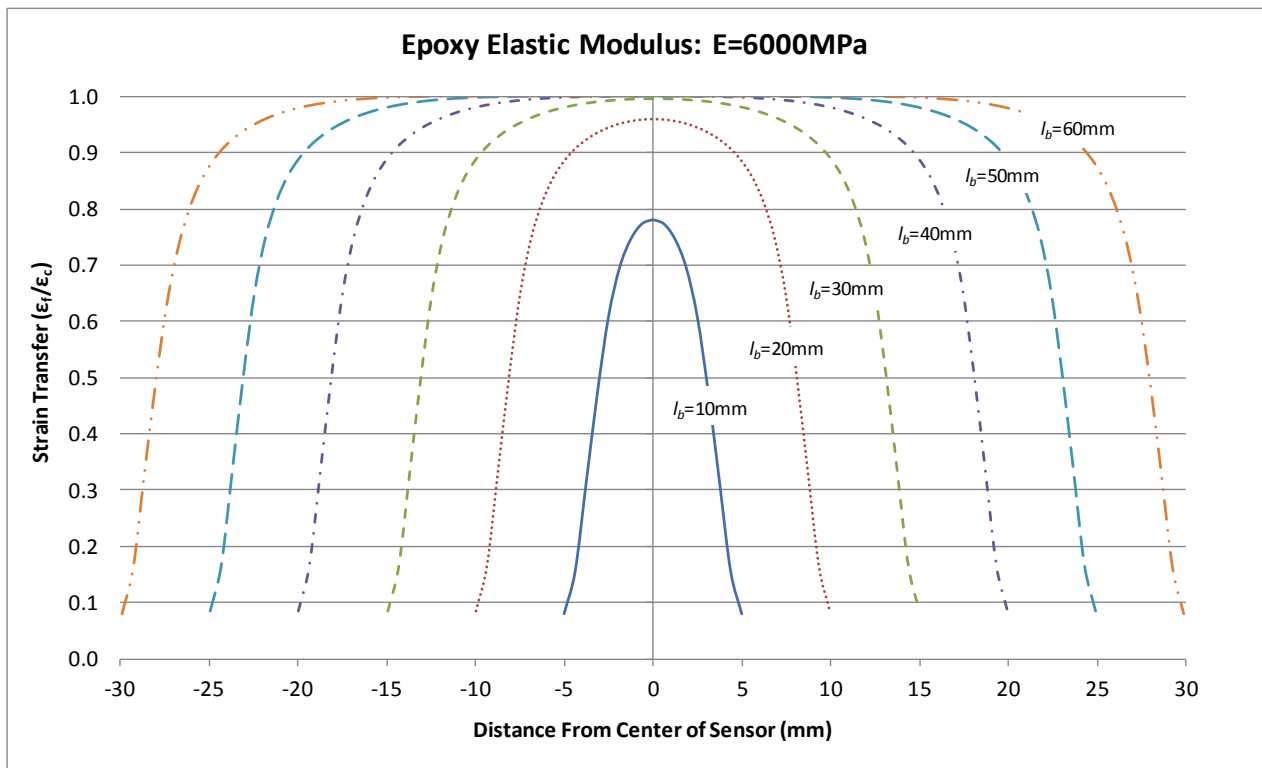


Figure A1-2d: Epoxy length comparison for 1.75 mm bond layer thickness v-notch configuration



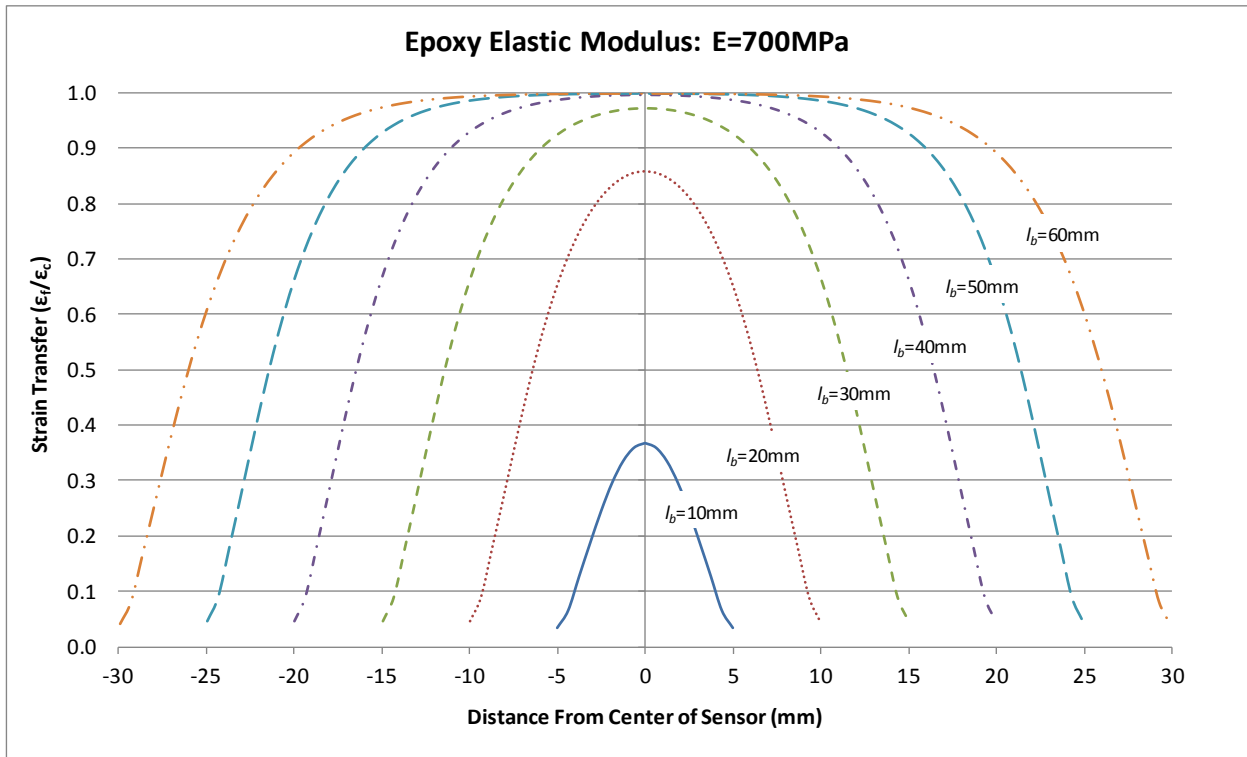


Figure A1-3a: Epoxy length comparison for 3.5 mm bond layer thickness v-notch configuration

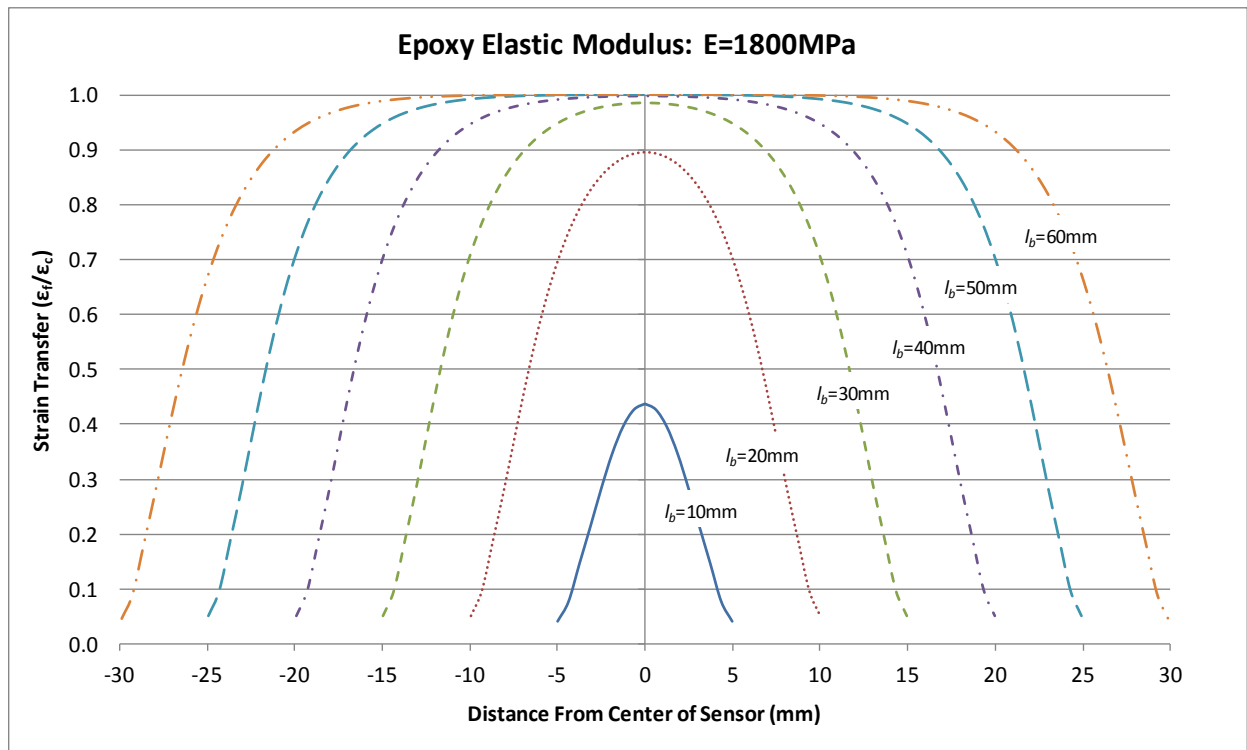


Figure A1-3b: Epoxy length comparison for 3.5 mm bond layer thickness v-notch configuration

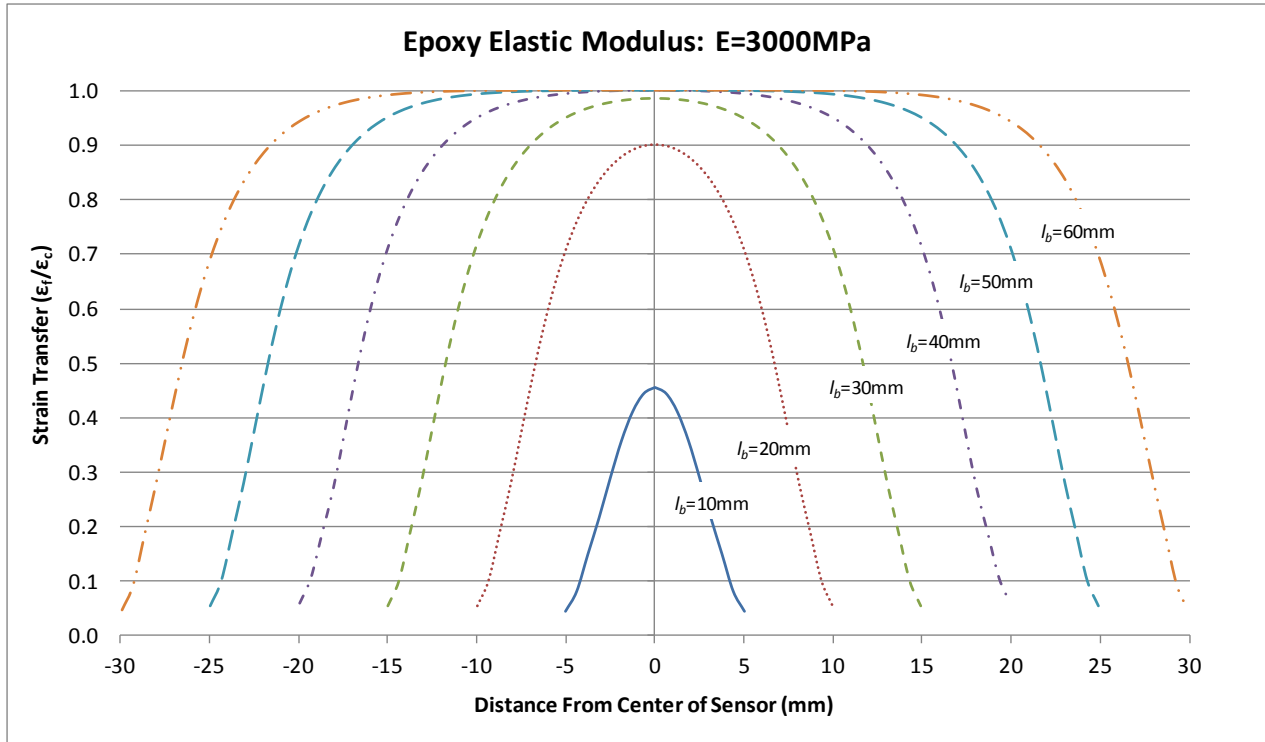


Figure A1-3c: Epoxy length comparison for 3.5 mm bond layer thickness v-notch configuration

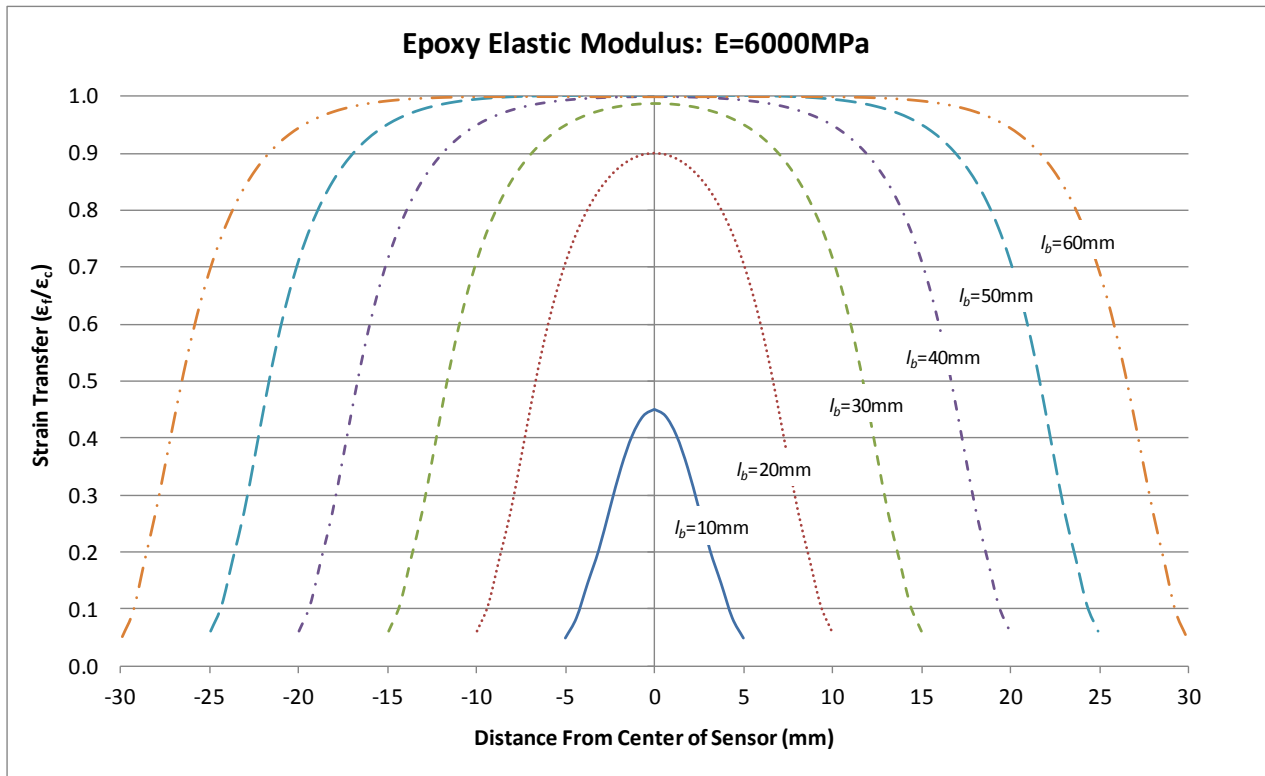


Figure A1-3d: Epoxy length comparison for 3.5 mm bond layer thickness v-notch configuration

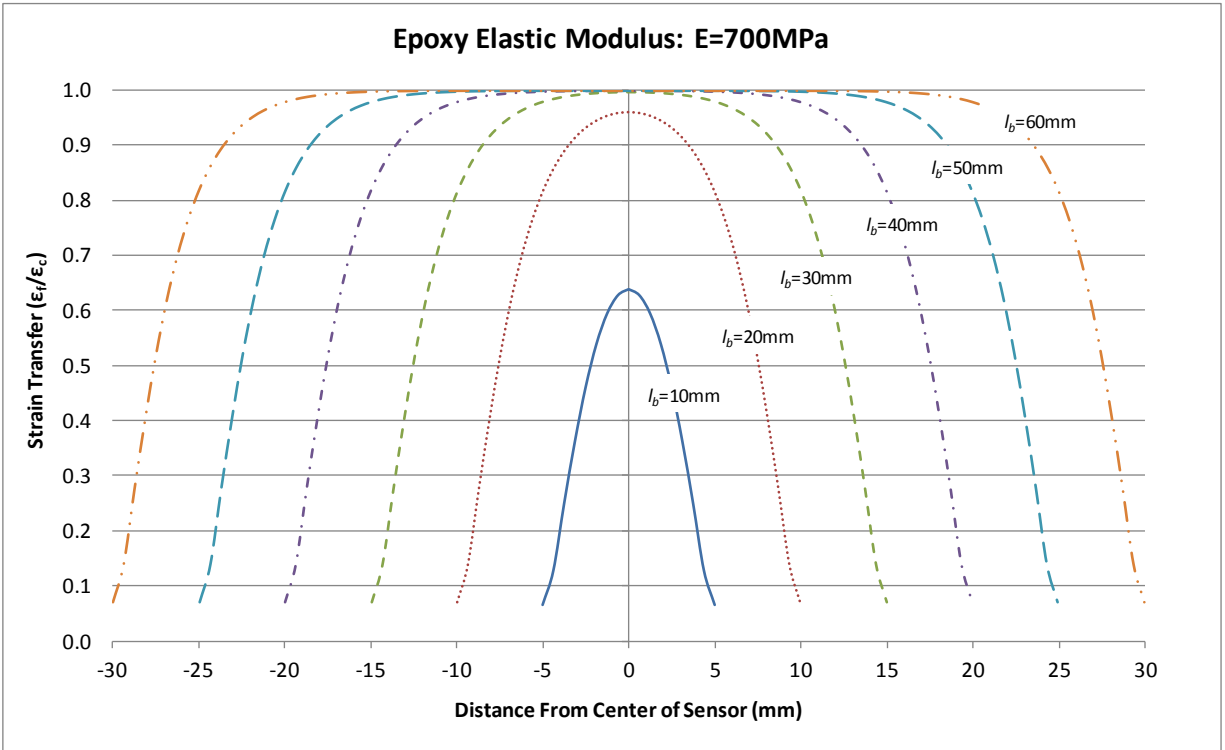


Figure A1-4a: Epoxy length comparison for 1.6 mm bond layer thickness saw-notch configuration

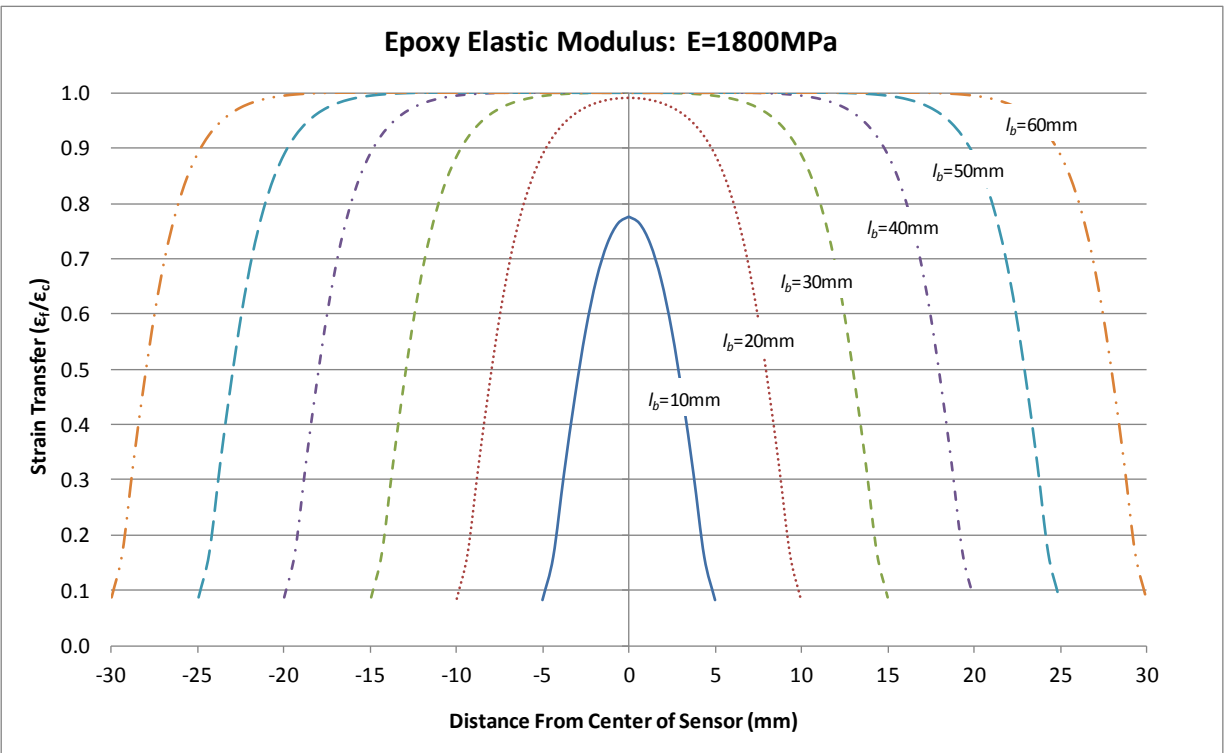


Figure A1-4b: Epoxy length comparison for 1.6 mm bond layer thickness saw-notch configuration

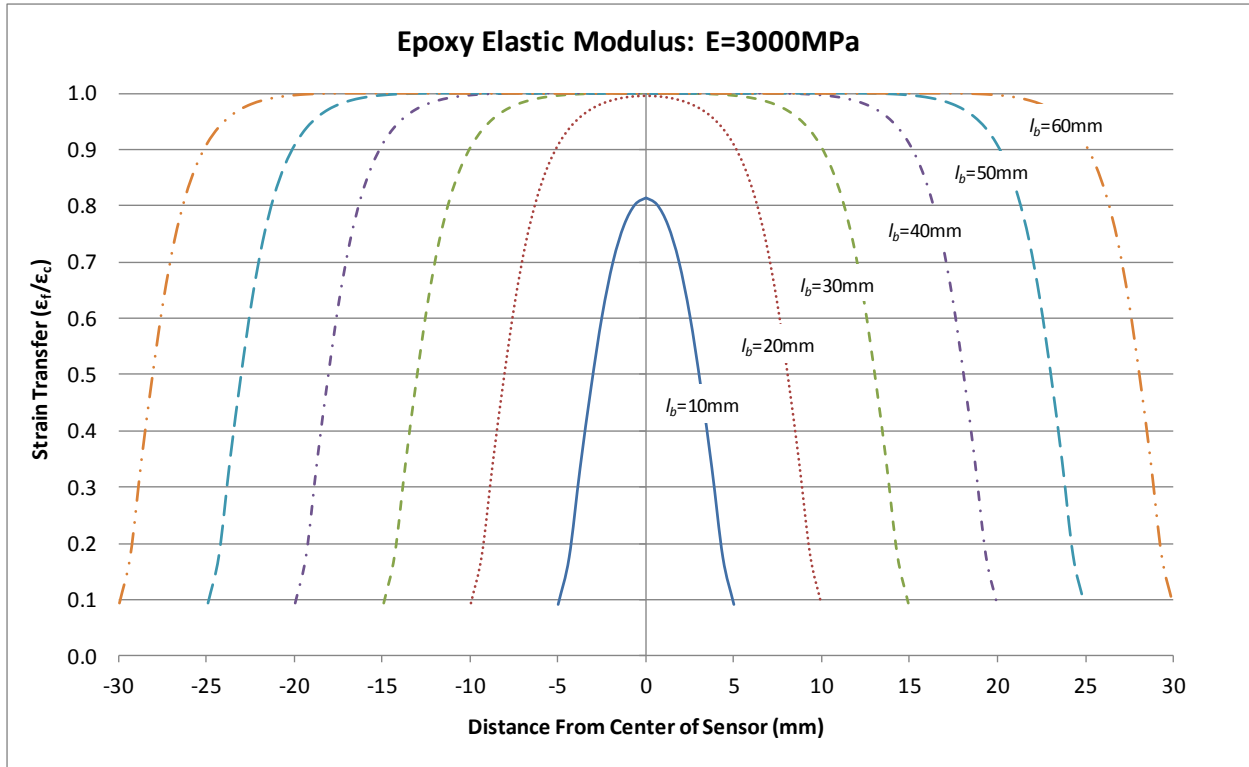


Figure A1-4c: Epoxy length comparison for 1.6 mm bond layer thickness saw-notch configuration

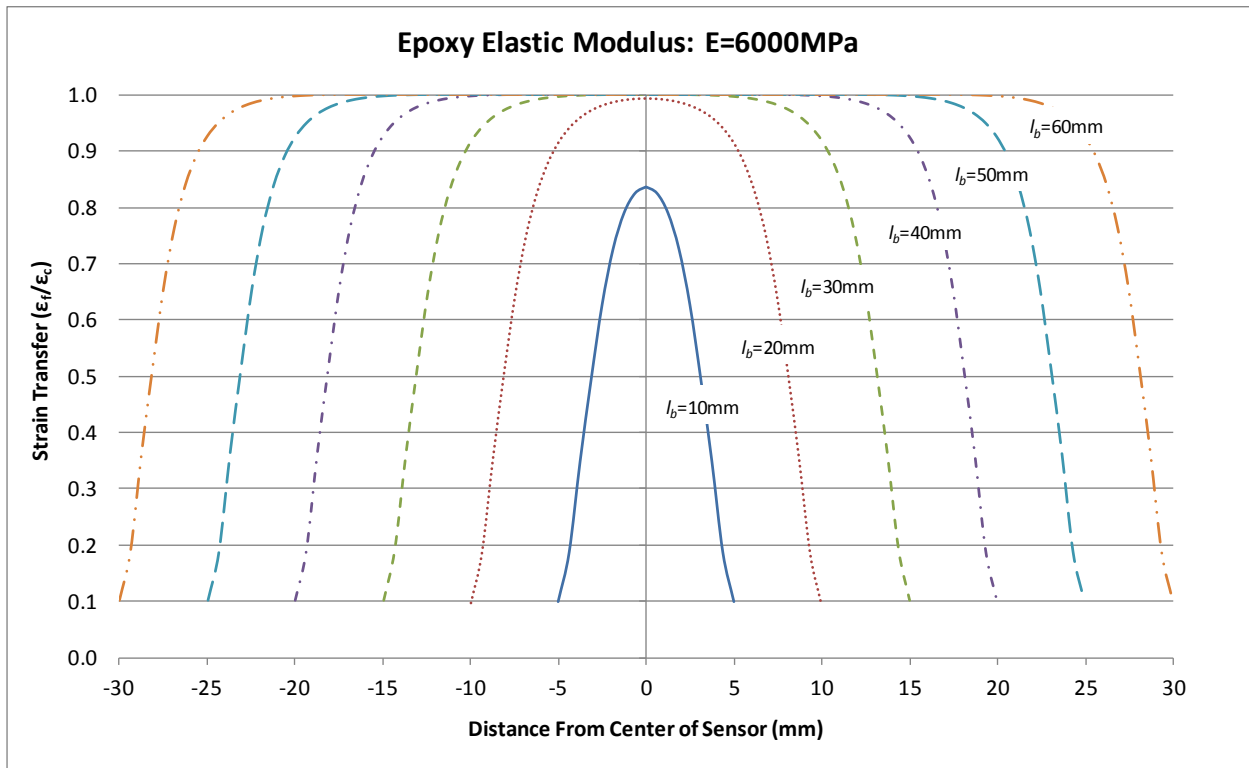


Figure A1-4d: Epoxy length comparison for 1.6 mm bond layer thickness saw-notch configuration

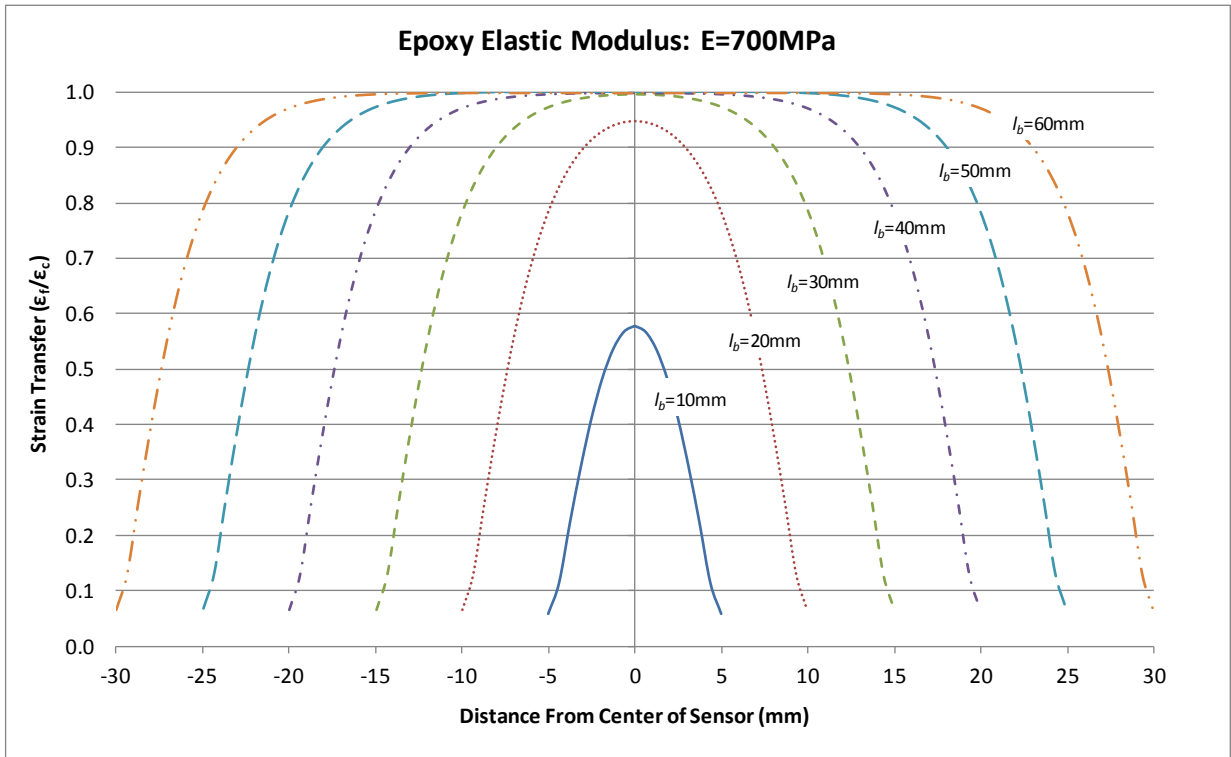


Figure A1-5a: Epoxy length comparison for 3.2 mm bond layer thickness saw-notch configuration

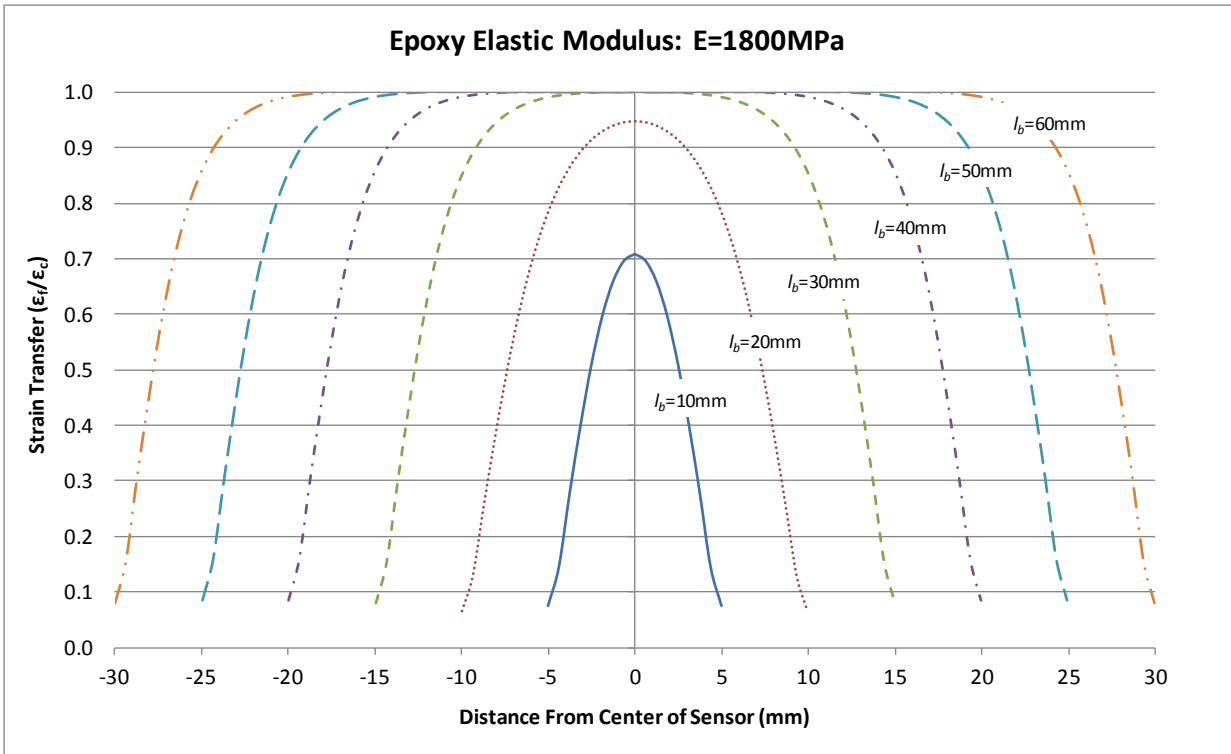


Figure A1-5b: Epoxy length comparison for 3.2 mm bond layer thickness saw-notch configuration

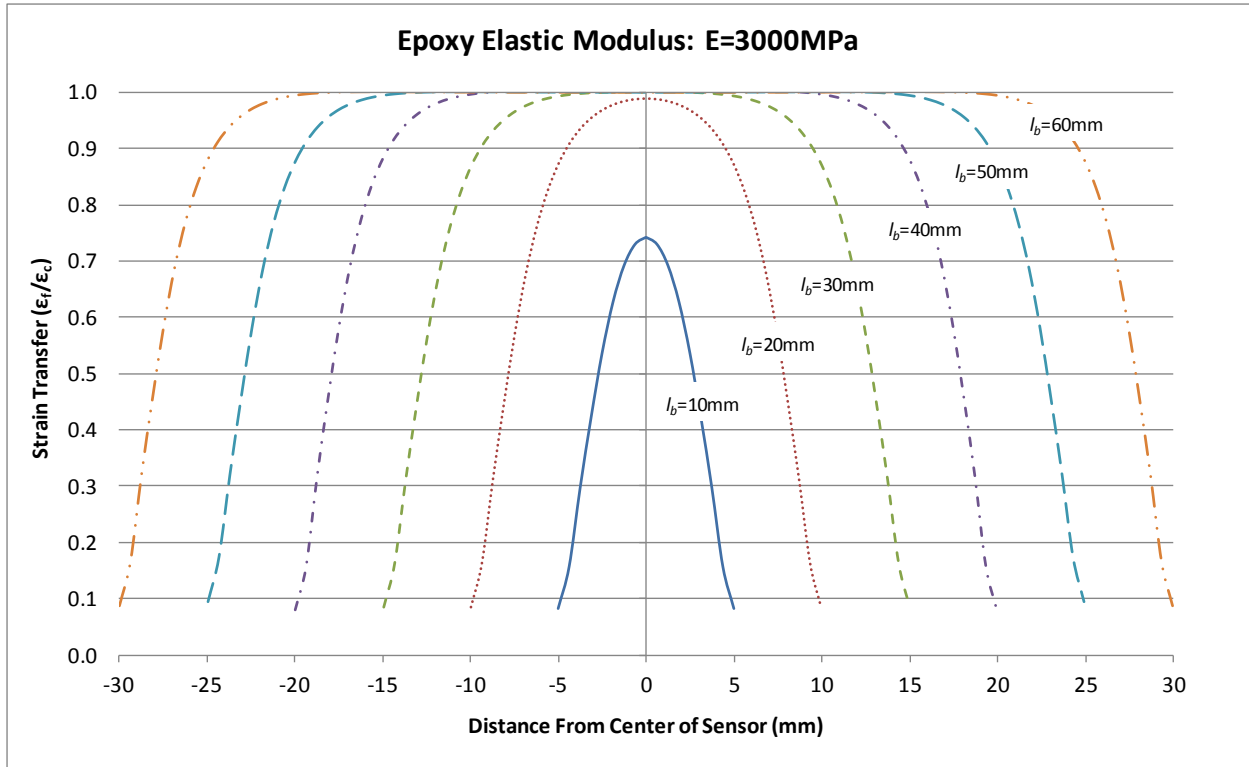


Figure A1-5c: Epoxy length comparison for 3.2 mm bond layer thickness saw-notch configuration

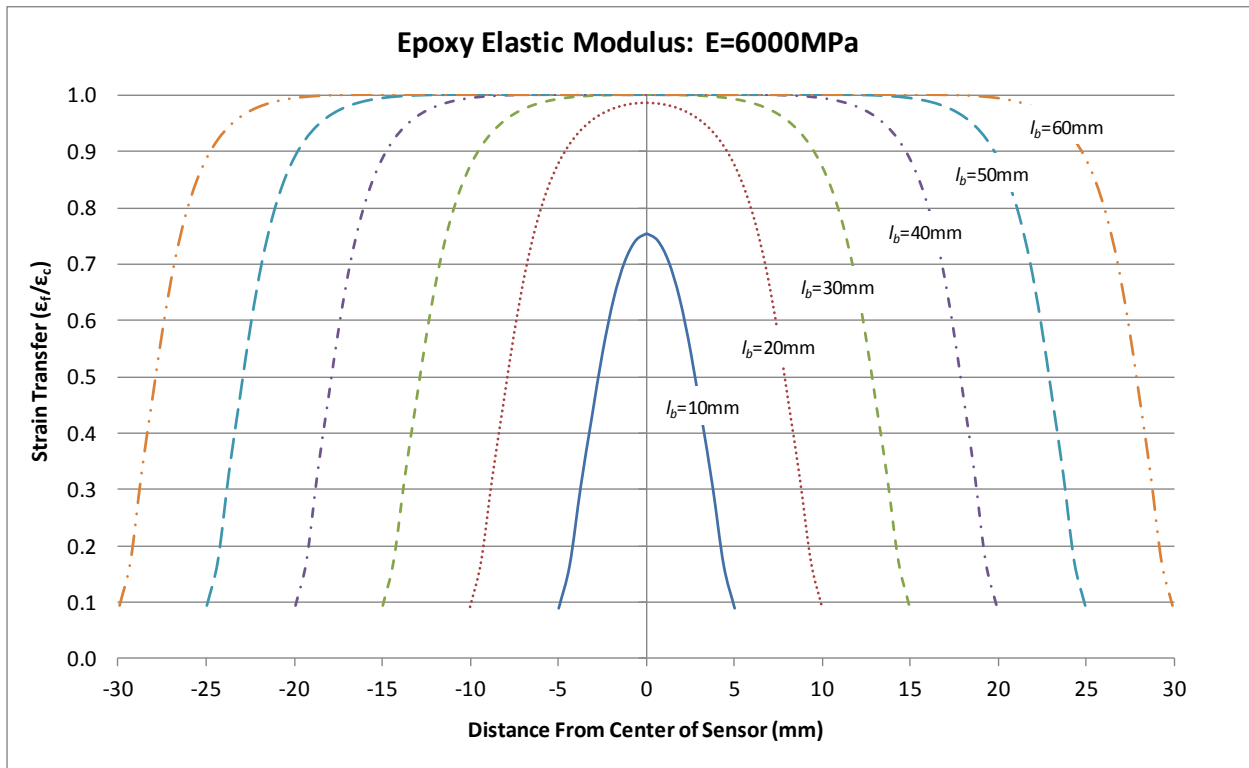


Figure A1-5d: Epoxy length comparison for 3.2 mm bond layer thickness saw-notch configuration

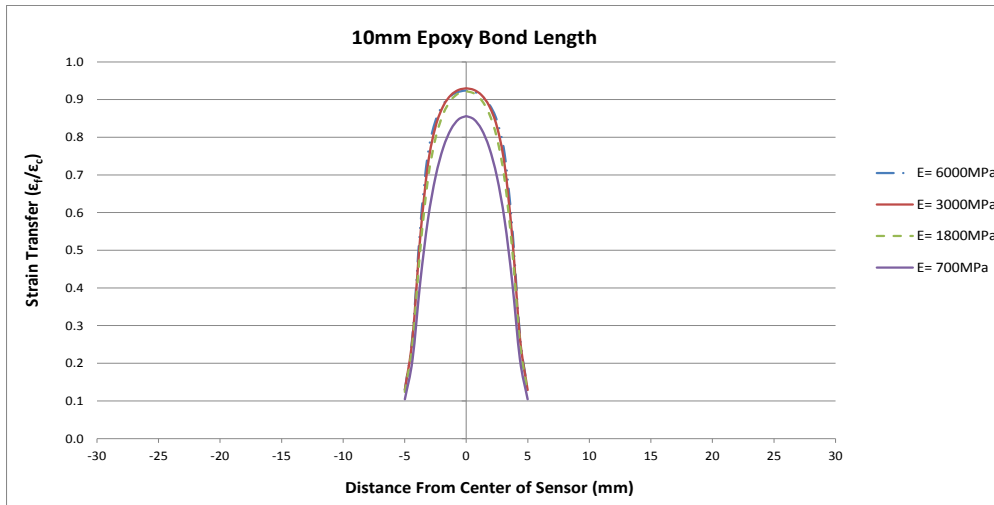


Figure A2-1a: Epoxy modulus comparison for 0.875 mm bond layer thickness v-notch configuration

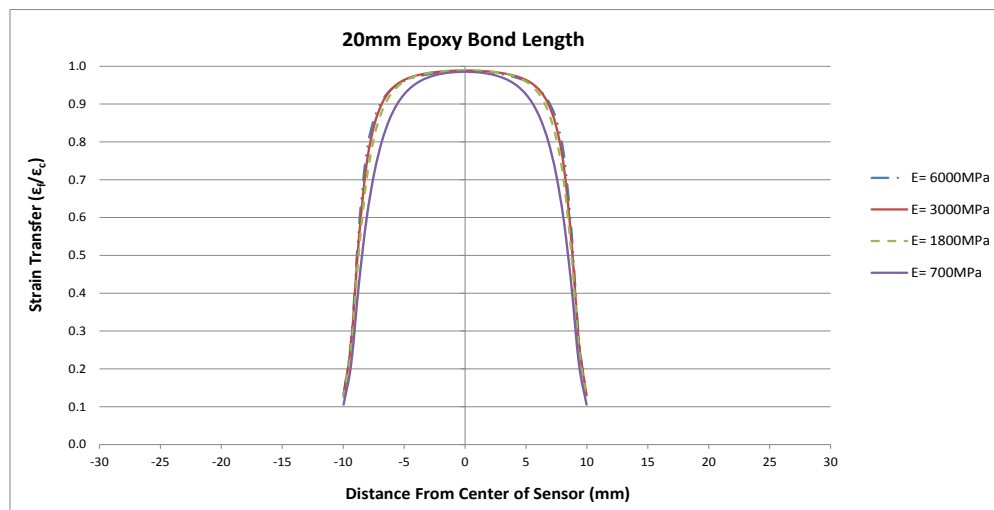


Figure A2-1b: Epoxy modulus comparison for 0.875 mm bond layer thickness v-notch configuration

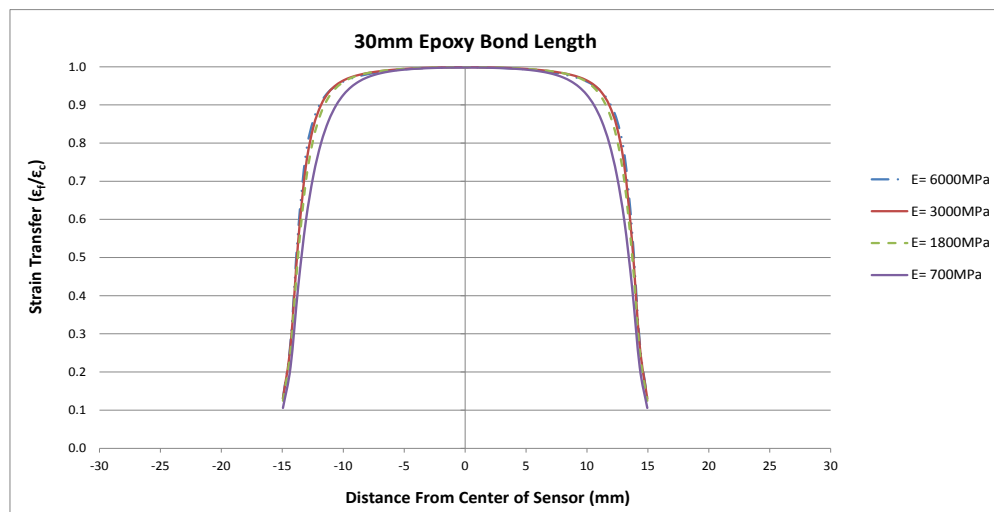


Figure A2-1c: Epoxy modulus comparison for 0.875 mm bond layer thickness v-notch configuration

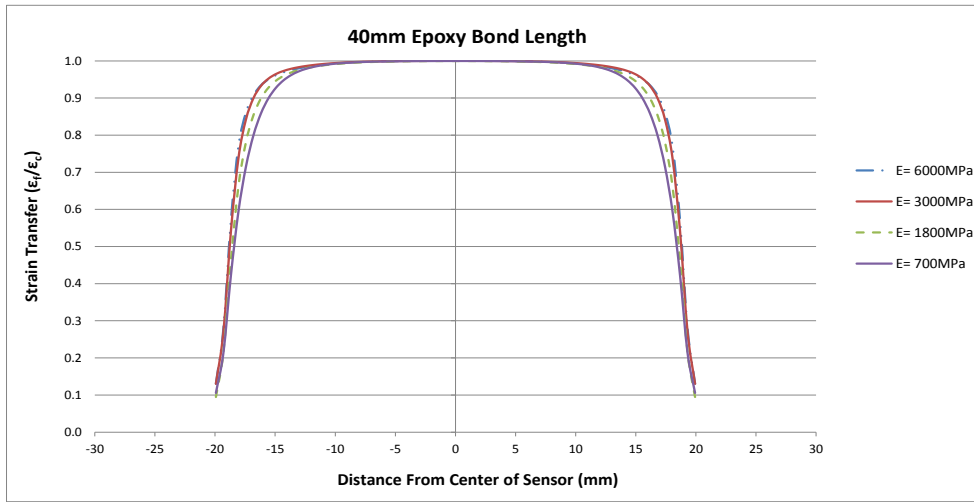


Figure A2-1d: Epoxy modulus comparison for 0.875 mm bond layer thickness v-notch configuration

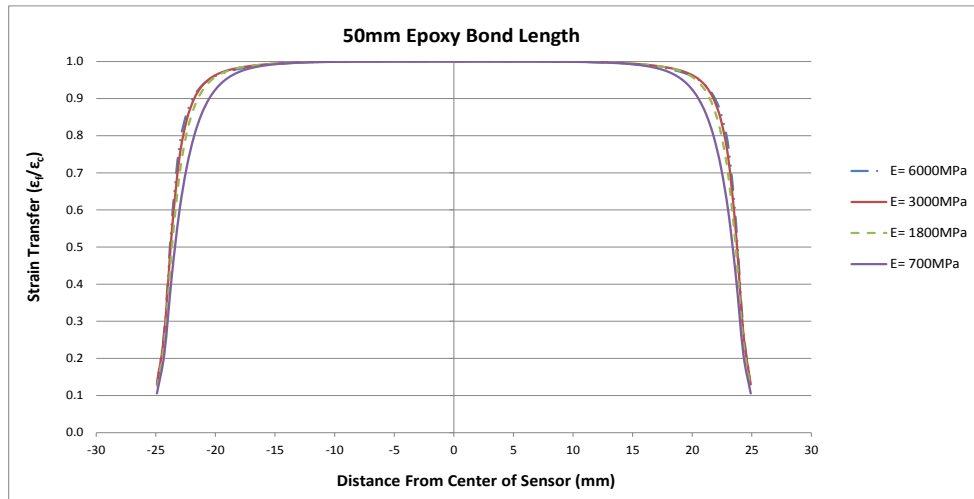


Figure A2-1e: Epoxy modulus comparison for 0.875 mm bond layer thickness v-notch configuration

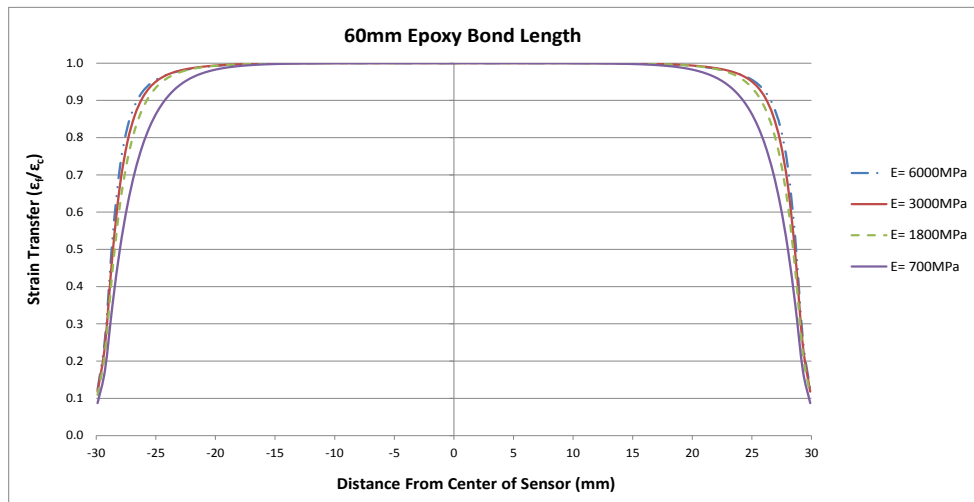


Figure A2-1f: Epoxy modulus comparison for 0.875 mm bond layer thickness v-notch configuration



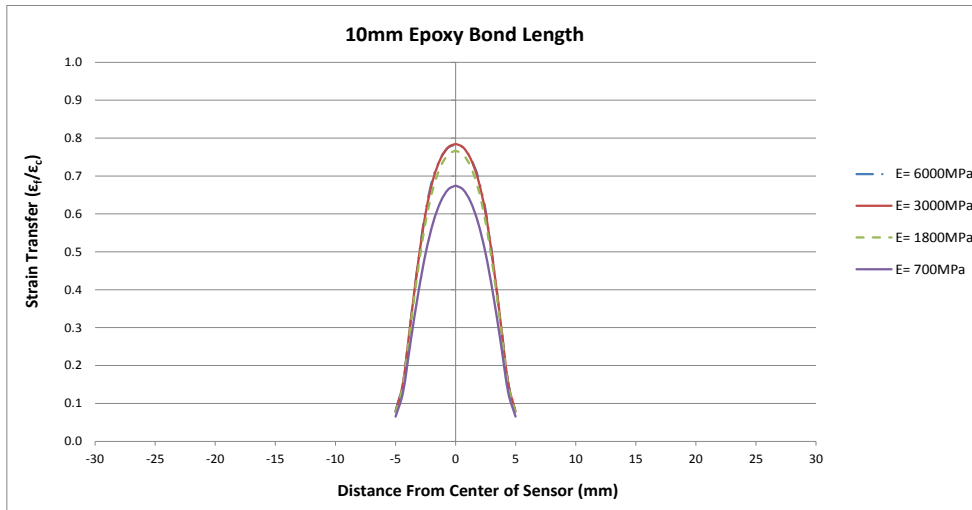


Figure A2-2a: Epoxy modulus comparison for 1.75 mm bond layer thickness v-notch configuration

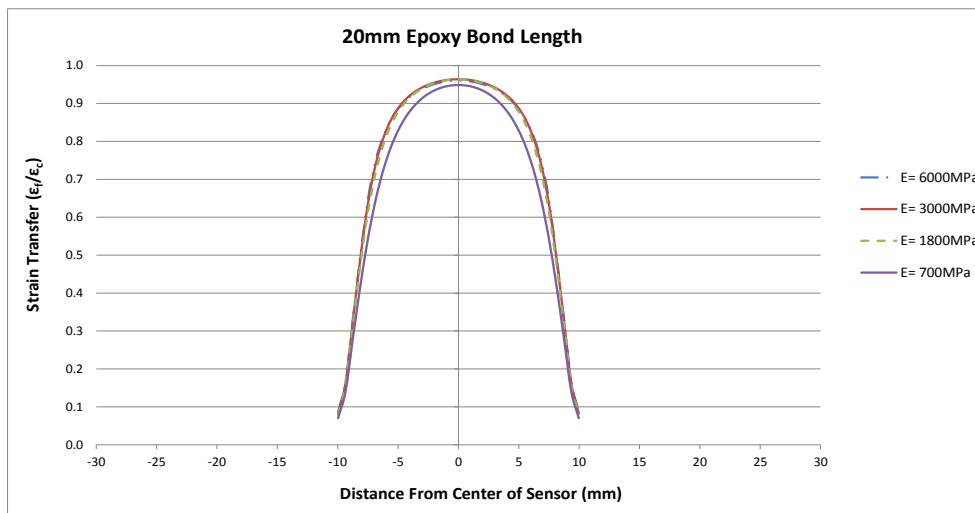


Figure A2-2b: Epoxy modulus comparison for 1.75 mm bond layer thickness v-notch configuration

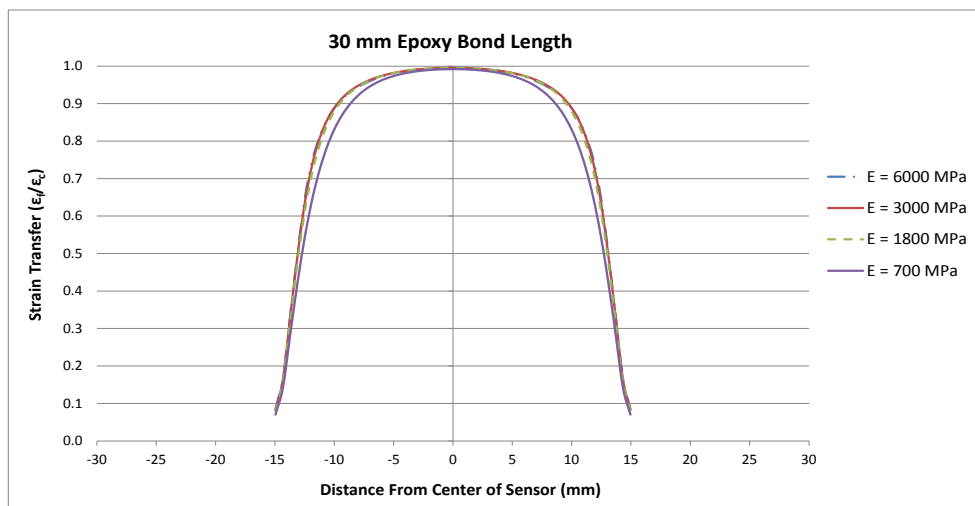


Figure A2-2c: Epoxy modulus comparison for 1.75 mm bond layer thickness v-notch configuration

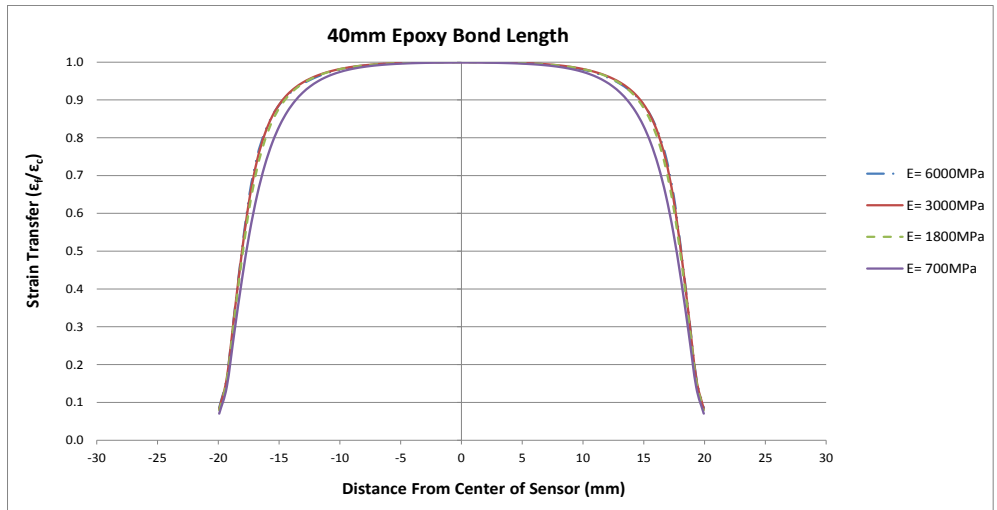


Figure A2-2d: Epoxy modulus comparison for 1.75 mm bond layer thickness v-notch configuration

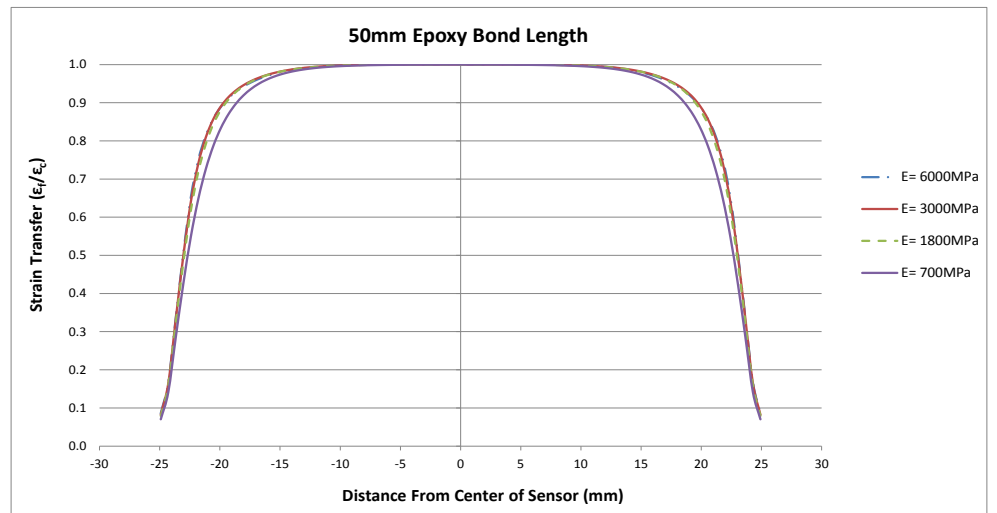


Figure A2-2e: Epoxy modulus comparison for 1.75 mm bond layer thickness v-notch configuration

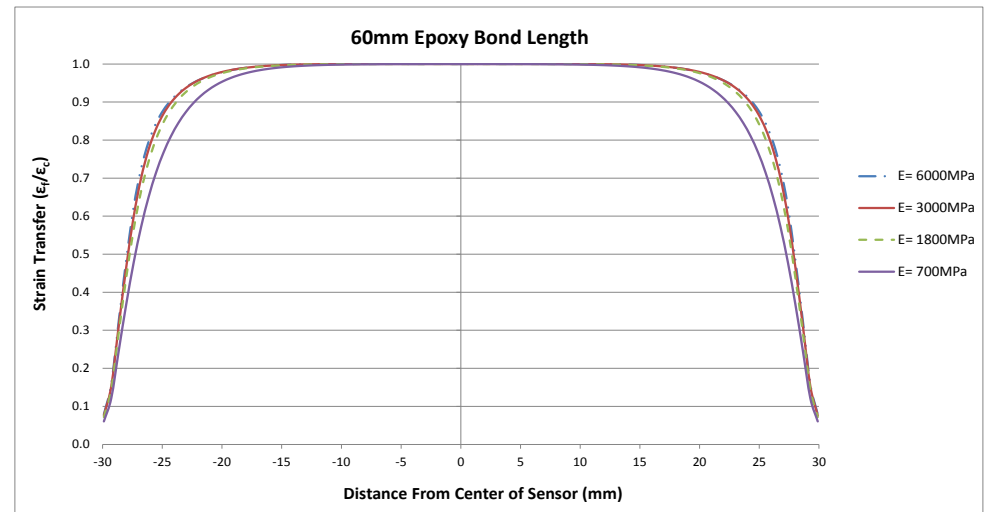


Figure A2-2f: Epoxy modulus comparison for 1.75 mm bond layer thickness v-notch configuration

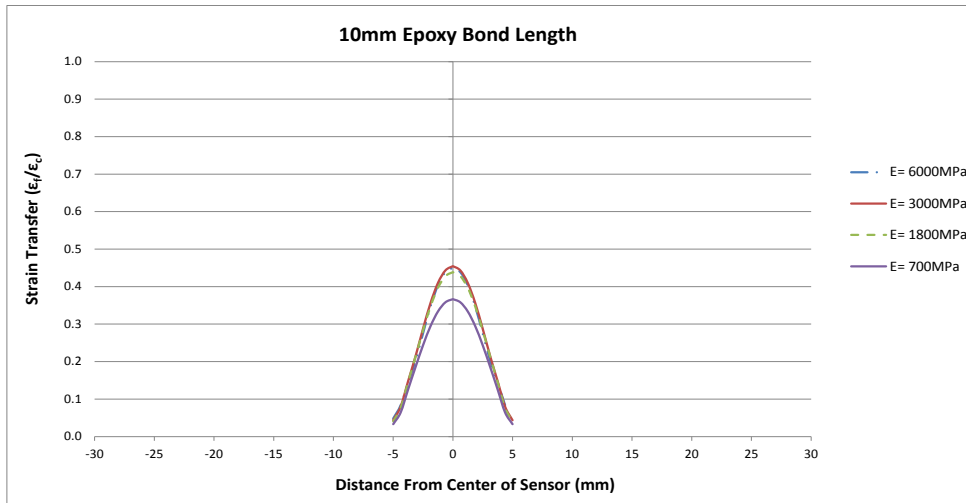


Figure A2-3a: Epoxy modulus comparison for 3.5 mm bond layer thickness v-notch configuration

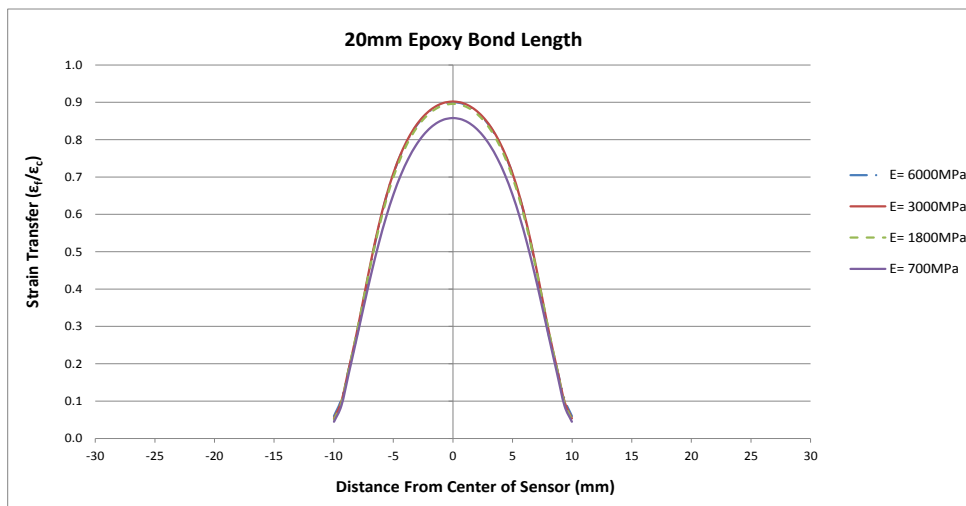


Figure A2-3b: Epoxy modulus comparison for 3.5 mm bond layer thickness v-notch configuration

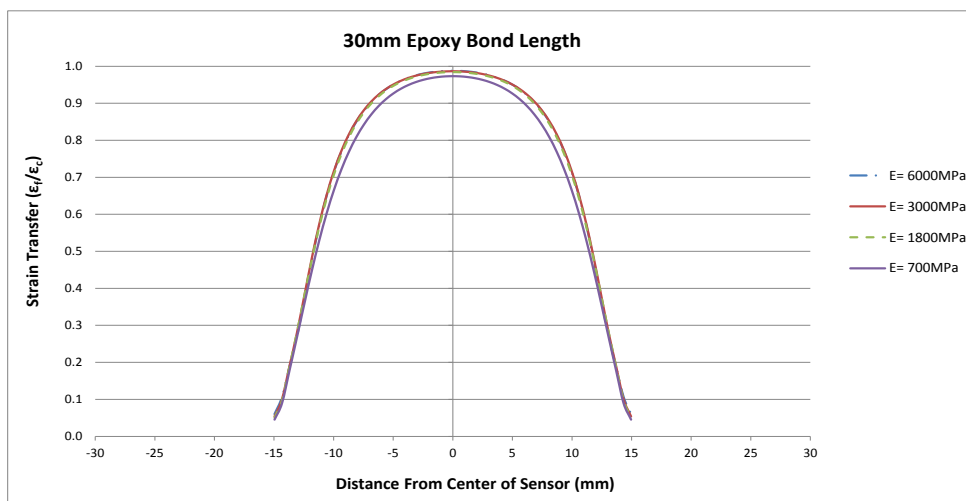


Figure A2-3c: Epoxy modulus comparison for 3.5 mm bond layer thickness v-notch configuration

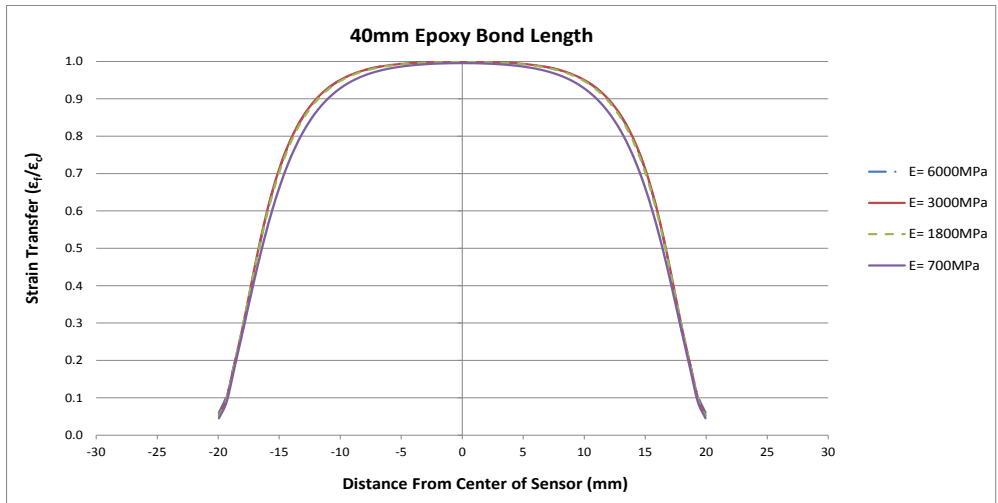


Figure A2-3d: Epoxy modulus comparison for 3.5 mm bond layer thickness v-notch configuration

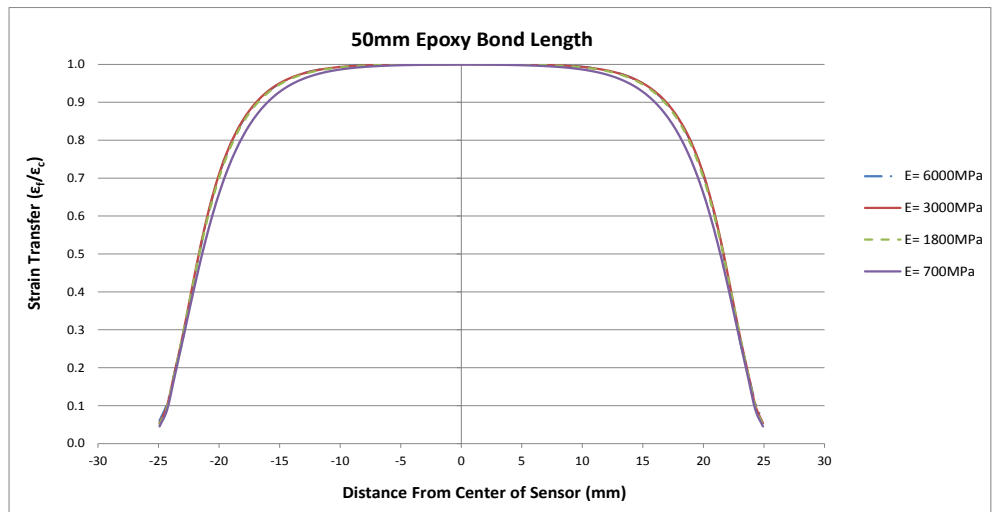


Figure A2-3e: Epoxy modulus comparison for 3.5 mm bond layer thickness v-notch configuration

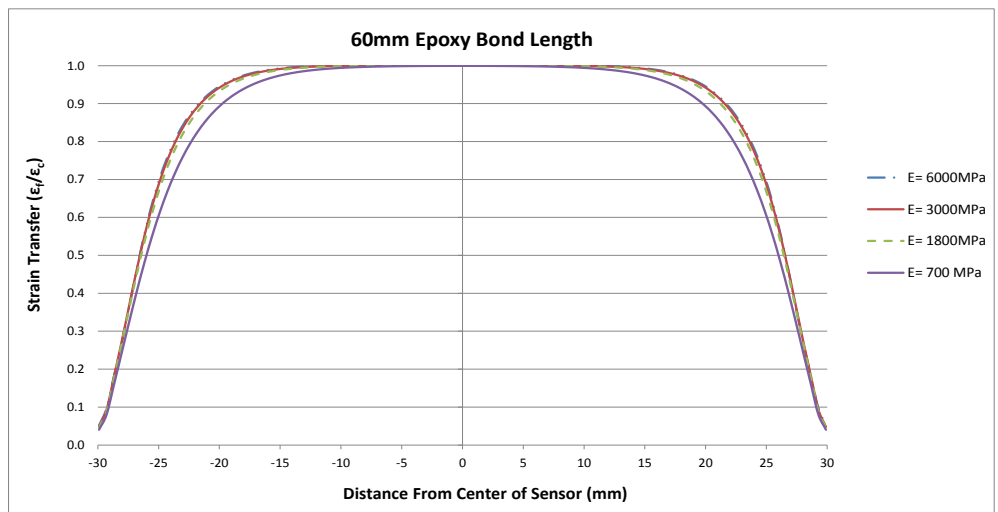


Figure A2-3f: Epoxy modulus comparison for 3.5 mm bond layer thickness v-notch configuration

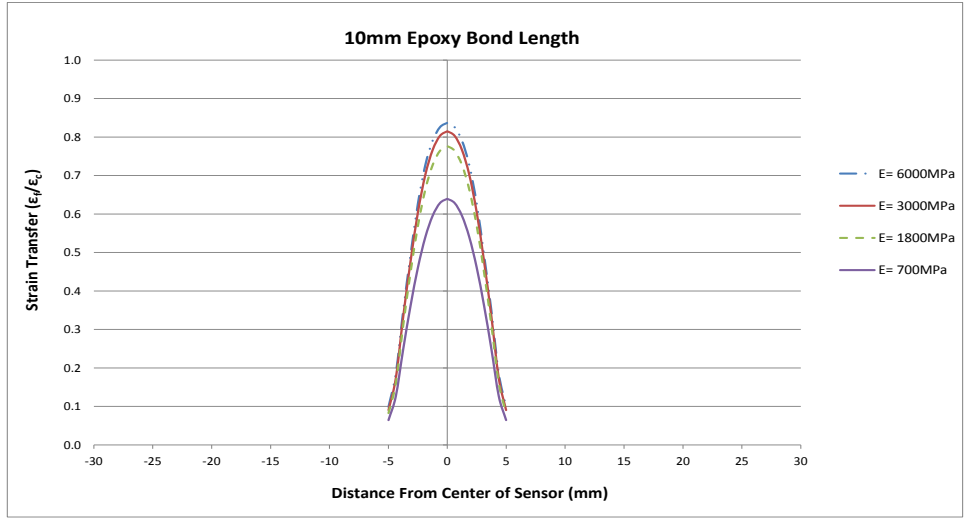


Figure A2-4a: Epoxy modulus comparison for 1.6 mm bond layer thickness saw-notch configuration

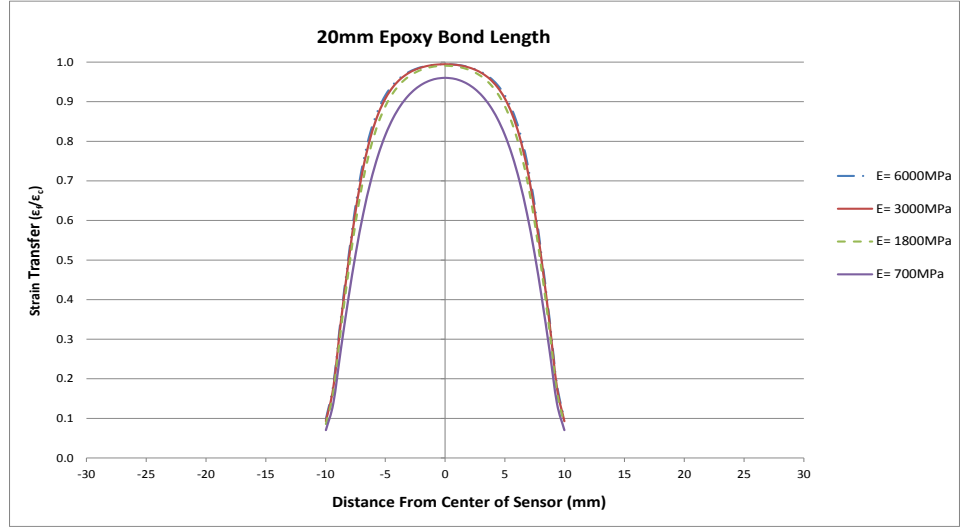


Figure A2-4b: Epoxy modulus comparison for 1.6 mm bond layer thickness saw-notch configuration

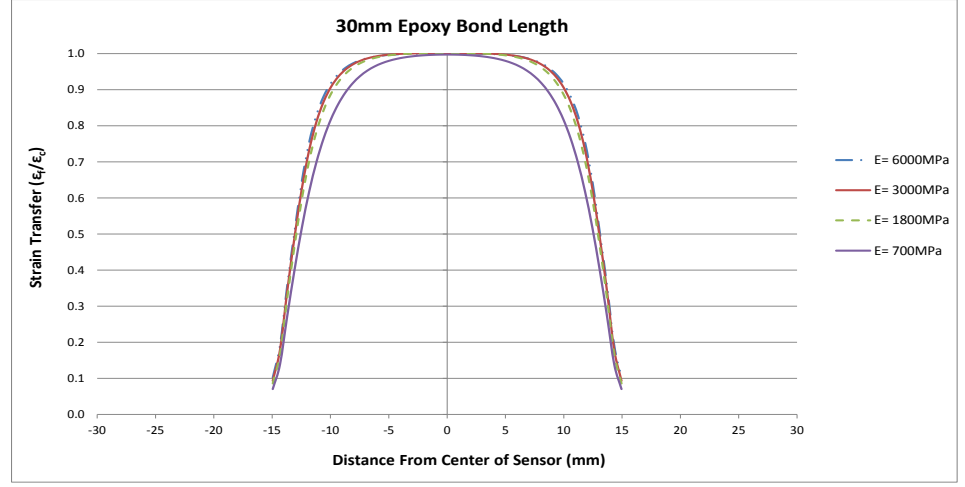


Figure A2-4c: Epoxy modulus comparison for 1.6 mm bond layer thickness saw-notch configuration

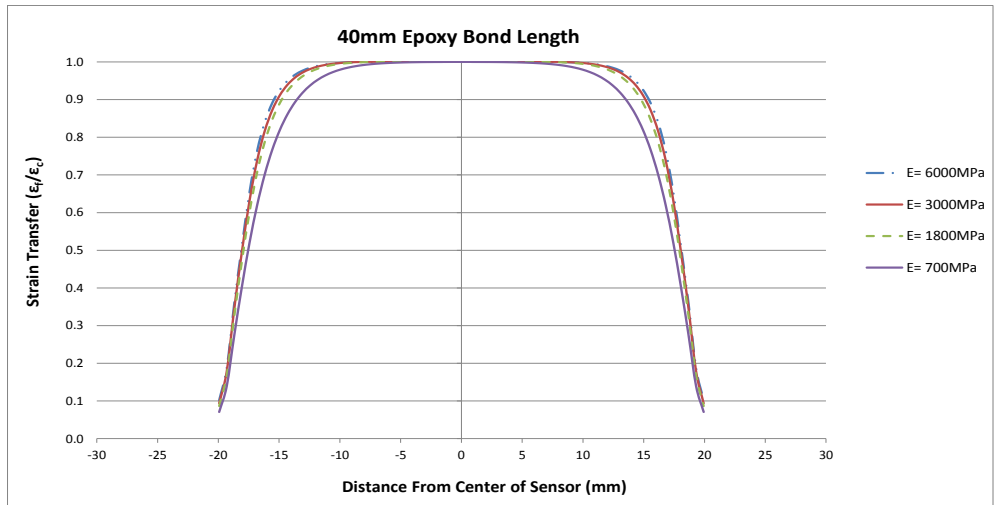


Figure A2-4d: Epoxy modulus comparison for 1.6 mm bond layer thickness saw-notch configuration

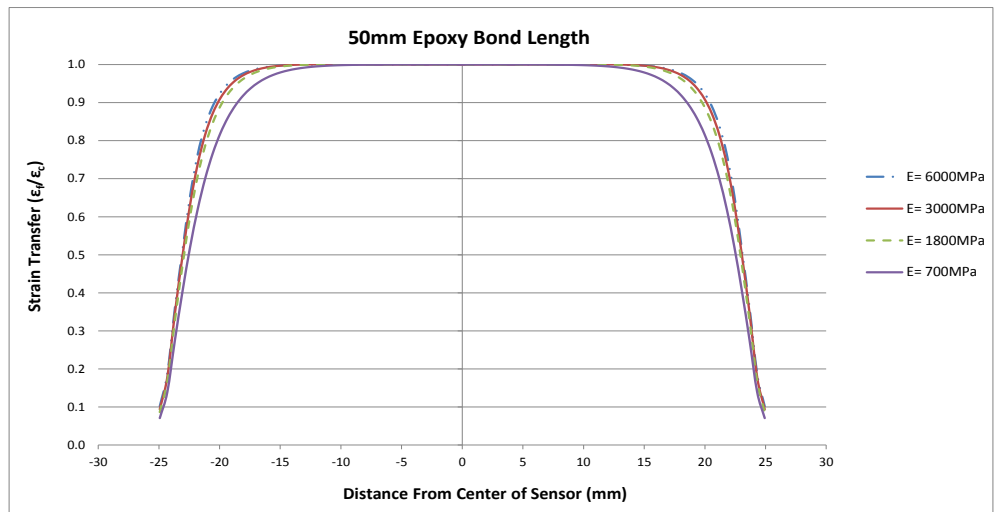


Figure A2-4e: Epoxy modulus comparison for 1.6 mm bond layer thickness saw-notch configuration

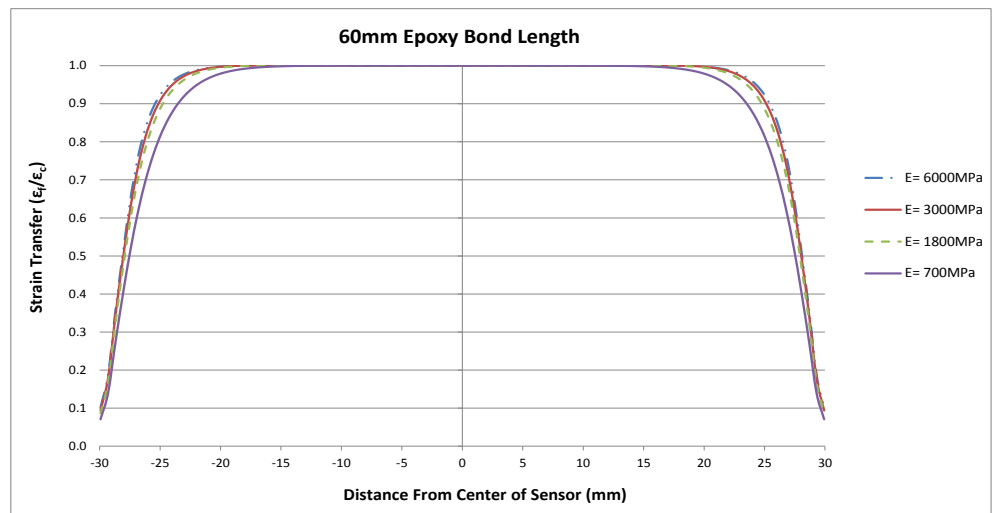


Figure A2-4f: Epoxy modulus comparison for 1.6 mm bond layer thickness saw-notch configuration

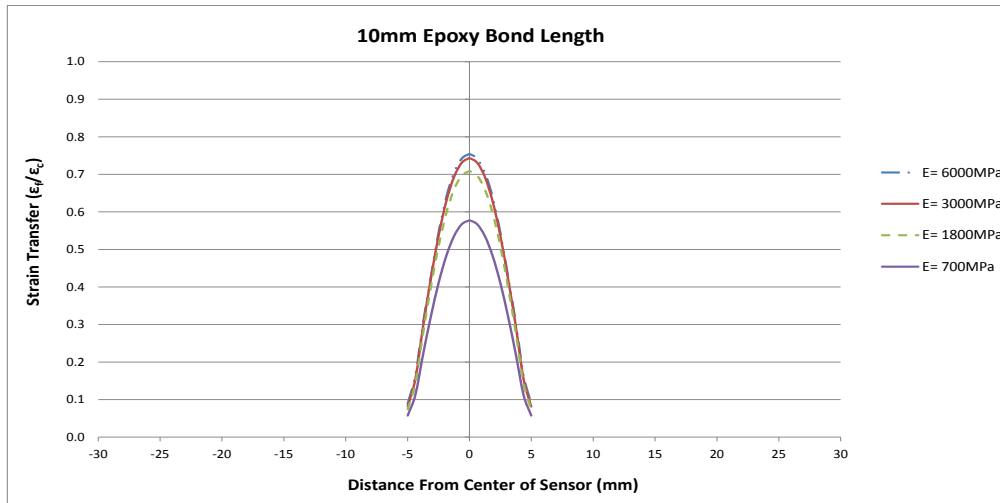


Figure A2-5a: Epoxy modulus comparison for 3.2 mm bond layer thickness saw-notch configuration

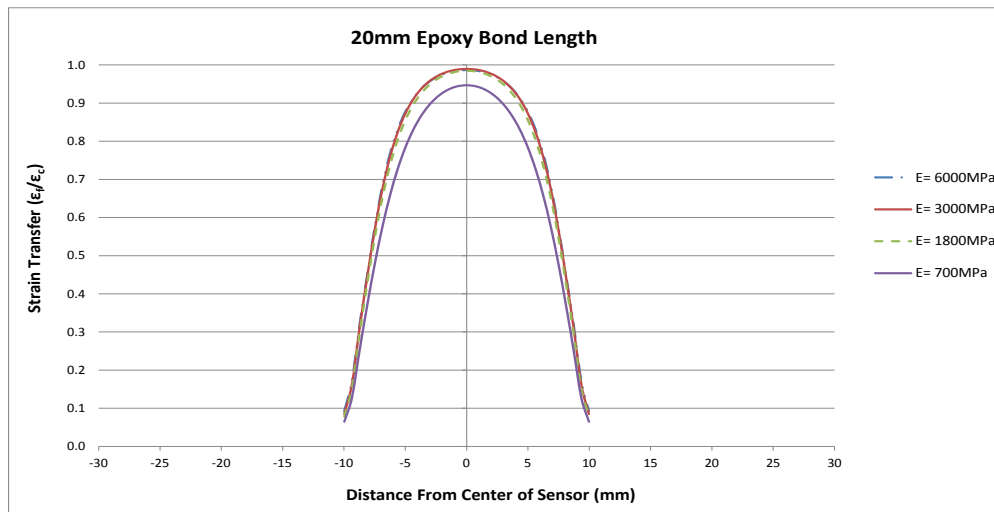


Figure A2-5b: Epoxy modulus comparison for 3.2 mm bond layer thickness saw-notch configuration

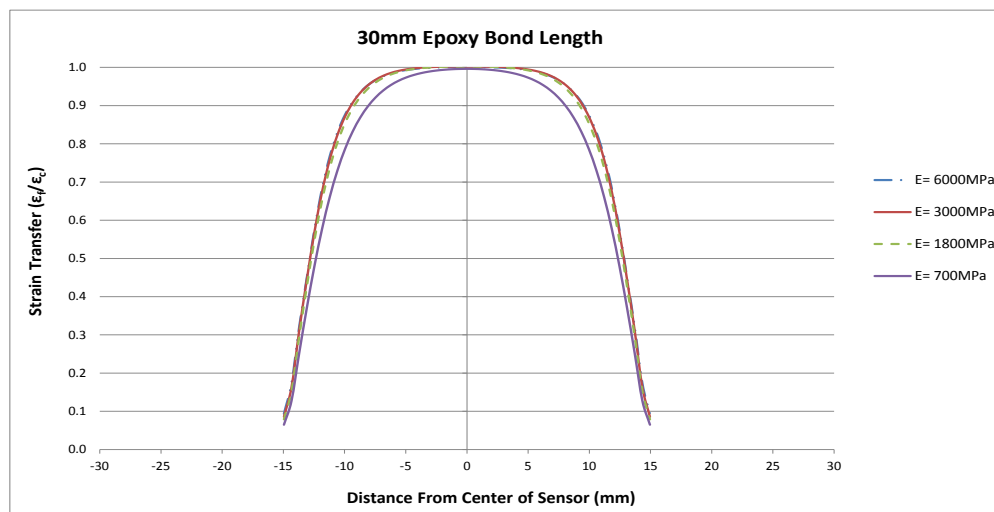


Figure A2-5c: Epoxy modulus comparison for 3.2 mm bond layer thickness saw-notch configuration

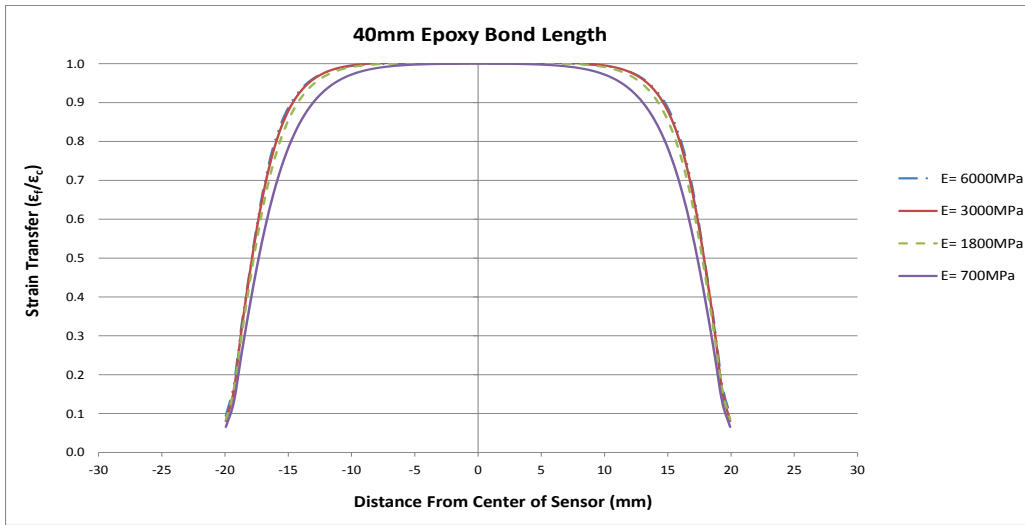


Figure A2-5d: Epoxy modulus comparison for 3.2 mm bond layer thickness saw-notch configuration

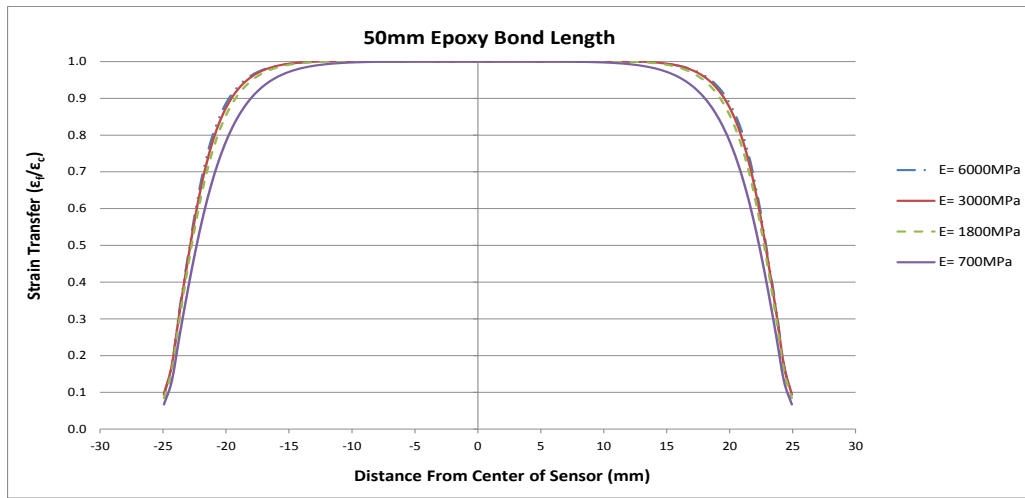


Figure A2-5e: Epoxy modulus comparison for 3.2 mm bond layer thickness saw-notch configuration

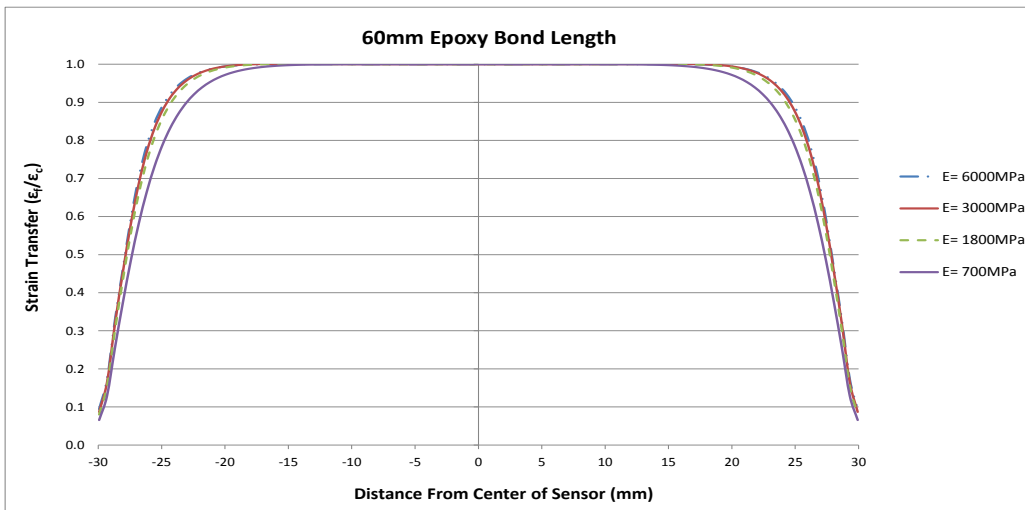


Figure A2-5f: Epoxy modulus comparison for 3.2 mm bond layer thickness saw-notch configuration



## APENDIX B: PICTURES OF TESTS

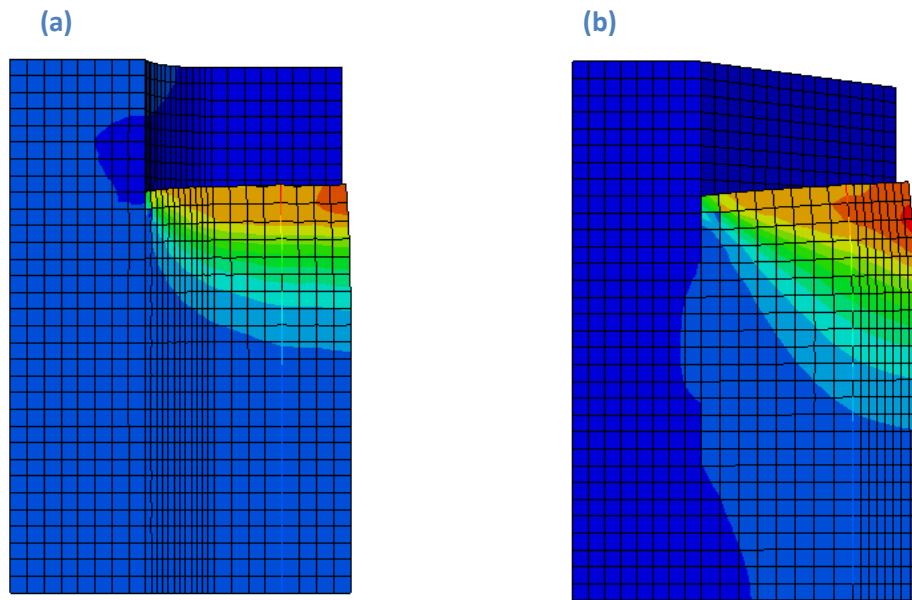


Figure B1: Example of FEA longitudinal strain distribution with deflected shape: (a) saw-notch model  
(b) v-notch model



Figure B2: Axially loaded concrete prism test setup

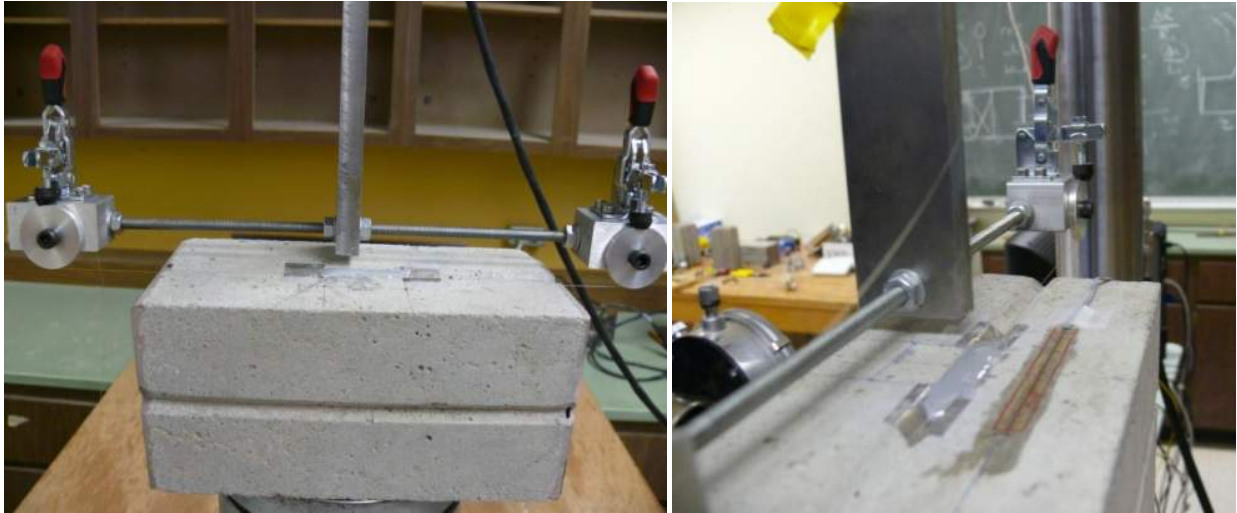


Figure B3: FBG epoxy embedment technique with tensioning devise



Figure B4: FBG compression range test setup



Figure B5: FBG gage factor calibration test



Figure B6: Epoxy stiffness test

**APPENDIX B-2**

**M.S. THESIS  
BY MICHAEL JUNG**

To the University of Wyoming:

The members of the Committee approve the thesis of Michael Jung presented on  
9/11/2014.

Dr. Richard Schmidt, Chairperson

Dr. David Walrath, External Department Member

Dr. Jay Puckett

APPROVED:

Dr. Anthony Denzer, Department Head, Civil and Architectural Engineering Department

Dr. Michael Pishko, Dean, College of Engineering and Applied Science

Jung, Michael, A., DEVELOPMENT OF A FIBER OPTIC BASED LOAD TESTING SYSTEM FOR HIGHWAY BRIDGES, M.S., Civil & Architectural Engineering, August, 2014.

## **ABSTRACT**

The present state of American infrastructure demands new solutions to prolong the life of civil structures and quantify the performance of aging structures that have suffered varying degrees of degradation. This is especially true of bridges, which are routinely subjected to environmental events and are depended upon to reliably and safely move huge quantities of goods and people. A structural health monitoring system can supplement traditional bridge inspection methods to aid in detecting deterioration in structures and to perform load rating tests to determine more accurate structural capacities than those predicted by analytical methods alone. With better information about bridge performance and condition, bridge management officials can better allocate resources for maintaining highway networks.

This thesis develops techniques for implementing a structural health monitoring system based on fiber Bragg grating strain sensors that may be used to perform diagnostic load rating tests after further development. This thesis discusses sensor placement, installation, protection methods, and analysis techniques. To develop the methods discussed, a scale model bridge was constructed in the laboratory consisting of a pre-stressed concrete beam and a steel beam. Thus, it was possible to develop methods for sensing behavior in concrete and steel elements.

The techniques for system design, sensor installation, and analysis developed in this thesis provide a preliminary groundwork for the future development of a structural health monitoring system that can be used to evaluate the capacity of bridges. These techniques will be refined, further developed, and field-tested in the next phases of this project. Additional parameters that were not studied in the laboratory are discussed and will also be studied in the next phases of research.

**DEVELOPMENT OF A FIBER OPTIC BASED LOAD TESTING  
SYSTEM FOR HIGHWAY BRIDGES**

By  
Michael A. Jung

A thesis submitted to the Civil and Architectural Engineering Department  
and the University of Wyoming

in partial fulfillment of the requirements

for the degree of

MASTERS OF SCIENCE  
in  
CIVIL ENGINEERING

Laramie, Wyoming

August, 2014



## **DEDICATION PAGE**

This thesis is dedicated to my wife Stephanie, to my family, and to my daughter Skye.

Thank you for your encouragement, support, sacrifice, and inspiration.

## ACKNOWLEDGMENTS

This research was made possible by research grants provided by the Wyoming Department of Transportation, the Mountain-Plains Consortium, and the Department of Civil and Architectural Engineering at the University of Wyoming. I am grateful for their support and dedication to research in the civil engineering field. Additionally, I would like to specifically thank Keith Fulton and Paul Cortez for their guidance and support during this project.

I would like to thank my adviser, Dr. Richard Schmidt, for providing me with the opportunity to attend graduate school at the University of Wyoming and for his guidance during my research and studies. Thank you also to my additional committee members: Dr. Jay Puckett and Dr. David Walrath.

I am also very grateful for my graduate colleagues who assisted me during my research, especially McKenzie Danforth, who will continue this research into the next phase; Dan Maurais, whose research preceded my work on this project; and James Branscomb, who has worked to develop the instrumentation for this system.

Finally, thank you to Dr. Rob Erikson for his guidance during the experiment design, to the UW machine shop for their work in fabricating the experiment, and to Bridget Schabron for her assistance with instrumentation and data collection.

**Table of Contents**

Chapter 1: Introduction..... 1

    1.1 Background..... 1

        State of Infrastructure..... 1

        Bridge Inspection ..... 2

        Structural Health Monitoring ..... 3

        Sensors ..... 7

    1.2 Research Overview ..... 9

        Research Phase 1 ..... 10

        Research Phase 2..... 12

    1.3 Thesis Objectives and Scope ..... 12

Chapter 2: Literature Review ..... 14

    2.1 Sensor Placement..... 14

    2.2 FBG Sensor Installation..... 16

    2.3 Guidelines and Codes Relating to Load Testing ..... 17

    2.4 Load Testing Case Studies..... 20

Chapter 3: Experiment Design ..... 25

    3.1 Field Bridge Analysis ..... 25

    3.2 Laboratory Scaling..... 26

    3.3 Experimental Setup..... 30

3.4 Sensor Locations.....	32
Chapter 4: Installation Techniques.....	36
4.1 Multiplexed Sensor System Design.....	36
4.2 Temperature Compensation.....	39
4.3 Sensor Installation.....	41
Sensing Steel Elements.....	43
Sensing Concrete Elements.....	48
Chapter 5: Experimental Procedures.....	58
Chapter 6: Analysis Procedures.....	61
6.1 FBG Data Analysis.....	61
Considerations for Long Gauge Sensors.....	63
6.2 Determination of Analytical Load Effects.....	64
Chapter 7: Concrete Beam Results.....	65
7.1 Calculated Analytical Properties.....	65
7.2 Cross-Section Sensor Placement.....	66
7.3 Static Tests.....	67
Neutral Axis Location.....	70
Comparison of Results.....	74
7.4 Moving Load Tests.....	77
Chapter 8: Steel Beam Results.....	81

8.1 Calculated Analytical Properties .....	81
8.2 Steel Cross-Section Sensor Placement .....	81
8.3 Secondary Load Effects .....	82
8.4 Static Tests .....	88
Neutral Axis Location .....	90
Comparison of Results .....	94
8.5 Moving Load Tests .....	96
Chapter 9: Summary of Findings & Conclusions.....	99
9.1 FBG Sensor Installation Techniques (Objectives 1 & 2) .....	99
9.2 Analysis of Test Data (Objective 3) .....	100
9.3 Cross-Section Sensor Location (Objective 4).....	101
9.4 Comparison of Test Data with Analytical Model (Objective 5).....	102
Chapter 10: Applications & Future Work .....	104
10.1 Cross-Section Sensor Placement .....	105
10.2 Load Distribution .....	105
10.3 Incidental Composite Action .....	106
10.4 Data Handling .....	106
10.5 Considerations for Load Rating Through Testing .....	107
10.6 Wide Implementation .....	108

## Table of Figures

Figure 1.1 Illustration of FBG Signal Transmission .....	8
Figure 1.2. Block Diagram of Instrumentation Being Developed for SHM System .....	11
Figure 3.1. Half Framing Plan of Field Bridge .....	26
Figure 3.2. Load Configuration of Moving Load Applied to SAP2000 Finite Element Model of Field Bridge, and Lab Bridge.....	28
Figure 3.3. Load Configuration of Laboratory Test Vehicle.....	29
Figure 3.4. Schematic of Load Cart for Laboratory Test .....	31
Figure 3.5. Laboratory Test Setup.....	31
Figure 3.6. Sensor Locations on Beam Cross-Sections.....	32
Figure 3.7. Sensor Locations Along Beam Length .....	32
Figure 3.8. Analytical Curvature Envelope for Laboratory Beam .....	35
Figure 4.1. Interrogation Overlap Due to Inadequate Sensor Spacing.....	37
Figure 4.2. Sensor Schematic for Sensors Placed at Extreme Fibers of Concrete Laboratory Beam.....	38
Figure 4.3. Temperature Compensation FBG .....	41
Figure 4.4. Test Setup for Strain Transfer of Surface Adhered FBG on Steel.....	44
Figure 4.5. Test Results for Strain Transfer of Surface Adhered FBG on Steel .....	44
Figure 4.6. Protected FBG Fiber on Steel Beam .....	47
Figure 4.7. Bond Resulting From Notch Embedded Epoxy Procedure For Concrete Fiber Installation .....	49
Figure 4.8. Minimum Configuration for Long-Gage Strain Sensing of Concrete Using an FBG .....	51

Figure 4.9. Photo of Long-Gage FBG Installed on Concrete Beam .....	52
Figure 4.10. Protection Method 2 for Fibers Installed on Concrete.....	56
Figure 6.1 Peak Strain Reported by Long Gauge Sensor.....	63
Figure 7.1. Curvatures Measured by Cross-Sectional Sensor Configurations on Concrete Beam.....	66
Figure 7.2. Sensor Locations on Concrete Beam Cross-Section.....	67
Figure 7.3. Curvature Measured by Side Sensors on Concrete Beam.....	69
Figure 7.4. Curvature Measured by Side Sensors on Concrete Beam.....	69
Figure 7.5. Curvature Measured by Side Sensors on Concrete Beam.....	70
Figure 7.6. Neutral Axis Height Measured by Side Sensors on Concrete Beam .....	71
Figure 7.7. Neutral Axis Height Measured by Top & Bottom Sensors on Concrete Beam.....	71
Figure 7.8. Neutral Axis Height Measured by Side Sensors on Concrete Beam .....	72
Figure 7.9. Neutral Axis Height Measured by Top & Bottom Sensors on Concrete Beam.....	72
Figure 7.10. Neutral Axis Height Measured by Side Sensors on Concrete Beam .....	73
Figure 7.11. Neutral Axis Height Measured by Top & Bottom Sensors on Concrete Beam...	73
Figure 7.12. Comparison of Analytical and Measured Curvatures for Concrete Beam.....	76
Figure 7.13. Comparison of Analytical and Measured Curvatures for Concrete Beam.....	76
Figure 7.14. Comparison of Analytical and Measured Curvatures for Concrete Beam.....	77
Figure 7.15. Averaged Curvature from Static, Pseudo-Static, and Full-Speed Tests .....	79
Figure 7.16. Curvature Influence Function for Concrete Beam at Mid-Span (2.05) .....	80
Figure 8.1. Curvatures Measured by Cross-Sectional Sensor Configurations on Steel Beam.	82
Figure 8.2. Orientation of Sensors and Load on Steel Beam Cross-Section.....	82
Figure 8.3. Curvatures Calculated from Individual Sensors on Steel Beam .....	83

Figure 8.4. Isometric View of Model for Analyzing Effects of Out-of-Plane Force Acting on Top Flange..... 85

Figure 8.5 Cross-Section of Deflected Shape Near Mid-Span..... 86

Figure 8.6. Static Test Results Adjusted for Differential Out of Plane Flange Bending..... 87

Figure 8.7. Averaged Curvature from Static Tests on Steel Beam ..... 89

Figure 8.8. Averaged Curvature from Static Tests on Steel Beam ..... 89

Figure 8.9. Averaged Curvature from Static Tests on Steel Beam ..... 90

Figure 8.10. Neutral Axis Location Measured by Inside Sensors on Steel Beam..... 91

Figure 8.11. Neutral Axis Location Measured by Outside Sensors on Steel Beam..... 91

Figure 8.12. Neutral Axis Location Measured by Inside Sensors on Steel Beam..... 92

Figure 8.13. Neutral Axis Location Measured by Outside Sensors on Steel Beam..... 92

Figure 8.14. Neutral Axis Location Measured by Inside Sensors on Steel Beam..... 93

Figure 8.15. Neutral Axis Location Measured by Outside Sensors on Steel Beam..... 93

Figure 8.16. Comparison of Analytical and Measured Curvatures on Steel Beam..... 95

Figure 8.17. Comparison of Analytical and Measured Curvatures on Steel Beam..... 95

Figure 8.18. Comparison of Analytical and Measured Curvatures on Steel Beam..... 96

Figure 8.19. Average Curvature Influence Function for Steel Beam at Mid-Span (2.05) ..... 98



# **CHAPTER 1: INTRODUCTION**

## **1.1 BACKGROUND**

### **State of Infrastructure**

The present state of American infrastructure demands new solutions to prolong the life of civil structures and quantify the performance of aging structures that have suffered varying degrees of degradation. This is especially true of bridges, which are routinely subjected to environmental events and are depended upon to reliably and safely move huge quantities of goods and people.

In 2012, the average highway bridge age in the U.S. was 42 years. Of the 607,380 bridges in the United States, 66,749 were considered structurally deficient (ASCE 2013). A structurally deficient bridge is defined as a "bridge that requires significant maintenance, rehabilitation, or replacement" due to "critical load-carrying elements found to be in poor condition from deterioration or damage" (ASCE 2013). If the structural deficiency becomes severe enough, bridge managers are required to post load restrictions to ban travel of heavy loads across the bridge, or in some cases ban use of the bridge altogether. Of the structurally deficient bridges cited above, 60,971 bridges have been posted with load restrictions, and 3,585 bridges have been totally closed (ASCE 2013). These conditions are the inevitable result of balancing limited resources against increasing bridge maintenance needs and illustrate the importance of developing more efficient strategies for infrastructure management.

## **Bridge Inspection**

The Federal Highway Act of 1968 established the National Bridge Inspection Standards (NBIS) (Federal Highway Administration 2014). In its current form, the NBIS requires that states maintain an inventory of all bridges and catalog any structural deficiencies. To maintain a current inventory, all highway bridges are required to be inspected a minimum of once every 24 months, and more frequently if the bridge condition necessitates it. The objective of a bridge inspection is to “...determine the physical and functional condition of the bridge; to form the basis for the evaluation and load rating of the bridge, as well as analysis of overload permit applications; to initiate maintenance actions; to provide a continuous record of bridge condition and rate of deterioration; and to establish priorities for repair and rehabilitation programs” (AASHTO 2010).

Routine inspections are performed visually by specially trained bridge inspectors who, upon finding indications of concern, may require in-depth inspections of structural elements to further quantify deterioration or confirm the performance of critical members. These in-depth inspections involve a close-up inspection of the identified elements and may require material sensing and field measurements of structural behavior or observed deterioration. Findings from these inspections may be integrated into the structural analysis of the bridge to assess its structural condition. The results of this analysis may be used to post load restrictions on the bridge, determine sufficiency for overweight permit vehicles, and plan future maintenance or replacement needs.

Although great care is taken to perform thorough inspections, because these inspections are performed only at discrete time intervals and rely predominantly on qualitative

techniques, there is potential for structural deterioration to go undetected, especially in regions of the structure that are difficult to access. Furthermore, because the condition of structural elements tends to be estimated based on qualitative assessments during inspections, they do not provide raters the confidence that can be achieved by testing (A.G. Lichtenstein and Associates, Inc. 1998).

### **Structural Health Monitoring**

Structural health monitoring (SHM) systems have the potential to supplement bridge inspection operations through structural testing and continuous monitoring of diagnostic instrumentation. Two primary focuses for structural monitoring are damage detection and load rating. In this thesis, "health monitoring" will refer to detecting and monitoring deterioration and damage in the structure, while the terms "load testing" or "load rating" will refer to methods to diagnose the structural capacity of a bridge.

### ***Health Monitoring***

Deterioration of some structural elements may be measured by comparing readings from sensors over time. The changes due to deterioration may be gradual for phenomena such as corrosion or crack propagation, or may occur suddenly due to a seismic or impact event.

Sensors may be applied locally to monitor areas of concern. These sensors may be used where cracks are observed and it is desired to measure crack growth, or in regions where corrosion has been observed. They may also be used to monitor novel structural details that have not been exhaustively studied or on details that are fracture critical or susceptible to fatigue failure. This method of sensor placement can only measure areas of concern that are known in advance.

Alternatively, sensors may be strategically placed to monitor global structural behavior; in which case, a change in structural behavior may indicate that deterioration has occurred, but may offer limited insight into the nature of the damage (Doornink, et al. 2006). Global level indicators may include resting-state strains, response to loads, or vibrational signatures. If the location of the deterioration sensed by the global indicators is determined from inspection, a local sensor may then be installed to monitor that location for further deterioration. Detection of damage by the SHM system can alert bridge managers of the need to schedule a bridge inspection, or in extreme cases, close the bridge via an incorporated communication network.

### ***Load Rating***

Load rating is the process of determining the live-load carrying capacity of an existing bridge (AASHTO 2010). Load rating is achieved through evaluation, testing and structural analysis. Traditional load rating techniques involve a visual inspection of the structure, in which the material strength, effective sections, and other structural parameters are estimated and then incorporated with the as-built plans to define the as-inspected condition of the structure. Structural analysis is then performed using the as-inspected condition to rate the structure. The general equation for a load and resistance factored rating (LRFR) is given by Equation 1.1.

$$RF = \frac{C - \gamma_{DC}DC - \gamma_{DW}DW \pm \gamma_P P}{\gamma_{LL}(LL + IM)} \quad (1.1)$$

(AASHTO 2010)

where:  $RF$  = rating factor ( $RF > 1.0$  implies an adequate load rating)  
 $C$  = factored capacity  
 $DC$  = component dead load effects  
 $DW$  = wearing surface and utility dead load effects  
 $P$  = permanent non-dead load effects  
 $LL$  = live load effects  
 $IM$  = dynamic load allowance  
 $\gamma_{DC}, \gamma_{DW}, \gamma_P, \gamma_{LL}$  = corresponding load factors

A load rating can be performed at three different levels: design, legal, and permit level. A design level rating assesses the structure according to AASHTO design standards, allowing for unlimited passage of legal and exclusionary vehicle loads on the structure. A legal load rating assesses the structure primarily at the strength limit state for a specific load configuration. This rating may form the basis for determining appropriate load postings or strengthening of the structure. For structures meeting the criteria for a design load rating, an additional permit load rating may be performed to determine the safety and serviceability of a bridge subjected to loads exceeding the legally established limits (AASHTO 2010).

### ***Load Testing***

Where inspection methods rely primarily on qualitative visual methods for estimating structural condition, load tests may be performed to directly measure and quantify structural performance, yielding more accurate and often more favorable load ratings.

Load testing is particularly advantageous for bridges that do not meet the criteria for a design-level load rating based on the as-inspected condition, as the measured capacity of a

structure will generally exceed predicted capacities (A.G. Lichtenstein and Associates, Inc. 1998). There are two types of load tests: diagnostic load tests and proof load tests. A description of proof load tests follows; however this thesis primarily focuses on developing techniques that may form the basis for diagnostic load testing.

### **Proof Load Test**

A proof load test consists of thoroughly instrumenting a bridge and incrementally increasing the loads applied to the bridge until either it is proven adequate for a predetermined desired load, or the structure shows significant distress indicating that the structure is inadequate for additional loading. Proof load tests provide a direct measure of structural performance and the most accurate measure of capacity. However, they are expensive, cumbersome to perform, and are generally used only for structures with unknown structural properties that are missing as-built plans or are of novel design. Because these tests involve applying strength-level loads to structures with unknown properties, they can be dangerous to perform and require extreme care and close monitoring.

### **Diagnostic Load Test**

A diagnostic load test involves instrumenting a bridge with sensors, and measuring the structural response to known load configurations. From these data, structural properties are calculated, and an extrapolated capacity can be determined. Unlike with a proof load test, where capacity is measured directly, diagnostic load test data must be carefully analyzed to determine specifically which sources are contributing to the structural capacity. This is because the test is not performed under strength-level loads, and certain factors that contribute to structural behavior under lesser load conditions break down and are not available to resist

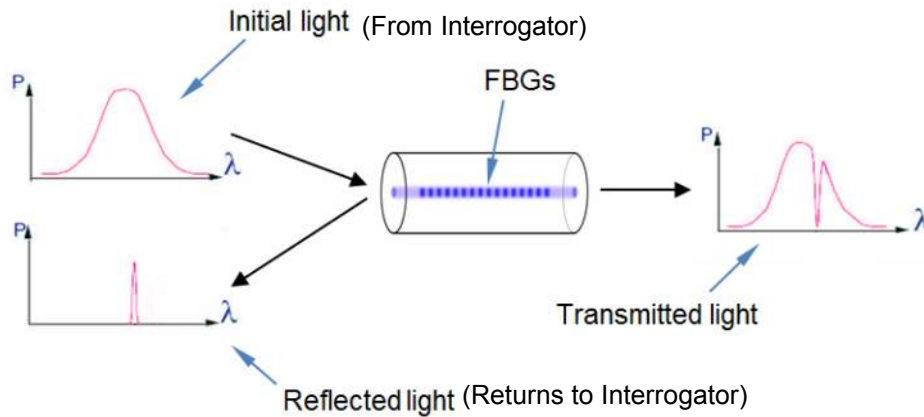
strength-level loads. The properties that are quantified during diagnostic tests and their effect on the rating of the structure are discussed in detail in subsequent chapters.

## **Sensors**

In order to successfully monitor or load test a bridge, the structure must be instrumented with appropriate equipment. There is a wide variety of sensors available on the market that can be incorporated into an SHM system. System designers must consider the goals of the system when determining which type of sensors to use. The ultimate goal for this research is to develop an SHM system that can operate long-term, remotely, and possibly with intermittent power. Based on these criteria, a fiber optic strain sensor, called a fiber Bragg grating, was selected.

### ***Fiber Bragg Gratings***

Fiber Bragg Grating (FBG) strain sensors are beginning to achieve broad acceptance by the civil engineering field because they offer many advantages over other sensors available on the market (Zhou and Ou 2004). FBG sensors have been widely studied and used in structural testing and health monitoring applications, but are still less common than traditional foil strain gages because of the high cost of FBG sensors and interrogators. An FBG is an optical sensing device that consists of a grating etched into the core of an optical fiber at a precise spacing. When light is passed through the grating, a portion of the light is reflected back toward the source at a narrow band of wavelength centered about the Bragg peak wavelength. This process is illustrated in Figure 1.1.



**Figure 1.1 Illustration of FBG Signal Transmission (Heininger 2009)**

A change in the pitch of the grating, which can be induced by straining the fiber, results in a shift in the peak wavelength that is reflected back. This shift in reflected wavelength is proportional to the strain. Using this property, the strain in the fiber can be determined by measuring the shift in the reflected wavelength. The relationship between strain and wavelength shift is given by Equation 1.2.

$$\varepsilon = \frac{\lambda - \lambda_0}{G\lambda_0} \quad (1.2)$$

where:  $\varepsilon$  = strain  
 $\lambda$  = reflected wavelength  
 $\lambda_0$  = unstrained reflected wavelength  
 $G$  = gage factor (typically 0.78)

An interrogator is used to both send and receive the light signals for the gratings. The interrogator may have multiple channels, and multiple FBG sensors can be installed on a single fiber and interrogated by a single channel. Installing multiple sensors on one channel is called multiplexing. Multiplexing permits a large number of sensors to be installed on a structure and read by a single interrogator. Fibers can run the entire length of the structure and



measure strains at multiple locations. Distributing a number of sensors along the length of just a few fibers simplifies the installation process and reduces the amount of equipment necessary to read the sensors. It is important to efficiently utilize the multi-channel and multiplexing capabilities of an interrogator in order to minimize the cost of an SHM system. Interrogators are by far the costliest components of a FBG monitoring system, accounting for as much as 70% of the component costs.

Because the Fiber Bragg Gratings operate using light signals, the sensors are immune to electromagnetic interference, the behavior of the gage is extremely stable and does not need to be recalibrated (Guemes and Sierra-Perez 2013), and the signal can travel extremely long distances with almost no losses. Additionally, the silica material for the sensors is resistant to corrosion. So, the sensors can be applied almost anywhere so long as the optical fibers are protected from mechanical breakage.

Due to their many benefits and long lifespan, FBG sensors are beginning to be widely implemented in critical civil structures. Their benefits, however, may extend beyond just high profile projects and critical structures. As the technology becomes more widespread the cost of FBG systems may reach a point where it becomes economically viable for widespread implementation of FBG-based bridge rating and monitoring systems on highway networks.

## **1.2 RESEARCH OVERVIEW**

The Wyoming Department of Transportation and the Mountain-Plains Consortium have collaborated with the University of Wyoming to develop a load rating and structural health monitoring system for the long-term assessment of bridge performance in the state. A burgeoning energy sector in Wyoming has resulted in a growing number of overweight

vehicles needing to pass over the many bridges in the state. The current load rating methods are thought to be overly restrictive for many bridges, resulting in unnecessary detouring and travelling restrictions for permit vehicles. Engineers are interested in quantifying the structural response of bridges to these permit-level loads, as well as monitoring the structures for damage. If a reasonable system can be developed, this system may be used to supplement the state's bridge inventory catalog and used to route overweight vehicles more effectively, detect damage, allocate repair funds, and refine bridge-design criteria.

The health monitoring system being developed uses FBG sensors to measure strains at specific locations. Data acquired from the sensors can be correlated with known load conditions and analyzed to calculate the structural response due to a load. This information can then be used to determine structural properties of the bridge and calculate a load rating according to the AASHTO Manual for Bridge Evaluation (AASHTO 2010). Results from similar tests performed over the lifetime of the structure can be compared and differences in results may indicate changes in bridge performance. The development of the structural monitoring system has been divided into two phases.

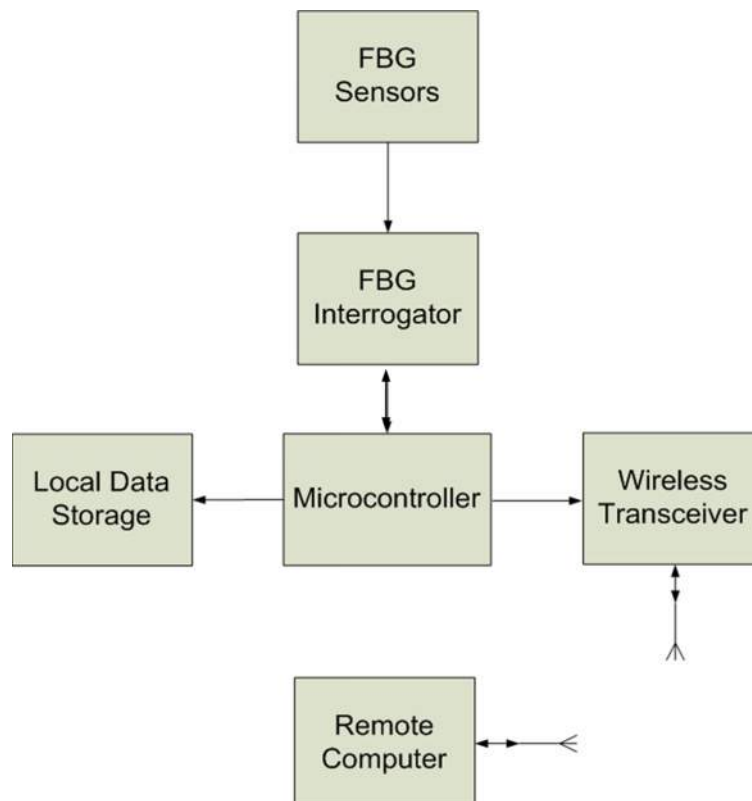
### **Research Phase 1**

Phase 1, which is the focus of this thesis, consists of developing installation, testing, and analysis methods for an FBG sensor network. Preliminary tests were performed on a scaled laboratory model of a bridge at the University of Wyoming to determine the abilities and limitations of the methods developed.

Previous work (Maurais 2012) entailed developing proper attachment techniques for adhering FBG sensors to concrete, which included studying the effects of epoxy stiffness,

embedment geometry, and development length on strain transfer between the concrete host material and the sensing fiber.

The remainder of Phase 1 includes developing an attachment method for steel material, determining viable options for protecting the fibers and sensors, developing analysis techniques for interpreting the FBG readings, and testing these techniques on a scale-model bridge in the laboratory. Additionally, work is being performed to develop the necessary instrumentation for collecting, processing, and communicating data from a remote bridge location. A basic block diagram of the instrumentation being developed for the structural health monitoring system is provided in Figure 1.2.



**Figure 1.2. Block Diagram of Instrumentation Being Developed for SHM System**  
(Branscomb 2013)

## **Research Phase 2**

In Phase 2 of the project, the devised system will be installed on a three-span bridge on Interstate 80 in Laramie, Wyoming to verify the techniques developed in Phase 1. Additional analysis techniques will be developed to account for variables that could not be measured in the laboratory experiments. Further work may entail the widespread implementation of the system to bridges across the state, and development of a structural health database.

### **1.3 THESIS OBJECTIVES AND SCOPE**

This research was focused on developing preliminary methods for performing load testing on bridges using FBG sensors, which may be further developed into a system capable of performing load ratings or structural health monitoring in the future. The scope of this study was limited to developing procedures that could be tested by a simple two-beam three-span bridge structure in the laboratory and determining areas for further study. The objectives of the study were as follows:

- 1. Develop and test techniques for installing FBG sensors on concrete elements.**

Previous work (Maurais 2012) was performed to develop and test a method for adhering FBG sensors to concrete elements by embedding the grouted fiber in a notch in the concrete surface and surrounding it with epoxy. This research investigates the feasibility of the previously developed approach on a larger scale, and develops methods for adhering and protecting the lead fiber between sensors to a concrete structure.

2. Develop and test techniques for installing FBG sensors on steel elements. A preliminary study was performed on adhering FBG sensors on steel elements in previous work (Maurais 2012). This research refines the methods developed in that study to develop techniques that can be used on a larger scale to install and protect the fibers.
3. Perform simplified preliminary load test analysis and present procedures for converting raw wavelength data from FBG sensors into strain values and calculating structural responses and properties from test data.
4. Verify that sensors installed at different locations on a member cross-section can produce similar curvature measurements. In the field, there are likely to be obstructions, such as bearing plates and decks, that may prevent sensor installation on the extreme fibers of a section. Therefore, it may be necessary to install sensors on the interior of the cross-section. This research investigates whether sensors installed at interior locations of a cross-section can produce similar measurements to sensors installed at the extreme fibers.
5. Compare the measured structural behavior of the laboratory bridge with the behavior predicted by structural analysis.

## **CHAPTER 2: LITERATURE REVIEW**

### **2.1 SENSOR PLACEMENT**

For the purpose of performing load tests, the Manual for Bridge Rating through Load Testing (A.G. Lichtenstein and Associates, Inc. 1998), published by the National Cooperative Highway Research Program (NCHRP), states that sensors should be placed on critical members and in locations to gather data that can be used to verify the analytical model.

In this paper, a three digit notation of the form X.XX is used to describe a point of interest (POI) on a bridge. The number on the left of the decimal place indicates which span the POI is located in, and the two digit number to the right of the decimal place indicates how many tenths of the span the POI is from the left end of the span. For example, 1.00 indicates a position just inside of the first support of a bridge. Location 1.05 describes the middle (5/10) of span 1, and 1.10 describes the location just to the left of the second support. Location 2.00 would then describe the location just to the right of the second support.

In Barker, et al. (1999), six different standardized testing plans are detailed for measuring the different factors that can affect a load rating on a steel girder bridge. These testing plans provide guidance for placing the necessary sensors for performing the required tests. The six plans vary in complexity and effort required based on the amount of information the tester would like gain from the test. The simplest plan consists of a single strain gage placed on the bottom flange of the critical girder at the location of maximum moment determined from analysis. This simple plan can be used to post a bridge. The most complex plan consists of multiple sensors on each of the girder webs at the maximum moment regions and near each support. This more complex configuration can be used to determine load rating

adjustments for: impact, lateral load distribution factors, bearing restraints, and composite behavior.

Chajes, Shenton III, & O'Shea (2000) performed diagnostic load tests on a bridge by placing sensors on the top and bottom flanges of girders at the middle of each of the three spans in a continuous multi-girder bridge. They did not discuss any analysis indicating that the mid-span locations were points of maximum load effect, and typical practice would indicate that the sensors in the exterior spans are not measuring the maximum load effects. The AASHTO Bridge Design Manual (AASHTO 2012) reports statistical moment data from the 1.04, 2.05, and 3.06 span locations from a number of bridges in the commentary discussing the calibration of the HL-93 live load and load factors. These span locations reflect a commonly accepted rule of thumb for estimating the anticipated maximum moment locations in a three-span bridge.

In Cardini and DeWolf (2008) sensors were placed on the web of the steel girders. They were located 2 inches below the top flange and 2 inches above the bottom flange. This placement allowed for the calculation of the neutral axis location. However, by being further from the extreme fibers, the strain gages were limited to measuring smaller strains. As it was a simple-span bridge being tested, sensors were installed only at mid-span for each of the girders on the bridge.

Doornink, et al. (2006) conducted a study to monitor a bridge for local failure in a girder web by placing sensors across the region of the expected failure and in other "non-target" areas. By tracking the paired response of these sensors to loading events over time,

they were able to prevent false alarms that could have been triggered by systems monitoring sensors in the critical locations alone.

In addition to placing sensors to measure critical member behavior, Seo, Phares, Lu, Wipf, & Dahlberg (2012) placed sensors on the underside of the bridge deck in order to determine the approximate wheel locations and axle spacing of a vehicle during a load event.

## **2.2 FBG SENSOR INSTALLATION**

Several considerations are important when determining an appropriate sensing system for bridge monitoring and testing. A good summary of issues to consider is presented in Farhey (2005). Many of the complications described in this summary are overcome by FBG sensors. However, the developed system must still consider appropriate sensor placement, ease of installation, gauge lengths, and procedures for protecting and replacing sensors. In addition, FBG sensors present some additional challenges that are not discussed in this paper, such as appropriately tensioning fibers, and adequately spacing the wavelengths of multiplexed sensors. These topics are addressed in this thesis.

In previous work performed at the University of Wyoming, techniques were developed for embedding FBG sensors into notches in concrete members using high-strength epoxy. These notches could either be formed into the member during casting or cut in to the face after curing using common tools like a masonry saw blade. Tests were also performed to validate the effectiveness of surface-mounting FBG sensors to steel using cyanoacrylate adhesive. Both methods showed satisfactory strain measurement. The results of these studies are summarized in Maurais (2012).



The FBG sensors used in the study by Todd, et al. (1999) were installed on steel girders using a cyanoacrylate adhesive and protected with a silicone RTV sealant. This method of protection is simple to apply and provides protection from weather. However, it may not be adequate to withstand vandals and wildlife.

In Doornink, et al. (2006) FBG sensors were embedded in carbon fiber reinforced polymer packaging, which is commercially available, and installed on steel bridge members using cyanoacrylate adhesive. The strain measurements showed excellent agreement with the traditional strain transducers that were installed to verify the accuracy of the FBGs.

A different type of fiber optic sensor, called a Brillouin Optical Time-Domain Reflectometry sensor, was used in Matta, et al. (2005). The installation required for this type of sensor is similar to that required for FBG sensors. For this study, the researchers ordered the fibers to be factory-embedded into an FRP tape. The sensors and tape were then adhered to the steel bridge girders using a two-part epoxy encapsulation resin. Prior to adhering the sensors, the steel was prepped by manually roughening the surface with steel brushes and applying a lacquer thinner for degreasing.

### **2.3 GUIDELINES AND CODES RELATING TO LOAD TESTING**

The Second Edition of the AASHTO Manual for Bridge Evaluation (AASHTO 2010) is the primary specification used for evaluating the condition and capacity of bridges. Chapter 8 of this specification deals specifically with evaluating the capacity of a bridge through nondestructive load testing. Procedures are set forth for analyzing the results for both proof load tests and diagnostic load tests to calculate safe load ratings.

The procedures set forth in this load testing chapter of the specification are adapted from the Manual for Bridge Rating through Load Testing (A.G. Lichtenstein and Associates, Inc. 1998) published by the NCHRP. The recommendations from the NCHRP report were adjusted to align with the Load and Resistance Factor Rating (LRFR) procedures and incorporated into the AASHTO specifications.

The AASHTO specification does not specify strict procedures for performing load tests, but rather it allows engineers the latitude to use their judgment to determine the appropriate procedures depending on the bridge being tested. The NCHRP manual provides more background and recommends more specific procedures for performing and analyzing load tests.

There are some areas where the specification deviates from the original report. For example, the NCHRP manual recommended that incidental composite action may be included in the load rating of a bridge if analysis showed that the shear stress at the interface between the girder and deck was less than a specified threshold. However, the AASHTO specification states that incidental composite action should not be included in the calculation of the bridge capacity.

Both manuals suggest that the vehicle used for load testing should have a similar load configuration to the vehicle that the bridge is being rated for. A load vehicle that has a similar configuration to the HL-93 design truck is often used. If a bridge is being rated for a specific permit vehicle, then a test vehicle with a similar load configuration to the permit vehicle is recommended. Additionally, for diagnostic tests, the test vehicle should have a sufficiently large load in order to accurately predict whether elastic behavior will persist at the rating level

based on results of the test. The AASHTO specification does not recommend increasing a load rating if the test vehicle used is less than 40% of the desired load rating. In order to take full advantage of the diagnostic load test results, the rating specification requires a test vehicle with a weight at least 70% of the desired load rating.

The specification lists the following steps as a general procedure for developing and documenting a load rating using nondestructive load testing. This thesis focuses on developing procedures that address steps 2-5 for a system using FBG sensors.

1. Inspection and theoretical load rating
2. Development of load test program
3. Planning and preparation for load test
4. Execution of load test
5. Evaluation of load test results
6. Determination of final load rating
7. Reporting

The two references discussed above focus on load testing and load rating of bridges. The Federal Highway Administration published a technical report (Aktan, et al. 2003) that provides guidance for designing and operating structural health monitoring systems intended to assess the structural reliability and lifecycle of bridges. This report offers insight from the infrastructure network management perspective, and suggests the use of load tests and modeling to assess and predict structural deterioration over the life of the structure. The report does not attempt to codify any procedures, rather it offers an overview of the state of the art, and provides a discussion of the major parameters that should be considered by an SHM system. This report also suggests a higher level "fleet monitoring" approach, in which statistical sampling of representative bridges outfitted with SHM systems is used to prescribe

appropriate maintenance regimens for all similar bridges based on measured and predicted deterioration models. This approach is similar to that used in the aviation industry to adequately maintain fleets of airplanes. This report suggests the following procedure for the design of an SHM system:

1. Characterize the structure and the monitoring
2. Identify the phenomena to be measured and characterize the parameters that will be measured
3. Select the sensors and data acquisition components
4. Calibrate system and verify suitability of components
5. Devise methods for data quality assurance, processing, and archival
6. Develop presentation and decision criteria

This thesis addresses steps 3, 4, and the processing aspect of step 5.

## **2.4 LOAD TESTING CASE STUDIES**

It was proposed by Cardinin and DeWolf (2008) that structural damage could be detected by monitoring structural properties for changes. Changes in distribution factors or maximum strain could indicate damage in the girders, and changes in the neutral axis depth or distribution factors could indicate damage to a concrete deck. However, because this is a long term monitoring project, and no deterioration has been observed in the structure yet, they were unable to verify the effectiveness of these methods. Monitoring the structure for maximum strains would provide the load-history data necessary for analyzing critical fatigue details. All of the parameters discussed in the paper can be determined from strain measurements.

A novel application of structural health monitoring was outlined by Okasha, Frangopol, and Orcesi (2011), in which the data from periodic diagnostic load tests was

automatically incorporated into a finite element model using an optimization algorithm. The updated FEM model was then used to adjust the resistance parameters of a structural reliability model for the structure to match the properties determined by the load test. This reliability model was then analyzed for a large sample of statistical simulations based on a characteristic extreme value distribution of loading and degradation parameters in order to predict its remaining lifecycle performance. This approach was used in a case study on a bridge on I-39 in Wisconsin. The updated reliability model for the bridge based on the load ratings resulted in an increase in the cumulative time failure probability function.

The appendices of Aktan, et al. (2003), which are summarized in the following paragraphs, provide an overview of a number of structural health monitoring projects that have been performed or are currently in service. Most of these involve monitoring major bridges for critical loading effects and providing instant alerts of critical behavior. However, a few novel applications are described as well.

- Appendix H describes a monitoring system that was installed on a bridge prior to construction in order to measure the structural response due to construction and service. The installed sensors measured the stresses induced by different loads at different resistance stages. The readings taken during construction provided an estimate of the locked-in stresses induced by the dead loads at points of interest.
- Appendix J summarizes the results of monitoring three bridges for damage caused by a permitted super-load vehicle. A diagnostic load test was performed to ensure the bridges had adequate capacity, and the models predicted that no permanent damage would occur. The bridges were monitored during the passage of the super-load vehicle, and an

additional diagnostic load test was performed after the event to measure any change in structural behavior. Based on the analysis of the event and comparisons of the two diagnostic tests, the owner concluded that no damage had occurred to the bridges from the overload event.

- Appendix K describes the application of the "fleet monitoring" concept for a population of approximately 1,600 T-beam bridges that were all constructed from standard design plans. Thus, bridges of similar spans were designed to be essentially identical. The purpose of the fleet monitoring is to develop a standard maintenance regimen for a population of similar bridges that will be susceptible to similar deteriorations during their lifecycle. When it is observed that maintenance is necessary on a representative bridge, this method recommends performing the prescribed maintenance on all similar bridges in the fleet. The variables that affected load ratings were assessed, and based on statistical distributions, it was determined that 60 representative bridges could be used to describe the condition of a fleet of 1,600 bridges. These representative bridges were subjected to varying levels of in-depth inspection, analysis, and diagnostic load testing. Based on the results of this analysis combined with statistical reliability analysis and inspection of the population, the authors determined that it would be possible to increase the load rating of the fleet of similar bridges by 6% to 40%.

A.G. Lichtenstein and Associates, Inc. (1998) provides an appendix that summarizes a number of load tests that have been performed to load-rate bridges. This summary includes both diagnostic tests and proof tests. For the majority of the structures tested, engineers were able to increase the load rating for the bridge, and for a number of structures, they were able

to remove load postings. The increase in load rating was significant for a number of bridges, on the order of 10% or more.

For five bridges out of 15 that were subjected to diagnostic load tests, the results confirmed deficient behavior and the load restrictions continued to be enforced. Of the seven reported proof load tests, four tests resulted in a more favorable load rating, while the remaining three tests indicated critical behavior and resulted in a decreased load rating for the bridge. These latter proof tests were especially critical, as all of these bridges were already under posted load restrictions.

Chajes, Sheton III and O'Shea (2000) performed diagnostic load testing on a bridge in Delaware, and based on the refined distribution factors calculated from testing, they were able to increase the load rating of the bridge by 15%. This increase was enough to remove load restrictions from the bridge, which opened up a more direct route for overweight vehicle traffic traveling through the state. This load test prevented state engineers from prematurely replacing the structure in question.

Seven bridges were load tested in North Carolina by Lawrence, Ritter, and Gergely (2011). The results of these tests indicated little dynamic impact for the live load, and they found distribution factors similar to those determined from the equations in section 4.6.2.2 of AASHTO (2012). While the dynamic impact is generally small, especially for heavier loads, the results of the distribution factor are surprising, as the AASHTO equations for load distribution factors are generally fairly conservative. The load tests indicated that the primary factor affecting the difference between the tested bending behavior and the analytically predicted bending behavior was concrete stiffness and strength. Direct nondestructive tests of

the girder strength confirmed that the concrete was far stronger than the concrete strength used in the analytical load rating, which was assumed to be very low due to a lack of design and as-built information.

Executives from the structural testing company Lifespan Technologies reported in an editorial (Vanderzee and Cooper 2005) that out of 175 bridges that have been tested, 75% of them possessed higher capacity than traditional analysis had predicted. Additionally, 5% of the tested bridges actually showed a lower capacity than the analysis predicted. These results indicate a high likelihood that testing bridges could result in less restrictive bridge ratings, but they also demonstrate that analytical ratings are not always conservative.



## **CHAPTER 3: EXPERIMENT DESIGN**

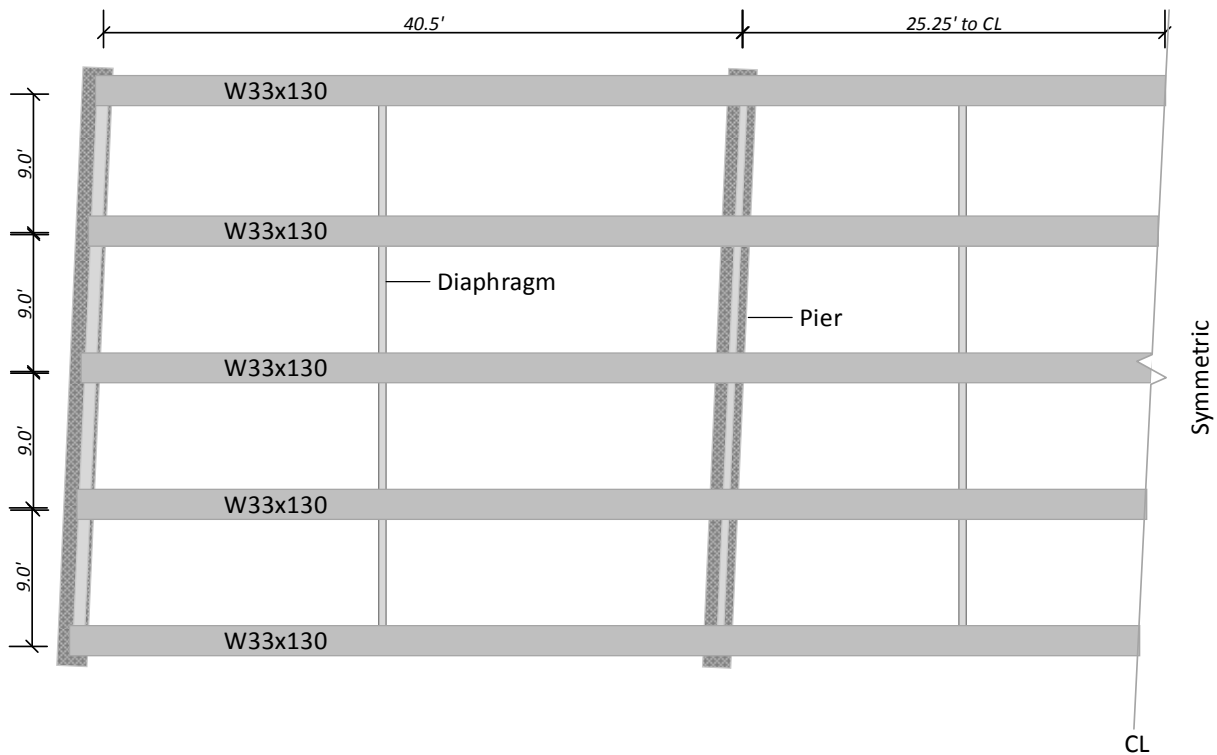
In order to develop sensor installation and data processing techniques, a laboratory model of a bridge and vehicle was designed and constructed. The model bridge consisted of two girders that were vertically supported at four points resulting in a three-span continuous configuration. Utilizing a three-span design allowed for the measurement of bridge behavior undergoing positive and negative bending. In order to develop techniques for sensing both steel and concrete structures, one girder was constructed of a wide flange steel beam, and the other utilized a post-tensioned concrete beam.

The design of the experiment was loosely modeled after a three-span bridge on Interstate 80, west of Laramie, Wyoming, which is targeted to serve as the site of the field study in the next phase of research. Analysis of this bridge provided some approximation of the magnitude of measurements that will be required of the resulting system. The field study will provide an opportunity to field test the methodology developed in this study.

### **3.1 FIELD BRIDGE ANALYSIS**

The field bridge that was approximated in the lab consisted of a three-span, continuous, non-composite steel girder design, utilizing W33x130 rolled-section girders spanning 40.5 feet, 50.5 feet, and 40.5 feet for a total length of 131.5 feet. The as-built plan view of the girder layout is provided in Figure 3.1. The bearing supports for this bridge consisted of sliding plate style connections. A girder-line model of this bridge was developed using SAP2000 (Computers & Structures, Inc 2011) finite element structural analysis software. In order to approximate the magnitude of curvature that would be induced by a typical diagnostic vehicle, the model was analyzed for an HL-93 design truck, where it was

assumed that one-half of each axle load would distribute to the beam-line, and no lane load was applied. Service-level loads were used to demonstrate that the SHM system will be capable of measuring the structural response of a bridge under elastic conditions. Based on this loading, the maximum curvature in the bridge was found to be  $0.000287 \text{ ft}^{-1}$  corresponding to a maximum strain in the extreme fiber of the cross-section of  $792 \mu\epsilon$ .



**Figure 3.1. Half Framing Plan of Field Bridge**

### 3.2 LABORATORY SCALING

Because the parameter being directly measured by the FBG sensors is strain, the laboratory experiment was designed to achieve the same maximum strains as those determined from analysis of the I-80 highway bridge. Due to constraints on support locations for the laboratory bridge, the span ratio for the laboratory setup was modified slightly, and the

laboratory beams spanned 9 feet, 12 feet, and 9 feet for a total length of 30 feet. This resulted in the average ratio of laboratory to field spans of 1:4.4.

In order to utilize the lightest loads possible for the sake of laboratory safety, a small cross-section rolled wide flange beam (W4x13) was used to form one girder for the laboratory bridge. Based on the flexural rigidity (modulus of elasticity and moment of inertia) of this section, the load necessary to induce a strain in the extreme fiber of the section equal to that predicted by the analysis of the highway bridge mentioned above was calculated by scaling the loads according to the section depths and resulting curvatures as illustrated below.

The relationship between moment and strain is given by:

$$\varepsilon = \frac{Mc}{EI} \quad (3.1)$$

where:  $M$  = moment  
 $E$  = modulus of elasticity  
 $I$  = moment of inertia  
 $\varepsilon$  = strain  
 $c$  = distance to the location of strain from neutral axis

By approximating the maximum moment as the moment induced by a point load  $P$  at mid-span of a simply supported beam,  $M = \frac{PL}{4}$ , and the distance from the neutral axis to the extreme fiber as  $c = \frac{d}{2}$ , where  $d$  is the total depth of the section, the strains in the laboratory beam were set equal to that of the field girder yielding:

$$\frac{d_L P_L L_L}{8E_L I_L} = \frac{d_F P_F L_F}{8E_F I_F} \quad (3.2)$$

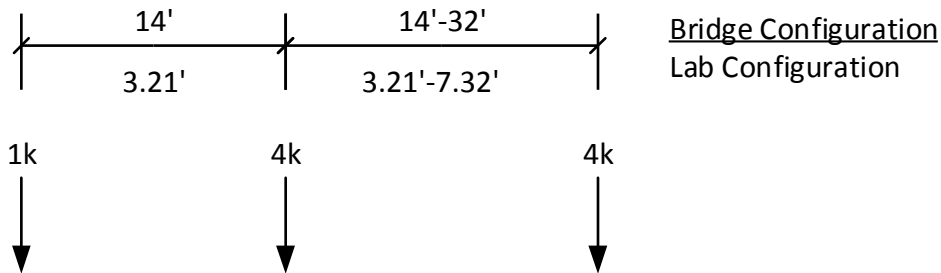
The subscripts  $L$  and  $F$  indicate values for the laboratory and field bridges respectively. Rearranging these terms gives:

$$P_L = \frac{d_F L_F E_L I_L}{d_L L_L E_F I_F} P_F \quad (3.3)$$

Substitution of the appropriate values gives  $P_L = 0.056P_F$ .

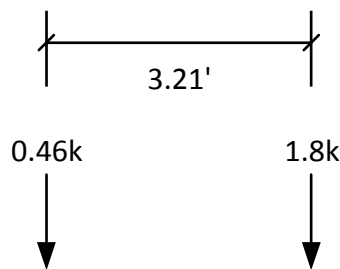
As an alternative analysis, the two span configurations were modeled in SAP2000 (Computers & Structures, Inc 2011), where a moving load was applied to each beam with the corresponding load configuration shown in Figure 3.2. The resulting maximum moments from the analysis were substituted into Equation 3.4. As the load effect is linearly proportional to the axle loads, this ratio gives the appropriate scaling for the laboratory loads. The result of this analysis was  $P_L = 0.057P_F$ , which is close to the value obtained by the original approximations.

$$\frac{M_L}{M_F} = \frac{d_F E_L I_L}{d_L E_F I_F} \quad (3.4)$$



**Figure 3.2. Load Configuration of Moving Load Applied to SAP2000 Finite Element Model of Field Bridge, and Lab Bridge**

Applying the scale factor to the loads for an HL-93 Design Truck resulted in a leading axle weighing 0.46 kips, and a trailing axle weighing 1.8 kips for the laboratory load vehicle. A third axle did not significantly impact the controlling load case, and was therefore omitted. The spacing of the axles was determined by dividing the 14 foot axle spacing for the HL-93 design vehicle by the laboratory span scale ratio of 4.40, resulting in an axle spacing for the test vehicle of 3.21 feet. The resulting load configuration for the laboratory test vehicle is shown in Figure 3.3.



**Figure 3.3. Load Configuration of Laboratory Test Vehicle**  
(Loads displayed are per axle.)

The post-tensioned concrete beam was sized to produce approximately the same flexural rigidity as the steel beam while providing adequate strength to carry the required loads. The resulting section was a rectangular beam 6 inches deep by 4.5 inches wide. Use of a pre-stressed beam allowed the beam to undergo the desired curvatures for the experiment while still supplying adequate strength to carry the necessary loads.

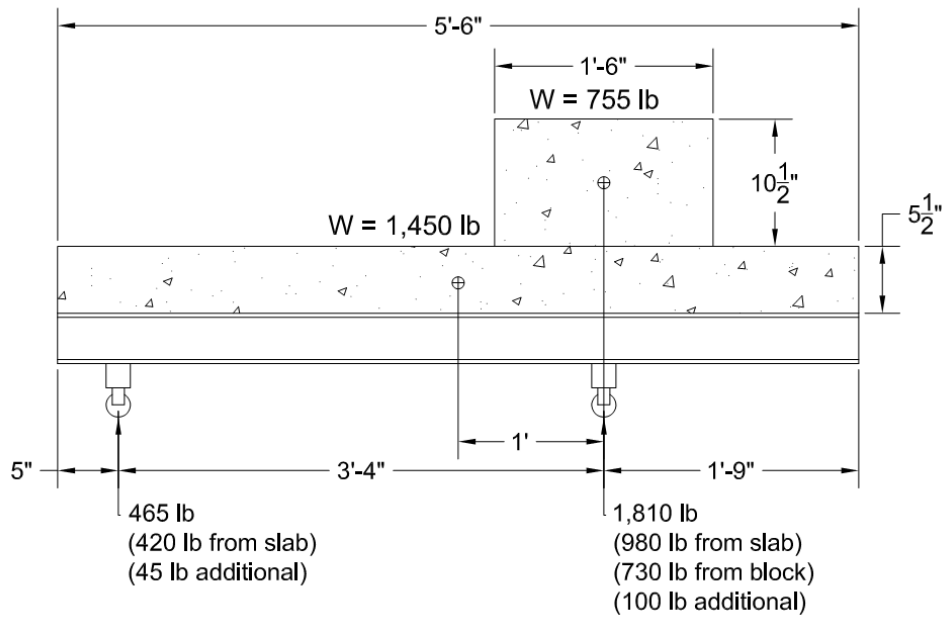
It was assumed that the axle loads evenly distribute between the two beams, and that they would both experience the same curvature due to the equal flexural rigidities. However, the concrete beam, due to its deeper cross-section, would experience a 33% larger strain in the extreme fibers.

### 3.3 EXPERIMENTAL SETUP

In the laboratory, the steel beam and the post-tensioned concrete beam were laterally spaced 3 feet apart. The beams are shown in Figure 3.5. At support locations, the beams bore on steel plates 4 inches wide in the direction of the span. This support configuration is similar to the conditions encountered in the field bridge where the girders bear on sole plates. At the mid-support locations, the beams were not attached to the supports to resist uplift. At the end-supports, the beams were attached with two hand-tightened bolts in order to provide stability to the system while still allowing rotation about the lateral axis. At each end of the two beams, there was a six-foot long runoff span to allow the load vehicle to completely exit the model bridge, allowing for the measurement of the unloaded structure. Steel angles were mounted along the entire length of the laboratory setup to provide a track for the load cart to ride upon. These angles were continuous across the 30 foot test beams and only attached at the end in order to minimize any stiffness contributions from the angles. There was a joint between the angles on the test spans and the angles on the runoff spans to ensure that there was no load transference when the cart was not on the test beams.

The load cart consisted of a concrete block, a concrete slab, two mounting beams, four load cells, and four non-swiveling V-notched casters. The wheel locations were determined to approximate the load configuration in Figure 3.3. The concrete block was placed directly above the rear wheels. A schematic of the load cart design is shown in Figure 3.4. Figure 3.5 shows the constructed laboratory experiment with the load cart.

Width of Cart & Block = 46"



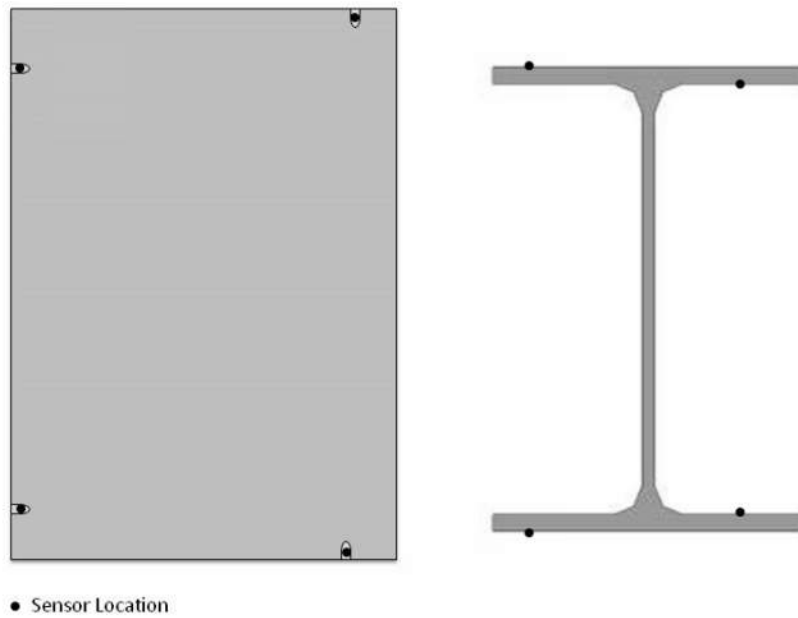
**Figure 3.4. Schematic of Load Cart for Laboratory Test**  
(Loads displayed are per axle)



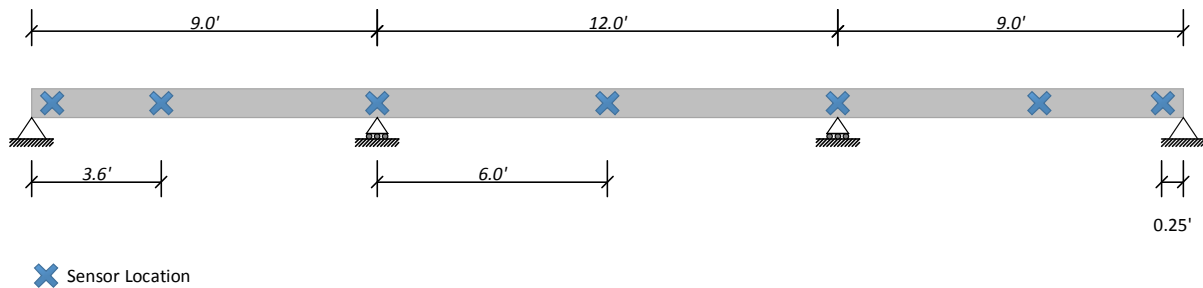
**Figure 3.5. Laboratory Test Setup**

### 3.4 SENSOR LOCATIONS

A total of 56 FBG sensors were installed on the beams for the laboratory experiment. For each beam, four sensors were installed about each beam cross-section at seven locations along the span of the beam. Figure 3.6 shows the sensor placement on the cross-section of each beam, and Figure 3.7 shows the locations of the sensors along the length of the beams.



**Figure 3.6. Sensor Locations on Beam Cross-Sections**  
Left: Pre-stressed concrete beam, Right: W4x13 steel beam



**Figure 3.7. Sensor Locations Along Beam Length**

On the cross-section of the beam, sensors were placed at the extreme fibers of the section for strong-axis bending to measure the curvature of the beam and the neutral axis



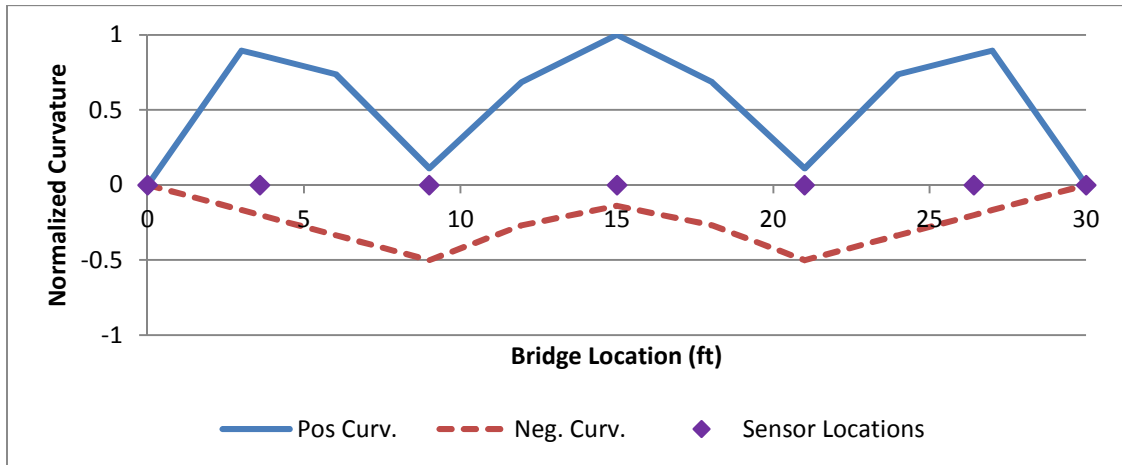
depth. Measuring strain at the extreme fibers allows the strain sensors to read larger measurements for the same value of curvature.

In practice, it may not always be possible or desirable to install sensors at the extreme fibers due to obstructions, cosmetic concerns, etc. In which case, the sensors would need to be installed on the interior of the section. In this configuration, sensors would be required to measure smaller values of strain. To show that the sensors are capable of measuring these smaller strains and producing reliable results, the second configuration of sensors was installed on the interior of the cross-sections. For the steel beam, the sensors were installed on the inside of the flanges, and for the concrete beam, the sensors were installed in the sides of the section.

Typically, three-span bridges achieve the maximum load effects due to bending over the supports, at mid-span of the middle span, and at approximately 40% of the span in from the end supports on the exterior spans. This rule of thumb is reflected in the AASHTO LRFD Design Specifications (2012) in the section discussing the calibration of the HL-93 live load and load factors and was echoed in discussions with WYDOT officials regarding points of interest for curvature measurement. Therefore, these locations were selected to take measurements on the bridge. The sensors placed at the end supports allowed for the measurement of rotational fixity in the supports, and the sensors located between the supports aided in determining the stiffness parameters of the beam. Furthermore, having the sensors at these locations would allow officials to monitor the maximum load effects on the structure to determine if critical behavior is experienced.

The span configuration was modeled in SAP2000 (Computers & Structures, Inc 2011), with a moving unit load used to determine the analytical curvature envelope for the laboratory structure. This distribution is shown in Figure 3.8, where the curvature envelope has been normalized. The maximum positive load effects in the first and third spans would have occurred at 3.00 ft from the ends of the bridge. These maxima are near the sensors placed at the 1.04 and 3.06 span locations, which were 3.60 ft from the ends of the bridge. According to the simulation, the curvature at the maximum locations in the exterior spans was 3.52% higher than the curvature at the sensor locations. For the middle span, the analytical model calculated that the maximum positive curvature would occur at the mid-span where the sensors were located.

The analytical models indicated that the maximum negative load effects would occur over the supports for the structure, as would be expected. Sensors were placed as near to the ends of the beams as possible to measure any curvature due to rotational fixity in the end supports. For the steel beam, sensors were placed within 2 inches of the end. However, sensors on the concrete beam needed to be moved in approximately 8 inches from the ends due to requirements for strain averaging and adhesive development length, which are discussed in detail later. Because the sensors in the tests were inset along the span due to interference from connections, they could only measure the moment near the ends of the beam, but not at the ends. However, as the analytical moment distribution was linear for the loading, the curvature at the end of the beam was found by linearly extrapolating from the values at the sensor locations.



**Figure 3.8. Analytical Curvature Envelope for Laboratory Beam**

The 1.04, 2.05, and 3.06 span locations are typical rule-of-thumb estimates for predicting the location of maximum moment in a continuous three-span bridge. These were reasonably close to where the maximum moments occurred in the lab test. However, it would be better practice to perform structural analysis on an analytical model of the structure to determine the locations of the maximum load effects, as different geometries will result in different behavior for each bridge.

Placing sensors at the locations where the maximum load effects will occur is important for accurate load rating of a structure, as the maximum values measured by the sensors will form the basis for the load rating. While structural analysis and extrapolation may be used to determine the maximum effects, advanced planning to measure these maximum effects directly would be a better approach.

## **CHAPTER 4: INSTALLATION TECHNIQUES**

Methods were developed for installing, protecting, and replacing FBG sensors on bridges. These installation techniques were developed while instrumenting the steel and concrete beams used in the laboratory experiment. Of primary concern was the feasibility and ease of using the installation methods in the field, the durability and ruggedness of the sensing system, and the practicality of repairing damaged fibers or sensors once installed.

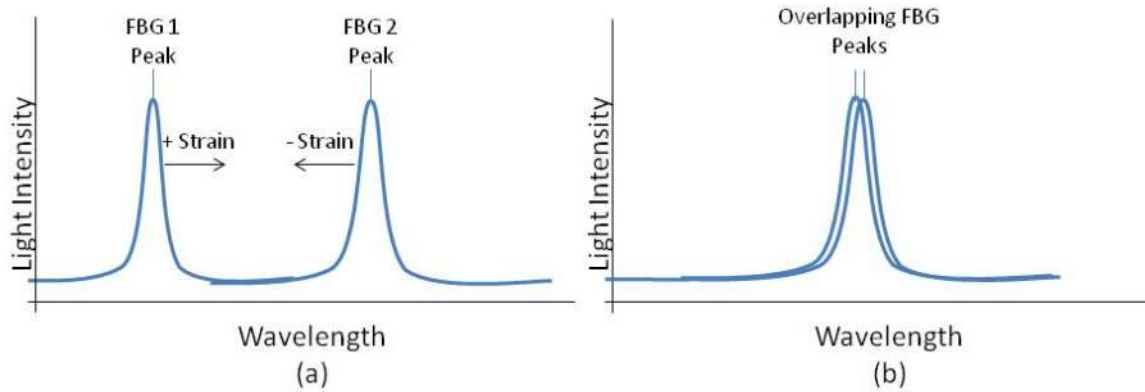
### **4.1 MULTIPLEXED SENSOR SYSTEM DESIGN**

Multiplexing, or the ability to attach multiple sensors on a single channel, is one of the main advantages of using an FBG based SHM system. It allows a single interrogator, which is generally the most expensive component of an FBG based system, to read a large number of sensors. Ideally, a single interrogator would be used to read all of the sensors on a bridge.

For a multiplexed FBG system, a sensor plan should be carefully developed prior to installing any sensors, to ensure that the operating wavelength spectrum of each channel of the interrogator is efficiently utilized. The operating spectrum of an interrogator is often the largest constraint on the number of sensors that can be effectively multiplexed, and interrogators with wider spectra or more channels will incur significant costs.

Therefore, consideration must be given to the wavelength range that multiplexed sensors will experience under operating conditions. If the reflected peaks from two FBG's on the same channel overlap during operation, interrogators cannot differentiate the light returning from the two sensors, and the reflected light will register as a single peak returning from a single FBG. This overlapped peak confuses the data collection, and renders those sensors ineffective. This problem occurs if the unstrained FBG peaks are not spaced far

enough apart on the wavelength spectrum to allow for the wavelength shift caused by the strain conditions. An illustration of this issue is provided in Figure 4.1.



**Figure 4.1. Interrogation Overlap Due to Inadequate Sensor Spacing**  
(a) Unstrained sensor reflected peaks, (b) Strained sensor reflected peaks

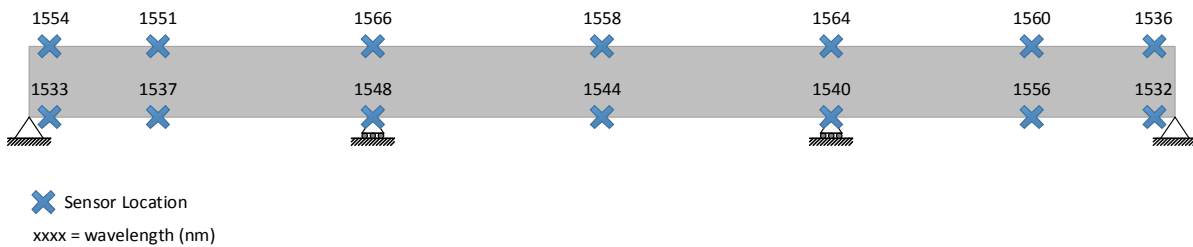
The wavelength spacing can be adjusted by applying different magnitudes of pretension to the fibers while they are being adhered to the structure. Enough pretension can be applied to a fiber to cause a wavelength shift of about 4nm without causing concern for over-tensioning the fiber during the FBG service.

To prevent overlapping peaks, preliminary analysis of the expected structural behavior should be performed to determine the appropriate location and pretensioning necessary to place multiplexed FBGs with adjacent wavelengths. The maximum shift on the light spectrum will be dictated primarily by the maximum strain that the fiber will undergo while in operation. For a maximum strain of 0.003, the corresponding shift in wavelength is approximately 4nm.

The maximum expected wavelength shift due to strain provides an estimate on the necessary spacing between wavelength peaks, but one must be judicious in spacing FBG

wavelengths to also maximize the number of sensors that can be multiplexed onto a single channel. In areas of the structure where large strains are unlikely to occur, the wavelength spacing may be reduced. However, if two fibers possess adjacent wavelength peaks on the spectrum and are likely to experience concurrent opposing strains (one fiber undergoing positive strain, while the other experiences negative strain), bringing the wavelength peaks toward each other, then the wavelength spacing between them should be increased appropriately. Often, care can be taken to place FBGs with adjacent wavelengths in areas of the structure that will undergo concurrent strains in the same direction allowing for a reduction in the wavelength spacing.

A sensor plan, which maps the locations of the FBGs on the structure with their corresponding wavelengths, helps to design an effective layout for the FBG sensors that can efficiently utilize the operational spectrum of the interrogator. System designers must determine appropriate wavelength spacings for the strains expected in the structural locations being measured. A sample sensor plan, which was used in the laboratory experiment design, is provided in Figure 4.2.



**Figure 4.2. Sensor Schematic for Sensors Placed at Extreme Fibers of Concrete Laboratory Beam**

## 4.2 TEMPERATURE COMPENSATION

FBG sensors are sensitive to changes in temperature and are not self-compensating for temperature variations. Therefore, it is necessary to separate the wavelength shift due to temperature variation from the wavelength shift due to mechanical strain in the host material. While the relationship between temperature and wavelength shift is well established (4.1), measuring temperature introduces complexity to the system. It is easier to measure the temperature effect on wavelength directly by using an FBG that is isolated from mechanical strain, and directly subtracting this apparent strain from the other bonded sensors on the structure to determine the resulting mechanical strain. The computations for this procedure are illustrated in the following.

The relationship between temperature change  $\Delta T$  and wavelength shift is given by:

$$\Delta\lambda_T = \lambda_0(\alpha_A + \alpha_\eta)\Delta T \quad (4.1)$$

(Chen and Lu 2011)

where:

- $\Delta\lambda_T$  = wavelength shift due to temperature change
- $\lambda_0$  = base wavelength of FBG
- $\alpha_A$  = thermal expansion coefficient of fiber ( $\approx 0.55 \times 10^{-6}/^\circ\text{C}$ )
- $\alpha_\eta$  = thermo-optic coefficient ( $\approx 8.60 \times 10^{-6}/^\circ\text{C}$ )
- $\Delta T$  = change in temperature

For a given change in temperature, the strain sensing FBG would read a total wavelength shift of:

$$\Delta\lambda = \Delta\lambda_M + \Delta\lambda_T \quad (4.2)$$

where:

- $\Delta\lambda$  = total wavelength shift
- $\Delta\lambda_M$  = wavelength shift due to mechanical strain
- $\Delta\lambda_T$  = wavelength shift due to temperature change

Rearranging the relationship between wavelength shift and strain presented in equation 1.2 gives:

$$\Delta\lambda_M = \lambda_0 G \varepsilon \quad (4.3)$$

where:  $G = \text{FBG gauge factor}$   
 $\varepsilon = \text{strain}$

Substituting for  $\Delta\lambda_M$  and  $\Delta\lambda_T$  gives:

$$\Delta\lambda = \lambda_0 G \varepsilon + \lambda_0 (\alpha_A + \alpha_\eta) \Delta T \quad (4.4)$$

The value for  $\Delta T$  can be obtained by the temperature compensating FBG by rearranging equation 4.1:

$$\Delta T = \frac{\Delta\lambda_{TC}}{\lambda_{0TC} (\alpha_A + \alpha_\eta)} \quad (4.5)$$

where the subscript TC denotes the values are obtained from the temperature compensating FBG sensor. Substituting equation 4.5 into equation 4.4 and simplifying results in the formula:

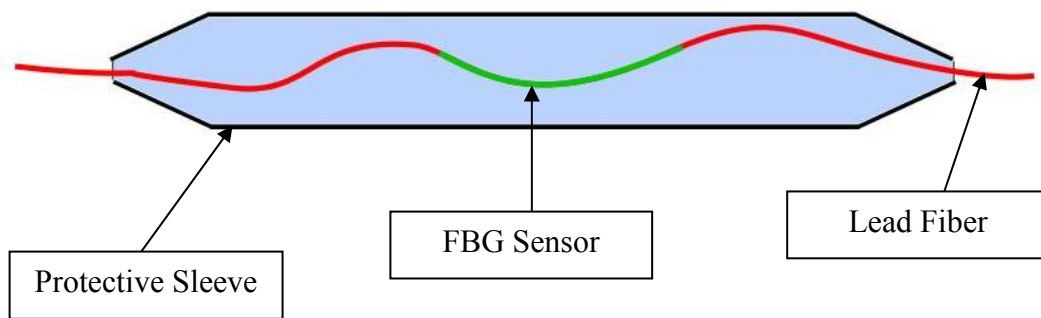
$$\Delta\lambda = \lambda_0 G \varepsilon + \frac{\lambda_0}{\lambda_{0TC}} \Delta\lambda_{TC} \quad (4.6)$$

Then solving equation 4.6 for strain  $\varepsilon$  gives the equation for field measured strain using a temperature compensating FBG sensor:

$$\varepsilon = \frac{\Delta\lambda - \frac{\lambda_0}{\lambda_{0TC}} \Delta\lambda_{TC}}{\lambda_0 G} \quad (4.7)$$



To measure the thermal effect on FBG readings, it was necessary to develop a method for isolating an FBG sensor from mechanical strain while providing adequate protection to ensure durable operation. To achieve this, an FBG sensor was inserted into a protective heat shrinking tube, which is typically used for protecting splices in optical fibers. Using a heat source, one of the tips was heated until it shrank and secured a bond with the fiber. Then the fiber was compressed to induce a buckled shape inside the protective sleeve. Then the other tip was heated to lock the fiber into place while being careful to maintain the buckled shape. The resulting protective sleeve was pinched at the ends, and a gap remained in the middle to allow the sleeve to expand and contract as temperature fluctuates without inducing mechanical strain in the fiber. The devised encasement for a temperature compensating FBG is illustrated in Figure 4.3.



**Figure 4.3. Temperature Compensation FBG**

### **4.3 SENSOR INSTALLATION**

In adhering the fiber Bragg gratings to bridges, care must be taken to ensure good strain transfer and reliable readings. The fibers need to be aligned along the desired axis of strain measurement, and it must be ensured that the fibers are securely attached to the host

material without any slack or buckling in the fiber across the sensing region. Slack and buckling in the fiber is prevented by applying a slight pretension to the fiber while adhering it to the host element.

While a nominal amount of pretension is necessary to ensure a sensor is installed straight and with a good bond, the specific amount of pretension necessary will be dictated by the wavelength required by the sensor plan. Often the sensors provided by an FBG manufacturer may not have base wavelengths corresponding to the necessary peak wavelengths required by the sensing plan. The peak wavelength can be increased by as much as 4 nm by applying pretension to the sensor during installation on the structure. Care must be taken not to over-tension the FBGs, as they can be brittle and have a tendency to break across the sensing region, which is slightly weakened during the manufacturing process (Li, Ren and Li 2012). Therefore, when ordering FBGs it is important to order sensors with base wavelengths that vary all across the effective spectrum of the interrogator.

It was desired to develop a simple and effective method for adhering FBG sensors to steel and concrete elements. Of primary concern was achieving an effective bond capable of delivering adequate strain transfer to the FBG and devising an efficient method for installation that would be simple to perform in field conditions.

After an FBG is installed, the sensor and lead fiber must be protected from weather, vandals, and wildlife. For the portions of the optical fiber between sensors or leading to the interrogator, a much more durable fiber that is secured in a 900 micron plastic sleeve should be spliced in. This additional sleeve provides much more flexibility and durability than the

standard acrylate coating. However, it would still be vulnerable to wildlife and vandals; so additional protection methods may be necessary.

Separate methods were developed for installing, protecting, and replacing FBG sensors for steel and concrete structures. The specific methodology is detailed in the following subsections.

## **Sensing Steel Elements**

### ***Installation on Steel Elements***

As steel is a homogeneous material, the strain sensor can be adhered directly to the region where measurement is desired. It was determined that adhering an FBG directly to the surface of steel elements using cyanoacrylate adhesive achieves satisfactory strain transfer. This was shown in previous work, (Maurais 2012), where an FBG was adhered to a steel dogbone specimen that was also instrumented with a traditional foil resistive strain gage and subjected to cyclic axial loading. The average discrepancy in strain measurements between the FBG and the strain gage at the peak load was 0.13%, demonstrating that this method of adhering FBGs produces strain readings comparable to commonly accepted practices for traditional strain gages. Figure 4.4 shows the test setup used to perform these tests, and Figure 4.5 illustrates the results of the tests.



Figure 4.4. Test Setup for Strain Transfer of Surface Adhered FBG on Steel

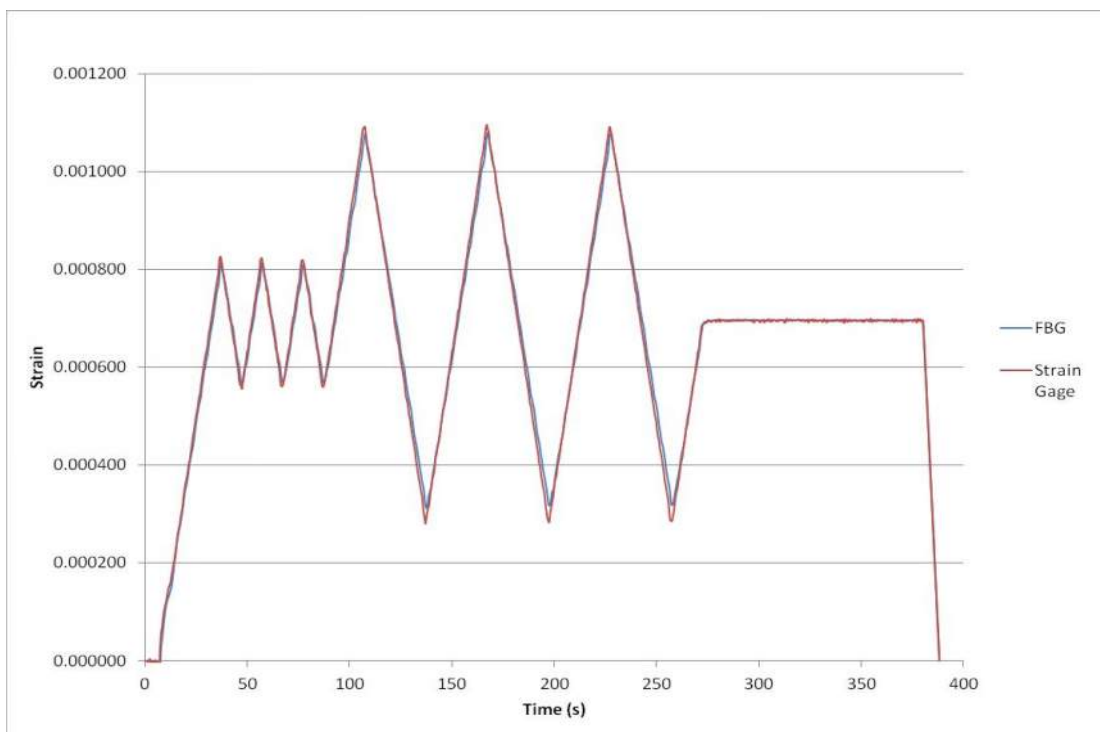


Figure 4.5. Test Results for Strain Transfer of Surface Adhered FBG on Steel

The specific type of adhesive used for the installation procedure on this project was a thickened fast curing cyanoacrylate adhesive called Lightning Bond™, which comes with an activator spray that accelerates the curing process. Loctite™ produces a similar product. Applying the FBGs to the steel material with the proper pretension requires methodical precision. The method devised for achieving an adequate bond with the appropriate pretension is as follows:

1. Remove any mill scale or paint using a grinder or wire brush. Then clean the material surface, removing all oil, and slightly roughen it with sand paper.
2. Carefully mark the location to be measured on the element and draw a straight line along the axis of measurement. Then position the fiber along the axis of measurement so that the FBG region of the fiber is positioned at the location of interest. Then tape one end of the fiber to the structure to aid in aligning the fiber for the next step.
3. Apply the cyanoacrylate adhesive approximately 2 inches away from the sensing region along the axis of measurement. Set the fiber into the adhesive so that the FBG is aligned and positioned correctly and spray the activator over the adhesive region to accelerate the curing process. Hold the fiber in place until the adhesive cures (about 30 seconds).
4. Once the adhesive has cured apply the cyanoacrylate adhesive to the region to be measured ensuring a minimum adhesive length of 1.5 inches. Then, gently adjust the tension on the fiber until the target wavelength is achieved. Next, press the fiber

against the steel so that it is aligned with the axis of measurement and in good contact with the adhesive. Hold the fiber steady, ensuring that it is tensioned to the appropriate wavelength, and apply the activator to the adhesive. Hold the fiber in place until the adhesive cures (about 30 seconds).\*

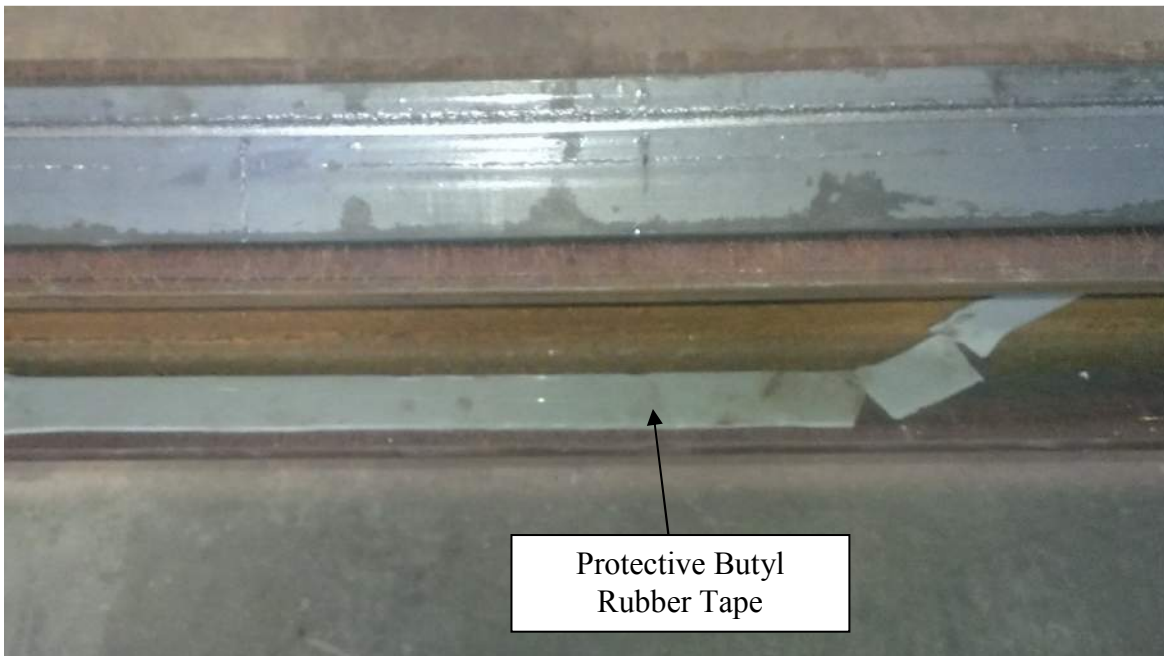
5. Slowly release hold of the fiber while monitoring the wavelength for any significant drop in wavelength. If the wavelength of the applied FBG fails to stabilize at a higher wavelength than the base wavelength, then adequate bond has not been achieved. If a satisfactory bond is not achieved, refer to the subsequent replacement procedure.

\* As an alternative to manually holding the fibers in place while the glue cures, a pair of flat clamps or strong magnets may be used to hold the fiber in tension against the steel member. For this approach, the fiber should be protected from the clamps or magnets using a thin piece of rubber or similar cushioning material. Prior to applying the activator spray, verify that the pre-tension is stable by monitoring the wavelength for any change.

Variations on these methods were tried during the installation of sensors on the laboratory structure as the procedure was refined. The devised attachment method was generally effective. Out of the 28 sensors installed on the steel beam, three experienced a loss of pretension greater than 25% between the time of installation and the time that test were performed. For the remaining sensors, the average pre-tension loss was 9.9%.

### ***Protection on Steel Elements***

For steel material it was decided that covering the fiber with a rugged, durable tape would be the simplest method for providing protection. The tape provides adequate protection and also holds the fibers in place. Fiber with the additional plastic protective coating should be spliced between FBG sensors to provide further durability under the tape. Various tapes were investigated for their bond quality, weatherproof capability, and ability to provide protection. A modified butyl rubber tape produced by Permatite™ was selected as the best option. It is rated for exterior exposure with a temperature range from -40°F to 250°F and a watertight seal. The tape is approximately 1/8" thick with a soft rubber / clay consistency, and it is available in various widths. The tape bonds well to steel, although no long term environmental exposure tests were performed. The steel should be clean and free of mill scale and oil prior to applying the tape. An example of this protection method is shown in Figure 4.6.



**Figure 4.6. Protected FBG Fiber on Steel Beam**

### ***Replacement on Steel Elements***

If a fiber breaks on a multiplexed channel, then the signal from all FBGs beyond the break will be lost. The location of the last FBG reflecting a signal back to the interrogator can be used to locate the break in the optical fiber, as the break will be located somewhere between this last reporting FBG and the next sensor on the fiber. To replace the damaged fiber, at least one foot of the protective tape must be removed from each side of the break to allow enough slack in the fiber to perform a splice. In regions where the lead fiber is protected by the additional sleeve, the tape can be carefully removed with a putty knife. In regions where the fiber lacks this protective sleeve it will be difficult to remove the tape without breaking the fiber.

If the break occurs near a sensor, where a fiber cannot be repaired by simply splicing in an additional length of fiber at the break, the damaged fiber will need to be removed and replaced. Once the tape has been removed, a putty knife or a razorblade can be used to scrape off the old fiber and adhesive. Sandpaper should be used to re-clean and roughen the surface. Then the new FBG can be spliced and installed according to the preceding installation instructions.

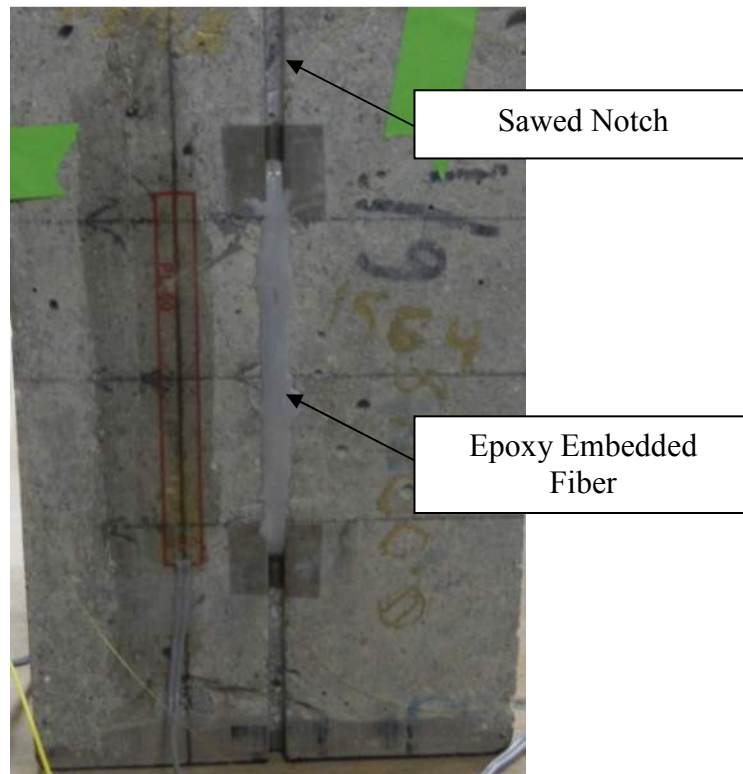
### **Sensing Concrete Elements**

#### ***Installation on Concrete Elements***

Because of the porous nature of concrete, it is difficult to achieve a high-quality, long-lasting bond using cyanoacrylate adhesive. In other studies, FBG fibers have been embedded in concrete using mechanical anchors or affixed to rebar. However the intent of this research was to develop methods for installing an SHM system post-construction. Therefore, a method



was necessary for applying FBG sensors to in-service concrete structures. In previous work (Maurais 2012), a methodology was developed and tested for adhering FBG to concrete by placing the fiber into a shallow channel on the surface, which can be cut using a masonry saw, and embedding the fiber in a stiff high-strength epoxy. The epoxy used in this study was Ultrabond 1300™. The resulting bond is shown in Figure 4.7.



**Figure 4.7. Bond Resulting From Notch Embedded Epoxy Procedure For Concrete Fiber Installation**

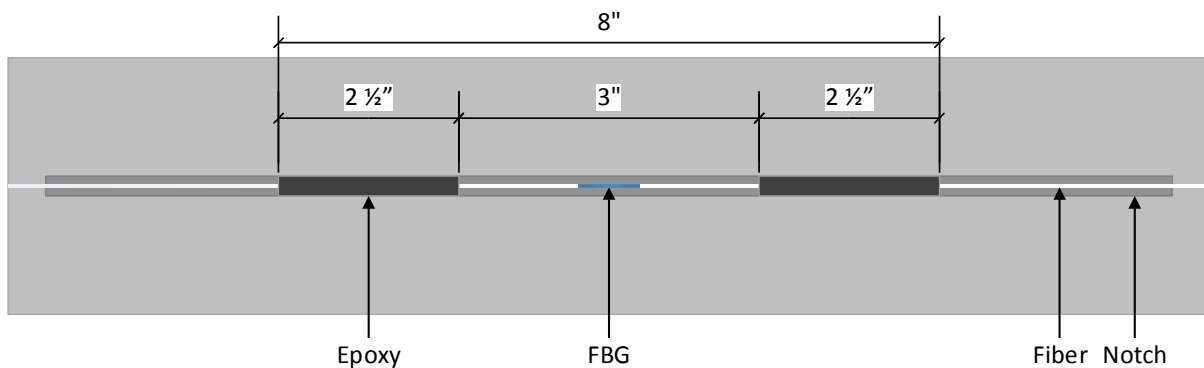
The primary variables that affected the strain sensing ability of the embedded FBGs were epoxy stiffness, embedment depth, and bond length. These effects were studied in finite element models and in laboratory tests, which showed good agreement. Stiff epoxies that possessed an elastic modulus similar to that of the host material produced the best results. Fibers that were embedded near the bottom of the notches presented the best strain transfer.

However, given an adequate bond length, quality strain transfer was achieved even in fibers with non-optimal embedment depths. Based on these tests, a bond length of 2.4 inches (60 mm) was deemed sufficient to achieve adequate strain transfer for fibers embedded at reasonable depths in saw notches 0.125 in wide and 0.125 in deep.

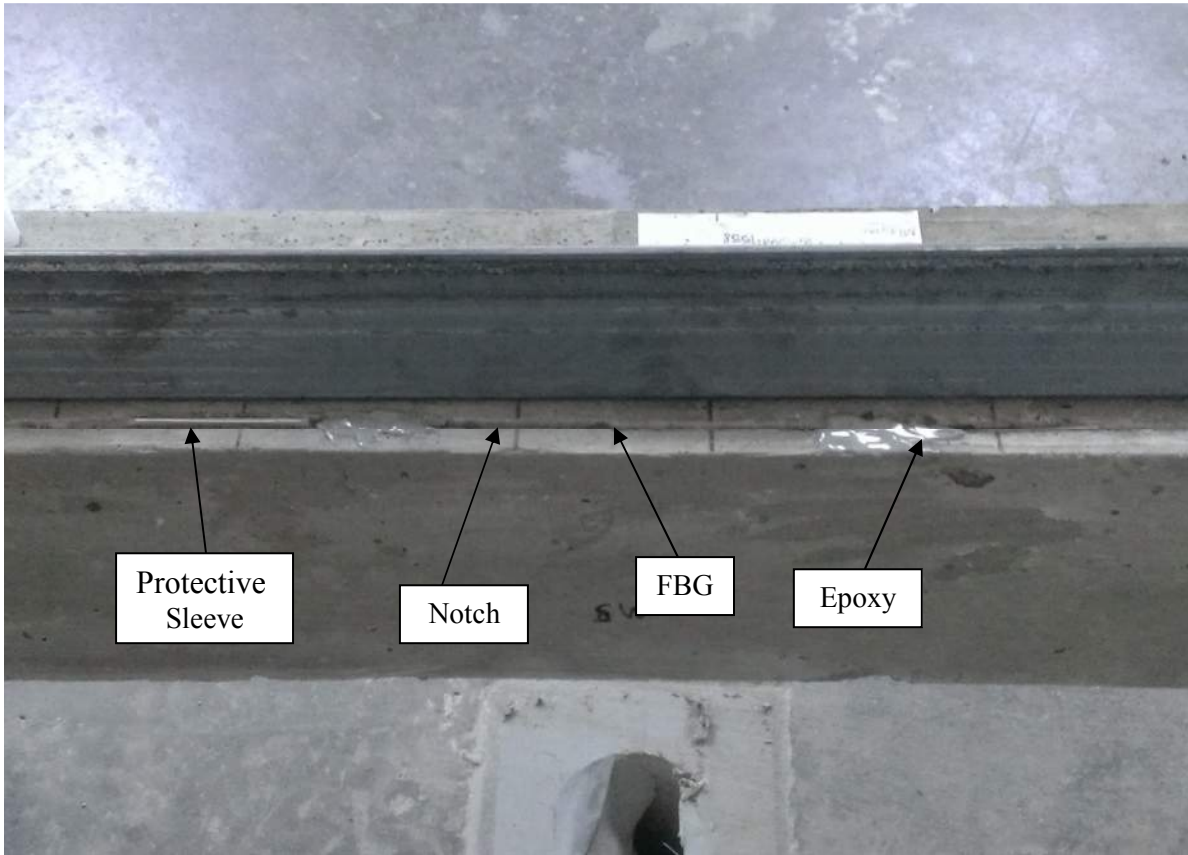
While embedding the fibers in a notch provides a good mechanism for strain transfer, it does present some accessibility challenges for installing fibers with adequate pretension. Furthermore, the majority of high-strength epoxies require at least 24 hours to fully cure. This makes it impractical for the fiber to be held in place manually until the epoxy reaches full strength. Therefore, a procedure was devised to apply an FBG fiber into a notch with adequate pretension and hold it in place long enough for the epoxy to cure. The devised method involves installing a heat shrink protective sleeve on the fiber, which bonds to the fiber and provides a means to grasp and tension the fiber. These protective sleeves can be affixed to concrete using cyanoacrylate. While this bond is not adequate for permanent installation in service conditions, it is sufficient to hold the fiber in place temporarily while the epoxy cures. This procedure is presented in detail in the following installation instructions for concrete.

Unlike steel, concrete is a heterogeneous material and the strain field is not constant across the material. For normal strength concrete, the stiffer aggregate will strain less than the cementitious material. As the strain increases, cracks will form, creating regions where most of the deformation is distributed into crack widening and almost no strain is experienced by the regions between cracks. Thus, it is necessary to average the strain across a long gage length for concrete rather than sensing strain locally. A gage length of 8 inches (20 cm) for concrete and asphalt materials has been suggested (Farhey 2005).

The configuration devised to achieve a long-gage strain sensor with adequate bond length consists of a shallow notch in the host concrete structure with two regions of epoxy approximately 2.5 inches long separated by an unepoxied region of at least 3 inches. The FBG is positioned in the center of the unepoxied region. A diagram of the long-gage FBG strain sensor is shown in Figure 4.8. This configuration shows the minimum gap between the epoxied regions. The strain over the epoxy region may not be truly averaged as the bond is developed. However, in the analysis the strain obtained will be treated as a reading at a localized point, likely located at a point of maximum strain. So using too large of a gage length may dilute the load effect being analyzed. For this experiment, an effort was made to balance these considerations and a gap of 5 inches between the epoxied regions was used. A photo of an FBG installed according to this configuration is shown in Figure 4.9. As the FBG is not directly affixed to the material, it is critical to maintain enough pretension in the fiber to prevent it from reaching a relaxed state during service. Therefore, the maximum expected compressive strain should be considered when determining the proper pretension to apply to the sensors for the system.



**Figure 4.8. Minimum Configuration for Long-Gage Strain Sensing of Concrete Using an FBG**



**Figure 4.9. Photo of Long-Gage FBG Installed on Concrete Beam**

The protocol developed for installing FBGs onto concrete members is as follows:

1. Prior to splicing the FBG into the channel line, slide a heat shrink protective sleeve onto each side of the FBG approximately 5 inches away from the center of the sensor. Being careful to keep the sleeve in place on the fiber, set each sleeve into the heating unit on the splicer to bond it into place. Once the sleeves are in place, the FBG fiber can be spliced onto other fibers or leads following typical procedures.
2. Carefully mark the location to be measured on the host structure and draw a straight line along the axis of measurement. Then, using a 1/8 in thick masonry blade, cut a

straight shallow notch into the beam along the axis of measurement approximately 1/8 inch deep and 12 inches long.

- 3.** Align the fiber with the notch and mark off the locations for the FBG sensor, the unepoxied region (approximately 3-5 inches), the epoxied regions on each side (2.5 inches), and the protective sleeves. Then using these marks as a guide, apply a thin layer of cyanoacrylate adhesive to one of the protective sleeves and position it in the notch. Ensure that it is in the appropriate position, and firmly press it down until the adhesive cures.
- 4.** Using a small flat head screwdriver or similar tool, distribute the epoxy into the bottom of the notch, filling it approximately halfway up in the epoxied regions.  
Note: For sensors being installed overhead or on vertical faces, it may be necessary to wait approximately 10 minutes after mixing the two parts of the epoxy for it to establish adequate viscosity to prevent it from running.
- 5.** Apply a thin layer of cyanoacrylate adhesive to the remaining unattached protective sleeve and to the corresponding region of the notch. Then, gently apply the appropriate pretension to the fiber and press the sleeve into the notch. Firmly hold the sleeve in place to maintain the pretension in the fiber. Then spray the activator on the cyanoacrylate adhesive and continue to hold the sleeve until the bond is secure.
- 6.** Using the flathead screwdriver, fill the epoxy region to the top of the notch with epoxy, being careful not to damage the fiber. Then monitor the wavelength for any

significant drop in wavelength. If the wavelength fails to stabilize above the base wavelength, it indicates an inadequate bond between the sensor and host material. If a satisfactory bond is not achieved, refer to the subsequent replacement procedure.

This procedure was used for installing the sensors on the concrete beam in the laboratory structure. Of the 28 FBG sensors installed using this approach, 3 sensors experienced a loss of pretension greater than 25%, and the average pretension loss in the remaining sensors was 12.9%.

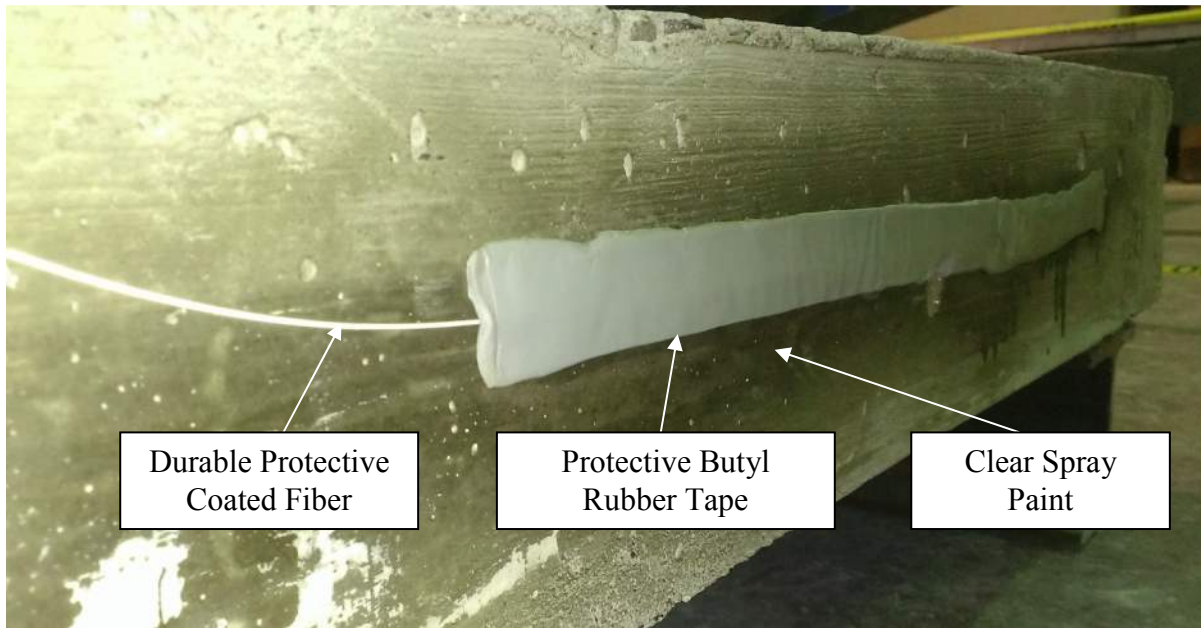
### ***Protection on Concrete Elements***

Affixing protective materials to concrete is more difficult than affixing to steel due to the rough surface, to which the tape does not adhere well. Two methods were developed to protect fibers attached to concrete elements.

The first method requires a more intricate installation process, but results in a more permanent system. However, if for some reason an element in the SHM system breaks, all of the sensors on the channel must be replaced. To begin, a notch is cut the full length of the bridge, and each sensor must be installed so that the fiber lies within the notch for the full length of the bridge. To ensure that the optical fibers fit into the notch, the fibers between sensors must be measured out to be the same length as the notch between sensors, so that the fibers can be installed onto the structure with very little slack. Once all of the sensors have been installed, the entire length of fiber for each channel is laid into the notch and covered with epoxy, except for the unepoxied regions where FBG's have been installed. Over the unepoxied regions, a thin 1 inch wide cover plate, made of either plastic or metal, can be attached to the concrete using epoxy to seal off the notch. This method results in a very

durable, permanent system. However, the installation process is complicated by the necessity of having a taught fiber between sensors, and it can be cumbersome to saw a notch the full length of the bridge. Finally, if a problem is discovered in any of the sensors after the protection system is in-place, then the entire line of sensors must be cut out, and new sensors must be installed.

The second method does not provide as robust protection, however it is easier to implement, and it allows for repairs to be performed without replacing all of the sensors on a channel. For this method, shallow, 1 foot long notches are cut at sensor locations, and the FBGs are installed according to the installation procedure. Between sensors the more durable fiber with a 900 micron protective sleeve is spliced leaving enough slack between sensors to maintain workability. A strip of clear spray paint is applied along the length of the element and allowed to dry in order to produce a smooth surface. Then the fiber is attached to the element using the butyl rubber tape discussed in the steel protection method section. The tape must be pressed firmly onto the concrete to ensure an adequate bond. If there is excess fiber, it can be wound into a loop and covered with butyl rubber tape. Care must be taken not to wind the fibers into too tight of a loop, which would result in a loss of signal. A diameter of about 2 to 3 inches is acceptable. The butyl rubber tape can be installed over the notched regions where sensors are installed, or a thin cover plate may be epoxied into place to provide extra protection for the bare fiber in the notch. A figure of the second protection method is shown in Figure 4.10.



**Figure 4.10. Protection Method 2 for Fibers Installed on Concrete**

### ***Replacement on Concrete Elements***

If protection method 1 was used, and it is discovered that a sensor is not performing, then all of the fiber will need to be removed from the notch, and new sensors will need to be installed. The epoxy may be removed using a file and similar hand tools, or it may be easier to recut the notch using a masonry blade. Once all of the sensors are removed, new sensors must be installed and protected according to the previous instructions.

If protection method 2 was used, the butyl rubber tape can be gently removed from the structure using a putty knife. Care must be taken not to damage the underlying protective coated fiber. If the break occurred along the fiber between sensors, then the disjointed fiber ends can be stripped, cleaved, and spliced according to common practice. The fiber can then be re-adhered to the structure using a fresh strip of the butyl rubber tape.



If the break occurred at, or close to, the sensor, then the sensor will need to be replaced. If a cover plate was used, it should be removed by scraping the underlying epoxy away with a putty knife. Otherwise the butyl rubber tape can be removed by gently pulling it back using a putty knife. Enough of the lead fiber should be liberated to splice a new FBG onto the channel. To remove the old sensor, the epoxy can be removed with a file, and the glued fiber protectors can be pried out using a flathead screwdriver. Once the old fiber is removed and the notch is cleaned, a new sensor can be installed according to the preceding instructions.

## CHAPTER 5: EXPERIMENTAL PROCEDURES

Experiments were performed on each beam to compare the measured behavior of the structure with the predicted behavior from analysis. For each beam, three types of tests were performed; a static test, a pseudo-static (crawl-speed) test, and a full-speed test. These are typical of the types of tests traditionally performed in load rating tests for bridges.

The static test provides the most reliable results, as there is less uncertainty about the position of the load, and any dynamic amplification is eliminated. The goal of the crawl speed test is to approximate the results of the static test with a less time-consuming method. Crawl speed tests were performed in the lab to verify their accuracy. Dynamic test results are typically compared to static or pseudo-static tests in order to calculate a dynamic impact factor.

During each test, three parameters were measured: the location of the wheels, the magnitude of the loads applied by the wheels, and the strains measured by the FBG sensors. In order to correlate these data, a stopwatch was used along with the timer mechanism built into the data acquisition software.

Due to fluctuations in the load distribution to the wheels of the cart during experiments, it was necessary to outfit each wheel with a load cell to measure how the loads were applied to the beams. In order to calibrate the load cells to account for their self-weight and the weight of the wheels, the cart was suspended by a crane and measurements from the load cells were recorded. These values were then combined with the measurements taken during tests to calculate the full force being applied on the beams.

The wheel loads were measured using a 2-kip Interface© 1210AF load cell connected to a computer using a data acquisition unit connected through a USB port. A program written in Labview© was used to record the data from the load cells along with the time of the measurement.

Initially, tests were performed with a load configuration similar to that shown in Figure 3.3. However, it was observed that all four wheels were not consistently bearing on the track during the experiment. The rigidity of the cart and wheel connections prevented the even distribution of the load to the wheels as the cart encountered variations in elevation of the track.

In order to achieve a more consistent load distribution during the tests, the cart configuration was modified to bear on three wheels rather than four. This was achieved by raising the height of one wheel on the cart until it was not in contact with the beam. The result was a load cart that was supported by three wheels, one on the measured beam, and two on the non-measured beam. This configuration provided a stable system that could produce a single point load traveling down the beam of interest with more consistent load distribution than the original four wheel configuration.

The sensors used in the laboratory experiment were 5 mm FBGs in SMF-28 acrylate fiber with base wavelengths ranging from 1530 nm to 1566 nm. The FBG data were recorded using a two-channel SmartScan© interrogator. Each channel was connected to 14 multiplexed FBG sensors installed along the length of the beam. One channel was connected to the sensors oriented on the extreme fibers of the cross-section of the test-beam. The other channel was connected to the sensors oriented on the inside of the test-beam cross-section. The sample rate

of the FBG data was set to 4 Hz, and the data were averaged to produce one data point per second. The averaging of the data was done to limit the quantity of data recorded during the test and to reduce the noise of the data collected. For the moving tests, the sample rate should have been increased to capture more precise measurements, but due to an oversight during the experimentation phase, this adjustment was not made.

For the static load test, the load cart was moved incrementally along the beam at 1 ft intervals for the entire length of the beam. At each interval the load cart was held in position for approximately 10 seconds while measurements were recorded. The interval that the load was held stationary for data collection is referred to as a load condition. Six static tests were performed on each beam to test the repeatability of the results. In-depth analysis was performed for the load condition that induced the largest curvatures measured in each span: a point load at 4 ft, a point load at 15 ft, and a point load at 26 ft.

For the pseudo-static and the dynamic tests, marks were placed at the locations of the sensors, and the cart was manually pushed down the length of the beams. A stopwatch was started at the same time that the FBG sensor data began recording. The time was recorded when the data for the load cells began recording, and the time was recorded as the wheel load passed each marked sensor. This timing data was then used to correlate the data between the FBG sensors, the load cells, and the location of the cart. For each beam, four pseudo-static tests and four dynamic tests were performed. The average speed of the cart was 0.788 ft/s for the pseudo-static tests and 2.083 ft/s for the full-speed tests. The cart speed for the full-speed test only scales to 13.4 mph (using the 1:4.4 ratio of bridge lengths). However, the velocity was limited by safety concerns in the laboratory.

## **CHAPTER 6: ANALYSIS PROCEDURES**

In-depth analysis was performed with the load positioned at three locations on each beam: at 40% of the first span (1.04), the middle of the second span (2.05), and 60% of the third span (3.06). Three types of raw data were collected for analysis: the position of the cart on the bridge, the load measured by the load cells, and the raw FBG wavelength data. The values of the raw measured data were correlated according to the time the measurements were taken. The load effects and the structural response were calculated from the raw data at each point, and the structural properties of interest were calculated for comparison with values found through analysis.

For the analysis of the static loads, multiple data points were collected while the load was held stationary at a single position. The data collected over the time that the load was held in position was averaged to produce a single average strain value for each load location, which was used in the analysis.

For the moving tests, strain data were collected at one-second intervals as the load cart was continuously moved down the length of the beam. The position and time data collected during the moving tests were used to linearly interpolate the FBG data to determine the strain response during the time that the load passed over the point of interest.

### **6.1 FBG DATA ANALYSIS**

The raw wavelength measurements from the FBG sensors were converted to strain using equation 1.2, which is reprinted below.

$$\varepsilon = \frac{\lambda - \lambda_0}{G\lambda_0} \quad (1.2)$$

where:  $\varepsilon$  = strain  
 $\lambda$  = reflected wavelength  
 $\lambda_0$  = unstrained reflected wavelength  
 $G$  = gage factor (typically 0.78)

The load applied by the cart wheel varied as it was moved along the beam. Equation 6.1 was used to normalize the measured curvatures for an average load so that data from different load configurations could be compared.

$$\varepsilon_{Adj} = \varepsilon_{Meas} * \frac{P_{Avg}}{P_{Meas}} \quad (6.1)$$

where:  $\varepsilon_{Adj}$  = adjusted strain  
 $\varepsilon_{Meas}$  = measured strain  
 $P_{Avg}$  = average of the loads measured from all tests and load conditions  
 $P_{Meas}$  = measured load that produced the measured curvature

Equation 6.2 was then used to calculate the curvature at each position on the bridge using these strain values. By considering the strain at two different cross-section depths, Equation 6.2 eliminates the need for knowing the neutral axis depth to calculate curvature, assuming that the strain distribution is linear through the depth of the bending member.

$$\phi = \frac{\varepsilon_T - \varepsilon_B}{d} \quad (6.2)$$

where:  $\phi$  = curvature  
 $\varepsilon_T$  = strain in top sensor  
 $\varepsilon_B$  = strain in bottom sensor  
 $d$  = depth between top and bottom sensors

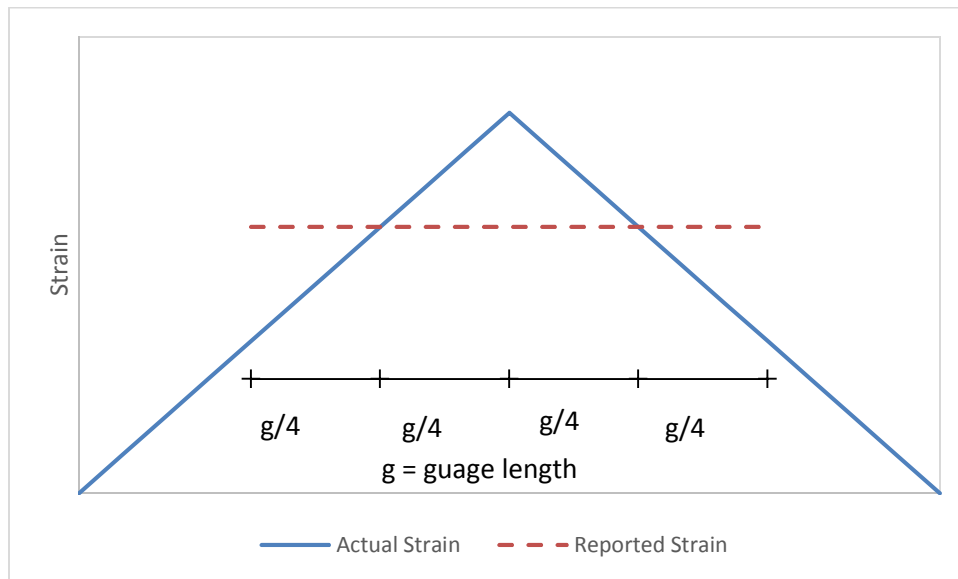
The neutral axis for various points was calculated using Equation 6.3.

$$NA = \frac{\varepsilon_B}{(\varepsilon_B - \varepsilon_T)} d + h_B \quad (6.3)$$

where:  $NA$  = distance from bottom of section to neutral axis  
 $\varepsilon_T$  = strain in top sensor  
 $\varepsilon_B$  = strain in bottom sensor  
 $d$  = depth between top and bottom sensors  
 $h_B$  = distance from bottom of section to bottom sensor

### Considerations for Long Gauge Sensors

As was mentioned previously, a long gauge sensor configuration was used to measure the strains on the concrete beam. The value reported by the long gauge sensor will be the average strain across the measured region. When the curve is linear over the length of the sensing region, the value reported should correspond to the value at the center of the gauge length. However, if the curve peaks in the region that is being measured, then the value reported by the long gauge sensor will tend to underestimate the peak as shown in Figure 6.1.



**Figure 6.1 Peak Strain Reported by Long Gauge Sensor**

To approximate the peak strain that occurs in the middle of a long gauge sensor, the measurement reported was assumed to equal the actual strain values at the  $\frac{1}{4}$  and  $\frac{3}{4}$  points of the sensing region. The curve was then linearly extrapolated to the midpoint of the gauge length to estimate the actual peak value.

## **6.2 DETERMINATION OF ANALYTICAL LOAD EFFECTS**

In order to calculate the analytical load effects for comparison with the laboratory measurements, a beam was modeled in SAP2000 (Computers & Structures, Inc 2011) with the flexural rigidity  $EI$  set to unity; nodes were placed at sensor locations, support locations, and load locations; a unit load was positioned at the appropriate location to replicate the load condition of the laboratory test; and the model was analyzed for the resulting moment. The supports were modeled to provide vertical and lateral restraint only. The values resulting from the simulation provided the moment function for a load at the location modeled. This moment function could then be scaled by the analytical flexural rigidity of the beam and the measured load magnitude to determine the analytical load effects, such as strains and curvatures, for a given load configuration.



## CHAPTER 7: CONCRETE BEAM RESULTS

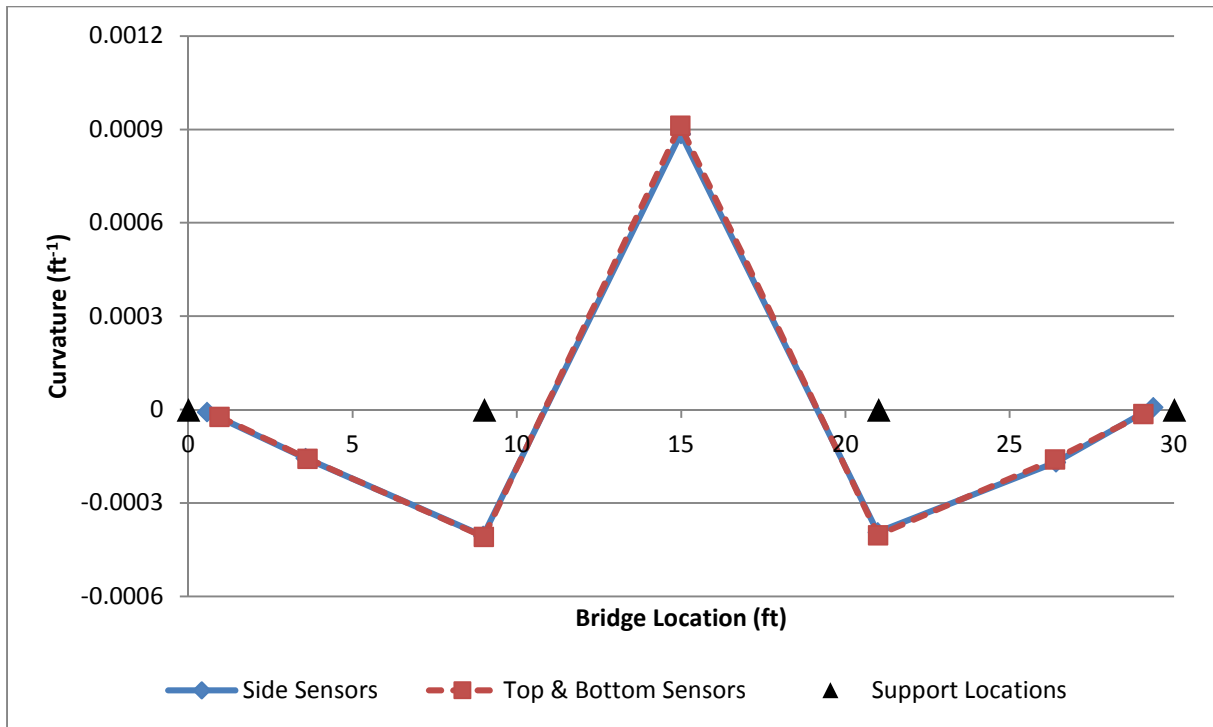
### 7.1 CALCULATED ANALYTICAL PROPERTIES

The concrete used for the beam was specified to have a 30 day compressive strength  $f_c$  of 5 ksi. An attempt was made to measure the strength of the concrete through compressive cylinder tests. However, the machine used was not correctly calibrated, and the results were not reliable. For the purpose of this analysis, it was assumed that the compressive strength was exactly 5 ksi. Based on this value, the compressive modulus of elasticity was calculated using Equation C5.4.2.4-1 from (AASHTO 2012) to be 4,031 ksi. The elastic modulus was assumed to be constant under the loading conditions.

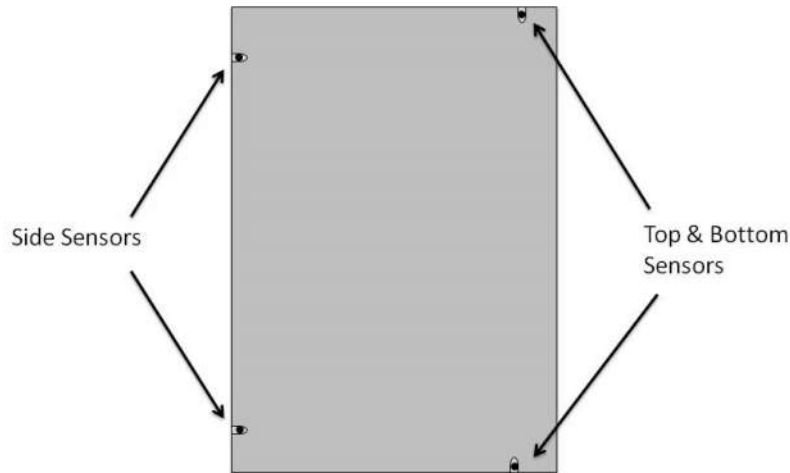
The design dimensions of the beam were 6 in deep by 4.5 in wide with a 1 in hole in the middle for the pre-stress tendon. The analytical moment of inertia of the concrete section was  $81 \text{ in}^4$ . However, the dimensions varied slightly due to irregularities in the concrete forms. The actual cross-sectional dimensions were measured at the sensor locations and were used to calculate the curvatures from the experimental strain values. The moment of inertia calculated from these measurements ranged from  $79.4 \text{ in}^4$  to  $88.5 \text{ in}^4$  with an average value of  $84.3 \text{ in}^4$ . The pre-stressed beam was designed for no cracking, and there was no mild steel reinforcement. The calculated flexural rigidity  $EI$  of the concrete section was  $326,421 \text{ kip-in}^2$ . The steel track angle (L2x2x3/16) had a moment of inertia about its bending axis of  $0.109 \text{ in}^4$  and an elastic modulus of 29,000 ksi. The track angle increased the flexural rigidity of the beam by  $3,161 \text{ kip-in}^2$  for a total flexural rigidity of the section equal to  $329,583 \text{ kip-in}^2$ .

## 7.2 CROSS-SECTION SENSOR PLACEMENT

For the concrete beam, comparing the results obtained from the sensors placed at the extreme fibers to those obtained from the sensors placed toward the inside of the cross-section shows good agreement between the sensor configurations. For the three load states analyzed during the six static load tests, the average discrepancy between curvature values measured by the two sensor configurations was 2.01% for the maximum positive curvature values and 1.32% for the maximum negative curvature values. The curvatures measured by the two sensor configurations for one of the analyzed load cases are illustrated in Figure 7.1. Other tests produced similar results. The sensor locations are shown in Figure 7.2.



**Figure 7.1. Curvatures Measured by Cross-Sectional Sensor Configurations on Concrete Beam**  
Static test with point load located at 15 feet (2.05).



**Figure 7.2. Sensor Locations on Concrete Beam Cross-Section**

### 7.3 STATIC TESTS

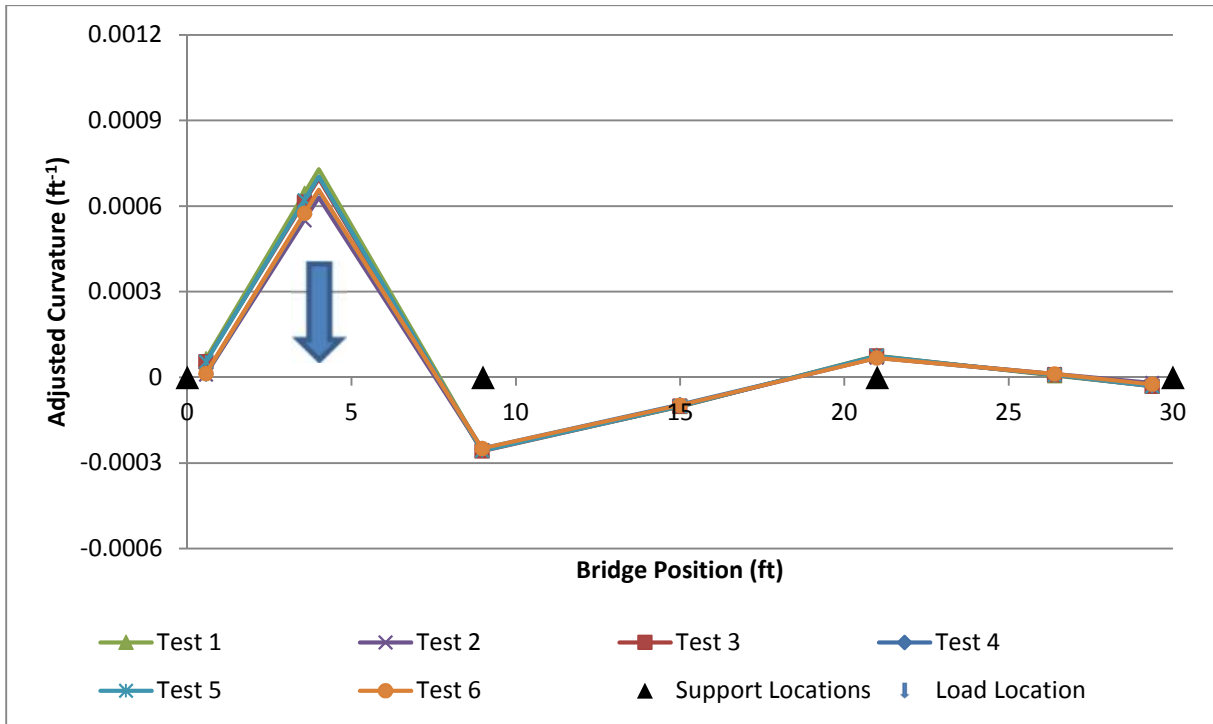
Six static load tests were performed on each beam in order to verify the repeatability of the results obtained from the SHM system. The curvature results from the six different tests on the concrete beam were compared for each of the three load conditions. After normalizing the values to account for variations in the magnitude of the loads between tests, the maximum positive and negative curvatures for each load condition were computed. The average coefficient of variation for these maximum normalized curvatures measured in each span was 0.0439. This indicates good repeatability for these measurements.

The curvatures at the end supports are used to detect any rotational fixity caused by the end support. As the sensor locations had to be inset from the ends of the bridge (6.5" to 11.5") to provide adequate space for the long gage sensors, the end curvatures could not be measured directly. Instead the curvature at the ends of the beams were calculated by linearly extrapolating the curvatures from the sensor measurements near the middle of the end spans (1.04, and 3.06 locations) and the sensor measurements inset from the ends of the end spans.

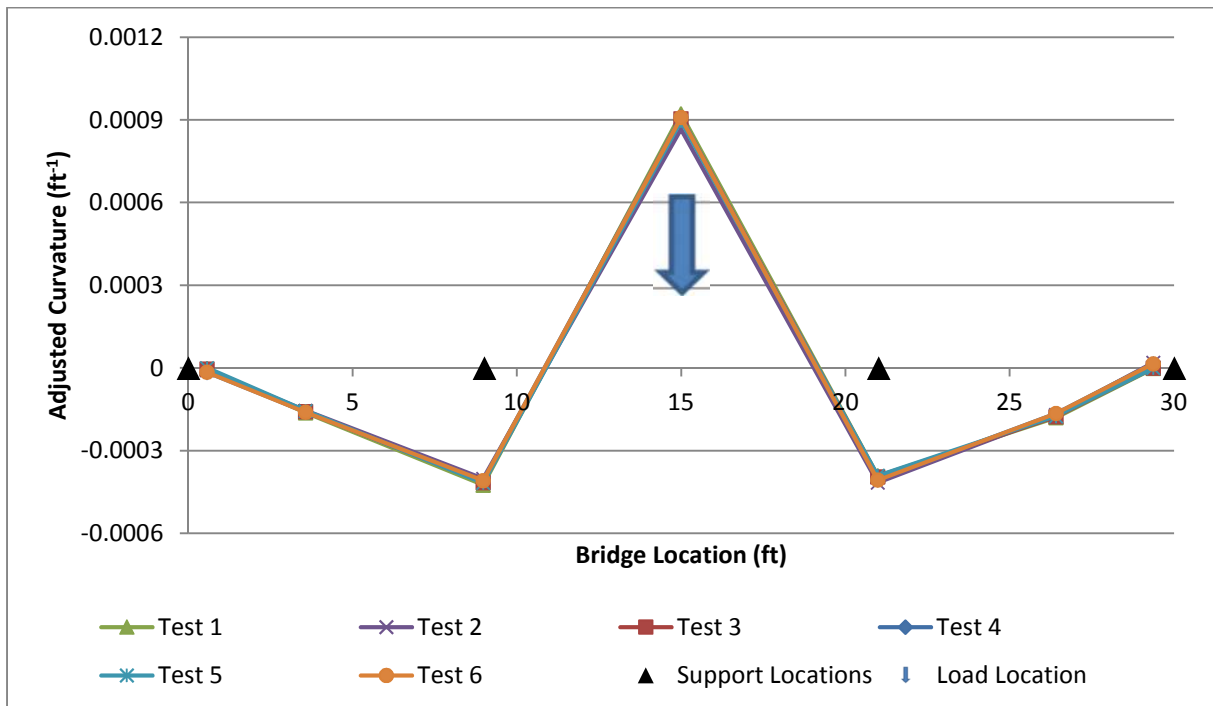
The average extrapolated end curvature was calculated to be  $-7.29 \times 10^{-5} \text{ ft}^{-1}$  at support 1.00 due to the point load at the 1.04 location and  $-13.72 \times 10^{-5} \text{ ft}^{-1}$  at support 3.10 due to the point load at the 3.06 location. The standard deviation for the end curvatures was  $3.43 \times 10^{-5} \text{ ft}^{-1}$ .

Plots of the curvatures obtained from the six static tests under the three different load conditions are shown in Figure 7.3, Figure 7.4, and Figure 7.5. The plots show the curvatures measured by the sensors located on the sides of the concrete beam cross-section. Similar values were obtained from the sensors located at the top and bottom of the cross-section. These plots show that the curvatures obtained from the SHM system are consistent for a given load configuration, and the curvature along the length of the span resembles the expected moment distribution for the load configurations analyzed.

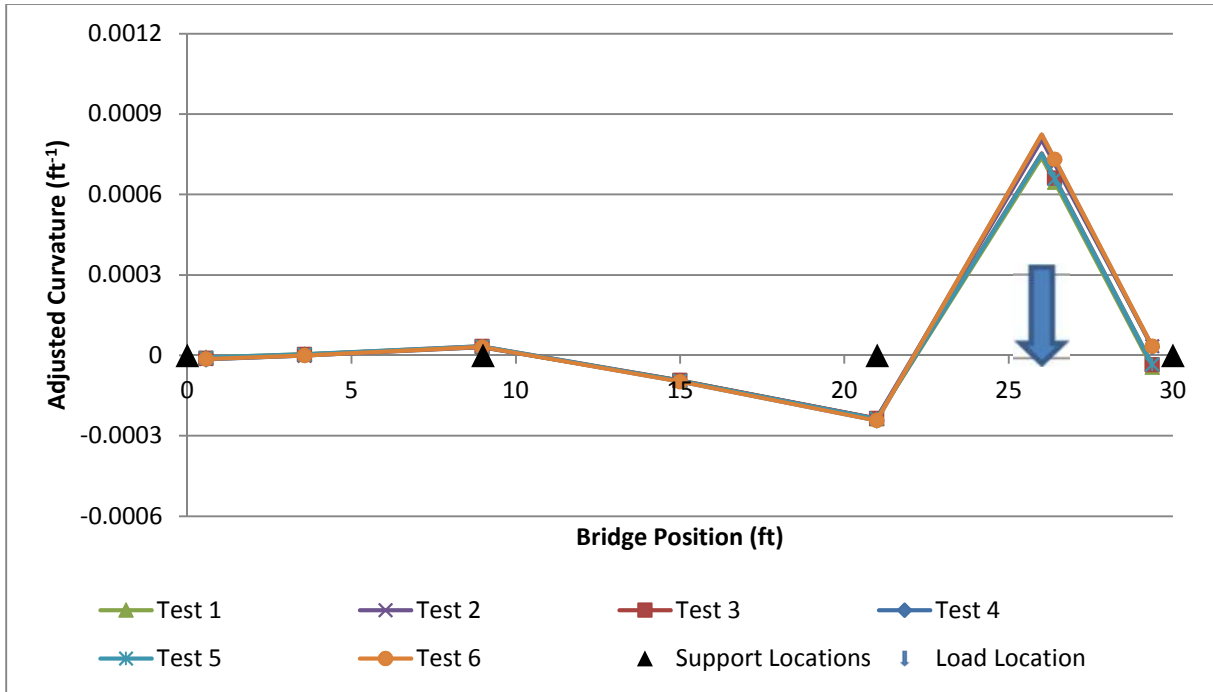
Note that in Figure 7.3 and Figure 7.5 the load location is slightly offset from the sensor location. The curves in these figures have been extrapolated to the load location to reflect the expected shape of the curvature diagram. Only the points with data markers reflect measurements taken during the experiment. This approach is taken for all of the figures showing the 1.04 or 3.06 load conditions throughout the rest of this paper.



**Figure 7.3. Curvature Measured by Side Sensors on Concrete Beam**  
 Static tests with point load located at 4 feet (~1.04). Curves are extrapolated to load location.



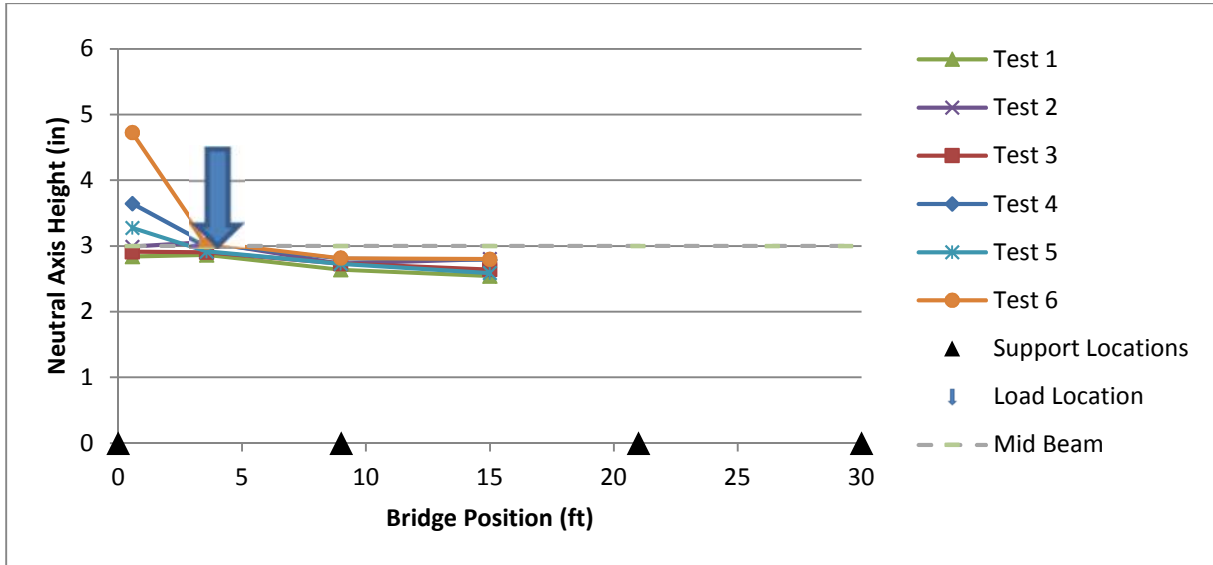
**Figure 7.4. Curvature Measured by Side Sensors on Concrete Beam**  
 Static tests with point load located at 15 feet (2.05).



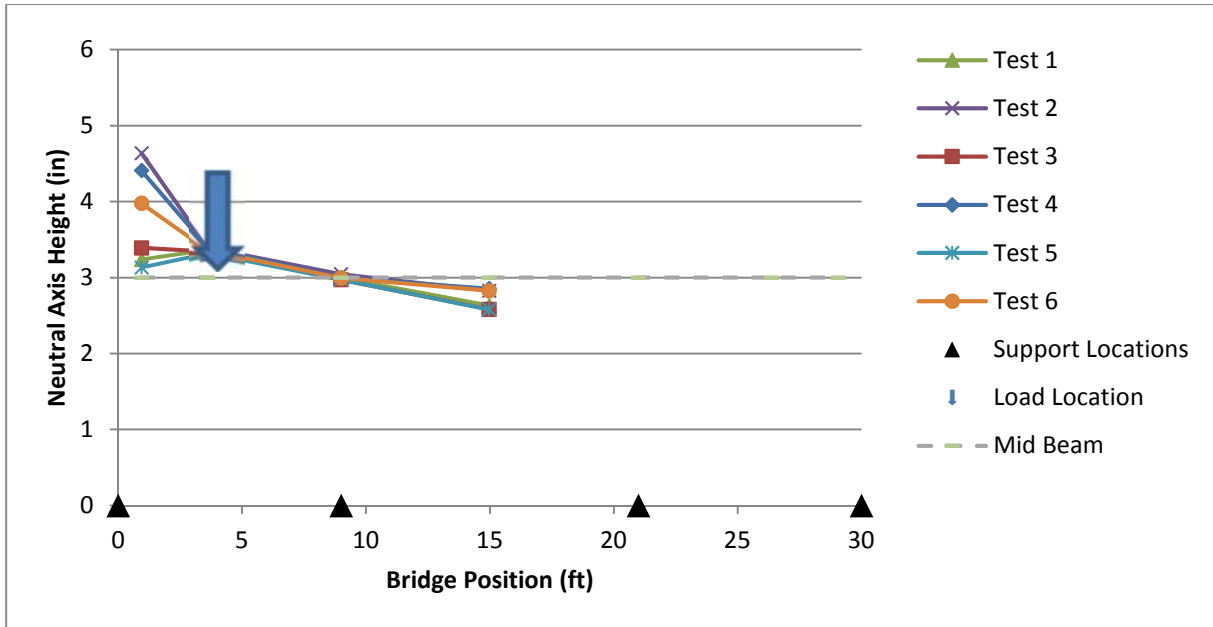
**Figure 7.5. Curvature Measured by Side Sensors on Concrete Beam**  
 Static tests with point load located at 26 feet (~3.06). Curves are extrapolated to load location.

### Neutral Axis Location

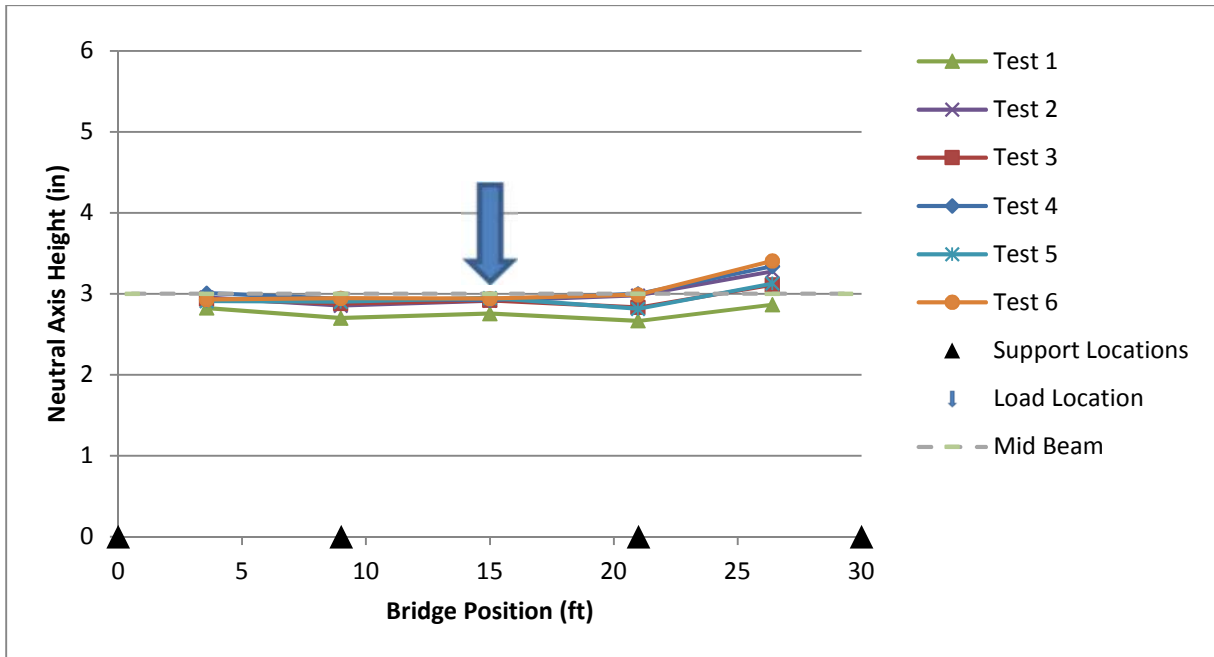
The neutral axis of the beam was calculated at each sensor location under the three load conditions for the six different tests. The neutral axis was calculated using strains recorded by the two sensor configurations shown in Figure 7.2. The neutral axis values are shown in the following figures. The strain values measured at locations away from the applied loads were too small to provide meaningful results; so the neutral axis values at those locations were omitted.



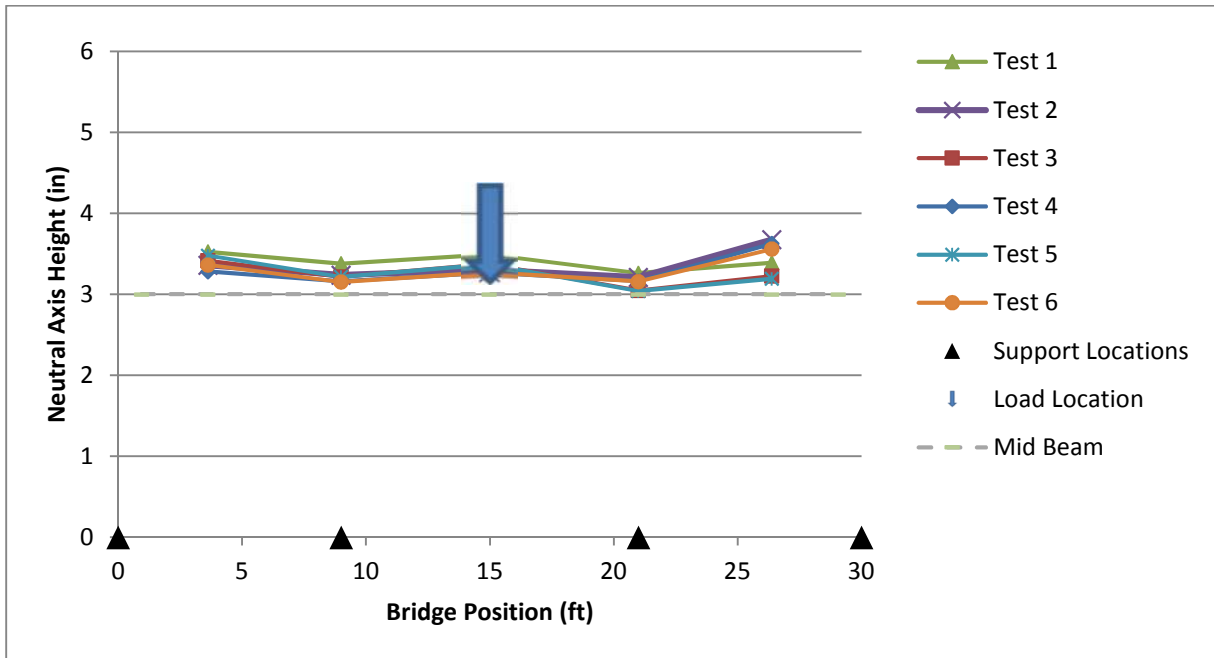
**Figure 7.6. Neutral Axis Height Measured by Side Sensors on Concrete Beam**  
 Static tests with point load located at 4 feet (~1.04).



**Figure 7.7. Neutral Axis Height Measured by Top & Bottom Sensors on Concrete Beam**  
 Static tests with point load located at 4 feet (~1.04).

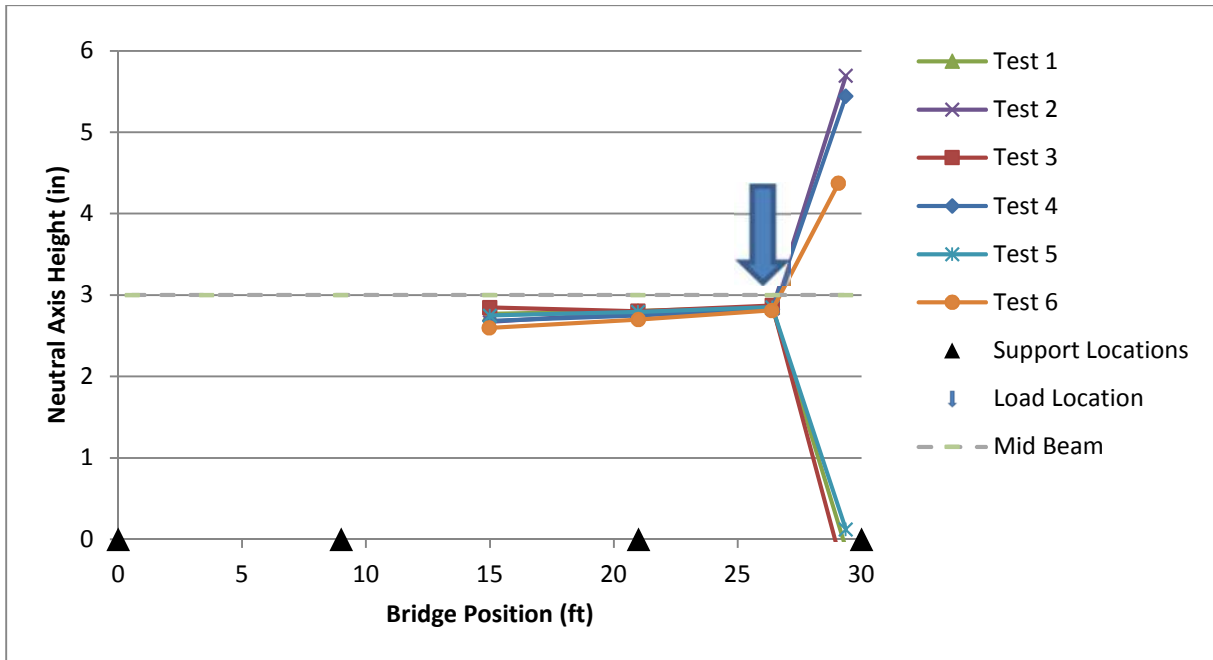


**Figure 7.8. Neutral Axis Height Measured by Side Sensors on Concrete Beam**  
 Static tests with point load located at 15 feet (2.05).

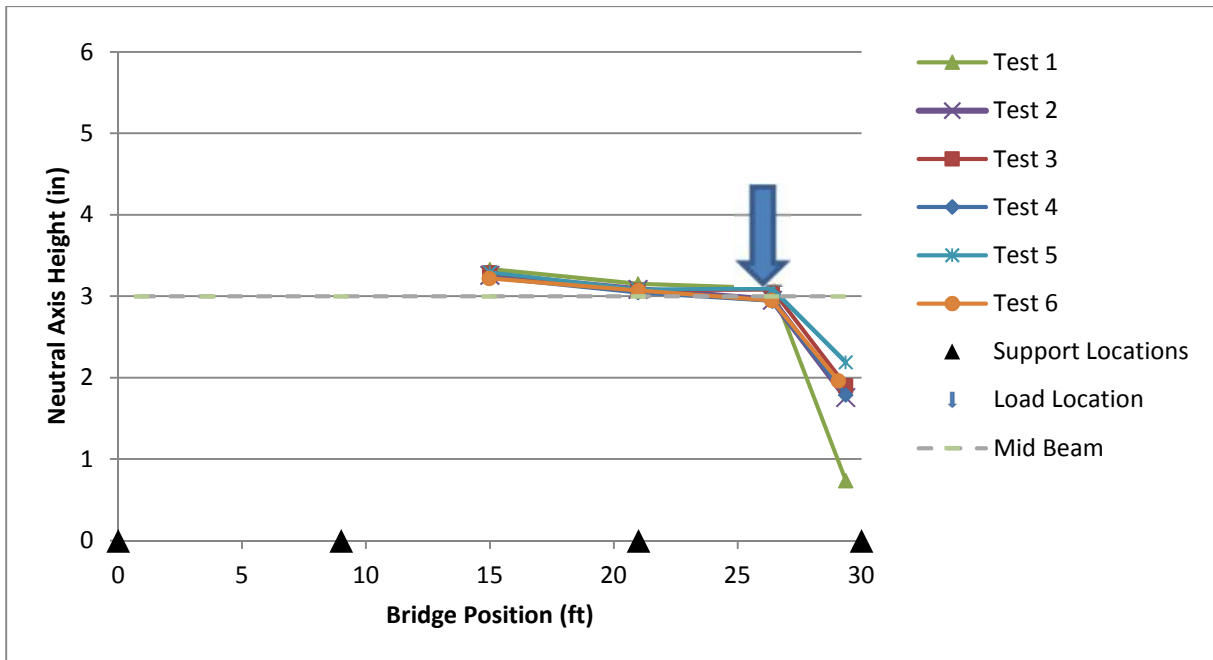


**Figure 7.9. Neutral Axis Height Measured by Top & Bottom Sensors on Concrete Beam**  
 Static tests with point load located at 15 feet (2.05).





**Figure 7.10. Neutral Axis Height Measured by Side Sensors on Concrete Beam**  
 Static tests with point load located at 26 feet (~3.06).



**Figure 7.11. Neutral Axis Height Measured by Top & Bottom Sensors on Concrete Beam**  
 Static tests with point load located at 26 feet (~3.06).

The large scatter in the neutral axis height measured at the end support locations could be explained by local bearing effects being read by sensors close to the supports; axial loads

caused by the attachment of the beam to the support; and the overall small magnitudes of strain measured by the sensors at those locations, which would exaggerate discrepancies between the top and bottom strain readings.

The neutral axis height calculated from the sensors located on the sides of the beams (left side of Figure 7.2) tended to be below the mid-height of the beam. Similarly, the neutral axis height calculated from the sensors located on the top and bottom of the beam (right side of Figure 7.2) were generally above the mid-height of the beam. Because the two sensor locations were located on opposite sides of the cross section, this may indicate minor axis bending, which may have been caused by the cart pulling the two beams towards each other as it proceeded down the tracks, which weren't perfectly straight. This observation is consistent with some of the behavior observed in the steel beam that will be discussed later.

### **Comparison of Results**

As was discussed in Chapter 6, an analytical model was developed to describe the behavior of the concrete beam based on properties typically used in design practice.

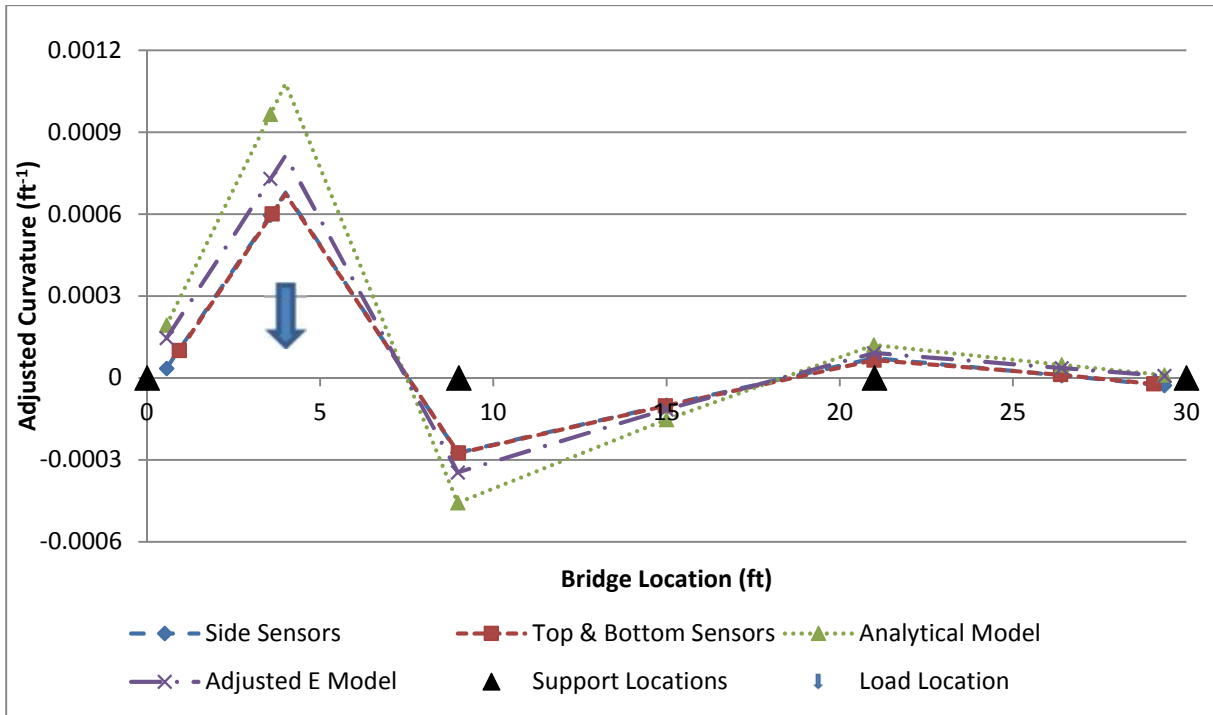
The results from all six static tests were averaged to produce a curvature distribution for each of the three load cases that were analyzed in depth: a point load at the 1.04, 2.05, and 3.06 locations.

In all three load cases, the analytical model predicted curvatures higher in magnitude than those measured during the tests, except at the beam ends, where the end-conditions assumed in the analytical model forced the curvature to a value of zero. The elastic modulus ( $E$ ) that was used for the analytical concrete model was based on Equation 5.4.2.4-1 in the

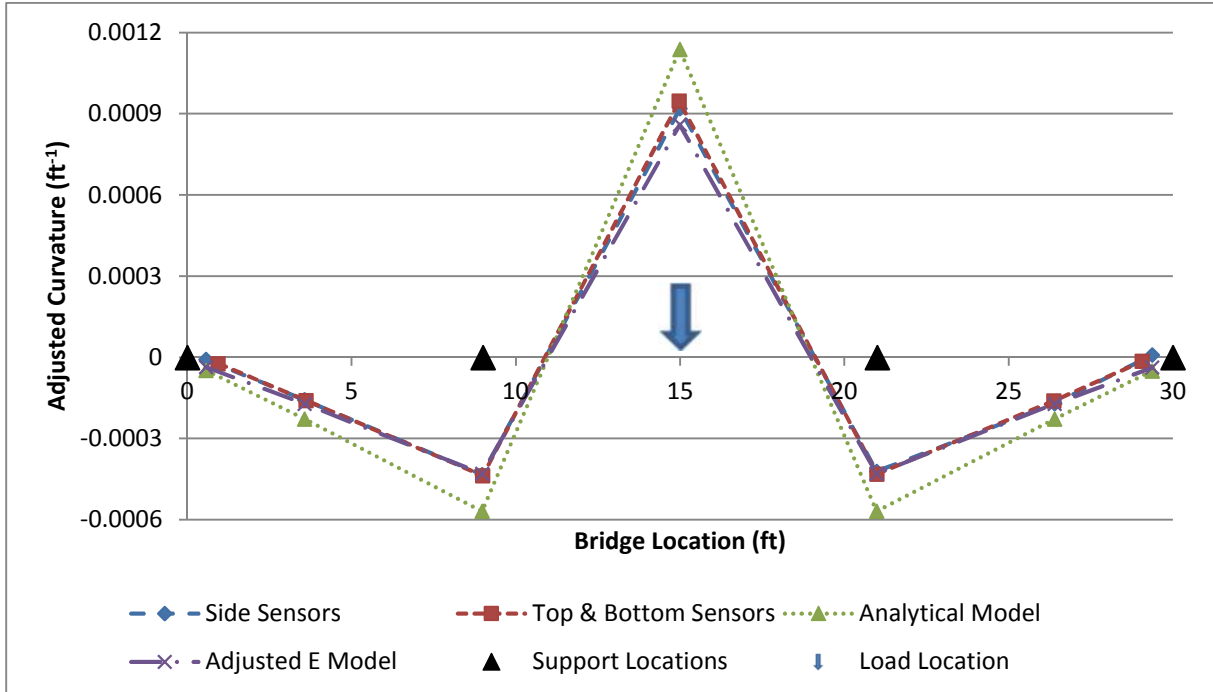
AASHTO LRFD Design Manual (2012). This equation does not account for the stiffness of the aggregate used. A direct test of the elastic modulus for the batch of concrete used to construct the beams would have given better results. However due to calibration issues with the testing machine, reliable data was not available.

In order to determine a modulus of elasticity that better approximated the experimental data than the value calculated using the AASHTO equation, the analytical static moment distribution was scaled by increasing the modulus of elasticity value to approximate the experimental curvature distribution. The resulting modulus of elasticity was increased by 32.3% from 4,031 ksi to 5,333 ksi. An additional analytical model was developed using this adjusted modulus of elasticity.

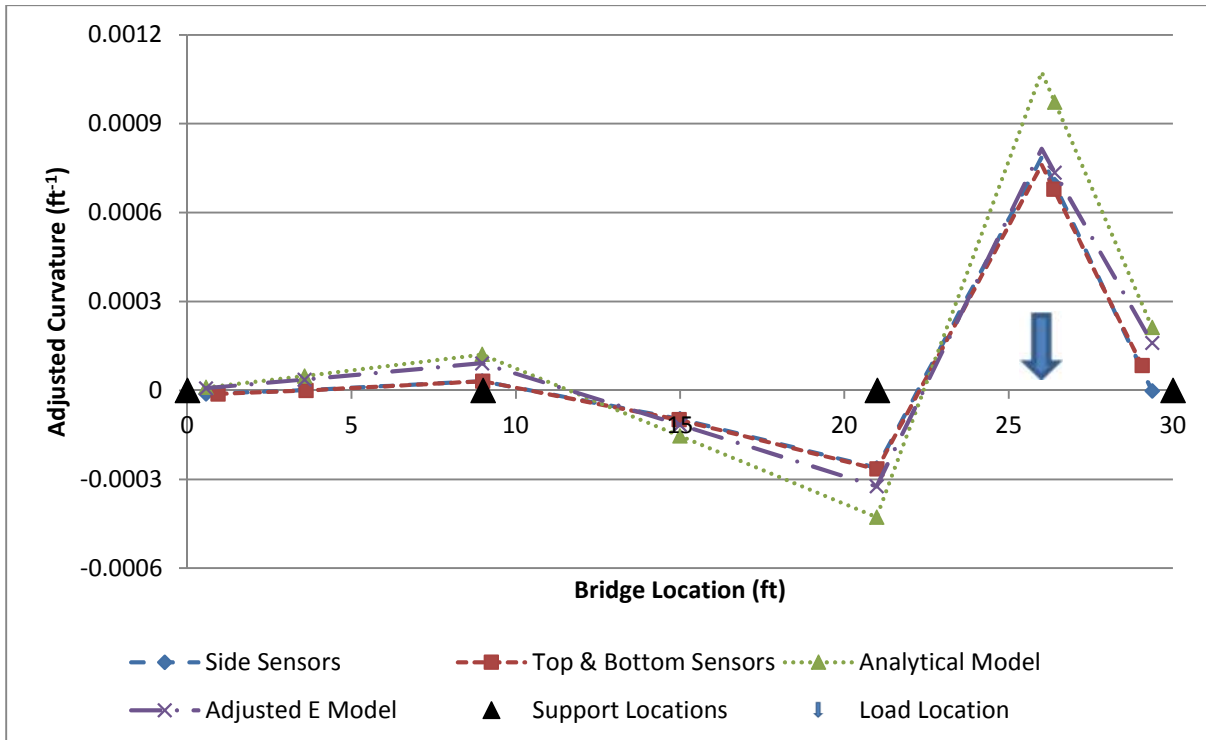
The curvature distributions calculated from the analytical model, the experimental data, and the adjusted modulus of elasticity analytical model are shown for comparison in Figure 7.12, Figure 7.13, and Figure 7.14 for the three load cases analyzed. As before, the curves in Figure 7.12 and Figure 7.14 have been extrapolated to the load location.



**Figure 7.12. Comparison of Analytical and Measured Curvatures for Concrete Beam**  
 Static tests with point load located at 4 feet (~1.04). Curves are extrapolated to load location.



**Figure 7.13. Comparison of Analytical and Measured Curvatures for Concrete Beam**  
 Static tests with point load located at 15 feet (2.05).



**Figure 7.14. Comparison of Analytical and Measured Curvatures for Concrete Beam**  
 Static tests with point load located at 26 feet (~3.06). Curves are extrapolated to load location.

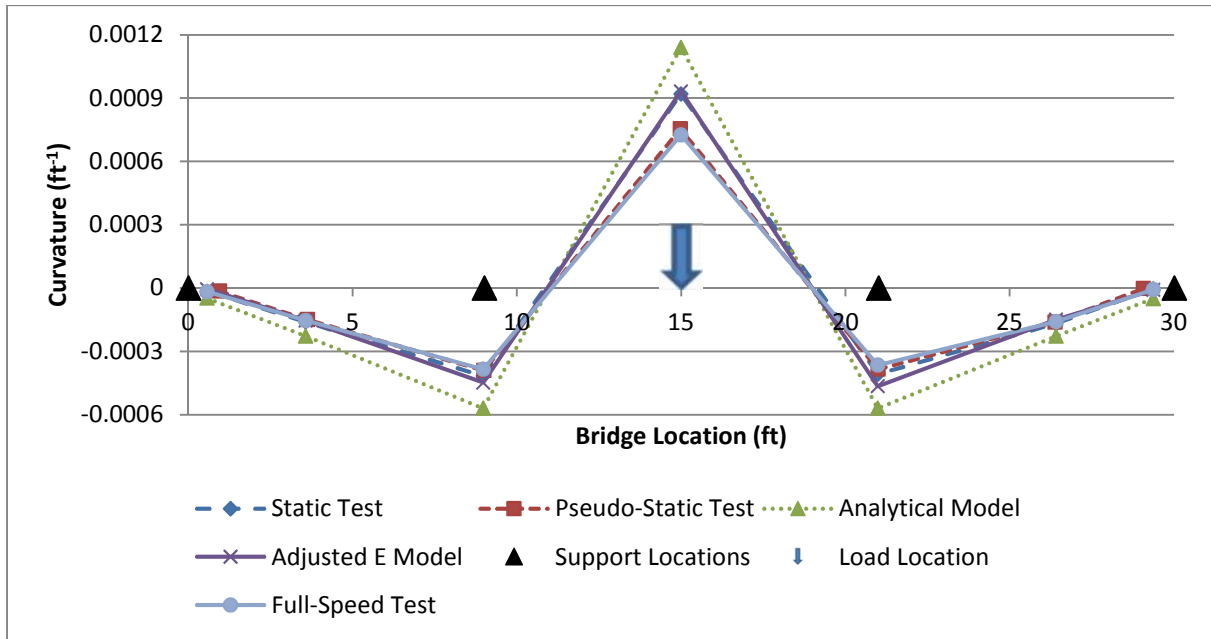
## 7.4 MOVING LOAD TESTS

The maximum positive and negative curvatures were calculated from the measurements corresponding to the three load conditions that were analyzed for the static load test results section. As the purpose of these tests was to quantify the effect of dynamic force interactions with the bridge, the curvatures were not adjusted based on the loads measured by the load cell. The maximum curvature measurements produced a coefficient of variation equal to 14.5% for the pseudo-static tests and 15.0% for the full-speed tests on the concrete beam. This variation is significant in that it is similar in magnitude to the difference between the maximum curvatures predicted by the analytical model and the values measured from static load test data.

During the moving tests, a significant side-to-side rocking was observed in the test cart that may have exaggerated the variability of the measurements. In practice the test vehicles traveling on bridges will have suspension systems and tires that will reduce some of the variability caused by oscillations. Additionally, the dynamic impact is typically less significant for heavier vehicles (AASHTO 2010).

The maximum load measured by the load cell attached to the wheel on the concrete beam over the course of the static load test was 1,338 lb. During the pseudo-static test, the maximum load measured was 1,347 lb, and during the full-speed test, the maximum load measured was 1,370 lb. This indicates a 0.63% dynamic impact factor for the pseudo-static test and a 2.33% factor for the full-speed test based on the load data alone. However, the dynamic impact factor is a function of the interaction between the bridge and the load and not just the load alone. Thus the dynamic impact factor should be calculated from the structural response.

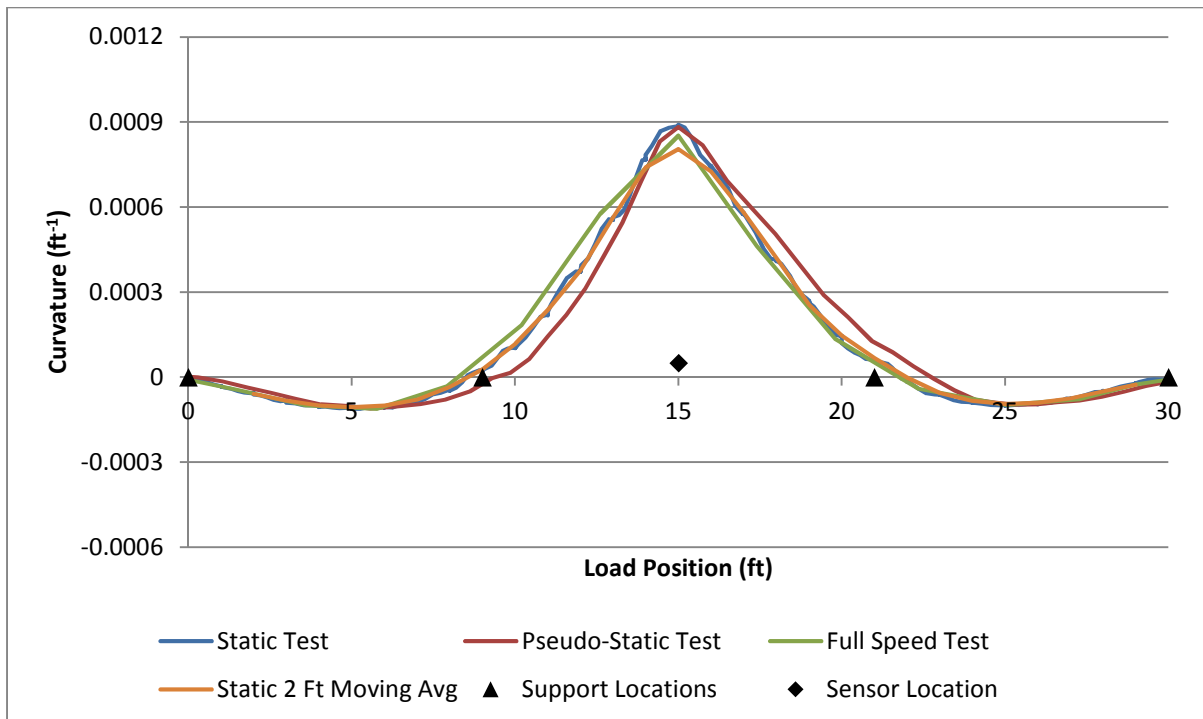
The curvatures from the static, pseudo-static, and full-speed tests were calculated and the values for each type of test and load case were averaged for comparison. These averaged curvatures are plotted alongside the analytical and adjusted models for curvature for one load case in Figure 7.15.



**Figure 7.15. Averaged Curvature from Static, Pseudo-Static, and Full-Speed Tests**  
 Tests with point load located at 15 feet (2.05).

The measured curvatures during the moving tests were actually lower in magnitude than the curvatures measured during the static tests, as shown in Figure 7.15. This apparent dynamic reduction was caused by an oversight in setting the time resolution used for collecting the strain data during the tests. Four measurements were taken each second during the test, but they were then averaged to produce only one recorded data point per second. During the static load tests, the load was held stationary for several seconds while data was collected, thus ensuring that the data was gathered while the load was in the desired location. However, during the moving tests, the cart continuously moved and was therefore only instantaneously in the location of interest. The data collection technique would have then collected data at points leading up to and passing the point of interest, then averaged these values into a single data point. Therefore, readings from the maximum curvature were combined with data from lower curvature conditions flattening the peaks of the curvature data. The result was a reduction in the maximum curvature reported from the moving tests.

Based on the velocity data, the maximum curvature reading during the full-speed test occurred with the load located between 14 ft and 16 ft from the end of the beam (span locations 2.042 and 2.058 respectively), and the measured value was an average of the curvatures experienced between these locations. For a more appropriate comparison, the static test curvatures between 14 ft and 16 ft were averaged to approximate a similar flattening of the response to that caused by the data collection procedure during the full-speed test. The ratio of the maximum curvature from the full-speed test to the averaged value from the static tests in this range yielded a dynamic impact factor of 7.0%. Following a similar approach over a correspondingly smaller range, the dynamic impact factor for the pseudo-static test was calculated to be 1.4%. The effect of averaging these values is illustrated by the 2 ft moving average, which is plotted in Figure 7.16.



**Figure 7.16. Curvature Influence Function for Concrete Beam at Mid-Span (2.05)**  
Measured by Sensors Located on Sides of Cross-Section at Mid-Span (2.05).



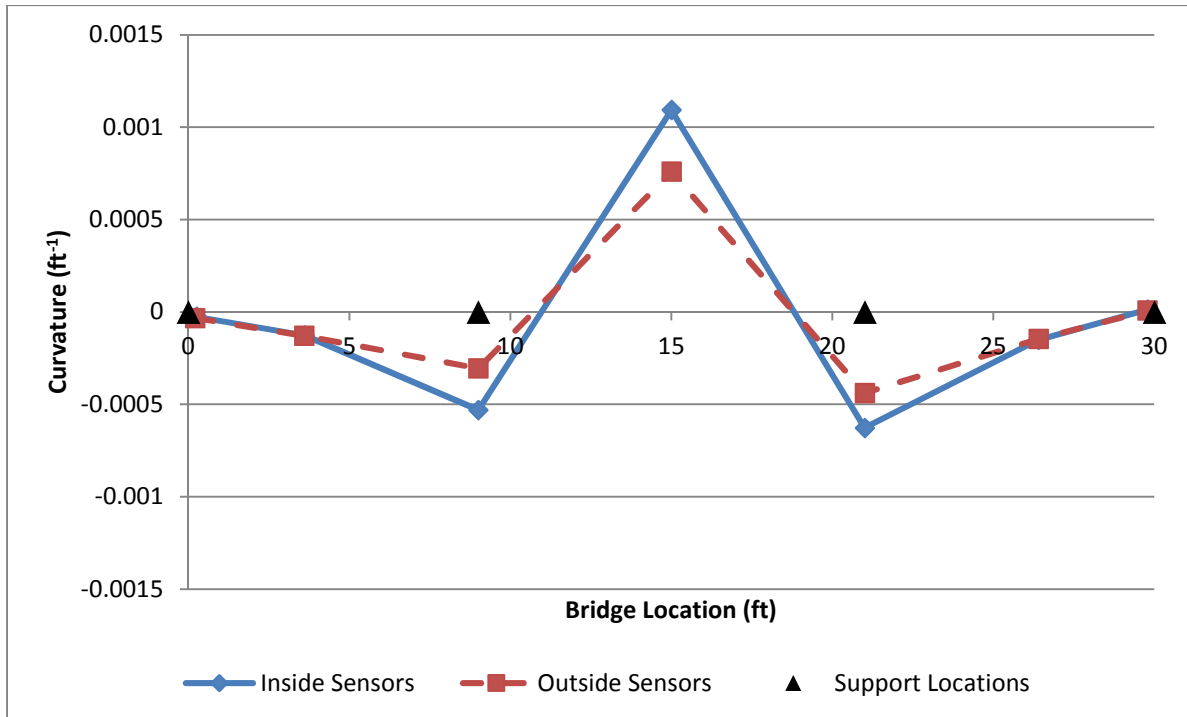
## **CHAPTER 8: STEEL BEAM RESULTS**

### **8.1 CALCULATED ANALYTICAL PROPERTIES**

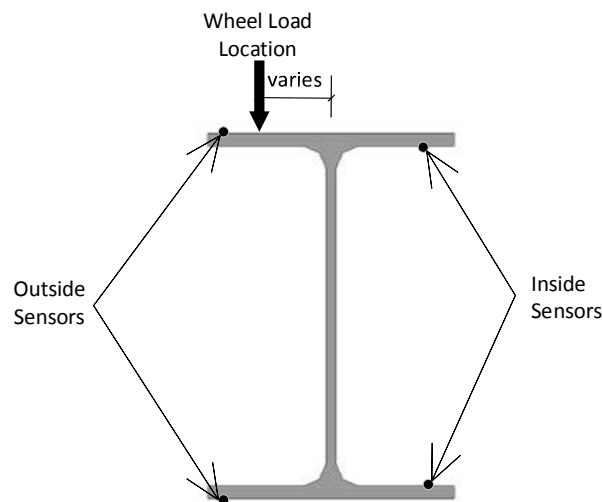
The W4x13 steel beam was made from ASTM A992 steel, and the properties for this beam were taken from (AISC 2006). The modulus of elasticity was taken to be 29,000 ksi, and the yield stress was taken as 50 ksi. The moment of inertia was  $11.3 \text{ in}^4$ . No stiffeners or braces were used. The flexural rigidity  $EI$  for the steel beam was  $327,700 \text{ kip-in}^2$ , and the contribution of the L2x2x3/16 steel track angle increased the flexural rigidity for the total section to  $330,861 \text{ kip-in}^2$ .

### **8.2 STEEL CROSS-SECTION SENSOR PLACEMENT**

On the steel beam, there were significant discrepancies between the curvatures from the sensors placed at the extreme fibers and the curvatures measured by the sensors placed on the inside of the flanges. Figure 8.1 shows the average curvatures measured for one of the load conditions analyzed. Figure 8.2 shows the orientation of the sensors installed on the steel beam. For the three load configurations analyzed during the six static load tests, the average discrepancy between values measured by the two configurations was 30.5% of the mean value for the maximum positive curvature values and 29.3% of the mean value for the maximum negative curvature values.



**Figure 8.1. Curvatures Measured by Cross-Sectional Sensor Configurations on Steel Beam**  
Static test with point load located at 15 feet (2.05).

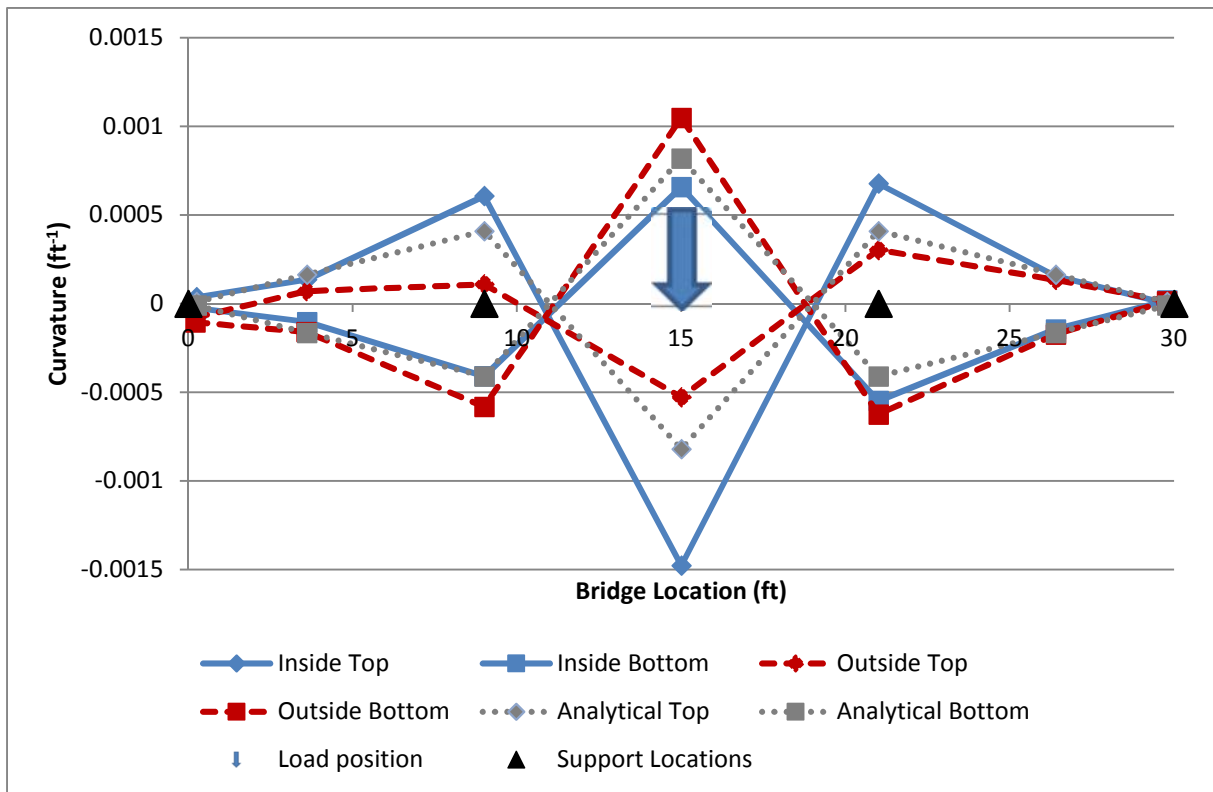


**Figure 8.2. Orientation of Sensors and Load on Steel Beam Cross-Section**

### 8.3 SECONDARY LOAD EFFECTS

Various factors may have contributed to the discrepancies in the measured values between the sensor configurations on the steel beam. Figure 8.3 shows the curvature

calculated from the strain measured in each sensor located on the steel beam. The locations of the sensors on the cross-section are illustrated in Figure 8.2. Curvature is shown rather than strain in order to account for the different distances between the sensors and the neutral axis of the beam. The top sensors at the mid-support locations (9 ft and 21 ft) for both the inside and outside configurations experienced significant loss in pretension during the installation process. So they may not represent accurate results. Additionally, the strains in these locations may be affected by local bearing effects induced by the supports.



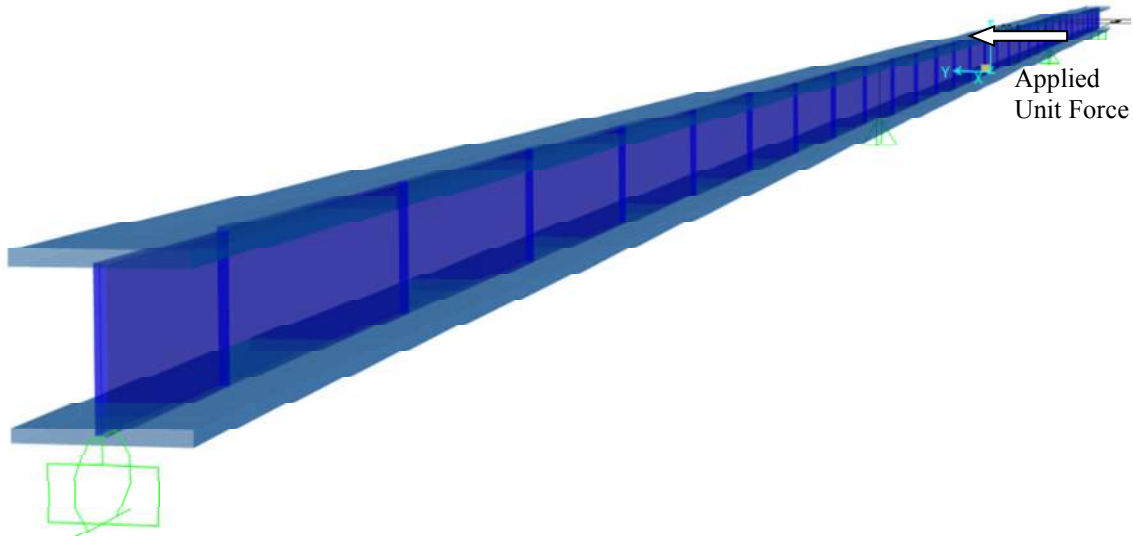
**Figure 8.3. Curvatures Calculated from Individual Sensors on Steel Beam**  
 Static test with point load located at 15 feet (2.05).

As shown in Figure 8.3, the curvature calculated from the top and bottom sensors on the same side of the beam were not equal in magnitude. However, there appears to be some correspondence in the strains measured by the inside top and outside bottom sensors, located

near the top right and bottom left corners of the cross-section shown in Figure 8.2 respectively. Similarly, there is an apparent correspondence between the outside top and inside bottom sensors, located near the top left and bottom right corners of the cross-section shown in Figure 8.2 respectively. This symmetry could indicate the presence of out of plane bending, which would result in a rotation of the neutral axis. During the experiment, it was observed that the cart's wheel was bearing close to the edge of the flange rather than directly over the web, as shown in Figure 8.2. The beams constructed in the lab were not perfectly straight and the rigidity of the load cart may have pulled the steel beam toward the stiffer concrete beam, resulting in minor-axis bending. This is consistent with observations from the neutral axis locations on the concrete beam. Furthermore, the eccentric load condition observed would result in a combined torsion and bending of the beam, which can result in secondary minor axis bending (Bremault, Driver and Grondin 2008). The minor axis bending would result in a tensile strain in both the top and bottom sensors on one side of the cross-section, and a compressive strain in the top and bottom sensors on the other side of the cross-section.

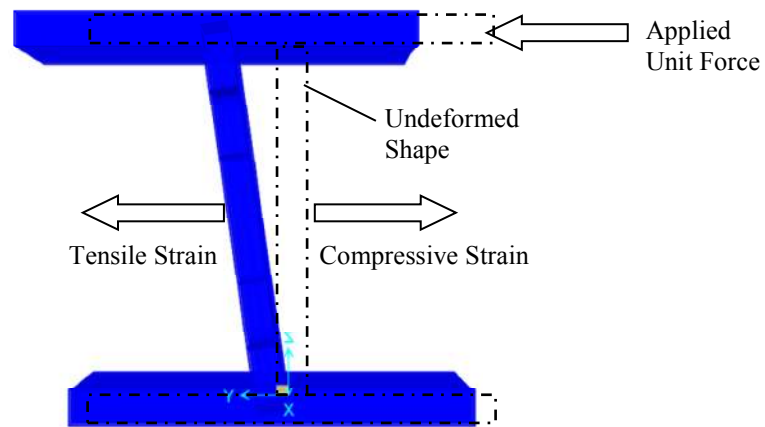
To demonstrate that out-of-plane bending is a feasible explanation for the observed behavior, a model was built in SAP2000 (Computers & Structures, Inc 2011) to approximate the W4x13 beam used in the experiment. The beam flanges and web were modeled as separate rectangular beam elements rigidly connected, and the fillets were neglected. The bottom flange was pin supported at the support locations and restrained from out of plane rotation at the end supports. The web and top flange were restrained only by rigid connections

to the other elements. A unit lateral load was applied to the top flange at mid-span (2.05). An isometric view of the model is shown in Figure 8.4.



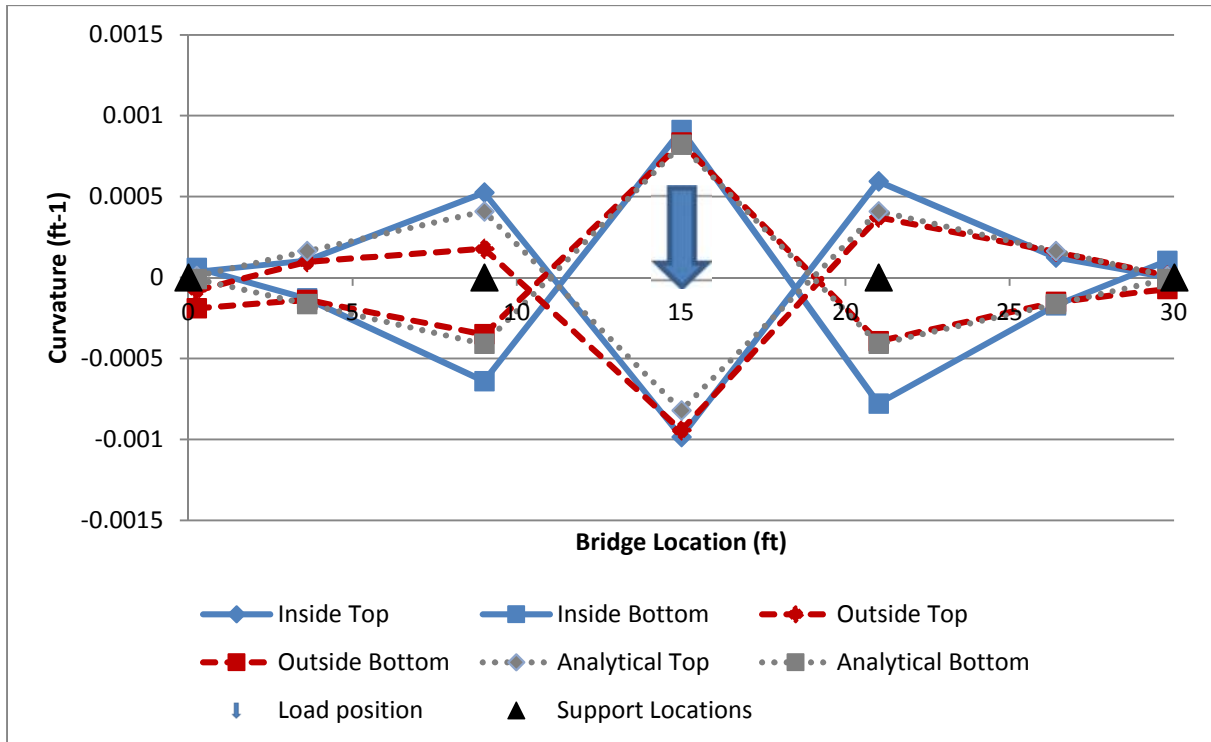
**Figure 8.4. Isometric View of Model for Analyzing Effects of Out-of-Plane Force Acting on Top Flange**

The lateral force applied to the top flange resulted in a larger out of plane deflection in the top flange than in the bottom flange as shown in Figure 8.5, which shows the deflected shape of the cross-section near mid-span (2.05). This differential out-of-plane flange bending would result in larger magnitudes of strains due to lateral forces in the top flange than in the bottom flange.



**Figure 8.5 Cross-Section of Deflected Shape Near Mid-Span**

The resulting strains in the top and bottom flanges were calculated from the model analysis, and subtracted from the strains measured during the experimental test. Then, the out-of-plane force effects were iteratively scaled until good agreement was achieved between the curvatures from the model and the test results. This analysis indicated that a lateral force of 230 lbs acting on the top flange would result in good agreement with the experimental results, as shown in Figure 8.6, which shows the resulting curvatures after the strains due to the out-of-plane force effects have been subtracted. This force is well within the range of lateral force that could be transferred by friction between the track and the top flange of the beam.



**Figure 8.6. Static Test Results Adjusted for Differential Out of Plane Flange Bending**  
 Static test with point load located at 15 feet (2.05).

Additionally, the beam supports provided some torsional restraint, and the connections at the ends of the beam provided some restraint against longitudinal strain. The combination of these restraints may have combined to provide some warping resistance, which would cause the torsion from the eccentric load condition on the beam to induce normal warping stress in the flanges of the I-section (Seaburg and Carter 2003). This warping stress would cause longitudinal strain in the flanges of the beam. The strains would be equal in sign and magnitude on opposing corners of the cross-section, i.e. tensile strain in the top right and bottom left corners and compressive strain in the top left and bottom right corners of the cross-section shown in Figure 8.2.

Further discrepancies could be the result of local effects caused by the load and the supports. As was mentioned previously, the top sensors at the mid-supports experienced

significant pretension loss during installation, and may not have been providing reliable measurements.

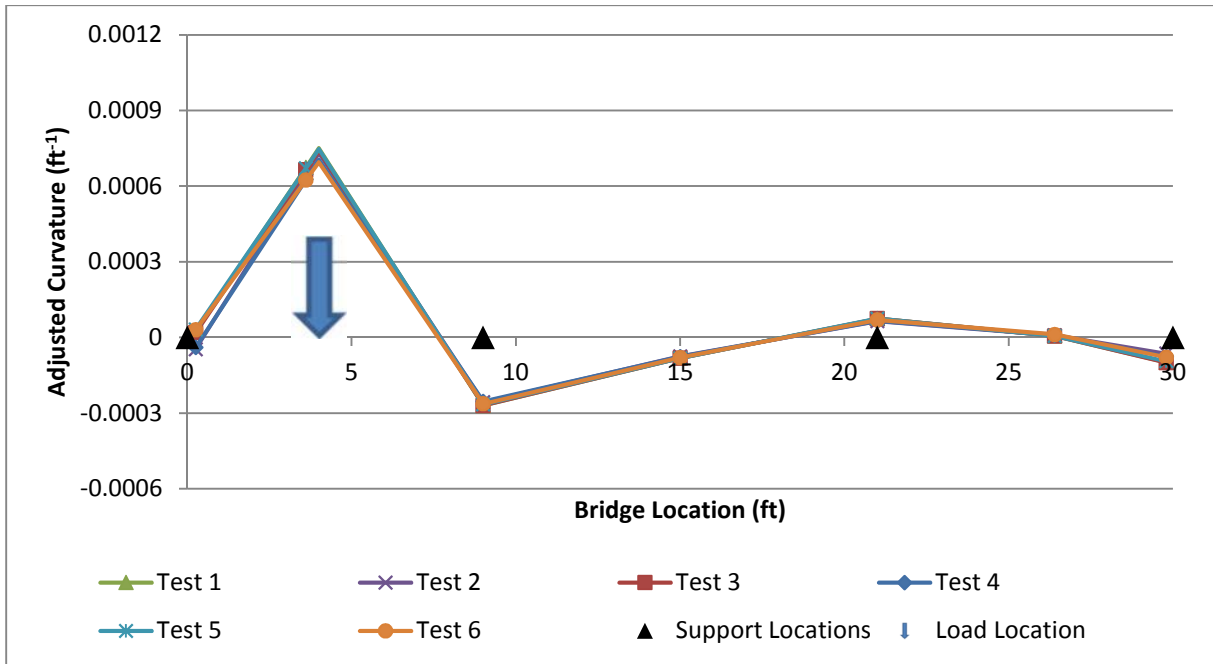
While the eccentric load condition was observed during experimentation, no measurements were taken to quantify lateral deflection or torsional rotation. Therefore, it was not confirmed that the steel beam underwent the load predicted by the previous analysis. However, out of plane bending and normal warping strain would result in a skewed neutral axis. This behavior would cause the strain to vary in both the strong and weak axis directions. So strains on one side of the web would not be equal to the strains on the other side of the web at the same depth.

#### **8.4 STATIC TESTS**

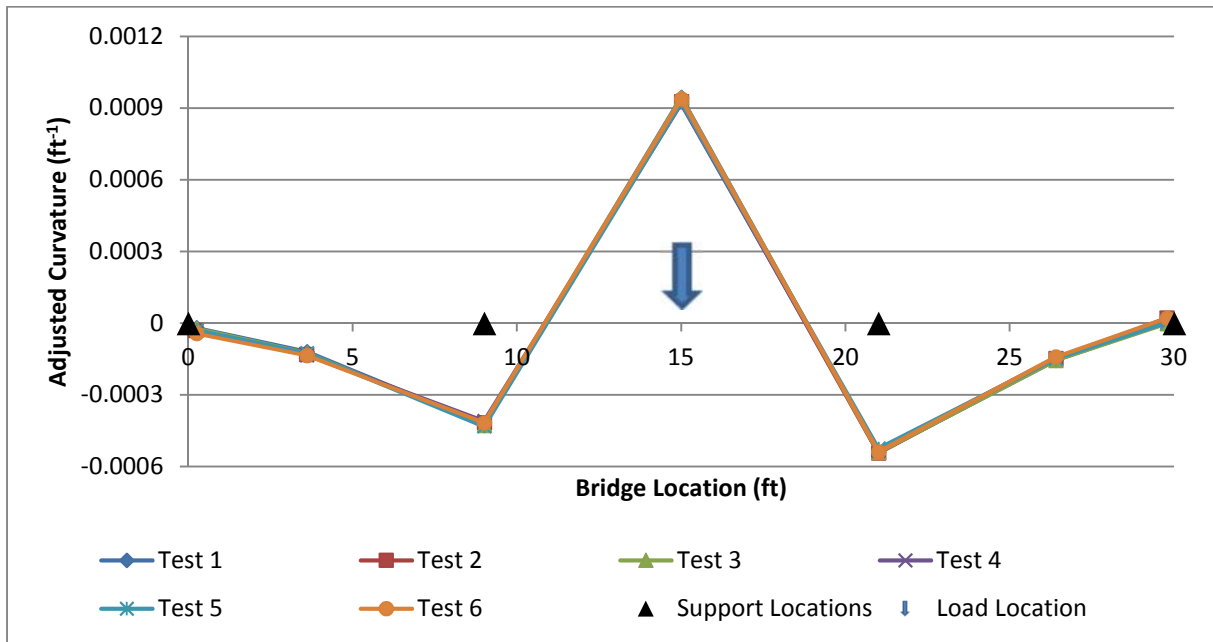
A similar procedure as that for the concrete beam was followed to calculate the results from the six different static tests performed on the steel beam. The coefficient of variation was 0.0388 for the maximum normalized positive and negative curvatures measured under each load condition. At support 1.00, the average curvature due to a load at the 1.04 location was calculated to be  $-4.46 \times 10^{-5} \text{ ft}^{-1}$ . At the 3.10 support, the average curvature due to a load at the 3.06 location was calculated to be  $-10.2 \times 10^{-5} \text{ ft}^{-1}$ .

Because there were significant discrepancies between the two sensor configurations used on the steel beam, Figure 8.7, Figure 8.8, and Figure 8.9 show the plots of the curvatures obtained from averaging the readings from all of the sensors on the cross-section at each location along the length of the beam.

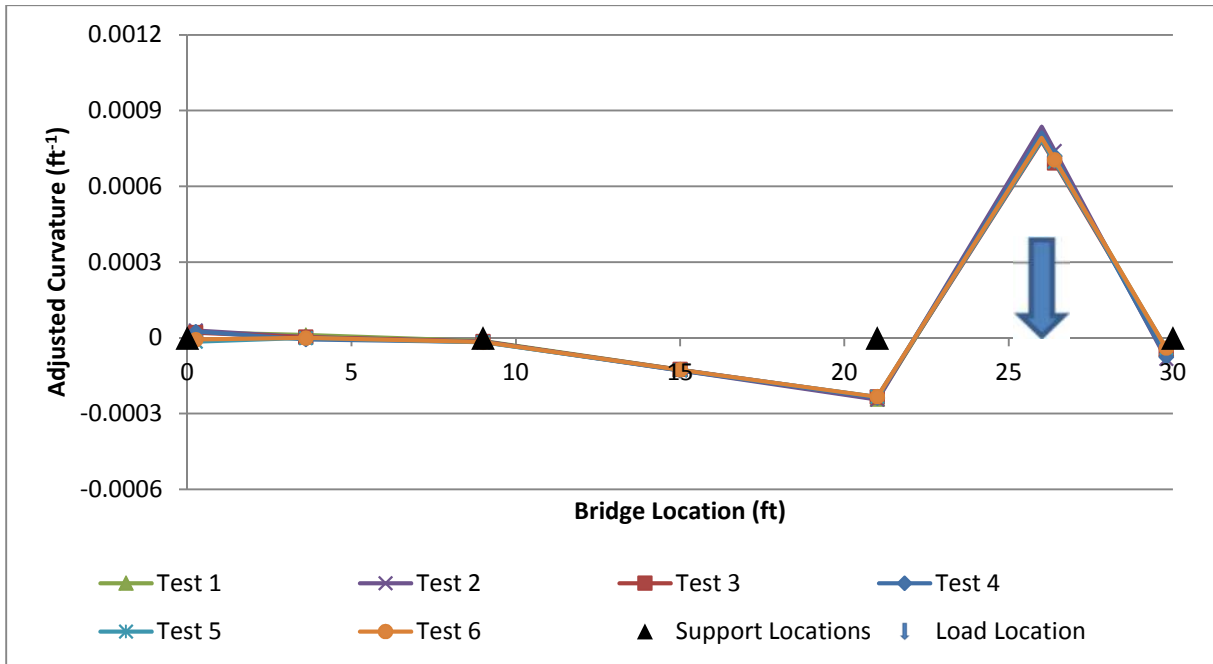




**Figure 8.7. Averaged Curvature from Static Tests on Steel Beam**  
 Static tests with point load located at 4 feet (~1.04). Curves are extrapolated to load location.



**Figure 8.8. Averaged Curvature from Static Tests on Steel Beam**  
 Static tests with point load located at 15 feet (2.05).

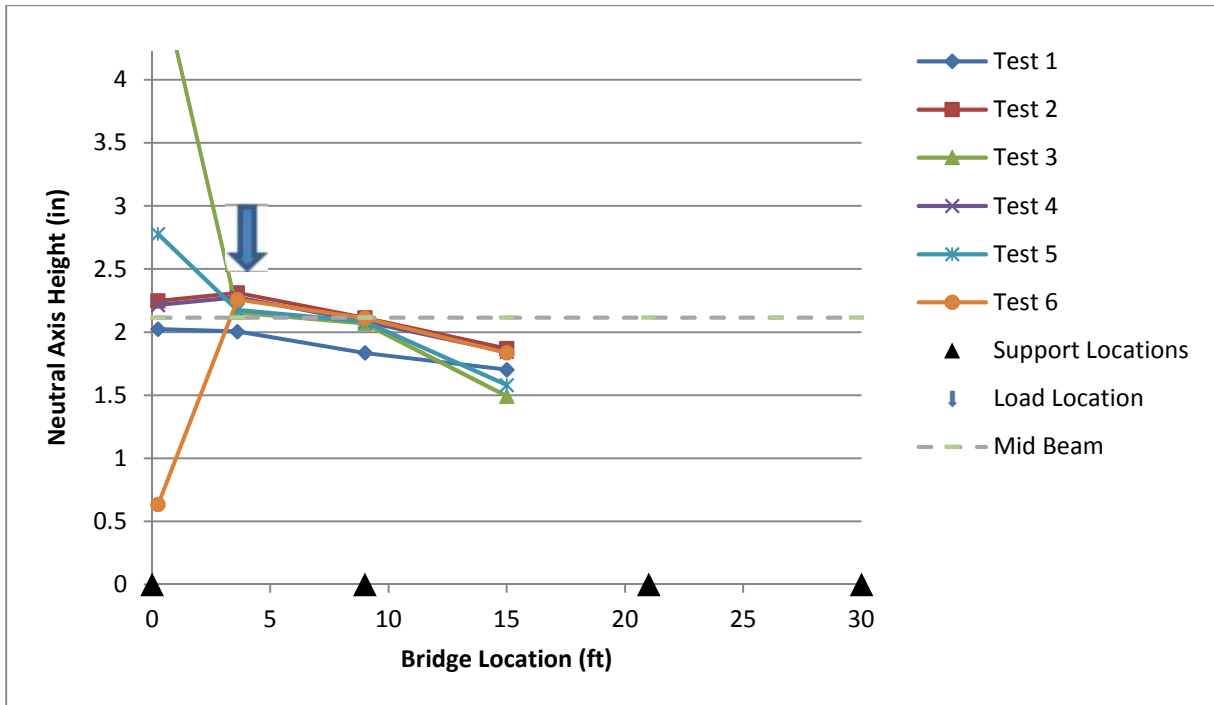


**Figure 8.9. Averaged Curvature from Static Tests on Steel Beam**  
 Static tests with point load located at 26 feet (~3.06). Curves are extrapolated to load location.

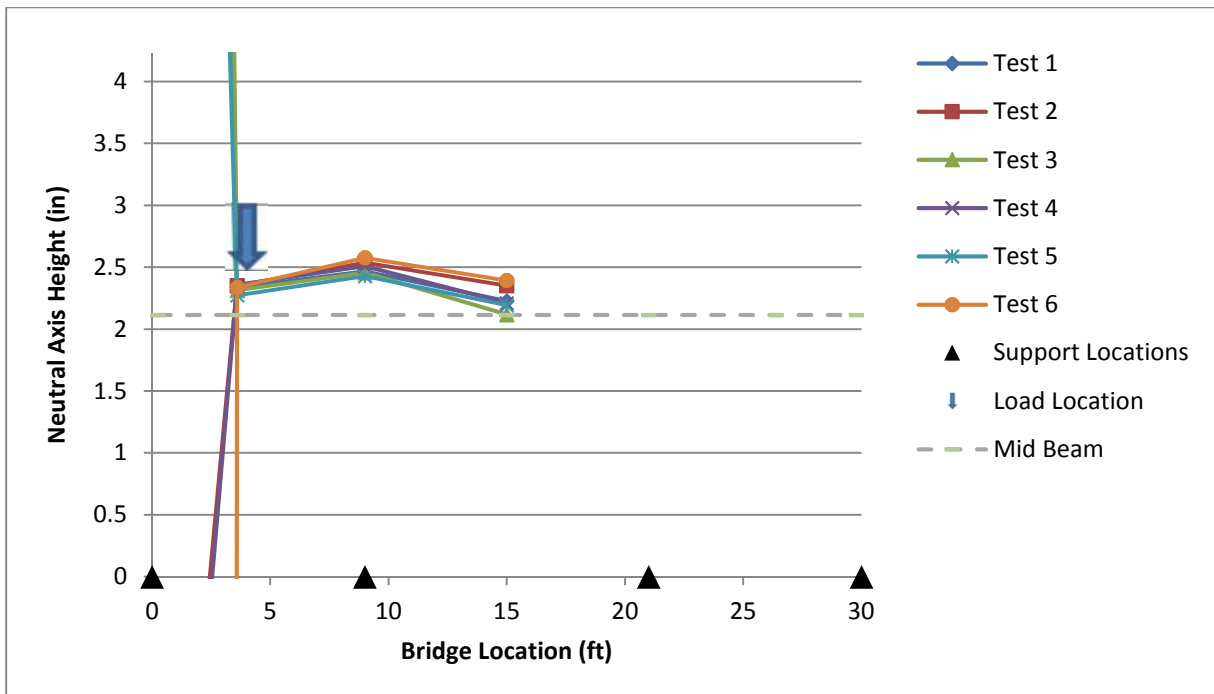
The consistency of the measurements taken during different tests indicates that the discrepancy in strain readings is likely not due to random error and further supports the conclusion that the beam experienced some secondary load effects in addition to major axis bending.

### Neutral Axis Location

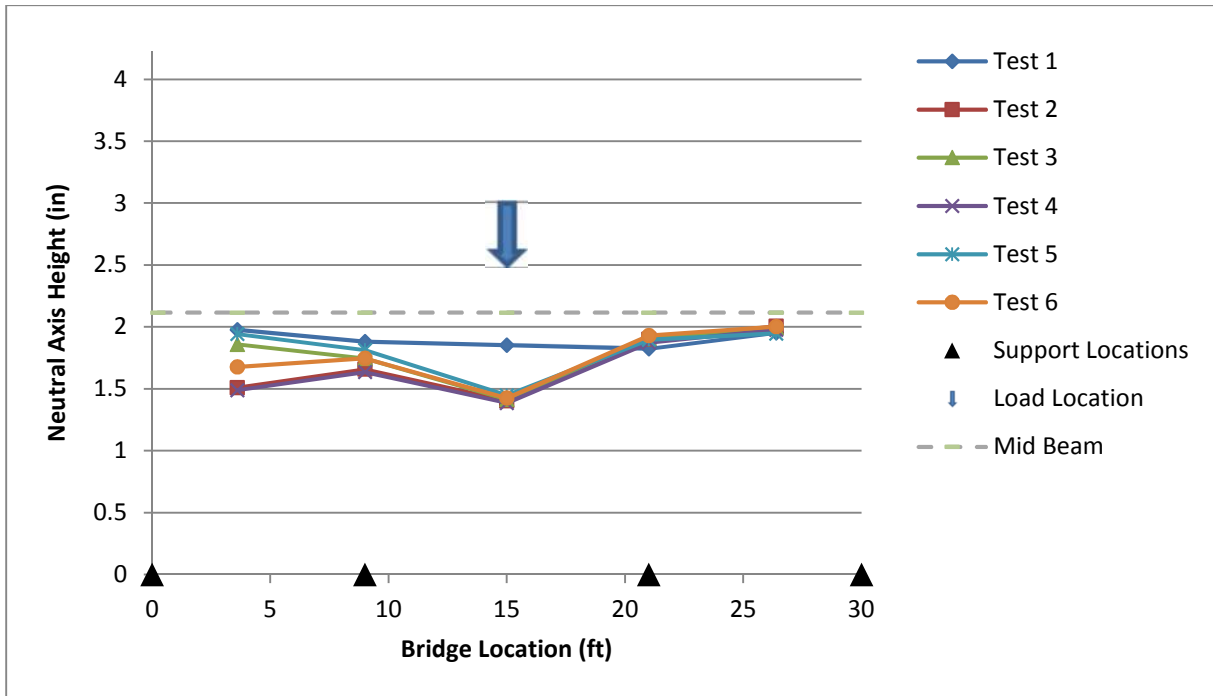
The neutral axis height was calculated for three load conditions for the two sensor configurations shown in Figure 8.2. The neutral axis height along the beam is shown in the following figures. Values away from the load location where the strain values were too small to yield meaningful results were omitted.



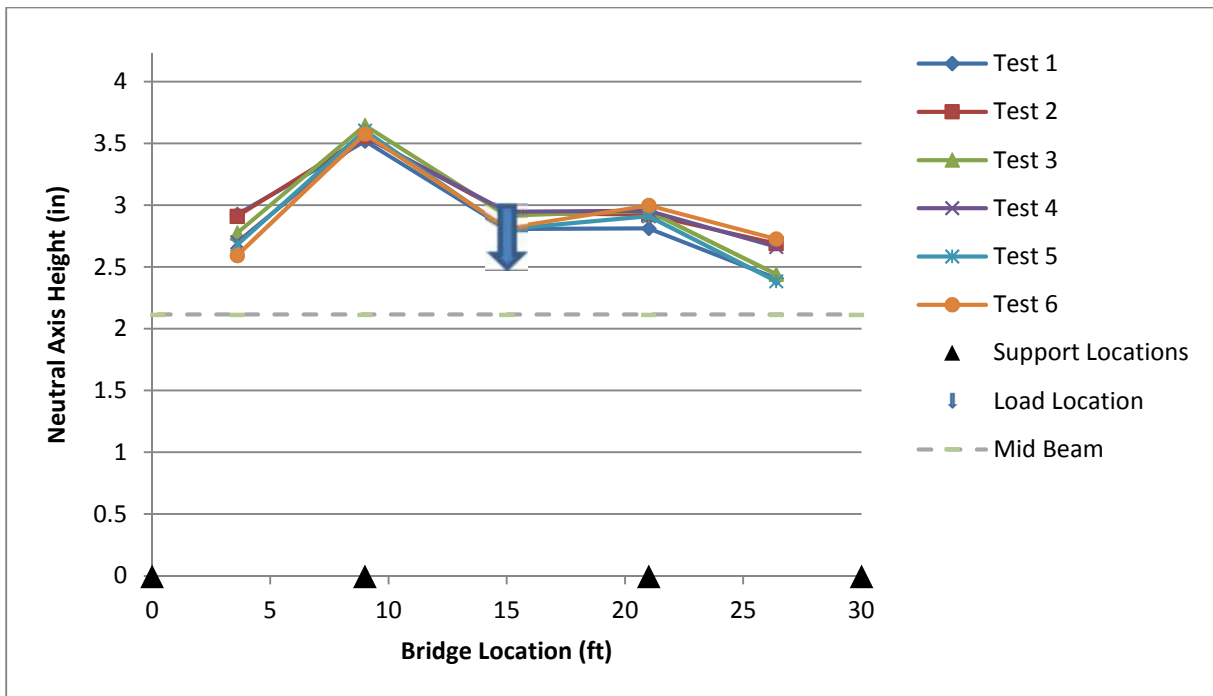
**Figure 8.10. Neutral Axis Location Measured by Inside Sensors on Steel Beam**  
Static tests with point load located at 4 feet (~1.04).



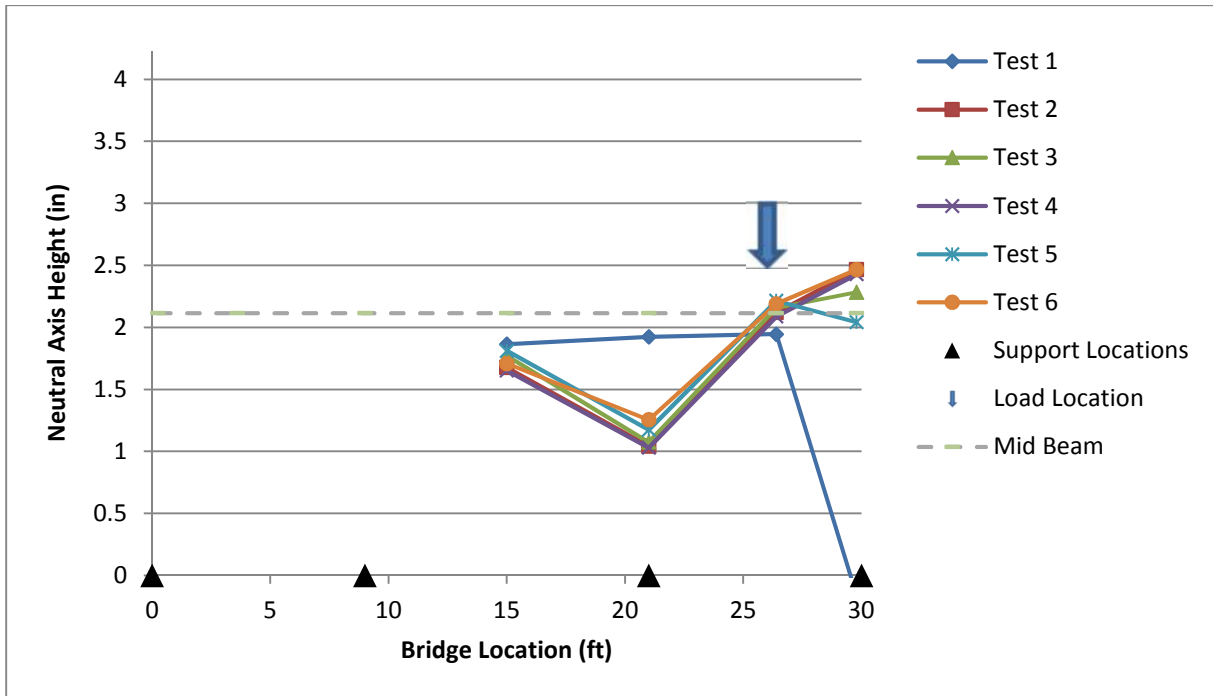
**Figure 8.11. Neutral Axis Location Measured by Outside Sensors on Steel Beam**  
Static tests with point load located at 4 feet (~1.04).



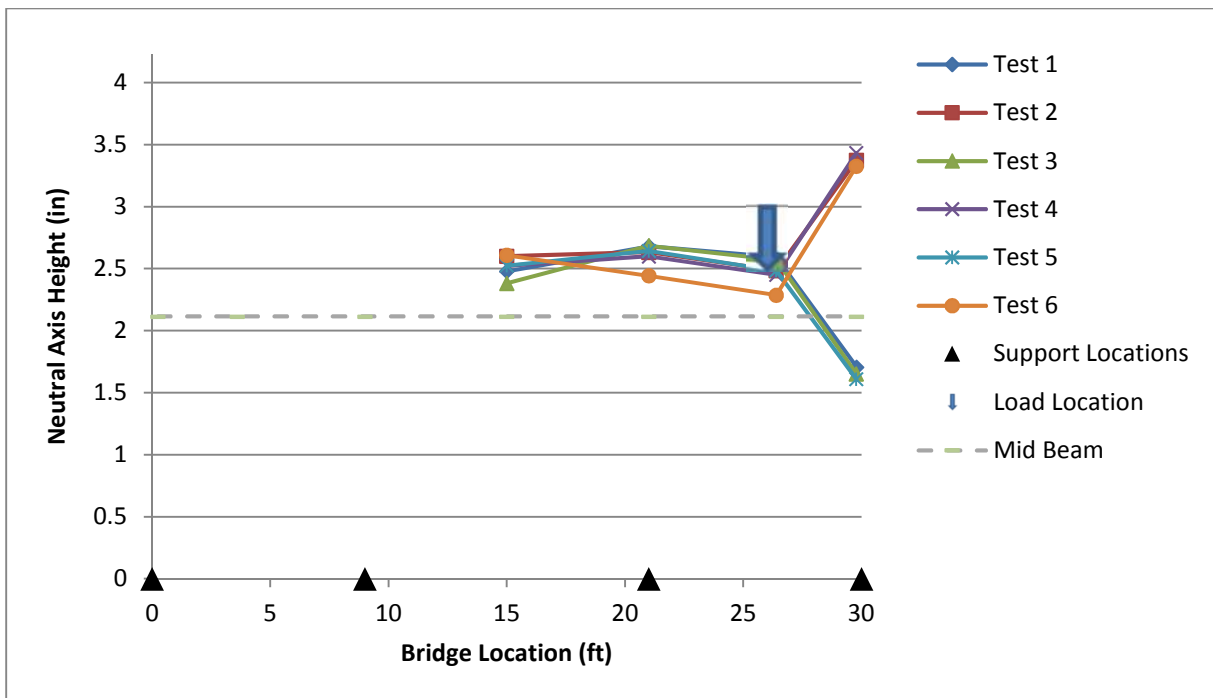
**Figure 8.12. Neutral Axis Location Measured by Inside Sensors on Steel Beam**  
 Static tests with point load located at 15 feet (2.05).



**Figure 8.13. Neutral Axis Location Measured by Outside Sensors on Steel Beam**  
 Static tests with point load located at 15 feet (2.05).



**Figure 8.14. Neutral Axis Location Measured by Inside Sensors on Steel Beam**  
 Static tests with point load located at 26 feet (~3.06).

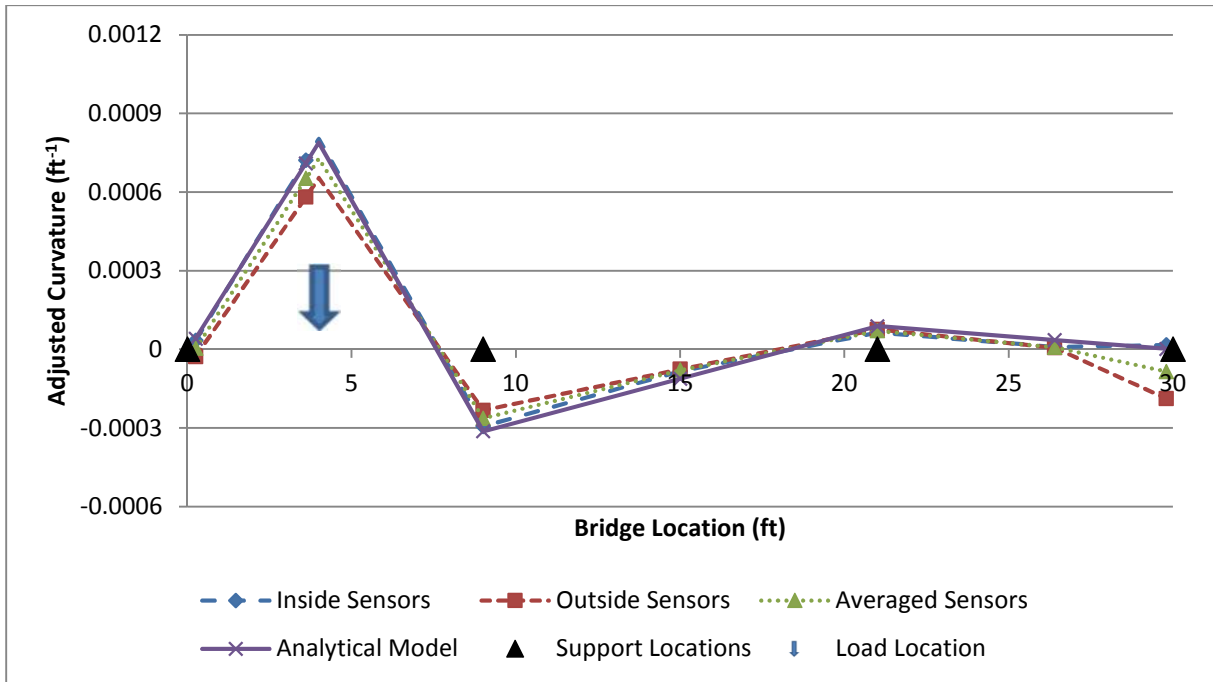


**Figure 8.15. Neutral Axis Location Measured by Outside Sensors on Steel Beam**  
 Static tests with point load located at 26 feet (~3.06).

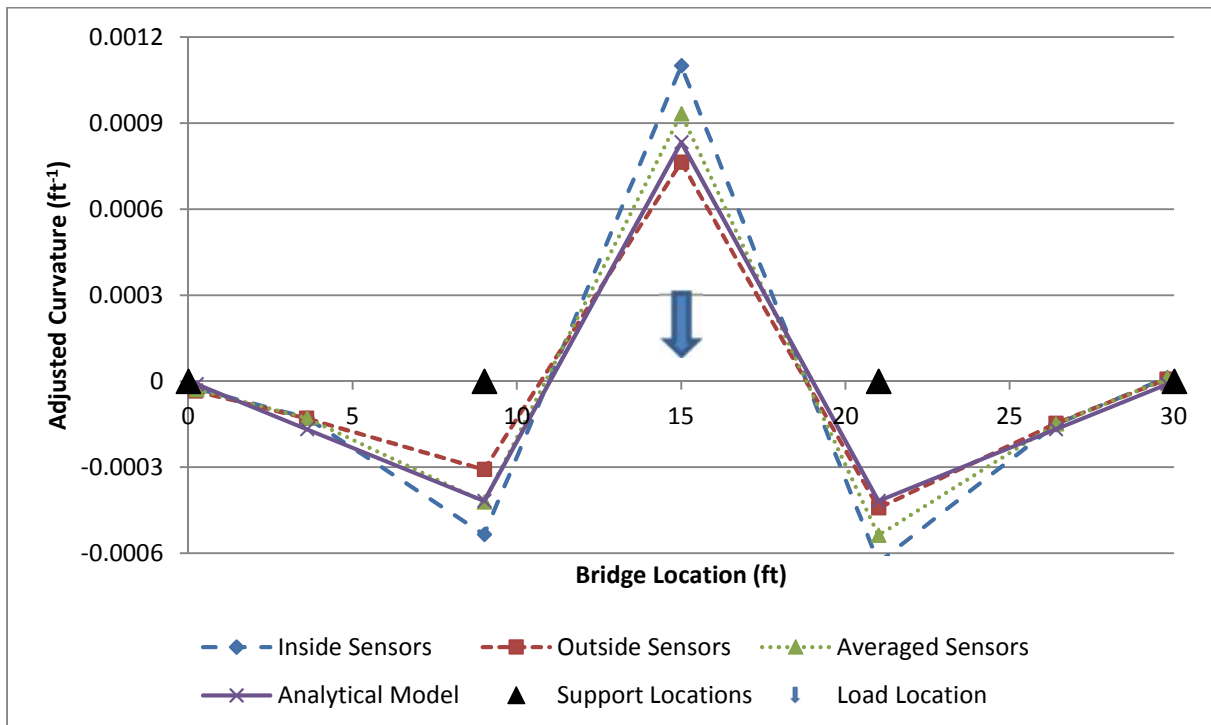
The neutral axis values for the steel beam were more variable than those calculated for the concrete beam. This could be due to the beam experiencing more significant secondary load effects and being more susceptible to local effects from the load and supports because of the short gauge sensor configuration used on the steel beam. Similar to the neutral axis results on the concrete beam, the neutral axis height determined by sensors on one side of the beam tended to be above the mid-height of the section and below the mid-height of the section on the other side of the beam, although this trend was not as pronounced as with the concrete beam. As with the concrete beam, the values for the neutral axis locations measured at the end supports were highly variable, likely due to effects from the bearing connection and exaggerated by the small strain magnitudes measured at those locations.

### **Comparison of Results**

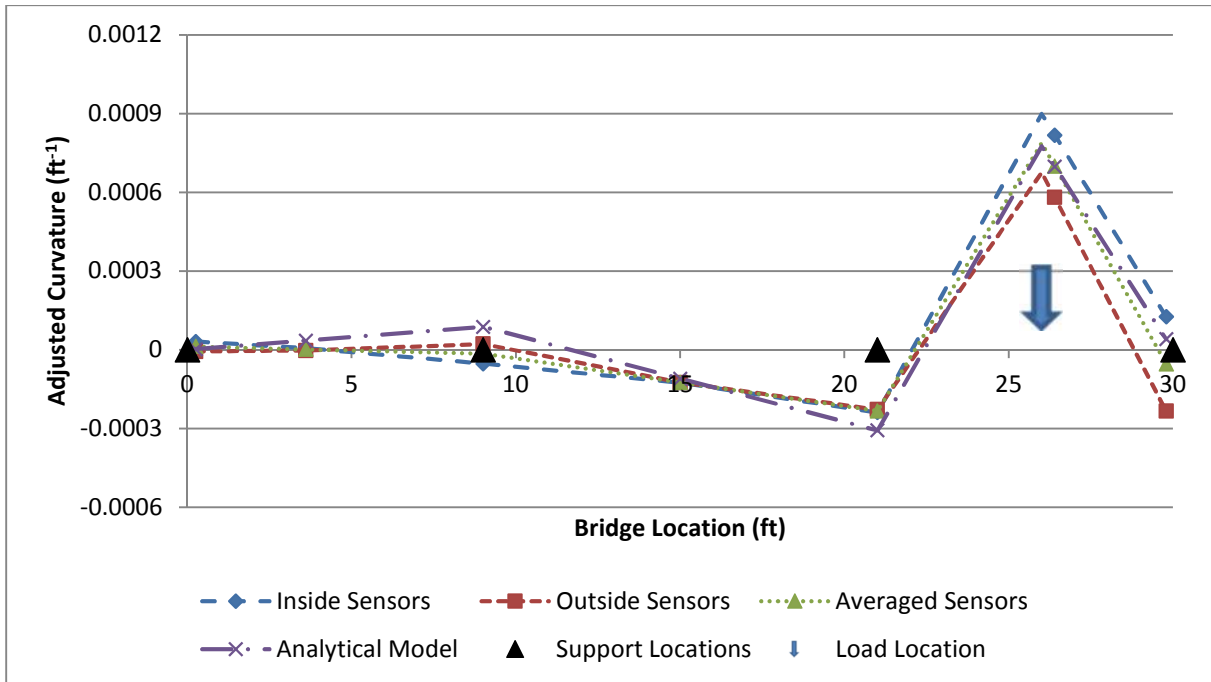
Figure 8.16, Figure 8.17, and Figure 8.18 compare the curvatures obtained from the sensors to the analytical values predicted by analysis of the steel beam subjected to strong axis bending only for the three load conditions studied.



**Figure 8.16. Comparison of Analytical and Measured Curvatures on Steel Beam**  
 Static tests with point load located at 4 feet (~1.04). Curves are extrapolated to load location.



**Figure 8.17. Comparison of Analytical and Measured Curvatures on Steel Beam**  
 Static tests with point load located at 15 feet (2.05).



**Figure 8.18. Comparison of Analytical and Measured Curvatures on Steel Beam**  
 Static tests with point load located at 26 feet (~3.06). Curves are extrapolated to load location.

As was previously discussed, the discrepancy between the measurements taken by the inside sensors and the outside sensors may be the result of secondary load effects like minor-axis bending. Averaging the measurements taken from all four sensors would have the effect of neutralizing these secondary load contributions on the data, as tensile strains on one side of the beam would be counteracted by compressive strains in the opposite side of the beam when the data is combined. The previous plots show some of this behavior, where the averaged curvatures tend to approach the analytically predicted values.

## 8.5 MOVING LOAD TESTS

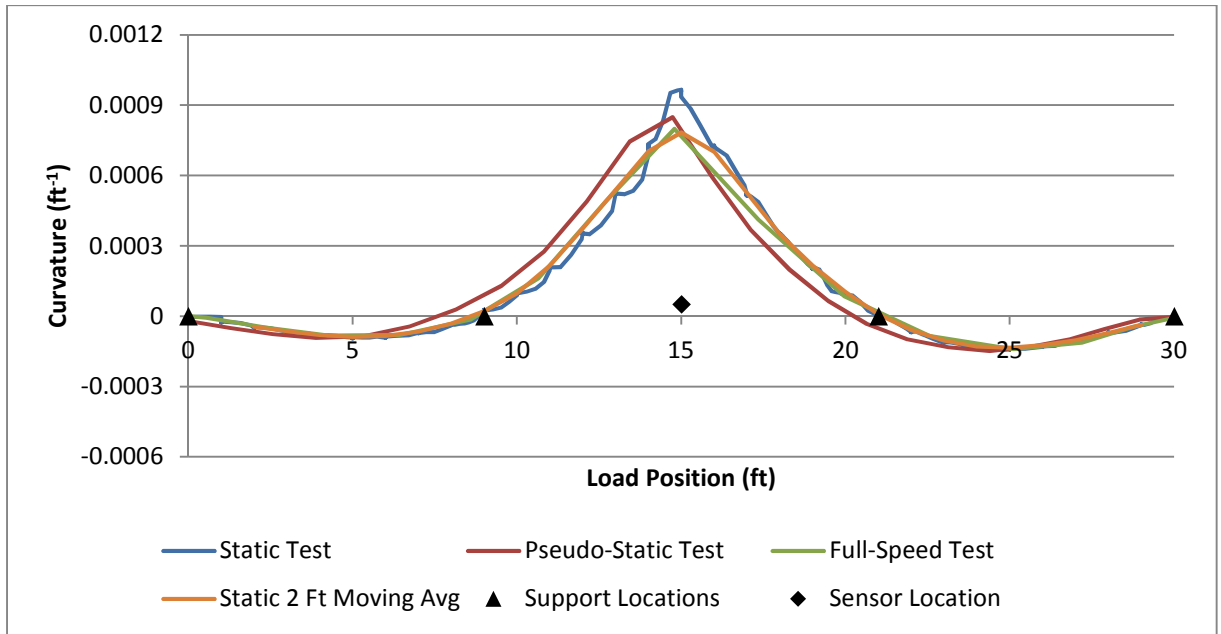
As with the moving load tests on the concrete beam, the moving load tests for the steel beam resulted in significant variability in the curvature values that was likely the result of the rocking observed in the cart during the tests. For the pseudo-static test curvatures, the coefficient of variation was 0.190 and for the full-speed test curvatures, the coefficient of



variation was 0.107. Once again, the suspension of a more traditional test vehicle on a field bridge will likely reduce this variability.

The maximum load recorded by the load cell during the static test was 1,005 lb. During the pseudo-static test, the maximum load measured was 9.77% higher than the static test value at 1,104 lb, and the full-speed test produced a maximum load reading of 1,099 lb, which was 9.23% higher than the maximum result from the static test. As was previously discussed, an increase in the measured load does not directly correlate to a higher dynamic impact factor.

As with the moving test performed on the concrete beam, the moving tests on the steel beam were performed with too low of a time resolution to capture accurate strain readings, and the results effectively produced a moving average of the load effects. The averaging of the strain data collected during the pseudo-static and full-speed tests effectively flattened the response curves from these tests. Therefore, the measurements from the static tests yielded the highest curvature values. However, by averaging the values measured during the static test over the appropriate ranges, a better indication of the dynamic impact factor was achieved. For the pseudo-static test, the dynamic impact factor was calculated to be 0.73%, when compared to the averaged adjusted static value. For the full-speed test, the dynamic impact factor was calculated to be 1.86% when compared to the averaged static value. Figure 8.19 shows the curvatures measured by the mid-span sensors during the course of a static test, pseudo-static test, and full-speed test along with the averaged static curvature.



**Figure 8.19. Average Curvature Influence Function for Steel Beam at Mid-Span (2.05)**  
 Measured by Sensors Located at Mid-Span (2.05).

## **CHAPTER 9: SUMMARY OF FINDINGS & CONCLUSIONS**

### **9.1 FBG SENSOR INSTALLATION TECHNIQUES (OBJECTIVES 1 & 2)**

In previous research, studies were performed to determine required bond properties to ensure adequate strain transfer between host elements and FBG sensors. Section 4.3 of this thesis outlines techniques for installing FBG sensors on concrete and steel elements that are suitable for use in the field. Additionally, methods for providing protection of the sensors and lead fibers were developed. The procedures outlined allowed for reliable sensor installation by a straight-forward procedure that could be mastered by an installer with a reasonable amount of training.

The sensors installed on the concrete beam using these methods provided measurements similar to, but lower in magnitude than, what was predicted by the analytical model. It was necessary to account for averaging effects caused by the long gauge sensor configuration. Further discrepancies between the test results and the analytical model could be explained by a difference between the predicted and the as-built modulus of elasticity for the concrete. However, the as-built modulus of elasticity was not measured, so this explanation cannot be confirmed.

The measurements taken on the steel beam were similar in magnitude to the values predicted by the analytical model. However, the measurements taken at different locations on the beam cross-section varied significantly, where they should have been similar. This variation could be explained by the presence of secondary load effects induced by an eccentricity in the load on the beam that was observed during the experiment. However, no measurements were made of secondary load effects. So, this explanation cannot be confirmed.

In a few locations on the steel beam, the sensors experienced a significant loss in pretension after installation. The wavelengths from these sensors did stabilize at a point that indicated that there was still adequate pretension to make the necessary measurements. However, the resulting measurements at these locations appeared inconsistent with measurements taken from other sensors during the tests. This may be due to an inadequate bond between the sensor and the beam. However, these sensors were located directly above the mid supports of the beam. So, the inconsistent measurements may have been the result of unpredicted localized effects from the supports.

## **9.2 ANALYSIS OF TEST DATA (OBJECTIVE 3)**

Section 6.1 outlines the typical procedures for converting the raw wavelength data recorded by the FBG sensors into strain. It also presents equations for determining curvature and the neutral axis height from strain data. These relationships are well-established and are presented in this thesis as a summary.

Analysis of the curvature and neutral axis height did not yield values similar to the analytical model. Comparing the measured experimental values with different hypothesized properties and loading scenarios on the analytical model allowed for reasonable postulations of the behavior that may have induced the recorded test data. However, these hypotheses were not confirmed by direct measurements.

The sensor data appeared to be significantly influenced by local effects at the support locations. Therefore, placing sensors directly over the support locations should be avoided. It may be necessary to offset the sensors a distance away from the support locations to minimize the influence of local bearing effects.

Moving tests were performed in order to illustrate the calculation of the dynamic impact factor. However, due to an oversight in the time resolution of the data collection, the moving tests did not yield meaningful results. This oversight underscores the importance of selecting appropriate data collection parameters for the type of test being performed.

### **9.3 CROSS-SECTION SENSOR LOCATION (OBJECTIVE 4)**

Section 7.2 discusses the placement of sensors on the cross-section of the concrete beam. The curvatures measured by the sensors located at the extreme fibers of the beam cross-section were similar to the curvatures measured by the sensors inset from the edges of the beam cross-section. This similarity in results supports the conclusion that the FBG sensors do not need to be located at the extreme fibers of the cross-section in order to measure accurate values. The neutral axis height values indicated that locating sensors near the sides of the cross-sections may incur unanticipated load effects due to minor-axis bending.

Section 8.2 discusses the placement of sensors on the cross-section of the steel beam. The sensors at the four locations on the cross-section each reported different magnitudes of curvature. It was postulated that this variation in results was caused by unanticipated secondary load effects such as minor-axis bending and torsional warping, based on observations of the load condition during the experiment. The presence of these incongruent curvature values makes it difficult to confirm that sensors located on the inside of the cross-section can accurately measure major-axis bending effects.

The presence of FBG sensors at multiple locations on the beam cross-section enabled the sensing system to detect discrepancies that were likely due to secondary load effects. To improve on the sensor arrangement used during these tests, sensors could be placed at the top

and bottom of the beam cross-section along the minor neutral axis in addition to near the side of the beam. The sensors on the minor neutral axis would provide a more direct measure of the major-axis bending, and could be compared to the measurements taken near the sides of the cross-section to quantify secondary load effects.

#### **9.4 COMPARISON OF TEST DATA WITH ANALYTICAL MODEL (OBJECTIVE 5)**

Section 7.3 compares the calculated load effects from the laboratory tests on the concrete beam with the values predicted by an analytical model based on common structural analysis and bridge design practices. The measured curvatures from the laboratory tests were consistently lower than those predicted by the analytical model. It was postulated that the modulus of elasticity of the laboratory beam was higher than what was assumed in the analytical model, but no measurement of the modulus of elasticity of the concrete was taken. So, this explanation remains unconfirmed.

Section 8.3 and Section 8.4 compares the curvatures measured by the sensors on the steel beam to the values predicted by the analytical model. There were significant discrepancies between the measurements taken by the different sensors, and it was postulated that these discrepancies were due to secondary load effects like minor-axis bending and torsional warping. After some analysis was done to quantify how these behaviors would affect the strains at the sensor locations, it was shown that adjusting the measured data to account for these load effects could achieve better agreement with the analytical model. However, because these assumptions were based only off of observations of the load position during the tests, and no measurements were made to quantify minor-axis bending or torsion, there was no way to confirm that these behaviors were the cause for the discrepancies in the test data.

The curvature values obtained by averaging the measurements taken by the four sensors located on the cross-section at each measured span location showed similar curvature distributions to the analytical model, with exception to the measurements taken at the support locations, where it appears that local interactions with the supports had influenced the measurements taken. Moving these sensors away from the support locations would reduce the local interactions with the sensors, but analysts would be required to extrapolate the tested data to determine the maximum negative load effects over the supports.

Additionally, the sensors on the top of the steel beam over the mid-supports experienced some pre-tension loss after installation and may not have been providing accurate readings. At these locations, the comparison with the analytical model were ignored.

## **CHAPTER 10: APPLICATIONS & FUTURE WORK**

The primary focus of this thesis was on developing and summarizing methods for installing FBG sensors and analyzing the results of a simplified preliminary load test. Future work on this project will include further development and refinement of the system and techniques outlined in this thesis in order to develop a system capable of performing a load rating on a bridge. It will be necessary to verify that the procedures for installation, protection, and analysis that were developed in the laboratory are feasible and appropriate for use in field conditions.

Methods need to be developed and tested for additional parameters that affect load ratings on structures that could not be measured by the laboratory tests. These include lateral load distribution, incidental composite action, and strength contributions from secondary bridge components like crash-barriers. Additionally, while this thesis has focused primarily on sensor installation and data analysis, techniques should be developed that focus on load rating bridges and monitoring them for damage and deterioration.

The testing in the laboratory was achieved with commercially available instrumentation. However, for continuous operation of the system from a remote structure, the current instrumentation is not adequate. Work has begun to develop the necessary electronics to automatically collect, filter, and send relevant data from the instrumented bridge to servers that can be accessed by engineers. The system will combine a commercially available interrogator, wireless data modem, and microprocessor using a custom designed printed circuit board.



## **10.1 CROSS-SECTION SENSOR PLACEMENT**

Sensors should be placed at a sufficient distance away from the neutral axis to ensure that they are measuring meaningful flexural strain values. For many structures, the concrete deck will act integrally with the primary structural elements. This composite behavior will shift the neutral axis toward the deck. Analysis should be performed for each structure to determine where the expected neutral axis will occur, and the neutral axis location should be considered when deciding where to locate the sensors on the cross-section.

A two-sensor configuration would make it difficult to distinguish any contribution from out-of-plane bending. If a sensor is located on a location of the cross-section where strains from one load effect act counter to strains from another load effect, these readings would underestimate the response of the structure to the loading. If these values were used to load rate a bridge, they would overestimate the capacity of the bridge. Placing the sensors close to the minor-neutral-axis of the beam would minimize the contributions from these secondary load effects. However, if there are significant secondary load effects, it would be important to consider them and the interaction of the stresses.

While the top flange of a girder is typically braced by the deck, the bottom flange often carries lateral loads along the girder line through bending until they reach a lateral brace that will transfer the loads into the deck (AASHTO 2012). The significance of these lateral loads should be investigated in the later phases of this research.

## **10.2 LOAD DISTRIBUTION**

The distribution of loads to the girders is one of the main parameters that can affect the load rating of a bridge. The equations used by the AASHTO Bridge Design Manual tend

to be conservative, and there is significant opportunity to calculate more favorable distribution factors through refined analysis. These factors can be measured directly during a load test by strategically locating a load vehicle on the bridge to induce the maximum value for the load effect of interest and measuring the response of the structure for use in equation 6.3. The final system will need to demonstrate reliable measurement of this parameter.

Crash barriers that are built integrally with the structure may contribute to the strength of the bridge by acting as inverted exterior girders. Their contribution can be measured by instrumenting them similarly to a girder and including them in the load distribution calculations. To include these contributions in a load rating, analysis should be performed to determine whether the barrier have sufficient capacity for the ultimate limit state.

### **10.3 INCIDENTAL COMPOSITE ACTION**

Structures with concrete decks will exhibit some composite behavior, even if the structure has not been designed to act compositely, due to adhesion between the deck and the girder. When performing a load rating on a non-composite structure, it is critical to quantify this contribution and ensure that it is not considered as part of the capacity of the structure. Erroneously including this contribution in the analysis could result in an unsafe load rating. This contribution can be inferred from the location of the neutral axis, which is found from the difference in strain measurements between sensors at different depths on the cross-section of the beam.

### **10.4 DATA HANDLING**

The SHM system will be capable of recording massive amounts of data. It will be necessary to develop methods to automatically decipher which data is significant and should

be transmitted and saved by the system. An algorithm to save data with readings that exceed a certain threshold or the maximum response each day may be appropriate. Taking a relaxed state reading each day may be appropriate for documenting changes in the structure or the sensing system.

Once the system is installed and data from the field loading conditions is available, more refined analysis can be performed to develop methods for recognition of load patterns, such as a method for differentiating truck loads from ambient traffic loads.

## **10.5 CONSIDERATIONS FOR LOAD RATING THROUGH TESTING**

Load testing can provide more accurate load ratings for an instrumented bridge than analytical predictions alone can achieve. However, care must be taken in performing the tests and interpreting the results. When calculating a load rating, the goal is to estimate the capacity of the bridge as accurately as possible without overestimating the capacity. Because of this necessity for a conservative load rating, the model developed from load testing may not exactly match the behavior of the bridge, but it should represent a lower bound of the bridge performance. Thus, it is important to consider which load effects will impact the rating of the structure when designing the sensing system.

Depending on which limit state is of critical interest, different sensor configurations may be necessary. The configuration used in these experiments was designed primarily to measure the behavior under pure major-axis bending. However, having sensors located at four different locations on the cross-section provided additional insight into the unexpected lateral load effects that were observed during testing. Sensors could also be placed to measure shear, the magnitude of strain cycles for fatigue considerations, and other parameters of interest.

It is critical that any observed behavior that is used to improve a load rating be understood and validated in the context of structural theory. If strong support cannot be found to explain the behavior being observed from measurements, then this data should not be used to improve a load rating, as it may not endure at the strength limit state.

It is also important to consider the variability of the test results when adjusting load ratings. If the coefficient of variation is similar in magnitude to the deviation between the analytical and test behavior, then the value that results in the more conservative load rating should govern. In order to ensure a conservative load rating, it is appropriate to use only the most restrictive test results.

Some variables, like the dynamic impact, require a higher time resolution for data collection. However, this process would yield a large amount of data that could encumber the transmission, storage, and analysis procedures. If properties that require high time resolution data collection are of primary concern, then it may be necessary to develop automated processing procedures to filter the relevant data.

## **10.6 WIDE IMPLEMENTATION**

After the development of the system is completed and tested at the conclusion of Phase 2, the next step would be wide implementation of the system. If successfully developed, the SHM system will be effective for load testing bridges and monitoring them for damage. The information gathered by the SHM systems would be beneficial for managing the maintenance, operations, and life-cycle of bridges. A network of instrumented bridges could enhance the bridge inspection program and be used to more effectively allocate limited

maintenance funds to the bridges and projects where they will have the most significant impact.

The system would also be capable of collecting other information of interest for bridge engineers. For example, statistics for average daily truck traffic, permit compliance, and fatigue limit cycles could be collected. Additionally, the system could be used to better quantify structural behavior. Additional sensors can be easily incorporated into the system in order to measure additional parameters that may be of interest to bridge engineers. The findings from measuring the behavior and loading of in-service bridges could be used to refine future design practices and codes.

## References

- A.G. Lichtenstein and Associates, Inc. 1998. "Manual for Bridge Rating Through Load Testing." *National Cooperative Highway Research Program Research Results Digest* (Transportation Research Board) (No. 234).
- AASHTO. 2012. *AASHTO LRFD Bridge Design Specifications*. Washington, D.C.: AASHTO.
- . 2010. *The Manual for Bridge Evaluation, 2nd Edition*. Washington D.C.: American Association of State Highway and Transportation Officials.
- AISC. 2006. *Steel Construction Manual - Thirteenth Edition*. Chicago: American Institute of Steel Construction.
- Aktan, Emin, Necati Catbad, Kirk Grimmelman, and Mesut Pervizpour. 2003. *Development of a Model Health Monitoring Guide for Major Bridges*. Drexel University.
- ASCE. 2013. *2013 Report Card for America's Infrastructure*. Reston, VA: American Society of Civil Engineers.
- Barker, Michael, Cory Imhoff, Travis McDaniel, and Troy Frederick. 1999. *Field Testing and Load Rating Procedures for Steel Girder Bridges*. Jefferson City, MO: Missouri Department of Transportation.
- Branscomb, James. 2013. "Presentation, Structural Health Monitoring of Highway Bridges Subjected to Overweight Vehicles." Cheyenne, Wyoming, March.

- Bremault, Dennis, Robert G Driver, and Gilbert Y Grondin. 2008. *Limit States Design Approach for Rolled Wide Flange Beams Subject to Combined Torsion and Flexure*. University of Alberta.
- Cardini, A, and J DeWolf. 2008. "Long-term Structural Health Monitoring of a Multi-girder Steel Composite Bridge Using Strain Data." *Structural Health Monitoring* 47-58.
- Chajes, Michael, Harry Shenton III, and Dennis O'Shea. 2000. "Bridge-Condition Assessment and Load Rating Using Nondestructive Evaluation Methods." *Transportation Research Record*.
- Chen, Qiyang, and Ping Lu. 2011. "Fiber Bragg Gratings and Their Applications as Temperature and Humidity Sensors." In *Atomic, Molecular and Optical Physics*, by L.T. Chen, 235-260. Nova.
- Computers & Structures, Inc. 2011. "SAP 2000 Version 15."
- Doornink, J.D., B.M. Phares, T.J. Wipf, and D.L. Wood. 2006. "Damage Detection in Bridges through Fiber Optic Structural Health Monitoring." *Proceedings of SPIE, the international society for optical engineering* 6371.
- Farhey, Daniel N. 2005. "Bridge Instrumentation and Monitoring for Structural Diagnostics." *Structural Health Monitoring* 301-318.
- Federal Highway Administration. 2014. *Questions and Answers on the National Bridge Inspection Standards 23 CFR 650 Subpart C*. May 3.  
<http://www.fhwa.dot.gov/bridge/nbis/index.cfm>.

- Guemes, Alfredo, and Julian Sierra-Perez. 2013. "Fiber Optic Sensors." In *New Trends in Structural Health Monitoring*, by W. Ostachowicz, 265-316. Udine: International Centre for Mechanical Sciences.
- Heininger, Hilmar. 2009. "Research proposal, Faseroptische Sensoren zur Bauwerksüberwachung." Mannheim.
- Lawrence, Timothy, Chad Ritter, and Janos Gergely. 2011. "Bridge Monitoring and Performance Evaluation." *Geotechnical and Geological Engineering* 29 (5): 919-926.
- Li, Dongsheng, Liang Ren, and Hongnan Li. 2012. "Mechanical Property and Strain Transferring Mechanism in Optical Fiber Sensors." In *Fiber Optic Sensors*, by Dr. Moh. Yasin, 439-458. Shanghai: InTech.
- Matta, F, F Bastianini, N Galati, P Casadei, and A Nanni. 2005. *In-Situ Load Testing of Bridge A6358*. MoDOT.
- Maurais, Daniel. 2012. *Strain Transfer of Notch Embedded Fiber Bragg Gratings*. Thesis, Laramie, WY: University of Wyoming.
- Okasha, Nader, Dan Frangopol, and Andre Orcesi. 2011. "Automated Finite Element Updating using Strain Data for the Lifetime Reliability Assessment of Bridges." *Reliability Engineering & System Safety* 139-150.
- Seaburg, Paul A, and Charles J Carter. 2003. *Design Guide 9: Torsional Analysis of Structural Steel Members*; . Chicago: American Institute of Steel Construction.



Seo, Junwon, Brent Phares, Ping Lu, Terry Wipf, and Justin Dahlberg. 2012. "Use of Structural Health Monitoring System for Assessment of Bridge Load Rating." *Forensic Engineering* 18-27.

Todd, M, C Chang, G Johnson, S Vohra, J Pate, and R Idriss. 1999. "Bridge Monitoring Using a 64-Channel Fiber Bragg Grating System." *17th International Modal Analysis Conference*. Kissimmee, FL: Society for Experimental Mechanics. 1719-1725.

Vanderzee, Peter, and James Cooper. 2005. "A Bridge Too Near." *International Bridge Conference*, 9-11.

Zhou, Zhi, and Jinping Ou. 2004. "Development of FBG Sensors for Structural Health Monitoring in Civil Infrastructures." *Sensing Issues in Civil Structural Health Monitoring*. Oahu: North American Euro-Pacific Workshop.

**APPENDIX B-3**

**M.S. THESIS  
BY MCKENZIE DANFORTH**

To the University of Wyoming:

The members of the Committee approve the thesis of McKenzie M. Danforth  
presented on 10/23/2015.

Dr. Richard Schmidt, Chairperson

Dr. Steven Barrett, External Department Member

Dr. Michael Barker

APPROVED:

Dr. Anthony Denzer, Department Head, Civil and Architectural Engineering Department.

Dr. Michael Pishko, Dean, College of Engineering and Applied Science

Danforth, McKenzie, M, Laramie River Bridge Load-Testing Plan with Sensor Verification and RFID Feasibility of Permitted Vehicles, M.S., Civil and Architectural Engineering, December, 2015.

Many mountain-west states, including Wyoming, are observing a rise in overweight and non-standard truck configurations due in part to an increase in demands from the energy sector. As a result, state department of transportations (DOTs) are under pressure to assure safe and efficient routes for overweight and non-standard vehicles transporting heavy equipment over highway bridges while investigating methods for increasing load ratings or removing postings. This thesis presents a method using fiber optic sensors to field test a bridge in order to determine the actual lateral distribution factors. Using field tested instead of analytical distribution factors could potentially increase the load rating of a bridge. The plan includes a sensor placement and vehicle load testing design. The specific fiber optic sensors used, called Fiber Bragg Gratings, are validated through laboratory tests. The thesis also explores a novel method to correlate known permitted vehicle loads to the response of an instrumented bridge using an RFID triggering system.

**Laramie River Bridge Load-Testing Plan with Sensor Verification and RFID Feasibility  
of Permitted Vehicles**

By

McKenzie M. Danforth

A thesis submitted to the Civil and Architectural Engineering Department

and the University of Wyoming

in partial fulfillment of the requirements

for the degree of

MASTER OF SCIENCE

in

CIVIL ENGINEERING

Laramie, Wyoming

December 2015

COPYRIGHT PAGE

© 2015 by McKenzie M. Danforth

## DEDICATION PAGE

To my parents, Linda and Luke, for your unconditional love and support and for teaching me the importance of education and the value of hard work.

## ACKNOWLEDGMENT

I would like to thank my advisor, Dr. Richard Schmidt, for his dedication to students, patience in teaching, and guidance throughout this research. I also appreciate the opportunity to continue my education at a higher level. I am also grateful for Dr. Michael Barker, Dr. Steven Barrett, and Dr. Jay Puckett for their guidance in research and commitment to students.

Thank you to the Wyoming Department of Transportation, the Mountain-Plains Consortium, and the Department of Civil and Architectural Engineering at the University of Wyoming for supporting and funding this research. Thank you specifically to members of the WYDOT Bridge Program: Keith Fulton, Paul Cortez, and Joe Ruess, who offered guidance and inspiration throughout this project.

A warm thank you goes to my graduate colleagues who contributed greatly to this research: Mike Jung, who previously developed this research, and James Branscomb, who advanced the instrumentation. Thank you also to my other graduate colleagues for your continuous inspiration and constant hard work.

Additional thank yous are addressed to Rob Erikson, Mike Schilt, Scott Wiseman, and Bridget Schabron for their technical assistance in the laboratories.



## TABLE OF CONTENTS

COPYRIGHT PAGE .....	ii
DEDICATION PAGE .....	iii
ACKNOWLEDGMENT .....	iv
TABLE OF CONTENTS .....	v
LIST OF TABLES AND FIGURES .....	x
Tables .....	x
Figures .....	x
CHAPTER 1: INTRODUCTION.....	1
1.1 Problem Statement .....	1
1.2 WYDOT’s Objective .....	3
1.3 Literature Review .....	3
1.3.1 Current Load-Rating Procedures and Validations .....	3
1.3.2 FBG Strain Transfer Behavior and Protection Techniques.....	5
1.3.3 Weigh-in-Motion Systems .....	9
1.4 Research Overview .....	10
1.5 Thesis Objectives and Scope .....	10
CHAPTER 2: LARAMIE RIVER BRIDGE.....	13
2.1 Selection of Laramie River Bridge .....	13
2.2 Description.....	14
2.3 Current Condition .....	16
CHAPTER 3: FIBER BRAGG GRATING SENSOR VERIFICATION .....	19
3.1 Objective.....	19

3.2 Fiber Bragg Gratings .....	20
3.2.1 Technical Information .....	20
3.3 Flexure Test Procedure .....	22
3.3.1 Instrumentation .....	23
3.3.2 Installation Techniques .....	26
3.3.3 Four-Point Bending Test Set Up .....	27
3.4 Results and Discussion .....	31
3.5.1 Set 1 .....	31
3.5.2 Set 2 .....	33
3.5.3 Set 3 and 4 .....	34
3.5.4 Set 5 .....	35
3.5.5 Set 6 .....	37
3.5.6 FBG Test 2 .....	38
CHAPTER 4: LATERAL DISTRIBUTION FACTOR .....	40
4.1 Objective .....	40
4.2 BRASS Software .....	40
4.2.1 BRASS-GIRDER Load Rating Analysis .....	41
4.2.2 Load Factor Rating .....	43
4.2.3 AASHTO Lateral Distribution Factors .....	44
4.3 Methodology for Determining the Instrumentation Plan .....	49
4.4 Instrumentation Plan .....	51
4.4.1 Factors Affecting Sensor Placement .....	51
4.4.2 Sensor Placement on Beams .....	52
4.4.3 Critical Longitudinal Locations .....	54

4.5 Vehicle Loading Plan.....	55
4.5.1 Experimental Test Vehicle.....	58
4.6 Data Collection.....	59
4.7 Data Analysis.....	59
4.8 Use of Experimental Lateral Distribution Factor.....	64
4.9 Summary of the Procedure to Determine the Lateral Distribution Factors.....	65
CHAPTER 5: RFID TRIGGERING DEVELOPMENT.....	67
5.1 Objective.....	67
5.2 Purpose.....	67
5.3 RFID Systematic Description.....	68
5.3.1 Port of Entry.....	68
5.3.2 Triggering.....	69
5.3.3 Data Collection.....	70
5.3.4 Data Storage.....	71
5.3.5 Data Transmission.....	71
5.3.6 Data Post Processing.....	71
5.4 Instrumentation Design (Branscomb, 2015).....	72
5.5 RFID Triggering Validation Procedure and Results.....	78
5.5.1 Proof of Concept Test Setup.....	79
5.5.2 RFID Transponder Position and Direction.....	81
5.5.3 RFID Vehicle Lane Position.....	82
5.5.4 RFID Tag Position in Windshield.....	83
5.5.5 Triggering at Full Speed.....	83
5.5.6 Data Collection and Storage.....	84

CHAPTER 6: CONCLUSIONS AND FUTURE RECOMMENDATIONS .....	85
6.1 Research Summary and Conclusions.....	85
6.1.1 Fiber Bragg Grating Sensor Verification.....	85
6.1.2 Lateral Distribution Factor.....	87
6.1.3 RFID Triggering Development.....	89
6.2 Future Recommendations .....	91
6.2.1 Fiber Bragg Grating Sensor Verification.....	91
6.2.2 Lateral Distribution Factor.....	91
6.2.3 RFID Triggering Development.....	93
REFERENCES.....	101
APPENDIX A .....	105
A.1 Literature Review of Current Load-Rating Procedures and Validations.....	105
A.2 Literature Review of FBG Strain Transfer Behavior and Protection Techniques .....	107
A.2.1 University of Wyoming Research on Notch Embedded FBGs.....	107
A.2.2 FBG Polyimide and Acrylate Recoat .....	109
A.2.3 FBG Strain Verification Cases Based upon Laboratory and Field Testing .....	111
A.3 Literature Review of Weigh-In-Motion Systems .....	115
APPENDIX B.....	120
B.1 Laramie River Bridge Load Rating Summary (WYDOT, 2015b).....	120
APPENDIX C.....	121
C.1 Micron Optics os3120 Epoxy Mount Installation Procedure.....	121
APPENDIX D .....	123
D.1 Printed Circuit Board Schematic Design (Branscomb, 2015) .....	123
APPENDIX E.....	125

E.1 Example of Stored Output Data from RFID Triggering System..... 125

APPENDIX F ..... 129

F.1 Common Applications to Wyoming to Move an Oversize and/or Overweight Load .. 129

## LIST OF TABLES AND FIGURES

### Tables

Table 1: Comparison of LFD and LRFD Lateral Distribution Factors .....	49
Table 2: Factors Taken into Consideration for Field Testing.....	52
Table 3 : Potential Controlling Vehicle Load Combinations .....	57
Table 4: Example Comparison Table for Analytical and Experimental Lateral Distribution Factors .....	65
Table 5: Main Characteristics of Different Fiber Coatings (Rivera et al. 2005).....	110

### Figures

Figure 1: Laramie River Bridge .....	14
Figure 2: Basic Section View of Laramie River Bridge.....	15
Figure 3: Exterior South Girder.....	15
Figure 4: Expansion Bearings at Abutment Two (left) and Pier Two (right) .....	16
Figure 5: Cross Frames Located in Spans One, Two, and Three and at the Piers .....	16
Figure 6: Laramie River Bridge Load Rating Summary (WYDOT, 2015b) .....	18
Figure 7: Fiber Bragg Grating Sensor .....	21
Figure 8: SmartScan Interrogator for Fiber Bragg Grating Sensors.....	25
Figure 9: National Instruments Modules for Foil Strain Gages .....	25
Figure 10: S3x5.7 Beam Cross-Section View .....	26
Figure 11: Traditional Foil Gage (left) and Micron Optics' os3120 Sensor (right).....	27
Figure 12: Top Plan View of Sensor Placement in Compression .....	28
Figure 13: Bottom Plan View of Sensor Placement in Tension.....	28
Figure 14: Right Side View of Sensor Placement .....	28
Figure 15: Left Side View of Sensor Placement .....	28
Figure 16: Cross-Section View with Sensor Placement.....	29
Figure 17: Four-Point Bending Test Set Up.....	29
Figure 18: Four-Point Bending Test Set Up.....	30

Figure 19: Set 1 Sensor Comparison of Stress vs. Strain in Compression.....	32
Figure 20: Set 2 Sensor Comparison of Stress vs. Strain in Compression.....	33
Figure 21: Set 3 Sensor Comparison of Stress vs. Strain in Tension.....	34
Figure 22: Set 4 Sensor Comparison of Stress vs. Strain in Tension.....	35
Figure 23: Set 5 Sensor Comparison of Stress vs. Strain in Tension.....	36
Figure 24: Set 6 Sensor Comparison of Stress vs. Strain in Tension.....	37
Figure 25: Test 2 FBG Results.....	38
Figure 26: Cross-Sectional View with FBG Sensors on the Web and Bottom Flange.....	53
Figure 27: Elevation View with Critical Locations for Sensor Placements.....	54
Figure 28: Plan View with Critical Locations for Sensor Placements.....	54
Figure 29: Vehicle Load Test Plan.....	56
Figure 30: HS20 AASHTO Approved Design Truck (Jaramilla and Huo, 2005).....	58
Figure 31: Strain Profile for Girder with Partially Composite Behavior.....	61
Figure 32: Total Moment for Girder with Partially Composite Behavior.....	62
Figure 33: Analytical and Experimental Moments.....	63
Figure 34: Block Diagram of Instrumentation at Weigh Station (Jung, 2015).....	69
Figure 35: Block Diagram of Instrumentation at Bridge (Jung, 2015).....	70
Figure 36: Exterior Top View (left) and Interior View with FBG Inputs (right) of Interrogator .....	73
Figure 37: Olimex Ethernet Controller (Branscomb, 2015).....	73
Figure 38: Top View of the Microcontroller Mounted onto an Adapter (Branscomb, 2015)..	74
Figure 39: Printed Circuit Board used to Control System Components (Branscomb, 2015)...	75
Figure 40: Data Passing Between the Interrogator, PCB, and Ethernet Network (Branscomb, 2015).....	76
Figure 41: LED Screen Displaying the System Running (Branscomb, 2015).....	76
Figure 42: Exterior Top (left) and Interior View (right) of PCB and LED Screen in Enclosure .....	77
Figure 43: Testing Location on Highway 17 with the West (left) and East (right) Views .....	79
Figure 44: Schematic Diagram of RFID Triggering Tests.....	80
Figure 45: Direction of RFID Transponder to Trigger Data Storage.....	81

Figure 46: Positioning of RFID Vehicle to Trigger Data Storage..... 82  
Figure 47: System Flow Chart (Jung, 2015) ..... 97  
Figure 48: Step 1 - Mix Epoxy ..... 121  
Figure 49: Step 2 - Surface Preparation ..... 121  
Figure 50: Step 3 - Position Sensor ..... 122  
Figure 51: Step 4 - Apply Epoxy..... 122  
Figure 52: Step 5 - Cure ..... 122



## CHAPTER 1: INTRODUCTION

### 1.1 Problem Statement

Most of the bridges in the United States were built in the early 1960s and were not originally designed for the loads or non-standard truck configurations called for today. Many mountain-west states, including Wyoming, are observing a rise in non-standard truck configurations due to an increase in demands from the energy sector. As a result, state department of transportations (DOTs) are under pressure to assure safe and efficient routes for overweight and non-standard vehicles transporting heavy equipment over highways and bridges.

It is important to distinguish the specific concerns that Wyoming infrastructure faces. An increase in the demand from the energy sector is forcing bridge managers to investigate methods for increasing load ratings or removing postings. Posting a bridge is required when the maximum legal load is greater than the maximum load capacity of a bridge (Puckett, 2013). Records show that in 2013, 166 of 3,099 bridges in Wyoming were posted, while another 20 bridges had recommended postings that were not enforced (FHWA, 2012a). Bridges with conservative load ratings can cause time-consuming and expensive permits to be obtained while postings force oversize or overweight vehicles to take alternative transportation routes, forcing costly detours.

Bridges are required by the American Association of State Highway and Transportation Officials (AASHTO) to be visually inspected at a minimum of every two years (Copel, 2014). States must submit their inspection data for compliance with the National Bridge Inspection Standards (NBIS) to receive federal funding. Visual inspections are vital because they provide general updates on the performance of existing bridges and can identify obvious structural damage. However, visual bridge inspections do not provide a quantitative analysis for how a

bridge reacts under certain load conditions, and inspections are usually conservative for safety measures. While traditional analysis of bridges can estimate their load capacity, often times these load ratings are conservative. Conservative load ratings cause expensive detours, increase bridge postings, and require more issued permits.

The Wyoming Department of Transportation (WYDOT) needed a method to potentially improve the accuracy of their current load rating software, Bridge Rating and Analysis of Structural Systems (BRASS) (WYDOT, 2003a). WYDOT has a thorough inventory of its bridges, and each federally owned bridge is load rated with BRASS. However, BRASS results are partly based on input from conservative inspections and design assumptions, so the true strength of a bridge may still be in question. By improving the understanding of a bridge's true behavior, WYDOT could potentially see an increase in load ratings or a reduction in postings throughout the state, thereby giving bridge managers a method to better allocate maintenance funds.

The University of Wyoming team utilized Fiber Bragg Gratings (FBG) to develop a field-testing plan that measures the actual lateral distribution factors to potentially improve load ratings, providing WYDOT with a long-term, more accurate, and in most cases, less conservative load rating. This system could potentially lead to an increase in load ratings, removal of postings, fewer rerouted permitted vehicles, and financial savings. The system would provide a more accurate quantitative analysis for how their bridges are performing while addressing the increasing energy sector demands, moving in the right direction of better evaluating the state's infrastructure.

## 1.2 WYDOT's Objective

WYDOT's main focus was to determine a method to potentially improve BRASS load rating results in Wyoming. The University of Wyoming team addressed WYDOT's request of determining a method for potentially improving BRASS load ratings by developing a field-testing plan to quantitatively measure the actual lateral distribution factors using FBG fiber optic strain sensors. This plan was combined with validating FBG sensors and determining the feasibility of a radio frequency identification (RFID) triggering system for permitted vehicles.

## 1.3 Literature Review

A literature review was conducted for the pertinent topics of the thesis. An introduction to each section is included followed by brief summaries of the reviews. Detailed reviews are located in Appendix A. A literature review was conducted for three topics. The first topic is current load-rating procedures and validations. This topic explains load-rating software that is prominent throughout many states and how field tests have been completed to verify more accurate load ratings than traditional load-rating calculations can predict. The second topic is FBG strain transfer behavior and protection techniques. New FBG technology is constantly developing, so it was important to ensure that the correct FBGs were used for testing and that they'd be adequately protected in the harsh Wyoming environment. The third topic is an overview of weigh-in-motion (WIM) systems. The research described in this thesis explored using Fiber Optic Sensors (FOS) coupled with a WIM system, so knowledge of existing WIM systems was necessary.

### 1.3.1 Current Load-Rating Procedures and Validations

Currently, there exists no national standardized load-rating software adhering to AASHTO LRFD Specifications for state departments of transportation (DOT). Each state has its

own methods of keeping inventory, analyzing structures, and developing load criteria for permits on bridges. WYDOT has a thorough inventory, in which each bridge is load rated by BRASS Software, and the bridge status is updated based upon scheduled bridge inspections. BRASS guides bridge engineers in designing highway bridges and quantifying a bridge's load capacity by using finite element analysis and current design specifications (WYDOT, 2003a). Thirty-two other state DOTs around the country utilize BRASS (Goodrich, 2014), validating its usefulness to the specific demands of a bridge management program.

In the past, most FBG systems have been developed for structural health monitoring (SHM) of bridge behavior to gain insight on long-term effects, for example deck deterioration or crack propagation. This type of monitoring has proven successful for small-scale endeavors, however it is more difficult to monitor the structure as a whole with the intent of improving the overall safety of aging infrastructure. More recently, research has expanded to establishing a framework that uses FBGs to verify load ratings instead of solely focusing on SHM systems. Few field cases have explored the potential of implementing FBG load-rating systems, and this research is typically funded through university or DOT grants. The remaining section gives a brief overview of field tests that used dynamic load rating in place of traditional load-rating calculations with details found in Appendix A.1.

The Iowa State University Bridge Engineering Center (BEC) completed a study to determine if their current load-rating calculations are overly conservative based upon dynamic load tests, instrumenting a total of 17 bridges with strain gages, 12 of them initially posted. Half of the posted bridges had their load restrictions removed, providing a safe alternative and saving DOTs money by avoiding excessive rerouting or permitting of vehicles. Near Ames, Iowa, a bridge on highway US 30 was instrumented with FOS to statistically estimate a load rating using

the bridge's response to ambient five-axle truck traffic and a weigh-in-motion (WIM) system (Seo, et al. 2012).

### 1.3.2 FBG Strain Transfer Behavior and Protection Techniques

Over the past two decades, FOS have developed into reliable strain sensors that are frequently replacing traditional foil gages due to their many benefits, described in Chapter 3. While the sensors have proven their validity through endless laboratory and field-testing procedures, engineers are still skeptical. A presentation by Micron Optics, one of the leading FOS manufactures in the United States, describes general misconceptions about the reliability of FOS (Micron Optics, 2014f).

- 1) A sense that FOS are still a “research” technology
- 2) Prior direct or anecdotal poor experiences with university or startup technology and/or deployments
- 3) Prior poor experiences stemming from inadequate understanding or training with regard to FOS strengths, weaknesses, and deployment techniques

Various topics have been explored by Micron Optics including fiber breakage susceptibility, poor or inconsistent strain transfer from carrier to FBG, spectral distortions leading to measurement distortions, fiber or carrier creep, fiber debonding, repeatable thermal response, humidity exposure and cycling, and fatigue cycling. Micron Optics laboratory and field qualification tests have proven that the right materials, processes, and controls can provide accurate and reliable strain results (Micron Optics, 2014f).

The University of Wyoming team has completed work related to certain aspects of testing by Micron Optics. This work included studies of strain transfer techniques and FBG testing with both polyimide and acrylate recoated fibers. Both topics are covered in this section through a literature review. Additionally, research by outside parties validated FBG sensors in various

types of carrier packages against traditional foil gages. A brief overview of the literature reviews is given below with a reference to Appendix A.2 for more details on each topic.

#### *University of Wyoming Research on Notch Embedded FBGs*

Maurais (2012) focused on the strain transfer methods of notch-embedded FBGs in concrete specimens. The types and applied lengths of epoxies varied from test to test using five different configurations. It was discovered that as the length of epoxy increased, the effective strain transfer increased as well. The strain transfer also increased with an epoxy that had a higher elastic modulus. Additionally, an increase in strain transfer was seen with a smaller bond layer thickness. Also researched were field implementation considerations and gage factor calibrations. Details of Maurais's work can be found in Appendix A.2.1.

#### *FBG Polyimide and Acrylate Recoat*

The protective coating on a FBG must be removed in order to create etches into the core of the fiber, which designates a base wavelength for that specific fiber. Afterward, the FBGs must have their inner cores protected by recoating the fiber, enhancing the fiber's strength and flexibility. The two most common types of recoating material currently available are polyimide and acrylate. The University of Wyoming team has used FBGs with both types of recoat materials for testing. It was important to distinguish the benefits and drawbacks of both polyimide and acrylate recoats for testing purposes, and it was concluded that FBGs with a polyimide recoat were better suited for both laboratory and field conditions. The following paragraph gives an overview of the literature review; details for each article can be found in Appendix A.2.2.

Kuang, et al. (2006) at the National University of Singapore studied the performance of FBGs embedded in carbon fiber composites; some were recoated with acrylate and some were bare FBGs after the recoated acrylate was removed. It was discovered that the bare FBGs performed more accurately compared to the recoated acrylate fibers, which saw a significant amount of stress relaxation. A study completed by the University of Manitoba (Rivera, et al. 2005) discusses the main differences between polyimide and acrylate recoating. Tension tests were carried for strain transfer performance; the FBGs were purchased from two different manufacturers, and the results were dependent on the manufacturer, not the type of recoat material. This finding led the researchers to believe that FBG recoating standards should be implemented. An e-mail from a representative at Micron Optics (Baez, 2014), one of the leading FBG manufacturers in the United States, described acrylate recoat as a “spongy” cladding, commenting that polyimide coating accomplishes strain transfer more successfully and has a wider temperature range.

#### *FBG Strain Verification Cases Based upon Laboratory and Field Testing*

Fiber optic sensors were first applied in the 1960s for commercial telecommunication purposes. They have been utilized in military and aerospace equipment fields, and have, within the last two decades, begun to gain acceptance into many fields including health monitoring for medicine, heritage culture, and various engineering fields. In the civil engineering industry, they are ultimately used to potentially increase the life of expensive and important structures as well as avoid crucial failures (Annamdas, 2011).

Fiber Bragg Gratings, a form of FOSs, are replacing traditional foil gages as they offer improved reliability, performance, safety, and optimized cost (Annamdas, 2011). Before laboratory and field testing took place at the University of Wyoming, it was important to identify

the success rate of FBGs in the civil engineering industry for use on bridge structures compared to traditional foil gages. This study encompassed a variety of factors including proof of adequate field protection, which is vital in harsh Wyoming conditions, and accurate strain readings. This section is an overview of various completed studies; details of each literature review can be found in Appendix A.2.3.

Ansari (2007) discussed the complications in using bare FBG sensors, or sensors without a type of carrier or protection method in field conditions. In Hong Kong China, forty sensors were installed on the Tsing Ma Bridge to measure temperature and strain. By using epoxy and a nitinol metal as a protection method, favorable strain results were seen from testing, agreeing with traditional foil gage measurements in similar locations (Chan, et al. 2005). Tests completed by a team at the University of Iowa Bridge Engineering Center displayed good agreement between FOS and traditional foil gage strain readings, which assured accuracy for field instrumentation on the US 30 Bridge near Ames, Iowa (Doornink, 2006). This study showed that FBGs perform accurately using a variety of different protection techniques.

Bridge Diagnostics Inc. (BDI) out of Boulder, Colorado was hired to install their strain sensors adjacent to the FOS installed on the US 30 Bridge to compare readings based upon ambient traffic loads. The results from BDI's sensors and the FOS were excellent, and the tests were deemed successful (Doornink, 2006). During construction of the Hulanhe Bridge, which crosses the Hulan River in northeast China, 15 FBGs and 15 traditional foil gages were installed. The FBGs performed as expected while only one traditional foil gage survived the installation procedure, proving the durability and reliability of FBGs over foil gages in this application (Zhou, et al.).



ISIS Canada and the University of Manitoba teamed up to install FOS onto various bridges in Canada (Tennyson, 2001). The Beddington Trail Bridge in Alberta, Canada was an example of FBGs as a reliable strain sensor with 18 out of 20 sensors still working accurately three years after installation. The Taylor Bridge in Manitoba, Canada was used to install 63 FBGs with traditional foil gages used to compare the data. Only 40% of the foil gages survived while the majority of the FBGs were still reading accurately.

### 1.3.3 Weigh-in-Motion Systems

Most of the nation's bridges were built in the early 1960's with an expected lifespan of 50 years, meaning that the majority of bridges are at the end of their lives or aren't built to withstand the demands of current everyday traffic. The economy is calling for trucks to carry heavier loads than in the past, some of these exceeding legal limits. Oversize and overweight vehicles on the highway deteriorate the infrastructure at a faster rate and cause a higher risk of traffic accidents.

In the last two decades, WIM systems have been effective in helping authorities minimize and control these effects (Jacob and Feypell-de La Beaumelle, 2010). Various WIM systems have been successful, as they typically don't disturb the flow of traffic and are cost effective; this has prompted continuous development in this field. This section briefly presents the history and recent research in the development of WIM systems; details for each summary are provided in Appendix A.3.

A journal article by Jacob and Feypell-de La Beaumelle (2010) discussed WIM technology from its origin in static weighing, to studies on bridge WIM systems, to the development of WIM systems today. The article does an excellent job of outlining major

research completed in the past, emphasizing that ongoing research and exchanging of ideas and experiences are key to moving forward. Two articles, one by Zhao, et al. (2014) and one by Leng (2015), discussed different approaches to improve established algorithms presented by O'Brien et al. (2006), which used the measured strain responses from a bridge to determine influence lines and calculate the axle loads of vehicles crossing the bridge. Research was completed in New York that developed a method to use data collected by WIM systems in order to distinguish overweight vehicles through a data mining procedure. The goal was to eventually assist state DOTs in creating a foundation for permit guidelines, weight enforcement procedures, and cost management analyses (Fiorillo, et al. 2014).

#### 1.4 Research Overview

The research for this report was conducted in three stages. The first stage of research was verifying the performance of FBG Micron Optics' os3120 sensors compared to traditional foil gages. The second stage was to develop a test design to determine lateral distribution factors on the Laramie River Bridge on Interstate 80 (I-80) in Wyoming. This procedure included a sensor installation and design vehicle placement plans. The last portion of the research was the development of a radio frequency identification (RFID) triggering proof-of-concept system to identify when a vehicle is present at a bridge. WYDOT and the University of Wyoming team developed the research objectives.

#### 1.5 Thesis Objectives and Scope

This thesis addresses three main objectives. The three objectives were all separately developed; this means that the results of one objective did not directly affect the results of another objective. The successful outcome of all three objectives has resulted in a method that WYDOT could use to measure the lateral distribution factors of a bridge, potentially increasing

load ratings, and conduct future studies on the effects of permitted vehicles on bridges throughout the state.

Objective 1 was to verify the performance of FBG sensors as compared to traditional foil gages. Its success was determined by the following:

- Verify the reliability of Micron Optics os3120 Fiber Bragg Gratings' strain results
- Understand and document the installation procedures of Micron Optics os3120 Fiber Bragg Gratings

The first objective was deemed successful by showing that FBG sensors produce reliable strain results compared to those from traditional foil gages. Tests were completed on various locations of a steel wide flange beam in the laboratory, however the extreme fibers of the bottom flange were the primary location of interest. Installation procedures were followed, understood, and documented to provide a basis for possible future installation of the sensors.

Objective 2 was to develop a test design plan for the Laramie River Bridge in order to determine the lateral distribution factors to potentially improve the load ratings produced by BRASS Software used by WYDOT. The test design plan is applicable for the HS20, HS25, Type 3, Type 3S2, and Type 3-3 truck configurations and would provide the means to determine a more accurate representation of a bridge's behavior. This objective required input from WYDOT and a literature review on applicable instrumentation methods.

Objective 3 was to develop a proof of concept for an RFID triggering system. The system was considered successful when the RFID reader detected the presence of the RFID tag then signaled the FBG interrogator to store strain data for an allotted amount of time. James Branscomb, an electrical engineer, participated in the development of this system.

This thesis is broken into six chapters discussing the three objectives. Chapter 1 is the introduction chapter. Chapter 2 highlights the Laramie River Bridge. Chapter 3 addresses objective 1, discussing FBG sensor verification. Chapter 4 reviews objective 2, lateral distribution factor determination. Chapter 5 focuses on objective 3, RFID triggering development. Lastly, Chapter 6 discusses conclusions and future work.

## CHAPTER 2: LARAMIE RIVER BRIDGE

### 2.1 Selection of Laramie River Bridge

The Laramie River Bridge, structure AXK, was chosen for instrumentation by members of the WYDOT Bridge Program and the University of Wyoming team. Selecting the bridge for installation of an SHM system considered a variety of factors; two major elements were the location and type of structure.

Structure AXK extends over the Laramie River and is located in Albany County in Wyoming; it was built for westbound traffic on Interstate 80 (I-80) at milepost 312.44. This is a primary route for permitted vehicles through Wyoming, and the westbound traffic indicates that the majority of the trucks have already passed through Cheyenne, which has two major ports of entry into the state. The location allows for a ten-minute drive, 3.5 miles, from the University of Wyoming campus. This location provides a reasonable commute for evaluating the condition, installing the sensor system, and completing field tests on the bridge in the future. This bridge is in an area with adequate cell phone coverage, which could be an important resource in future phases of the research, as discussed in Chapter 4.

The Laramie River Bridge, a three-span slab-on-steel girder bridge, represents a typical bridge in the WYDOT inventory. By installing a load-rating system on a common type of structure, methods for future instrumentation, testing, and analysis of bridges throughout the state could be the result. The University of Wyoming team initially focused more time working with and understanding the installation process of the sensors adhering to steel material. It is important to note that installing the sensors on concrete is just as straightforward and reliable as installing the sensors on steel; it only requires purchasing a different model of sensor.

Additional factors were also considered in the selection of this structure. For simplicity purposes, the chosen structure is a three-span continuous bridge with no skew. Although a river runs beneath the bridge, an under-bridge machine, also known as a Snooper, can reach the underside of a bridge to access the main structural components for sensor installation. Lastly, the bridge had to be approved by WYDOT; considered factors were the life expectancy, past inspection reports, and the current load rating of the bridge.

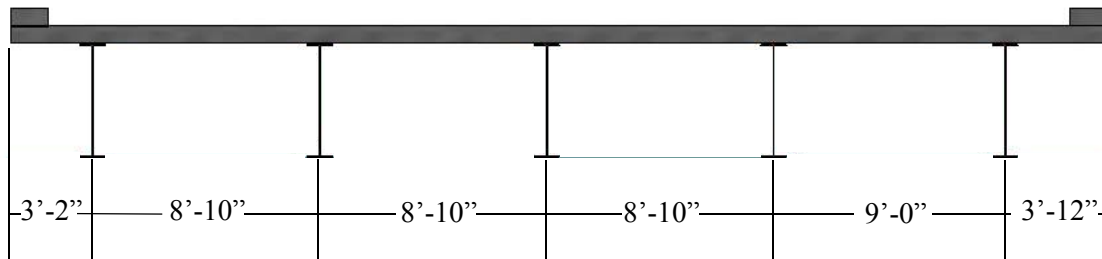
## 2.2 Description

The Laramie River Bridge is a three-span, continuous, welded, plate-girder bridge. It is non-composite with span lengths of 60-feet, 75-feet, and 60-feet, respectively. The roadway width is 40-feet with 1-foot 4-inch curbs on each side, and it has two westbound traffic lanes. A picture of the bridge is displayed in Figure 1 with the traffic headed west toward Rawlins.



**Figure 1: Laramie River Bridge**

The bridge was originally constructed in 1961 with four girders; it was widened in 1995 to include a fifth girder on the north side. From the south side to the north side of the bridge, the girders are spaced at 8-feet 10-inches, 8-feet 10-inches, 8-feet 10-inches, and 9-feet apart, respectively, as displayed in Figure 2.



**Figure 2: Basic Section View of Laramie River Bridge**

The plate girders are made of 50-ksi steel and have webs 7/16-inch by 51-inches and top and bottom flanges 3/4-inch by 12-inches. Figure 3 displays the exterior south girder.



**Figure 3: Exterior South Girder**

The bridge has expansion bearings at abutment number two, located on the east side of the bridge toward Cheyenne, and at both piers; bearings at the abutment and pier two are seen in Figure 4. The bridge has fixed bearings at abutment number one, located on the west side of the

bridge toward Rawlins. Diaphragms exist at the abutments, piers, and are spaced every 20-feet in spans one and three and every 25-feet in span two, as displayed in Figure 5.



**Figure 4: Expansion Bearings at Abutment Two (left) and Pier Two (right)**



**Figure 5: Cross Frames Located in Spans One, Two, and Three and at the Piers**

### 2.3 Current Condition

The Laramie River Bridge load-rating summary from January 9, 1997 was generated by BRASS and provided by WYDOT. The load-rating method used was the load factor method.

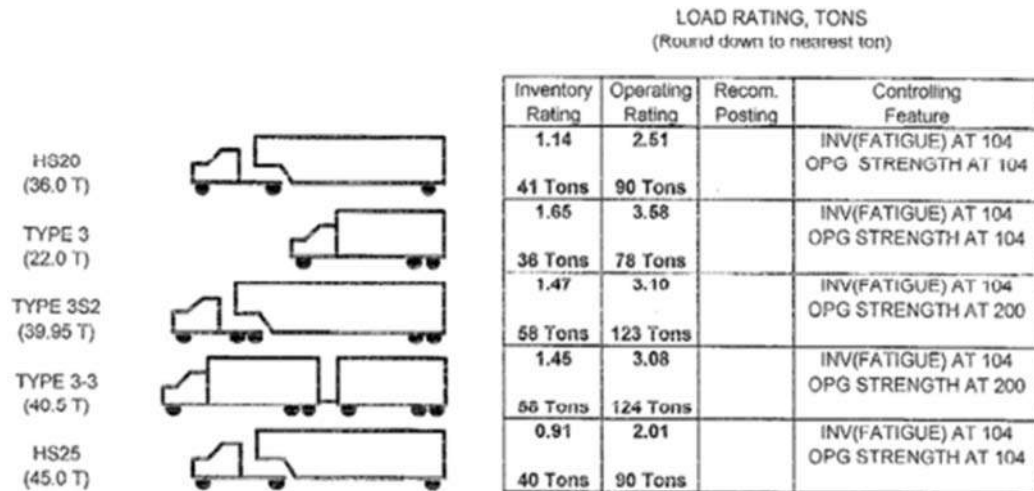


The bridge was rated with an 18-psf future wearing surface (FWS) and rated as the new exterior girder being as strong as the interior girder. The BRASS documentation was submitted on January 10, 1997.

The load ratings for five different vehicle types are included and rounded down to the nearest ton in terms of capacity. The HS 20 was one of the first designated vehicles with specific axle loads and spacing. Since then, other configurations thought to better represent loading conditions have been developed including the HS 25 vehicle, which has a 25% higher truck load (Munkelt, 2010). The American Association of State Highway and Transportation Officials (AASHTO) determined Types 3, 3S2, and 3-3 as model vehicles that represent common 3-axle single trucks, 5-axle tractor semi-trailers, and 6-axle tractor trailers. The group meets the federal weight limit and vehicle configuration and represents the most common trucks on the nation's interstates (FHWA, 2014c).

Included in the summary are the inventory ratings, operating ratings, and controlling features. An inventory rating is the structural load that the bridge can carry for an indefinite time period where the live load is not a concern according to AASHTO design. An operating rating is the maximum allowed load that the bridge can be subjected to for the specific vehicle type (FHWA, 2015b). The controlling features section denotes the point of the structure with the maximum load effects for each vehicle configuration.

The load rating summary is presented in Figure 6 with the full report in Appendix B.1.



**Figure 6: Laramie River Bridge Load Rating Summary (WYDOT, 2015b)**

The visual inspection report was provided by WYDOT and indicates only the visual condition of the bridge, which is different than the load rating summary. The evaluation did not propose any improvements for the structure. The Laramie River Bridge received a rating on February 14, 2011 of 97.356 out of 100, and the rating from the March 21, 2013 visual inspection was 97.4 out of 100. This would indicate no change in the visual condition of the bridge between the two inspection dates.

## CHAPTER 3: FIBER BRAGG GRATING SENSOR VERIFICATION

### 3.1 Objective

Both Fiber Bragg Gratings (FBG) and traditional foil gages (TG), also called electrical resistance sensors, have been validated in the structural engineering field through the test of time and performance. FBGs can measure strain greater than 10,000  $\mu\epsilon$  (Kreuzer, 2014), which is more than sufficient for strain detection in bridges. There were two main focuses when testing FBGs in the laboratory:

- Verify the reliability of Micron Optics os3120 Fiber Bragg Gratings' strain results
- Understand and document the installation procedures of Micron Optics os3120 Fiber Bragg Gratings

The first focus was deemed successful by showing that FBG sensors produce reliable strain results. The resulting FBG strain measurements were compared to those from TGs. The slopes of the moduli of elasticity were compared to see the difference in strain measurements because the averaged results were linear, so one slope value accurately represented the entire data set. Also, the moduli of elasticity were useful to quickly judge the results closest to the commonly accepted value of 29,000,000 psi for steel.

For the location of the underside of the bottom flange of the girder, an average of 5% difference when comparing the moduli of elasticity of FBGs and TGs was deemed successful. Tests were completed on various locations of a steel wide flange beam in the laboratory, however the main focus of the experimentation was the extreme fibers of the bottom flange. This strain sensor location is the absolute minimum required to determine lateral distribution factors.

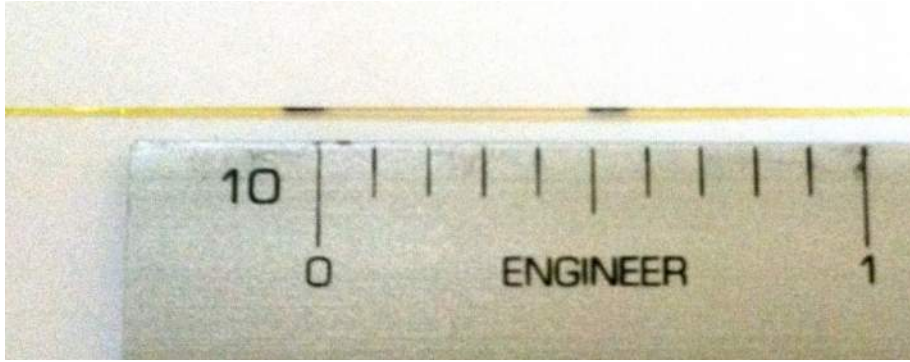
Installation procedures were practiced, understood, and documented to provide a basis for possible sensor installation projects in the future.

## 3.2 Fiber Bragg Gratings

In the past, the development of Fiber Bragg Gratings for use on bridges has been in the structural health monitoring (SHM) field. An example of these types of studies would be to obtain the behavior of the structure over its lifespan to gain insight on long-term effects such as deck deterioration or crack propagation. Instead of using this approach, the University of Wyoming team will take advantage of the unique capabilities of FBGs to install a system to determine the lateral distribution factors of the Laramie River Bridge.

### 3.2.1 Technical Information

FBGs are fiber optic sensors that are manufactured by creating etches, or gratings, into the refractive index of the glass fiber core by subjecting it to a variation of ultraviolet light. The various patterns of exposure will allow a specific base wavelength to be reflected back to the interrogator when light from a LED or laser is passed through the core of the fiber. The gratings are located between the two black marks, about 0.5-inch apart, pictured below in Figure 7. Changes in the spacing of the gratings will alter the reflected wavelength, which can be converted into a strain reading for future calculations. The spacing variation will occur with any applied strain, assuming the FBG is properly adhered to the material.



**Figure 7: Fiber Bragg Grating Sensor**

FBGs were developed in the 1960s and have been used commercially in multiple fields. They have rapidly become a well-respected and commonly used strain sensor within the field of civil engineering due to their many advantages (Kreuzer, 2014):

- Life expectancy, approximately 30 years
- Electromagnetic interference (EMI) immunity
- Noise free properties
- Long range capabilities
- Remote capabilities
- Multiplexing
- Reliability, perform as well as traditional gages
- Flexibility
- Embeddability
- Performance in extreme environment conditions, specialized FBGs can operate at temperatures  $> 700\text{ }^{\circ}\text{C}$
- Competitive pricing

FBGs are ideal for use on infrastructure and have been verified for various field conditions including fatigue and temperature effects, making them an ideal fit for field implementation. Micron Optics developed and tested its os3120 sensors, the same sensors used in testing at the University of Wyoming, to validate their long-term dependability under extreme environmental conditions, which included thermal cycling, high temperature humidity, and fatigue. Fatigue tests included bending and tensile strain tests completed at low-frequency strain

cycling at high strain rates to determine the long-term durability of the sensors (Micron Optics, 2007c). The number of cycles tested on the sensors ranged from 13 million to 102 million, and no signs of deterioration resulted (Micron Optics, 2007b).

Micron Optics provides various types of sensors depending on the structural material and application purpose. Os3120 sensors were selected for use in the laboratory under constant temperature conditions, however in the field, temperature-compensating FBGs will need to be purchased. They are designed to remove the temperature-induced strain effects so that only the mechanical strain is recorded. Temperature-compensating sensors are more costly and are unnecessary for laboratory conditions. Equation 1 is used to calculate the mechanical strain reading in  $\mu\epsilon$  (Micron Optics, 2015e):

$$\epsilon = \frac{\left(\frac{\Delta\lambda}{\lambda_0}\right)}{F_G} \mathbf{1x10^6} - \epsilon_{TO} \quad \text{(Equation 1)}$$

where  $\Delta\lambda$  is the wavelength shift or the interrogated value in nm;  $\lambda_0$  is the nominal wavelength or the initial value in nm;  $F_G$  is the gage factor, which is equal to 1.00 at room temperature; and  $\epsilon_{TO}$  is the thermally induced apparent strain in  $\mu\epsilon$ , which is zero at constant temperature.

### 3.3 Flexure Test Procedure

A four-point bending test was chosen to validate the FBGs using TGs as the baseline strain measurement. The four-point bending test procedure has an advantage over the three-point bending test procedure because it produces a constant moment at midspan of the beam along with constant shear values at the beam supports. This allowed a more straightforward comparison between FBG and TG strain results.

Six four-point bending tests were performed; the displacement, time, load, FBG strains, and TG strains were all recorded throughout the duration of each test. For each test, the beam was loaded monotonically to maximum load, held for 30 seconds, and then unloaded back to the starting position. There were six points of interest for each test with a FBG and TG at each location; this totaled to 12 strain gage results for each of the six tests. The testing required specific instrumentation equipment, precise sensor installation techniques, and a detailed testing plan.

### 3.3.1 Instrumentation

The test required specialized loading equipment. This included a MTS hydraulic actuator, last calibrated in August of 2014, and MTS TestStar IIs software, last updated in 1999. The Instron Model 1332 applied the loads measured by a 10-kip load cell.

Two types of strain gages were used: FBGs and TGs along with their respective data capturing equipment. The TGs used for testing were model C2A-13-250LW-12, from Micro Measurements. The Fiber Bragg Gratings, os3120s, were purchased from Micron Optics. These specific sensors were chosen because they are protected by a steel carrier, installed easily with an epoxy, and used frequently in the field. This is beneficial as opposed to a spot welding model, because field welding on WYDOT bridges is prohibited. Micron Optics provides the following performance properties for the os3120 gages (Micron Optics, 2010a):

- Strain sensitivity  $\sim 1.4 \text{ pm}/\mu\epsilon$
- Gage length = 22 mm
- Operating temperature range =  $-104^\circ$  to  $248^\circ \text{ C}$
- Strain limits  $\pm 2,500 \mu\epsilon$
- Fatigue life =  $100 \times 10^6$  cycles,  $\pm 2,000 \mu\epsilon$

As discussed in Section 3.2.1, the interrogator, displayed in Figure 8, was the device used to record the reflected wavelengths from the six FBGs. All six FBGs were spliced onto one fiber, utilizing Channel 1 of the two available channels. Data was captured at one reading per half-second, which was a considerably lower rate than the TG readings. The FBG interrogator has the following specifications (SmartScan, 2014):

- Scan frequency = 2.5Hz
- Repeatability < 1 pm
- Wavelength stability < 5 pm over operative temperature range, +/- 20 pm over 25 years
- Dynamic range = 27 dB
- Gain control = 9 levels, per channel or per sensor
- Onboard processing
- Operative temperature = -15° to +55° C

Additionally, the interrogator has a wavelength range of 1528 nm to 1560 nm in order to achieve the required base wavelength spacing for the FBGs. Spacing of 4 nm between wavelengths per channel is suggested in order for the interrogator to distinguish the individual wavelength peaks, which takes into account a shift in wavelength due to either compression or tension. Two channels for simultaneous FBG data collection were available in the lab, however more channels are typically required for field implementation.





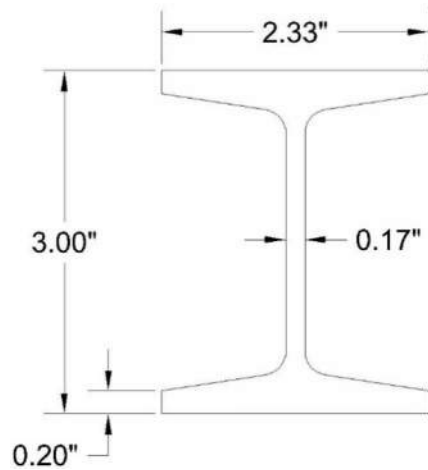
**Figure 8: SmartScan Interrogator for Fiber Bragg Grating Sensors**

The device that transmitted the voltage readings to strain measurements for the TGs was from National Instruments, more specifically Module 2, and is shown in Figure 9. NI LabVIEW 2013 was the software used to record the displacement, time, load, and TG readings. The rate of measurements taken was approximately 900 readings per second. Since the FBG data rate was two readings per second, linear interpolation was used to correlate the recorded load with the time of the strain readings for each type of software.



**Figure 9: National Instruments Modules for Foil Strain Gages**

An S3x5.7 beam with dimensions shown in Figure 10 was chosen as the test specimen. Using a small S-beam allowed for loads under 10 kips to be applied while reaching desired strain values. Because the flanges sloped down to the web, it made the placement of the sensors on the inside of the flanges more challenging than a typical wide-flange beam.



**Figure 10: S3x5.7 Beam Cross-Section View**

### 3.3.2 Installation Techniques

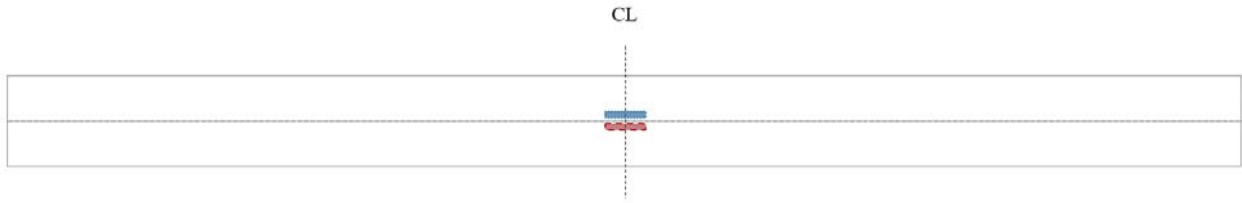
Two types of installation procedures were administered to prepare the S3x5.7 beam for the four-point bending test. Both procedures began with, in this order, abrading, degreasing, conditioning, and neutralizing the steel area in which the sensors were to be installed. The TGs were applied according to Micro Measurements' specifications for strain gage model C2A-13-250LW-12. The FBG installation process was administered following Micron Optics' procedures without any issues. The sensors were allowed to cure for 24-hours before being tested. A detailed installation procedure for the os3120 sensors can be found in Appendix C: "Micron Optics os3120 Epoxy Mount Installation Procedure" and is a vital resource for field instrumentation. Figure 11 shows sensor set 4 with the TG applied next to the Micron Optics FBG sensor.



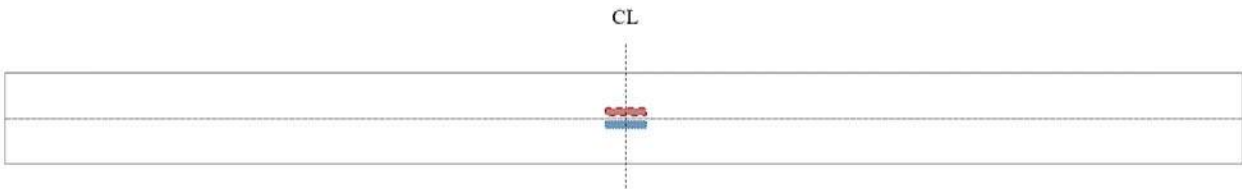
**Figure 11: Traditional Foil Gage (left) and Micron Optics' os3120 Sensor (right)**

### 3.3.3 Four-Point Bending Test Set Up

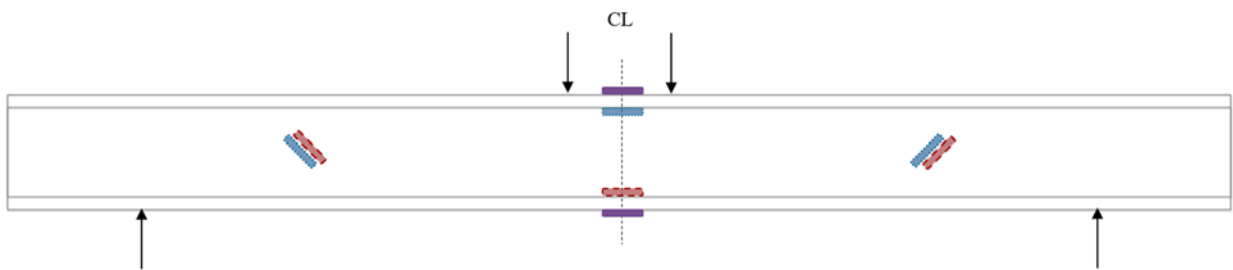
Sensor placement on the S-beam is displayed in the following five figures. Figure 12 is a top plan view of the S-beam and includes FBG 1 and TG 1, which comprises set 1 sensors. Figure 13 is a bottom plan view of the S-beam and includes FBG 6 and TG 6, making up set 6 comparisons. Figure 14 is a right side view of the beam where FBG 2 and TG 5 are displayed on the inside of the flanges, and FBG 3, FBG 4, TG 3, and TG 4 are on the inside of the web. Figure 15 is the left side view of the beam displaying TG 2 and FBG 5 on the inside of the flanges. The cross-sectional placements of the sensors are shown in Figure 16, where the four strain sensors on the web are represented by one rectangle.



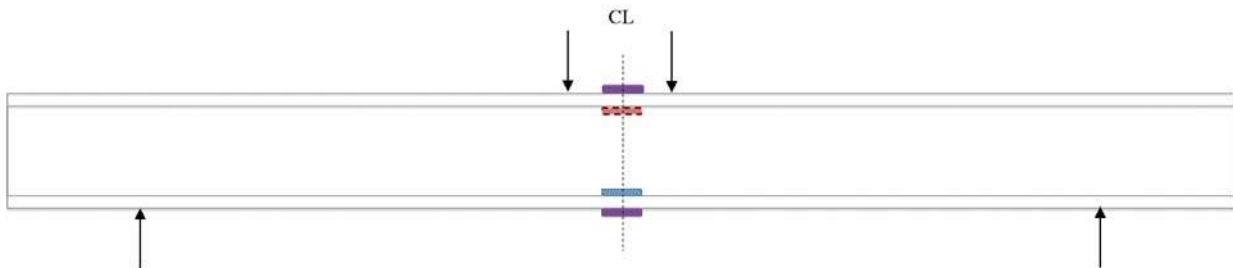
**Figure 12: Top Plan View of Sensor Placement in Compression**



**Figure 13: Bottom Plan View of Sensor Placement in Tension**




**Figure 14: Right Side View of Sensor Placement**



**Figure 15: Left Side View of Sensor Placement**

 Fiber Bragg Grating

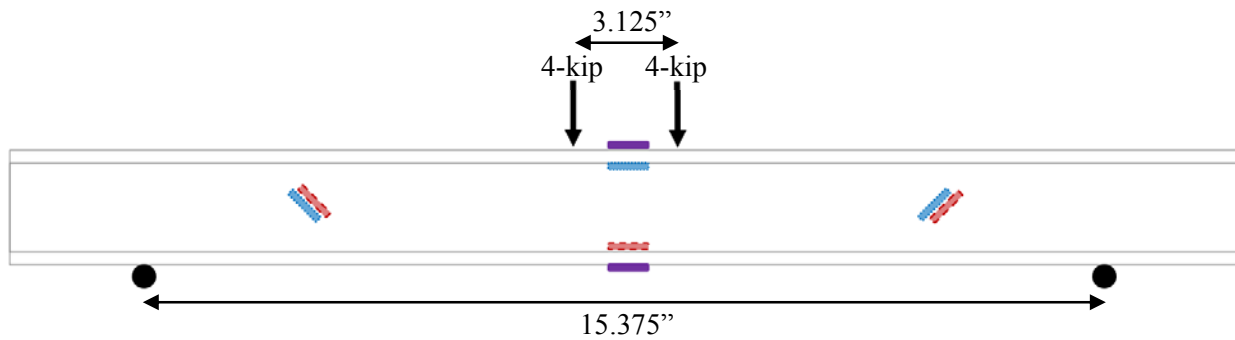
 Foil Strain Gage

 Side View, Both Sensors



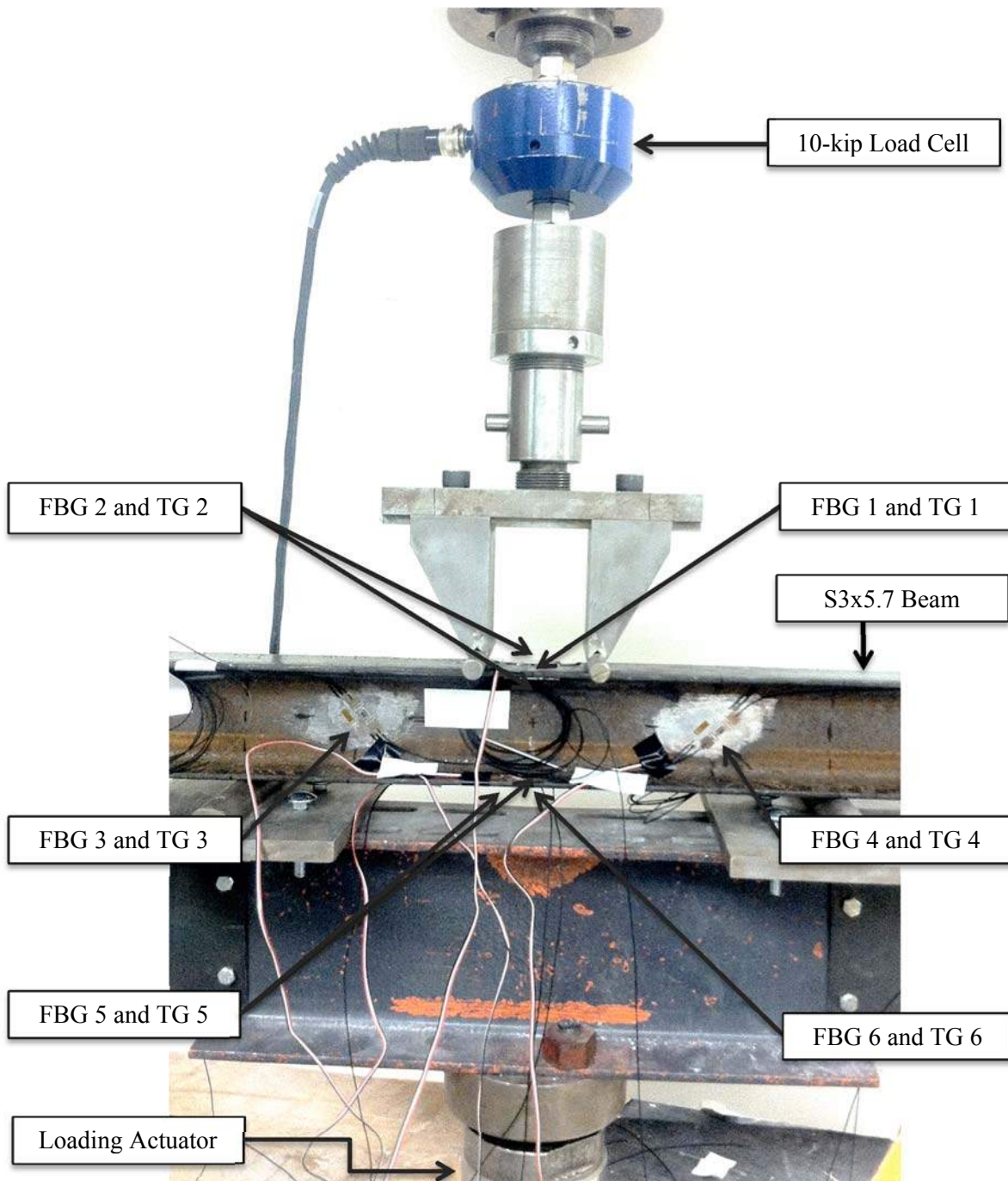
**Figure 16: Cross-Section View with Sensor Placement**

The total load applied was 8-kips, maximum spacing was 15.375-inches, and load spacing was 3.125-inches, as displayed in Figure 17.



**Figure 17: Four-Point Bending Test Set Up**

Figure 18 displays the test set up, including a loading actuator; 10-kip load cell; S3x5.7 beam; and the 12 sensors, six FBG and six TG.



**Figure 18: Four-Point Bending Test Set Up**

### 3.4 Results and Discussion

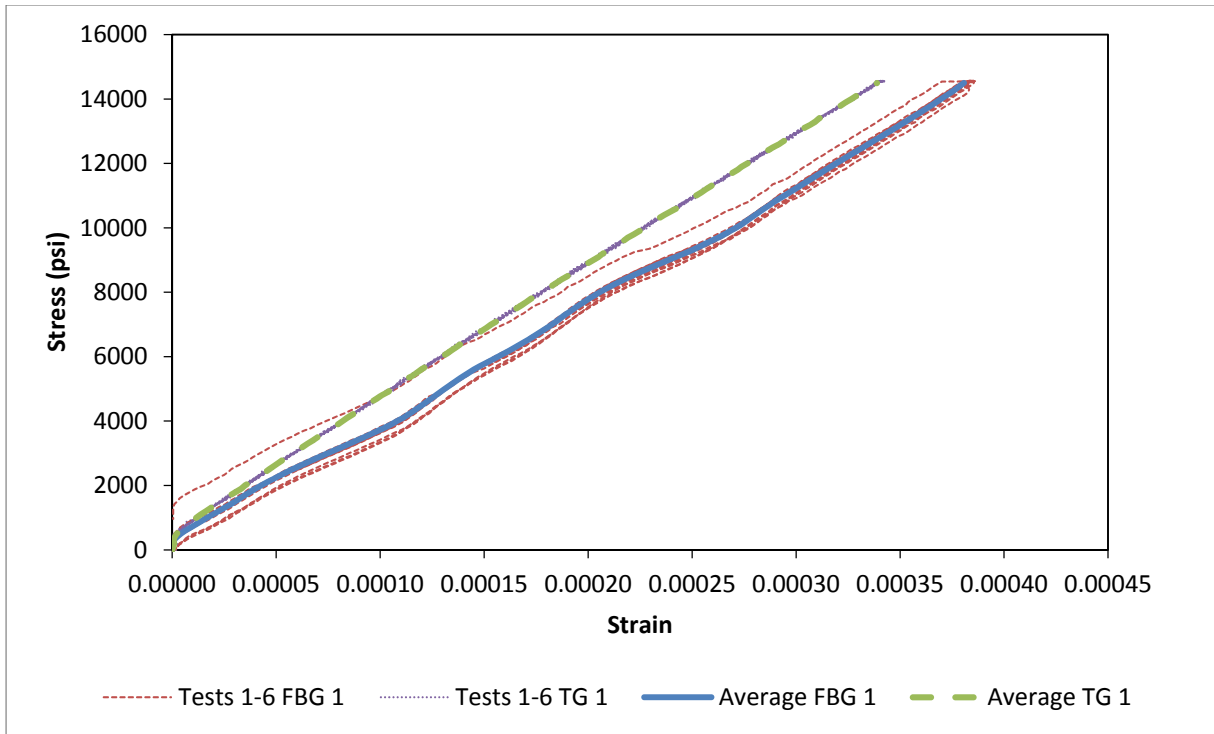
Six graphs display the results from six different tests comparing an FBG and a TG in similar locations on the S-beam. The stress versus strain averaged results for loading and unloading the specimen are shown for each sensor type. The data was averaged so that comparisons between FBGs and TGs were clear. The individual sensor results are also displayed to show the repeatability of each test. Additionally, the stress values were calculated based upon the applied load and location of the specific strain gage.

The results from each set of sensors are discussed after the graph is presented. Sensor sets 1 and 2 were in compression, resulting in negative strain values and sets 3, 4, 5, and 6 were in tension, resulting in positive strain values. The sensor set located on the bottom of the bottom flange was the main focus for the study because it is the critical location required to determine the lateral distribution factors.

It should be noted that neither the FBG nor the TG results were consistently greater than the other. If one type of sensor had higher or lower results for each test, then instrumentation malfunctioning could possibly be an explanation for the results. However, because both FBG and TG sensor results varied from higher or lower than the other, the averaged strain gage results in each beam location, as described in Section 4.4.2, could potentially lead to more accurate strain measurement results for field tests.

#### 3.5.1 Set 1

Figure 19 displays the results comparing set 1, which includes FBG 1 and TG 1. The sensors were located adjacent to each other on the top of the top flange.



**Figure 19: Set 1 Sensor Comparison of Stress vs. Strain in Compression**

The results comparing set 1 would ideally resemble the results from set 6. Both sets had an FBG and TG installed side by side on the outsides of the flanges where the test configuration would cause a constant moment at this location. While the TG results averaged to 11.3% higher strain readings than the FBG result averaged, some observations should be noted.

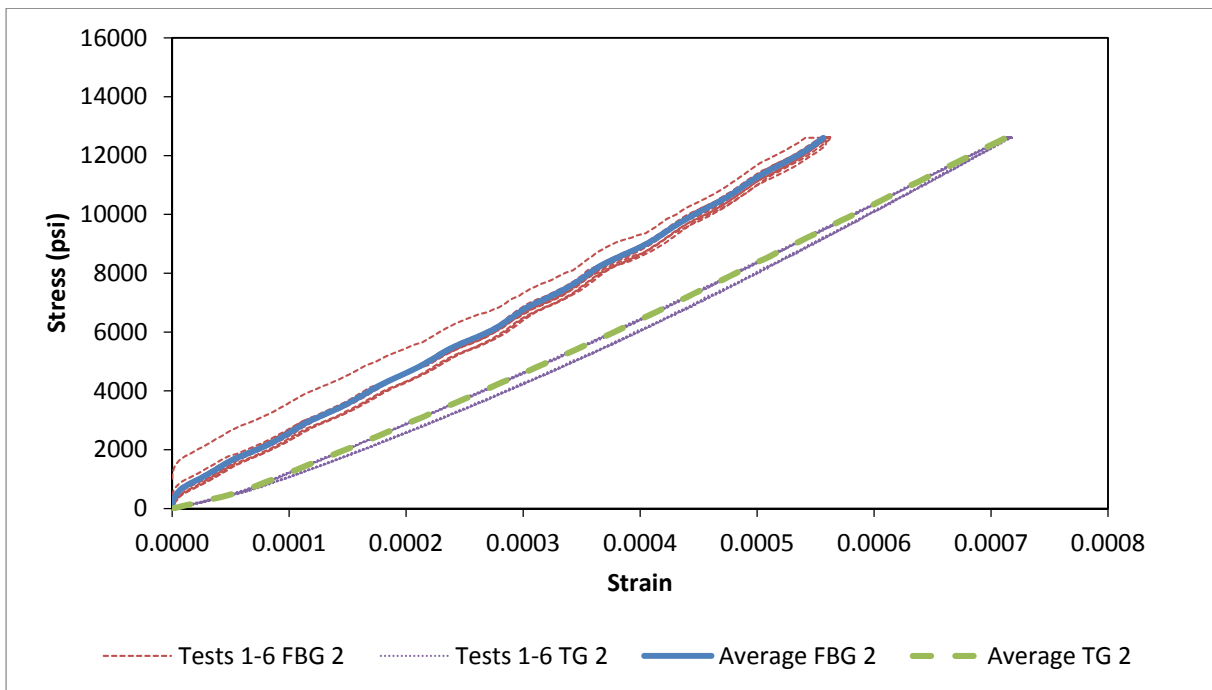
First, FBG 1 was the only sensor that was preinstalled on the beam from previous tests. When the surface was abraded in preparation for installation of TG 1, the surface area adjacent to FBG 1 became heated, possibly weakening the bond between the surface and FBG 1. A bond may be damaged and not as effective when heated to high temperatures then cooled again; the result could be slight or drastic inaccurate strain readings. Second, unlike the bottom surface of the beam, the top surface of the beam was slightly uneven; the top flange area over the web was slightly lower than flange area toward the edges of the beam. The difference was not large



enough to affect the application of the strain gages, however it could cause varying strain readings due to the exact distance from the neutral axis being slightly different.

### 3.5.2 Set 2

Figure 20 displays the results comparing set 2, which includes FBG 2 and TG 2. Both sensors were located on the bottom of the top flange on opposite sides.



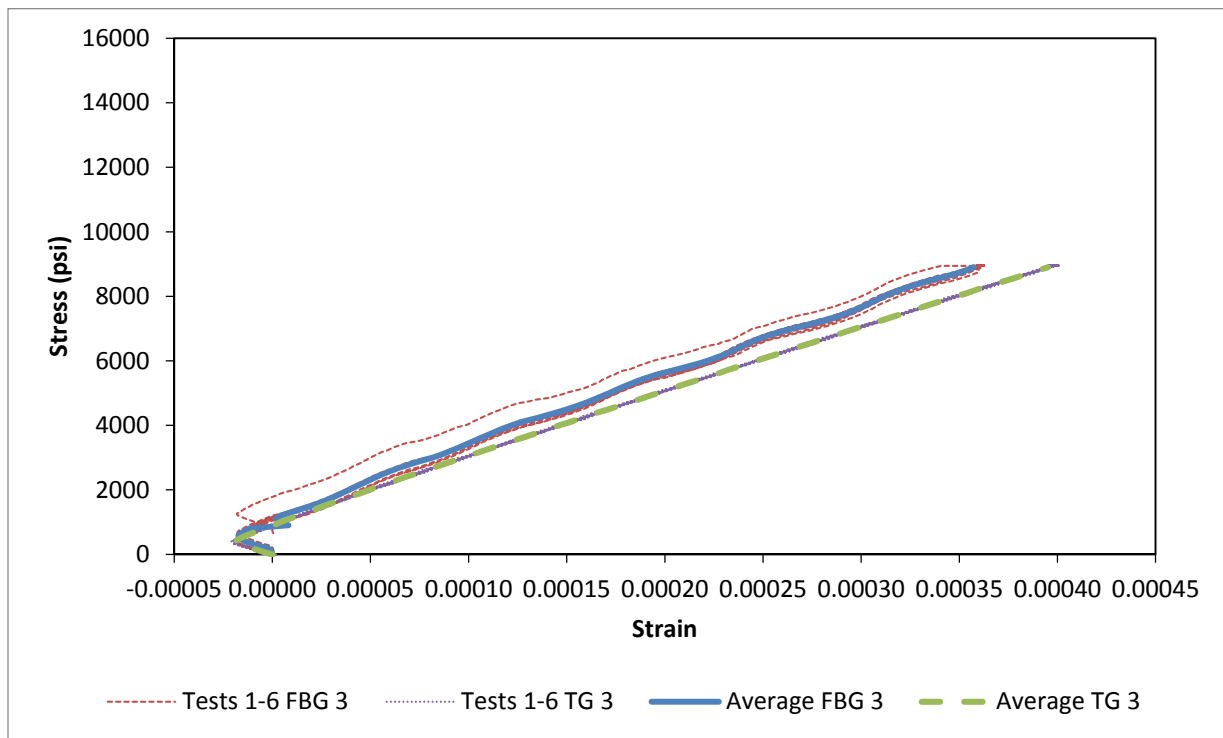
**Figure 20: Set 2 Sensor Comparison of Stress vs. Strain in Compression**

Set 2 showed the widest spread of results; the FBG strain averaged 14.8% higher than the TG averaged. The S-Beam had gradual slopes from the outside flanges to the web as seen in Figure 10, therefore it was important to measure and install the sensors at the same distance from the edge of each flange to the middle of each sensor. For set 2, FBG 2 was located 1/4-inch from the edge of the flange while TG 2 was located 3/16-inch from the edge directly on the opposite

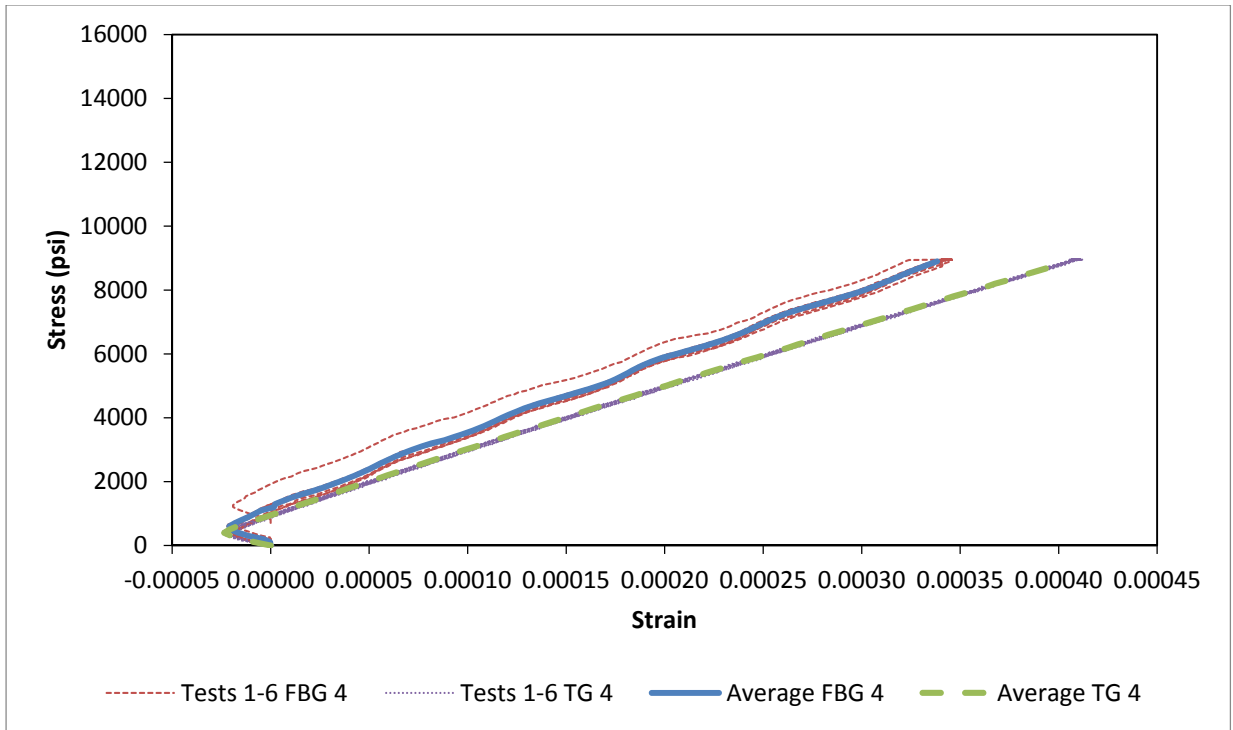
side. It should be noted that the small size of the S-beam enhances any inaccuracies in sensor placement relative to the actual I-80 plate-girder application.

### 3.5.3 Set 3 and 4

Figure 21 and Figure 22 display the results comparing sets 3 and 4, respectively. These results include FBG 3, TG 3, FBG 4, and TG 4. All four sensors were located on the web of the beam on the same side at a 45-degree angle to measure shear strain. For both sets of data, FBG and TG results showed a negative strain reading between the 0-1000 psi stress ranges. This behavior could have be a result of the beam adjusting its position on the support rollers when the load was initially applied.



**Figure 21: Set 3 Sensor Comparison of Stress vs. Strain in Tension**

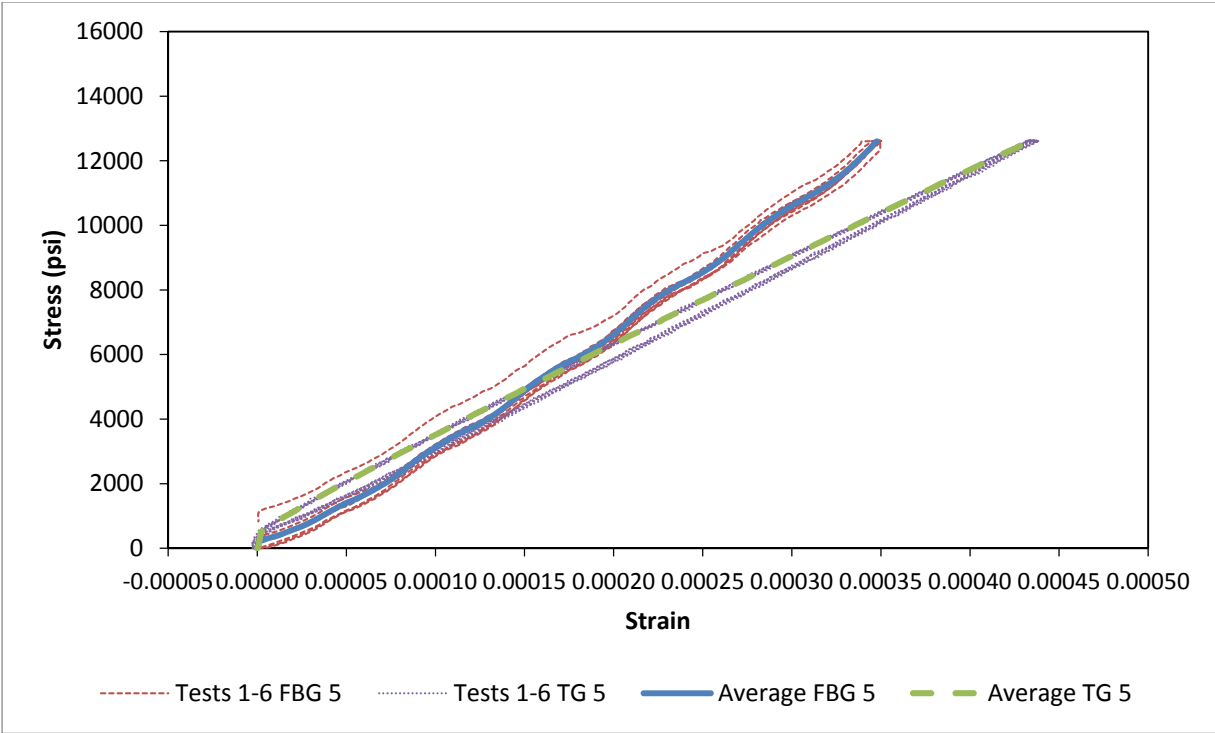


**Figure 22: Set 4 Sensor Comparison of Stress vs. Strain in Tension**

The results showed FBGs with higher strain readings than the TGs in sets 3 and 4. Set 3 had an average FBG strain of 8.8% higher than the TG strain, and set 4 had an average FBG strain of 14.2% higher than the TG strain. The sensors were angled at 45-degrees to obtain the strain readings in tension, but any variation in the angle placement could have affected the results. Additionally, the sensors appeared to be installed at the center of the web, but again, any slight variation could have yielded the given results.

### 3.5.4 Set 5

Figure 23 displays the results comparing set 5 as shown, which includes FBG 5 and TG 5. Both sensors were located on the top of the bottom flange on opposite sides.

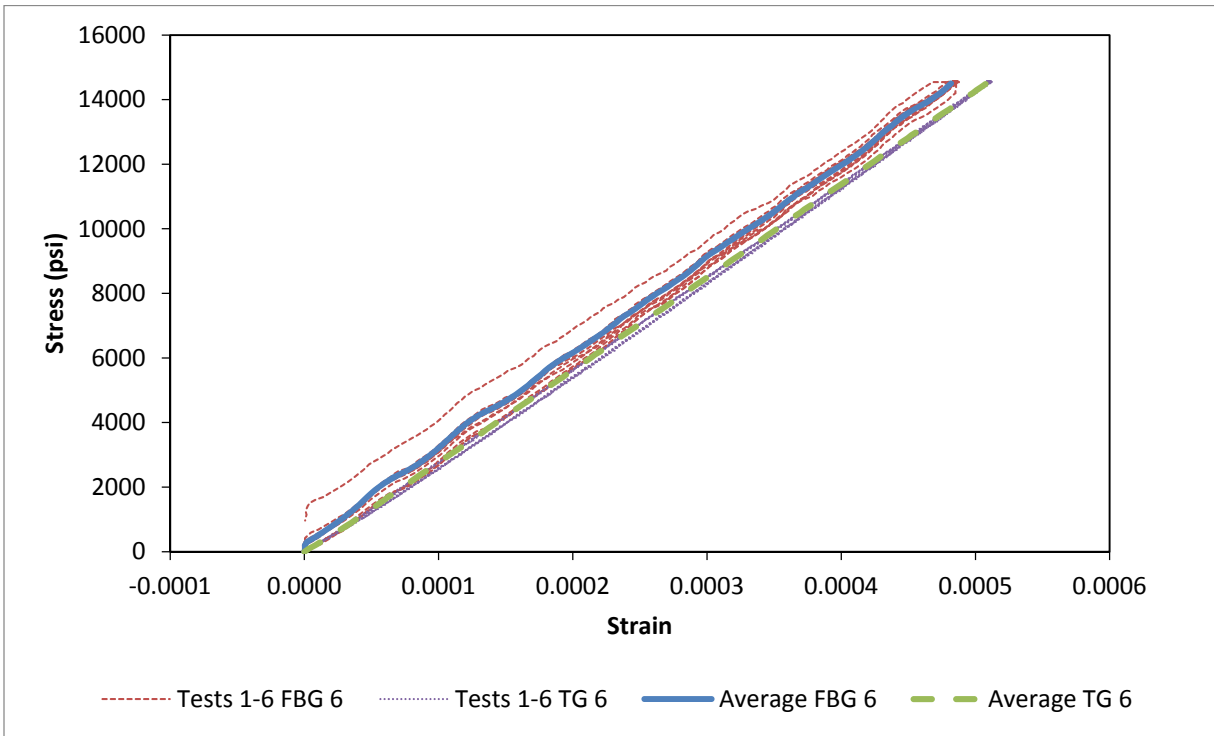


**Figure 23: Set 5 Sensor Comparison of Stress vs. Strain in Tension**

Set 5 results showed similar strain trends as the other sets for the first half of the test. Then, the FBG began to read higher strain levels than the TG during the second half of the test for an average of 20.3% difference in the moduli of elasticity between the two sensors. This trend was unusual and could possibly be an epoxy issue; the results have been sent into the manufacturer. Similar to the top flange, the S-Beam had gradual slopes from the outside flanges to the web as seen in Figure 10, therefore it was important to measure and install the sensors at the same distance from the edge of each flange to the middle of each sensor. For set 5, FBG 5 was located 3/16-inch from the edge of the flange while TG 5 was located 7/32-inch from the edge directly on the opposite side.

### 3.5.5 Set 6

Figure 24 displays the results comparing set 6, which includes FBG 6 and TG 6. Both sensors were located adjacent to each other on the bottom of the bottom flange.

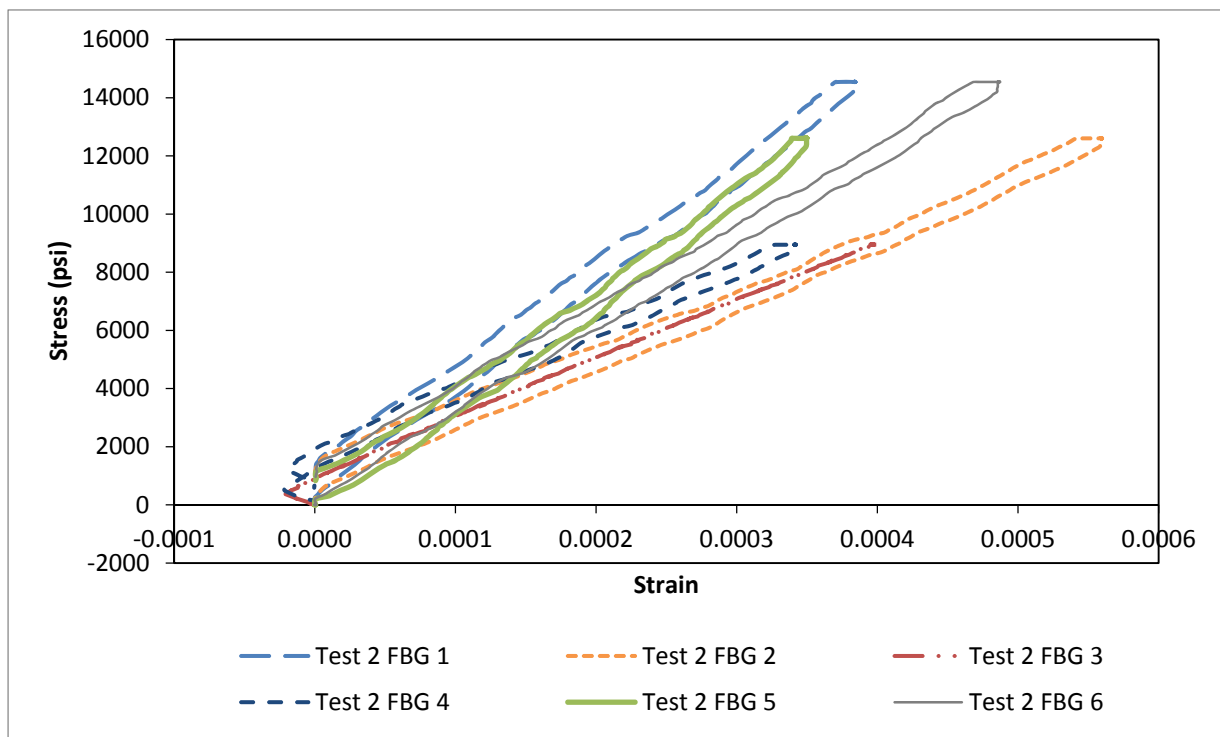


**Figure 24: Set 6 Sensor Comparison of Stress vs. Strain in Tension**

Set 6 has the least variation with a 2% higher modulus of elasticity reading from the FBG versus the TG. These results make sense because the two sensors were installed side by side and were the farthest away from the loading equipment, minimalizing local effects. Also, unlike the top surface of the S-beam, the bottom surface appeared to have a perfectly flat surface. Both sensors were installed after all abrading of the sensor attachment locations, so bond loss or reheating of the surface was not a concern.

### 3.5.6 FBG Test 2

Figure 25 displays the results from all six Fiber Bragg Grating sensors during test 2. These stress and strain values are displayed as positive values on the graph, however FBG 1 and FBG 2 were both in compression during the test. The purpose of displaying FBG results from this specific test and each location is to compare the unusual differences in the strain reading behavior between loading and unloading the specimen, along with a drop off of data between the 0-2000 psi stress ranges. In all other tests, the FBG strain behavior was the same for loading and unloading. The outlier is clear in set 1 through set 6 graphs where one dotted line, representing an FBG during test 2, lies above the remaining data.



**Figure 25: Test 2 FBG Results**

The FBG test 2 results were placed on a graph to compare the abnormal behavior of the six sensor locations. A common trend could be found when comparing FBGs 5 and 6 where the

stress drops to zero just under the 2000-psi mark due to an FBG interrogator malfunction. A similar characteristic can be seen in the test 5 data, although the results were less obvious with the data dropping around the 1000-psi mark.

In a comparison of the slopes of the FBGs stress-strain curves, the slope closest to the 29,000,000-psi modulus of elasticity of steel was consistently achieved by FBG 6, with all six tests with a slope of approximately 28,400,000-psi. The FBG sensor verification was most critical at this location and was within a 5% strain difference. The remaining sensor readings had slopes both lower and higher with FBG 2, FBG 3, and FBG 4 lower than FBG 6 and FBG 1 and FBG 5 higher than FBG 6. FBG 5 had an unusually high strain discrepancy in the results, however the difference for the remaining FBG strain results was reasonable for the reasons previously discussed. This trend was consistent throughout all six of the tests performed.

## CHAPTER 4: LATERAL DISTRIBUTION FACTOR

### 4.1 Objective

The primary objective of instrumenting the Laramie River Bridge, described in Chapter 2, was to obtain the lateral distribution factors (DFs) to validate or potentially improve the existing load ratings. A load rating is an indication of a structure's live load capacity. This chapter presents the process behind obtaining the DFs through the means of experimental field testing. A discussion on BRASS software, the methodology used for instrumentation design, the instrumentation plan, the design vehicle loading plan, and the data collection and analysis procedures is included.

### 4.2 BRASS Software

The Laramie River Bridge requires biennial visual inspections. DOTs are required to send the updated bridge data to the National Bridge Inventory (NBI) in order to receive federal funding. Bridge inspections also help state bridge managements to allocate their funds most effectively to maintain, retrofit, and replace highway bridges. In Wyoming, the relevant data gathered at each bridge inspection is updated into its corresponding BRASS file. BRASS then generates an updated load rating using current rating specifications (WYDOT, 2003a). By installing a system using strain sensors, more accurate DFs can be entered into the BRASS analysis engine to produce a more accurate and potentially increased load rating.

BRASS is an analysis program created to guide bridge engineers in the design and load rating of bridges. The program is current with the AASHTO *Standard Specifications for Highway Bridges*, 17<sup>th</sup> Edition, 2002; *LRFD Bridge Design Specifications*, 7<sup>th</sup> Edition, 2014 with 2015 interim revisions; and *Manual for Bridge Evaluation*, 2<sup>nd</sup> Edition, 2010 with 2011, 2013,



2014, and 2015 interim revisions (WYDOT, 2003a). Various subprograms within BRASS software can be obtained for a variety of bridge types. BRASS-Girder is used for highway bridges, including steel welded-plate continuous bridges.

#### 4.2.1 BRASS-GIRDER Load Rating Analysis

For research purposes, BRASS-Girder was used to calculate the load ratings for the Laramie River Bridge. To determine the girder-line analysis is a simplified method using the Standard Specifications, LRFD Specifications, the rigid method, and the lever rule. The BRASS-Girder method used does not provide a rigorous analysis of the DFs (Puckett, et al. 2011a).

Most federally owned bridges in Wyoming are defined in a BRASS-Girder file by an engineer. These inputs include the following (WYDOT, 2003a):

- 1) Bridge deck
- 2) Typical girder cross sections
- 3) Bridge span data
  - Length
  - Web depth variation
  - Typical cross-section limits
  - Cable path geometry
  - End restraints
  - Hinges
- 4) Material properties
- 5) Dead and live loads
- 6) Allowable stresses

Typical default values are automatically selected for any parameter left blank. Based upon the defined values, the system calculates moments, shears, axial forces, deflections, and rotations as a result of dead loads, live loads, settlements, and temperature changes. The user controls the degree of detail for the output report, so this method provides the calculation results at any

longitudinal point of interest along the bridge. The output is also able to decipher the critical longitudinal points of the bridge taking into account failure criteria for load ratings.

One of the input parameters selected by the user is the preferred analysis method. Either Load Factor Rating (LFR) or Load and Resistance Factor Rating (LRFR) can be selected for the analysis method. The FHWA supports both LFR and LRFR since the adoption of the AASHTO LRFD Specifications. For bridges designed before October 1, 2007 that followed Allowable Stress Design (ASD) or Load Factor Design (LFD) criteria, either LFR or LRFR may be used; for bridges designed on or after October 1, 2007, states must adhere to LRFR Specifications. For bridges that were designed using ASD or LFD standards, WYDOT chooses to load rate them using LFR Specifications (Ruess, 2015). Therefore, in order to stay consistent with WYDOT practices, the AASHTO LFR criteria were used to determine load ratings in BRASS-Girder for the Laramie River Bridge.

Included in the load-rating summary are the inventory ratings, operating ratings, and controlling features. An explanation of these terms can be found in Section 2.3. The load ratings for five different vehicle configurations are included and capacities were rounded down to the nearest ton. These configurations included the HS20, HS25, Type 3, Type 3S2, and Type 3-3 trucks. This vehicle group meets the federal weight limit and vehicle configuration requirements and represents the most common trucks on the nation's interstate highways (FHWA, 2014c). Additionally, AASHTO selected Types 3, 3S2, and 3-3 as model vehicles that represent common 3-axle single trucks, 5-axle tractor semi-trailers, and 6-axle tractor trailers, respectively.

By importing the bridge file and identifying the pertinent analysis factors, including the load configurations applied, a LFD load rating is produced by BRASS-Girder. Section 2.3 discusses the Laramie River Bridge load-rating summary that was provided by WYDOT.

#### 4.2.2 Load Factor Rating

The LFR method is based on the ultimate member capacity and is still used throughout state DOTs despite the fact that LRFR Specifications have become the required method of design and rating for newly constructed bridges. The basic LFR procedure is presented in this section for a simple span bridge for both inventory and operating ratings. The equations are meant to give the reader a basic idea of the LFD load rating process and to present the origin of the DF within the equation. BRASS-Girder was used to complete the analytical LFD load ratings for the purpose of this research.

The inventory rating for a bridge using the LFR method is displayed in Equation 2 (AASHTO, 2011):

$$RF_I = \frac{M_N - A_1 M_D}{A_2 M_{LL+IM}} \quad \text{(Equation 2)}$$

where  $RF_I$  is the inventory rating,  $M_N$  is the nominal moment capacity,  $A_1$  is the dead load factor equal to 1.3,  $M_D$  is the moment due to the dead load on the member,  $A_2$  is the live load factor equal to 2.17, and  $M_{LL+IM}$  is the live load moment on the member including the impact and DFs.  $M_{LL+IM}$  was calculated by Equation 3:

$$M_{LL+IM} = M_{LL}(1 + IM)DF \quad \text{(Equation 3)}$$

where  $M_{LL}$  is the maximum live load moment without impact.  $DF$  is the lateral distribution factor.  $IM$  is the impact factor determined by Equation 4:

$$IM = \frac{50}{L+125} \leq 0.3 \quad \text{(Equation 4)}$$

where  $L$  is equal to the length of the bridge in feet.

The operating rating for a bridge using the LFR method is the same as the inventory rating shown in Equation 2 except that  $A_2$  is equal to 1.3.

#### 4.2.3 AASHTO Lateral Distribution Factors

The DFs are used to determine the percent of total live load supported by an individual girder. AASHTO has developed DF methods that have been adopted by the FHWA, however mathematical models (Puckett, et al. 2005b) and completed field experiments have proven that the actual DFs are generally less than the conservative specification equations. Field-tested DFs have been shown to be up to 24% less than specification values, making a significance difference in experimental load-rating results (Barker, 2001). Fu, et al. (1996) provided field results demonstrating that the DFs were reduced for four bridges by an average of 22% from the analytical LRFD factors and 35% from the analytical LFD factors. These results were consistent throughout published research and validated the reasoning for determining more accurate DFs as a means for increasing load ratings.

It is important to note that the LFD Specifications and the LRFD Specifications use different units when determining the DFs. LFD is in terms of wheel lines per girder. LRFD is in terms of lanes per girder. When determining the DFs through the design specifications, the LFD factor must be divided by 2 to be compared to the LRFD factor, since there are two wheel lines per one vehicle lane. When determining the DFs by field testing for LFD, the calculated DF must be multiplied by however many wheel lines there are in the maximum load case to be used for LFD design comparisons and for BRASS-Girder inputs.

*AASHTO Standard Specifications for Highway Bridges*

It was important to determine the analytical DFs in order to have preliminary expectations for field-test results for the Laramie River Bridge. WYDOT used the AASHTO *Standard Specification for Highway Bridges* to calculate the DF based on wheel lines for both positive and negative moment regions. This approach is considered conservative and is based on the spacing between girders for the wheel load distribution. In order to compare the analytical calculations from LFD to LRFD, each LFD total was multiplied by 0.5. The displayed DF was multiplied by 1.0 for one- and two-lanes loaded; it was multiplied by 0.9 for three-lanes loaded, accounting for the multiple presence factors.

Equation 5 was applied to calculate the DF for the interior girders for one-lane loaded:

$$DF_{m1}^i = \frac{S}{7} \quad \text{(Equation 5)}$$

where  $S$  is equal to the spacing between girders in feet.  $S$  was rounded to 9-feet for the Laramie River Bridge, since that was the largest girder spacing. For one-lane loaded, the DF resulted in 1.29 wheel lines per girder or 0.64 lanes per girder.

Equation 6 was used to calculate the DF for the interior girders for two- or more-lanes loaded (AASHTO, 2011):

$$DF_{m2}^i = \frac{S}{5.5} \quad \text{(Equation 6)}$$

where  $S$  is again equal to the spacing between girders in feet. For two-lanes loaded, the DF resulted in 1.64 wheel lines per girder or 0.82 lanes per girder. For three-lanes loaded, the outcome was 0.74 lanes per girder.

Equation 7 was applied to calculate the DF for the exterior girders:

$$DF^e = \frac{S}{4 + \frac{S}{4}} \quad \text{(Equation 7)}$$

where  $S$  is again equal to the girder spacing. For one- and two-lanes loaded, the DFs resulted in 1.44 wheel lines per girder or 0.72 lanes per girder, respectively. For three-lanes loaded, the outcome was 0.65 lanes per girder.

### *AASHTO LRFD Bridge Design Specifications*

The 2014 AASHTO LRFD Specifications, used for bridges designed today, include DFs that are typically more accurate than LFD Specifications indicate. For research purposes, the Laramie River Bridge DFs were calculated using LRFD Specifications to evaluate a more precise range for a preliminary analysis than LFD criteria would otherwise signify. The calculations were in terms of lanes per girder and considered both the positive and negative moment sections. The multiple presence factor,  $m$ , is embedded in the LRFD Equations 8, 9, 11, and 12 that follow and is equal to 1.2 for one-lane loaded, 1.0 for two-lanes loaded, and 0.85 for three-lanes loaded as determined by AASHTO.

First, the positive moment section was calculated. This calculation included interior girder DFs. The DF for moment and one-lane loaded,  $mg^i_{m1}$ , was equal to 0.53 lanes per girder, presented in Equation 8, and for moment and two-lanes loaded,  $mg^i_{m2}$ , was equal to 0.73 lanes per girder, displayed in Equation 9. The DF for moment and three-lanes loaded was equivalent to that for two-lanes loaded.

$$mg^i_{m1} = 0.06 + \left(\frac{S}{14}\right)^{0.4} \left(\frac{S}{L}\right)^{0.3} \left(\frac{K_g}{12.0Lt_s^3}\right)^{0.1} \quad \text{(Equation 8)}$$

$$mg^i_{m2} = 0.075 + \left(\frac{S}{9.5}\right)^{0.6} \left(\frac{S}{L}\right)^{0.2} \left(\frac{K_g}{12.0Lt_s^3}\right)^{0.1} \quad \text{(Equation 9)}$$

where  $S$  is the girder spacing equal to 9-feet.  $L$  is the span length equal to 65-feet, and  $t_s$  is the thickness of the slab equal to 8-inches.  $K_g$  is the longitudinal stiffness parameter equal to 367,620-inches<sup>4</sup>.

$K_g$  was determined using Equation 10:

$$K_g = n(I + Ae_g^2) \quad \text{(Equation 10)}$$

where  $n$  is the ratio of the modulus of elasticity of the beam material to the modulus of elasticity of the deck material equal to 9.  $I$  is the moment of inertia of the girder equal to 16,197-inches<sup>4</sup>.  $A$  is the area of the girder equal to 37.12-inches<sup>2</sup>.  $e_g$  is the distance between the neutral axis of the girder to the slab equal to 26.25-inches. It was assumed that the design calculations did not transform the cross section to include the behavior of the concrete deck because it is a noncomposite bridge. Therefore, a transformed section was omitted in the initial LRFD calculations. If the engineer is interested in the experimental section modulus, the experimental transformed moment of inertia would need to be calculated by first determining the experimental total moment as discussed in Section 4.7.

The exterior girder DFs were calculated using the lever rule. One-lane loaded  $mg^e_{m1}$  was equal to 0.67 lanes per girder and was determined by Equation 11.

$$mg^e_{m1} = \frac{d_v}{S} \quad \text{(Equation 11)}$$

where  $d_v$  is the distance from the center of the vehicle load with its outside wheel directly over the exterior girder to the second interior girder in feet. The DF for moment and two- and three-lanes loaded  $mg^e_{m2}$  was equal to 0.73 lanes per girder. These values were calculated by Equation 12:

$$mg_{m2}^e = e(mg_{m2}^i) \quad \text{(Equation 12)}$$

where the factor  $e$  is equal to 1.0 and calculated in Equation 13.

$$e = 0.77 + \frac{d_e}{9.1} \geq 1.0 \quad \text{(Equation 13)}$$

where  $d_e$  is the distance from the exterior girder to the edge of the curb in feet, which is equal to 2-feet where the wheel load can be applied.

Second, the negative moment section was calculated. These calculations included interior and exterior girder DFs. The same equations that were used for positive moment calculations were used for negative moment calculations. The only difference was the value of  $L$ , the length of the span. For negative moment, this value was taken as the average of the lengths of span one and span two equal to 67.5-feet. The negative moment results are displayed in Table 1.

Table 1 compares the LFD and LRFD lateral distribution factor results in lanes per girder. As shown, there are two highlighted values in the table. These were the factors used for design purposes in BRASS-Girder where the user has an option to define the standard wheel fraction for both one-lane loaded and two- or more-lanes loaded. For this reason, the controlling, or highest, value for one-lane loaded is highlighted, and the controlling value for two- or more-lanes loaded is highlighted. The controlling cases for both one-lane and two- or more-lanes loaded were using the LFD Specifications.



**Table 1: Comparison of LFD and LRFD Lateral Distribution Factors**

Analysis	Bending Moment	One Lane Loaded		Two Lanes Loaded		Three Lanes Loaded	
		Interior Girder	Exterior Girder	Interior Girder	Exterior Girder	Interior Girder	Exterior Girder
LFD	Positive and Negative	0.64	<b>0.72</b>	<b>0.82</b>	0.72	0.74	0.65
LRFD	Positive	0.53	0.67	0.73	0.73	0.73	0.73
	Negative	0.50	0.67	0.70	0.70	0.70	0.70

### 4.3 Methodology for Determining the Instrumentation Plan

The University of Wyoming team used FBGs to develop a system that could validate DFs at any given time. While FBGs have been available for strain monitoring for a long period of time, they were typically used for structural health monitoring purposes in the civil engineering field. As stated in *Fibre Optic Methods*, the data is generally used to “plan and design maintenance activities, increase safety, verify hypotheses, reduce uncertainty, and widen the knowledge concerning the structure being monitored” (Glisic, 2007). More recently, FBGs have been utilized to study the practicability of improving traditional load ratings of bridges through field testing. The University of Wyoming team approached the DF system design using FBGs, which were discussed in Chapter 3, and field testing methodology established by Barker and colleagues at the University of Missouri (McDaniel and Barker, 1998).

There are various methods used for field testing bridges to determine more accurate analyses of structures. A common method is to fully instrument a bridge with strain sensors, conduct field load rating tests, gather and analyze strain data to develop a field-tested model, and then compare this model to the analytical design model. By comparing the two models, a tuned analysis of the bridge can result in a quantitative representation of the structure’s true behavior.

While this method results in a fairly accurate representation of a bridge's response, the data acquisition system and analysis are costly and time consuming due to the price and number of sensors, installation time, and data reduction and analysis procedures. A tuned model and analysis of a bridge is not always necessary, depending on the goals of the field tests.

A simplified and economical field instrumentation plan may be implemented to measure accurate DFs. Then, these DFs can be used in an analytical rating, such as BRASS- Girder, to determine more accurate load ratings. Barker and colleagues at the University of Missouri developed a total of six instrumentation plans to be used on slab-on-steel girder bridges (McDaniel and Barker, 1998). The premise is based on the idea that the majority of bridges have a higher capacity than design indicates. Their team focused on the following eight factors that could contribute to additional bridge performance capacity, which are not initially accounted for in design specification procedures (McDaniel and Barker, 1998):

- 1) Impact factor
- 2) Experimental dead load
- 3) Actual dimensions
- 4) Unintended composite action
- 5) Lateral distribution factor
- 6) Bearing restraint
- 7) Longitudinal distribution
- 8) Unaccounted system stiffness

One of the goals of their research was to develop various instrumentation plans that could be referenced for installing strain sensors onto bridges based upon which of the eight factors were parameters of interest. The bridge engineer must decide which factors should be accounted for based upon an initial analysis, determining the complexity of the instrumentation plan for the field tests. For the research completed in Missouri, traditional foil and welded strain gages were

used; however, the instrumentation plan is applicable to any type of reliable strain gage that is well suited for the bridge materials and field conditions.

#### 4.4 Instrumentation Plan

The experimental response of the noncomposite Laramie River Bridge would include contributions from all eight factors that could affect the additional bridge capacity over design procedures as previously discussed. Because the purpose of instrumenting the bridge is to obtain DFs, various parameters suggested by McDaniel and Barker (1998) were considered insignificant for this field testing. These considerations are discussed in depth in this section as they formed the basis for developing the strain sensor instrumentation plan.

##### 4.4.1 Factors Affecting Sensor Placement

After careful consideration and input from WYDOT bridge engineers, it was decided that the DFs were the most vital parameters for establishing an experimental load rating capacity. The experimental DFs are input values for BRASS load rating analysis and affect the load rating of a structure. It provides bridge engineers a more accurate representation of the bridge's behavior and allows potentially higher load ratings without the cost to develop a fully tuned bridge model.

Since the objective of the field test is to determine the DFs, an instrumentation plan that determines the DFs has been developed; all other factors that affect the bridge response were considered irrelevant. Table 2 is a summary of the eight contributing factors and describes why each factor is or is not considered relevant for the purpose of this work.

**Table 2: Factors Taken into Consideration for Field Testing**

<b>Contributing Factors</b>	<b>Considered</b>	<b>Reasoning</b>
1. Impact Factor	No	Expensive to determine as it involves in-depth static and dynamic testing and analysis.
2. Experimental Dead Load	No	Assumed to be equal to design dead loads.
3. Actual Dimensions	No	Assumed that actual dimensions are equal to design dimensions because measuring the true dimensions of each member would take additional time to complete during bridge inspections.
4. Unintended Composite Action	No	Cannot be relied upon for determining the ultimate capacity of a bridge.
5. Lateral Distribution	Yes	Can be quantified as an input factor for BRASS analysis, affecting the load rating of a structure. Can provide bridge engineers a general idea of the bridge's behavior in order to calculate a potentially higher load rating without the cost for a tuned bridge model.
6. Bearing Restraint	No	Cannot be relied upon for determining the ultimate capacity of a bridge.
7. Longitudinal Distribution	No	Is not quantified or accounted for as an input parameter to improve a calculated load rating through BRASS.
8. Unaccounted System Stiffness	No	Is not quantified or accounted for as an input parameter to improve a calculated load rating through BRASS.

#### 4.4.2 Sensor Placement on Beams

In order to calculate an approximate DF for each girder, Plan III from McDaniel and Barker (1998) states that a strain gage must be placed only on the bottom flange of each girder. This would allow Equation 14 to be used:

$$DF = \frac{\epsilon_{GirderMax}}{\sum \epsilon_{AllGirders}} \quad \text{(Equation 14)}$$

where the DF for the girder of interest is equal to the maximum strain measured of that girder divided by the sum of all the girder strains at the critical locations.

This approach is straightforward, however this simplified sensor configuration will result in approximated DFs, and it does not provide redundancy of experimental sensors or the means to calculate cross-sectional stress, moments, or the location of the neutral axis. Although this was

designed as a noncomposite bridge, the bridge will act at least partially composite. Because of this behavior, the location of the neutral axis must be determined in order to obtain a more accurate DF. By calculating the actual neutral axis and total bending moment, the engineer is also able to check global equilibrium to validate the system's performance.

Instead of having one FBG installed at the extreme fibers of the bottom flange, there will be a total of four FBGs. This will include two FBGs located on the web, each positioned at middepth of the girder but on different sides of the web. Additionally, two FBGs will be located on the underside of the bottom flange, each placed an equal distance away from the longitudinal center of the flange and the outside edge of the flange. This configuration is displayed in Figure 26.



**Figure 26: Cross-Sectional View with FBG Sensors on the Web and Bottom Flange**

The strain measurements can be averaged at the two locations to remove the effects of weak axis bending and torsion. The two different locations for strain measurements allow the

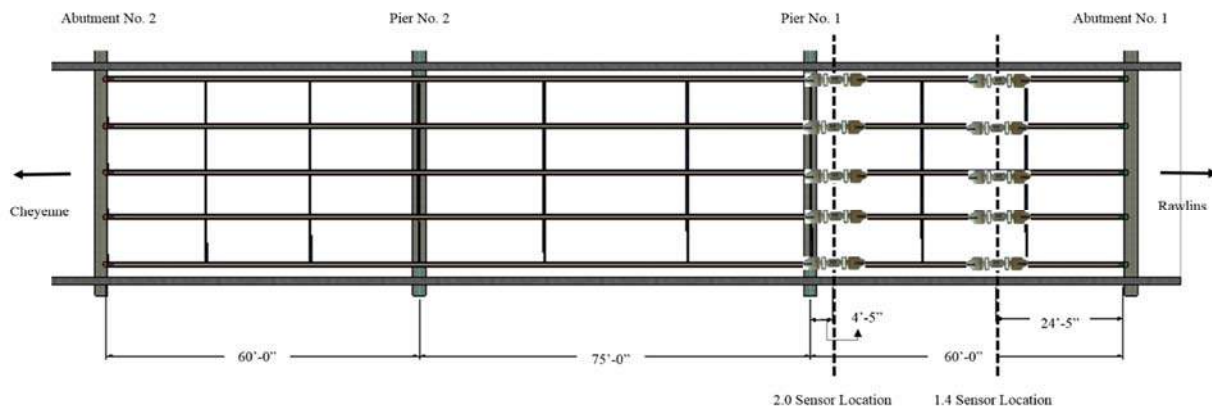
strain profile for the section to be calculated, and then the location of the neutral axis can be determined. This process is described in Section 4.7.

#### 4.4.3 Critical Longitudinal Locations

McDaniel and Barker (1998) state that the sensors must be placed on the cross section of the critical longitudinal location. Referring to the BRASS LFR load rating analysis, the critical cross section for sensor placement is at the 1.4 location, which is at 40% of the first span, and at the 2.0 location, which is the start of the second span. The 1.4 critical location is controlled by the following commercial vehicle configurations for the strength limit state: HS20, HS25, and Type 3. The 2.0 critical location is also controlled by the strength limit state for Type 3S2 and Type 3-3 vehicles. The critical locations are shown in an elevation view in Figure 27 and a plan view in Figure 28.



**Figure 27: Elevation View with Critical Locations for Sensor Placements**



**Figure 28: Plan View with Critical Locations for Sensor Placements**

One should note that the sensors are not directly placed at the 1.4 or 2.0 locations. Oesch and Barker (2003) discussed concentrated load effects taking place directly over supports or even over cross frames. By installing the sensors a distance of the height of the girder away from these occurrences, these effects can be avoided. The initial 1.4 location of 24-feet from abutment one was adjusted an additional 5-inches due to a cross frame. The 2.0 sensor location also shifted 4-feet 5-inches toward abutment one to avoid concentrated load effects due to pier one.

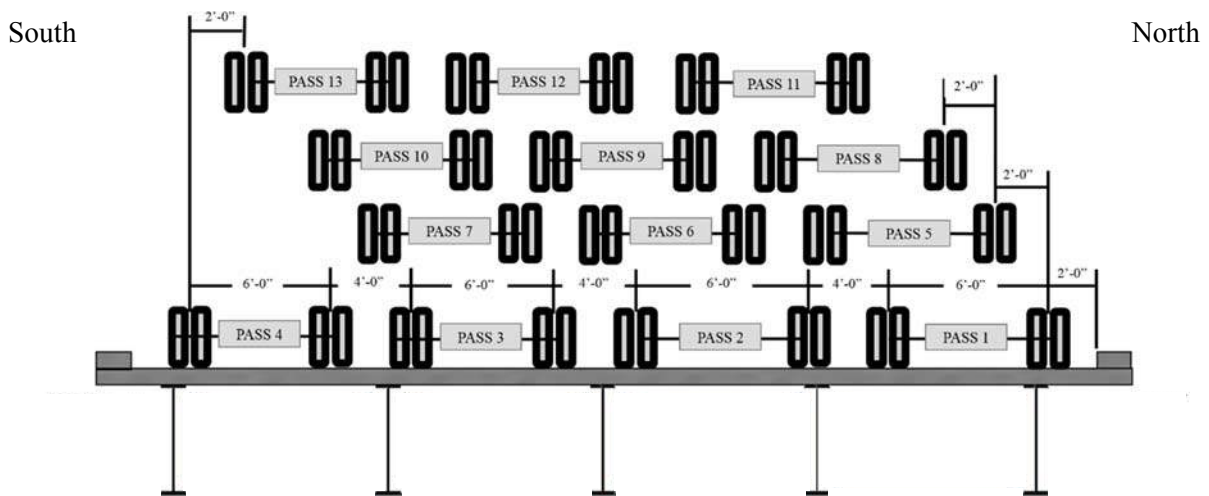
#### 4.5 Vehicle Loading Plan

The purpose of developing a vehicle-loading plan is to determine the maximum resistance of each girder against a known load. It is important that each girder is tested for its maximum live-load effect under static testing of individual vehicle loads. Static testing can be accomplished by driving a vehicle at crawl speed without the concern of dynamic impact affecting the results. Most field tests are not completed with multiple test load vehicles. Thus to induce the effect of multiple vehicles, the method of superposition is applied.

As long as the bridge stays within its elastic range, which can be verified using a displacement transducer, the effect from an individual vehicle can be added or superimposed on the effect of another vehicle when loaded in an adjacent lateral position. Superposition pertains to strain measurements from the girder of interest when maximized under vehicle load effects. Field testing should take place first where an individual vehicle passes over the bridge in a predetermined lateral position. Based upon the field testing results, an engineer can determine which truck position combinations caused the greatest stress in the girder of interest. The strain effects from the selected truck positions that cause the beam maximum stress can be superimposed, or added together, resulting in the maximum total strain induced from the vehicle passes on the girder of interest.

The design vehicle placement plan is displayed in Figure 29 where the principle of superposition should be used to maximize the load effects on each girder for a total of 13 passes. The outside wheel was placed 2-feet from the right, or north, curb because the overhang on the north side is wider and should produce a greater DF. With a design lane load of 10-feet, four design vehicle loads are included. However, it is not expected that four lanes loaded would control.

From the north side, the design vehicle should be placed 2-feet toward from the north curb for passes 1, 2, 3, and 4. Then the vehicle's path should be 2-feet toward the south for passes 5, 6, and 7 and then another 2-feet for passes 8, 9, and 10. Passes 11, 12, and 13 should be positioned 2-feet north from the south most wheel load of pass 4. By completing each pass with an individual test vehicle, load combinations of design vehicles can dictate the maximized live-load effects of each girder. It is important that various traffic positions are tested to determine the worst-case scenario.



**Figure 29: Vehicle Load Test Plan**



The tests are designed so that passes 1 through 13 are completed in sequential order with the layout of the passes marked on the bridge. As stated earlier, deflections should be measured throughout the duration of the testing. After the strain data is collected, the values should be used to find stresses. By plotting stress versus time for the girder of interest, one is able to distinguish which load cases created the maximum moment on the girder. The critical vehicle passes must be selected, which forms a maximized load case combination. The combination should be checked to assure that the selected load cases all fit on the clear roadway width with 4-feet in between axles as some passes are overlapped in the vehicle load test plan. Superposition of the applicable load cases will determine the maximum response for each girder.

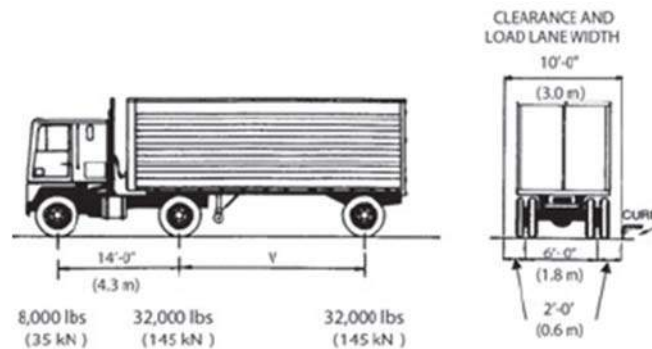
Table 3 gives examples of which vehicle load cases may maximize the live load effects of each girder and should be analyzed.

**Table 3 : Potential Controlling Vehicle Load Combinations**

<b>Girder</b>	<b>Load Combination</b>
South	Pass 3 + Pass 4
South Interior	Pass 3 + Pass 4 Pass 4 + Pass 12 Pass 12 + Pass 13
Middle	Pass 2 + Pass 3 Pass 6 + Pass 7 Pass 8 + Pass 9 Pass 9 + Pass 10 Pass 11 + Pass 12
North Interior	Pass 1 + Pass 2 Pass 5 + Pass 6
North	Pass 1 + Pass 2

#### 4.5.1 Experimental Test Vehicle

The purpose of using an experimental load truck is to accurately measure the bridge's strain responses to known loads using typical highway truck configurations. Typically during field testing, any type of available truck with the appropriate dimensions that can be loaded to the required axle weights may be used. When developing a field tested load rating factor using LFR Specifications, the load testing vehicle used must be analytically equated to an AASHTO approved vehicle. Often this approved vehicle is an HS20 design truck, which is displayed in Figure 30 for reference.



**Figure 30: HS20 AASHTO Approved Design Truck (Jaramilla and Huo, 2005)**

The determination of the DFs is based on the gage distance of the test vehicle, not the longitudinal configuration of the axles. Any load-testing vehicle that has wheel lines that are 6-feet apart can be utilized where the next adjacent vehicle is separated by 4-feet. This configuration creates a lane width of 10-feet used for applying the live load. An experienced bridge engineer should determine the actual weight placed in the testing vehicle, however it should not exceed the operating rating tonnage limit.

## 4.6 Data Collection

The main components of the data collection process are include the FBG sensors and interrogator; their design specifications and data collection process are described in Section 3.3.1. Other important components include the load vehicle, displacement transducers, and laptop computer, the appropriate software, and an external hard drive. During the field tests, the strain measurement data should be stored on the external hard drive for post processing at the University of Wyoming. The FBGs and interrogator are suitable for harsh environments and field testing after enclosing them in the proper weather-proof protection materials.

## 4.7 Data Analysis

Ultimately, the goal of the Laramie River Bridge field testing is to determine the actual DFs. Although Equation 14 determines an approximate DF, it cannot determine girder moments. A more accurate procedure for determining the DF is to place additional sensors as shown in Figure 26 and determine individual girder moments. Procedures by McDaniel and Barker (1998) are employed where the DF is calculated using Equation 15:

$$DF = \frac{M_{GirderMax}}{\left(\frac{\sum M_{AllGirders}}{2}\right)} \quad \text{(Equation 15)}$$

where  $M_{GirderMax}$  is the maximum moment in the girder of interest, and  $\sum M_{AllGirders}$  is the sum of the concurrent moments in the individual girders across the bridge section.

To account for one-lane loaded, to compare to LFD DFs, the sum is divided by 2 because two vehicle wheels lines are applied. If for example, the superimposed load consisted of two vehicles to maximize the girder, the sum should be divided by 4, etc. Additionally, the multiple presence factors should be included. If one- or two-lanes loaded controls, then Equation 14 is

multiplied by 1.0. If three- or more-lanes loaded controls, which is unlikely, Equation 14 is multiplied by 0.9.

Two methods will be described for finding the maximum moment for the bridge girders. The first method assumes full composite action using the transformed section and could be used for a preliminary analysis. The second method is the more accurate and suggested method as it takes into account the partial composite action from field testing.

The first method uses the calculation for the bending moment shown in Equation 16:

$$M_{Girder} = S_{TR} E \epsilon \quad \text{(Equation 16)}$$

where  $E$  is equal to the modulus of elasticity of steel;  $\epsilon$  is the maximum superimposed strain value obtained from field testing.  $S_{TR}$  is the transformed section modulus shown by Equation 17:

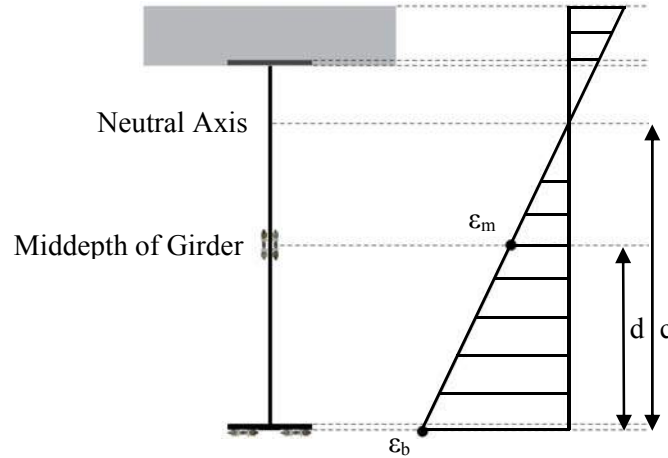
$$S_{TR} = \frac{I_{TR}}{c} \quad \text{(Equation 17)}$$

where  $I_{TR}$  is the transformed analytical moment of inertia of the cross section, and  $c$  is the distance to the neutral axis from the bottom of the bottom flange.

The strain sensor configuration described in Section 4.4.2 allows the location of the neutral axis location to be determined as explained in Equation 18 and displayed in Figure 31.

$$c = \frac{\epsilon_b}{(\epsilon_b - \epsilon_m)} d \quad \text{(Equation 18)}$$

where  $\epsilon_b$  is the strain measured at the bottom of the bottom flange,  $\epsilon_m$  is the strain measured at middepth of the girder, and  $d$  is the distance between the two sets of sensors.



**Figure 31: Strain Profile for Girder with Partially Composite Behavior**

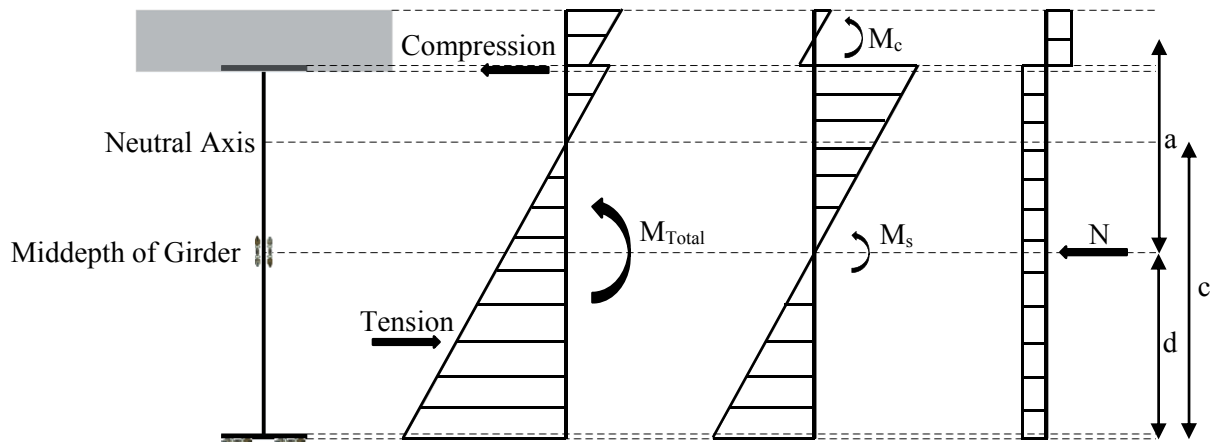
The second method calculates the total moment shown in Equation 19 (McDaniel and Barker, 1998). This calculation is useful because it takes into account the bending moment contributions from the steel girder and the concrete deck. This method accounts for the experimental moment of inertia, including the moment contribution of the concrete slab; yields more accurate DFs; and provides the means to complete a global equilibrium check.

$$M_{GirderTotal} = M_s + M_c + Na \quad \text{(Equation 19)}$$

where the total moment is equal to the sum of  $M_s$ , the steel girder bending about its own neutral axis,  $M_c$ , the concrete area bending about its own neutral axis, and  $Na$ , a function developed to quantify the unintended composite action between the steel and concrete.

This process is demonstrated in Figure 32 where the total stress distribution is shown, and a breakdown of the individual total moment components is displayed. Typically a noncomposite beam would have the neutral axis close to middepth of the girder. Although the Laramie River Bridge was built to perform noncompositely, unintended composite action will occur. This behavior causes the neutral axis location to be higher than middepth of the girder where a larger

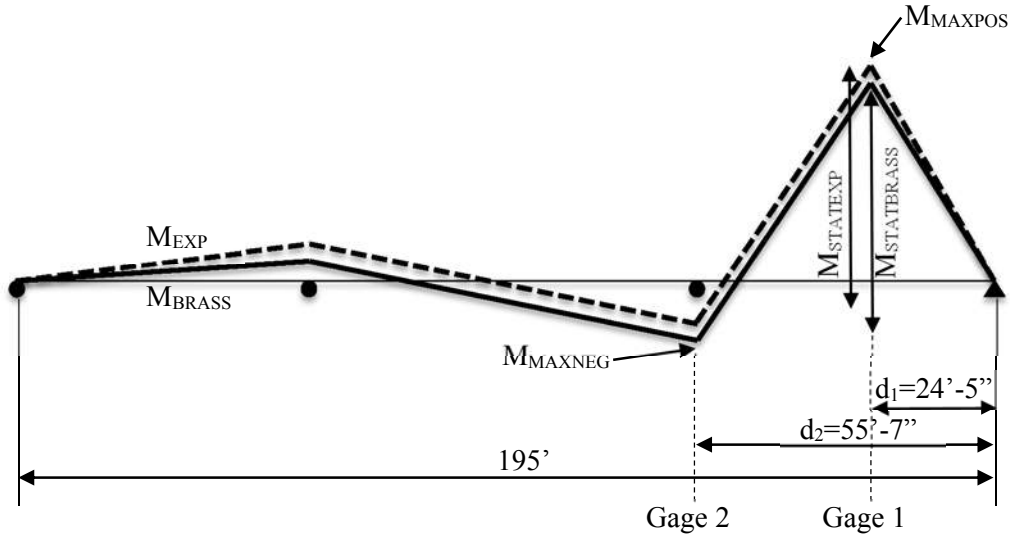
area of the girder is in tension with the concrete area acting in compression. Chapter 2 of *Standardization of Bridge Load Test Procedures* by McDaniel and Barker (1998) presents a detailed procedure for calculating each component.



**Figure 32: Total Moment for Girder with Partially Composite Behavior**

Engineers are able to verify the accuracy of the system by checking that static equilibrium exists, where the sum of the moments in the girders is equal to the applied moment. Comparisons can be made between the experimental statical moments and the analytical statical moments to gain a better overall understanding of a bridge’s true behavior. Often the bridge performs better than the design model.

Figure 33 is an example of the statical moment with the load located for maximum positive moment, the 1.4 location, plotted along the length of the Laramie River Bridge. The solid line represents moment results one might see from the BRASS-Girder file, while the dashed line represents possible experimental results from field testing. The figure also shows a strain gage located near the 1.4 location and another strain gage near the 2.0 location.



**Figure 33: Analytical and Experimental Moments**

The experimental statical moment can be determined by Equation 20:

$$M_{STATEXP} = \frac{d_1}{d_2} \times M^{NEG-GAGE} + M^{POS-GAGE} \quad (\text{Equation 20})$$

where  $d_1$  is equal to the distance to the strain gage located near the 1.4 location, and  $d_2$  is equal to the distance to the strain gage located near the 2.0 location.  $M^{NEG-GAGE}$  is the maximum negative moment measured by strain gage 2, and  $M^{POS-GAGE}$  is the maximum positive moment measured by strain gage 1.

The analytical moment can be determined by Equation 21:

$$M_{STATEXP} = \frac{d_1}{d_2} \times M^{NEG-BRASS} + M^{POS-BRASS} \quad (\text{Equation 21})$$

where  $d_1$  is again equal to the distance to the strain gage located near the 1.4 location, and  $d_2$  is equal to the distance to the strain gage located near the 2.0 location.  $M^{NEG-BRASS}$  is the maximum negative moment from the BRASS-Girder analysis near the 2.0 location, and  $M^{POS-BRASS}$  is the maximum positive moment from the BRASS-Girder analysis near the 1.4 location.

## 4.8 Use of Experimental Lateral Distribution Factor

The purpose of field testing the Laramie River Bridge is to obtain the accurate DFs as input parameters for BRASS-Girder. These input values are controlled by the user under the “Wheel Fractions” control panel, which uses the LFR Standard Specifications for load ratings. There are two options presented in the control panel: one-lane loaded and multiple-lanes loaded. If the input values are left empty, the load rating analysis will be determined automatically using the AASHTO Specification values as described in Section 4.2.3. However, by specifying the field-tested DFs calculated from Equation 15, a more accurate load rating can be determined.

Again, it is important to have the DFs in the correct form because BRASS-Girder uses the values as a wheel fraction. When using Equation 15, one must take note of how many load vehicles create the maximum moment in the girder of interest because it affects the DFs, described in Section 4.7. If the engineer is interested in comparing the experimental DFs with the analytical LRFR factors, the values should be in terms of lanes per girder, and determined by multiplying Equation 15 by 0.5 to account for two wheel lines per lane.

The user should calculate the experimental DFs for one-lane loaded and multiple-lanes loaded to input into BRASS-Girder. A table could be formed comparing the difference between the LFR Specifications versus the experimental DFs, where a percent difference is presented. An example of how this comparison may be arranged is displayed in Table 4 with the highlighted values examples of the BRASS-Girder input values.



**Table 4: Example Comparison Table for Analytical and Experimental Lateral Distribution Factors**

Analysis	Bending Moment	One Lane Loaded		Two Lanes Loaded		Three Lanes Loaded	
		Interior Girder	Exterior Girder	Interior Girder	Exterior Girder	Interior Girder	Exterior Girder
Analytical	Positive and Negative	0.64	0.72	0.82	0.72	0.74	0.65
Experimental (Example)	Positive	<b>0.62</b>	0.58	0.61	<b>0.65</b>	0.59	0.53
	Negative	0.56	0.61	0.63	0.59	0.61	0.50
Percent Difference		14		21			

The experimental DFs for one-lane loaded for BRASS-Girder will be the maximum value from the 1.4 and 2.0 critical locations, including the interior and exterior girders for one-lane loaded. The maximum experimental value will be divided by the maximum LFD analytical value to obtain the percent difference; for this example the difference would be 0.62 divided by 0.72 to obtain a 14% improvement. The experimental DFs for multiple-lanes loaded will be the maximum value from the 1.4 and 2.0 locations, including the interior and exterior girders for two- or more-lanes loaded. Again, the maximum experiment value will be compared to the maximum LFD factor to obtain the percent difference of the DFs; for this example the difference would be 0.65 divided by 0.82 resulting in a 21% increase.

It should be noted that the composite action between the steel girder and concrete deck could also be added into the comparison table in order to quantify the percentage of unintended composite action within the bridge. Since the research team was focused on the DFs, the contribution of the unintended composite action was not included.

#### 4.9 Summary of the Procedure to Determine the Lateral Distribution Factors

First, a strain sensor instrumentation plan was developed, in which two sensors are placed on the bottom flange and two at middepth of the web. Next, a vehicle load testing plan was developed to maximize the load effects on each girder by passing a loaded vehicle over

designated routes. One can use a stress versus time graph for each girder to decipher which vehicle passes caused the maximized stress to develop a load combination. The strain data from the critical load combination of the girder of interest should be superimposed for each girder during the respective vehicle passes to determine the maximum and concurrent responses for interior and exterior girders.

After field testing occurs, the data must be analyzed. The first step is to develop the strain profiles of the girders to determine the location of the neutral axis. The total girder moments will be calculated for each girder at the two critical locations to determine the DFs. Static equilibrium should be checked to assure that the system is performing as expected and that the data is accurate and repeatable. The calculated DFs will need adjustment depending on the number of vehicles accounted for in the critical load combinations.

Finally, a comparison should be made to the analytical LFR values in order to identify the improved DFs. If one would like to compare the DFs to the analytical LRFR factors, the factors would need to be multiplied by 0.5 to account for the wheel fraction conversion. The maximum DF for one-lane loaded, including the 1.4 location, 2.0 location, interior girders, and exterior girders, should be entered into the BRASS-Girder input panel. Additionally, the maximum factor for multiple-lanes loaded, including the 1.4 location, 2.0 location, interior girders, and exterior girders, should be recorded as the other input value. Entering the experimental DFs could result in improved load ratings for various truck configurations using LFD Specifications.

## CHAPTER 5: RFID TRIGGERING DEVELOPMENT

### 5.1 Objective

The objective of testing the proof of concept for an RFID triggering system was to successfully use an RFID reader to detect the presence of an RFID tag in an approaching vehicle and then signal the FBG interrogator to store strain data for an allotted time period. The field tests focused solely on event triggering, data collection, and data storage. However, the entire process, including data transmission, is explained in this chapter for future development purposes. When further developed, the data collected from the system could potentially be used to better understand in-service bridge behavior, refine bridge design and rating methods, and yield safer and more efficient transportation for the public. James Branscomb, an electrical engineer, participated in the development of this system. This chapter includes the purpose of developing the RFID system, the RFID systematic description, the instrumentation design, and the validation procedures and results for the proof of concept field tests.

### 5.2 Purpose

One challenge with managing a continuous, long-term bridge monitoring system is collecting, storing, and prioritizing the copious amounts of bridge response data. The RFID triggering system was developed as a method to prioritize the collection and storage of data by triggering the system with a predetermined and recognizable vehicle. The triggering is important because storing continuous strain data can result in an unmanageable amount of information to be stored or to be passed through a cellular modem. The outcome of the system would provide the means to collect and store only the meaningful FBG strain data.

### 5.3 RFID Systematic Description

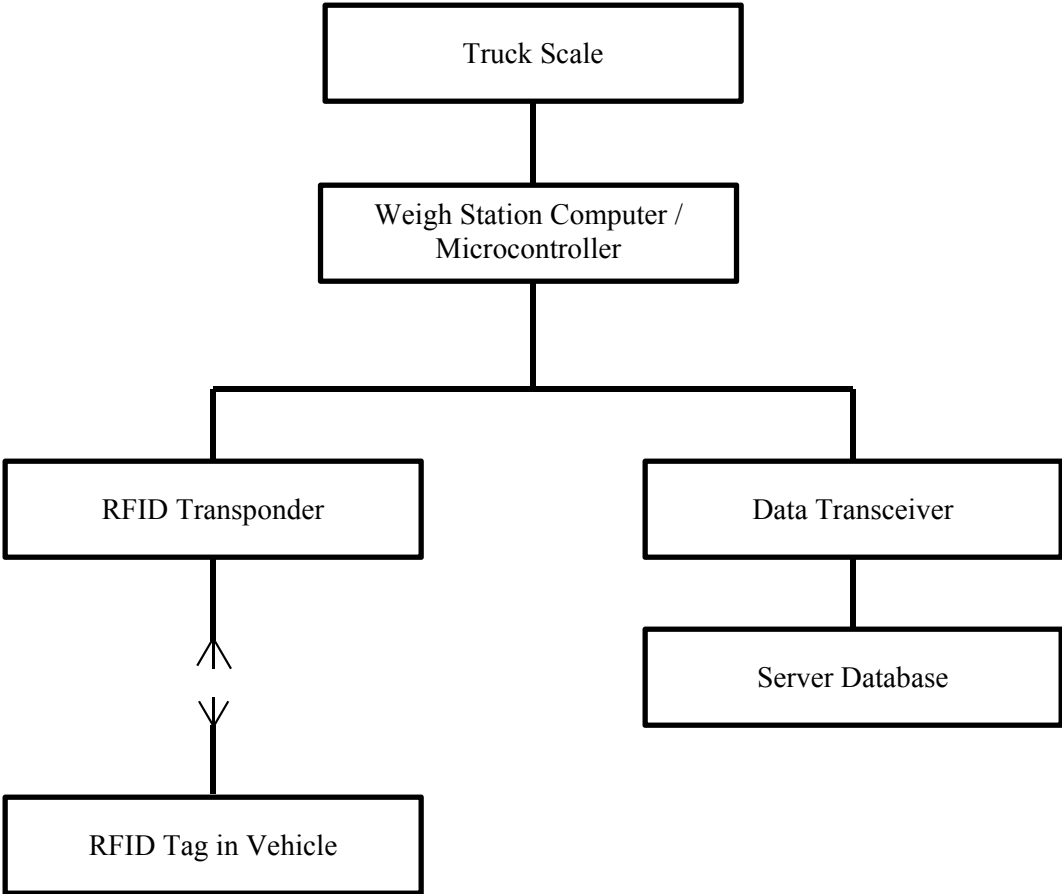
The RFID system operates by transferring information using radio-frequency electromagnetic fields, utilizing a transponder that wirelessly transmits data to and from the tags. In this specific application, an RFID reader and antenna combination, or transponder, will be installed at a weigh station at a Wyoming port of entry and at the bridge of interest. At the port of entry, the permitted truck information, including the axle weights and configuration, will be assigned to an RFID tag with an identification code. The tag would then be placed on the windshield of the vehicle. At the bridge, a different transponder will detect the presence of the RFID tag and will trigger the data acquisition system to store the bridge strain data while the permitted vehicle passes over the bridge. The following subsections describe the process in detail.

#### 5.3.1 Port of Entry

The first transponder should be placed at a Wyoming port of entry. Along with detecting the presence of a tag, the transponder has the capabilities of writing specific information to a tag, enabling a transponder to read the data from the tag at a different point in time. To incorporate this system into the previously discussed instrumented Laramie River Bridge, it is advised that the transponder be placed at the Cheyenne I-80 Port of Entry. This port of entry has a high volume of traffic, is a gateway for a primary trucking route through Wyoming, and has vehicles travelling west on I-80 that will typically pass over the Laramie River Bridge.

All permitted vehicles are required to stop at the ports of entry when crossing over the state line to assure that they remain in compliance with their specified axle loads and gross vehicle weight requirements. When a permitted vehicle is weighed, it will be assigned a tag encoded with a vehicle identification number. At the weigh station, the axle weights, gross

vehicle weight, and axle configuration will be determined. This information can then be entered into a database and associated with its assigned vehicle identification number. The vehicle will then travel across the highway with the tag in the vehicle. Figure 34 is a block diagram of the instrumentation at the weigh station.

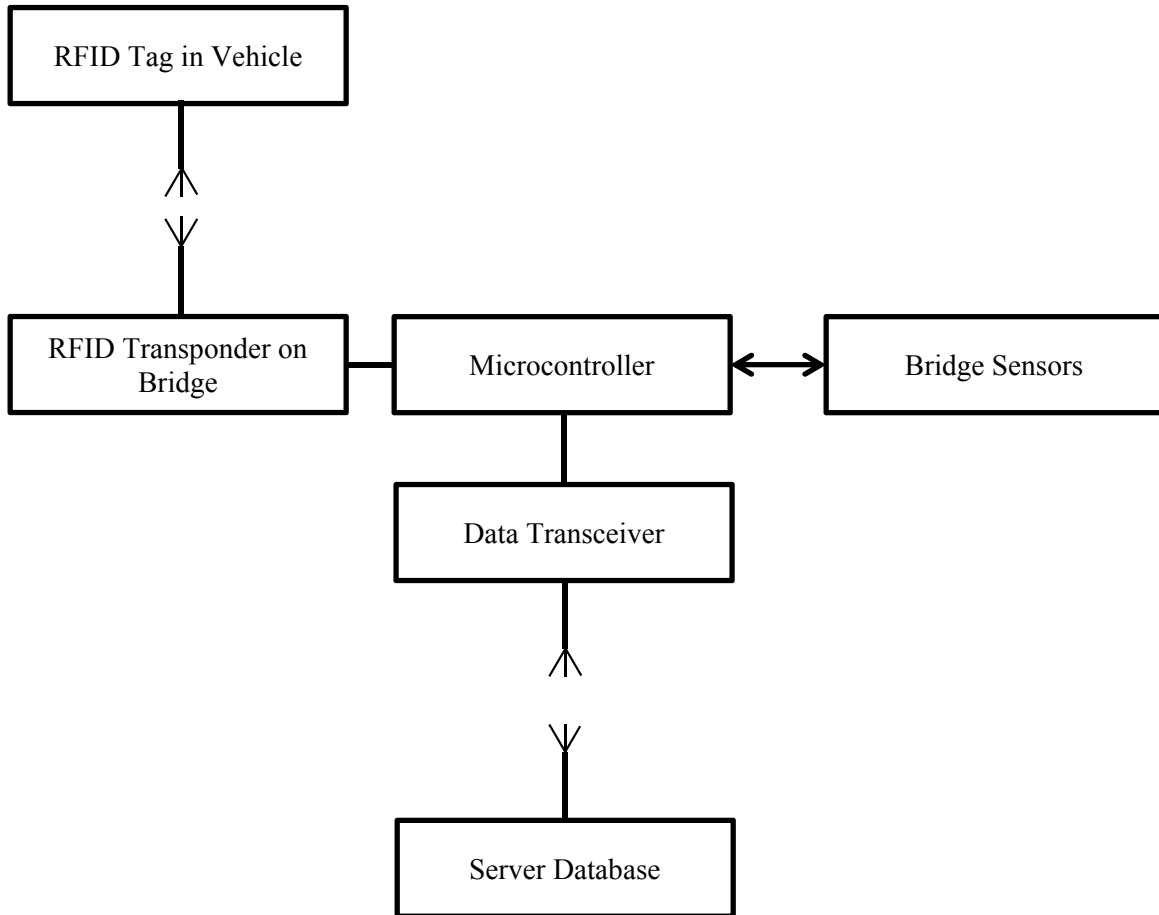


**Figure 34: Block Diagram of Instrumentation at Weigh Station (Jung, 2015)**

5.3.2 Triggering

When a tagged vehicle approaches an instrumented bridge and the tag is within range of the transponder, the transponder will send a signal to the data acquisition unit on the bridge to activate the data storage. The transponder will read the vehicle identification number written on

the tag and send its information and the bridge's response to a database (Jung, 2015). Figure 35 is a block diagram of the instrumentation at the bridge.



**Figure 35: Block Diagram of Instrumentation at Bridge (Jung, 2015)**

### 5.3.3 Data Collection

The FBG interrogator will be powered on and will interrogate its FBG sensors continuously. Once an RFID tag has been identified, the transponder will send a signal to the data acquisition unit to begin data storage and transmission to the server. The data system will collect and record data for an allotted time period. This system will provide controlled data collection because it is triggered by the presence of a tag in a permitted vehicle. It will also limit the amount of data to analyze because only data from permitted vehicles crossing the bridge will

be collected. As the system develops, additional triggering features may be considered, for example when a certain strain threshold is reached.

#### 5.3.4 Data Storage

The data collected from the interrogator will be stored on an external hard drive. The extent of required storage space will depend on the duration over which data for a vehicle is recorded, the number of sensors on the bridge, the sensor scan rate, and the frequency of triggered traffic events. Initially, for the lateral distribution factor field testing of the Laramie River Bridge, 5-megabytes of storage capacity should be available to store strain data from 13 vehicle passes plus extra storage in the event of additional tests ensuing. As the RFID development continues, the storage must be sufficient to store strain measurement data until cellular data transmission is established.

#### 5.3.5 Data Transmission

Data transmission will be implemented by means of a cellular module. The FBG strain measurements will be temporarily stored on an external hard drive, and then after the triggered event occurs, the database would receive the bridge response data. To provide a secure connection, Verizon Wireless recommended the Feeney Wireless Skyus and the Option Cloudgate as suitable options.

#### 5.3.6 Data Post Processing

The data will be transmitted through the cellular network to the database. The RFID identification number assigned to the permitted vehicle at the weigh station with the axle loads and configuration will correlate with the same identification number recorded at the bridge site with the bridge response data. This would form a single case that contains the vehicle

identification number, vehicle axle weights, vehicle gross weight, vehicle axle configuration, the time the vehicle passed over the bridge of interest, and the bridge strain measurement data. The vehicle load effects can then be associated with the measured structural response data obtained from the FBGs.

The database will work in conjunction with software to provide limited access to the combined vehicle and bridge information. Individuals, such as WYDOT bridge engineers, will be able to log into the database to view the most recent bridge activity. This software will allow the bridge owner to perform the necessary analysis procedures, whether they be load rating procedures, permitted vehicle hysteresis, or long term monitoring to determine changes in bridge behavior.

#### 5.4 Instrumentation Design (Branscomb, 2015)

The instrumentation design was developed in collaboration with an electrical engineer, James Branscomb. Field instrumentation necessary for the discrimination of bridge strain data based on identified permitted vehicles primarily relies upon a robust FBG sensor interrogator, Ethernet controller, data processing microcontroller, data storage module, cellular transmission module, reliable power source, RFID transponder, and RFID tags. The FBG interrogator purchased for the research was the FS2200 extended temperature BraggMETER by FiberSensing because of its programming capabilities, Ethernet interface, and ability to handle harsh environments. The interrogator is 11 ¼-inches by 8 ½-inches by 3 ¾-inches, displayed in Figure 36.





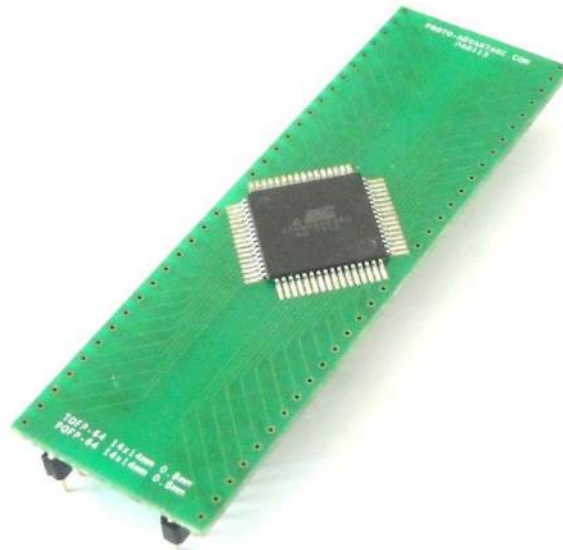
**Figure 36: Exterior Top View (left) and Interior View with FBG Inputs (right) of Interrogator**

Two Olimex mod-enc624J600 boards create the Ethernet to the serial peripheral interface (SPI) data link from the interrogator and cellular network to the microcontroller. The boards' main components are Microchip's enc624J600 10/100 Base-T Ethernet controllers, shown in Figure 37.



**Figure 37: Olimex Ethernet Controller (Branscomb, 2015)**

By using the Ethernet controller to form the SPI connection, the Atmel ATxmega64a3 microcontroller is able to receive continuous strain data from the FBG interrogator. The microcontroller, seen in Figure 38, allows the user to define which parameters will trigger the data storage of field measurements. As of now, the detection of an RFID tag is the trigger for storing the field test data.

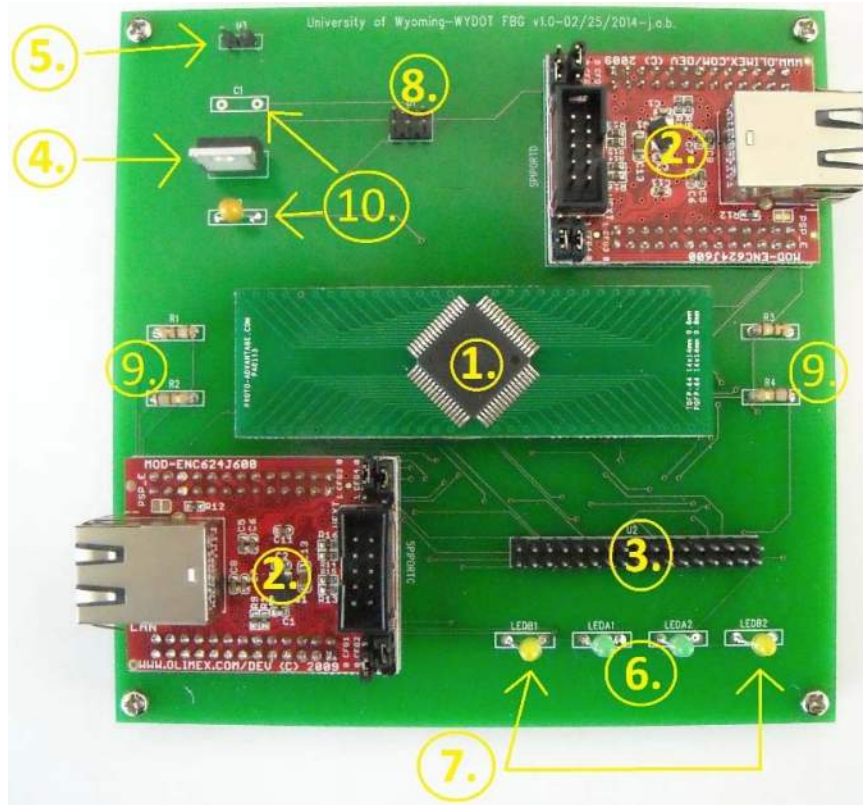


**Figure 38: Top View of the Microcontroller Mounted onto an Adapter (Branscomb, 2015)**

As previously mentioned, two cellular modules, as advised by Verizon Wireless, are being explored. A second Ethernet controller will be used to link the microcontroller and the cellular module. The purpose of the controller is to convert SPI signals back to Ethernet so that the field strain data can be directed through the cellular network.

The current system development can be seen in Figure 39. The printed circuit board (PCB) consists of the two Ethernet controllers, microcontroller, programming port, voltage supply and regulator, LED indicators, and general purpose input/output (GPIO) pins to be used

for future programming. Following the figure is the detailed component information. A complete circuit board schematic is located in Appendix D.

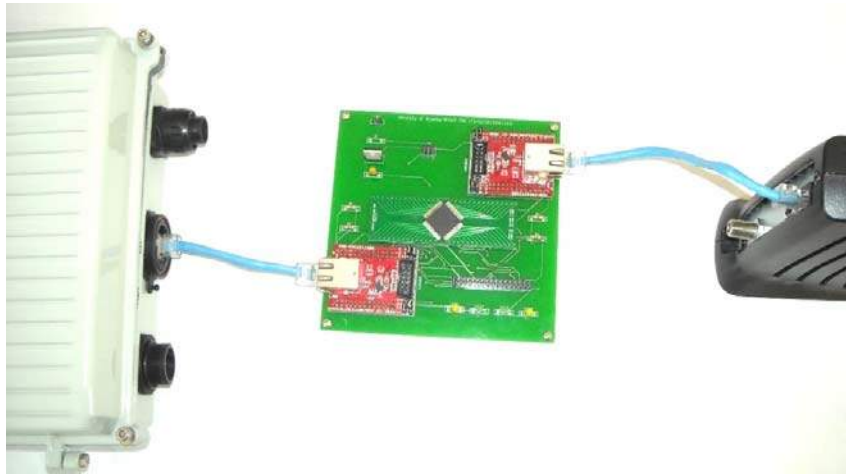


**Figure 39: Printed Circuit Board used to Control System Components (Branscomb, 2015)**

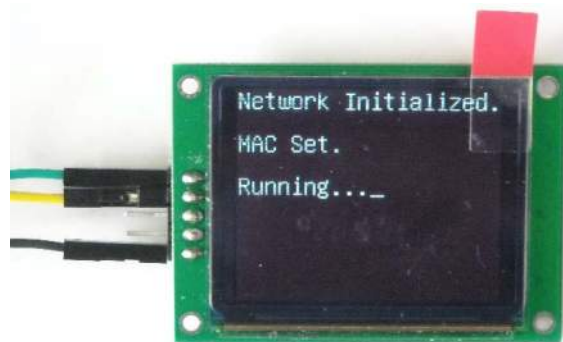
The PCB contains the following components:

- 1) Atmel Atmega64a3 microcontroller
- 2) Olimex mod-enc624J600 Ethernet controllers
- 3) General purpose input/output (GPIO) pins/UART/SPI/VCC/GND for future device implementation
- 4) LM1085it-3.3v fixed voltage regulator (27V maximum input-to-output differential)
- 5) Voltage Supply
- 6) LED Ethernet link status indicators for the two Ethernet controllers (programmable)
- 7) LED Ethernet activity indicators for the two Ethernet controllers (programmable)
- 8) PDI programming port for the Atmega64a3 microcontroller
- 9) 180Ω current-limiting resistors for LED Ethernet indicators
- 10) 10uF Bypass capacitors (capacitors not shown, but will be incorporated in the future)

An example of the connection between the interrogator, PCB, and wireless Ethernet network can be seen in Figure 40 using the Ethernet ports for passing data. Also, an LED screen was installed for debugging purposes, shown in Figure 41.

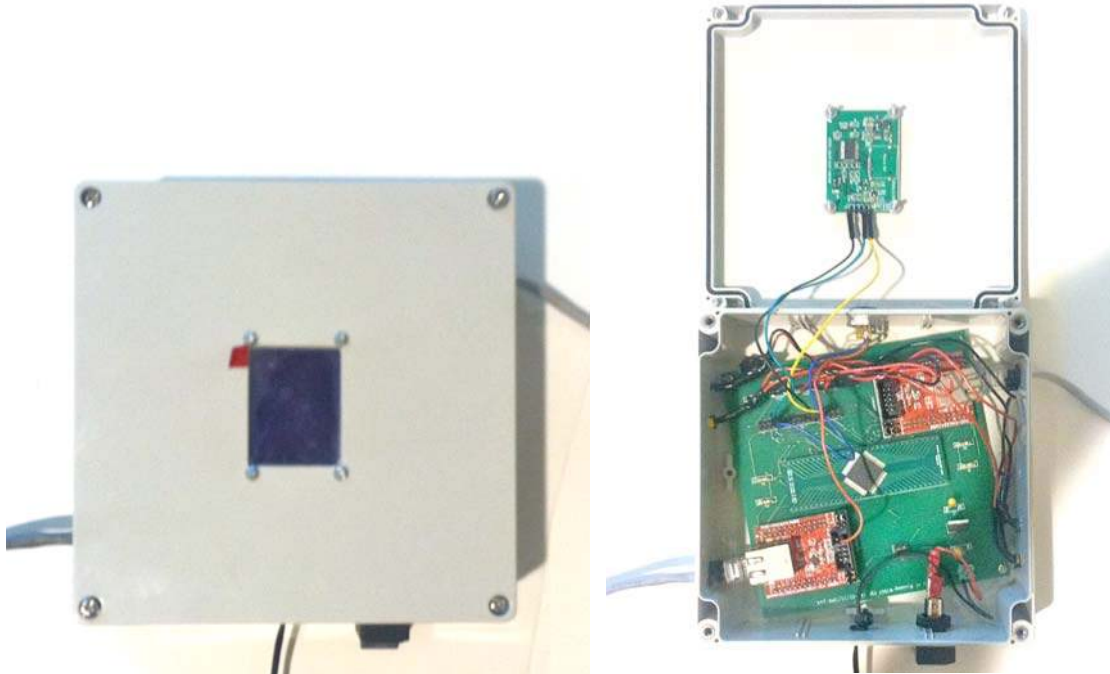


**Figure 40: Data Passing Between the Interrogator, PCB, and Ethernet Network (Branscomb, 2015)**



**Figure 41: LED Screen Displaying the System Running (Branscomb, 2015)**

The protection box that houses the PCB and LED screen is displayed in Figure 42. The unit is 6 ¼-inches by 6 ¼-inches by 2 ½-inches. For field implementation, the weatherproof enclosure will require a larger box for protection of all the instrumentation components, including the interrogator.



**Figure 42: Exterior Top (left) and Interior View (right) of PCB and LED Screen in Enclosure**

Not pictured is a solar panel along with minimal batteries that will be used as the primary power source. Solar panels would be effective for the RFID system for a few reasons. Bridges in Wyoming are often located in remote areas, so access to power supply is limited. The Wyoming weather conditions often provide enough sunlight to power various electronic devices, for example the variable speed limit signs use this technology. Also, solar panels are economically feasible and are practical to install.

The RFID system that triggers the microcontroller consists of three main physical components: an RFID reader, antenna, and tags.

The CS203ETHER Integrated RFID reader both reads and writes information to the tags and transmits data. It is designed to withstand extreme weather conditions, including water and dust, with a high read rate. The RFID antenna communicates with the tags using radio frequency

signals. The antenna has a range of approximately 30-feet, however it can be coupled with an additional IP67 antenna for extended radio frequency range. The reader and antenna have thus far been referred to as the transponder, as they are physically enclosed in one unit that can be powered through an Ethernet connection. The unit is 1-foot by 1-foot by 3-inches.

The CS6710 Windshield RFID tags are each assigned a unique identification number, and they can store data transmitted from one transponder that can be read by another transponder at a different location. The tags are designed to be coupled with the CS203 integrated reader and placed on the inside of cars, buses, and trucks. The tags are passive, meaning that they do not require batteries in order to communicate with the reader and antenna and are more economical than active tags that need batteries. The tag is approximately 2 ½-inches tall by 4 ½-inches wide.

## 5.5 RFID Triggering Validation Procedure and Results

The proof of concept field tests for the triggering mechanism validated the performance of the RFID system components. The validation procedure was considered successful when the RFID transponder recognized the presence of the RFID tag in an approaching vehicle, recorded the tag identification number, and triggered the storage of FBG strain data for a predetermined amount of time. This procedure was designed to test the system for a possible deployment project, so the focus was to demonstrate the capabilities of the triggering mechanism to provide a basis for future work.

Two modes were developed for the system: software and hardware. The software mode required use of a Dell laptop computer in order to command the microcontroller to store strain sensor data. This mode was utilized for field tests. Having a laptop in the field is not ideal, because it cannot handle extreme weather conditions, requires additional space in a weatherproof



enclosure, and calls for an increase in power supply. The hardware mode was created to prevent this scenario, and if the hardware mode is used, the laptop is not needed in the field. The hardware mode was under development at the time of testing; therefore, the software mode was used for field tests. The hardware mode has since been systematically validated, and it will be functional for field tests in the future.

#### 5.5.1 Proof of Concept Test Setup

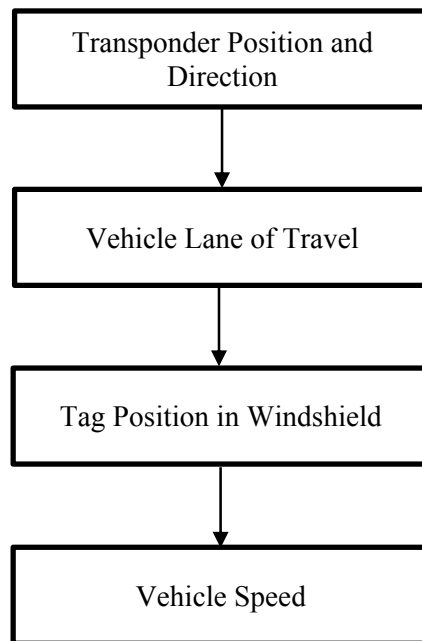
The RFID triggering tests were located between Timber Canyon Road and Domino Road on Highway 17, or Roger Canyon Road, located north of Laramie. The section of highway is straight with low traffic volume. The equipment was powered by means of a vehicle using a power convertor and an extension cord. The location is displayed in Figure 43.



**Figure 43: Testing Location on Highway 17 with the West (left) and East (right) Views**

Highway 17 has two lanes that are each 11-feet wide, unlike interstate lanes that are typically 12-feet wide. The distance from the edge of the lane to the transponder was 6-feet, and the distance from the ground to the bottom of the transponder was also 6-feet. The transponder was on the south side of the highway facing west. The RFID tag that was placed in the car was 5-feet above the ground.

The tests were organized so that the initial positioning of each RFID component was established prior to testing the system at full speed, including the position and direction of the RFID transponder, RFID vehicle, and RFID tag. A schematic of this process is displayed in Figure 44. For all tests, the vehicle was driven in the east direction toward the transponder. It should be noted that each time the transponder detected the tag, the FBG strain data from three sensors were recorded for the allotted 30-second time frame.



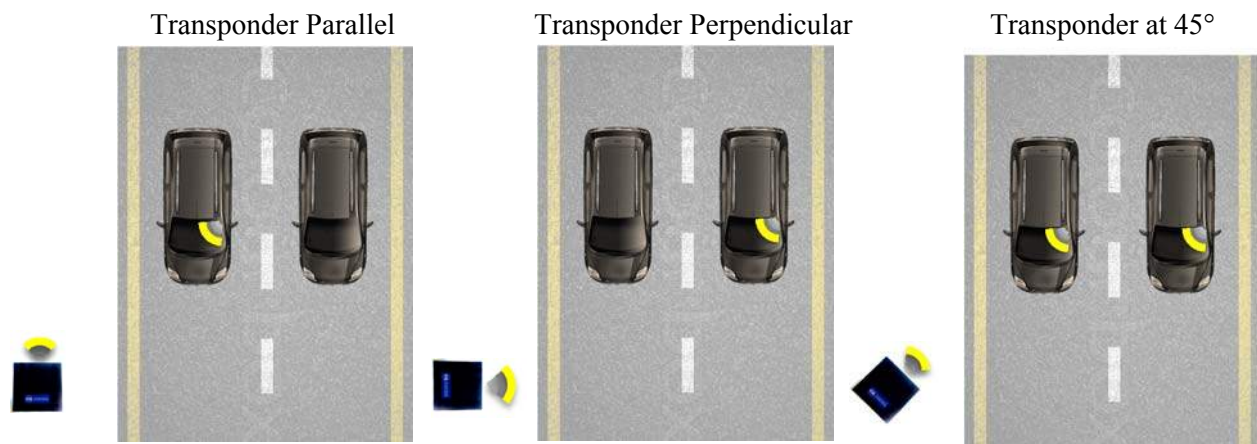
**Figure 44: Schematic Diagram of RFID Triggering Tests**



### 5.5.2 RFID Transponder Position and Direction

The horizontal direction to which the transponder would detect the tag most effectively was determined by three different arrangements. The tag was placed in the upper left-hand corner of the windshield, and the vehicle travelled at 65-MPH.

First, the transponder was faced parallel to the oncoming vehicle, or straight toward the tag. This method was successful when the vehicle travelled in the closest lane, however the transponder did not detect the tag when the vehicle was in the farther lane. Second, the transponder was directed perpendicular to the road. This angle was effective for the vehicle in the farthest lane, however it did not trigger when the vehicle was in the closest lane. Third, the transponder faced the northwest direction at a 45-degree angle. When the vehicle was located in the closest and farthest lanes, the transponder identified the tag and triggered the data to be saved onto a file. The three cases are displayed in Figure 45.



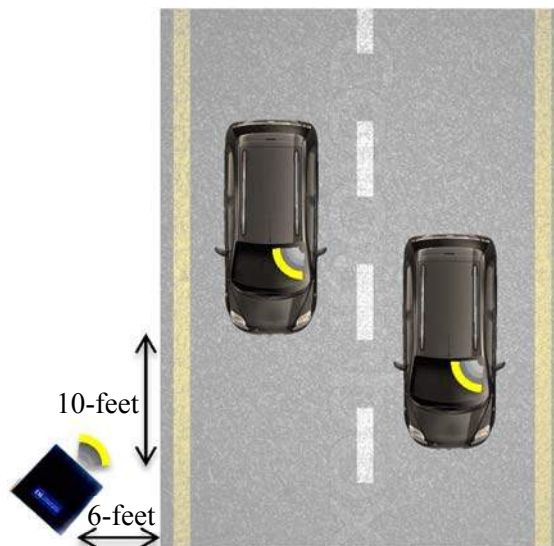
**Figure 45: Direction of RFID Transponder to Trigger Data Storage**

The position of the transponder from the ground also varied throughout testing. It was determined that the system was triggered occasionally at a height of 5-feet, consistently at 6-feet, and rarely at 7-feet. Clearly, this distance will alter depending on the height of the tag target for

permitted vehicles in future testing. Additionally, the transponder was initially located at a distance of 8-feet from the edge of the lane, however the distance was decreased to 6-feet for reliable triggering. The vertical angle that the transponder was directed was not tested because it is a feature that should be considered based upon the setup of the system in the future.

### 5.5.3 RFID Vehicle Lane Position

The range from the transponder to the tag was identified, shown in Figure 46. Similar to the previous tests, the tag was placed in the upper left-hand corner of the vehicle windshield. The transponder was directed at a 45-degree angle northwest. The vehicle was located in the lane closest to the transponder and travelled at a speed of 10-MPH. The transponder detected the presence of the tag when the vehicle was approximately 10-feet from the reader, measuring parallel on the road. The vehicle then travelled in the farthest lane, again headed east. With the tag farther away, the transponder detected the tag when the vehicle was in line with the reader, or at zero feet parallel on the road.



**Figure 46: Positioning of RFID Vehicle to Trigger Data Storage**

#### 5.5.4 RFID Tag Position in Windshield

The tags were designed to be placed on the inside of a vehicle's windshield. For the field tests, the tag was initially placed on the upper left-hand corner of the windshield. The vehicle was driven at 65-MPH in the closest lane, and the transponder detected the tag six out of six times consecutively. The vehicle was then driven in the farthest lane with the same tag positioning, and the tag was identified in two out of four runs. As a result, an additional tag was added to the upper right-hand corner of the vehicle. The transponder then detected the tag two out of two times while the vehicle was in the farthest lane. This test suggests that the maximum perpendicular distance for consistent triggering is approximately 18-feet, and inconsistent triggering occurs at a distance of 28-feet for a system using one antenna.

#### 5.5.5 Triggering at Full Speed

To trigger the system to record strain measurement data, the full vehicle speed was set at 65-MPH. While most interstates in Wyoming have a speed limit of 75-MPH, it is predicted that most overweight or non-standard configuration permitted vehicles will not be travelling at that rate for safety precautions. Nevertheless, the triggering was briefly tested for the vehicle travelling at 70, 75, and 80-MPH as well.

Up to this point, the positions of the transponder, vehicle, and tag were established, and the outcome of the three tested parameters had to be confirmed. The transponder was angled at 45-degrees facing the northwest direction; the vehicle was located in the farthest lane to test the worst-case scenario for vehicle placement; and the tag was placed in the upper right-hand corner of the windshield. The vehicle was driven at 65-MPH, and the transponder recognized the tag, triggering the data saving system six out of six times. These tests were sufficient to determine that the RFID triggering system functioned as intended.

Additional tests were completed with the same parameters except with varying speeds. The vehicle was driven at 70-MPH, and the transponder did not trigger the system the first time but did the second time. The vehicle was then driven at 75-MPH, and the transponder again did not recognize the tag the first time but did recognize it the second time. Lastly, the vehicle was driven at 80-MPH, and the transponder did not trigger for either of the two tests.

#### 5.5.6 Data Collection and Storage

After the vehicle event was triggered, the FBG strain measurement data automatically saved to a file onto the computer hard drive. The file included the wavelength readings, tag identification number, date, and time, respectively. A portion of a data file from one field test is included in Appendix E, where one full second of wavelength data is labeled as “:TS:1”, and includes approximately 100 wavelength readings per second for each of the three sensors. The entire file contains wavelength data through “:TS:30:” or 30 seconds of recorded data.

The wavelength readings were recorded from three of the four available interrogator channels, where one FBG was located on each channel. The sensors were not the focus of the field tests nor were they adhered to a host material affected by traffic events, so the readings fluctuated only slightly due to noise and marginal temperature variations. As stated in Chapter 3, each channel has the ability to be multiplexed with 20 FBG sensors when spliced onto the same optical line. The channels were labeled as “CH0”, “CH1”, and “CH2” in the document output. The tag identification number was recorded after “EPC:”. The date was ordered by year, month, and day with the time of day defined in standard time.

For a deployment project in the future, the data transmission and post processing techniques would ensue as described in Section 5.3.5 and Section 5.3.6.

## CHAPTER 6: CONCLUSIONS AND FUTURE RECOMMENDATIONS

### 6.1 Research Summary and Conclusions

A rise in the energy sector has resulted in a greater number of trucks travelling with overweight loads or non-standard vehicle configurations. State bridge managers are responsible for assuring safe and efficient routes for these permitted vehicle loads over bridges. As a result, bridge engineers are developing methods to quantify the actual capacities of in-service bridges, which are generally higher than the analytical analysis indicates. A field tested bridge analysis can lead to improved load ratings or the removal of bridge postings, allowing permitted vehicles to travel through the state safely without costly detours.

The University of Wyoming worked with WYDOT to develop the research objectives:

- 1) Verify the performance of Fiber Bragg Grating sensors
- 2) Develop a plan to determine the lateral distribution factors for the Laramie River Bridge
- 3) Validate a proof of concept for an RFID triggering system

The research objectives were achieved. For each objective, this section provides a brief summary, including the test purpose, procedures, and results, followed by a conclusion.

#### 6.1.1 Fiber Bragg Grating Sensor Verification

Fiber Bragg Gratings have been used in various fields for decades; more recently, they have been introduced into the structural engineering field. FBGs are more commonly replacing TGs for field testing bridges. Appendix A, Section A.2.3, describes cases where FBGs have been proven to be more robust, outlasting TGs in a number of applications while performing to the same standard. Regardless, some engineers are skeptical of replacing the TGs. To reestablish

confidence in the performance of FBGs and to understand and describe the installation process for future possible deployment, the University of Wyoming used TGs to verify FBGs.

The FBGs and TGs were installed on an S3x5.7 steel beam. There were six of each type of sensor, where one FBG and one TG were located in six different locations on the beam. The beam was loaded by a hydraulic actuator to a predetermined load, held for 30-seconds, and then unloaded back to zero load.

The averaged results from each FBG and TG set at the various locations were compared for the six tests. Additionally, a graph with the FBG results from test 2 was described because the FBGs exhibited unusual strain behavior in that particular test. The moduli of elasticity values were used for comparison because the averaged results were linear, so one slope value accurately represented the data set.

Set 1 had an FBG and TG located at the extreme compression fiber. At this location, the TG results were 11.3% higher than the FBG results. Set 2 was located on the underside of the top flanges with FBG results 14.8% higher than the TG results. Sets 3 and 4 were installed on the web of the beam on the same side at a 45-degree angle to record shear strain results. Set 3 FBG results were 8.8% higher than TG results while set 4 showed FBG results 14.2% higher. Set 5 was located on the top of the bottom flanges and the FBG results were 20.3% higher than TG results. Lastly, set 6 was mounted on the bottom of the bottom flange; the FBG resulted in an average of 2% higher than the TG results.

The FBG results based upon the six tests were within a reasonable range of the TG results. Set 5 is an exception that displayed unusual results, possibly due to an epoxy bond failure. Many assumptions were made for the verification tests that could explain the strain

measurement discrepancies. Assumptions include a perfectly flat, sanded, and clean surface; flawless sensor application, resulting in a perfect bond; reliable foil gage measurements; exact angle alignment of sensors at 45-degrees and sensors parallel to each other; the beam stays within its elastic range; and that a difference in strain due to the distance between sensor sets is negligible. Although the assumptions represent ideal testing conditions, this is rarely the case.

Given the assumptions of the tests and additional test properties, the results are within a reasonable range. Typically, when comparing strain gages on the market to foil gages through laboratory testing, strain results within 5% are a reasonable expectation. Set 6 displayed this comparison with a 2% difference. However, based upon the assumptions and additional test properties, results within 15% are realistic. The possible factors contributing to strain discrepancies, including the various test properties, are described in detail in Section 3.4.

Objective 1 was successful as the FBG sensors were verified by comparison to the TGs. Additionally, the FBG installation procedures were completed, understood, and documented for possible future use on a deployment project. The sensors can be applied with confidence for field tests on a bridge.

#### 6.1.2 Lateral Distribution Factor

Plans were developed for field instrumentation and testing of the Laramie River Bridge on I-80 to provide engineers with a tool to determine the field tested DFs. The determined factors could replace the more conservative AASHTO DFs when defined in BRASS-Girder. Using field-measured values, engineers could calculate a potentially higher and more accurate load rating. To determine more accurate DFs, there were four main focuses of the research: strain

sensor placement plan for girders, vehicle load test design, data analysis to determine the DFs, and use of DFs in the BRASS-Girder program.

The sensor placement plan was developed based upon methodology established by McDaniel and Barker (1998) then modified for optimization for the Laramie River Bridge. The cross-section sensor placement plan includes two sensor readings located on the underside of the bottom flange and two sensors located on the web. The two sensors at each location should be averaged to provide redundancy and to remove the effects of weak axis bending and torsion. Two different sensor locations allow a strain profile to be developed, providing the data necessary to determine the neutral axis location. Additionally, the sensors should be placed at the critical longitudinal sections, which are near the 1.4 and 2.0 longitudinal locations of the Laramie River Bridge.

The vehicle loading plan was created to maximize the live load effects of each girder to identify the critical case for the DF analysis. Thirteen vehicle passes and potential controlling vehicle load combinations were suggested. As long as the bridge is performing within its elastic range, the values from the controlling load combinations can be superimposed to determine the maximum strain response for each girder. Additionally, the experimental test vehicle is required to have a gage distance of 6-feet with the next adjacent vehicle separated by 4-feet, however the longitudinal configuration of the axles is not a vital consideration as it does not contribute to the DF analysis.

The data analysis to determine the DFs is presented by three different equations and is based upon the desired accuracy of the system results. Approximate DFs can be determined by Equation 14 and Equation 16. More accurate DFs can be calculated by Equation 19, and this



method is the recommended approach as it provides the means to verify the accuracy of the system by completing a global equilibrium check.

To use the determined DFs factors as BRASS-Girder input values, the worst-case DFs have to be determined for both one-lane loaded and multiple-lanes loaded. The experimental DFs for one-lane loaded used by BRASS-Girder will be the maximum value from the positive and negative critical locations, including the interior and exterior girders for one-lane loaded. The experimental DFs for multiple-lanes loaded will be the maximum value from the positive and negative locations, including the interior and exterior girders for two- or more-lanes loaded. The load ratings can then be determined using BRASS-Girder and the field tested DFs.

Objective 2 was considered successful. The aforementioned test designs and methods are sufficient to determine the field tested DFs for the Laramie River Bridge. The process of defining the DFs in BRASS-Girder is described in detail in Section 4.8 to potentially improve load ratings.

### 6.1.3 RFID Triggering Development

The purpose of the work completed at the University of Wyoming was to validate a proof of concept of the RFID triggering system for data collection and data storage capabilities. The research was focused on permitted vehicles. Additionally, the system is designed to correlate known vehicle data with the measured response of a bridge. The work focused on the RFID systematic description, the validation procedure, and the validation results for the proof of concept field tests.

The RFID system utilizes a transponder that wirelessly transmits data to and from the RFID tags. RFID transponders will be installed at a weigh station at a Wyoming port of entry and at the bridge of interest. At the port of entry, the permitted truck information, including the axle weights and configuration, will be assigned to an RFID tag with an identification code that would be placed on the windshield of the vehicle. Another transponder placed near the bridge will detect the presence of the RFID tag and trigger the system to store the bridge strain data when the tagged permitted vehicle passes over the bridge.

James Branscomb assisted in developing the instrumentation for the RFID triggering system. For the proof of concept testing, the triggering mechanism, data collection, and data storage were the specific parameters tested.

The proof of concept tests took place on Highway 17, Roger Canyon Road, north of Laramie. The tests were organized so that the initial positioning of each RFID component was established prior to testing the system at full speed, including positioning of the RFID transponder, RFID tag, and RFID vehicle. For all tests, the vehicle was driven in the east direction toward the transponder. Each time the transponder detected the tag, the FBG strain data from three sensors were continuously recorded for the allotted 30-second time frame.

After the ideal placements were determined for the vehicle, transponder, and tag, the proof of concept tests were conducted. The vehicle was located in the farthest lane to test the worst-case scenario for vehicle placement; the transponder was angled at 45-degrees facing the northwest direction; and the tag was placed in the upper right-hand corner of the vehicle windshield. The vehicle was driven at a constant speed of 65 MPH. When the transponder

detected the presence of the tag, the system triggered the data to save on the hard drive six out of six times.

Objective 3 was successful as the proof of concept for the RFID triggering system was validated. It was determined that the success of the triggering is dependent upon the position of the tagged vehicle; the transponder, including the height and horizontal position; and the tag location in the vehicle. The proof of concept tests provided admissible results that were sufficient to move on to the next phase of instrumentation design and testing.

## 6.2 Future Recommendations

Each of the research objectives involves multiple materials and methods of evaluation that are at different stages of development. The details of the future work for each objective reflects those current stages.

### 6.2.1 Fiber Bragg Grating Sensor Verification

The durability of Fiber Bragg Gratings has been validated by their sustained performance in laboratory experiments and field tests. Special attention should be taken when purchasing FBGs. Knowledge about existing technologies and manufacturers will help to assure accurate, consistent, and reliable strain sensor results.

### 6.2.2 Lateral Distribution Factor

Future work should be performed before, during, and after determining the DFs. Before the field tests takes place, the following factors should be considered:

- Sensor installation equipment
- Temperature compensating FBGs
- Displacement transducers
- Paint removal on girders for sensor installation
- Weather-proof enclosure
- Power-source details
- Available load vehicles
- Vehicle passes marked on bridges
- Closure of bridge for field tests

An additional task that could be completed before testing takes place is to perform a more rigorous analysis of the Laramie River Bridge using a grillage model. As opposed to the girder-line analysis performed by BRASS-Girder, a 3-D grillage model better approximate the DFs. The analysis can define nodes connecting multiple bridge members that are broken into smaller sections and applies live loads, taking into account transverse load distributions. The grillage model can consider a variety of factors that the girder-line analysis cannot, including various bridge effects, such as skew. This method provides more accurate analytical DFs than BRASS-Girder and could be compared to the field tested DFs.

During the field tests, enough personnel should be available to conduct a number of tasks including strain measurement and displacement monitoring; vehicle control; and safety precaution supervision. Using the RFID triggering system, the bridge measurement data automatically saves to an Excel file, however the data can be converted to any program of choice. After the field tests are complete, there should be qualified personnel to perform analysis procedures. For the BRASS-Girder load rating, WYDOT engineers should be consulted to assure their procedures are followed.

As discussed in Section 5.2, the Iowa Bridge Engineering Center has completed sufficient field tests to begin classifying bridges with similar design characteristics into families. After

testing a number of structurally similar bridges, bridge behavior characteristics, such as the DFs, were determined for that family of bridges. These more accurate values replaced the AASHTO Specification values in load ratings in Iowa. A similar approach could be implemented in Wyoming. After testing a large number of three-span, plate-girder, concrete-deck bridges, a new range of DFs can be determined. These values would better represent the actual behavior of this type of bridge and could replace the specification DFs, potentially improving load ratings for that family of bridges.

### 6.2.3 RFID Triggering Development

The future work for the RFID system is broken into two different sections. The first section discusses the improvements needed to finish the RFID system development. The second section discusses the potential uses of the RFID system that could be developed, with respect to the interests of the bridge owner.

#### *RFID System Development*

The RFID proof of concept triggering system included the event triggering of the system to collect data and save the file to a hard drive. The system as a whole was described Section 5.3 and the instrumentation components in Section 5.4. For the system to perform as described, progress needs to be made on several components. Developments include the port of entry system installation, firmware advancement, larger transponder range capabilities, cellular data transmission capabilities, database establishment, and software formation, respectively.

The first focus for system development should be the port of entry implementation. Implementation includes the installation of an RFID transponder with a method to correlate the RFID tag identification number to the load axles and total gross weight where the information

would be send to a central database. Fifteen states in the United States currently incorporate RFID instrumentation into their daily traffic needs through E-ZPASS, an automated RFID based system.

E-ZPASS allows vehicles to travel over toll roads or weigh scales, without inconveniencing the driver to stop. At the Cheyenne I-25 Port of Entry, approximately 800 to 1500 trucks use the E-ZPASS system every day as a method to bypass port of entry stations (Fresquez, 2015). In order to obtain a pre-pass for the system, the truck company must register, purchase a pass, and pay a monthly fee. Only trucks in compliance with legal weight and legal size standards may use the E-ZPASS system.

An RFID transponder is located 1-mile from the port of entry. When passing the transponder, if the vehicle is in good standing with the E-ZPASS system, the truck driver receives a signal that indicates that the truck may continue without stopping at the port of entry. If the company is not in good standing, for example if it has not paid its monthly fee, then the truck driver receives a signal to stop at the port of entry to be evaluated. The Cheyenne I-80 Port of Entry has a similar system. (Fresquez, 2015). The E-ZPASS is used for legal vehicle loads while all permitted loads must stop at the weigh station. The success of this system suggests that incorporating an additional RFID system for permitted vehicles is reasonably achievable.

Firmware development needs to occur before field implementation takes place. Both the software and hardware modes are completed and the next stage is to verify its performance. A safety feature must also be programmed to warn the user if any system components are not functioning as designed. For example, a signal could be sent to and from the microcontroller and interrogator every 24-hours for a power status check. Another addition is to develop a feature

that discriminates interrogator data as an additional triggering mechanism where the system stores strain data when a live load causes a sensor to reach a predetermined threshold value. Additionally, sleep and wake commands should be integrated to increase energy efficiency and prolong battery life.

During the proof of concept tests, the transponder did not have a large enough detection range to trigger the system consistently when the tag was located on the left-hand corner of the windshield. Additionally, the interstate lanes are 1-foot wider than the lanes on Highway 17. As a result, it is suggested that an additional antenna be added to the system on the opposite side of the highway for consistent and confident triggering.

The cellular data transfer from the instrumented bridge needs to be further explored to determine which module will best suit the needs of the RFID system. As previously discussed, two cellular modems were suggested by Verizon Wireless: the Feeney Wireless Skyus and the Option Cloudgate. Depending on the amount of data collected and the needed transfer rate, one modem may be beneficial over the other.

A database should be established that can manage a large amount of vehicle and bridge information and can be accessed by approved personnel, for example WYDOT bridge engineers. Software must be developed as well as algorithms for automatic post-processing. One company that has been researched, Chandler Monitoring Systems, Inc., has developed some of these processes, and it may be worthwhile to pursue their guidance or services. Once the RFID system development is finished, bridge managers could determine how the system would best serve their specific needs. Examples of RFID system applications are explained in the next section.

### *Potential RFID System Uses*

In the literature review, field cases are discussed that use various WIM systems as methods to better monitor the live-load traffic that highways and bridges experience. Examples include low-speed, high-speed, and bridge WIM systems. The RFID system discussed in this research is another application of a WIM system. Utilizing a static WIM system that already exists at the port of entries, bridge engineers can correlate that load to the bridge responses induced by permitted live loads.

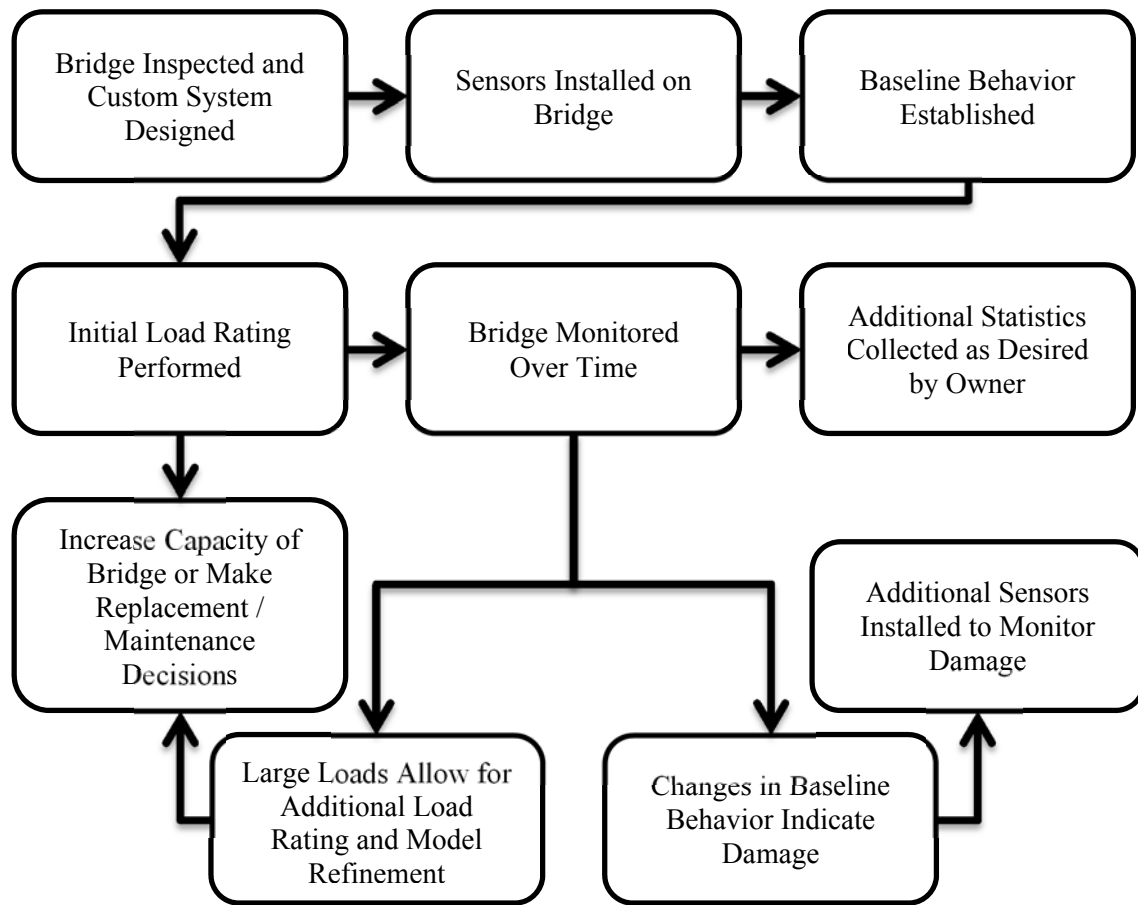
There are various benefits to the procedure, many of which arise due to the system being created specifically for permitted vehicles. Unlike many of the other available systems, an additional scale does not need to be introduced, potentially resulting in great economic savings. The load does not need to be determined based on complicated algorithms that are still in their trial stages. Instead, the system takes advantage of pre-existing technology to correlate vehicle information to bridge measurement data.

Because of the various advantages that this system has over other developed WIM systems, a variety of applications and studies could be applied once the system is ready for implementation. Depending on the purpose of the RFID system, there is potential for economic favorability as bridge managers could better allocate their funds, prioritize the needs of existing bridges, and generate safer and more efficient highways and bridges. Development of the devised system could result in a variety of purposeful uses.

One possible development is a continuous load-rating system for permitted vehicles. Over time, a standard baseline could be determined for specific permitted vehicles and bridge families. Instead of relying on a conservative analysis completed by BRASS-Girder, the actual



responses would be measured and monitored for a variety of applied vehicle configurations. Algorithms and procedures would need to be developed to determine real-time bridge load ratings from bridge measurement data. By continuously monitoring the bridge, bridge management officials could potentially determine practices to safely increase the load ratings. As stated in Section 5.2 and Appendix A.3, other states are in the process of developing the procedures to complete this type of analysis. A diagram of this system is shown in Figure 47 (Jung, 2015).



**Figure 47: System Flow Chart (Jung, 2015)**

Load ratings for permitted vehicles in Wyoming are restricted to an analysis performed by BRASS-Girder. Typically, the loads that have to be analyzed by a bridge engineer are over

250,000-pounds. An application must be submitted to WYDOT to receive approval to travel through the state. Examples of common permitted loads and applications were provided by WYDOT and are located in Appendix F. Based on the information provided by the application, the bridge engineer must open the BRASS-Girder bridge file for each structure on the vehicle's route and apply the specific load to the structure to determine whether or not the vehicle must take detours. Bridge engineers do not know how conservative their analysis is using this method (Ruess, 2015). Establishing a real-time load rating system would alleviate the majority of grey area resulting from analytical analysis procedures.

To complete this type of system, BRASS-Girder should be used initially to determine the critical cross sections of the bridge of interest. Appendix G contains three types of permitted loads that are typically seen by the WYDOT Bridge Program (Ruess, 2015). Using the BRASS-Girder analysis developed from the application of common permitted loads, the critical cross sections could be instrumented for field testing purposes. Time would be required to initially analyze and install the system, however with wide implementation, the system could have a large economical savings over time.

Other applications for the RFID system include fatigue life cycle and load hysteresis analysis. The fatigue life predicted from the robust data set and would ideally be instrumented and monitored, starting when the bridge is constructed. A load hysteresis of permitted vehicles would provide bridge engineers with a better understanding of the loading conditions presented from average daily truck traffic.

Permit compliance is where law enforcement assures that overweight or oversize vehicles file for a legal vehicle permit. Companies with overweight or oversize vehicles will often not file

for a permit in an attempt to by-pass permit fees. However, overweight and oversize vehicles cause more wear to highways and bridges than typical daily truck traffic, and in extreme cases, they can cause significant damage, resulting in higher maintenance and rehabilitation costs that could have been avoided.

The RFID system could assist in identifying the illegal loads and notifying law enforcement. As stated in Section A.3, other countries have implemented different versions of this system and have had a substantial decrease in illegal vehicles. One method to explore would be the application of a trigger based on a strain threshold being reached. When the threshold is reached without a tag present, a picture could be taken of the vehicle's license plate and sent to law enforcement. There are many different approaches that could be taken for this procedure. If pursued, highways and bridges would be safer without as many illegal loads and would potentially last longer before needing replacement.

A variety of other studies could benefit bridge owners or national agencies, such as the AASHTO or FHWA. More refined design values could be determined after field tests take place for bridge families. The refined analysis could provide more accurate design specification values for today's highway bridges.

After the RFID system is fully developed for permitted vehicles, numerous applications could ensue. Examples include real-time load ratings, fatigue life-cycle analysis, load hysteresis analysis, permit compliance, and beneficial studies for national agencies. Processes to improve these applications have already been, or are in the process of being, established, however research should be completed on the topics to determine the extent of development. The bridge owner, such as WYDOT, could determine the best method based upon the requests of the state

bridge management. A successful system would result in safer, more efficient highway bridges throughout the state and financial savings for state DOTs.

## REFERENCES

- AASHTO (2011). "Appendix A: Illustrative Examples." *The Manual for Bridge Evaluation*. 2nd ed. Washington: American Association of State Highway and Transportation Officials. A7, A43-A50. Print.
- Annamdas, Venu Gopal Madhav (2011). "Review on Developments in Fiber Optical Sensors and Applications." *IJME International Journal of Materials Engineering*: 1-16. Scientific & Academic Publishing. Web. 20 July 2015. <<http://article.sapub.org>>.
- Ansari, Farhad (2007). "Practical Implementation of Optical Fiber Sensors in Civil Structural Health Monitoring." *Journal of Intelligent Material Systems and Structures* 18.8: 879-89. *Engineering Village*. Web. 4 May 2014. <[www.engineeringvillage.com](http://www.engineeringvillage.com)>.
- Baez, Michael (13 May 2014). "Phase II." Message to McKenzie Danforth. Personal communication.
- Barker, Michael G (2001). "Quantifying Field-Test Behavior for Rating Steel Girder Bridges." *Journal of Bridge Engineering* 6.4: 254-61. Print.
- Branscomb, James (Mar. 2013-Oct. 2015). Electrical Design Engineer. Wyoming Department of Transportation. Personal communication.
- Chan, T.h.t., L. Yu, H.y. Tam, Y.q. Ni, S.y. Liu, W.h. Chung, and L.k. Cheng (2005). "Fiber Bragg Grating Sensors for Structural Health Monitoring of Tsing Ma Bridge: Background and Experimental Observation." *Engineering Structures* 8.5: 648-59. *Engineering Village*. Web. 5 May 2014. <[www.engineeringvillage.com](http://www.engineeringvillage.com)>.
- Copel, Larry (24 Apr. 2014). "Analysis: Nation's Bridges Desperately Need Repair." *USA Today*. Gannett. Web. 5 Oct. 2014.
- Doornink, J. D., B. M. Phares, T. J. Wipf, and D. L. Wood (2006). "Damage Detection in Bridges Through Fiber Optic Structural Health Monitoring." *Photonic Sensing Technologies* 6371. *Engineering Village*. Web. 5 May 2014. <[www.engineeringvillage.com](http://www.engineeringvillage.com)>.
- FHWA (31 Dec. 2012a). "Bridges by Posting Status (2013)." *Bridges and Structures*. Federal Highway Administration. Web. 11 Oct. 2014.
- FHWA (28 Mar. 2015b). "NBI Elements." *National Bridge Inventory [NBI] - Data Dictionary*. Federal Highway Administration. Web. <[http://nationalbridges.com/nbiDesc.html#ITEM\\_66](http://nationalbridges.com/nbiDesc.html#ITEM_66)>.

- FHWA (2014c). "Questions and Answers Load Rating of Specialized Hauling Vehicles." 7, 8, 9. Federal Highway Administration. Web. 31 Aug. 2015. <[https://www.fhwa.dot.gov/bridge/loadrating/shv\\_qa.pdf](https://www.fhwa.dot.gov/bridge/loadrating/shv_qa.pdf)>.
- Fiorillo, Graziano, and Michel Ghosn (2014). "Procedure for Statistical Categorization of Overweight Vehicles in a WIM Database." *Journal of Transportation Engineering* 140.5. *Engineering Village*. Web. 3 June 2015. <[www.engineeringvillage.com](http://www.engineeringvillage.com)>.
- Fresquez, Leroy (Mar. 2015). Lead Officer, I-25 Port of Entry Cheyenne. Personal communication.
- Fu, Chung C., Maged Elhelbawey, M. A. Sahin, and David R. Schelling (1996). "Lateral Distribution Factor from Bridge Field Testing." *Journal of Structural Engineering* 122.9: 1106-109. *Engineering Village*. Web. 27 Jan. 2015. <[www.engineeringvillage.com](http://www.engineeringvillage.com)>.
- Glisic, Branko, and Daniele Inaudi (2007). "Introduction to Structural Health Monitoring." *Fibre Optic Methods for Structural Health Monitoring*. West Sussex: John Wiley & Sons. 1-2. Print.
- Goodrich, Brian (22 Oct. 2014). "RE: States using BRASS." Message to McKenzie Danforth. Personal communication.
- Jacob, Bernard, and Véronique Feypell-de La Beaumelle (2010). "Improving Truck Safety: Potential of Weigh-in-Motion Technology." *IATSS Research* 34.1: 9-15. *Science Direct*. Web. 3 June 2015. <[www.sciencedirect.com](http://www.sciencedirect.com)>.
- Jaramilla, Becky, and Sharon Huo (Aug. 2005). Standard HS20 Truck. Digital image. *Federal Highway Administration Research and Technology*. FHWA. Web. 21 Sept. 2015. <<https://www.fhwa.dot.gov/publications/publicroads/05jul/09.cfm>>.
- Jung, Michael (4 Feb. 2015). "Method for Correlating Vehicular Loads with Structural Response Data for Structural Health Monitoring and Load Rating". U.S. Provisional Patent. Print.
- Kuang, K. S. C., M. Maalej, and S. T. Quek (2006). "Hybrid Optical Fiber Sensor System Based on Fiber Bragg Gratings and Plastic Optical Fibers for Health Monitoring of Engineering Structures." *Smart Structures and Materials 2006: Sensors and Smart Structures Technologies for Civil, Mechanical, and Aerospace Systems* 6174. *Engineering Village*. Web. 5 May 2014. <[www.engineeringvillage.com](http://www.engineeringvillage.com)>.
- Kreuzer, Manfred (28 Nov. 2014). "Strain Measurement with Fiber Bragg Grating Sensors." *Micron Optics*. HBM. Web.
- Leng, Sio-Song (2015). "Bridge Influence Line Estimation for Bridge Weigh-in-Motion System." *Journal of Computing in Civil Engineering* 29.1. *Engineering Village*. Web. 3 June 2015. <[www.engineeringvillage.com](http://www.engineeringvillage.com)>.

- Maurais, Dan (2012). "Strain Transfer Behavior of Notch Embedded Fiber Bragg Gratings." Print.
- McDaniel, Travis, and Michael Barker (1998). "Load Posting Plans for Diagnostic Field Testing." *Standardization of Bridge Load Test Procedure*. 2, 184-187. Print.
- Micron Optics (2010a). "Optical Strain Gage os3100." Web. 19 Mar. 2014. <<http://www.sengenia.com/pdfs/os3100.pdf>>.
- Micron Optics (2007b). "os3100 Style Strain Sensor Comprehensive Fatigue Test Report." 1-6. Print.
- Micron Optics (2007c). "os3100 Style Strain Sensor Long Term Test Summary." Print.
- Micron Optics (23 April 2009d). "os3120 Epoxy Mount Installation Demo." Online video clip. *YouTube*. Web. 5 May 2014.
- Micron Optics (25 May 2015e). "os3120 Optical Strain Gage-Epoxy Mount." *Sensor Information Sheet*. Web. <[http://www.micronoptics.com/uploads/documents/os3120\\_Sensor\\_Information\\_Sheet\\_0906.1.doc](http://www.micronoptics.com/uploads/documents/os3120_Sensor_Information_Sheet_0906.1.doc)>.
- Micron Optics (13 May 2014f). "Requirements and Considerations for Successful FBG Sensing Solutions." PowerPoint.
- Munkelt, Gary (28 July 2010). "HL93 Truck Loads vs. HS20 Truck Loads." *National Precast Concrete Association*. Precast Inc. Magazine. Web. 31 Aug. 2015.
- O'Brien, E.J., Quilligan, M.J., and Karoumi, R. (2006). "Calculating an IL from Direct Measurements." *Proceedings of the Institution of Civil Engineers, Bridge Engineering*, 159, 31-34.
- Oesch, Everett Ralph (2003). "University of Missouri Field Testing System and Data Reduction Process." *Strength and Performance Field Testing of Hybrid HPS Bridge A6101*. 24. Print.
- Phares, Brent (21 Jan. 2015). Personal communication.
- Puckett, Jay A., Sharon X. Huo, Mark Jablin, and Dennis R. Mertz (2011a). "Framework for Simplified Live Load Distribution-Factor Computations." *Journal of Bridge Engineering* 16.6: 777-91. *Engineering Village*. Web. 15 Oct. 2015. <[engineeringvillage.com](http://engineeringvillage.com)>.
- Puckett, J., X. Huo, M. Patrick, M. Jablin, D. Mertz, and M. Peavy (2005b). "Simplified Live Load Distribution Factor Equations for Bridge Design." *Transportation Research Record: Journal of the Transportation Research Board*: 67-78. Print.

- Rivera, E., D. J. Thomson, and A. A. Mufti (2005). "Comparison of Recoated Fiber Bragg Grating Sensors Under Tension on a Steel Coupon." *Nondestructive Evaluation and Health Monitoring of Aerospace Materials, Composites, and Civil Infrastructure IV* 5767.1: 163-74. *Engineering Village*. Web. 6 May 2014. <[www.engineeringvillage.com](http://www.engineeringvillage.com)>.
- Ruess, Joseph (18 Sept. 2015). "BRASS Analysis." Personal communication.
- Seo, Junwon, Brent M. Phares, Ping Lu, Terry J. Wipf, and Justin Dahlberg (2012). "Use of a Structural Health Monitoring System for the Assessment of Bridge Load Rating." *Forensic Engineering 2012*: 18-27. *Engineering Village*. Web. 13 May 2014. <[www.engineeringvillage.com](http://www.engineeringvillage.com)>.
- Smart Fibres (11 Dec. 2014). "SmartScan Interrogator for Fiber Bragg Grating Sensors." *Smart Fibres*. Web. <<http://www.smartfibres.com/docs/SmartScan.pdf>>.
- Tennyson, R. C., A. A. Mufti, S. Rizkalla, G. Tadros, and B. Benmokrane (2001). "Structural Health Monitoring of Innovative Bridges in Canada with Fiber Optic Sensors." *Smart Materials and Structures* 10: 560-73. IOP Science. *Engineering Village*. Web. 3 Oct. 2014. <<http://www.engineeringvillage.com/>>.
- Wipf, Terry, and Travis Hosteng (1 Dec. 2010). "Diagnostic Load Testing May Reduce Embargoes." *Iowa State University Institute for Transportation*. Web. 15 Oct. 2014.
- WYDOT (1 Feb. 2003a). "BRASS Bridge Rating & Analysis of Structural Systems." *Wyoming Department of Transportation*. Web. 3 Oct. 2014.
- WYDOT (27 Aug. 2015b). "Laramie River Bridge Load Rating Summary." *Wyoming Department of Transportation*. Print.
- Zhao, Hua, Nasim Uddin, Xudong Shao, Ping Zhu, and Chengjun Tan (2014). "Field-Calibrated Influence Lines for Improved Axle Weight Identification with a Bridge Weigh-in-Motion System." *Structure and Infrastructure Engineering* 11.6: 721-43. *Engineering Village*. Web. 3 June 2015. <[www.engineeringvillage.com](http://www.engineeringvillage.com)>.
- Zhou, Zhi et al (20 July 2015). "The Application of FBG Sensing in Monitoring Hulanhe Bridge in Heilong Jiang Province." *Micron Optics*. Web.



## APPENDIX A

### A.1 Literature Review of Current Load-Rating Procedures and Validations

The Iowa State University Bridge Engineering Center (BEC) completed a study to compare the load ratings of bridges determined by two methods. The first load ratings were calculated using AASHTO Specifications; the second load ratings were determined by dynamic field testing. A total of 17 bridges were instrumented; 12 of those bridges were initially posted and had a negative effect on the flow of traffic. Strain data measurements were taken at predetermined locations where sensors were installed at critical spans, sections, and member locations. The BEC determined lateral distribution factors and studied the composite action and end restraint behavior of the bridges. The field tests showed that the traditionally calculated load ratings were overly conservative, and as a result, 6 of the 12 postings were removed (Wipf, 2010).

Wipf (2010) suggested using the outcome of the research to ensure safe load ratings that were not overly conservative. This conclusion included the following suggestions:

- Re-evaluate older bridges
- Determine the capacity for bridges with insufficient design data
- Evaluate the need to impose temporary load restrictions on damaged bridges
- Reduce the number of bridges that restrict access to overweight trucks
- Verify the effectiveness of new strengthening techniques
- Remove load restrictions imposed on additional bridges due to implementation of new test-vehicle weight laws
- Determine the behavior of structures under heavy loads with calculated load ratings below anticipated capacity needs

The work completed was vital as it pertains to each state for determining the conservatism of load ratings, more specifically load ratings for posted bridges. By conducting a study justifying

the removal of 50% of the posting on the bridges, other states could use this research as a blueprint to improve the use of posted bridges and increase load ratings while maintaining safety (Wipf, 2010). This study is promising as the University of Wyoming team looks to produce similar results where postings can be removed or load ratings improved.

A bridge on US 30 near Ames, Iowa crossing the Skunk River was utilized in a study where FOS were used to measure a bridge's response at critical locations to various truck loads whose data is known based on a weigh-in-motion (WIM) system from the State of Iowa highways. The data was used to better calculate a load rating for the bridge based on a calibrated computer model. The steps taken to effectively produce a load rating for the bridge were as follows: obtain the strain data from ambient trucks, calibrate a computational model of the bridge, create a Load Factor Design (LFD) rating using the calibrated model, develop the load rating distribution, and then statistically estimate a load rating (Seo, et al. 2012).

The bridge's response based on five-axle trucks was measured, and truck configurations and travel lanes were discovered by analyzing the patterns of the data from the sensor placed on the bottom of the deck. Random five-axle trucks were used for the model calibration. The computer model was calibrated by importing the actual properties such as the moments of inertia of the girders, stringers and floor beams; the modulus of elasticity of the concrete deck; and the rotational restraint at the supports of the abutments (Seo, et al. 2012).

Statistical analysis and graphs were used to prove that the calibrated model responses were in close agreement with the field responses. Load ratings were developed by following the AASHTO Standard for HS-20 trucks; results varied from 1.26 to 1.54. The structural capacity was anywhere from 26 to 54 percent above what is required for the five-axle trucks (Seo, et al.

2012). This study was similar to the testing plan at the University of Wyoming in regards to using a WIM system with FOS placed at critical locations of a bridge to determine a more accurate load rating. The process differs in that the University of Iowa team developed a method to use real-time bridge ratings for ambient five-axle truck loads, and the University of Wyoming will focus on traditional load rating field tests to determine potentially less conservative load ratings.

## A.2 Literature Review of FBG Strain Transfer Behavior and Protection Techniques

The University of Wyoming team has completed work related to various testing performed by Micron Optics. This work included studies of strain-transfer techniques and FBG testing with both polyimide and acrylate recoated fibers. Additionally, research by outside parties validated FBG sensors in various carrier packages against traditional foil gages. The three topics are covered in this section through a literature review.

### A.2.1 University of Wyoming Research on Notch Embedded FBGs

Maurais (2012) completed analysis and laboratory research at the University of Wyoming on strain transfer behavior of notch embedded FBGs in concrete specimens. The experimental results were compared to a finite element analysis (FEA) model to determine the most effective method of installation, studying strain-transfer configurations. Also considered was the feasibility of using the developed procedures for field implementation. It was determined that the methods are “effective and obtainable” for installation in the field with an Ultrabond 1300 epoxy being nearly ideal for typical applications, while an epoxy with a higher viscosity would be optimal for overhead applications.

The strain transfer comparisons showed a 1%-9% difference between the FEA and experimental test results for five different configurations. This difference is small, since many assumptions were made in the FEA model, including a complete bond between the epoxy and the concrete as well as between the epoxy and the FBG; completely clean concrete surface; long-gage strain transfer, meaning no local strain effects from aggregate in the concrete; and perfect notch shape with flawless epoxy application. The strain transfer was most effective with an increase in epoxy bond length for all bond layer thicknesses and epoxy elastic moduli. The experimental strain transfer was also most accurate with the highest epoxy elastic modulus, suggesting that the closer the epoxy modulus is to the modulus of concrete, the better the strain transfer. Successful strain transfer was also seen with the smallest layer of epoxy thickness. Lastly, the saw-notch configuration was more effective compared to the v-notch configuration with a consistent epoxy modulus, epoxy bond length, and bond layer thickness in both specimens (Maurais, 2012).

FBGs have a predetermined gage factor to use in calculations for converting the wavelength change into strain values. Tensile tests using dogbone steel specimens were completed to confirm that the gage factor of 0.78 provided by the manufacturer was accurate. It was concluded that the experimental factor was within 0.5% of the provided gage factor and therefore was validated for FBG calculations (Maurais, 2012). Maurais work was important because it gave the University of Wyoming team an in-depth understanding of the transfer behavior of FBGs; this information was helpful in determining the best suited FBGs for future research.

### A.2.2 FBG Polyimide and Acrylate Recoat

Kuang, et al. (2006) at the National University of Singapore performed a variety of tests that included tensile, flexural, and cyclic flexural tests to study the performance of various FBG configurations, types of adhesives, and plastic optical fibers. The study of interest to the University of Wyoming team was the comparison of FBGs recoated with acrylate and bare FBGs with the recoated acrylate removed and the fibers then embedded in carbon-fiber composites. Flexural tests were completed using both types of FBGs and traditional foil gages surface adhered to the bottom surface of an aluminum I-beam by means of cyanoacrylate-based adhesive. The I-beam was loaded from rest, held briefly, and unloaded back to zero.

The results showed that both sensor types showed acceptable linearity of the loading curves, however while the loading was held, the acrylate recoated FBG showed noticeable stress relaxation. As the loading continued, the recoated FBG displayed a non-linear loading curve while the bare FBG consistently reported similar results as the traditional foil gage throughout the testing period. The behavior of the recoated FBG could be due to a variety of factors including slipping between the recoating and the fiber core. Kuang, et al. (2006) suggested to further study the effects of polyimide recoated FBGs, suspecting better strain transfer results.

A study completed by the University of Manitoba in Winnipeg, Canada discusses the main differences between polyimide and acrylate recoating shown in Table 5.

**Table 5: Main Characteristics of Different Fiber Coatings (Rivera et al. 2005)**

<b>Property</b>	<b>Acrylate Microcoating</b>	<b>Polyimide Microcoating</b>
Stripping	Mechanical or chemical	Chemical
Transmission of strain across coating	Good for short times, low tensions and $T < 95^{\circ}\text{F}$	Excellent
Mechanical protection	Very poor	Very poor
Chemical protection	Moderate	Moderate
Thermal expansion coefficient	Very low $0.5 \times 10^{-6}$	Very low $0.5 \times 10^{-6}$
Cost	Low	High

Tension tests were carried out using a cold rolled steel specimen to test the strain transfer performance of each recoat. The test coupon had 11 sensors installed, including traditional foil gages, FBGs with polyimide and acrylate recoat from Supplier 1, and FBGs with acrylate recoat from Supplier 2. The coupon was set in an MTS machine, loaded until the strain reached a specific value, held for 1.5 minutes, incrementally dropped back to zero load, then repeated two more times (Rivera, et al. 2005).

The results showed that the sensors from Supplier 1 with both the polyimide and acrylate recoat had favorable outcomes with strain readings within 3% of the foil gages. Supplier 2 provided acrylate fibers where the strain values were between 7% and 13% of the foil gages. Even though some fibers from Supplier 1 and Supplier 2 had the same acrylate recoat, the results appeared to be based solely on the manufacturer, not the recoat material. This outcome led the researchers to believe that FBG recoating standards should be implemented in the future. (Rivera, et al. 2005). While additional testing has been completed since this study, this experiment relates back to the Chapter 1 discussion where Micron Optics pointed out that careful consideration must be taken when selecting the manufacturer for purchasing FBGs (Micron Optics, 2014f). These findings were important to keep in mind when selecting the FBGs to

purchase for testing and should be a high consideration when looking into sensors for field implementation.

Baez (2014) from Micron Optics, one of the leading FBG manufacturers in the United States, commented on the use of polyimide versus acrylate recoats. Micron Optics does not use an acrylate recoat for any of their applications, because it results in poor strain transfer. Instead, polyimide recoat is utilized for all applications because it provides better strain transfer and a wider temperature range. One drawback to using polyimide versus acrylate recoat is that the only form of removing the recoat, which is a procedure needed to splice the fibers together, is through chemical means. This process involves burning the recoat with a lighter and wiping it clean with a cloth soaked in alcohol. The acrylate recoat can be removed either chemically or mechanically, making the splicing process quicker.

Baez (2014) also discussed the use of bare FBGs versus FBGs with a protective carrier. Micron Optics suggested not using bare FBGs, or FBGs without protective carriers, for field applications; the installation process is time consuming, and results can be difficult to distinguish. The carriers from Micron Optics consistently compress and tension the gage length for optimal strain readings with a strain range of  $\pm 2,500 \mu\epsilon$ . The fibers purchased for research at the University of Wyoming were from Micron Optics, model os3120, which used a polyimide recoated FBG protected by a steel carrier.

### A.2.3 FBG Strain Verification Cases Based upon Laboratory and Field Testing

Ansari (2007) discussed the use of protection methods of FBGs in a variety of fields, recognizing that civil engineering infrastructure is a more recent application that has new factors to consider, including the large sizes of structures, the variety of building materials, and the harsh

environmental conditions they endure. The use of bare sensors initially sounds promising; it is inexpensive with smaller sensor sizes, easier to multiplex the sensors onto one fiber, and involves cheaper labor. However the bare FBG sensors installed in the past for monitoring purposes were not generally used long-term and were expected to have very little intrusion onto the surface material. The installation process becomes time consuming, as the fibers must be handled carefully to prevent breaking. Care must be taken for installation during construction or on already existing structures. For this reason, many companies have resorted to various types of surface-adhered, embedded, or attached sensors to produce more durable sensors. This information was vital for the research completed at the University of Wyoming in order to seek out well-protected fibers for field instrumentation.

In Hong Kong, China, forty FBGs were installed on the Tsing Ma Bridge on the hanger cables, rocker bearings, and truss girders to measure temperature and strain for a structural health monitoring system. A method of protecting FBGs was being tested where the coating was removed, then the fiber was placed on nitinol strips. Nitinol is known for being an elastic metal and having corrosion resisting capabilities. The FBGs were adhered onto the nitinol with high-strength epoxy, allowed to bake at 176° F for 5 hours, and then cooled. The sensors were placed close to traditional foil gages, which were used to validate the packaged FBG responses. The sensors displayed excellent correlation and the dynamic strain was validated (Chan, et al. 2005). Since this study, other types of protections techniques have developed for an even more accurate and improved performance in field conditions.

A team at the University of Iowa Bridge Engineering Center compared FOS manufactured by Avensys, Inc. to traditional foil gages to confirm accuracy for use on a field instrumentation project. The FBGs were protected by carbon fiber reinforced polymer (CFRP)



packaging and provided easier installation. The FBGs and traditional foil gages were installed adjacent to each other on a steel coupon and were tested through tensile cyclic loading at various magnitudes and number of cycles. The wavelength recordings were taken continuously for the FBGs, and strain was measured at specific intervals for the foil gages. All tests showed good agreement between the results of the FBGs and foil gages, so the FBGs were used for instrumentation on the US 30 Bridge near Ames, Iowa (Doornink, 2006). Within the last decade, researchers have made tremendous strides in the development of FBGs, making them even more accurate and durable in harsh environments.

The Iowa State University Bridge Engineering Center teamed up with Iowa DOT to install a structural health monitoring system, using FOS on a fracture-critical bridge constructed in the 1960s (Doornink, 2006). The bridge, the same structure previously discussed, is located on highway US 30 near Ames, IA and crosses the Skunk River. It has three spans: 97.5 feet side spans and 125 feet middle span, and is 30 feet wide, supporting two traffic lanes.

The bridge was one of many in the state that was retrofitted to fix the lack of connection plates and stiffeners attached to the girder tension flanges. It was retrofitted by removing sections of the floor beam connection plates and stiffeners in the negative moment regions. This procedure eliminated a large portion of the stress concentrations stemming from out-of-plane bending, however there was a still concern about the formation of fatigue cracks. This test served as a prototype for similar bridges around the state, so assuring that the equipment and sensors were running properly was key for future success. Bridge Diagnostics Inc. (BDI) out of Boulder, Colorado was hired to install their sensors adjacent to the FOS to compare readings based upon ambient traffic loads. The results from BDI's sensors and the FOS were excellent, and the tests were deemed successful (Doornink, 2006).

The bridge on US 30 was successfully instrumented, and a reliable and respectable company validated the sensor results. While the University of Iowa and Iowa DOT were focused on the structural health monitoring aspect of the project, sensor validation completed in this project was important to recognize in moving the University of Wyoming's project forward. It should also be noted that data was collected to define typical relationships between sensors so that any outliers could be addressed; this analysis was vital in order to identify any irregular bridge behavior. Determining the sensor outliers is not the focus of this research paper, however specific data reduction information can be found in Doornink's article (2006).

Zhou, et al. installed FOS onto the Hulanhe Bridge, which crosses the Hulan River in northeast China, with the goal of creating a bridge-monitoring system. In 2001, the bridge was fully instrumented during the construction phase. Installation consisted of 15 FBGs provided by Micron Optics and 15 traditional foil gages that were installed on the rebar and the surface of the bridge. A traditional foil gage was adjacent to every FBG sensor. It should be noted that multiple FBGs did break during installation and were initially replaced. The installed FBGs performed as expected while only one traditional foil gage survived the installation procedure. The results showed that FBGs are much more durable and reliable than foil gages, especially when installed during the construction phase of a bridge. The sensors provided accurate strain measurements and were beneficial for determining temperature changes. The results bode well for a system in Wyoming where field conditions are less than ideal and temperature changes are frequent.

ISIS Canada and University of Manitoba teamed up to install FOS onto various bridges in Canada (Tennyson, 2001). The Beddington Trail Bridge in Alberta, Canada had 20 FBG sensors embedded into the concrete girders in 1993. Measurements were again made in 1996 and found that 18 of the 20 sensors were still working properly and no problems were found with the

structural health of the bridge (Tennyson, 2001). This case validates the accountability of FBGs in extreme weather conditions in the field.

The Taylor Bridge in Manitoba, Canada was reinforced by fiber reinforced plastic (FRP) and had prestressed concrete girders. Sixty-three FBG sensors were installed on the girders at midspan and at the girder ends with the majority of them reading accurately after installation. Electric strain gages were also used to monitor the effectiveness of the fiber optic sensors; however 60% of the electric strain gages failed (Tennyson, 2001). This case study demonstrated the reliability of FBGs in harsh field conditions compared to traditional electrical resistance strain sensors.

### A.3 Literature Review of Weigh-In-Motion Systems

A journal article by Jacob and Feypell-de La Beaumelle (2010) discusses WIM technology and its importance to the safety and efficiency of today's daily truck operations. WIM systems have come a long way within the last two decades. In the mid-1990's, the only legal weight limit enforcement in the United States was static weighing, including three types of scales: fixed, semi-portable, and portable. Systems have been improved today because of the limitations that static weighing exhibits including the time it takes to weigh vehicles, personnel required to weigh vehicles, interruption of traffic, and necessary legal action for truck violations. The following is a review of a wide variety of WIM systems; however there exists more systems than are listed.

Each WIM system has demonstrated its drawbacks in the field thus far. Low-speed WIM (LS-WIM) systems are the most accurate technology and use wheel or axle scales; the drawback is that the speed of the vehicle must generally be between about 3 to 9 miles per hour. High-

speed WIM (HS-WIM) systems are sensors installed in traffic lanes to measure normal-speed traffic loads; their advantages include a fully automated system at a reasonable cost while their main disadvantage is accuracy due to road surface characteristics and truck suspension performance. Other technologies used in the past include bending and load-cell plates embedded in the road; strip sensors fixed in traffic lanes measuring pressure, strain, or forces; and multiple sensor systems that are arranged at specific spacing for load measurements (Jacob and Feypell-de La Beaumelle, 2010).

Bridge WIM (B-WIM) systems have been developed by obtaining the strain values from sensors installed on a bridge then determining the load induced from the calculated influence lines. It was determined that strain sensors were sensitive enough to calculate axle loads without the need for axle detectors. This system typically doesn't require road closures, interruption in traffic, or drivers to be aware of the location of the WIM system. This type of system has been completed using both complex and simple strain sensors that can be removed and installed on another bridge. The disadvantages to this system are that sensors take time and expertise to install, and a high level of engineering is required to analyze the data (Jacob and Feypell-de La Beaumelle, 2010). Additionally, the accuracy at which the axle loads can be detected is still being developed and is discussed in additional article reviews.

A more recent development in WIM technology is the use of video and automatic vehicle identification (AVI). If a truck exceeds the legal axle weight or gross vehicle weight, then a picture of the vehicle, including license plate number, is sent to the authorities that have the opportunity to address the vehicle at a weighing area. This type of procedure has taken place in the Netherlands, France, Sweden, Japan, and various other countries; some have seen up to a 50% decrease in overloaded vehicles (Jacob and Feypell-de La Beaumelle, 2010). In the future,

this type of system could be combined with the WIM system being developed by the University of Wyoming to become more effective.

One of the most recent developments in WIM technology is to require a standard, tamper proof, and on-board weighing system for trucks using load cells and air pressure transducers. Australia has been focusing on advancements in this field, however progress must be made before it can be relied upon for legal purposes. Eventually, this process could lead to real-time monitoring coupled with a GPS system for law enforcement (Jacob and Feypell-de La Beaumelle, 2010). This method would take a long time to develop for legal use in the United States; however if widely deployed, it could assist managers and law officials to make highways and bridges safer and more cost efficient.

Two articles, one by Zhao, et al. (2014) and one by Leng (2015), discuss methods of using the measured strain responses and the determined influence lines to calculate the axle loads of vehicles crossing a bridge. These articles were both based off of work completed by O'Brien, et al. (2006), which studied one calibration truck passing over strain sensors on a bridge one time to determine the loads. The articles agree that the method by O'Brien, et al. is beneficial because it can determine a general function to define the influence lines. However, the system is limited because it doesn't take into account all effects of the calibration vehicle and the mathematical approach is complex.

Zhao, et al. (2014) used the methodology completed by O'Brien, et al. (2006) but applied two calibration vehicles to resemble a more accurate simulation by presenting transverse behavior, improving the overall accuracy of the influence lines. This method was proven successful after completing a field test on a bridge on highway US 78 in Alabama. Leng (2015)

improved the approach by O'Brien, et al. (2006) by using the maximum likelihood estimator method to generalize the model. Two calibration vehicles along with 113 vehicles in the traffic flow were used to validate the method on the Millau Viaduct in France. The result of the developed methodology was a more accurate and robust assessment of the applied loads. The University of Wyoming team will be installing strain sensors onto a bridge, and the methodology presented herein could be applied for use as a B-WIM system in the future after this methodology has been further developed and established.

Fiorillo and Ghosn (2014) worked with the New York State DOT in developing a method to use data collected by WIM systems in order to distinguish overweight vehicles that have permits from those that are illegal. Permits are issued regularly to overweight trucks; therefore WIM data on its own does not provide ample information to determine how many of the overweight vehicles are illegal. The goal was to eventually assist state DOTs in creating a foundation for permit guidelines, weight enforcement procedures, and cost management analyses.

The New York State DOT maintains annual records of the permitted vehicle information, including axle configurations and maximum allowed axle and gross weights. Data mining algorithms were separated into two categories. First, the Federal Highway Administration has vehicle classifications that helped create parameters that categorized overweight trucks. These vehicle classifications were again divided into groups based upon the total axle length, and a method was created to identify axle configurations. Overweight vehicles that did not match the trucks extracted from the database were considered illegal. Second, the pattern recognition used Bayesian updating to create a statistical distribution of vehicles considered illegal based upon vehicle configurations that resembled permitted trucks (Fiorillo and Ghosn, 2014).

To test the accuracy of the algorithm, the New York State DOT utilized a WIM system and a camera to manually identify the percentage of permitted and illegal trucks for a group of vehicles. The conclusion from the survey displayed good agreement with the data-mining algorithms, which resulted in similar percentages of both permitted and illegal trucks. Specific details of the categorizations and algorithms can be found in Fiorillo and Ghosn (2014). Although this type of bridge WIM system is not specifically explored in this thesis, the article addresses the complications of distinguishing permitted from illegal overweight trucks, which has been a topic of discussion with WYDOT for possible future studies.

APPENDIX B

B.1 Laramie River Bridge Load Rating Summary (WYDOT, 2015b)

Form BR-FR3  
Load Rating Summary  
Date 1/9/97  
By JOL  
✓ By JAY

WYOMING DEPARTMENT OF TRANSPORTATION  
BRIDGE BRANCH  
LOAD RATING SUMMARY




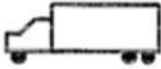


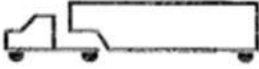
**STRUCTURE IDENTIFICATION**

Route I-80  
Station 120+09.25  
County ALBANY  
Feature Intersection LARAMIE RIVER  
Structure Type 3 CONT WELDED PLATE GIRDER  
Project Number BRI-80-5(121)312  
Drawing Number 6295  
T 15 N R 73 W Sec 5

On  Off  System Date 1/9/97  
Structure Number AXK  
Milepost 312.44  
Structure ID EBC & WBL

LOAD RATING METHOD: X Allowable Stress Load Factor

LOAD RATING, TONS  
(Round down to nearest ton)

HS20 (36.0 T)   
TYPE 3 (22.0 T)   
TYPE 3S2 (39.95 T)   
TYPE 3-3 (40.5 T)   
HS25 (45.0 T)   
OTHER  
(Show Sketch)

Inventory Rating	Operating Rating	Recom. Posting	Controlling Feature
1.14	2.51		INV(FATIGUE) AT 104 OPG STRENGTH AT 104
41 Tons	90 Tons		
1.65	3.58		INV(FATIGUE) AT 104 OPG STRENGTH AT 104
36 Tons	78 Tons		
1.47	3.10		INV(FATIGUE) AT 104 OPG STRENGTH AT 200
58 Tons	123 Tons		
1.45	3.08		INV(FATIGUE) AT 104 OPG STRENGTH AT 200
55 Tons	124 Tons		
0.91	2.01		INV(FATIGUE) AT 104 OPG STRENGTH AT 104
40 Tons	90 Tons		
0.00	0.00		

BRASS DOCUMENTATION SUBMITTED: Yes X No   
HAND COMPUTATIONS SUBMITTED: Yes  No X

Please indicate the data file location:  
 Disk  Network (g:\bridgelshared\)

STORAGE REQUEST (Include structure number in data file name)  
Data File Name LARAMRAT.dat

1-10-97 Date Archived into /brass/archive/  
dcy (MIS tech use only)

Number of Data Sets 1 (Usually 1)

Comments: Rated with 18 psf FWS and rated the new exterior girder as strong as the interior girder.



## APPENDIX C

### C.1 Micron Optics os3120 Epoxy Mount Installation Procedure

The Fiber Bragg Grating sensors used in the University of Wyoming Lab in the four-point bending tests are also the sensors planned for field instrumentation. The pictures and installation steps were acquired from the installation procedure video produced by the manufacturers, Micron Optics (2009d). Safety precautions include wearing gloves and laboratory safety glasses; the steps for installation are stated below.

#### 1. Mix Epoxy

- a) Fill dropper with Curing Agent 10 exactly to the number ten, and dispense the contents into the center of the jar of Resin AE. Immediately cap the bottle of Curing Agent 10 to avoid moisture absorption.
- b) Mix thoroughly for five minutes, using one of the plastic stirring rods. Discard the dropper after use.



Figure 48: Step 1 - Mix Epoxy

#### 2. Surface Preparation

- a) Sand surface.
- b) Spray Degreaser directly onto surface and wipe down.
- c) Apply Conditioner directly onto surface. Use new cloth to wipe surface.
- d) Apply Neutralizer directly onto surface. Use new cloth to wipe surface.



Figure 49: Step 2 - Surface Preparation

### 3. Position Sensor

- a) Place sensor along the axis of measurement.
- b) Tape sensor to surface then pull back one side.

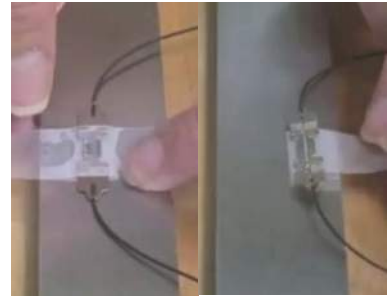


Figure 50: Step 3 - Position Sensor

### 4. Apply Epoxy

- a) Apply enough epoxy to cover each end using wooden dowel.
- b) Tape sensor onto surface.

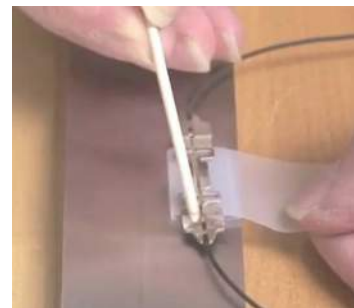


Figure 51: Step 4 - Apply Epoxy

### 5. Cure Epoxy

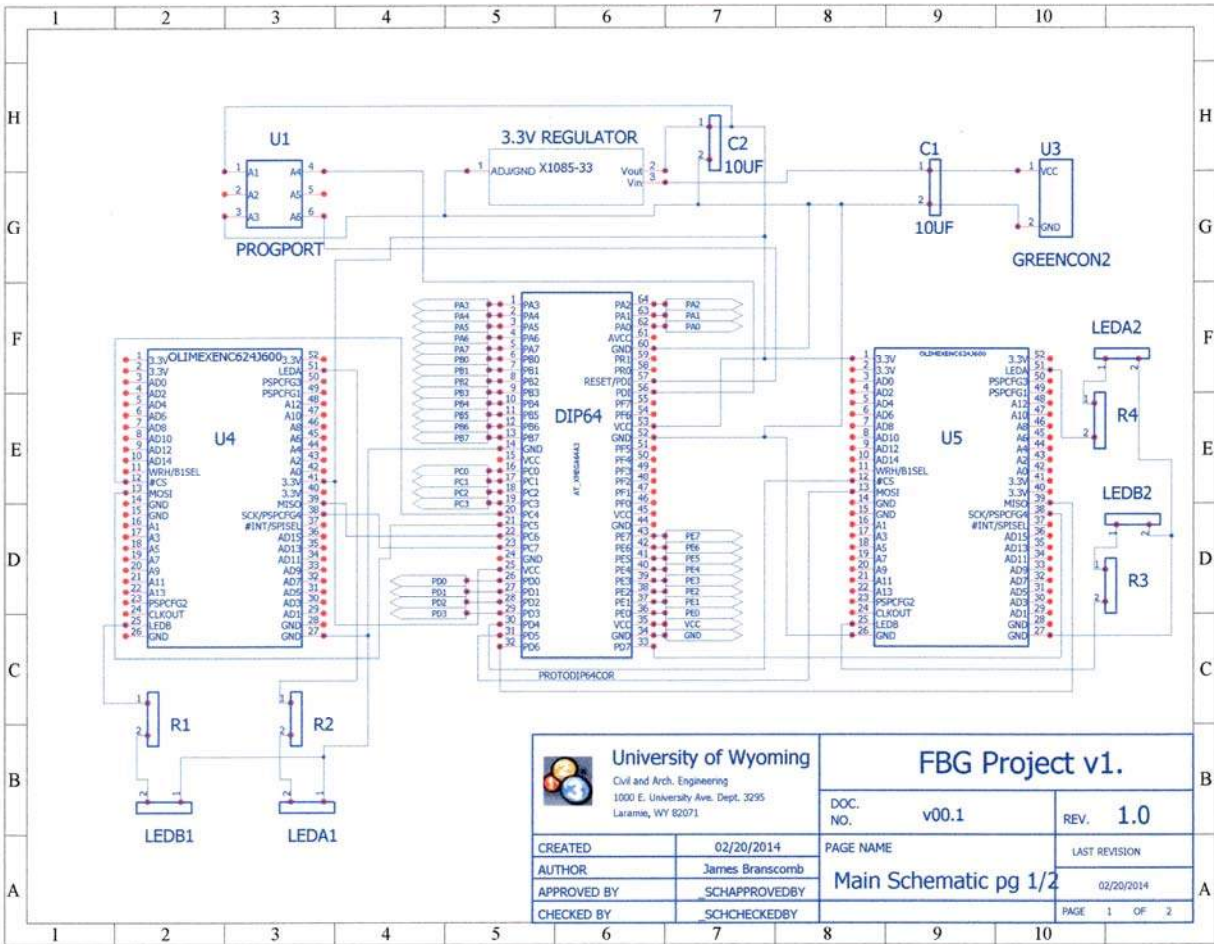
- a) Place metal plate over os3120 and secure by taping.
- b) Clamp plate to surface.
- c) Epoxy will take approximately six hours to cure at room temperature.

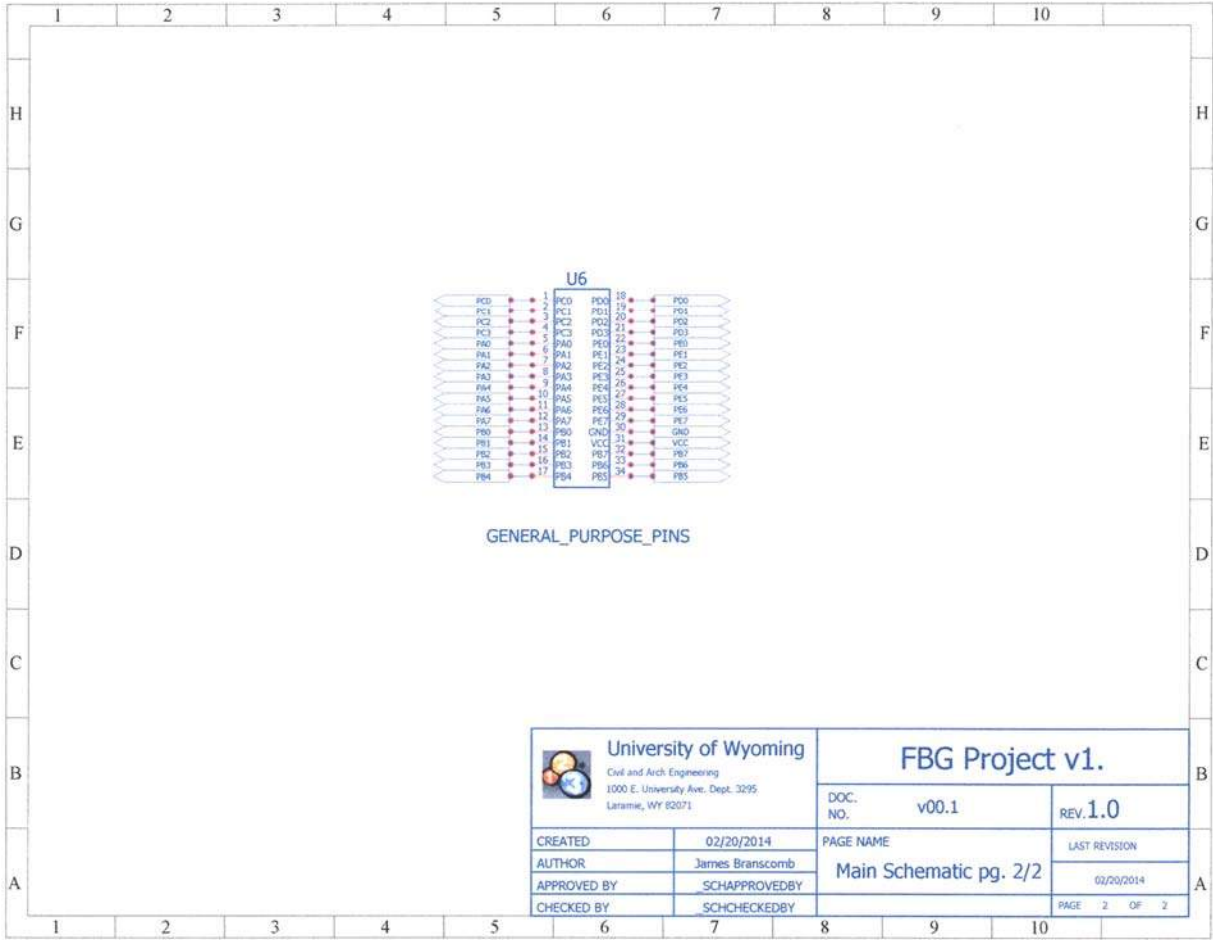



Figure 52: Step 5 - Cure

# APPENDIX D

## D.1 Printed Circuit Board Schematic Design (Branscomb, 2015)





 <b>University of Wyoming</b> Civil and Arch Engineering 1000 E. University Ave. Dept. 3295 Laramie, WY 82071		<b>FBG Project v1.</b>	
		DOC. NO. v00.1	REV. 1.0
CREATED	02/20/2014	PAGE NAME	
AUTHOR	James Branscomb	Main Schematic pg. 2/2	
APPROVED BY	SCHAPPROVEDBY		
CHECKED BY	SCHCHECKEDBY	LAST REVISION	
		02/20/2014	
		PAGE 2 OF 2	

## APPENDIX E

### E.1 Example of Stored Output Data from RFID Triggering System

CH0	CH1	CH2
::1566.1577	1543.945	1531.9843::
::1566.1579	1543.9456	1531.9855::
::1566.1579	1543.9455	1531.9855::
::1566.1578	1543.944	1531.9844::
::1566.1346	1543.927	1531.9588::
::1566.1333	1543.9274	1531.9580::
::1566.1341	1543.9253	1531.9589::
:TS:1		
::1566.1340	1543.9263	1531.9585::
::1566.1351	1543.9257	1531.9581::
::1566.1347	1543.9262	1531.9588::
::1566.1344	1543.9261	1531.9590::
::1566.1345	1543.9279	1531.9575::
::1566.1348	1543.9275	1531.9586::
::1566.1348	1543.9259	1531.9585::
::1566.1347	1543.927	1531.9579::
::1566.1342	1543.925	1531.9580::
::1566.1342	1543.9282	1531.9582::
::1566.1353	1543.9283	1531.9605::
::1566.1345	1543.9251	1531.9570::
::1566.1340	1543.9241	1531.9581::
::1566.1343	1543.9264	1531.9598::
::1566.1358	1543.9283	1531.9585::
::1566.1353	1543.9269	1531.9591::
::1566.1352	1543.9261	1531.9578::
::1566.1353	1543.9269	1531.9585::
::1566.1349	1543.9277	1531.9574::
::1566.1345	1543.9256	1531.9585::
::1566.1339	1543.9258	1531.9594::
::1566.1345	1543.9266	1531.9586::
::1566.1355	1543.926	1531.9603::
::1566.1354	1543.9272	1531.9557::
::1566.1343	1543.9277	1531.9590::
::1566.1342	1543.9264	1531.9591::
::1566.1342	1543.9262	1531.9579::
::1566.1346	1543.9268	1531.9586::
::1566.1349	1543.9265	1531.9577::
::1566.1347	1543.9267	1531.9580::
::1566.1345	1543.9256	1531.9563::

::1566.1346 1543.9284 1531.9594::  
::1566.1345 1543.9257 1531.9580::  
::1566.1345 1543.9256 1531.9587::  
::1566.1352 1543.9269 1531.9593::  
::1566.1352 1543.9266 1531.9583::  
::1566.1332 1543.9255 1531.9585::  
::1566.1344 1543.9273 1531.9592::  
::1566.1362 1543.9303 1531.9587::  
::1566.1352 1543.926 1531.9585::  
::1566.1348 1543.9267 1531.9564::  
::1566.1349 1543.9263 1531.9594::  
::1566.1355 1543.9286 1531.9593::  
::1566.1346 1543.9269 1531.9582::  
::1566.1351 1543.9262 1531.9591::  
::1566.1354 1543.927 1531.9584::  
::1566.1357 1543.9263 1531.9595::  
::1566.1347 1543.9249 1531.9594::  
::1566.1343 1543.9254 1531.9569::  
::1566.1345 1543.9275 1531.9596::  
::1566.1361 1543.928 1531.9598::  
::1566.1350 1543.9275 1531.9581::  
::1566.1349 1543.9254 1531.9574::  
::1566.1348 1543.926 1531.9578::  
::1566.1350 1543.9267 1531.9590::  
::1566.1340 1543.9273 1531.9577::  
::1566.1346 1543.9265 1531.9574::  
::1566.1346 1543.926 1531.9591::  
::1566.1354 1543.9258 1531.9584::  
::1566.1352 1543.9244 1531.9583::  
::1566.1348 1543.9252 1531.9577::  
::1566.1343 1543.9273 1531.9568::  
::1566.1342 1543.9257 1531.9574::  
::1566.1351 1543.9266 1531.9592::  
::1566.1345 1543.9277 1531.9571::  
::1566.1356 1543.926 1531.9577::  
::1566.1347 1543.9259 1531.9588::  
::1566.1342 1543.9262 1531.9591::  
::1566.1351 1543.9261 1531.9605::  
::1566.1346 1543.9277 1531.9572::  
::1566.1362 1543.9286 1531.9592::  
::1566.1339 1543.9256 1531.9590::  
::1566.1340 1543.927 1531.9578::  
::1566.1340 1543.9265 1531.9578::

::1566.1347 1543.9253 1531.9579::  
::1566.1341 1543.9246 1531.9580::  
::1566.1345 1543.9261 1531.9579::  
::1566.1351 1543.9276 1531.9581::  
::1566.1347 1543.9265 1531.9599::  
::1566.1346 1543.926 1531.9586::  
::1566.1351 1543.9272 1531.9586::  
::1566.1342 1543.9268 1531.9573::  
::1566.1349 1543.9258 1531.9583::  
::1566.1347 1543.9275 1531.9579::  
::1566.1345 1543.928 1531.9581::  
::1566.1339 1543.9266 1531.9591::  
::1566.1343 1543.9255 1531.9585::  
::1566.1348 1543.9266 1531.9588::  
::1566.1344 1543.9261 1531.9561::  
::1566.1339 1543.9251 1531.9579::  
::1566.1359 1543.9249 1531.9598::  
::1566.1347 1543.9252 1531.9583::  
::1566.1342 1543.9276 1531.9564::  
::1566.1347 1543.926 1531.9564::  
::1566.1355 1543.9267 1531.9583::  
::1566.1345 1543.9264 1531.9581::  
::1566.1350 1543.9269 1531.9580::  
::1566.1346 1543.927 1531.9589::  
::1566.1356 1543.9268 1531.9594::  
::1566.1348 1543.9279 1531.9577::  
:TS:2  
::1566.1346 1543.9262 1531.9576::  
::1566.1346 1543.9271 1531.9593::  
::1566.1355 1543.9279 1531.9581::  
::1566.1353 1543.9266 1531.9584::  
::1566.1344 1543.9276 1531.9588::  
::1566.1352 1543.9255 1531.9581::  
::1566.1344 1543.9272 1531.9584::  
::1566.1344 1543.9266 1531.9581::  
::1566.1347 1543.9272 1531.9575::  
::1566.1345 1543.9258 1531.9571::  
::1566.1343 1543.9273 1531.9601::  
::1566.1348 1543.9274 1531.9576::  
::1566.1342 1543.9282 1531.9578::



## APPENDIX F

### F.1 Common Applications to Wyoming to Move an Oversize and/or Overweight Load

**APPLICATION TO WYOMING TO MOVE AN OVERSIZE AND/OR OVERWEIGHT LOAD**

This is for **SUPER LOADS ONLY** to be cleared through the Office of Overweight Loads  
 Submitting this application in **NO** way authorizes the move of any vehicle or load. You **MUST** receive an  
 authorization number from the permit issuing authority before moving the load on any Wyoming State highway.

\*\*\* **THIS IS NOT A PERMIT** \*\*\*

**CARRIER INFORMATION:**

USDOT #: \_\_\_\_\_ WY Docket #: \_\_\_\_\_  
 Company Name: \_\_\_\_\_

**CONTACT INFORMATION: (Only individuals that have read the cover sheet may submit this request)**

Name: \_\_\_\_\_ Phone #: \_\_\_\_\_ E-mail: \_\_\_\_\_

TO MOVE: For locations within WY be specific (i.e. MP 109 on WY-59)

Truck Unit #: \_\_\_\_\_ License #: \_\_\_\_\_ State: \_\_\_\_\_ Trailer License #: \_\_\_\_\_ State: \_\_\_\_\_

Description of Load: Cat 992C Loader

From: US 189 @ 9 miles N of I-80 To: WY 150 & CR 166 S of Evanston

Routes: US 189, I-80, Bus 189 (Bear River Dr.), WY 89, WY 150

Date & Time of Movement: 9-16-15

SIZE INFORMATION: Show all Sizes: Feet-Inches (i.e. 12 feet 6 inches is shown as 12-6)

Overall Length: 128 Single Vehicle Length: 112 Rear Overhang: \_\_\_\_\_

Width: 15 Height: 16

Approximate

WEIGHT INFORMATION: Total # of Axles: 12 Gross Weight: 270000

Entered by WYDOT Only. Maximums: 25,000 single, 55,000 tandem, 65,000 triple, 74,000 quad unless noted in COMMENTS

A plus B	B plus C	C plus D	D plus E	E plus F	F plus G	G plus H
H plus I	I plus J	J plus K	K plus L	L plus M	M plus N	

Enter the approx. weight of each axle group. Below each weight, select the number of axles in the group:

A) 20000	B) 55000	C) 65000	D) 65000	E) 65000	F)	G)
O	O O	O O O	O O O	O O O		
H)	I)	J)	K)	L)	M)	N)

Spacing between each axle: feet-inches (i.e. 4 feet 6 inches is shown as 4-6)

1-2	2-3	3-4	4-5	5-6	6-7	7-8	8-9	9-10	10-11	11-12	12-13	13-14	14-15	15-16	16-17
16-6	4-6	16-2	5	5	42-6	5	5	14-2	5	5					
17-18	18-19	19-20	20-21	21-22	22-23	23-24	24-25	25-26	26-27	27-28	28-29	29-30	30-31	31-32	32-33

COMMENTS/REMARKS/ADDED RESTRICTIONS: Indicate all axles that have a width over 10' in this area

AUTHORIZATION: The driver **MUST** have this information.

Entered by WYDOT Only

Authorization is given by: Darrin to proceed to the:  
 with authorization number: \_\_\_\_\_ Valid Through: \_\_\_\_\_

Escort Requirements: P & S: Front Rear Interstate: Front Rear  Height Pole on front escort

No travel during school hours on P & S 0600-0900 hrs & 1430-1630 hrs

Time Sensitive: If the move is delayed anywhere along the route, the carrier must contact 307-777-4376 immediately during office hours.

BROWL# 4409 is assigned for the weights shown above with the following Restrictions on Structures:

5 MPH, no shifting or braking  Center line and no other vehicles  No added Restrictions on structures

Comments from Bridge Dept:

Authorization will be sent to the location above and a reply to the original e-mail. A citation may be issued if incorrect information is provided. Owl office must be notified if the load is canceled.

**APPLICATION TO WYOMING TO MOVE AN OVERSIZE AND/OR OVERWEIGHT LOAD**

This is for **SUPER LOADS ONLY** to be cleared through the Office of Overweight Loads  
 Submitting this application in **NO** way authorizes the move of any vehicle or load. You **MUST** receive an  
 authorization number from the permit issuing authority before moving the load on any Wyoming State highway.

\*\*\* **THIS IS NOT A PERMIT** \*\*\*

**CARRIER INFORMATION:**

USDOT #: \_\_\_\_\_ WY Docket #: \_\_\_\_\_  
 Company Name: \_\_\_\_\_

**CONTACT INFORMATION: (Only individuals that have read the cover sheet may submit this request)**

Name: \_\_\_\_\_ Phone #: \_\_\_\_\_ E-mail: \_\_\_\_\_

TO MOVE: For locations within WY be specific (i.e. MP 109 on WY-59)

Truck Unit #: \_\_\_\_\_ License #: \_\_\_\_\_ State: \_\_\_\_\_ Trailer License #: \_\_\_\_\_ State: \_\_\_\_\_

Description of Load: Lampson Crane

From: Rozet To: Jeffrey City

Routes: Hwy 51 north to Adon Rd onto I-90 at exit 141 to exit 128, Hwy 51, Garner Lake Rd, 59, 387, I-25S, 20/26BP, 254, 20/26BP, 20/26, 258, 220, 287

Date & Time of Movement: 9/23/15

**SIZE INFORMATION: Show all Sizes: Feet-Inches (i.e. 12 feet 6 inches is shown as 12-6)**

Overall Length: 137-7 Single Vehicle Length: 106-4 Rear Overhang: 0

Width: 12-6 Height: 16

**WEIGHT INFORMATION:** Total # of Axles: 13 Approximate Gross Weight: 275,000

Entered by WYDOT Only. Maximums: 25,000 single, 55,000 tandem, 65,000 triple, 74,000 quad unless noted in COMMENTS

A plus B	B plus C	C plus D	D plus E	E plus F	F plus G	G plus H
H plus I	I plus J	J plus K	K plus L	L plus M	M plus N	

Enter the approx. weight of each axle group. Below each weight, select the number of axles in the group:

A}17000	B}65000	C}63000	D}65000	E}65000	F}	G}
O	O O O	O O O	O O O	O O O		
H}	I}	J}	K}	L}	M}	N}

Spacing between each axle: feet-inches (i.e. 4 feet 6 inches is shown as 4-6)

1-2	2-3	3-4	4-5	5-6	6-7	7-8	8-9	9-10	10-11	11-12	12-13	13-14	14-15	15-16	16-17	
16-10	4-7	4-7	14	5	5	39-5	5	5	14-3	5	5	28-29	29-30	30-31	31-32	32-33
17-18	18-19	19-20	20-21	21-22	22-23	23-24	24-25	25-26	26-27	27-28	28-29	29-30	30-31	31-32	32-33	

COMMENTS/REMARKS/ADDED RESTRICTIONS: Indicate all axles that have a width over 10' in this area

**Reference Brawl 4411**

**AUTHORIZATION:** The driver **MUST** have this information.

Entered by WYDOT Only  
 Authorization is given by: \_\_\_\_\_ to proceed to the:  
 with authorization number: \_\_\_\_\_ Valid Through: \_\_\_\_\_

Escort Requirements: P & S: Front Rear Interstate: Front Rear  Height Pole on front escort

No travel during school hours on P & S 0600-0900 hrs & 1430-1630 hrs

Time Sensitive: \_\_\_\_\_ If the move is delayed anywhere along the route, the carrier must contact 307-777-4376 immediately during office hours.

BROWL# 4415 is assigned for the weights shown above with the following Restrictions on Structures:  
 5 MPH, no shifting or braking  Center line and no other vehicles  No added Restrictions on structures  
 Comments from Bridge Dept: **NOT Authorized on STR BGE on WYO 51 at MP 143.6**

Authorization will be sent to the location above and a reply to the original e-mail. A citation may be issued if incorrect information is provided. Owl office must be notified if the load is canceled.

**APPLICATION TO WYOMING TO MOVE AN OVERSIZE AND/OR OVERWEIGHT LOAD**

This is for **SUPER LOADS ONLY** to be cleared through the Office of Overweight Loads  
 Submitting this application in **NO** way authorizes the move of any vehicle or load. You **MUST** receive an  
 authorization number from the permit issuing authority before moving the load on any Wyoming State highway.

\*\*\* **THIS IS NOT A PERMIT** \*\*\*

**CARRIER INFORMATION:**

USDOT #: \_\_\_\_\_ WY Docket #: \_\_\_\_\_  
 Company Name: \_\_\_\_\_

**CONTACT INFORMATION: (Only individuals that have read the cover sheet may submit this request)**

Name: \_\_\_\_\_ Phone #: \_\_\_\_\_ E-mail: \_\_\_\_\_

TO MOVE: For locations within WY be specific (i.e. MP 109 on WY-59)

Truck Unit #: \_\_\_\_\_ License #: \_\_\_\_\_ State: \_\_\_\_\_ Trailer License #: \_\_\_\_\_ State: \_\_\_\_\_

Description of Load: GAS COMPRESSOR

From: GILETTE - 1844 Schoonover To: COLORADO

Routes: WY 59, Garner Lake, WY 51, Gillette POE, WY 51, Garner Lake, WY 59, WY 450, US 16, US 16 Truck  
 Route, US 16, US 85, WY 156, US 85, WY 154, WY 152, US 85, WY 213, I-80 to exit 370, I-80, WY  
 214, CR 203, CR 151.

Date & Time of Movement: 4-29-15

**SIZE INFORMATION: Show all Sizes: Feet-Inches (i.e. 12 feet 6 inches is shown as 12-6)**

Overall Length: 135 Single Vehicle Length: 105 Rear Overhang: 0'-0

Width: 23-6 Height: 18-10

**WEIGHT INFORMATION:** Total # of Axles: 10 Gross Weight: 295,000  
 Approximate

Entered by WYDOT Only. Maximums: 25,000 single, 55,000 tandem, 65,000 triple, 74,000 quad unless noted in COMMENTS

A plus B	B plus C	C plus D	D plus E	E plus F	F plus G	G plus H
H plus I	I plus J	J plus K	K plus L	L plus M	M plus N	

Enter the approx. weight of each axle group. Below each weight, select the number of axles in the group:

A}20000	B}65000	C}67000	D}67000	E}67000	F}	G}
O	O O O	O O	O O	O O		
H}1	I}	J}	K}	L}	M}	N}

Spacing between each axle: feet-inches (i.e. 4 feet 6 inches is shown as 4-6)

1-2	2-3	3-4	4-5	5-6	6-7	7-8	8-9	9-10	10-11	11-12	12-13	13-14	14-15	15-16	16-17
16	5	5	13-1	6	55-0	6	16-9	6							
17-18	18-19	19-20	20-21	21-22	22-23	23-24	24-25	25-26	26-27	27-28	28-29	29-30	30-31	31-32	32-33

COMMENTS/REMARKS/ADDED RESTRICTIONS: Indicate all axles that have a width over 10' in this area

**AXLES 4-10 TRUNION 10' WIDE TRACK; revised axle weights**

AUTHORIZATION: The driver **MUST** have this information.

Entered by WYDOT Only  
 Authorization is given by: Darrin to proceed to the:  
 with authorization number: \_\_\_\_\_ Valid Through: \_\_\_\_\_

Escort Requirements: P & S: Front Rear Interstate: Front Rear  Height Pole on front escort

No travel during school hours on P & S 0600-0900 hrs & 1430-1630 hrs  
 If the move is delayed anywhere along the route, the carrier must  
 Time Sensitive: contact 307-777-4376 immediately during office hours.

BROWL# 4215 is assigned for the weights shown above with the following Restrictions on Structures:  
 5 MPH, no shifting or braking  Center line and no other vehicles  No added Restrictions on structures  
 Comments from Bridge Dept: \_\_\_\_\_

